

AD A063792

AGARD-CP-238-VOL. II

DDC FILE COPY

LEVEL III

AGARD-CP-238-VOL. II

AGARD

ADVISORY GROUP FOR AEROSPACE RESEARCH & DEVELOPMENT

7 RUE ANCELLE 92200 NEUILLY SUR SEINE FRANCE

AGARD CONFERENCE PROCEEDINGS No. 238

Operational Modelling of the Aerospace Propagation Environment

Edited by
H. Soicher

Volume II

This document has been approved
for public release and sale; its
distribution is unlimited.

DDC
REF ID: A63792
JAN 29 1978
LIBRARY

NORTH ATLANTIC TREATY ORGANIZATION



DISTRIBUTION AND AVAILABILITY
ON BACK COVER

79 01 26 085

NORTH ATLANTIC TREATY ORGANIZATION
ADVISORY GROUP FOR AEROSPACE RESEARCH AND DEVELOPMENT
(ORGANISATION DU TRAITE DE L'ATLANTIQUE NORD)

AGARD Conference Proceedings No.238

6. OPERATIONAL MODELLING OF THE
AEROSPACE PROPAGATION ENVIRONMENT, Volume II.
(IN TWO VOLUMES)

Edited by

H. Soicher
DRDCO-COM-RF
US Army CORADCOM
Fort Monmouth, NJ 07703
USA

VOLUME 2

Papers presented at a Meeting of the Electromagnetic Wave Propagation Panel
held in Ottawa, Canada, 24-28 April 1978.

400 0413 79 01 26 035

THE MISSION OF AGARD

The mission of AGARD is to bring together the leading personalities of the NATO nations in the fields of science and technology relating to aerospace for the following purposes:

- Exchanging of scientific and technical information;
- Continuously stimulating advances in the aerospace sciences relevant to strengthening the common defence posture,
- Improving the co-operation among member nations in aerospace research and development;
- Providing scientific and technical advice and assistance to the North Atlantic Military Committee in the field of aerospace research and development;
- Rendering scientific and technical assistance, as requested, to other NATO bodies and to member nations in connection with research and development problems in the aerospace field;
- Providing assistance to member nations for the purpose of increasing their scientific and technical potential;
- Recommending effective ways for the member nations to use their research and development capabilities for the common benefit of the NATO community.

The highest authority within AGARD is the National Delegates Board consisting of officially appointed senior representatives from each member nation. The mission of AGARD is carried out through the Panels which are composed of experts appointed by the National Delegates, the Consultant and Exchange Programme and the Aerospace Applications Studies Programme. The results of AGARD work are reported to the member nations and the NATO Authorities through the AGARD series of publications of which this is one.

Participation in AGARD activities is by invitation only and is normally limited to citizens of the NATO nations.

A large part of the content of this publication has been reproduced directly from material supplied by AGARD or the authors; the remainder has been set by Technical Editing and Reproduction Ltd.

ACCESSION TO

NTIS
FDC
UNCLASSIFIED
JOS 11 12 1978

By
NORTH ATLANTIC TREATY ORGANIZATION
SECRETARY GENERAL

DATE
11/12/78

WPA Section ☒
PAC Section ☐

NOES
SP. CIAL

[Signature]

Published November 1978

Copyright © AGARD 1978
All Rights Reserved

ISBN 92-835-0224-8



Printed by Technical Editing and Reproduction Ltd
Harford House, 7-9 Charlotte St. London, W1P 1HD

CONTENTS

VOLUME 2

SESSION VII – OPTICAL/IR ENVIRONMENT

Reference

CHAIRMAN'S SUMMARY	VII
ATMOSPHERIC OPTICAL TRANSMISSION MODELLING AND PREDICTION SCHEMES by R.A.McClatchey and E.P.Shettle	33
MODELLING THE TRANSFER OF RADIATION IN THE ATMOSPHERE by H.J.Jung, M.Kerschgens and E.Raschke	34
CALCULATION OF EXTINCTION AND SCATTERING IN THE WAVELENGTH RANGE FROM 0.25–15 μ m BY HYDROMETEORS AND FOR GENERAL GERMAN WEATHER SITUATIONS by W.Eckl, H.J.Fluss and H.Hallwachs	35
A BAROCLINIC MODEL FOR THE PREDICTION OF THE VERTICAL TEMPERATURE AND MOISTURE STRATIFICATION IN THE BAROCLINIC BOUNDARY LAYER by W.Behnke	36

SESSION VIII – OPTICAL SYSTEMS/PROJECTS

CHAIRMAN'S SUMMARY	VIII
A REVIEW OF THE NAVAL RESEARCH LABORATORY PROGRAM IN ATMOSPHERIC MEASUREMENTS AND APPLICATION TO MODELING by J.A.Dowling, J.A.Curcio, S.T.Hanley, R.F.Horton, K.M.Haught, D.H.Garcia, A.Guttman, C.O.Gott, W.L.Agambar, G.L.Trusty and T.H.Cosden	37
A MODELING PROGRAM FOR THE PREDICTION OF ATMOSPHERIC EFFECTS ON E-O SENSOR PERFORMANCE by R.B.Gomez	38
INTERPRETATION OF AIRBORNE MEASUREMENTS OF ATMOSPHERIC EXTINCTION AND IRRADIATING FLUXES IN GERMANY AND THE NETHERLANDS by H.von Redwitz, G.H.Ruppersberg, K.Schellhase and J.Weidner	39
THE INFLUENCE OF METEOROLOGICAL PARAMETERS ON ATMOSPHERIC TRANSMISSION AT 10.6 μ m (CO ₂ LASER RADIATION) AND 0.63 μ m (He-Ne-LASER RADIATION) FROM MEASUREMENTS AND CALCULATIONS by J.Abele, H.Raidt, W.Jessen, R.Kirschmer	40
ELECTRO OPTICS SYSTEMS PERFORMANCE ANALYSIS IN SELECTED MARINE ENVIRONMENTS by B.S.Katz and K.C.Hepfer	41

SESSION IX – TROPOSPHERIC TURBULENCE

SESSION SUMMARY	IX
OPTICAL PHASE AND SCINTILLATION AT AMOS: COMPARISON BETWEEN OBSERVATION AND PREDICTION by H.T.Yura	42
REAL TIME SIMULATION OF TURBULENT ATMOSPHERIC PROPAGATION by J.D.Lyon	43
TEMPERATURE TURBULENCE MEASUREMENTS AT AMOS by D.W.Hanson	44

SESSION X – EHF PROPAGATION

CHAIRMAN'S SUMMARY	X
--------------------	---

	Reference
ATMOSPHERIC MEDIUM CHARACTERIZATION AND MODELLING OF LHF PROPAGATION IN AIR by H.J.Liebe and J.D.Hopponen	45
A COMPUTER MODEL DESCRIBING ATMOSPHERIC PROPAGATION OF MICROWAVES FROM 1 to 300 GHz INCLUDING DETAILED ATMOSPHERIC CONDITIONS AND COMPARISON WITH EXPERIMENTAL DATA by H.J.Fluess	46
CARACTERISATION DE LA DISTORSION DU CANAL TROPOSPHERIQUE par A.Marguinaud	47
AEROSPACE PROPAGATION PREDICTION CAPABILITIES ASSOCIATED WITH THE IF-77 MODEL by M.E.Johnson and G.D.Gierhart	48
THE CRC VHF-UHF PROPAGATION PREDICTION PROGRAM: DESCRIPTION AND COMPARISON WITH FIELD-MEASUREMENTS by F.H.Palmer	49
A STOCHASTIC DYNAMIC MODEL OF RAIN ATTENUATION by T.Maseng and P.M.Bakken	50
Appendix A GENERAL DISCUSSION PROCEEDINGS	A
Appendix B LIST OF PARTICIPANTS	B

SUMMARY OF SESSION VII

OPTICAL/IR ENVIRONMENT

by

Dr H.J. Albrecht
Session Chairman

The programme of the session resulted in a reasonable coverage of the subject concerned, namely the operational modelling in the optical and infrared environment. Following an excellent review paper on the entire field (R.A. McClatchey, E.P. Shettle, atmospheric optical transmission modelling and prediction schemes), three contributions dealt with models regarding the transfer of radiation in the atmosphere (H.J. Jung, M. Kerschgens, E. Raschke), the extinction and scattering by hydrometeors in the range between 0.25 and 15 μm considering general weather situations (W. Eckl, H.J. Flüss, H. Hallwachs), and the prediction of vertical temperature and moisture stratification in the baroclinic boundary layer (W. Behnke).

The above-mentioned review paper covered the present state of the art; it was mainly based on computer programmes for transmission characteristics in the spectral range between 0.25 μm and 1.4 μm , designated HITRAN with appropriately high resolutions as, for instance, required for the description of LASER transmission spectra, and LOWTRAN with less resolution and more reasonable computer time-requirements. A comprehensive data base is being used together with the HITRAN programme, as far as the optical properties of atmospheric molecules are concerned. Assumptions are made with regard to the absorption line shapes as a function of atmospheric pressure. Between 8 and 14 μm as well as 3.5 and 4.2 μm water vapour continua are evident, a quasi-continuous absorption feature around 4.3 μm due to nitrogen molecules has also been taken into account. Absorption and scattering of aerosols have been treated as a slowly varying continuum function which is added to the more rapidly varying molecular absorption. Complex refractive index, size distribution, and origin of aerosols are examples of parameters used. In summary, problem areas and the present state of the art have been reported in this review.

The second paper in this session discussed the use of atmospheric radiative transfer models to describe effects in optical, infrared and microwave spectral ranges; special applications were illustrated, such as estimates of cloud effects as a function of altitude, optical thickness and droplet size distribution, and of a relationship in the microwave region between brightness temperature at the top of the atmosphere and cloud thickness expressed in terms of precipitation rate. The possibility of estimating precipitation intensities from brightness temperature was mentioned, with particular reference to rainfall above ocean surfaces.

The contribution on calculation of extinction and scattering between 0.25 and 15 μm by hydrometeors concerned relevant meteorological conditions during general weather situations typical for the central NATO-region, or, in other words, the geographic area of the Federal Republic of Germany. For this purpose, a modified version of the LOWTRAN model was utilized to consider scattering and extinction by precipitation and clouds. Meteorological input data typical of the most common weather situations included profiles of barometric pressure, temperature, humidity, and data on precipitation and clouds. Although the accuracy of data assessment has to be considered variable and may be marginal for some parameters, the experiment as such is interesting; it represents a first attempt of system-oriented predictions on the basis of recognized general conditions and their trend.

The final paper in this session referred to vertical temperature and moisture stratification in the baroclinic boundary layer up to an altitude of one to two kilometres. The model aims at a determination of heights of inversion layers as a function of ground roughness and baroclinic conditions. Effects on the stratification of the refractive index were mentioned.

Discussions related to this session generally supplemented the information contained in papers presented. In some cases, questions addressed new fields of research in electromagnetic wave propagation and in the appropriate behaviour of propagation media. This summary refers to the more significant discussion areas.

An example of research-related discussion topics is the artificial modification of propagation media. Full applicability is indicated for most models, results being generally as useful as the input data are reliable. Specific comments again emphasized the discrepancy in the present state of the art as far as the rather advanced identification of molecular characteristics is concerned, in comparison to that of aerosol effects.

The evaluation of humidity effects on rural aerosol models was mentioned as a possibility of using such dependence as a method of estimating humidity.

Several comments referred to limitations governing determination as well as consideration of precipitation characteristics, in addition to adjacent problems, such as their vertical distribution as an example of applicability in satellite communication links on microwave frequencies. Reference was made to the use of microwave images to investigate the extent of precipitation cells.

The presentation of a new model using general weather situations typical of geographically limited regions led to the discussion of relevant aspects. Criteria of mesh density and validity of data for portions of such a region were discussed with respect to the field of application in modelling propagation characteristics. Although such questions did not only refer to the area covered by this session on optical and infrared environment, they were here touched upon as a means of evaluating the feasibility of such a new approach.

Differing levels of validity were identified for different parameters with precipitation rate and dropsize distribution as examples of low reliability due to the existing difficulties in appropriately assessing data. Keeping in mind such limitations, the approach seems to lead to more useful predictions of propagation characteristics; further investigations are necessary.

In conclusion, papers presented and discussions of relevant aspects during this session on optical and infrared environment have led to a review of the state of the art in relevant operational modelling, to reports on current activities, as well as to an identification of areas in which further research appears to be particularly promising.

ATMOSPHERIC OPTICAL TRANSMISSION MODELLING AND PREDICTION SCHEMES

R.A. McClatchey, (OPI)
E.P. Shettle, (OPA)
Air Force Geophysics Laboratory
Hanscom AFB, Massachusetts 01731

SUMMARY

The optical modelling of the atmosphere requires a detailed knowledge of the physical and optical properties of the atmosphere including temperature, pressure and the distribution of molecular and aerosol constituents responsible for atmospheric extinction. Our knowledge of the optical properties of atmospheric molecules is embodied in the AFGL Atmospheric Absorption Line Parameters Compilation, so this data base together with the HITRAN code provides the basis for high spectral resolution atmospheric optical modelling. The properties of aerosols can not be handled in quite so straightforward a manner. The major difficulty in dealing with the atmospheric aerosols is the large natural variability of their properties. Our work in modelling these properties will be described. The LOWTRAN code provides a moderately low spectral resolution atmospheric propagation model of both the atmospheric molecules and aerosols without the extensive computer time requirements of HITRAN. Recent work in developing an atmospheric radiance version of LOWTRAN, and LASER which is a version of HITRAN including continuum absorption and aerosol extinction will also be discussed.

1. INTRODUCTION

The ultimate objective of atmospheric transmission modelling is to be able to predict the opacity of the atmosphere along any geometric path under any atmospheric condition at any wavelength given a set of measured or predicted meteorological parameters. We would like to carry out such predictions at extremely high spectral resolution pertinent to the transmission of laser radiation or at low spectral resolution consistent with broad-band systems. For the purpose of this presentation, the spectral range will be limited to the region from 0.25 μm to the submillimeter region (about 22 GHz).

Our ability to attain this ultimate objective has been substantially advanced in the past several years, but there are still a number of outstanding issues which require further effort. To the extent possible, we have attempted to embody these advances in the two atmospheric transmission prediction codes: HITRAN and LOWTRAN. We will describe the state-of-the-art of each of these prediction codes and also indicate those areas where further work is necessary.

Equation 1 indicates the need to determine four extinction coefficients as a function of wavelength (or frequency) across this broad spectral region: σ_m and σ_a are the scattering coefficients due to atmospheric molecules and aerosols respectively and k_m and k_a are absorption coefficients due to molecules and aerosols. The total extinction coefficient is then given in Equation 2 and the transmission, τ , is given by application of Equation 3 where L represents the atmospheric path.

$$\sigma(\lambda) = \sigma_m(\lambda) + \sigma_a(\lambda); k(\lambda) = k_m(\lambda) + k_a(\lambda) \quad (1)$$

$$\gamma(\lambda) = \sigma(\lambda) + k(\lambda) \quad (2)$$

$$\tau(\lambda) = e^{-\int \gamma(\lambda) dL} \quad (3)$$

Except for k_m , these extinction coefficients are slowly varying functions of wavelength. The molecular absorption coefficient, however, in the vicinity of discrete absorption lines and bands is a very rapidly varying function of wavelength. This distinction requires us to treat molecular absorption in a considerably different way than we treat the remaining three extinction processes. Furthermore, even the molecular absorption is composed of a rapidly varying component and a more slowly varying component generally characterized as "continuum" absorption. We will treat this separately in the discussion to follow.

The complexity of atmospheric absorption is indicated in Figure 1 in which a series of solar spectra in the infrared are shown from various altitudes. The detailed fine structure is all due to molecular absorption, and the slowly varying extinction mentioned above has been normalized out in these spectra. For comparison, Figure 2 provides a synthetic spectrum generated with the AFGL HITRAN code in the region around 10.5 μm and includes the total effect of molecular absorption including a model of the molecular absorption continuum based on laboratory measurements. The variation with wavelength of the remaining three extinction coefficients is indicated in Figure 3 for two of our model atmospheres and two visibility conditions.

The prediction of atmospheric transmission requires us to model the meteorological properties of the atmosphere and the optical properties of the pertinent atmospheric constituents. We will now describe the status of these modelling efforts.

2. ATMOSPHERIC MODELS

The atmospheric path, over which the atmospheric transmission is to be computed, must be completely described in terms of the parameters responsible for both molecular and aerosol extinction. As will become more clear later, the description of the atmosphere in terms of its temperature, pressure and the concentrations of molecular species along the path will completely describe the meteorological properties of the atmosphere for purposes of molecular scattering and absorption. For practical purposes, several of the molecular constituents of the atmosphere can be assumed uniformly mixed. Table 1 identifies these species and lists concentration values. Two outstanding exceptions are ozone and water vapor and Figure 4 indicates some typical variations with altitude. Fortunately, the required quantities for the computation of atmospheric molecular absorption are regularly measured at most meteorological stations around the world. In the case of aerosols, however, this is not so. The only quantity measured routinely at some stations is visibility and there is great non-uniformity in the methods of measurement. Furthermore, the relationship between a measured visibility at visible wavelengths and the required aerosol quantities (concentration, size distribution and refractive index) is not straightforward and is certainly not unique. Therefore, we must depend on our general understanding of aerosol distributions and properties to develop models for general use. We must then develop the relationships between these models and standard meteorological information so that the models can be optimally applied to real atmospheric situations or to atmospheric statistics.

Figure 5 provides a set of models for the vertical distribution of the number of aerosol particles. This set of curves is based on an extensive set of extinction coefficient measurements made by a large number of investigators. Further information on these aerosol models may be found in the AGARD report by Shettle and Fenn¹. Figure 6 compares the boundary layer models with measurements and indicates the variability of the concentration of aerosols in the lowest layers of the atmosphere since the extinction coefficient variation (the abscissa) is primarily due to variations in particle number density.

3. OPTICAL DATA (MOLECULAR)

The AFGL Atmospheric Absorption Line Parameters Compilation² is the data base available for computing the contributions from discrete molecular absorption lines to the atmospheric extinction. It forms the basis of the various HITRAN transmission codes. The molecules for which the line parameters are contained in this compilation are indicated in Table 2 together with a figure indicating the number of molecular absorption lines of each molecular species for which parameters are included. The parameters which make up this data compilation include (for each absorption line) the line position (frequency), intensity, half-width, energy of the lower state, quantum numbers, isotopic identification and molecular identification. Efforts have continued to update this compilation^{3,4} as new experimental results become available. The basis for inclusion in this data compilation is the line intensity criterion indicated in Figure 7. All lines of sufficient strength to produce an optical depth exceeding 0.1 over the indicated atmospheric path are included in the compilation.

The utilization of the Line Parameters Compilation requires a knowledge of molecular absorption line shapes. Our HITRAN model currently assumes a Lorentz line shape in the lower atmosphere for all pressures less than 10 mb, a Voigt shape in the region from 10 mb to 0.1 mb and a pure Doppler line shape at lower atmospheric pressures. Although the applicability of the Lorentz line shape remains in some doubt for distant line wings, it has generally been found to represent experimental data adequately within a few wavenumbers of the centers of absorption lines. The Lorentz line shape is indicated in Figure 8 and the mathematical form is given in Equation 4. Equation 5 represents the temperature dependence of the line intensity.

$$k = \frac{S \alpha}{\pi [(v - \nu_0)^2 + \alpha^2]} \quad S = \int k dv \quad (4)$$

$$\text{where } \alpha_L = \alpha_0 \sqrt{\frac{T_0}{T}}$$

$$S(T) = S(T_0) \left(\frac{T_0}{T} \right)^n \exp \left[- \frac{hc}{k} E'' \left(\frac{T_0 - T}{T_0 T} \right) \right] \quad (5)$$

Apart from constants, an examination of Equations 4 and 5 show that the absorption coefficient as a function of frequency is determined if the line position (frequency), intensity, half-width at standard conditions of temperature and pressure, and the energy of the lower state (E'') are defined for each line. These are the four fundamental parameters used in the HITRAN calculations for each absorption line.

The application of the molecular data compilation to the generation of a monochromatic transmission or to a high resolution spectrum then follows the straightforward application of Equations 6-9. Equation 6 computes the monochromatic transmittance due to a single line of a single molecular species. Equation 7 then sums the contributions to the absorption coefficient at the frequency, ν , from all lines associated with a given molecular species as well as all lines associated with different molecular species. Equation 8 indicates the necessity to integrate this result through an atmospheric path containing temperature, pressure, and concentration gradients. Finally Equation 9 indicates that, in general, it is necessary to convolve the resulting monochromatic transmittance results with some kind of finite instrument spectral response function if one is to generate a spectrum for comparison with measurements.

$$\tau(\nu) = \exp - [k(\nu)m] \quad (6)$$

$$\tau(\nu) = \exp - \left[\sum_j \sum_i k_{ji}(\nu) m_j \right] \quad (7)$$

$$\tau(\nu) = \exp - \sum_j \left[\int \left(\sum_i k_{ji}(\nu) dm_j \right) \right] \quad (8)$$

$$\bar{\tau}(\nu) = \frac{\int \tau(\nu) g(\nu - \nu_0) d\nu}{\int g(\nu - \nu_0) d\nu} \quad (9)$$

Applications of this calculation scheme repeatedly at small frequency increments will generate a high resolution absorption spectrum. An example of such a calculation is shown in Figure 9 compared with a laboratory measurement in the wing of the 15 μm CO_2 band. A second example is shown in Figure 10 where a computed spectrum is compared with a segment of one of the spectra shown in Figure 1.

As noted above, in addition to molecular absorption by discrete absorption lines, there exists a slowly varying component of the absorption coefficient which is observed experimentally in the laboratory under certain conditions when absorption by some atmospheric gases is studied. This same kind of absorption has also been observed in the atmosphere, particularly in "window" regions where absorption by discrete lines is small.

It is difficult to separate this "continuum" absorption from absorption in the distant wings of strong discrete absorption lines. Indeed, for our purposes, it really doesn't matter as long as we understand the dependence of this continuum absorption on the physical parameters describing the atmospheric path. In regions of more substantial line absorption, the problem reduces to that of deciding how far into the wings of each line to assume individual line contributions and how much of the experimentally observed absorption to model as a "continuum", even when we are quite certain that most of this contribution results from line wings. Two significant absorption features, treated as continuum absorption and of particular significance in atmospheric window regions will now be described.

Water Vapor Continuum

The absorption coefficient per precipitable centimeter of water vapor is given in Equation 10 where $C_s(\nu, T)$ is a self-broadening coefficient due to collisions of water molecules with other water molecules, $C_N(\nu, T)$ is a nitrogen broadening coefficient due to collisions of water molecules with air (primarily nitrogen) molecules, P_w is the partial pressure (in atmospheres) of water vapor and P_a is the partial pressure of the remainder of the atmosphere (primarily nitrogen). It is necessary to establish the C_s and the C_N quantities and their frequency and temperature dependence in both the 8-14 and 3-5 micrometer regions. As of this writing, existing laboratory measurements have been analyzed thoroughly and the resulting coefficients and temperature dependences are described here. The laboratory evidence for the 8-14 μm continuum absorption is given in Figure 11 (Taken from Burch⁵).

- i) The 8-14 micrometer continuum^{5,6,7}

$$C_s(\nu, T) = C_s(\nu, 296) \exp - 1800 \left(\frac{1}{T} - \frac{1}{296} \right) \quad (11)$$

where $C_s(\nu, 296) = 4.18 + 5578 \exp (-7.87 \times 10^{-3} \nu)$ (pr. cm)⁻¹ atm⁻¹

and $C_N(\nu, T) = 0.002 \times C_s(\nu, 296)$ (pr. cm)⁻¹ atm⁻¹

- ii) The 3.5-4.2 micrometer continuum⁸

$$C_s(\nu, T) = C_s(\nu, 296) \exp - 1350 \left(\frac{1}{T} - \frac{1}{296} \right) \text{ (pr. cm)}^{-1} \text{ atm}^{-1} \quad (12)$$

$$C_N(\nu, T) = 0.12 \times C_s(\nu, T)$$

where the $C_s(\nu, 296)$ values are given in Table 3.

Using these continuum functions and a series of atmospheric models⁹, Figure 12 has been constructed to show the relative effects of the water vapor continuum at 4 and 10 μm .

Nitrogen Continuum

In addition to the more or less continuous absorption due to water vapor described above, there is another quasi-continuous absorption feature due to molecular absorption by the nitrogen molecule centered near $4.3 \mu\text{m}$ (2350 cm^{-1}). In the spectral region from 2400 cm^{-1} to about 2800 cm^{-1} this absorption feature is of particular importance to laser transmission as it tends to provide a background transmission level for paths in the lower atmosphere regardless of the presence or absence of absorption lines and regardless of how dry the atmosphere may be. It is of little importance at frequencies smaller than 2400 cm^{-1} due to the overwhelming absorption by atmospheric carbon dioxide. Figure 13 represents the absorption coefficient as a function of frequency for this nitrogen absorption as used in the LOWTRAN and HITRAN models.

4. OPTICAL DATA (AEROSOLS)

In addition to the continuum absorption by atmospheric molecules described above, extinction by aerosols (absorption and scattering) is treated in much the same way in our transmission models. That is, it can be thought of as a slowly varying continuum function which is added to the more complex rapidly varying molecular absorption coefficients. The primary difficulty in the case of aerosol extinction is our lack of a complete description of the physical models for any given atmospheric path.

The fundamental quantities required in the determination of extinction coefficients due to aerosols are the concentration and size distribution of the particles and the complex index of refraction of the aerosol material. Assuming spherical particles, Mie theory can then be applied and extinction coefficients for both scattering and absorption determined. A great deal of work has been carried out to determine the complex index of refraction of atmospheric aerosols^{10,11}. Figure 14 presents the complex refractive index data used in the construction of the Rural and Maritime models.

In addition to the complex refractive index, the size distribution of aerosols plays an important role in determining the extinction as a function of wavelength, particles having a dimension similar to the wavelength having a greater effect on scattering coefficients than other particle sizes. Particle size distribution measurements made by a large number of investigators^{1,12,13} indicate that they can best be represented by some form of bimodal distribution. Examples of the size distributions used in constructing the Rural and Maritime aerosol models are provided in Figure 15.

Aerosols can be continental in origin (dust and organic matter) or maritime in origin (sea-salt component). In urban industrial regions the aerosols can include soot-like particles. At stratospheric altitudes the background aerosols are predominantly about 75% sulfuric acid solution, although significant amounts of volcanic particles may also be present. At higher altitudes (above 30 km), a significant portion of the larger aerosols may be meteoric dust. They can be dry or they can contain substantial quantities of liquid water, especially as relative humidities increase above 70%. A series of models representing a Rural, Urban, Maritime, and Tropospheric environment have been constructed based on a variety of experimental data and these models have been incorporated into our LOWTRAN transmission model.

The application of Mie theory to the complex index of refraction data and particle size distributions produces the normalized extinction coefficient (scattering plus absorption) curves shown in Figure 16. These aerosol models have been included in the current (LOWTRAN 3B)⁶ transmission model. Applying these models to a 10-km horizontal path at sea level for a visual range of 23 km and including all molecular absorption effects generates the transmittance spectra given in Figure 17.

Low values of the visibility (less than 2 km) are usually associated with the transition from haze to fog and the concurrent growth of particles by accretion of liquid water. This occurs more rapidly the higher the relative humidity. These effects are not accounted for by the present aerosol models. Therefore, we are currently extending our aerosol modelling efforts to describe this particle growth with increasing relative humidity. Figure 18 shows the results of applying our knowledge of this particle growth process to the Rural aerosol model. It is apparent that the wavelength dependence becomes much less as the relative humidity is increased. Such humidity effects are being included in our LOWTRAN transmission model.

5. LOW SPECTRAL RESOLUTION PROPAGATION (LOWTRAN)

Although we have already discussed certain elements of the LOWTRAN code, it is easiest to discuss it in the framework of HITRAN, continuum absorption models, and aerosol models. The highest spectral resolution obtainable with the LOWTRAN model is 20 cm^{-1} . Therefore, it smears out (or averages) the results of individual absorption lines. This averaging process is at the root of the construction of the LOWTRAN model. Aside from this averaging associated with molecular line absorption, LOWTRAN simply adds in the extinction due to the more slowly varying functions associated with molecular scattering, aerosol scattering and aerosol absorption. Particular efforts have been made to create an efficient and flexible transmission model and this element of LOWTRAN is one of its primary assets. In the molecular absorption area this has required some approximation and concurrent compromise in accuracy. But this slight compromise in accuracy simply allows the solution of problems which would be impossible with more detailed calculations of molecular absorption. An example of the kind of results obtained with the LOWTRAN computer code is shown in Figure 9 in which the LOWTRAN 3B results have been compared with field measurements. There has been great interest in the effect of the water vapor continuum modifications described above, so Figure 20 has been developed to show the effects of this recent modification. We have recently developed a version of the LOWTRAN model capable of computing atmospheric radiance¹⁴ for any of the same geometries associated with the transmission model. A comparison of the LOWTRAN 3B-Radiance model with atmospheric radiance measurements made at an altitude of 18 km is shown in Figure 21.

6. LASER TRANSMISSION

The addition of continuum extinction functions associated with both molecular scattering and absorption and aerosol scattering and absorption have been made to several of the HITRAN transmission models: An example of a high resolution computed spectrum compared with field measurements is shown in Figure 22 (taken from Reference 15). A special version of such a HITRAN model (to be called LASER) is in publication¹⁶ and will generate extinction coefficient charts such as that shown in Table 4. The four extinction coefficients indicated in Equation 1 can be obtained from such charts for a wide variety of atmospheric models. Extinction coefficients for any atmospheric path can then be obtained by summing appropriate entries.

REFERENCES

1. Shettle, E.P. and Fenn, R.W. (1975) Models of the Atmospheric Aerosols and Their Optical Properties, AGARD Conference Proceedings No. 243, Optical Propagation in the Atmosphere, pp. 2.1-2.16, presented at the Electromagnetic Wave Propagation Panel Symposium, Lingby, Denmark, 27-31 Oct. 1975. (Available from NTIS, Acc. No. N76-29817.) (Note: A more complete version of this report will soon be published as an AFGL Technical Report.)
2. McClatchey, R.A., Benedict, W.S., Clough, S.A., Burch, D.E., Calfee, R.F., Fox, K., Rothman, L.S. and Garing, J.S. (1973) AFCRL Atmospheric Absorption Line Parameters Compilation, AFCRL-TR-73-0096.
3. Rothman, L.S. and McClatchey, R.A. (1976) Updating of the AFCRL Atmospheric Absorption Line Parameters Compilation, Applied Optics, 15, p. 2616.
4. Rothman, L.S. (1977) Atmospheric Optics, OSA Technical Group Meeting, Tucson, 19 October 1976, Applied Optics, 16, No. 2, p. 277, February 1977.
5. Burch, D.E. (1970) Semiannual Technical Report, Investigation of the Absorption of Infrared Radiation by Atmospheric Gases, U-4784, January 1970.
6. Selby, J.E.A., Shettle, E.P. and McClatchey, R.A. (1976) Atmospheric Transmittance from 0.25 to 28.5 μ m: Supplement LOWTRAN 3B (1976), AFGL-TR-76-0258, ERP 587, November 1976.
7. Roberts, R.E., Selby, J.E.A. and Biberman, L.M. (1976) Infrared Continuum Absorption by Atmospheric Water Vapor in the 8-12 μ m Window, Applied Optics 14:2085.
8. Burch, D.E., Gryvnak, D.A., and Pembroke, J.D. (1971) Phico-Ford Corp., Aeronutronic Report U-4887, ASTIA (AD882876).
9. McClatchey, R.A., Fenn, R.W., Selby, J.E.A., Volz, F.E., and Garing, J.S. (1972) Optical Properties of the Atmosphere (Third Edition), AFCRL-72-0497, ERP No. 411, 1972.
10. Volz, F.E. (1972) Infrared Refractive Index of Atmospheric Aerosol Substances, Applied Optics, 11, 755-759.
11. Volz, F.E. (1972) Infrared Optical Constants of Ammonium Sulfate, Sahara Dust, Volcanic Pumice and Flyash, Applied Optics, 12, 564-568.
12. Junge, C.E. (1953) Air Chemistry and Radioactivity, pp. 382, Academic Press, N.Y.
13. Whitby, K.T., Husar, R.B. and Liu, B.Y.H., (1972) The Aerosol Size Distribution of Los Angeles Smog, J. Colloid and Interface Science, 39, 177-204.
14. Selby, J.E.A., Knsizys, F.X., Chetwynd, J.H. Jr., and McClatchey, R.A. (1978) Atmospheric Transmittance/Radiance: Computer Code LOWTRAN 3B-Radiance, To be published as AFGL Technical Report, 1978.
15. Haught, K.M. and Dowling, J.A. (1977) Long-path High-resolution Field Measurements of Absolute Transmission in the 3.5 to 4 μ m Atmospheric Window, Optics Letters, 1, 4, October 1977.
16. McClatchey, R.A. and D'Agati, A.P. Atmospheric Transmission of Laser Radiation: Computer Code LASER (1978). To be published as AFGL Technical Report, 1978.

TABLE 1 - Atmospheric Constituents

<u>MOLECULE</u>	<u>FRACTION BY VOLUME</u>
NITROGEN (N ₂)	0.78
OXYGEN (O ₂)	0.21
ARGON (A)	0.0093
CARBON DIOXIDE (CO ₂)	0.00033
METHANE (CH ₄)	1.6×10^{-6}
NITROUS OXIDE (N ₂ O)	3.5×10^{-7}
CARBON MONOXIDE (CO)	7.5×10^{-8}
OZONE (O ₃)	VARIABLE (10^{-8})
H _e , N _e , K _r	$< 10^{-4}$
WATER VAPOR	VARIABLE ($< .03$)
AEROSOLS	} VARIABLE
DUST	
SALT	
LIQUID WATER	

TABLE 2 - AFGL Line Compilation

<u>MOLECULE</u>	<u>NO. OF ENTRIES</u>
H ₂ O	38,350
CO ₂	57,288
O ₃	19,327
N ₂ O	15,500
CO	383
CH ₄	2,519
O ₂	1,726

PARAMETERS INCLUDED

FREQUENCY	ENERGY OF LOWER STATE
INTENSITY	QUANTUM NUMBERS
HALF-WIDTH	ISOTOPIC I.D.

TABLE 3 - Self-Broadening Absorption Coefficients for Water Vapor Continuum
(3.3 - 4.2 μm)

$\nu(\text{cm}^{-1})$	$C_s(\nu, 296) (\text{PR. CM}^{-1})(\text{ATM.}^{-1})$	ν	$C_s(\nu, 296) (\text{PR. CM}^{-1})(\text{ATM.}^{-1})$
2350	0.230	2700	0.120
2400	0.187	2750	0.147
2450	0.147	2800	0.174
2500	0.117	2850	0.200
2550	0.097	2900	0.240
2600	0.087	2950	0.280
2650	0.100	3000	0.330

TABLE 4 - Extinction Coefficient for Laser Transmission at 10.6 μm

10.531033 MICROMETERS 933.195 WAVELENGTH															
WAVELENGTH = FREQUENCY =		WIDIA- SUMMER		MIDLAT WINTER		SUBARCTIC SUMMER		SUBARCTIC WINTER		CLEAR		HAZY			
U.S. STANDARD		TROPICAL		WIDIA- SUMMER		MIDLAT WINTER		SUBARCTIC SUMMER		SUBARCTIC WINTER		CLEAR		HAZY	
1	1.255-03	0	1.075-01	3.105-01	7.575-02	1.035-01	3.365-02	2.935-03	4.005-03	3.255-02	4.355-02	3.255-02	4.355-02		
2	1.065-01	0	3.15-01	2.465-01	5.725-02	1.505-01	3.325-02	1.935-03	2.545-03	3.255-02	4.355-02	3.255-02	4.355-02		
3	1.065-02	0	2.535-01	1.505-01	5.475-02	1.035-01	3.775-02	2.225-04	4.805-04	4.055-03	7.555-04	4.055-03	7.555-04		
4	1.065-02	0	1.15-01	0.595-01	4.575-02	7.335-02	2.335-02	1.735-03	2.655-03	5.735-04	1.235-04	5.735-04	1.235-04		
5	1.065-02	0	1.15-02	0.545-02	3.755-02	5.805-02	2.355-02	1.035-04	2.005-04	3.745-04	7.035-05	3.745-04	7.035-05		
6	1.065-02	0	5.135-02	5.135-02	3.045-02	4.385-02	2.325-02	8.495-03	1.145-03	1.335-04	2.535-05	1.335-04	2.535-05		
7	1.065-02	0	4.205-02	4.205-02	2.495-02	3.495-02	1.945-02	6.915-03	1.115-03	1.235-04	3.335-05	1.235-04	3.335-05		
8	1.065-02	0	3.535-02	3.535-02	2.035-02	2.715-02	1.445-02	4.435-03	7.315-03	1.035-04	1.335-05	1.035-04	1.335-05		
9	1.065-02	0	3.025-02	2.865-02	1.655-02	2.155-02	1.125-02	2.345-03	5.035-03	5.715-03	1.235-05	5.715-03	1.235-05		
10	1.065-02	0	2.505-02	2.315-02	1.335-02	1.705-02	9.235-03	4.735-03	5.035-03	5.715-03	9.035-03	5.715-03	9.035-03		
11	1.065-02	0	1.335-02	1.145-02	1.065-02	1.325-02	3.375-03	3.355-03	5.035-03	5.715-03	5.335-05	5.715-03	5.335-05		
12	1.065-03	0	1.065-02	1.065-02	9.375-03	1.175-02	5.355-03	3.035-03	5.035-03	5.715-03	5.335-05	5.715-03	5.335-05		
13	1.065-03	0	1.065-02	1.065-02	9.375-03	1.175-02	5.355-03	3.035-03	5.035-03	5.715-03	5.335-05	5.715-03	5.335-05		
14	1.065-03	0	1.065-02	1.065-02	9.375-03	1.175-02	5.355-03	3.035-03	5.035-03	5.715-03	5.335-05	5.715-03	5.335-05		
15	1.065-03	0	1.065-02	1.065-02	9.375-03	1.175-02	5.355-03	3.035-03	5.035-03	5.715-03	5.335-05	5.715-03	5.335-05		
16	1.065-03	0	1.065-02	1.065-02	9.375-03	1.175-02	5.355-03	3.035-03	5.035-03	5.715-03	5.335-05	5.715-03	5.335-05		
17	1.065-03	0	1.065-02	1.065-02	9.375-03	1.175-02	5.355-03	3.035-03	5.035-03	5.715-03	5.335-05	5.715-03	5.335-05		
18	1.065-03	0	1.065-02	1.065-02	9.375-03	1.175-02	5.355-03	3.035-03	5.035-03	5.715-03	5.335-05	5.715-03	5.335-05		
19	1.065-03	0	1.065-02	1.065-02	9.375-03	1.175-02	5.355-03	3.035-03	5.035-03	5.715-03	5.335-05	5.715-03	5.335-05		
20	1.065-03	0	1.065-02	1.065-02	9.375-03	1.175-02	5.355-03	3.035-03	5.035-03	5.715-03	5.335-05	5.715-03	5.335-05		
21	1.065-03	0	1.065-02	1.065-02	9.375-03	1.175-02	5.355-03	3.035-03	5.035-03	5.715-03	5.335-05	5.715-03	5.335-05		
22	1.065-03	0	1.065-02	1.065-02	9.375-03	1.175-02	5.355-03	3.035-03	5.035-03	5.715-03	5.335-05	5.715-03	5.335-05		
23	1.065-03	0	1.065-02	1.065-02	9.375-03	1.175-02	5.355-03	3.035-03	5.035-03	5.715-03	5.335-05	5.715-03	5.335-05		
24	1.065-03	0	1.065-02	1.065-02	9.375-03	1.175-02	5.355-03	3.035-03	5.035-03	5.715-03	5.335-05	5.715-03	5.335-05		
25	1.065-03	0	1.065-02	1.065-02	9.375-03	1.175-02	5.355-03	3.035-03	5.035-03	5.715-03	5.335-05	5.715-03	5.335-05		
26	1.065-03	0	1.065-02	1.065-02	9.375-03	1.175-02	5.355-03	3.035-03	5.035-03	5.715-03	5.335-05	5.715-03	5.335-05		
27	1.065-03	0	1.065-02	1.065-02	9.375-03	1.175-02	5.355-03	3.035-03	5.035-03	5.715-03	5.335-05	5.715-03	5.335-05		
28	1.065-03	0	1.065-02	1.065-02	9.375-03	1.175-02	5.355-03	3.035-03	5.035-03	5.715-03	5.335-05	5.715-03	5.335-05		
29	1.065-03	0	1.065-02	1.065-02	9.375-03	1.175-02	5.355-03	3.035-03	5.035-03	5.715-03	5.335-05	5.715-03	5.335-05		
30	1.065-03	0	1.065-02	1.065-02	9.375-03	1.175-02	5.355-03	3.035-03	5.035-03	5.715-03	5.335-05	5.715-03	5.335-05		
31	1.065-03	0	1.065-02	1.065-02	9.375-03	1.175-02	5.355-03	3.035-03	5.035-03	5.715-03	5.335-05	5.715-03	5.335-05		
32	1.065-03	0	1.065-02	1.065-02	9.375-03	1.175-02	5.355-03	3.035-03	5.035-03	5.715-03	5.335-05	5.715-03	5.335-05		
33	1.065-03	0	1.065-02	1.065-02	9.375-03	1.175-02	5.355-03	3.035-03	5.035-03	5.715-03	5.335-05	5.715-03	5.335-05		
34	1.065-03	0	1.065-02	1.065-02	9.375-03	1.175-02	5.355-03	3.035-03	5.035-03	5.715-03	5.335-05	5.715-03	5.335-05		
35	1.065-03	0	1.065-02	1.065-02	9.375-03	1.175-02	5.355-03	3.035-03	5.035-03	5.715-03	5.335-05	5.715-03	5.335-05		
36	1.065-03	0	1.065-02	1.065-02	9.375-03	1.175-02	5.355-03	3.035-03	5.035-03	5.715-03	5.335-05	5.715-03	5.335-05		
37	1.065-03	0	1.065-02	1.065-02	9.375-03	1.175-02	5.355-03	3.035-03	5.035-03	5.715-03	5.335-05	5.715-03	5.335-05		
38	1.065-03	0	1.065-02	1.065-02	9.375-03	1.175-02	5.355-03	3.035-03	5.035-03	5.715-03	5.335-05	5.715-03	5.335-05		
39	1.065-03	0	1.065-02	1.065-02	9.375-03	1.175-02	5.355-03	3.035-03	5.035-03	5.715-03	5.335-05	5.715-03	5.335-05		
40	1.065-03	0	1.065-02	1.065-02	9.375-03	1.175-02	5.355-03	3.035-03	5.035-03	5.715-03	5.335-05	5.715-03	5.335-05		
41	1.065-03	0	1.065-02	1.065-02	9.375-03	1.175-02	5.355-03	3.035-03	5.035-03	5.715-03	5.335-05	5.715-03	5.335-05		
42	1.065-03	0	1.065-02	1.065-02	9.375-03	1.175-02	5.355-03	3.035-03	5.035-03	5.715-03	5.335-05	5.715-03	5.335-05		
43	1.065-03	0	1.065-02	1.065-02	9.375-03	1.175-02	5.355-03	3.035-03	5.035-03	5.715-03	5.335-05	5.715-03	5.335-05		
44	1.065-03	0	1.065-02	1.065-02	9.375-03	1.175-02	5.355-03	3.035-03	5.035-03	5.715-03	5.335-05	5.715-03	5.335-05		
45	1.065-03	0	1.065-02	1.065-02	9.375-03	1.175-02	5.355-03	3.035-03	5.035-03	5.715-03	5.335-05	5.715-03	5.335-05		
46	1.065-03	0	1.065-02	1.065-02	9.375-03	1.175-02	5.355-03	3.035-03	5.035-03	5.715-03	5.335-05	5.715-03	5.335-05		
47	1.065-03	0	1.065-02	1.065-02	9.375-03	1.175-02	5.355-03	3.035-03	5.035-03	5.715-03	5.335-05	5.715-03	5.335-05		
48	1.065-03	0	1.065-02	1.065-02	9.375-03	1.175-02	5.355-03	3.035-03	5.035-03	5.715-03	5.335-05	5.715-03	5.335-05		
49	1.065-03	0	1.065-02	1.065-02	9.375-03	1.175-02	5.355-03	3.035-03	5.035-03	5.715-03	5.335-05	5.715-03	5.335-05		
50	1.065-03	0	1.065-02	1.065-02	9.375-03	1.175-02	5.355-03	3.035-03	5.035-03	5.715-03	5.335-05	5.715-03	5.335-05		
51	1.065-03	0	1.065-02	1.065-02	9.375-03	1.175-02	5.355-03	3.035-03	5.035-03	5.715-03	5.335-05	5.715-03	5.335-05		
52	1.065-03	0	1.065-02	1.065-02	9.375-03	1.175-02	5.355-03	3.035-03	5.035-03	5.715-03	5.335-05	5.715-03	5.335-05		
53	1.065-03	0	1.065-02	1.065-02	9.375-03	1.175-02	5.355-03	3.035-03	5.035-03	5.715-03	5.335-05	5.715-03	5.335-05		
54	1.065-03	0	1.065-02	1.065-02	9.375-03	1.175-02	5.355-03	3.035-03	5.035-03	5.715-03	5.335-05	5.715-03	5.335-05		
55	1.065-03	0	1.065-02	1.065-02	9.375-03	1.175-02	5.355-03	3.035-03	5.035-03	5.715-03	5.335-05	5.715-03	5.335-05		
56	1.065-03	0	1.065-02	1.065-02	9.375-03	1.175-02	5.355-03	3.035-03	5.035-03	5.715-03	5.335-05	5.715-03	5.335-05		
57	1.065-03	0	1.065-02	1.065-02	9.375-03	1.175-02	5.355-03	3.035-03	5.035-03	5.715-03	5.335-05	5.715-03	5.335-05		
58	1.065-03	0	1.065-02	1.065-02	9.375-03	1.175-02	5.355-03	3.035-03	5.035-03	5.715-03	5.335-05	5.715-03	5.335-05		
59	1.065-03	0	1.065-02	1.065-02	9.375-03	1.175-02	5.355-03	3.035-03	5.035-03	5.715-03	5.335-05	5.715-03	5.335-05		
60	1.065-03	0	1.065-02	1.065-02	9.375-03	1.175-02	5.355-03	3.035-03	5.035-03	5.715-03	5.335-05	5.715-03	5.335-05		

ALTERNATE BOUNDARY LAYER APPROXIMATIONS

...

HAZY

[illegible]

INFRARED ATMOSPHERIC TRANSMISSION

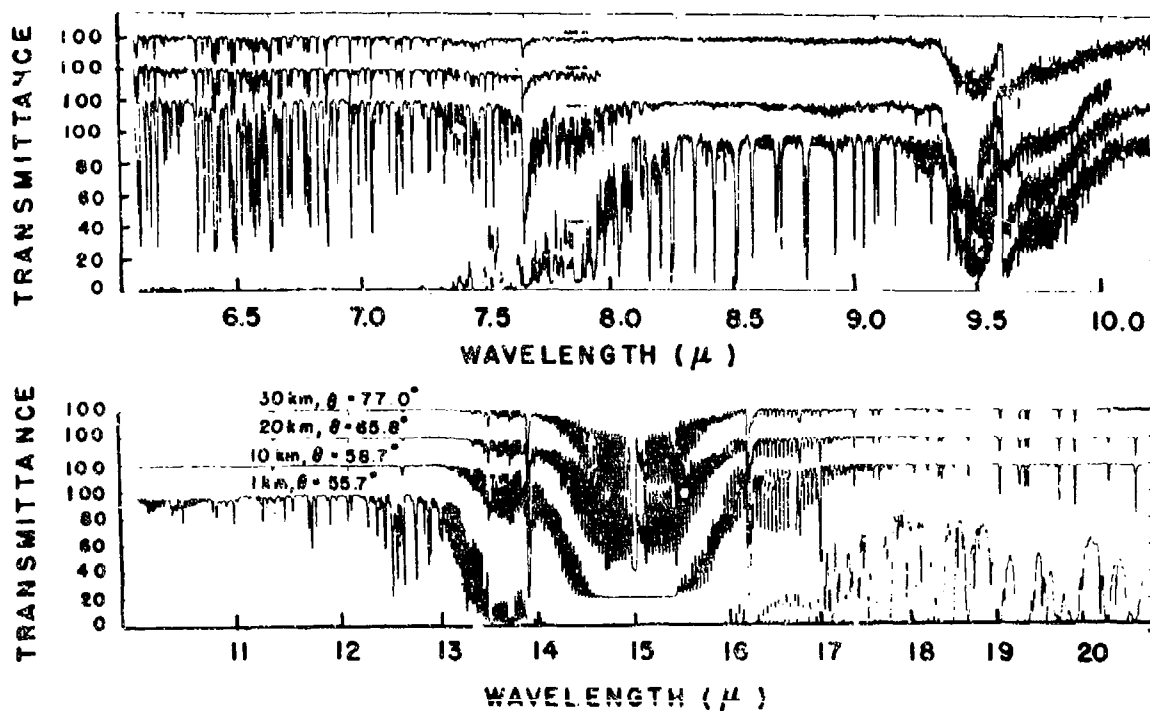


FIGURE 1 - High Resolution Measurements of Solar Spectra

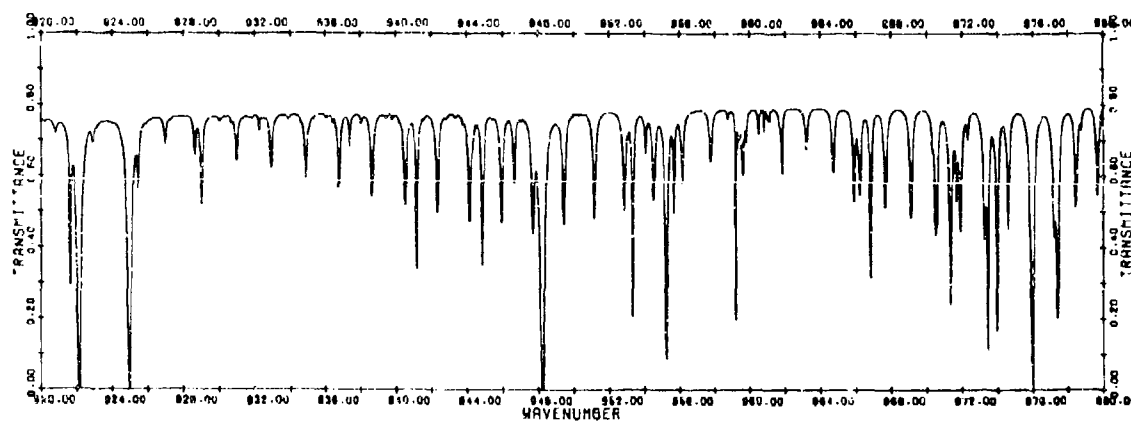


FIGURE 2 - Computed Atmospheric Spectrum for 10-km Sea Level Path

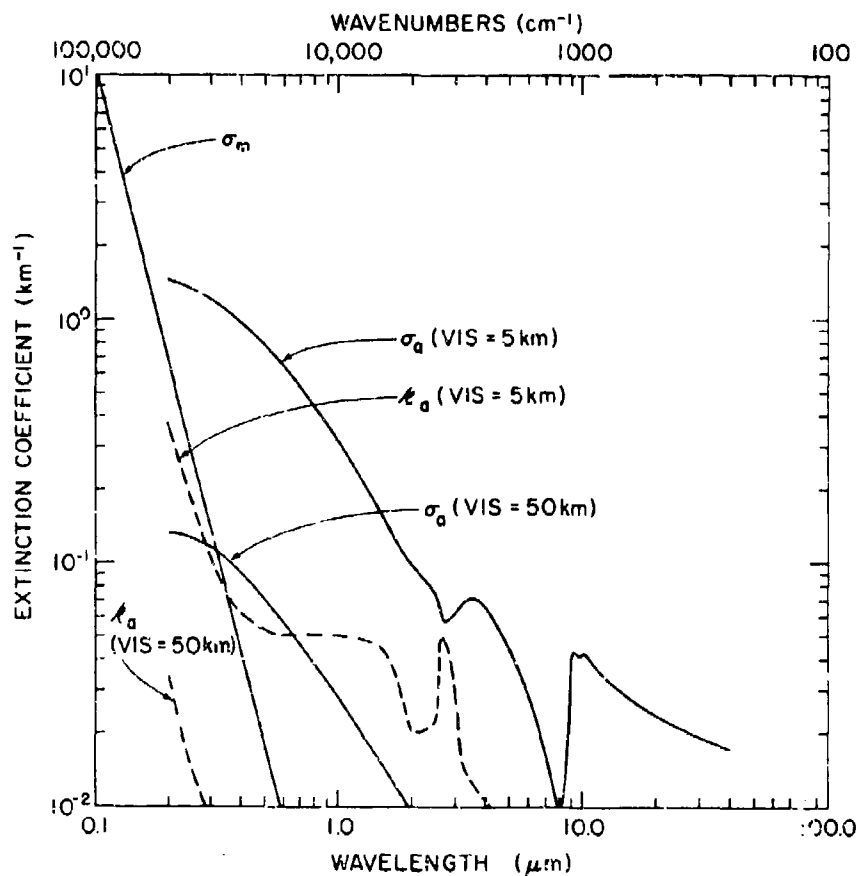


FIGURE 3 - Wavelength Dependence of Molecular Scattering, Aerosol Absorption, and Aerosol Scattering

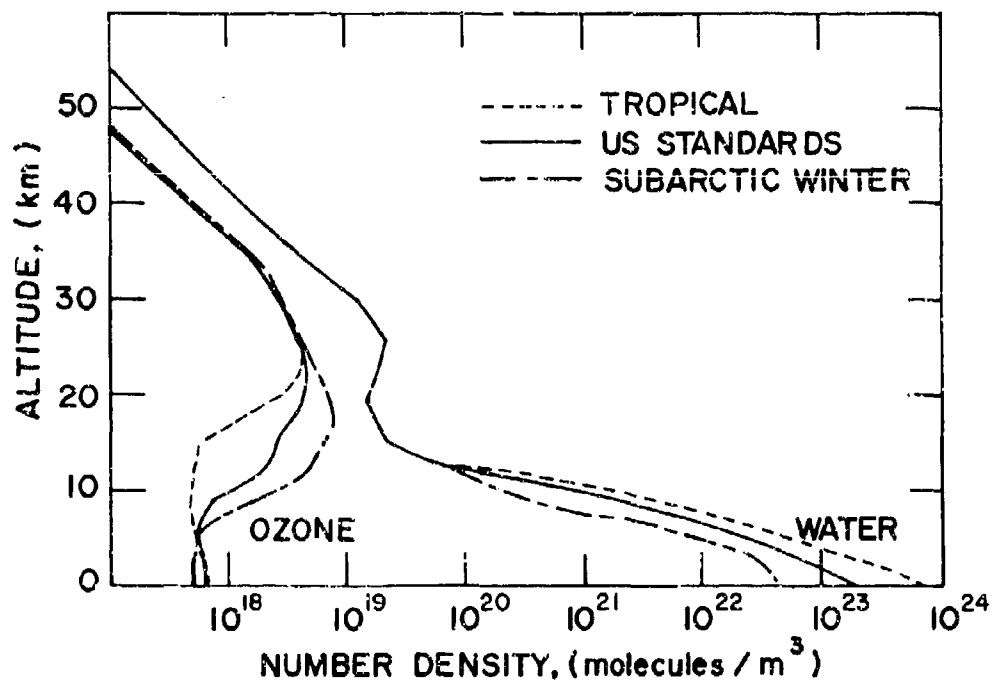


FIGURE 4 - Standard Vertical Distributions of Water Vapor and Ozone

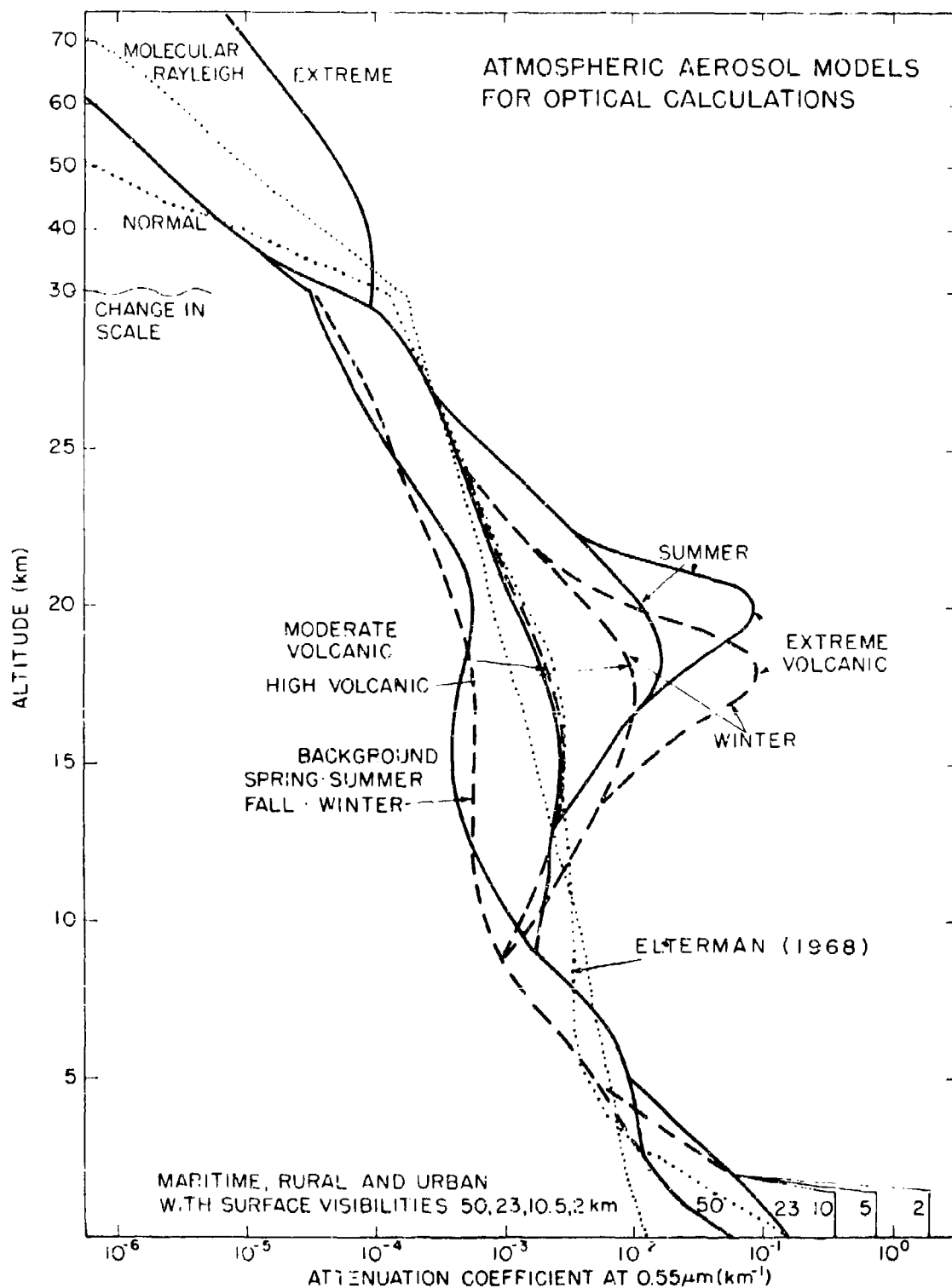
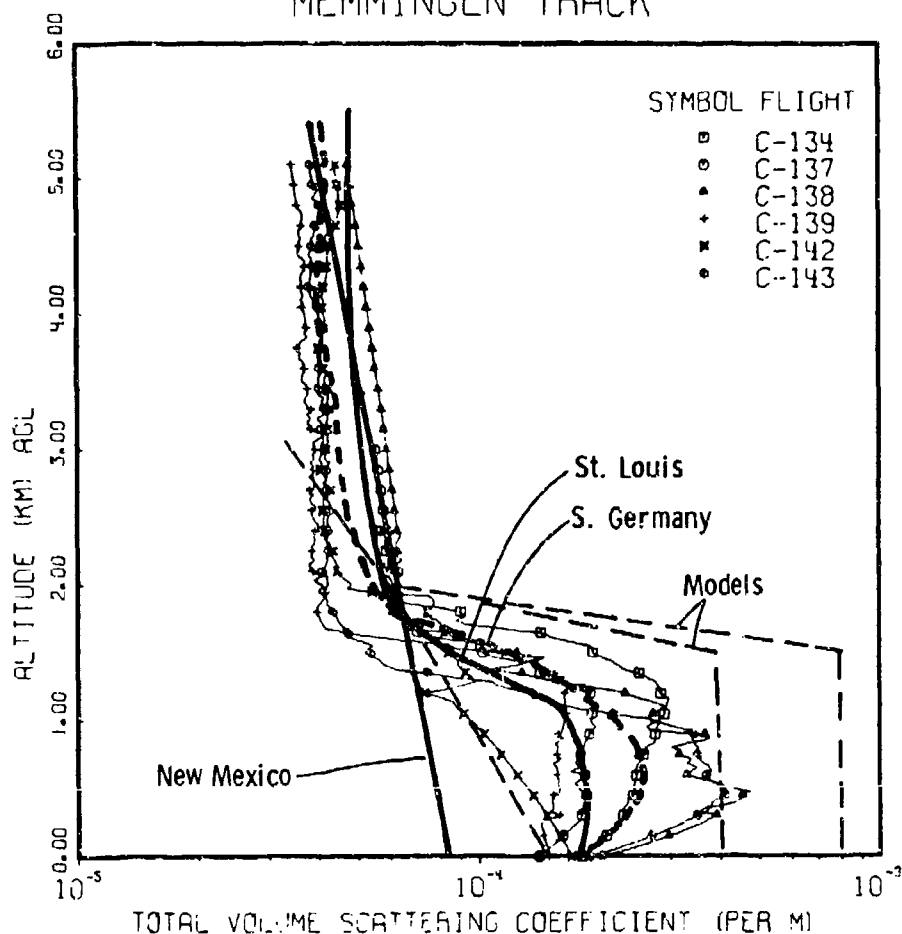


FIGURE 5 - Vertical Structure of Aerosol Models

SCATTERING FOR HAVENVIEW FLIGHTS FILTER 5 PSEUDO-PHOTOPIC MEMMINGEN TRACK



Total Volume Scattering Coefficient for Filter 5 (Pseudo-Photopic)
for the Six HAVEN VIEW Flights.

FIGURE 6 - Comparison of Aerosol Models with Measured Distributions in the Boundary Layer

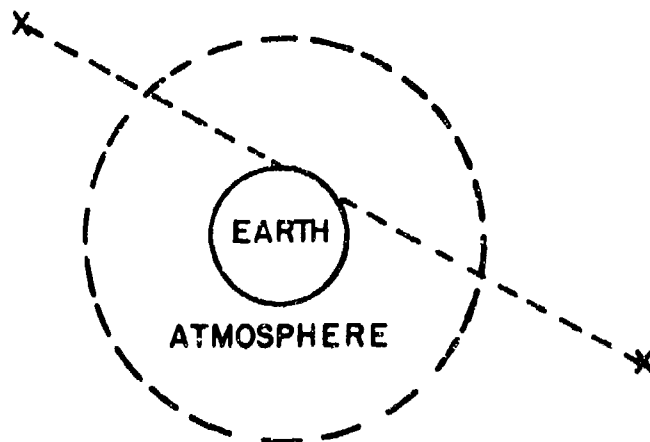


FIGURE 7 - Line Intensity Criterion

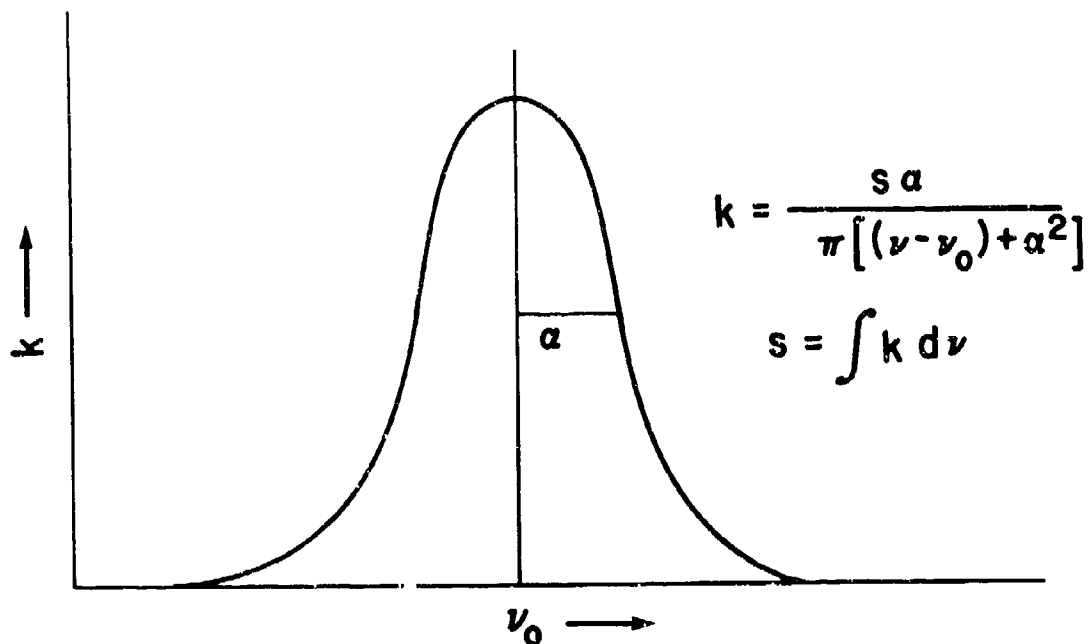


FIGURE 8 - Lorentz Line Shape

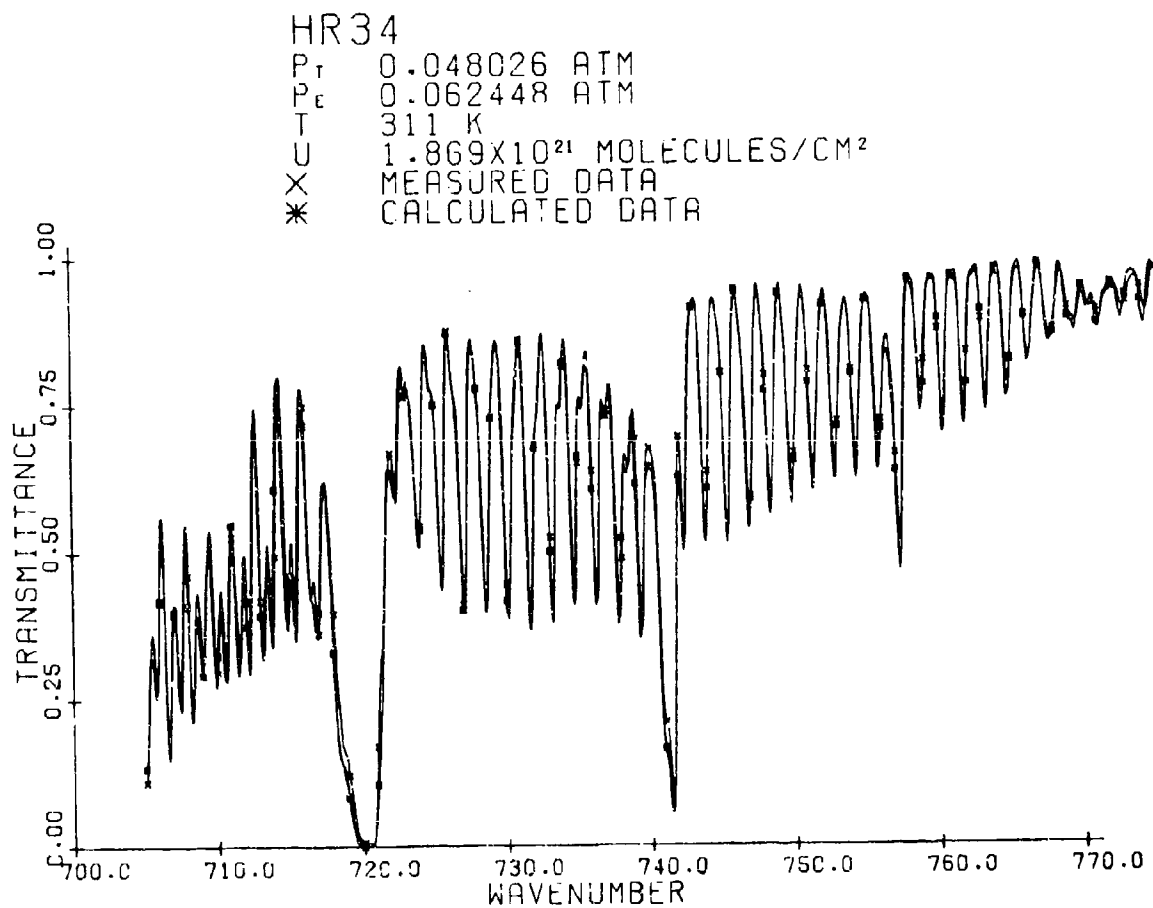


FIGURE 9 - Comparison of Calculated Transmission Spectrum with Laboratory Measurement

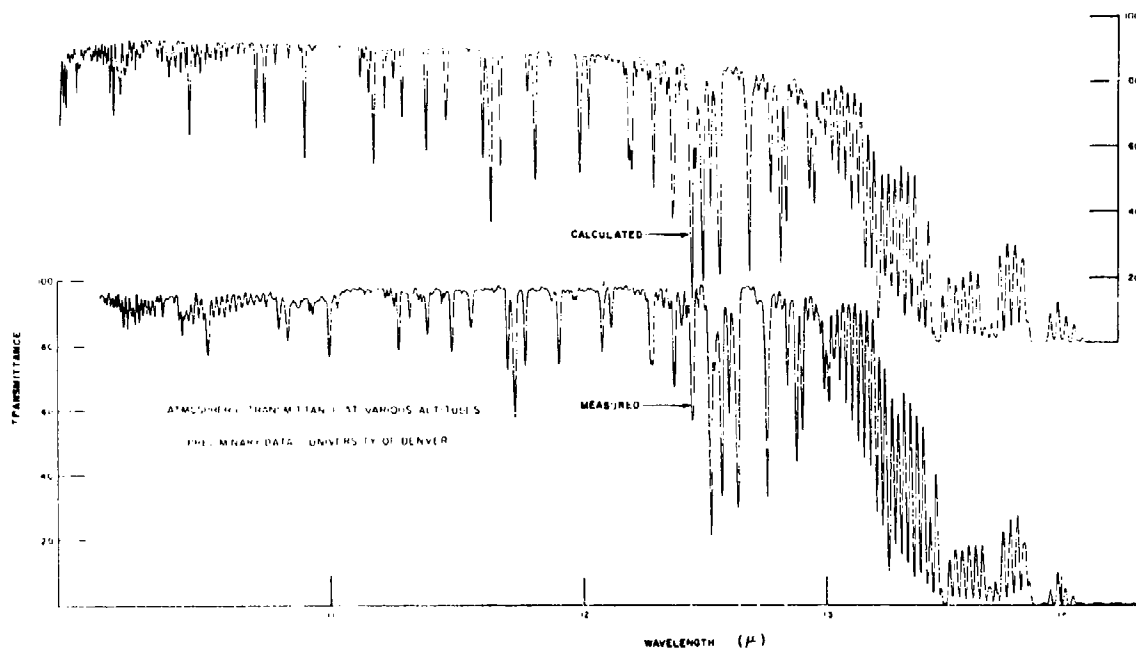


FIGURE 10 - Comparison of Calculated Spectrum with Solar Spectrum in the 10-14 μm Region

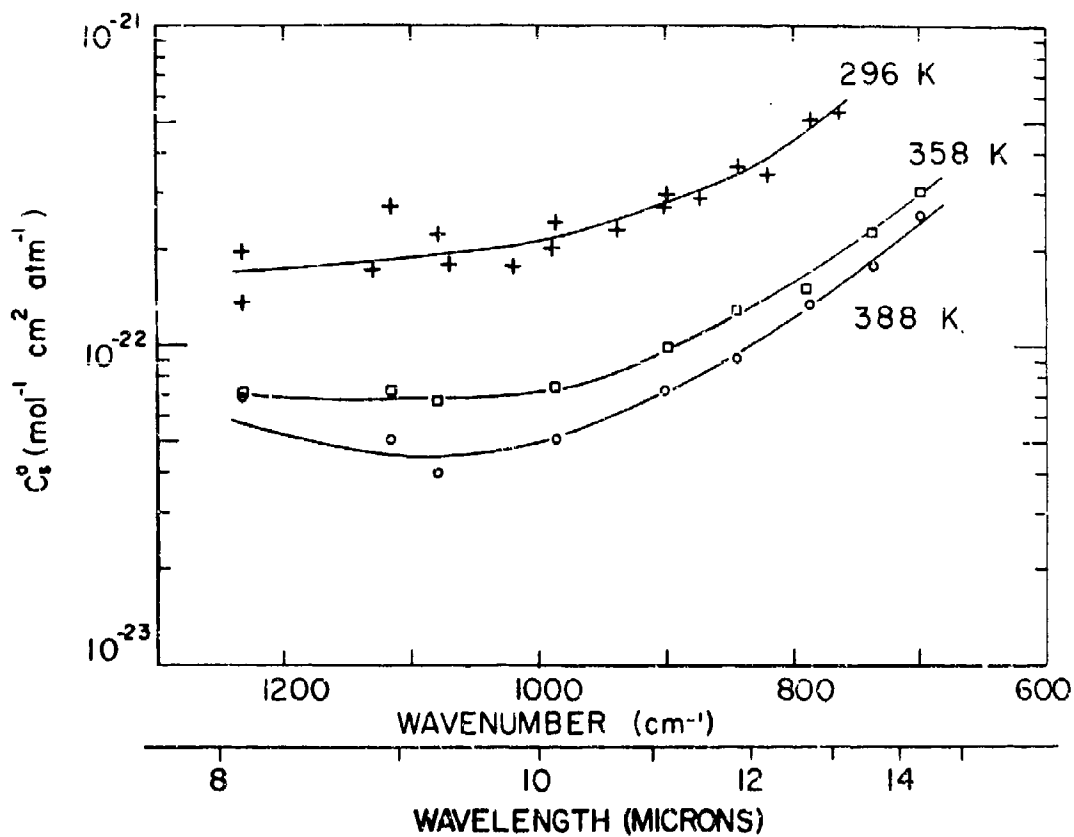


FIGURE 11 - Laboratory Measurements of Self-Broadened Water Vapor Continuum Coefficients

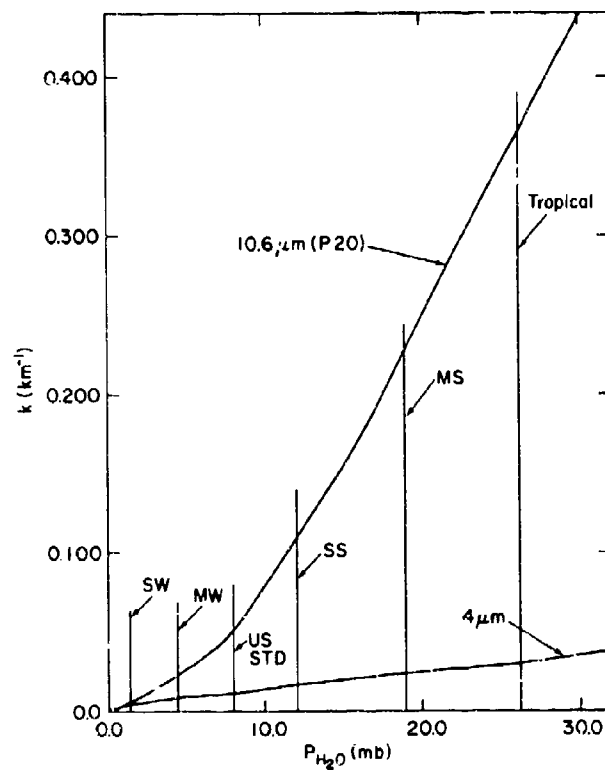


FIGURE 12 - Absorption Coefficients Due to Water Vapor Continuum at $4 \mu\text{m}$ and $10.6 \mu\text{m}$

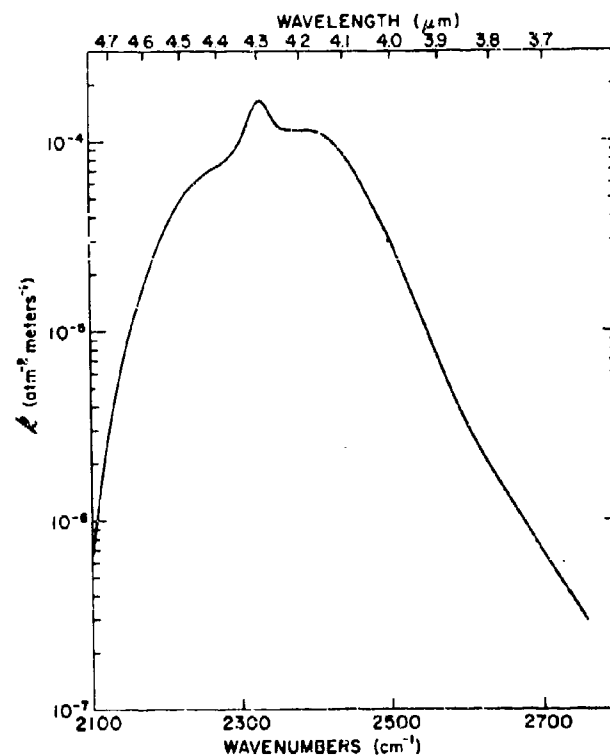


FIGURE 13 - Absorption Coefficient Due to Pressure - Induced Nitrogen Band

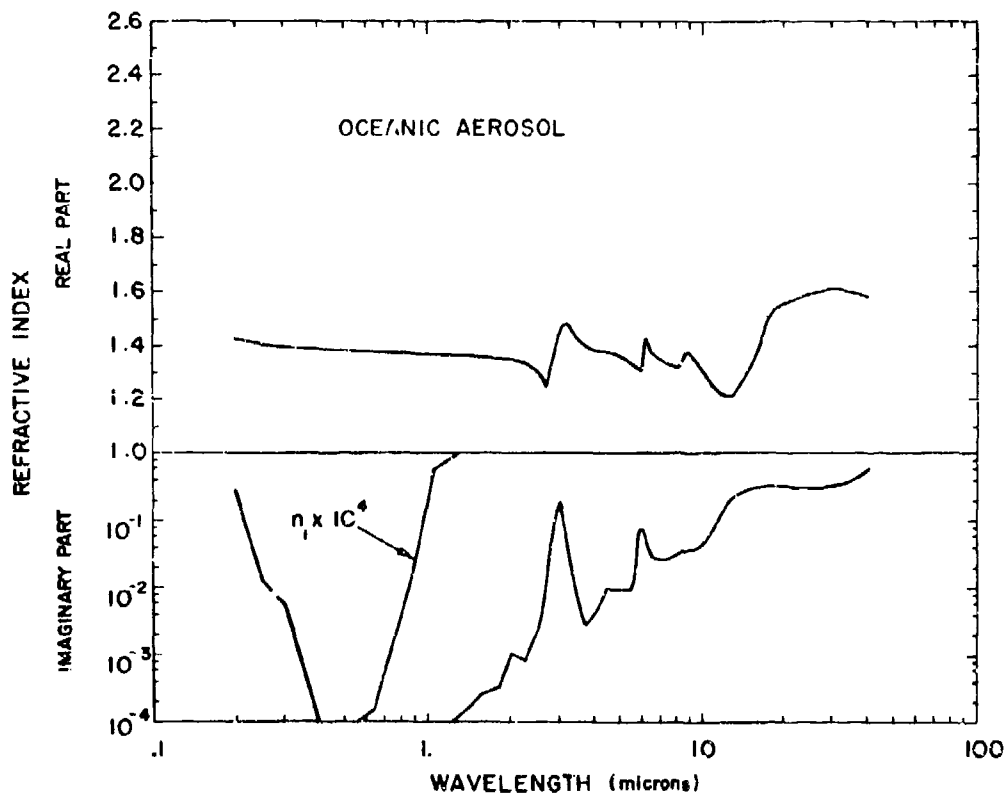
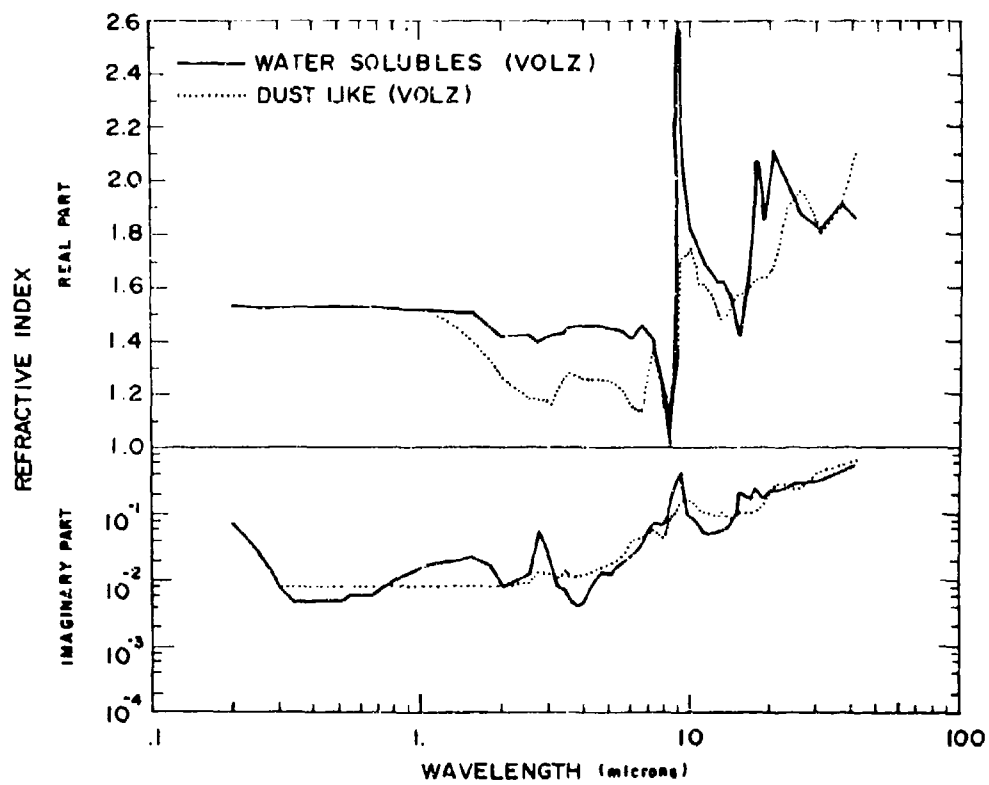


FIGURE 14 - Complex Refractive Indices for Rural and Maritime Aerosol Models

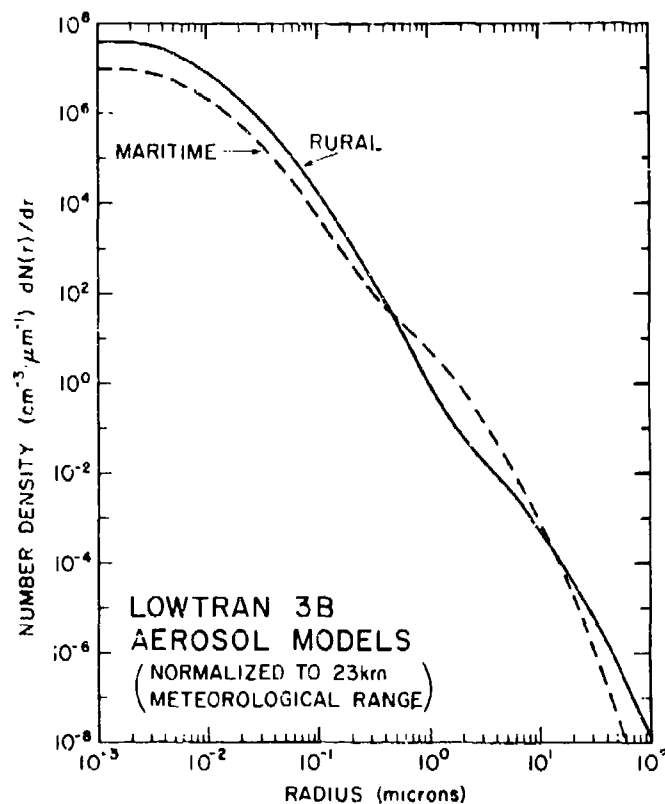


FIGURE 15 - Particle Size Distributions for the Rural and Maritime Aerosol Models

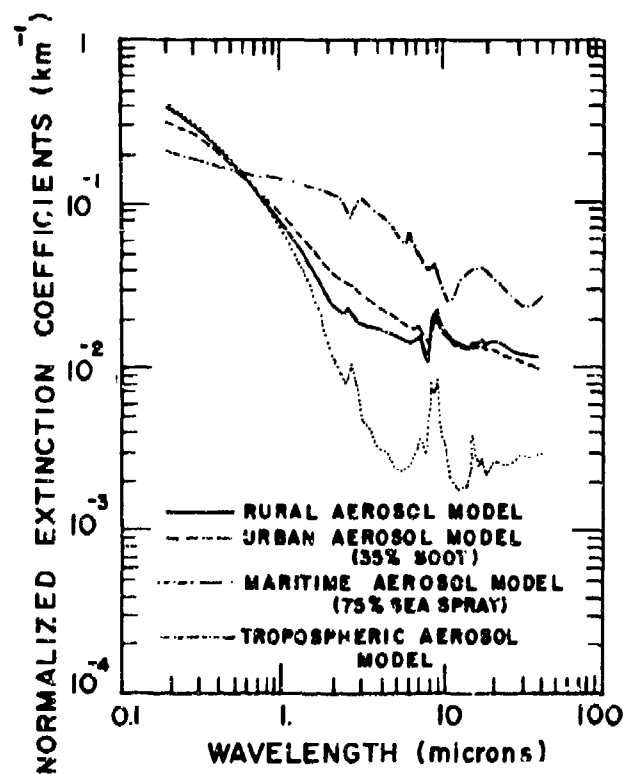
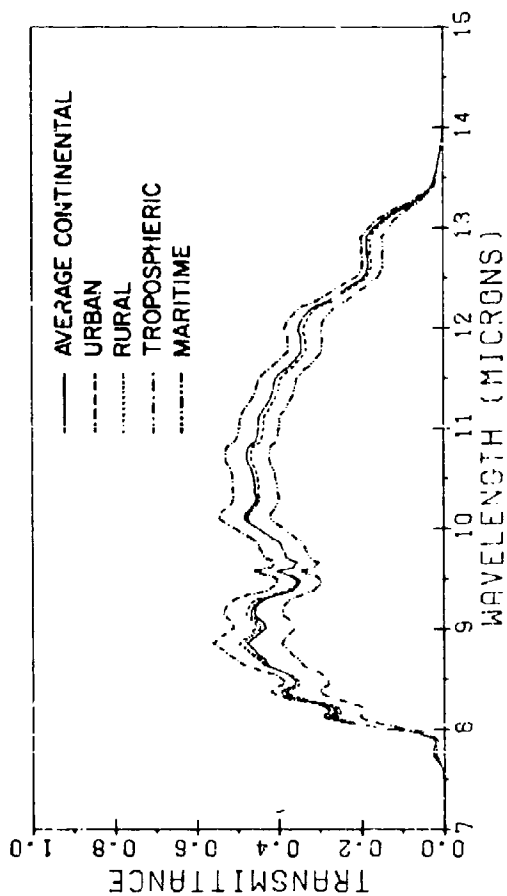
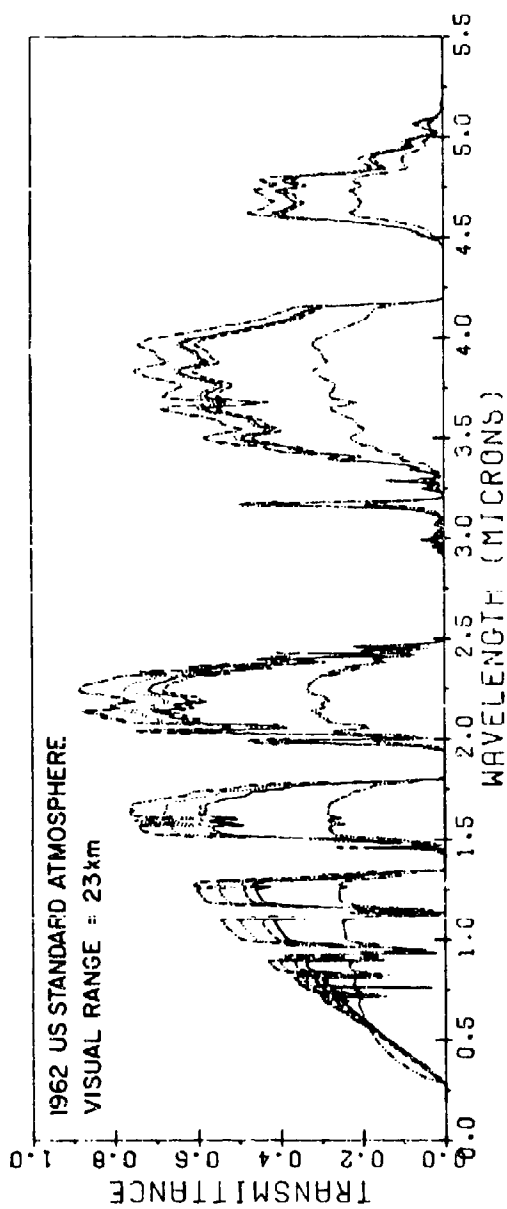


FIGURE 16 - Extinction Coefficients for Aerosol Models



TRANSMITTANCE FOR A 10 km PATH AT SEA LEVEL FOR 5 AEROSOL MODELS

FIGURE 17 - Transmission Variation for Various Aerosol Models

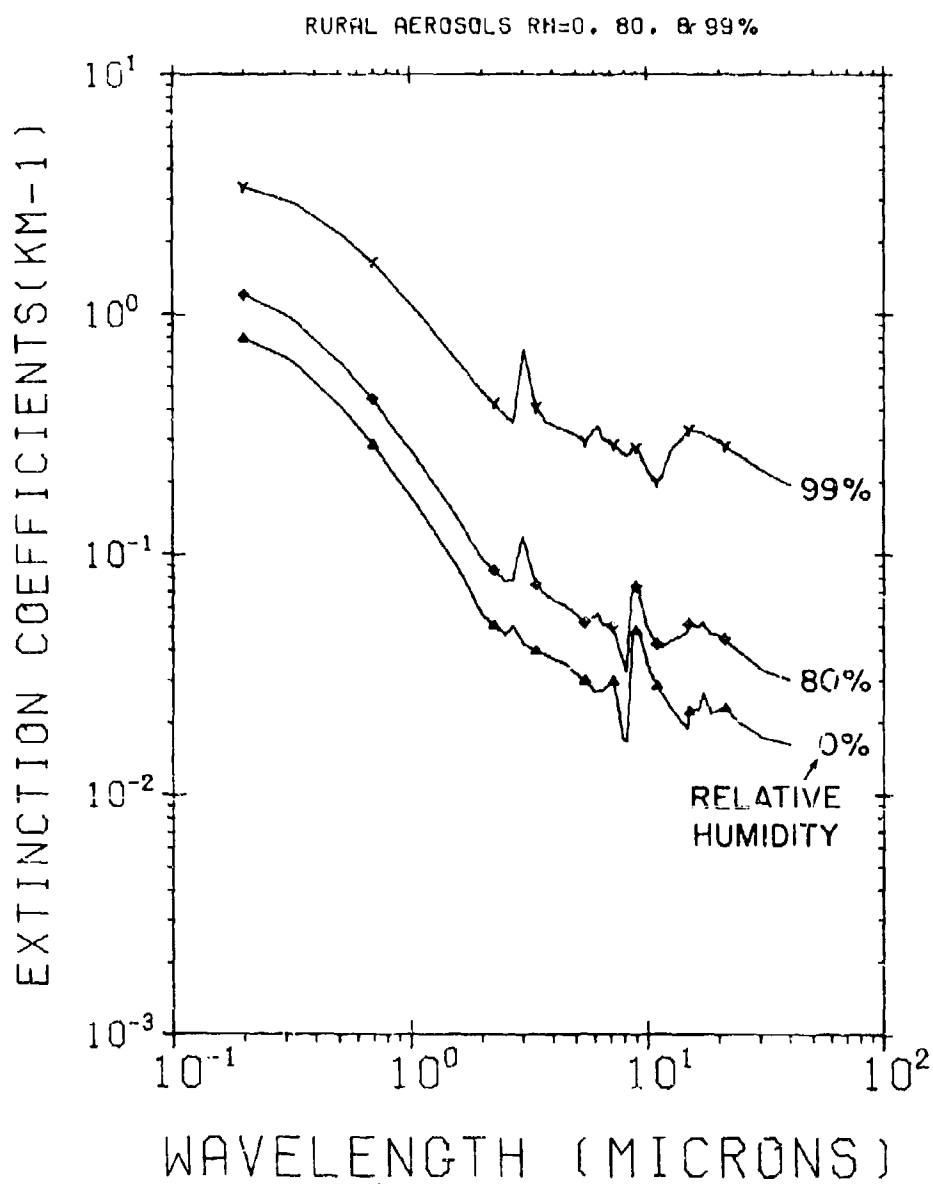
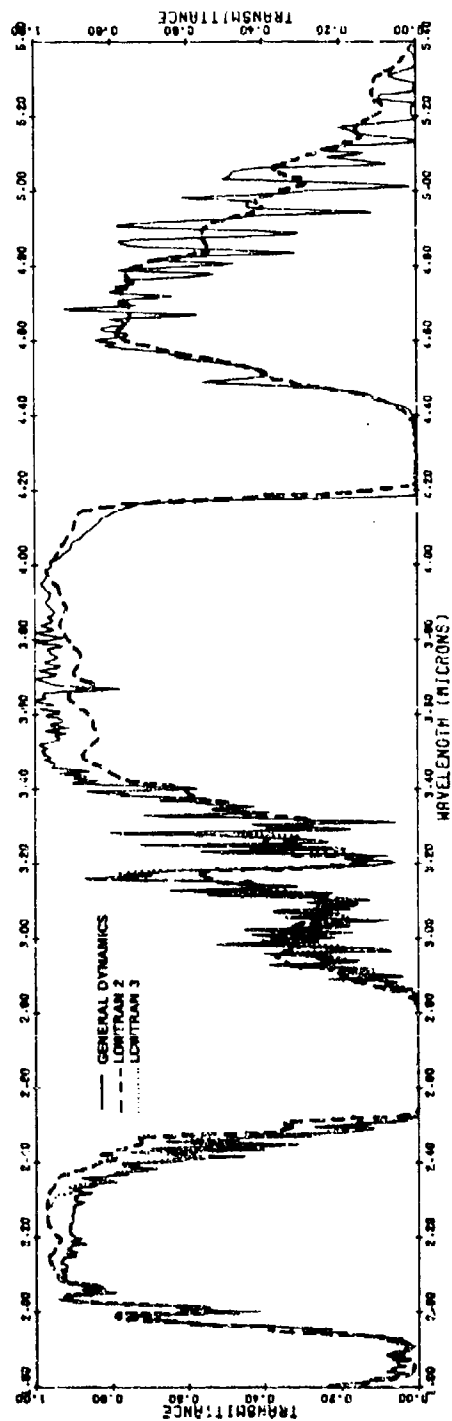


FIGURE 18 - Humidity Effect on Rural Aerosol Model

8 ATMOSPHERIC TRANSMISSION 9-23-72. R=1300M. T=0218. TF/RH=52/64 M20= .72 SWL



9 ATMOSPHERIC TRANSMISSION 9-22-72. R=1300M. T=0145. TF/RH=52/64 M20= .72 LWL

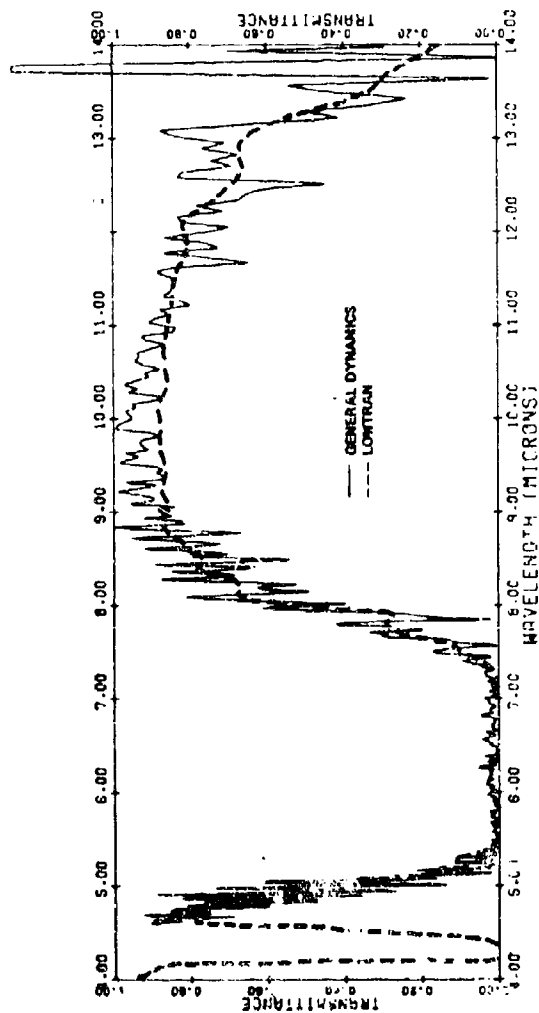
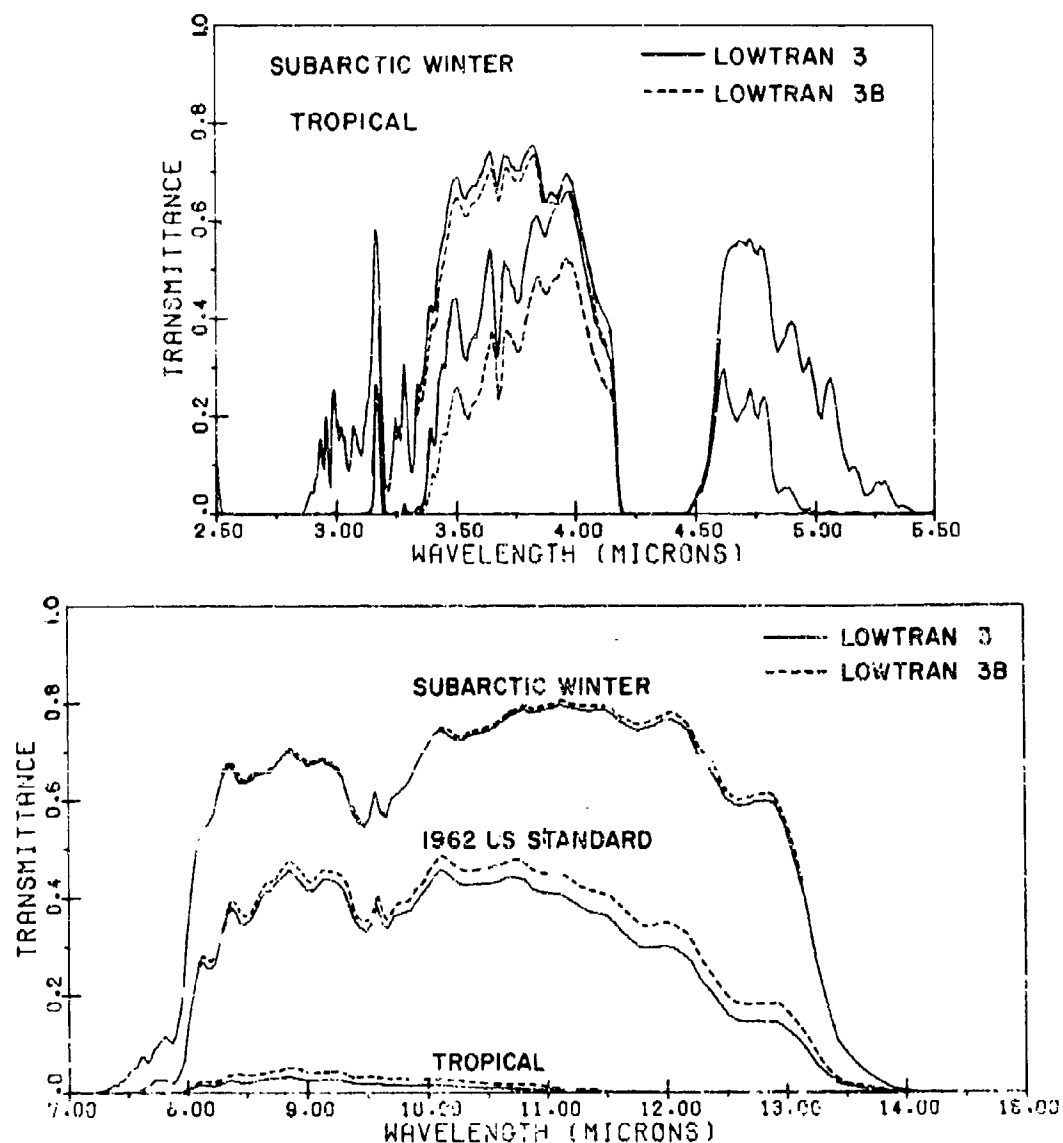


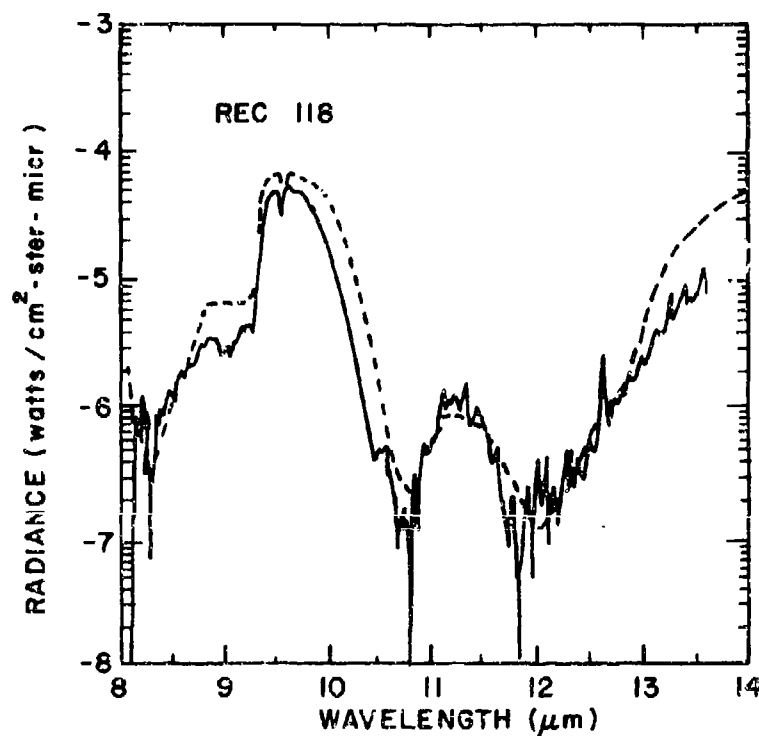
FIGURE 19 - Comparison of LOWTRAN Transmission Calculation with Field Measurement



10 km PATH AT SEA LEVEL FOR 3 ATMOSPHERIC MODELS

FIGURE 20 - Comparison of LOWTRAN 3 and LOWTRAN 3B in 3-5 and 8-14 μ m Regions

— MURCRAY ET AL. HOLLOMAN AFB, NEW MEXICO,
19 FEBRUARY 1975
---- LOWTRAN



SAMPLE SPECTRUM OF SHORT WAVELENGTH REGION OBSERVED
AT AN ALTITUDE OF 18.0 km AND A ZENITH ANGLE OF 63° ON
19 FEBRUARY 1975.

FIGURE 21 - Comparison of LOWTRAN 3B Radiance with Field Measurement

ATMOSPHERIC TRANSMISSION SPECTRUM

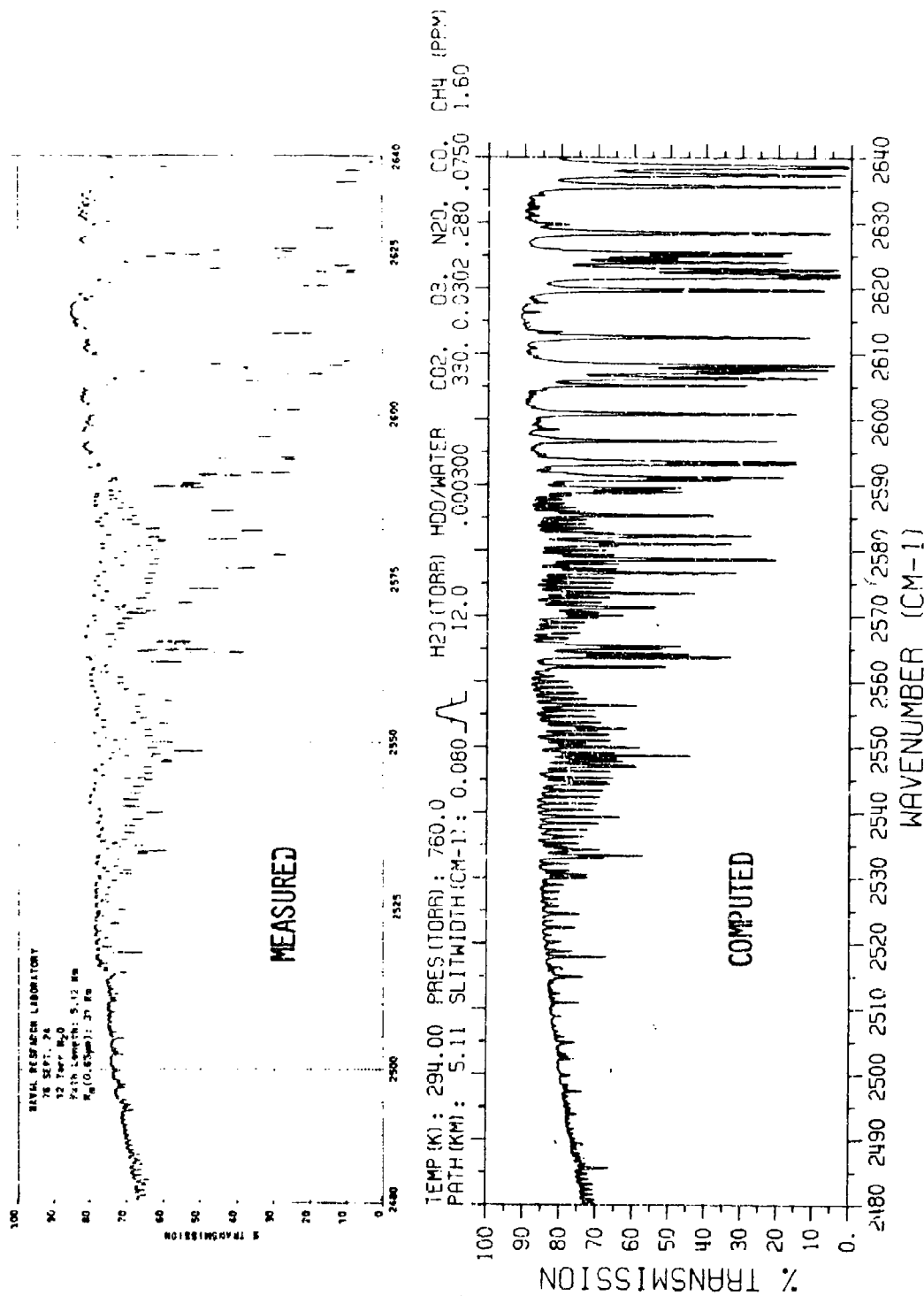


FIGURE 22 - Comparison of Computed High Resolution Spectra with Measurement (after Naught and Dowling)¹⁵

DISCUSSION

B.S.Katz, US

What is the status of improvements in HITRAN lines in order to develop hot aircraft and missile plume band models?

Author's Reply

There is a need for more high-resolution data if high-resolution calculations are to be done. For band model calculations with inherently less resolution constants are available to extend the time compilation to higher vibrational and rotational states.

H.Fluess, FRG

What is the spectral resolution of HITRAN in comparison to LOWTRAN?

Author's Reply

The HITRAN spectral resolution is infinite, limited only by the real width of spectral lines in the atmosphere. The LOWTRAN spectral resolution is 20 cm^{-1} .

C.Fengler, Canada

- (1) Is there a need to consider the shape of aerosols?
- (2) Have you to consider interactions depending on charges dwelling in aerosols?

Author's Reply

- (1) Yes, but such effects are probably small compared to uncertainties in aerosol size distribution and complex indices of refraction for a given atmospheric path.
- (2) I don't know the magnitude of such effects.

I.D.Lyon, UK

How do we obtain copies of up-to-date HITRAN and LOWTRAN programs?

Author's Reply

Reports can be obtained by writing to me directly. The HITRAN data tape, LOWTRAN and LASER card decks can be obtained by writing to:

National Climatic Center
NOAA
Federal Building
Asheville, North Carolina, USA

The HITRAN data tape costs \$60.00. The card decks cost \$20.00 each.

M.Tavis, US

- (1) What do you do about long tails on absorption lines not accounted for by Lorentzenian or Gaussian Type Lines?
- (2) LOWTRAN: Is curvature due to index of refraction accounted for?
- (3) Is the Diermendjian type model used for modeling aerosol distribution for each of the bimodal components?

Author's Reply

- (1) Empirical Line Shape adjustments are made. Future HITRAN codes will assume standard line shape to 64 half-widths and then add empirical "continuum".
- (2) Yes.
- (3) Early LOWTRAN models used a Diermendjian aerosol size distribution. Current and future models are similar, but different in order to be consistent with recent aerosol size distribution measurements.

MODELLING THE TRANSFER OF RADIATION IN THE ATMOSPHERE

H. J. Jung, M. Kerschgens, E. Raschke
 Universität Köln, Fed. Rep. of Germany

Summary

In this paper the concept of radiative transfer is discussed by reference to computations of the radiative energy in the solar, infrared and microwave spectral range. The radiation fields and spatial divergencies are dependent on the absorption, scattering and thermal emission by air molecules, aerosols, cloud and rain droplets. Additional parameters which influence the radiation fields in the atmosphere are the reflection and emission properties of the ground.

1 Introduction

A detailed knowledge on the radiation transfer properties and on the boundary conditions at the upper and lower bound of the atmosphere is required to model the transfer of radiation in the atmosphere. In the solar (0.2 - 3.6 μm), infrared (3.6 - 200 μm) and the microwave (0.8 cm) spectral ranges the radiative transfer is determined by the same basic laws, but the extinction characteristics of the gases and the atmospheric particles as well as the emission and reflection properties of the earth surface are different with respect to the wavelength region. In principle the complex index of refraction is an easy mean to describe this wavelength dependence.

The radiative transfer theory is applied for many purposes, in particular studies of communication links and of the energy balance of the earth and the atmosphere. For these purposes many computation schemes have been developed which are described comprehensively in the standard literature (cf. Kondratyev 1969, Paltridge 1976).

Studies of the radiative transfer are also performed for remote sensing of atmosphere, and oceanic and ground parameters. The number and the selection of these parameters depends on the radiation properties of the target and of the intermediate medium.

This paper intends to give a brief review about the basic laws of the radiation transfer theory. In particular it discusses some results of computations in the three wavelength regions demonstrating the influence of clouds in the solar and infrared and the determination of rainfall rates in the microwave spectrum.

2 Radiation transfer equation

For an arbitrary geometry of a transfer medium the radiative transfer equation takes the form (Lenoble 1975):

$$\vec{R} \cdot \vec{\nabla} L_v(\vec{r}, \vec{R}) = -\sigma_{\text{ext}}(\vec{r}) \cdot (L_v(\vec{r}, \vec{R}) - J(\vec{r}, \vec{R})) \quad (1)$$

where:

$L_v(\vec{r}, \vec{R})$: Spectral radiance at a point defined by vector \vec{r} and for radiation propagating in direction \vec{R} (watts m^{-2} sterad $^{-1}$)
 v : wave number (cm^{-1})

$\sigma_{\text{ext}}(\vec{r})$: Volume extinction coefficient (km^{-1})

$J(\vec{r}, \vec{R})$: Source function (due to internal or external sources of radiation)

This equation describes only the transfer of unpolarized radiation in the atmosphere. By introducing the four Stokes Parameter (L, Q, U, V) one is able to represent completely the state and the degree of polarization of arbitrarily polarized monochromatic radiation (Deirmendjian 1969, Chandrasekhar 1950). The Stokes Parameters may be defined in the following manner (e.g. Van de Hulst 1957):

$$\begin{aligned} L &= L_1 + L_2 \\ Q &= L_1 - L_2 \\ U &= Q \cdot \tan 2\chi \\ V &= L \cdot \sin 2\beta \end{aligned} \quad (2)$$

L_1 and L_2 represent the radiance of two orthogonal states of radiation in the transverse plane of a wave, U and V give respectively the direction of polarization and the ellipticity.

In the case of polarized radiation, $L_\nu(\vec{r}, \vec{\Omega})$ is to be considered as a vector, while the source function $J(\vec{r}, \vec{\Omega})$ must be replaced by a matrix. Calculations show, that the state of polarization must be taken into consideration, if meteorological parameters are inverted from radiometric data especially in the microwave region. There is a great variety of computation schemes for the solution of the radiative transfer equation in a plane parallel or spherical shell atmosphere with absorbing and scattering constituents.

One can choose between accurate but often much computer time consuming solution methods (cf. Monte Carlo, spherical harmonics or successive orders of scattering method) or approximate but fast methods (cf. modified two stream approximation, Delta Eddington) which compute without significant loss on accuracy the radiation field in the atmosphere (Lenoble 1975, Özisik 1973).

For the computations in the solar spectral range discussed here a modified two stream approximation (Kerschgens et al. 1978) is applied, while the radiances in the infrared and the microwave spectral range are determined by the method of successive orders of scattering (Raschke 1972). The atmospheric model under consideration is horizontally homogeneous and plane-parallel, but inhomogeneous into the vertical direction.

3 Dependence of radiative transfer on atmospheric constituents

3.1 Absorption

The atmospheric gases O_2 , O_3 , H_2O , CO_2 and also the aerosols and cloud- and rain droplets act as absorbers. The intensity of the absorption processes depends on the concentration and on the spectral distribution of the absorption lines of the gases and the particles.

Besides the rain droplets all mentioned absorbers influence the radiation transfer in the short wave spectral range (Moskalenkov 1968, Shettle and Fenn 1975). Taking into account the highly variable amount of absorber concentrations (H_2O) the prediction of the absorption intensity is very difficult. Regions of high transparency, the atmospheric windows, can be used for remote sensing of the earth surface.

One assumption for determining the absorption quantities in the infrared is the validity of the concept of the local thermodynamic equilibrium (LTE). The main gaseous absorbers in this wavelength region are H_2O , CO_2 and O_3 which have strong absorption bands at $6.3 \mu m$, $\lambda > 17 \mu m$ (H_2O), $15 \mu m$ (CO_2) and $9.6 \mu m$ (O_3).

Absorption data of high spectral resolution are tabulated by McClatchey (1975). The absorption by cloud droplets becomes important especially in the atmospheric window ($8 - 12 \mu m$), whereas in regions of high absorptivity the optical thickness of the cloud is so high, so that the cloud can be considered as a black body.

The transparency in the microwave region is determined by the absorption properties of H_2O , O_2 , cloud- and rain droplets (Staelin 1966).

3.2 Scattering

The scattering properties of atmospheric particles can be expressed in terms of the dimensionless Mie size parameter $x = 2\pi r/\lambda$ (λ : wavelength, r : droplet radius) and the complex index of refraction.

For the case $x < 1$ (particle radius is small compared to the wavelength) the well known Rayleigh approximation is valid (cf. scattering on air molecules in the solar spectral range), while for $x > 1$ a more elaborate theory developed at first by Mie (1908) should be applied for the estimation of the highly anisotropic scattered radiation of cloud-, aerosols- and rain droplets (Deirmendjian 1969).

Generally the radiation transfer is strongly dependent on the scattering behaviour of the atmosphere especially in spectral regions of high transparency. In the infrared, however, the scattering effect can be neglected, if the absorptivity is high.

Fig. 1 shows three phase functions describing the intensity distribution of the scattered radiation as a function of the scattering angle for three wavelengths.

The computations have been done for the wavelength ($\lambda = 0.5 \mu m$ and $\lambda = 10.6 \mu m$ for a N_s droplet size distribution (size range: $0.1 < r < 20 \mu m$), while in the microwave region a Marshall Palmer (1948) raindrop size distribution (size range: $0.1 < r < 3.5 mm$) has been used.

As a result of computations for a single scattering event (programm obtained from Quenzel 1976) the portion of the radiation scattered in forward direction is reduced, if the wavelength increases. At $\lambda = 0.8 cm$ the ratio of the forward and backward scattered radiation reaches unity. Extensive studies of single scattering processes have been reported by many authors, e.g. Giese (1971).

3.3 Boundary conditions

Boundary conditions of radiation models are the direct solar beam incident at the top of the atmosphere and the emission and reflection properties of the ground. The latter are depending on the refractive index and the surface roughness. In particular the effect of roughness of ocean surfaces is described in our calculations by the model of Cox and Munk (1954).

In the solar the radiation reflected at the earth surface is highly anisotropic because the surface acts as a diffuse reflector. This anisotropy can be in particular detected over water surfaces behaving like a mirror. Additionally over oceans the absorption and scattering properties of seawater must be known, since there is a radiation exchange between

ocean and atmosphere in the solar spectral range. Comparing the values of the albedo (= ratio of the outgoing to the incoming radiation) at the top of the atmosphere and at the ocean surface one can estimate the effects of various chlorophyll concentrations (Fig. 2).

With sufficient accuracy the emissivity in the infrared is assumed to be unity. Deviations from this value cause a variation of the profiles of temperature changes especially in the planetary boundary layer.

The reflected radiation from ocean surface in the microwave range is highly polarized. The vertical and horizontal polarized components of the radiation show a different behaviour, if the wind speed and therefore the surface roughness increases (Stogryn 1972). To estimate the effects of varying wind speed reflection values for both polarizations are derived from the Fresnel formula with application of the Cox - Munk (1954) model for the sea roughness (Raschke 1972). (Fig. 3)

A change of the emissivity is also caused by sea foam and white caps (Hollinger 1970). The composition of sea foam, its thickness and its density, is subject of measurements and theoretical model calculations (Rosenkrantz 1972).

4 Some radiative transfer calculations

Under consideration of all mentioned absorbers and scatters a calculation over the solar and infrared spectral range is performed using a frequency model with a high spectral resolution. Fig. 4 demonstrates the effects of all this constituents in the presence of a Ns (Nimbostratus) cloud between 1 and 2 km altitude. At the top of the cloud there is a strong cooling, while in the region beneath the cloud both spectral ranges contribute to an increase in the heating rate.

The influence of clouds on the radiation energy budget depends on the height, on the optical thickness and on the droplet size distribution of the clouds. Variations of these parameters determining the radiative properties of clouds are considered in radiative transfer calculations by many authors, e.g. Kerschgens et al. (1978).

In the microwave region there exists a relationship between the brightness temperature at the top of the atmosphere and the thickness of the cloud expressed in terms of rainfall rates. Fig. 5 shows the behaviour of the radiation temperature for three different cloud models. The LWC (liquid water content) is the dominating effect, while other absorbers like H_2O or O_2 contribute only at a low rate to the radiation temperature of this wavelength.

Remote sensing in the microwave range seems to be a good tool for estimating rainfall intensities especially over ocean surfaces. Derivations of rainfall rates from brightness temperatures are obtainable by considering the boundary conditions at the ocean surface (roughness) and the effects of varying raindrop size distributions in or below the cloud (Savage 1976).

References

- Chandrasekhar, S., 1975: Radiative Transfer, Dover Publication Inc., New York
- Cox, C., Munk, W., 1954: Measurements of the roughness of the sea surface from photographs of the sun's glitter, J. Opt. Soc. Am., Vol. 44, 838 - 850
- Deirmendjian, D., 1969: Electromagnetic scattering on spherical polydispersions, American Elsevier Publishing Company, Inc., New York
- Giese, R. H., 1971: Tabellen von Mie - Streufunktionen I. Gemische dielektrischer Teilchen, BMBW - FB W 71 - 23, Ruhr Universität Bochum
- Hollinger, J. P., 1970: Passive microwave measurements of the sea surface, J. G. R., Vol. 75, 5209 - 5213
- Kerschgens, M., Pilz, U., Raschke, E., 1978: A modified two - stream approximation for computations of the solar radiation budget in a cloudy atmosphere, accepted for publication in Tellus
- Kondratyev, K. Y., 1969: Radiation in the atmosphere, Academic Press New York and London
- Lenoble, J., 1975: Standard procedures to compute atmospheric radiative transfer in a scattering atmosphere, Laboratoire d'Optique Atmosphérique Lille, Vol. I
- Marshall, T. S., Palmer, W. McK., 1948: The distribution of raindrops with size, J. Met. 5, 165 - 166
- McClatchey, R. A., Selby, J. E. A., 1975: Atmospheric transmittance from 0.25 to 28.5 μm : Computer Code Lowtran 3, AFGL - TR - 75 - 0255
- Mie, G., 1908: Beiträge zur Optik trüber Medien, Ann. der Physik, 8, 377 - 445
- Moskalenkov, N. I., Golibitskiy, B. M., 1968: Spectral transmission functions in the H_2O and CO_2 bands, Izv. Atm. and Oce. Phys., 4, 346 - 359
- Özisik, M. N., 1973: Radiative transfer and interactions with conduction and convection, John Wiley Sons, New York
- Paltridge, G. W., Platt, C. M. R., 1976: Radiative processes in meteorology and climatology, Elsevier Scientific Publishing Company, New York

Raschke, E., 1972: Multiple scattering calculations of the transfer of solar radiation in an atmosphere - ocean system, Beitr. Phys. Atm., 45, 1 - 19

Rosenkrantz, P. W., Staelin, D. H., 1972: Microwave emissivity of ocean foam and its effects on nadir radiometric measurements, J. G. R., Vol. 77, 6528 - 6537

Savage, R., 1976: The transfer of thermal microwaves through hydrometeors, University Microfilms International, Ann Arbor, Michigan, U. S. A.

Shettle, E. P., Fenn, W., 1975: Models of the atmospheric aerosols and their optical properties, AGARD, conference proceedings No 183 on Optical Propagation in the Atmosphere, 2 - 1 - 2 -16, 1975

Staelin, D. H., 1966: Measurements and interpretations of the microwave spectrum of the terrestrial atmosphere near 1 cm wavelength, J. G. R., Vol. 71, 2875 - 2881

Stogryn, A., 1967: The apparent temperature of the sea at microwave frequencies, IEEE Transactions on Antennas and Propagation, Vol. Ap - 15, No 2, 278 - 286

Van de Hulst, H. C., 1957: Light scattering by small particles, John Wiley Sons, Inc., New York

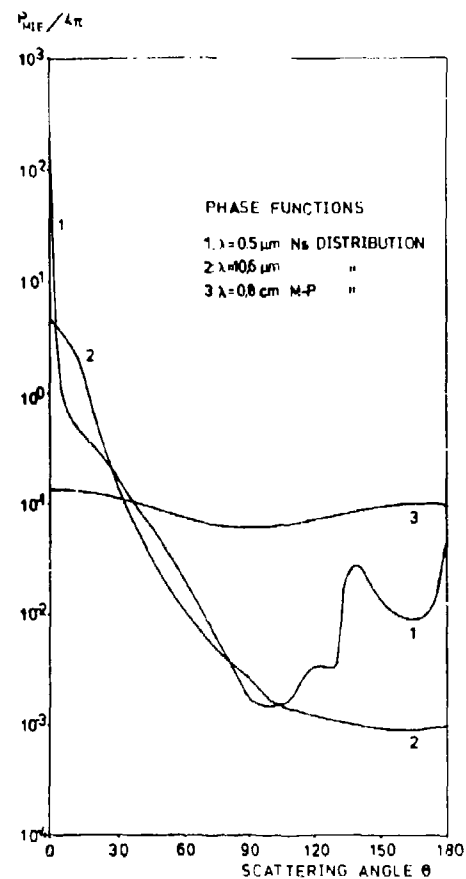


Fig. 1: Phase functions for different wavelengths and dropsize distributions

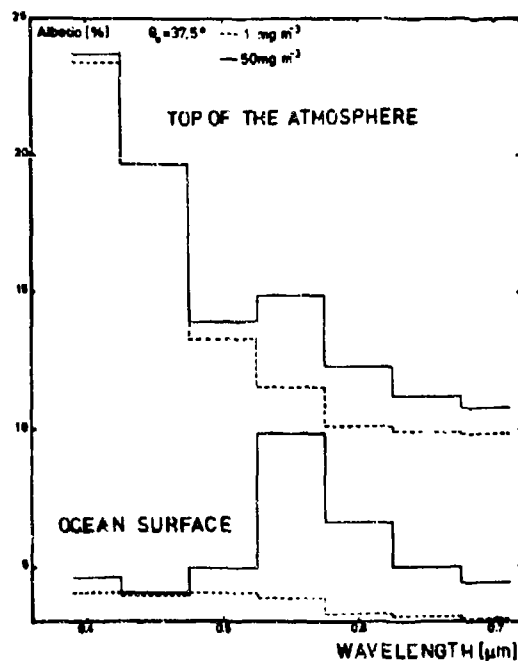


Fig. 2: Effect of two chlorophyll concentrations on albedo values of the atmosphere-ocean system

REFLECTIVITY (%)

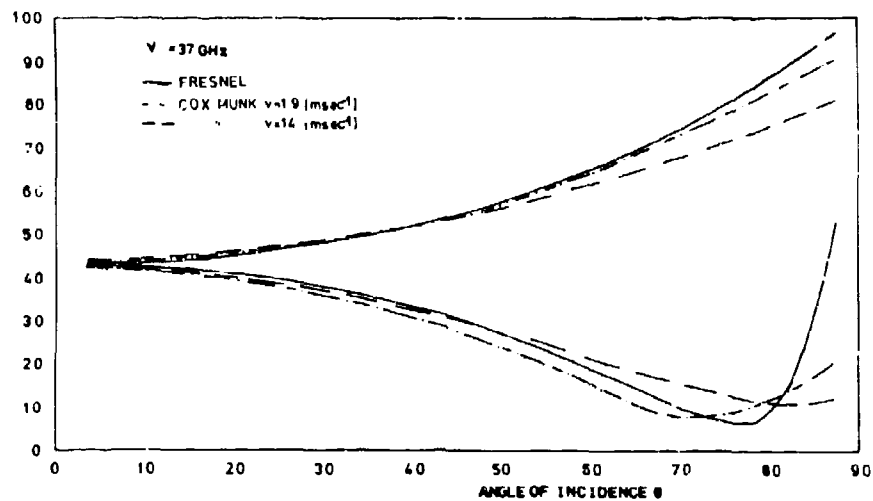


Fig. 3: Reflectivity of a ocean surface for various roughness scales

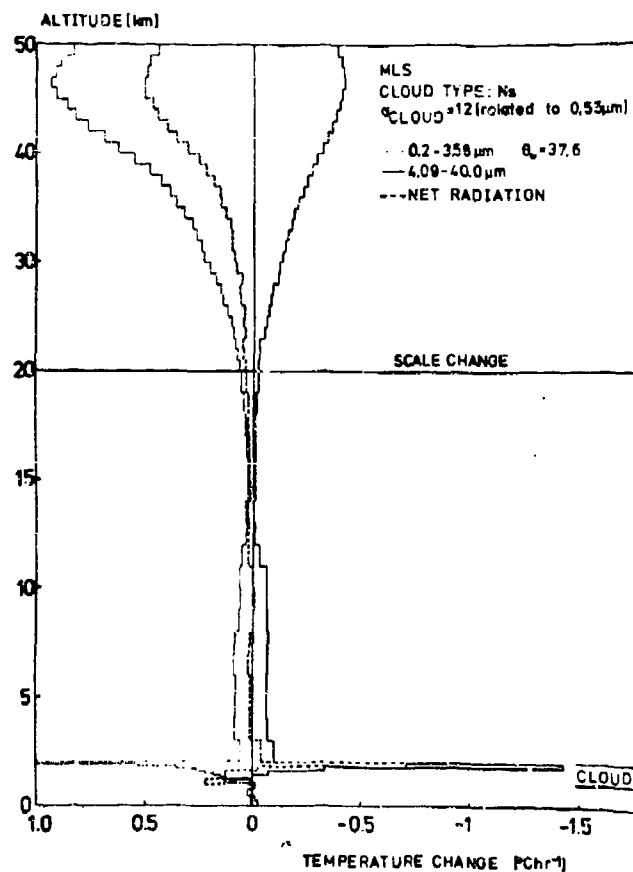


Fig. 4: Contributions of the solar and the infrared spectral range to the net radiation in a MLS (midlatitude summer) atmospheric model

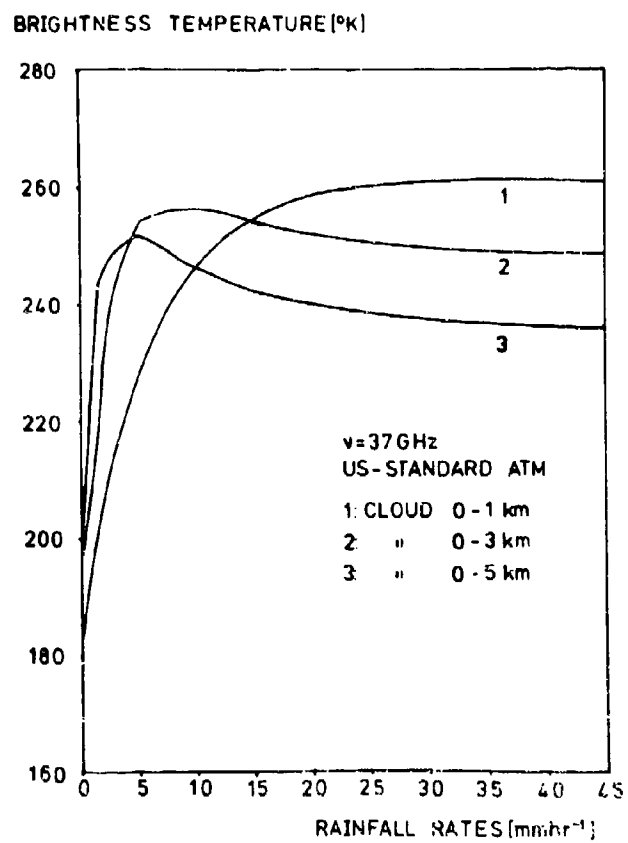


Fig. 5: Brightness temperatures for three different cloud models as a function of rainfall rates

CALCULATION OF EXTINCTION AND SCATTERING IN THE WAVELENGTH
RANGE FROM 0,25 to 15 μm BY
HYDROMETEORS AND FOR GENERAL GERMAN WEATHER SITUATIONS

W. Eckl *, H.J. Flüß ** , H. Hallwachs **

* Elektronik-System-GmbH, Vogelweideplatz 9
8000 München 80, W. Germany

** Messerschmitt-Bölkow-Blohm GmbH,
Postfach 801160, 8000 München 80,
W. Germany

SUMMARY

For system design and operational research purposes a computer program "KATTA" was written for the description of absorption and scattering of electromagnetic waves by hydrometeors (water droplets in rain, fog and clouds). The calculation is based upon the Mie-theory and single scattering. It is valid for Mie-parameters up to 10,000 and includes the angular dependency of the scattering function. Much effort has been done to achieve fast convergence of numerical values. The program is compatible with existing LOWTRAN-codes.

For application of the integrated KATTA + LOWTRAN-code to European scenario detailed European atmospheric input data were used. They contain statistical meteorological data and German significant weather map types including precipitation, fog and clouds. The results presented here show the variation of calculated atmospheric transmission for the different weather situation with and without precipitation.

1. INTRODUCTION

The influence of the atmosphere on the performance of sensors in the various spectral regions depends on

- the sensor itself,
- the spectral sensitivity of the sensor,
- the actual atmospheric data, and
- the probability of its occurrence.

For system design and operational research (OR) purposes it is necessary to know not only the technical data of a sensor but much more its operability in a given tactical scenario. This scenario must be described with sufficient details and equal depth, i.e. for each spectral region. That means also that it has to set a reference acknowledged by industry and government agencies.

For the description of the influence of atmosphere such a reference can be derived either

- from time consuming measurement series or by
- a theoretical approach.

Encouraged by the work of Selby and McClatchey /1/ describing the transmission through the atmosphere without hydrometeors in the spectral region from 0,25 μm to 28 μm two computer programs were written:

1. The program RATRAN /2/ for the description of atmospheric attenuation, scattering and refraction in the microwave region from 0,5 to 300 GHz.
2. A supplement to LOWTRAN 3B called KATTA describing the influence of hydrometeors in the wavelength range from 0,25 to 15 μm .

As these programs should be used primarily for European weather conditions appropriate atmospheric input data had to be used instead of the data, i.e. in LOWTRAN 3B. The German Military Geophysical Office (AW Geophys) took over this time-consuming task and provided very detailed atmospheric data to these programs /3/.

In this paper therefore the influence of hydrometeors in the 0,25 to 15 μm region and of the German general weather situations will be presented.

2. EXTINCTION OF ELECTROMAGNETIC WAVES BY HYDROMETEORS

Water droplets in rain, clouds and fog are considered. They are regarded as a dielectric sphere with a complex index of refraction. Extinction of e.m.w. is caused by absorption and scattering. The extinction coefficient is calculated by:

1. Calculation of extinction cross-sections σ according to Mie-theory as a function of Mie-parameter ($\alpha = \frac{\pi d}{\lambda}$) for values of α up to 10,000 including angular distributions, and
2. Multiplying σ_{ext} with the number of hydrometeors/volume unit and diameter, and
3. Integrating over the whole distribution $N(\alpha)$ of hydrometeors.

2.1 Calculation of Mie-Extinction Cross-Section

2.1.1 The extinction cross-section σ is calculated according to Mie /4/. Fig. 1 shows the relation of the effective cross-section to the geometrical one as a function of α . It can be seen that for values of α up to 20 high oscillations occur for the scattering and extinction coefficient. For greater Mie-parameters absorption and scattering coefficients approach to unity, which means that the extinction cross-section is twice the geometrical one.

The numerical solution depends on the value of α and is carried out as follows:

A straightforward calculation was done for $0 < \alpha \leq 20$ (Mie-scattering). Recursive calculation of the non-selective scattering was performed for $20 < \alpha \leq 2000$ because of numerical instabilities according to Kattawar and Plass /5/. For $\alpha > 2000$ the laws of geometric optics and Huygen's principle according to Van de Hulst /6/ were applied.

The calculations were performed with double word length on an IBM 370 machine and a single word length on a Cyber 175 machine.

2.1.2 Angular Dependency of Scattering Function

According to theory scattering is not uniform, but has an increasing forward component with decreasing wavelength. This angular dependency of the scattering function was taken into account in the program. Fig. 2 shows the scattering functions for 3,5 μm and 10,6 μm and scattering angles between 0 and 20 degrees. The change of the scattering function by more than 5 orders of magnitude and the frequency dependency can easily be seen.

2.2 Influence of Droplet Distributions

The extinction coefficient ρ is proportional to

- the extinction cross-section σ and
- the number of hydrometeors $N(\alpha)$ per volume unit and diameter α according to equation 2.1:

$$\rho = \pi \int_{D_0}^{D_{\max}} (m, \alpha, \lambda) N(\alpha) \alpha^2 d\alpha \quad (2.1)$$

with

- m = complex index of refraction for water droplets
- α = Mie-parameter
- λ = Wavelength

The influence of the variation of the water droplets' index of refraction by temperature changes is negligible according to Irvine and Pollack /7/.

The influence of particle density distribution $N(\alpha)$ is, however, essential and shown in the following.

2.2.1 Droplet Distributions for Rain

For rain the two main different distributions are according to

- Marshall-Palmer (MP) /8/ and
- Laws-Parson (LP) /9/.

They are shown in Fig. 3 for rain rates of 2,5 mm/h and 12,5 mm/h respectively. The MP-distribution is characterized by an essentially higher density of particles with a diameter between 0 and 1 mm. This difference results in different extinction coefficients as shown in Fig. 4 for a wavelength of 10,6 μm . The four curves were calculated with a

- MP-distribution of rain droplets and starting integration with a minimum diameter D_0 of 0,5 mm (curve 1) and 1 mm (curve 2) respectively and in addition with a
- LP-distribution and $D_0 = 0,5$ mm (curve 3) and $D_0 = 1$ mm (curve 4) respectively.

Besides curve 1 the other 3 curves are lying close to each other especially for higher rain rates. That means that the main contribution to the extinction coefficient in this spectral region is based upon particles smaller than about 1 mm diameter. The choice of the distribution to be used was based upon the agreement of available experimental data /10,11/ with these theoretical data, which are shown together in Fig. 5. From this figure it can be seen that the LP-distribution fits better to the experimental data, especially at rain rates less than 5 mm/h which are the most likely ones.

For the calculation D_0 was 0,5 mm and D_{\max} was 7 mm.

2.2.2 Distributions of Droplets in Clouds

The drop distributions for eight different types of clouds, namely

- cumulus congestus /12/
- cumulus humilis /13/
- cumulus fractus /14/
- strato-cumulus, cumulus fractus /15/
- altocumulus /14/
- altostratus /14/
- stratus /14/
- cirrus /15/

are taken from the literature cited and are used for the calculations of extinction by clouds.

Fig. 6 shows an example of the extinction coefficient calculated as a function of wavelength for

- a strato cumulus and
- a cumulus humilis.

Both curves are related to their extinction coefficient at $0,55 \mu\text{m}$. A significant narrow window at about $10,5 \mu\text{m}$ appears for both clouds in the calculations. Experimental data, i.e. by Moerl /16/, have confirmed these theoretical results.

3. METEOROLOGICAL INPUT DATA

For the computer model two different meteorological input data sets were used, namely

- statistical data evaluated from the year 1973 and
- general weather situation.

Both are briefly described in the following.

3.1 Statistical Meteorological Data

For a short analysis of system performance one of 12 statistical meteorological data can be called up which are differentiated by

- location (north or south Germany)
- season (winter or summer)
- probability of occurrence

They contain the pressure, temperature and humidity profile as a function of height above MSL, but no precipitation, fog or clouds, and no detailed description of the boundary layer.

For the southern part of Germany and the summer season Fig. 7 shows the 3 pressure profiles, Fig. 8 shows the 3 temperature profiles, and Fig. 9 shows the 3 humidity profiles together with the corresponding values of the US-Midlatitude-Summer-atmosphere.

The lower curve is identified as the "lower extreme value" with a 10 % probability of occurrence, the curve in the middle is referred to as that of "mean values" and the upper curve is called "upper extreme value" (10 % probability of occurrence).

Especially the variation of humidity influences the achievable atmospheric transmission as shown in Fig. 10.

3.2 German Significant Weather Map Types

The lack of information about type and density of precipitation, probability of occurrence and density of fog, distribution and type of clouds, the limited number of atmospheric models and the requirements for detailed meteorological data of the boundary layer for heights up to 2 km resulted in the generation of meteorological data which are based upon 4 significant weather types. These 4 weather map types and their probability of occurrence in summer and winter are shown below:

Probability of occurrence in:

Type	Winter	Summer
West	55,9 %	50,4 %
North	20,2 %	18,6 %
East	9,4 %	13,2 %
High	14,2 %	18,08 %

The vertical profiles are recorded at

- 100 m intervals from 0 to 2 km in order to respect possible atmospheric irregularities, and at
- 1 km intervals between 2 and 12 km.

A concentrated extract of one of these sets is shown in Table 1 of Filles /2/.

4. CALCULATED RESULTS

With both meteorological data sets some calculations have been made. The results achieved are shown and discussed in the following.

4.1 Calculated Results with Statistical Meteorological Data

The variation of atmospheric parameters, especially humidity, results in a change of atmospheric transmission characteristics. For the summer values in the southern part of Germany (area around Munich) Fig. 10 shows the transmission per km for the upper and lower extreme values. Especially at longer wavelengths a significant reduction of transmission results with the upper extreme values of the statistical atmospheric data. This variation is about the same for the winter data.

Curve 3 in Fig. 10 shows the calculated results with the US-Midlatitude summer data. These results correspond in good approximation with those of the upper extreme values. The reason may be found in the fact that both atmospheres have a humidity content of about 13 g/m^3 at MSL.

The lower extreme values for summer 1973 correspond quite well with "the US-Standard Atmosphere 1962" with a humidity of about 6 g/m^3 at MSL.

A comparison of the mean values of winter and summer enables Fig. 11. Due to the lower humidity content in winter the atmospheric transparency is higher than in summer.

4.2 Calculated Results with General Weather Map Type Data

The superposition of probability, type and intensity of precipitation, type and extension of clouds and fog to the pressure, temperature and humidity profile in general weather situation data permits the calculation of realistic transmission coefficients. Fig. 12 shows the transmission per km for

- the general weather situation: north in winter, northern Germany with and without rain of 4 mm/h which occurs with an 8 % probability during this weather situation.

The significant reduction of transmission in all spectral regions can easily be seen.

5. CONCLUSION

The existing LOWTRAN 3B-code was supplemented by a computer program describing the extinction of electromagnetic waves by hydrometeors. The extended program is in use in Germany for OR and system design purposes. According to the requirements detailed atmospheric parameters including hydrometeors were inserted based upon a detailed evaluation of the AW Geophys. The program is compatible with the program RANRAN describing the atmospheric influence in the microwave region.

Due to the limited computing time allowed for operational research. (OR) purposes only single scattering was respected. Multiple scattering calculations may improve the accuracy of the results.

The concentration of rain droplets was assumed to be based upon Laws-Pearson distributions. A verification of the full truth of this preliminary decision has still to be made.

Due to the lack of related data the influence of atmospheric turbulences could not yet be respected.

6. ACKNOWLEDGEMENT

The work for this paper was performed under contract No. T/R420/60002/62006 of BMVg-Bonn. The authors are very grateful to the German Military Geophysical Office (AW Geophys) for the large amount of detailed meteorological data and for their excellent cooperation.

7. REFERENCES

- /1/ Selby J.E.A.
Shettle, E.P.
McClatchy, R.A. 1976 "Atmospheric Transmittance from 0,25 to 28,5 μ m: Supplement LOWTRAN 3B", Air Force Geophysics Lab., Rep. No. ATR76-0258
- /2/ Flüß, H. 1978 A Computer Model describing Atmospheric propagation of Microwaves from 1 to 300 GHz including Detailed Atmospheric Conditions and Comparison with Experimental Data, Proceedings of AGARD-Symposium on "Operational Modelling of the Aerospace Propagation Environment" this issue
- /3/ German Military Geophysical Office 1976 "Vertikalprofile, Tropfenspektren und daraus abgeleitete Größen für die Atmosphäre in Mitteleuropa" Studie Nr. 76148
- 1977 Das Referenzjahr 1973, Studie Nr. 77135
- Das Bodenwetter-Szenarium, Studie Nr. 77169
- /4/ Mie, G. 1908 "Beiträge zur Optik trüber Medien, speziell kolloidaler Metallösungen" Ann. Phys., 25, 377-445
- /5/ Kattawar, G.W. 1967 Electromagnetic Scattering from Absorbing Spheres Appl. Optics 5, 8
- /6/ Van de Hulst, H.C. 1957 Light Scattering by Small Particles John Wiley & Sons, Inc. New York
- /7/ Irvine, W.M. 1968 Infrared Optical Properties of Water and Ice Spheres Pollack, J.B. Icarus, 8, 2, 337
- /8/ Marshall, J.S. 1948 The Distribution of Raindrops with Size J. Meteorol., 5, 165-166
- /9/ Laws, J.O. 1943 The Relation of Raindrop Size to Intensity Am. Geophys. Union Pt. II 24, 452-460
- Parson, D.A.
- /10/ Chu, T.S. 1968 Effects of Precipitation on Propagation at 0,63, 3,5 and 10,6 Microns Hogg, D.C. Bell Syst. Techn. Journal 47, 3
- /11/ Farrow, J.B. 1970 Influence of the Atmosphere on Optical Systems Optical Acta 17, 317
- /12/ Huan Mei-Yuan 1963 Izv., Akad. Nauk SSSR, 2, 362-376
- /13/ Warner, J. 1973 J. Atm. Sc., 30, 256-261
- /14/ Paltridge, G.W. 1974 J. Geophys. Res. 79, 4053-4058
- /15/ Weickmann, H. 1954 Berichte des DWD in der US-Zone, Nr. 6
- /16/ Moerl, P. 1974 Measurements of the Transmittance of Fog at 10,6 μ m Wavelength Int. Rep. DFVLR - Institut für Physik der Atmosphäre

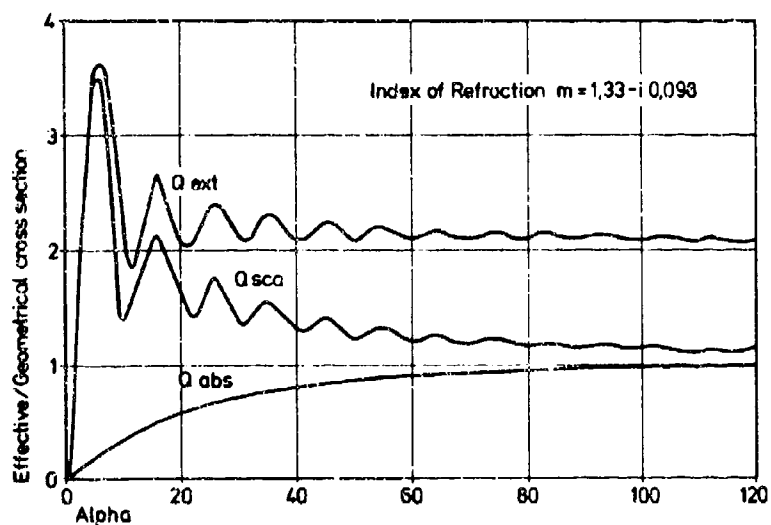


Fig. 1: Effective cross-section/geometrical cross-section as a function of Mie-parameter

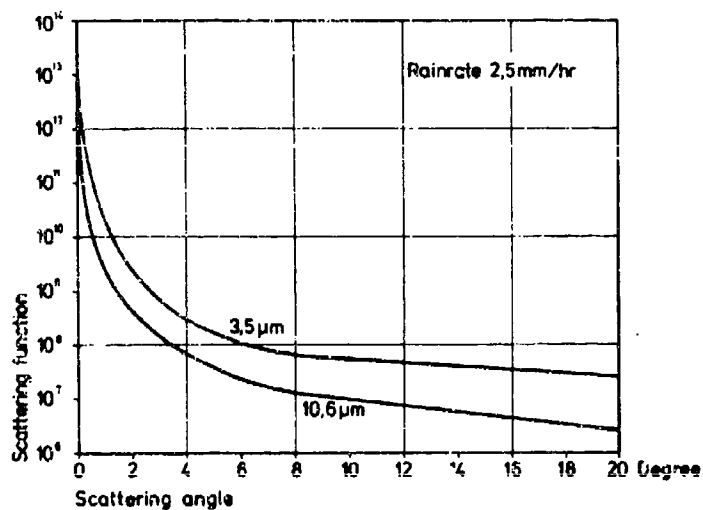


Fig. 2: Scattering function for 3, 5 μm and 10,6 μm for scattering angles between 0 and 20 degrees

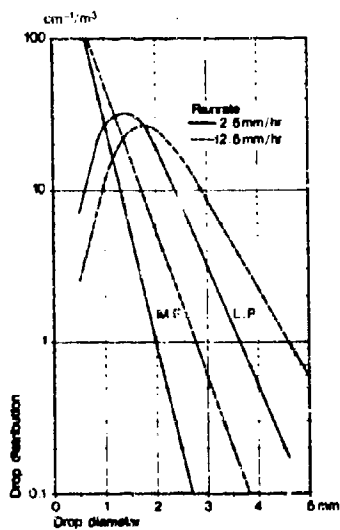


Fig. 3: Marshall-Falmer and Laws-Parson drop distributions for rain rates of 2,5 and 12,5 mm/h

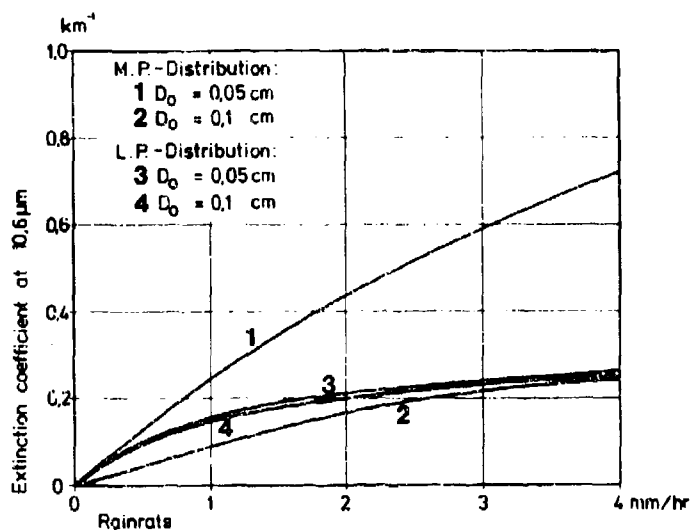


Fig. 4: Extinction coefficient at $10.6 \mu\text{m}$ for MP- and LP-distributions with different integration parameters

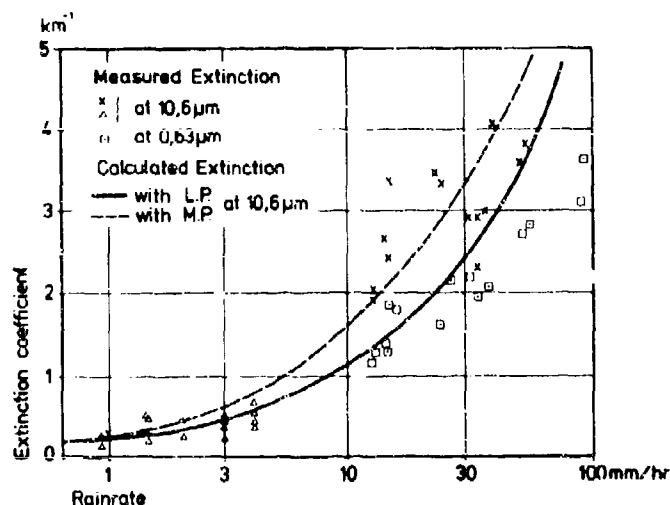


Fig. 5: Comparison of experimental and calculated extinction coefficients as a function of rain rate

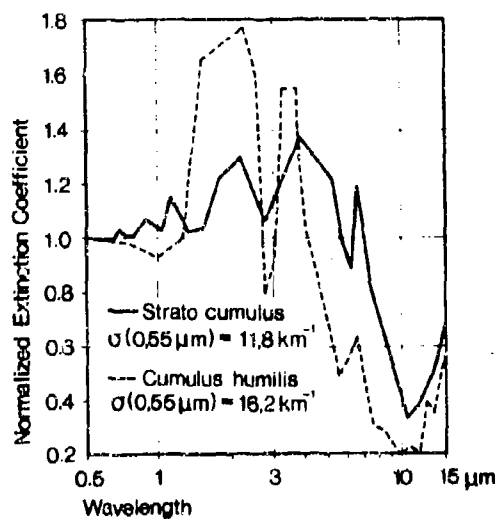


Fig. 6: Calculated extinction coefficient for 2 cloud types as a function of wavelength

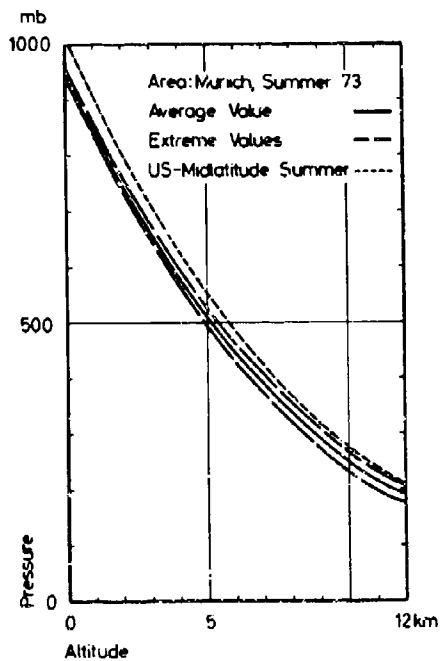


Fig. 7: Pressure profiles as a function of height above MSL

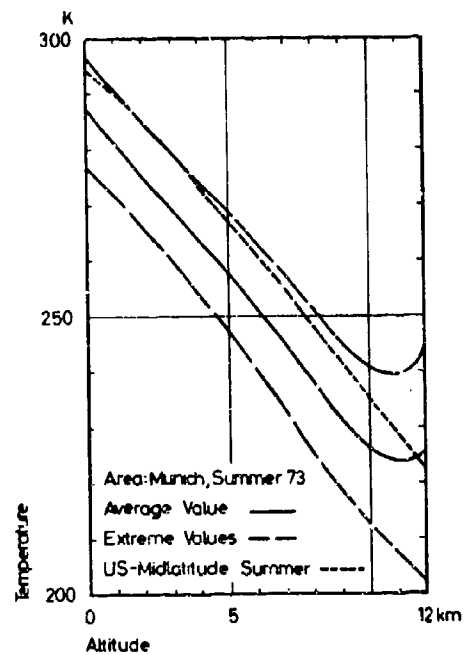


Fig. 8: Temperature distribution as a function of height above MSL

Statistical Meteorological Data

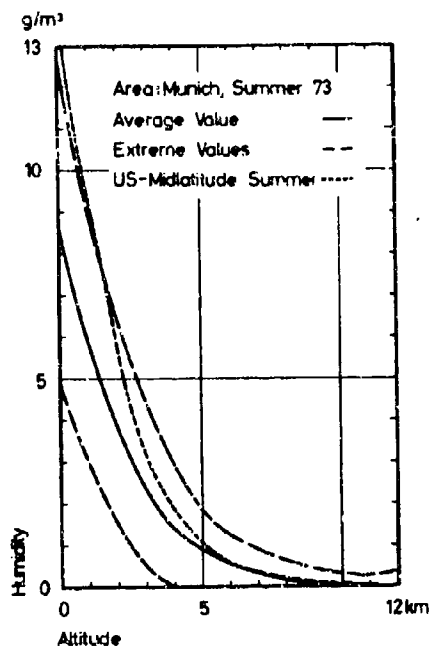


Fig. 9: Humidity as a function of height above MSL

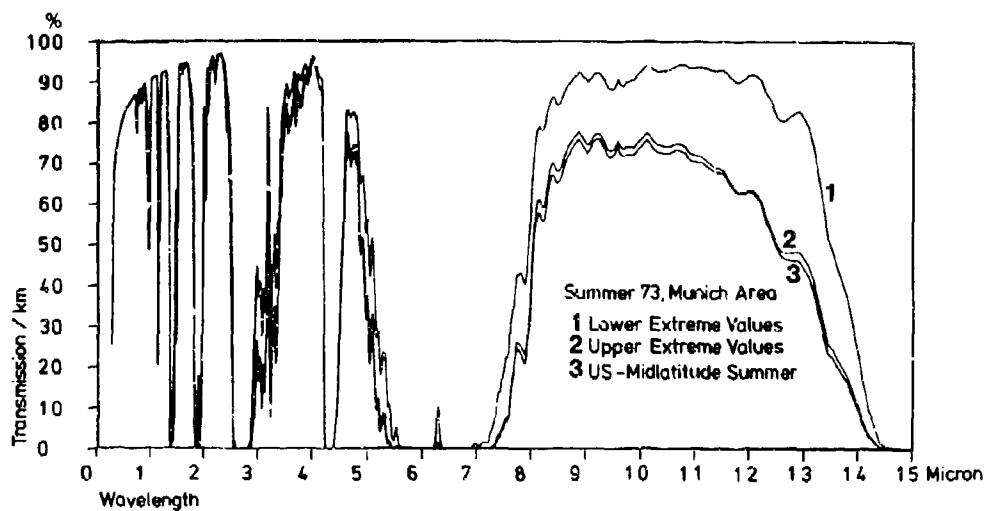


Fig. 10: Atmospheric transmission for different meteorological data sets as a function of wavelength

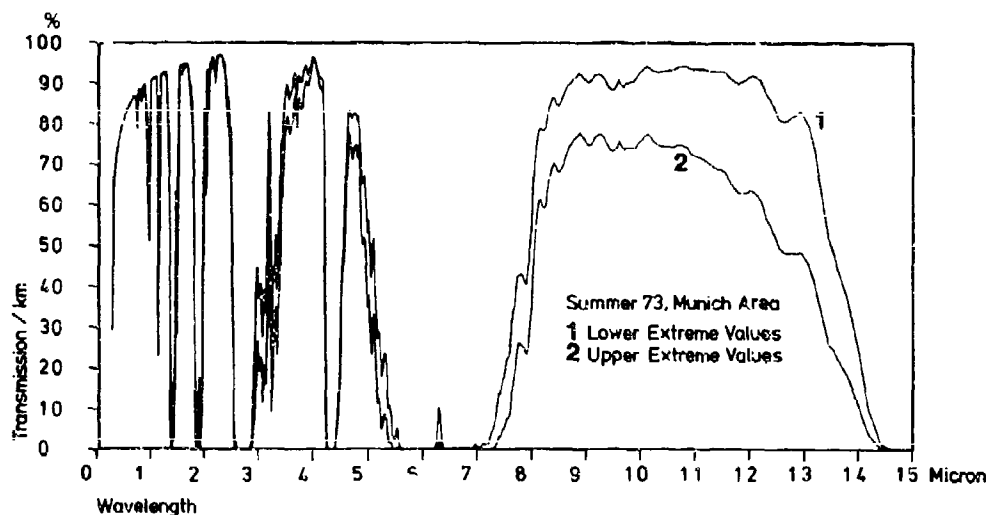
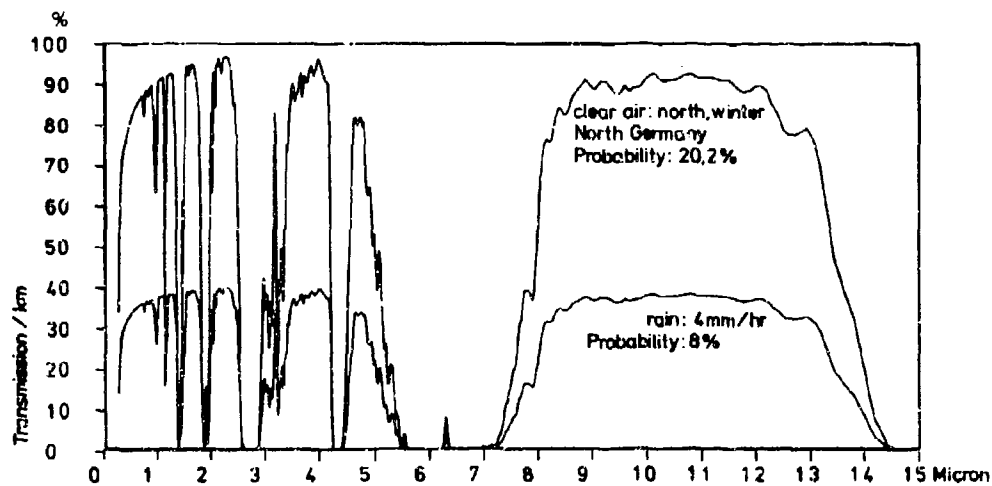


Fig. 11: Atmospheric transmission for mean values of summer and winter as a function of wavelength



DISCUSSION

R.A. McClatchey, US

It was indicated that the LOWTRAN 3D Program as modified was applied to laser transmission. In regions of molecular absorption, this application would be inapplicable. Would the author please comment?

Author's Reply

It is intended to use the improved version of the LOWTRAN-Code together with the supplements of our program.

J. Röttger, FRG

Turbulence might give rise to strong signal scintillation which can detract the circuit reliability. Would you assume a necessity to include models of (clear air) turbulence for further improving your calculations?

Author's Reply

The program is in the first stage of development. During the improvement stage of the program we expect to receive input data describing the influence of turbulence in an appropriate way.

M. Tavis, US

Is molecular absorption included in cloud propagation calculation along with the hydrometeor effects?

Author's Reply

The molecular absorption of water vapor and oxygen is included in the calculation of rainfall rates at 37 GHz. But in comparison with the scattering and absorption effects of different raindrop distributions the contributions of atmospheric gases don't play a dominant role at this wavelength.

A BAROCLINIC MODEL FOR THE PREDICTION OF THE VERTICAL TEMPERATURE AND MOISTURE STRATIFICATION IN THE BAROCLINIC BOUNDARY LAYER

by

W. Behnke

Universität Köln, Fed. Rep. of Germany

Abstract

A baroclinic but otherwise horizontally homogeneous model of the planetary boundary layer, which considers inatationarity, is used to compute the different influences of roughness and baroclinity on inversion height. Computations are compared with the measurements of an acoustic echo sounder.

1. Introduction

The planetary boundary layer, i.e. the lowest part of the atmosphere of about 1-2 km thickness, became subject of increasing interest in atmospheric research and modeling. It is the transit layer for all exchanges of energy and momentum between the free troposphere and the ground. Therefore, its vertical structure determines to a large extent these processes. Since it is also largely affected by the large-scale circulation processes and by the structure and thermal properties of its lower boundaries, its modeling requires a detailed understanding of both these properties.

Recent considerable efforts to investigate the properties of the planetary boundary layer primarily arose from the need to model the physical processes in it within the frame-work of numerical forecast models. Such work has been recently summarized by the European Centre for Medium Range Weather Forecasts (1976). But also the research of the effect of urban areas on the climate in the immediate environment requires a basic physical understanding of the physical processes taking part within the boundary layer. Such work earned increasing interest as the general interest for environmental problems increased (e.g. Chandler, T.J., 1976).

Within the context of this meeting also an exact physical modeling of the planetary boundary layer and perhaps a forecast of its vertical structure and perhaps also its turbulent behaviour is of great interest. For instance, within or near inversions the vertical profiles of temperature and moisture exhibit drastic changes, thus effecting the propagation of electromagnetic waves of the cm- and m-regions (Jeske, H., 1965; Früchtenicht, H.W., 1971). Horizontal communication lines will have major profit from an exact forecast of such properties, e.g. of the profiles of the refraction index. This includes also the evaporation ducting frequently observed over the oceans. This paper does not present a general survey on recent research of the properties of the planetary boundary layer. Such results are reviewed in recent publications by Businger (1973) or by Tennekes (1973). Instead, it contains the description of a time-dependent and baroclinic boundary layer model, which could be used for short-range forecasts of the vertical temperature and moisture structure - and thus also the refractive index.

2. The model

The model makes use of the Boussinesq-approximation and considers all processes as instationary. It is horizontally homogeneous, but baroclinic. Its original version for a barotropic model atmosphere has been developed by Venkatram and Viskanta (1975). These authors determine the turbulent exchange with the equation for turbulent kinetic energy E , as derived by Monin and Yaglom (1971). It is

$$\bar{E} = \frac{1}{2} (\overline{u'^2} + \overline{v'^2} + \overline{w'^2}) \quad (1)$$

where u' , v' , w' are small deviations from the respective mean wind components. The total change of E with time is given by

$$\frac{DE}{Dt} = \frac{\partial}{\partial z} (F^{1/2} \& \frac{\partial E}{\partial z}) + F^{1/2} \& \{ (\frac{\partial u}{\partial z})^2 + (\frac{\partial v}{\partial z})^2 \} + F^{1/2} \& \frac{\alpha}{\gamma} \frac{\partial}{\partial z} (\frac{\partial \theta}{\partial z} - \gamma) - \epsilon \quad (2)$$

where $\&$ is the mixing length and γ is the so-called counter gradient (Deardorff, J.W., 1966); g , T are the gravitational acceleration and temperature, respectively. The first three terms on the right-hand-side of eq. (2) determine the divergence, shear production and thermal production of turbulent kinetic energy, the last term describes its dissipation. It is

$$\epsilon = c F^{3/2} / \& \quad (3)$$

where c has to be determined experimentally. $c = 0.09$ is a commonly accepted value (Launder and Spalding, 1972). We assume the ratio for the exchange coefficients for heat and momentum as constant (as derived by Businger et al. (1972)) for neutral stratification.

$$\alpha = \frac{K_H}{K_M} = 1.35 \quad (4)$$

It is further after Blackadar (1962)

$$K_M = \epsilon^{1/3} l^{4/3} \quad (5)$$

where the mixing length l depends on the height of the planetary boundary layer. The height is determined by the energy and momentum fluxes at the surface, but also by the gradients of the wind and temperature fields above the inversion, capping the boundary layer.

In the equation of motion we consider the baroclinicity as expressed by the geostrophic wind shear Δu (x-direction) and Δv (y-direction)

$$\begin{aligned} \frac{\partial u}{\partial t} &= \frac{\partial}{\partial z} (K_M \frac{\partial u}{\partial z}) + f(v - (v_g + \Delta v \cdot z)) \\ \frac{\partial v}{\partial t} &= \frac{\partial}{\partial z} (K_M \frac{\partial v}{\partial z}) - f(u - (u_g + \Delta u \cdot z)) \end{aligned} \quad (6)$$

u_g and v_g describe the geostrophic wind components at the surface and f is the Coriolis parameter.

The diabatic heating of the model by solar and terrestrial radiation has been computed with a modified two stream approximation (Kerschgens et al., 1978) and in the infrared by a simplified flux equation model, which is similar to that by Rodgers and Walshaw (1966). The diurnal variation of the solar zenith angle is considered with time steps of one minute.

The equations of motion and equations for the conservations of energy and moisture have been solved with a finite difference approximation. A first order finite difference scheme has been used to solve the equation for turbulent kinetic energy.

3. Some results

Results have been obtained for the following boundary conditions:

thermal diffusion in the ground = $1.33 \cdot 10^{-2} \text{ cm s}^{-1}$
(Verkatram, A., et al., 1976)

evaporation at the surface: as determined by the Halsteadt
parameter $H = 0.1$ (Halsteadt, M.R., et al., 1957)

Coriolis parameter $f = 1.11 \cdot 10^{-4} \text{ s}^{-1}$

The initial conditions are based on synoptic observations and a radiosonde sounding obtained on July 11th, 1977 at noon (13.00 GMT) over Cologne, Germany. At this particular day the large scale circulation over that area was determined by an anticyclone with warm air advection; the geostrophic wind at ground was about 10 ms^{-1} , the height of the boundary layer amounted to 1800 m.

In these model considerations we prescribe the baroclinicity (Fig. 1) by

$\beta = 120^\circ, 300^\circ$ (β - angle between the geostrophic
wind at the surface and the thermal
wind)

and the wind shear magnitude

$$(\Delta u^2 + \Delta v^2)^{1/2} = 5 \cdot 10^{-3} \text{ s}^{-1}$$

and the roughness parameter

$$z_0 = 10 \text{ cm} \quad (\text{roughness parameter})$$

3.1 Effect of the baroclinicity on the height of the planetary boundary layer

Some results on the vertical profiles of magnitudes of the shear and thermal production terms (erg/s) are shown in Fig. 2 for a labile stratification. The inversion height is 1650 m for $\beta = 120^\circ$ (warm air advection) and much smaller for $\beta = 300^\circ$ when artificially a cold air advection is considered. In the first case the wind shear at the lower boundary of the inversion is larger, and thus also the downward entrainment of heat through the inversion. After sunset the height of the boundary layer suddenly breaks down and the nocturnal inversion arises. Fig. 3 shows a comparison of the computed inversion height with that measured by an acoustic sounder on evening of 11th July 1977 over the city of Cologne.

A wind speed maximum is frequently observed at the top of the nocturnal inversion (Lettau, H., 1954; Blackadar, A.K., 1955; Thorpe, A.J., 1977). This sharp maximum is supergeostrophic and is often associated with extremely large values of wind shear. Blackadar (1957) has shown that this inversion wind maximum (also described by Reiter, F.R., 1961) is caused by an inertia oscillation in the region above the inversion, where all the turbulent exchange is suppressed, that only a jet-like profile with a wind maximum at the top of the inversion yields a stable configuration. Whereas, the existence of a wind maximum above the level of the inversion is liable to result in a chaotic breakdown of the inversion.

The model computations show that not only an increasing geostrophic wind with height but also an increasing ageostrophic wind component at the evening and the inertia oscillations of this component at night create a wind maximum several hundred meters above the top of the nocturnal inversion.

During cold air advection ($\beta = 300^\circ$), the ageostrophic component of wind speed decreases with height, as can be observed also for a barotropic atmosphere. But computations assuming warm air advection (the synoptic situation of 11th July) give a growth of the ageostrophic wind component with height.

During the night of the 11th July two breakdowns of the inversion occur in the computations: the first at 22.00, the second at 4.00 local time. Such breakdowns can be found at nearly the same time in the facsimile acoustic sounder chart. About half an hour after breakdown the inversion regenerates and it is distributed among a deeper layer as before.

3.2 Effect of the roughness parameter z_0 on the height of the PBL

For both cases of labile and stable stratification $\beta = 60^\circ$, computations were made assuming a rather smooth surface ($z_0 = 0.1 \text{ cm}$, representative for mown grass) and a very rough surface ($z_0 = 100 \text{ cm}$, representing a city). Figs. 4, 4b and 4c show again vertical profiles of the shear and thermal production terms of turbulent kinetic energy, computed for 8.30, 11.30 and 14.30 local time. In case of stable stratification the roughness lifts the height of the boundary layer from 300 to 550 m, since it is entirely determined by the wind shear. With increasing labilization the thermal production term becomes of increasing importance. However with increasing roughness the evaporation also rises, lowering then the flux of sensible heat. Thus the PBL grows faster over areas with lower roughness.

4. Conclusions

This is a one-dimensional boundary layer, where baroclinicity is introduced. Its results, however, exhibit the behaviour of the PBL as it can be also quite frequently observed. In this paper we demonstrate the results with the aid of two terms of the equation of turbulent kinetic energy (2). In the oral presentation our discussions will be extended to the effect of these changes on the stratification of the refractive index in the microwave region.

5. References

- Blackadar, A.K., 1955, "The Low Level Jet Phenomenon", Institute of the Aeronautical Sciences Reprint No. 519.
- Blackadar, A.K., 1957, "Boundary Layer Wind Maxima and Their Significance for the Growth of Nocturnal Inversions", Bull. Amer. Meteor. Soc., vol. 38, pp 283-290.
- Blackadar, A.K., 1962, "The Vertical Distribution of Wind and Turbulent Exchange in a Neutral Atmosphere", J. Geophys. Res. 67, pp 3095-3102.
- Businger, J.A., 1972, "Turbulent Transfer in the Atmospheric Surface Layer", Workshop in Micrometeorology, D.A. Haugen, Ed., Amer. Meteor. Soc., Boston, pp 67-100.

- Centre for Medium Range Weather Forecasts, 1976, "Seminars on the Treatment of the Boundary Layer in Numerical Weather Prediction", Reading 6-10th September 1976.
- Chandler, T.J., 1976, "Urban Climatology and its Relevance to Urban Design", Technical Note No. 149, WMO, Geneva.
- Deardorff, J.W., 1966, "The Counter-Gradient Heat Flux in the Lower Atmosphere and in the Laboratory", J. Atm. Sci., 23, pp 503-506.
- Früchtenicht, H.W., 1971, "Atmosphärische Einflüsse auf die Ausbreitung elektromagnetischer Wellen (cm-Band) über See innerhalb des radioptischen Horizonts", Hamburger Geophys. Einzelschriften, Heft 14.
- Halstead, M.R., Richman, R., Covey, W., and Merriman, J., 1957, "A Preliminary Report on the Design of a Computer for Micrometeorology", J. Meteor. 14, pp 308-325.
- Jeske, H., 1965, "Die Ausbreitung elektromagnetischer Wellen im cm- bis m-Band über Meer unter besonderer Berücksichtigung der meteorologischen Bedingungen in der maritimen Grenzschicht", Hamburger Geophys. Einzelschriften, Heft 6.
- Kerschgens, M., 1978, "Berechnungen des solaren Strahlungstransports in Atmosphäre und Ozean mit Hilfe einer Zweistrommethode", Inaugural-Dissertation zur Erlangung des Doktorgrades der Math./Nat. Fak. der Univ. zu Köln.
- Launder, B.E., and Spalding, D.B., 1972, "Lectures in Mathematical Models of Turbulence", Academic Press, London and New York.
- Lettau, H., 1954, "Graphs and Illustrations of Diverse Atmospheric States and Processes Observed During the Seventh Test Period of the Great Plains Turbulence Field Program", Occasional Report No. 1, Atmospheric Analysis Laboratory, Air Force Cambridge Research Center.
- Monin, A.S., and Yaglom, A.M., 1971, "Statistical Fluid Mechanics of Turbulence", Vol. 1, The M.I.T. Press, Cambridge, Mass..
- Reiter, E.R., 1961, "Meteorologie der Strahlströme", Wien, Springer Verlag.
- Rodgers, C.D., and Walshaw, C.D., 1966, "The Computation of Infrared Cooling Rate in Planetary Atmospheres", Qu. J. R. M. S., 92, pp 67-92.
- Tennekes, H., 1972, "Similarity Laws and Scale Relations in Planetary Boundary Layers", D.A. Haugen, Ed. Amer. Meteor. Soc., Boston, pp 177-214.
- Thorpe, A.J., Guymer, T.H., 1977, "The Nocturnal Jet", Qu. J. R. M. S., 103, pp 633-655.

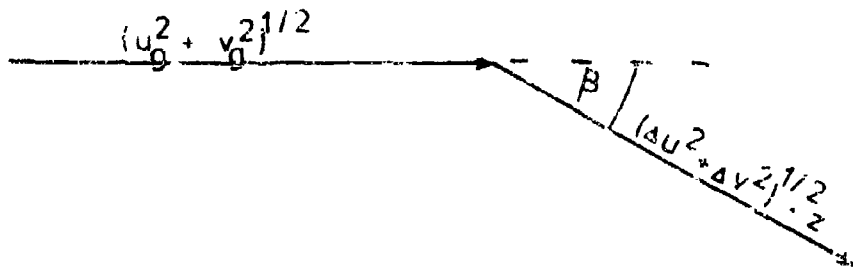


Fig.1. The angle β between the surface geostrophic wind and the thermal wind shear.

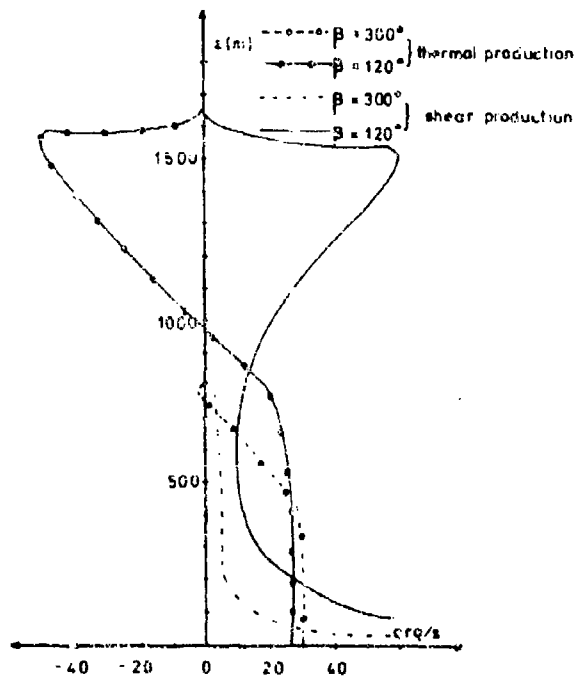


Fig.2: The computed thermal and the shear production terms (equation 2) and the inversion height at 14.30 local time for warm air advection ($\beta = 120^\circ$) and cold air advection ($\beta = 300^\circ$).



Fig.3: Acoustic sounder facsimile obtained during the 11 - 12 July 1977 over Cologne, Germany and the computed lapse rate.

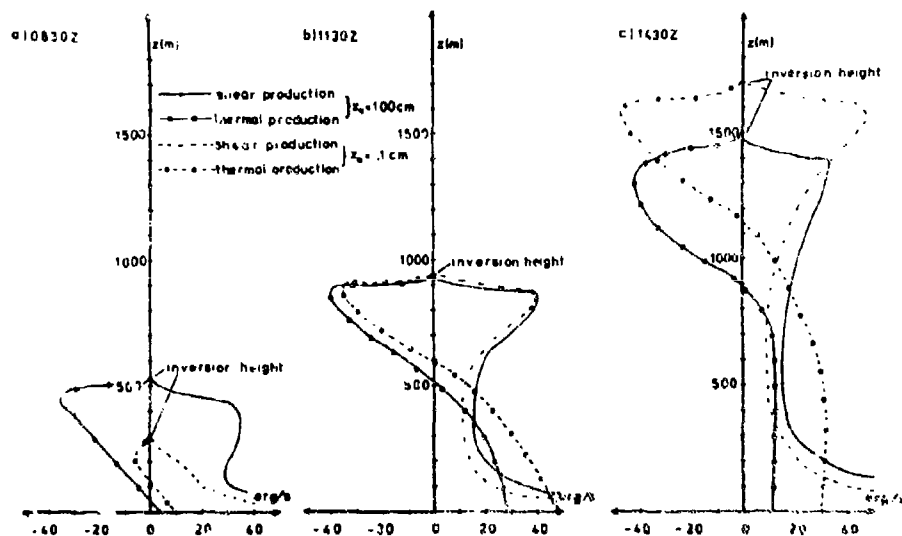


Fig.4: the shear and thermal production terms (e.g. equation 2) and the inversion height at 8.30, 11.30, 14.30 local time computed for two different values of the surface roughness ($z_0 = 0.1, 100$ cm).

DISCUSSION**M. Tavis, US**

Do you have any comment on the possibility of the effect of gravitational waves on the inversion layer causing scintillation of received microwave signals at low observation angles, i.e., 5° .

Author's Reply

As far as I know, the decrease or increase of inversion height is often combined with gravitational waves as measurements of an acoustic sounder system indicate. But, I can give no comment about the effects on the mentioned wave propagation problem. At this particular point, I must refer to the author, W. Behnke.

SUMMARY OF SESSION VIII
OPTICAL SYSTEMS/PROJECTS

by

Dr L.F.Drummeter
Session Chairman

The session provided several views of programs which are concerned with: either the acquisition of data for the verification or improvement of propagation models, or the generation of modelling procedures for evaluating or predicting optical system performance.

The emphasis is in the region of the lower atmosphere. The US Navy outlined two widely different programs. The work of Dowling et al and Trusty and Cosden, from the US Naval Research Laboratory is concerned with the acquisition of field data to help improve the well-known HITRAN and LOWTRAN models of the Air Force Geophysics Laboratory. The program of Katz and Hepfer, of the Naval Surface Weapons Center, is designed to provide statistical performance prediction capability for at-sea electro-optical systems.

The work of the US Army Atmospheric Sciences Laboratory, as described by Gomez, is concerned with problems of the battlefield environment on electro-optical systems. The large scale effort involves laboratory measurements, field measurements, modelling, etc. in a complicated area. In Europe, somewhat similar concerns are developed under the OPAQUE project which has major measurement programs underway. In Germany, H. von Redwitz et al from the Institute für Physik der Atmosphäre (DFVLR) have had a program for airborne photometric measurements which help connect scattered OPAQUE stations through visibility-type information.

Also in Germany, Abele et al from the Forschungsinstitute für Optik have been examining transmission in the important CO₂ region and comparing it to visible transmission. It appears predictions from visible to 10 μ meters are not adequate -- an important operational finding.

IN ATMOSPHERIC MEASUREMENTS AND APPLICATION

TO MODELING

I - Precision Atmospheric Transmission Measurements and Model Comparisons

J. A. Dowling, J. A. Curcio, S. T. Hanley,
R. F. Horton, K. M. Taught, D. H. Garcia,
A. Guttman, C. O. Gott and W. L. Aganbar

Naval Research Laboratory
Washington, D. C. 20375

SUMMARY

Extensive field measurements of atmospheric extinction at several infrared laser wavelengths have been performed using procedures and facilities described in this paper. Recent additions to these experiments include a high resolution Fourier transform spectrometer (FTS) and a gas filter correlation spectrometer (GFCS) which uses H₂O as the filter gas. The combination of laser extinction, FTS and GFCS measurements provide well characterized and precisely calibrated high resolution transmission spectra useful in comparisons to computational models. Examples of comparisons between these data and line-by-line computer calculations for several spectral regions are presented and discussed.

1. INTRODUCTION

For several years, NRL scientists have been conducting field experiments dealing with atmospheric propagation of infrared laser beams. Earlier experiments were designed to study the effects of beam spreading and beam wander caused by atmospheric turbulence (Dowling, J. A., and P. M. Livingston, 1973). Recently, measurements of atmospheric extinction at several laser wavelengths of interest to the Navy High-Energy Laser Project—primarily those of the DF laser operating near 3.8 μ m—have been emphasized.

During 1975, two extensive experiments were conducted at coastal sites in Florida and later in California. The Florida experiment followed initial DF laser transmission measurements performed at the Cape Canaveral Air Force Station (CCAFS) early in 1974. The California experiment was performed in conjunction with high-power, DF laser propagation tests conducted during the Joint Army-Navy Propagation Experiments at the IRW Capistrano Test Site during May through October 1975. (Dowling, J. A., et al, 1977).

Several hundred measurements of DF and Nd-YAG laser transmission, along with supporting meteorological data, were used to test the validity of transmission predictions based on a line-by-line computer code calculation. The results of comparisons of the field measurements with predictions based on a Hi-TRAN type calculation using the AFGL spectral line atlas are summarized in this article.

Recent modifications to the trailer-based measurement system used in the earlier Florida and California experiments include two significant additions; a) a high-resolution atmospheric measurement capability based on a Fourier transform spectrometer (FTS) system and a gas-filter correlation spectrometer (GFCS).

This paper describes the apparatus used in the three types of measurements, the philosophy underlying the experiments, and the more important results obtained in recent studies. Examples of data collected in these experiments are used to illustrate the application of high resolution transmission measurements to the understanding and accurate modeling of infrared laser and infrared target signature propagation.

2. LASER EXTINCTION MEASUREMENTS

The Infrared Mobile Optical Radiation Laboratory (IMORL) used to collect the laser calibrated high-resolution atmospheric transmission spectra discussed in this paper comprises several infrared laser and blackbody sources, large, stable telescope optics, a scanning Michelson interferometer (SMI) system, and various support equipment, all of which are transported in and operated from several large semi-trailers. The usual measurement configuration consists of an optical transmitter trailer housing HeNe, Nd-YAG, DF, CO, and CO₂ single-line cw laser sources, relay optics, and a large stably-mounted and precisely-pointed 91 cm aperture, f/35 Cassegrain collimating telescope. The small cw combustion-driven DF laser used for much of the laser extinction work previously carried out requires a large (1600 cfm) vacuum system for operation. This pump is housed in a separate trailer; a 20 cm diameter, vacuum line is installed once the two trailers are properly located at the measurement site. Two additional trailers contain office space, meteorological signal processing and recording electronics, and bottled gas and other consumable supplies used during the course of an experiment.

The FTS system and apparatus used for laser extinction measurements is housed in a receiver trailer which contains a 120 cm aperture, f/5 newtonian telescope. The large receiver telescope aperture insures that the entire laser beam used during long path (typically 5 km) extinction measurements can be entirely collected, thereby providing reliable absolute transmission calibrations for the FTS measurements. High resolution transmission spectra are taken by substituting a 1300 K blackbody source for the laser source in the transmitter optical system and adjusting the receiver optical system so as to couple the FTS system to the 120 cm collecting telescope. Repeated calibrations and extensive experience with this measurement system in field experiments have demonstrated that absolute transmission can be readily measured for long atmospheric paths with an uncertainty less than $\pm 3\%$.

Figure 1 is a photograph of the transmitter station taken during a recent experiment at the Patuxent Naval Air Station, Patuxent River, Maryland. From left to right in the figure can be seen an office trailer and meteorological system electronics, vacuum pump trailer, optical transmitter trailer (the 91 cm aperture telescope frame may be seen through the open doors), and the supply trailer respectively.

Figure 2 is a schematic depicting the experimental arrangement used for laser extinction measurements. The output beam from any of the several laser sources used is first collimated by auxiliary optics to a diameter of approximately 18 mm. The beam is then focused via the off-axis parabolic mirror shown in the upper left and then diverged to fill the 91 cm transmitter telescope aperture. A 37 Hz, 50% duty cycle chopper modulates the beam near the focus formed by the off-axis parabola. The beam is alternately transmitted through the telescope and reflected onto the stationary detector as shown. The Mobile detector shown in the figure is placed in the "XMTR" position for calibration measurements in which the relative response of the two detectors is measured. The mobile detector is then placed near the focus of the 120 cm aperture receiver telescope for a) calibration of the large telescope optical efficiencies or b) long path extinction measurements. The calibration measurements are carried out with the transmitter and receiver trailers immediately opposite one another, i.e. for \sim zero atmospheric path. When the trailers are separated for long path measurements the two types of calibration data are then used to determine absolute atmospheric transmission for the several laser lines studied. The signal produced by the mobile detector in the receiver trailer at one end of the measurement path is relayed to the transmitter by means of a pulse-rate-modulated (PRM) GaAs-laser-based data link. This signal, proportional to laser power at the receiver, is connected to the numerator input of a special purpose analog ratiometer. The stationary detector signal, proportional to the transmitted laser power is connected to the denominator input of the ratiometer. Thus, a real time measure of transmission for the laser line being studied is available at the transmitter site. The ratiometer reading must be corrected for the relative response of the two detectors for that laser line (monitored daily) and the efficiency of the large optical elements beyond the chopper in order to obtain absolute transmission readings. As shown in Figure 2, the voltage-controlled oscillator (VCO) and frequency-to-voltage (FVC) converter used with the GaAs data link are also connected in the numerator circuit of the ratiometer when the mobile detector is used in the "XMTR" position, so that their combined transfer function is normalized out of the final extinction ratio.

A comparison between observed extinction (which includes aerosol scattering effects) and calculated molecular absorption for 22 DF laser lines between 3.6 and 4.1 μ m is shown in Figure 3. One would expect a constant offset between the two sets of points, due to aerosol scattering. As seen in the figure, the agreement is quite good when the trends between the two sets of points are compared.

Data from both the Florida and California experiments, such as that in Figure 3, were corrected for aerosol effects and compared with molecular absorption calculations. An example of such a comparison for the PL-8 DF laser line is shown in Figure 4. The squares are data taken at Cape Canaveral, Florida, the crosses are data taken at the TRW Capistrano Test Site, California.

A summary of comparisons such as shown in Figure 4 is presented in Table I for the midlatitude-summer water-vapor partial pressure of 14.26 Torr. Column five of the table lists the differences between measured and calculated absorption coefficients for each of the DF laser lines listed in column one. The calculations utilized recently measured HDO line strengths and widths; the agreements between theory and field measurements are quite good, with the worst case differences remaining about 20%.

3. GAS FILTER CORRELATION SPECTROMETER MEASUREMENTS

Figure 5 illustrates the basic operation of the GFCS device. The average transmission of an atmospheric constituent in the spectral interval $\Delta\nu$ is given by the expression equated to T_a . The energy from a graybody source, spectrally modulated by absorption due to one or more atmospheric constituents, is collected by the receiver optical system. This selectively transmitted energy is alternately passed through a spectrally nonselective attenuation arm with transmission T_R or through a cell containing a known amount of the absorber under study, whose transmission is $T_C(\nu)$. The nonselective transmission (T_R) is initially balanced against the average transmission of the cell during calibration. If the spectral character of the atmospherically transmitted energy resembles that of the cell absorber $T_C(\nu)$, then a difference in transmission and hence a modulation signal will result when the light from the distant source is alternately passed through the GFCS instrument's two arms.

If the atmospheric abundance of HDO along the 5-km path used for the laser extinction and FTS measurements is sampled by the GFCS, then a path integral value for atmospheric water vapor may be obtained by using the isotopic abundance of HDO/H₂O of 0.030%. Since water vapor is an important absorber in the infrared regions of interest for atmospheric transmission studies, this path integral is very important for use in comparisons of transmission data to calculational models. Path integral measurements, like those provided by the GFCS, are particularly useful for overwater transmission experiments where midpoints along the path are not readily accessible to standard dew-point observations.

The GFCS measurement cannot utilize normal water vapor as the filter gas, because an amount of water in a 5-km path at standard conditions cannot be maintained in the vapor state in the local reference cell. However, there is very little HDO in the atmosphere, so that a greatly enhanced concentration of that vapor can be held in a multipass absorption cell. A 5-km path equivalent amount of HDO is contained in the GFCS multipass reference cell, which affords a total path of 40 m.

Figure 5 is a plot of data taken during recent experiments at the Patuxent Naval Air Station, comparing water vapor measurements obtained with the GFCS and EG&G model 110 dew-point hygrometers located on shore at each end of the 5.12-km overwater path. When an HDO/H₂O ratio of 3×10^{-4} is used in reducing the GFCS data, the results are consistently lower than the fixed point measurements, by \sim 30%. Independent HDO/H₂O ratios derived from spectra taken during the GFCS measurements using individual H₂O and HDO spectral lines, together with recent line strength data show that the 3×10^{-4} abundance ratio cannot be universally applied to all sea level locations. This is an important result since the HDO/H₂O ratio profoundly affects DF laser propagation.

4. LASER CALIBRATED FTS MEASUREMENTS

The procedure used in calibrating the relative FTS transmission spectra by means of measured laser-line extinction is illustrated graphically in Figure 7. The upper portion of the figure shows a portion of a transmission spectrum recorded at NATC, Patuxent River, Maryland. The lower portion shows the FTS response to the P1-8 DF laser line at 2717.538 cm^{-1} . By use of the procedures outlined earlier for laser extinction measurements a 52% transmission was measured at this line and used to calibrate the FTS spectra shown. The traces in Figure 7 are copies of records produced by the FTS data system plotter and show actual signal-to-noise ratios observed in the 5-km transmission spectra.

Figure 8 shows results obtained with the FTS system by use of several DF laser transmission-calibration points. The lower portion of the figure shows a calculation of molecular absorption for the conditions listed above the plot. The calculations employ the same HI-TRAN code used in the DF laser line calculations discussed earlier. The overall agreement with measurements is remarkably good throughout this spectral region. Improved agreement is obtained when the $\text{HDO}/\text{H}_2\text{O}$ ratio used in the calculation is reduced to $\sim 2 \times 10^{-4}$, consistent with the GFCs results cited earlier.

Comparisons of experimental spectra to HI-TRAN calculations in several spectral regions have been performed and an example of such a comparison is shown in Figure 9. The upper trace shows a measured transmission spectrum of a 5.1 km path between 1950 cm^{-1} and 2120 cm^{-1} for 12.0 torr partial pressure of H_2O and a visibility of 31 km. The lower trace shows a HI-TRAN calculation for the same conditions. It is readily apparent that the calculated spectrum substantially overestimates transmission in the "clear" sub-intervals near 1980 cm^{-1} , 2000 cm^{-1} , 2030 cm^{-1} , 2070 cm^{-1} , 2085 cm^{-1} , etc. The density of atmospheric absorption lines (mostly H_2O) throughout this region is very high, with the result that only selected sub-intervals show appreciable transmission. However these sub-intervals may be important for low water vapor conditions. The calculated spectrum was generated by using an unmodified Lorentz line shape for the water vapor absorption lines. Based on the comparison shown here, it is possible that the far wing absorption for H_2O lines in this region exceeds that of a pure Lorentz line shape. Work in our laboratory is currently being devoted to studying H_2O line shape variations in this region which can account for the discrepancies shown in Figure 9. It is anticipated that a "super Lorentz" modified line shape will be found which, when used in a HI-TRAN calculation, will generate agreement with the experimental spectrum. Using the variety of experimental spectra already obtained in the NRL measurements and additional data for conditions and ranges of interest which have yet to be examined, a "best fit" modification to the Lorentz line shape for the spectral region shown will be obtained. When incorporated into the HI-TRAN calculation, reliable transmission predictions will be available for the laser propagation and plume signature applications as well as other transmission related problems occurring in this spectral region.

Measured transmission for the region 2578 cm^{-1} to 2573 cm^{-1} is shown in the upper portion of Figure 10. A calculated spectrum for the measurement conditions is shown in the lower portion. The calculation was carried out using the modified line shape suggested by Winters, Silverman, and Benedict, (Winters, B. H., et al, 1964) and confirmed by Burch, et al. (Burch, D. E., et al 1969). A significant difference exists between calculated and measured spectra in the CO_2 band edge region. Work is currently underway to obtain a modified line shape which results in a closer fit to the experimental observations. The problem is complicated by the presence of an N_2 pressure-induced continuum absorption which becomes more important than the CO_2 wing absorption for higher wavenumbers beyond $\sim 2420\text{ cm}^{-1}$ and gives rise to the shape of the absorption envelope shown in Figure 10 out to approximately 2500 cm^{-1} . The $3\text{--}5\text{ }\mu\text{m}$ water vapor continuum absorption which has been studied by Burch, et al (Burch, D. E., et al, 1974) and by Watkins and White (Watkins, W. R., and White, K. O., 1977) contributes absorption throughout the higher transmission region shown in the figure, although the empirical expressions representing laboratory measurements have been carried out for the region between 2400 cm^{-1} and 2600 cm^{-1} . Based on an examination of several long path transmission spectra measured for absolute humidities ranging between 2 and 20 torr of H_2O , the water vapor contribution to absorption in the CO_2 band edge region is secondary, changing the transmission by less than 10% at 2935 cm^{-1} over the observed range in water vapor partial pressures.

Figure 11 shows a HI-TRAN calculation for the conditions specified in the figure without the inclusion of a calculated $3\text{--}5\text{ }\mu\text{m}$ H_2O continuum. Note that there are several locations where $> 96\%$ transmission is measurable over the 5 km path for a water vapor partial pressure of 12 torr. (e.g. 2510 cm^{-1} , 2603 cm^{-1} , 2615 cm^{-1} , 2668 cm^{-1} , etc.) By examining high resolution spectra recorded for high visibility conditions, these maximum transmission locations constitute a useful approximation to the $3\text{--}5\text{ }\mu\text{m}$ H_2O continuum absorption. Maximum transmission values for several spectra corresponding to a range of water vapor partial pressures between 2 and 18 torr have been determined throughout the $3\text{ to }5\text{ }\mu\text{m}$ region. These data show the water vapor dependence of the window envelope and correspond to H_2O continuum limited transmission in the region 2400 cm^{-1} to 2800 cm^{-1} but are strongly affected by local line wing contributions below 2400 cm^{-1} and above 2920 cm^{-1} . Outside this region the transmission peaks define a maximum transmission envelope and the edges of the $3\text{--}5\text{ }\mu\text{m}$ window.

Figure 12 is a plot of experimental peak transmission values extracted from measured long-path spectra for the several values of water vapor indicated in the figure. In each case the measured visibility exceeded 30 km. The peak transmission values are shown for the entire $3\text{--}5\text{ }\mu\text{m}$ window in order to demonstrate the strong dependence of the window edges upon absolute humidity. The region between 2950 cm^{-1} and 3150 cm^{-1} is consistently opaque for all but very low values of water vapor while transmission across the long wavelength edge between 2000 cm^{-1} and 2200 cm^{-1} changes rather uniformly with changes in absolute humidity.

Figure 13 shows a comparison of smooth curves representing the 2, 12, and 18 torr (H_2O) data shown in Figure 12 to the continuum model of Burch et al. (Burch, D. E., et al 1974). The experimental data exhibit a flatter behavior throughout the region 2500 cm^{-1} to 2900 cm^{-1} than does the calculation. The magnitude of the Burch model is close to the observed values for 12 torr near 2500 cm^{-1} but shows considerably less absorption throughout the rest of the region and poorer agreement for humidities higher or lower than 12 torr.

Figure 14 is a comparison of the same peak transmission curves to the continuum model of Watkins and White (Watkins, W. R., and K. O. White, 1977). This model shows better agreement with the field measurements at 12 torr throughout the entire spectral range although the curves derived from the long path data are consistently flatter than the model for water vapor pressures of 12 torr and higher. Near 2800 cm^{-1} the Watkins and White model shows higher absorption for 12 and 18 torr than does the field data which are relatively flat out to 2920 cm^{-1} .

We have used several examples of high accuracy, long path atmospheric transmission spectra to demonstrate the importance of this information for understanding various infrared atmospheric transmission problems. Laser propagation and infrared target signature transmission calculations must be carried out using an accurate, high-resolution model to properly account for individual line effects in the interaction of the source emission with the absorbing atmosphere. Infrared surveillance and imaging systems operating in moderately wide spectral bands may be affected by spectrally uniform absorptions in the atmospheric windows, therefore such continua must be accurately modeled as well. The use of laser-extinction-calibrated, high-resolution data for continuum estimates and comparisons to current model values has been discussed and significant variations with calculations identified. While the line-by-line correspondence of measured and calculated spectra are generally in excellent agreement, several variations between measured spectra and HI-TRAN calculations have been identified and work directed toward the derivation of improved line parameters and an empirical representation of the 3-5 μm H_2O continuum, based on the long path atmospheric measurements is in progress.

A REVIEW OF THE NAVAL RESEARCH LABORATORY PROGRAM

IN ATMOSPHERIC MEASUREMENTS AND APPLICATION

TO MODELING

II - Aerosol Size Distributions for Modeling and the Prediction of Optical Extinctions

Gary L. Trusty and Thomas H. Cosden

Naval Research Laboratory
Washington, D. C. 20375

SUMMARY

In the winter of 1975 the Optical Radiation Branch of NRL was making outdoor, long-path, laser transmission measurements. As part of that measurement program we began assembling instruments which could monitor the aerosol that contributed to the laser extinction. This paper will give a brief description of the resultant aerosol-monitoring Mobile Laboratory in its present state of development and will present an overview of the many particle size distributions obtained in various locations in the last three years.

1. INSTRUMENTATION

Particle Measuring Systems Particle Spectrometers measured the aerosol size distributions. These probes function as part of the Mobile Laboratory schematic shown in Figure 15, which indicates two primary sets of sensors. The meteorological set on the upper left includes devices for monitoring air temperature, dewpoint, wind speed and wind direction. On the upper right are two Particle Spectrometers. One is an Active Aerosol Spectrometer Probe, which measures particles in the size range of 0.1 to 2.0 micrometer radius. The second is a High Volume Classical Scattering Probe, which covers a size range of 1.0 to 15 micrometer radius. The electronics which handle the data from the sensors are in the Mobile Laboratory and are illustrated in three columns. The center column shows the Particle Measuring Systems (PMS) electronics, which include the data buffer and a digital magnetic tape where the information from all sensors is stored every second.

Simultaneously, the system feeds the information into the PDP 11/34 Data Acquisition System for real time processing. The user may specify averaging times. Data reduction includes the generation of aerosol size distributions from the probe data and the calculation, from these distributions, of extinction coefficients for five arbitrary wavelengths by the Mie scattering theory. A disc stores resultant extinction coefficients, size distributions, and averaged meteorological parameters at the end of each averaging period; this data later produces time plots or cross-correlation plots.

2. EXPERIMENTAL RESULTS

Figure 16 an example of real time output from the computer program. The top line shows the year, day, time of day, and the averaging time. The next line of numbers gives the air temperature, dewpoint, wind speed, wind direction, barometric pressure, partial pressure of water vapor, and the relative humidity. The plot is dN/dR plotted versus R in a log-log form, where N is the particle concentration and R is the particle radius.

The on-line program uses the distribution to calculate in real time, the particle number density, the cross-sectional area density, and the volume density. The results of those calculations appear directly beneath the plot. Finally, from the distribution, the extinction coefficients at five wavelengths are calculated in real time, as shown on the last line. These extinction coefficients, obtained from Mie theory, give only the extinction due to the aerosols; no molecular absorption or Rayleigh scattering is included.

Figure 17 is a list of the twelve field experiments where we have obtained aerosol size distribution data. They include inland, coastal, and open sea locations. Those marked with the circled crosses indicate the locations reported in this paper.

As the first example, Figure 18 is a set of size distributions obtained on the open sea 65km off the coast of Nova Scotia. These result from the ship encountering a fog bank. Distributions are shown for the aerosol outside, near the edge, and inside the fog. Note that for the three locations the shape of the distributions are quite similar except for the bimodal property of the curve for the INSIDE case.

Figure 19 shows another set of distributions obtained on the ship cruise of the previous example. The circles indicate a distribution from the middle of the North Atlantic. The triangles are for an aerosol in the middle of the Mediterranean. Note that neither display an obvious sea-spray hump in the large particle region. The solid curve denotes the Maritime Aerosol used in LOWTRAN 3B.

Figure 20 is an example of data for a beach environment, obtained on the coast of Florida. The variation in the three curves seems to be a result of different relative humidity and wind direction conditions. The diamonds are for a low humidity case where the wind was primarily from the open sea, but in such a direction that it was nearly parallel to the beach at the point of measurement; very little surf existed. The solid circles are for a case of wind from the land, again of low humidity. The circled crosses are for wind from the sea nearly normal to the beach; the surf spray blew directly toward the particle counters.

Although the distributions of the last example seem to have quite different shapes, when we calculate the extinction coefficients as a function of wavelength as shown in Figure 21 we find those resultant curves to be quite similar. This is, however, not the usual case, as the next example will show. (The calculated points are for the wavelengths of 0.55, 1.05, 3.8, and 10.0 micrometers.)

Before going further, we should point out that results from measurements with humidities less than 70% are suspect in several ways. The size distributions are suspect in themselves because low humidity causes an uncertainty in both the index of refraction and the sphericity of the particles. The particle counters are not strongly sensitive to index changes because of the near-forward scattering angles used in the measurement process. However, they are certainly affected by the sphericity. The second stage of uncertainty comes in the calculation of the extinction coefficient. Here both the index and the sphericity affect the answer. A sensitivity study of index changes can give an estimate of the effect for that portion of the problem, but the effect of the sphericity is harder to predict.

Thus, we consider our results here to be good for the higher humidity cases, but to have obvious problems for conditions of low humidity. However, in the general references to distribution shapes, although several of those shown have low humidities, similar examples exist with high humidities, such that the comments still pertain.

Figure 22 shows two distributions from a series of measurements at Dahlgren, Virginia on the banks of the Potomac River. Although the large size counts are nearly identical, the smaller particles are much more numerous for the higher humidity case. Wind and temperature conditions were similar for the two measurement periods.

Figure 23 shows calculated curves for extinction coefficients from the distributions shown in Figure 22. Here, the curves are quite different. Note, in particular, that an attempt to predict the IR extinction from a visibility measurement would not produce satisfactory results for both cases; i.e., the ratios of visible to IR are definitely not the same for the two cases.

The distributions shown in Figure 24 were measured at a site 6.5km inland from San Clemente, California. The solid circles are representative of the typical aerosol we measured over a two week period on a twenty four hour basis. The circled crosses show the distribution from an unusually clear day; Santa Catalina Island, at a distance of 80km, could be seen clearly. A morning fog is responsible for the distribution shown by the diamonds. Because of the large number of particles beyond the limits of the counters an extinction calculation for the fog case would not be accurate. To correct this deficiency, we have recently added a third counter will extend the particle size range to 150 micrometers radius.

The two distributions shown in Figure 25 were obtained at the NRL Chesapeake Bay Division, 60km east of Washington, D.C. The circled crosses show a distribution which is typical of a clear winter day in the area. The solid circles denote a measurement result which was actually obtained from a light fog, even though the distribution is not typical of other fogs we have measured. The primary difference is the lack of large particles. For this case an extinction calculation for the fog would not be confronted with the accuracy problem mentioned before.

The distribution comparison shown in Figure 26 shows two winter measurement results from similar locations 60km apart on the Chesapeake Bay. These are presented together because the distributions cross in the center, making the difference in the overall slopes obvious.

Similarly, the extinction coefficient curves shown in Figure 27, derived from the distributions in Figure 26 also cross, indicating once again, the difficulty of predicting IR extinction from visibility measurements alone.

3. CONCLUSIONS

The purpose of presenting this paper is twofold: One is to show the widely varying shapes a particle size distribution can assume--even in seemingly similar clear air conditions. The other is to report to the community that we have an enormous collection of aerosol size distributions which will soon be available. These distributions were obtained over a wide variety of documented conditions in different locations. Hopefully, these data will prove useful in the validation of aerosol models.

References

- Dowling, J. A. and P. M. Livingston, 1973 "The Behavior of Focused Beams in Atmospheric Turbulence: Measurements and Comments of the Theory," J. Opt. Soc. Am. 63, 846 (1973).
- Dowling, J. A., K. M. Haught, R. F. Horton, G. L. Trusty, J. A. Curcio, T. H. Cosden, S. T. Hanley, C. O. Gott and W. L. Agambar, "Atmospheric Extinction Measurements at Nd-YAG and DF Laser Wavelengths Performed in Conjunction with the JAN Propagation Tests, June-September 1975." NRL Report 8058, Naval Research Laboratory, Washington, D. C., February 1977.
- Winters, B. H., S. Silverman, and W. S. Eenedict, "Line Shape in the Wing Beyond the Band Head of the 4.3 μ m Band of CO₂," J. Quan. Spectroscopy and Radiative Transfer, 4 527 (1964).
- Burch, D. E., D. A. Gryvnak, and J. D. Pembroke, "Investigation of the Absorption of Infrared Radiation by Atmospheric Gases: Water, Nitrogen, Nitrous Oxide," Philco-Ford Aeronautronic Division Report U-4784, (AFCRL-71-0124) Air Force Geophysics Laboratory, Hanscomb AFB, Massachusetts, (January 1974).
- Burch, D. E., D. A. Gryvnak, R. R. Patty, and C. E. Bartky, "Absorption of Infrared Radiant Energy by CO₂ and H₂O. IV. Shapes of Collision Broadened CO₂ Lines," J. Opt. Soc. Am. 59, 267 (1969).
- Watkins, W. R. and K. O. White, "Water-Vapor-Continuum Absorption Measurements (3.5-4.0 μ m) Using HDO-depleted Water," Opt. Ltrs. 1, 31 (1977).

List of Tables

- Table 1. Comparisons of Measured and Calculated Molecular Absorption for 22 DF Laser Lines for a Water Vapor Partial Pressure of 14.26 torr.

List of Figures (Part I)

- Figure 1. Transmitter Station for Long Path Laser Extinction Measurements. From Left to Right: Office Trailer and Meteorological System Electronics, Vacuum Pump Trailer, Optical Transmitter Trailer, Supply Trailer.
- Figure 2. Schematic for Laser Extinction Measurement Configuration.
- Figure 3. Comparison of Measured Extinction and Calculated Molecular Absorption for 22 DF Laser Frequencies.
- Figure 4. Comparison of Measured and Calculated Molecular Absorption Versus Water Vapor Partial Pressure for the P1-8 DF Laser Line.
- Figure 5. Operational Schematic for the HDO Gas Filter Correlation Spectrometer.
- Figure 6. Comparisons of GFCS and Dew-point Hygrometer Water Vapor Measurements.
- Figure 7. Fourier Transform Spectrometer Measurements of a Greybody Source (upper trace) and the P1-8 DF Laser Line (lower trace) over a 5.1 km Path.
- Figure 8. Comparison of Measured DF Laser-Calibrated Transmission Spectra to HI-TRAN Calculations.
- Figure 9. Comparison of Measured and Calculated Transmission Spectra of a 5.1 km Path Between 1950 cm^{-1} and 2120 cm^{-1} for 12.0 torr H_2O and 31 km Visibility.
- Figure 10. Comparison of Measured and Calculated Transmission Spectra of a 5.1 km Path Between 2400 cm^{-1} and 2578 cm^{-1} for 12.0 torr H_2O and 31 km Visibility.
- Figure 11. Calculated Transmission of a 5 km Atmospheric Path for 12.0 torr Partial Pressure of H_2O Excluding a Water Vapor Continuum Calculation.
- Figure 12. Experimental Peak Transmission Values Between 2000 cm^{-1} and 3200 cm^{-1} Derived From Long Path High Resolution Transmission Spectra.
- Figure 13. A Comparison of Data Shown in Figure 12 to the N_2 Continuum and H_2O Continuum Models of Burch, et al (see text for reference).
- Figure 14. A Comparison of Data Shown in Figure 12 to the N_2 Continuum Model of Burch, et al, and the H_2O Continuum Model of Watkins and White (see text for reference).

List of Figures (Part II)

- Figure 15. Mobile Aerosol Measurement Laboratory Schematic.
- Figure 16. Example of Real Time Output of Aerosol Distribution Measurement.
- Figure 17. List of Recent Field Operations Conducted by the Laser/Aerosol Interaction Section, Optical Radiation Branch (NKL Code 5565).
- Figure 18. Aerosol Distribution Measurements Obtained on the Open Sea.
- Figure 19. Measured Aerosol Distributions from the North Atlantic (circles) and the Mediterranean (triangles) Compared to the Maritime Aerosol Model Used in LOWTRAN 3B.
- Figure 20. Aerosol Distribution Measurements Obtained on the Coast of Florida for Different Relative Humidity and Wind Conditions.
- Figure 21. Extinction Coefficients for Various Wavelengths Calculated from the Data Shown in Figure 20.
- Figure 22. Aerosol Distributions from a Series of Measurements at Dahlgren, Virginia.
- Figure 23. Extinction Calculations for Four Wavelengths Based on the Data Shown in Figure 22.
- Figure 24. Aerosol Distributions Measured at a Site 6.5 km Inland from San Clemente, California.
- Figure 25. Aerosol Distributions Measured on the Shore of the Chesapeake Bay, 60 km East of Washington, D. C.
- Figure 26. A Comparison of Aerosol Distributions Measured at Two Locations on the Shore of the Chesapeake Bay During Winter Conditions.
- Figure 27. Extinction Calculations for Four Wavelengths Based on the Data Shown in Figure 26.

Table 1. Comparisons of Measured and Calculated Molecular Absorption for 22 DF Laser Lines for a Water Vapor Partial Pressure of 14.26 torr.

LINE	POSITION (cm ⁻¹)	α (km ⁻¹)		(EXP-CAL)/CAL % DIFF	σ EXP/CAL %
		EXP	CAL		
P3(10)	2496.721	.0516	.0514	.4	4.7
P3(9)	2521.769	.0364	.0366	-.5	12.5
P2(12)	2527.391	.0340	.0346	-1.7	4.0
P3(8)	2546.375	.0561	.0511	9.9	9.3
P2(11)	2553.952	.0360	.0365	-1.3	16.0
P3(7)	2570.522	.0701	.0648	8.2	5.7
P2(10)	2580.096	.0736	.0678	8.7	17.7
P3(6)	2594.197	.0364	.0308	18.1	8.8
P2(9)	2605.806	.0554	.0513	8.0	16.2
P3(5)	2617.386	.0221	.0229	-3.5	10.7
P2(8)	2631.067	.0302	.0360	-16.0	13.3
P2(7)	2655.663	.1023	.1004	1.8	4.4
P1(10)	2665.219	.0460	.0381	20.5	16.7
P2(6)	2680.179	.0639	.0600	6.6	7.2
P1(9)	2691.606	.0435	.0463	-6.1	6.9
P2(5)	2703.999	.0284	.0300	-5.3	12.0
P1(8)	2717.538	.1456	.1437	1.3	2.5
P2(4)	2727.309	.0437	.0574	-23.8	4.5
P1(7)	2742.997	.0311	.0350	-11.1	12.3
P2(3)	2750.094	.0457	.0425	7.6	11.0
P1(6)	2767.968	.0764	.0876	-12.3	8.1
P1(5)	2792.434	.0661	.0705	-6.3	9.6

JULY 1976



Figure 1. Transmitter Station for Long Path Laser Extinction Measurements. From Left to Right: Office Trailer and Meteorological System Electronics, Vacuum Pump Trailer, Optical Transmitter Trailer, Supply Trailer.

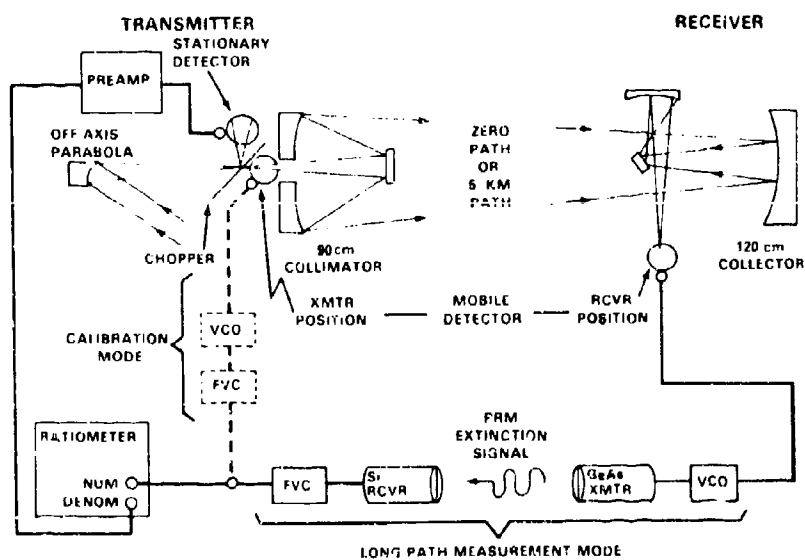


Figure 2. Schematic for Laser Extinction Measurement Configuration.

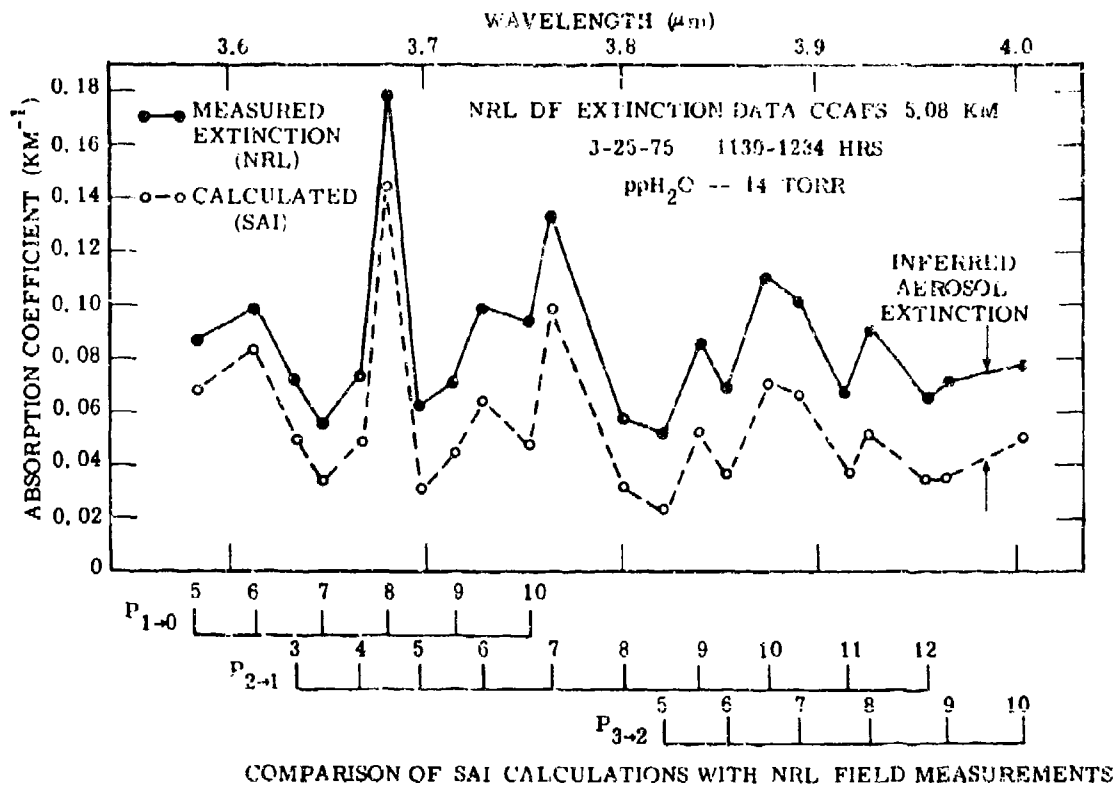
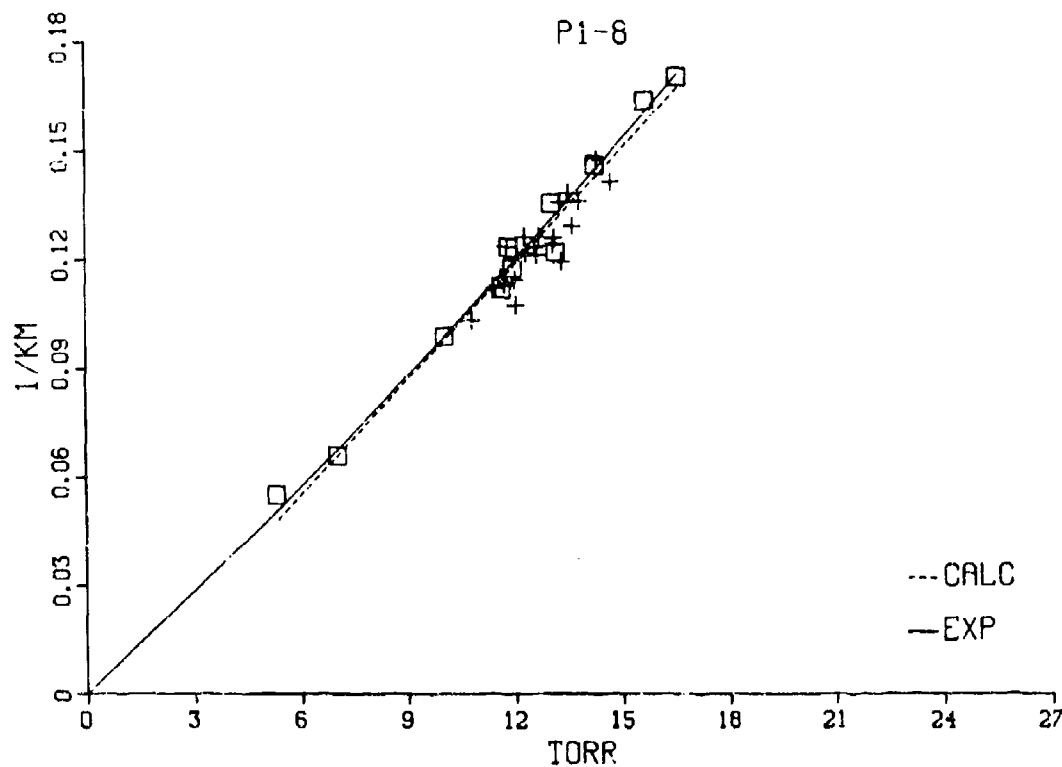


Figure 3. Comparison of Measured Extinction and Calculated Molecular Absorption for 22 DF Laser Frequencies.



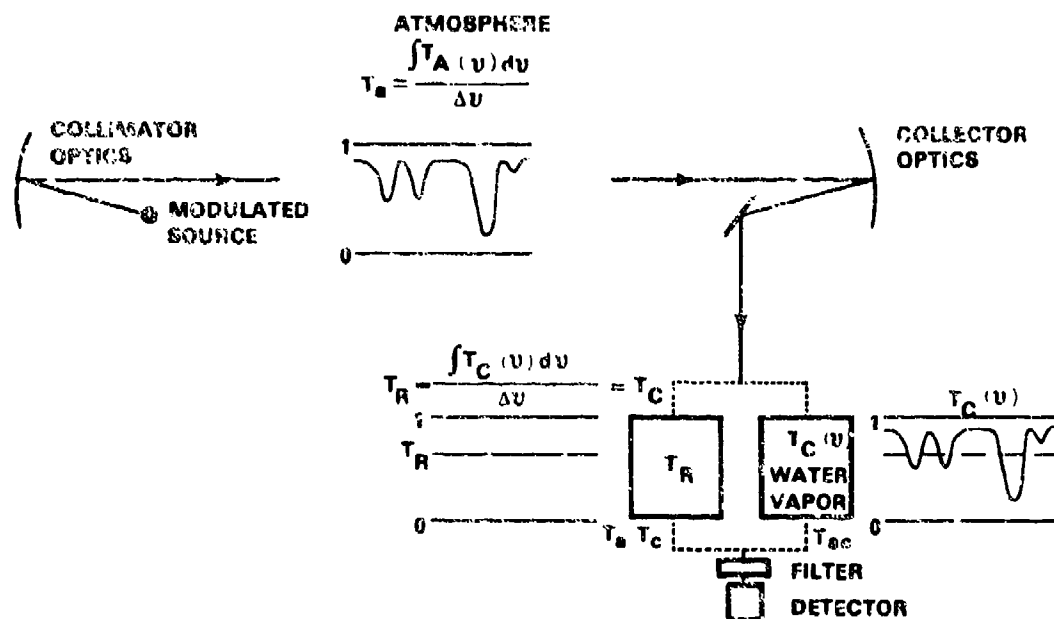


Figure 5. Operational Schematic for the HDO Gas Filter Correlation Spectrometer.

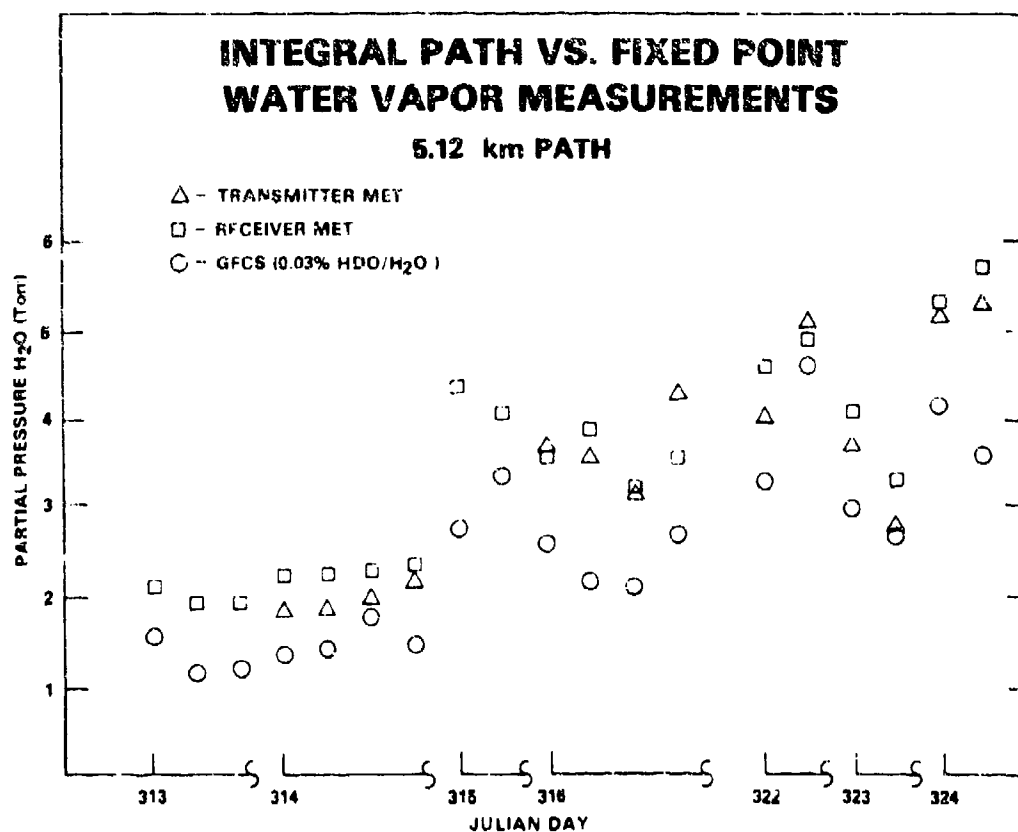


Figure 6. Comparisons of GFCS and Dew-point Hygrometer Water Vapor Measurements.

NAVAL RESEARCH LABORATORY

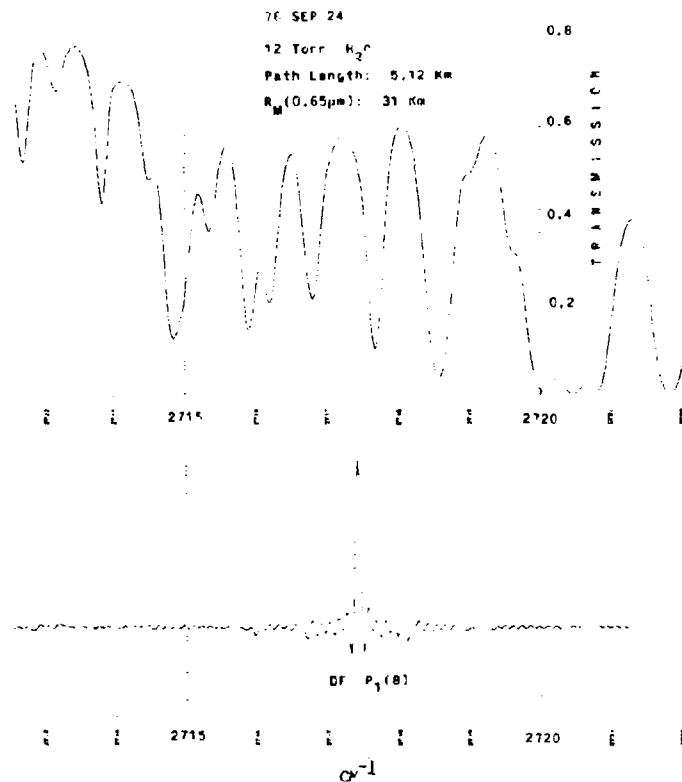


Figure 7. Fourier Transform Spectrometer Measurements of a Greybody Source (upper trace) and the P1-8 DF Laser Line (lower trace) over a 5.1 km Path.

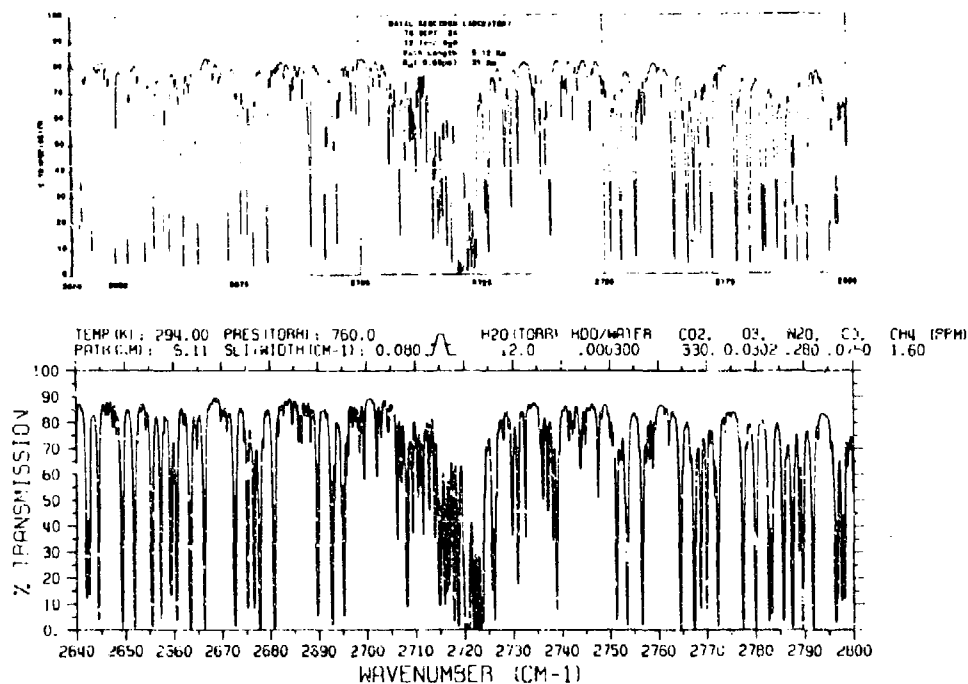


Figure 8. Comparison of Measured DF Laser-Calibrated Transmission Spectra to HITRAN Calculations.

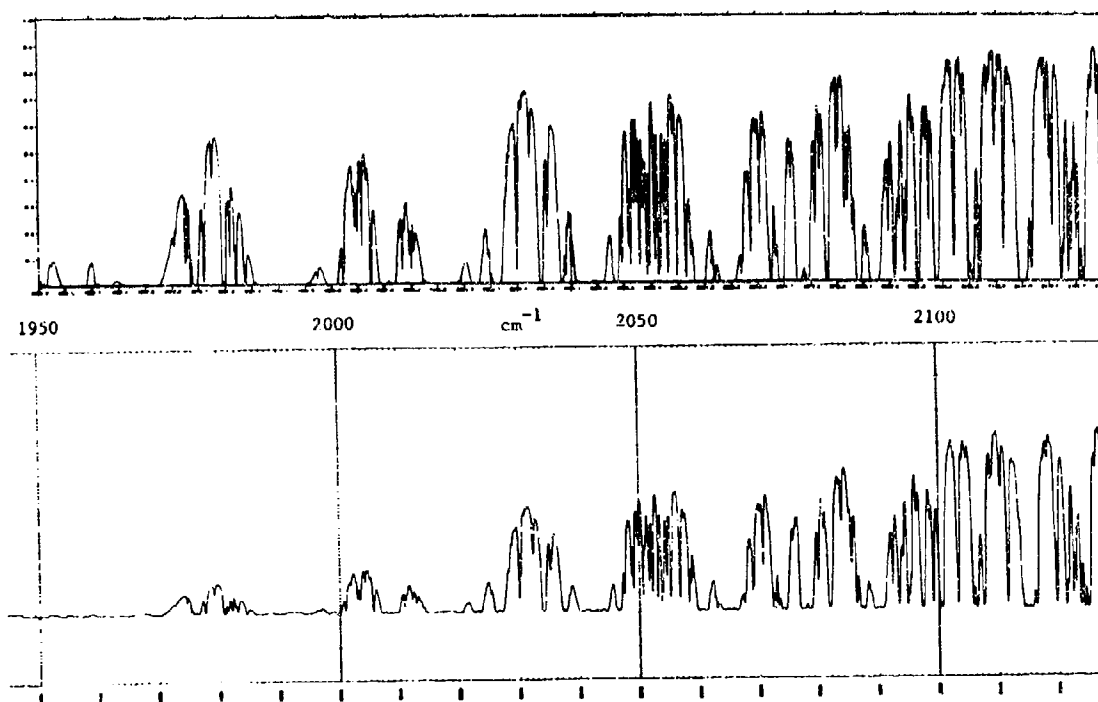


Figure 9. Comparison of Measured and Calculated Transmission Spectra of a 5.1 km Path Between 1950 cm^{-1} and 2120 cm^{-1} for 12.0 torr H_2O and 31 km Visibility.

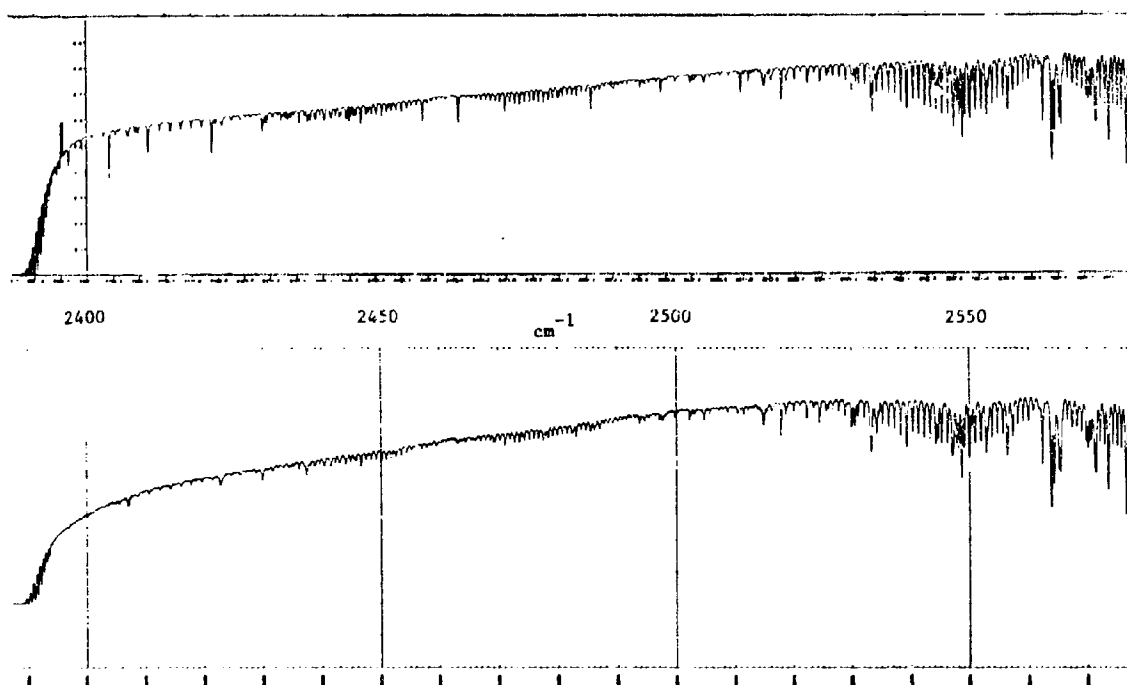


Figure 10. Comparison of Measured and Calculated Transmission Spectra of a 5.1 km Path Between 2400 cm^{-1} and 2578 cm^{-1} for 12.0 torr H_2O and 31 km Visibility.

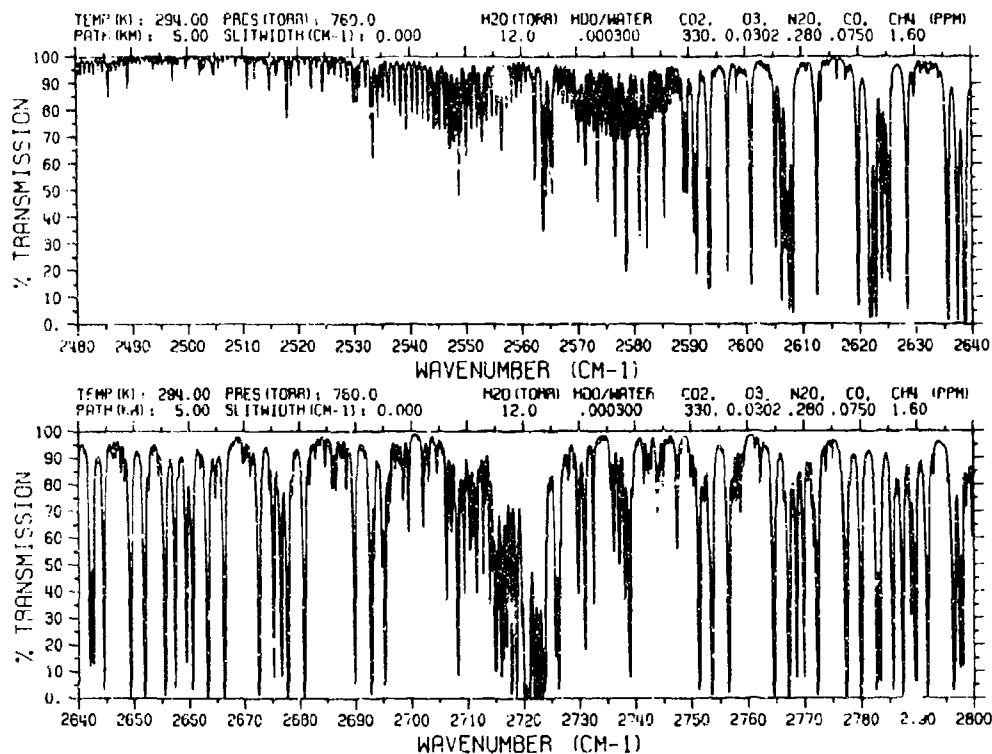


Figure 11. Calculated Transmission of a 5 km Atmospheric Path for 12.0 torr Partial Pressure of H_2O Excluding a Water Vapor Continuum Calculation.

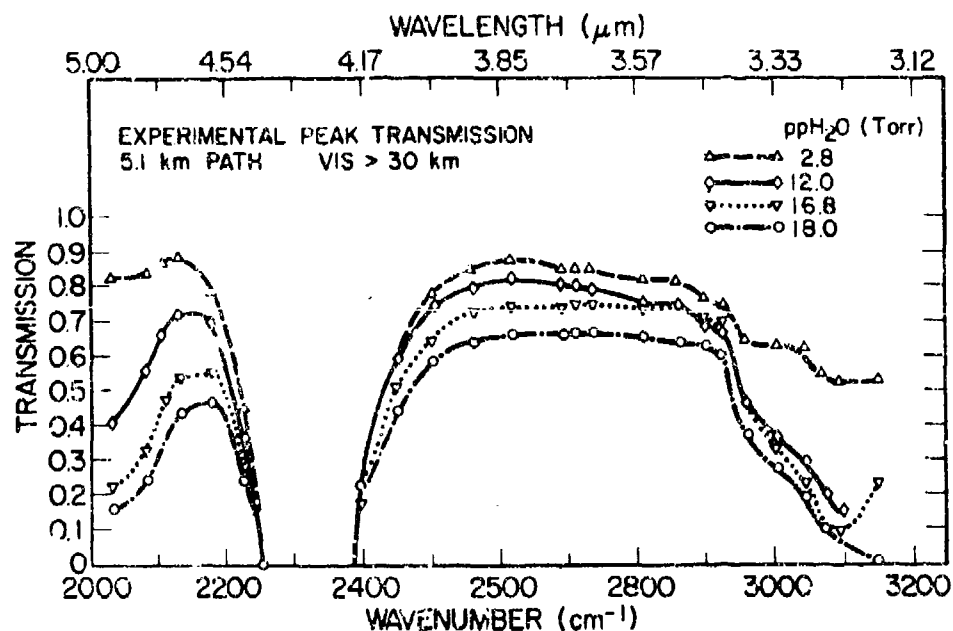


Figure 12. Experimental Peak Transmission Values Between 2000 cm^{-1} and 3200 cm^{-1} Derived From Long Path High Resolution Transmission Spectra.

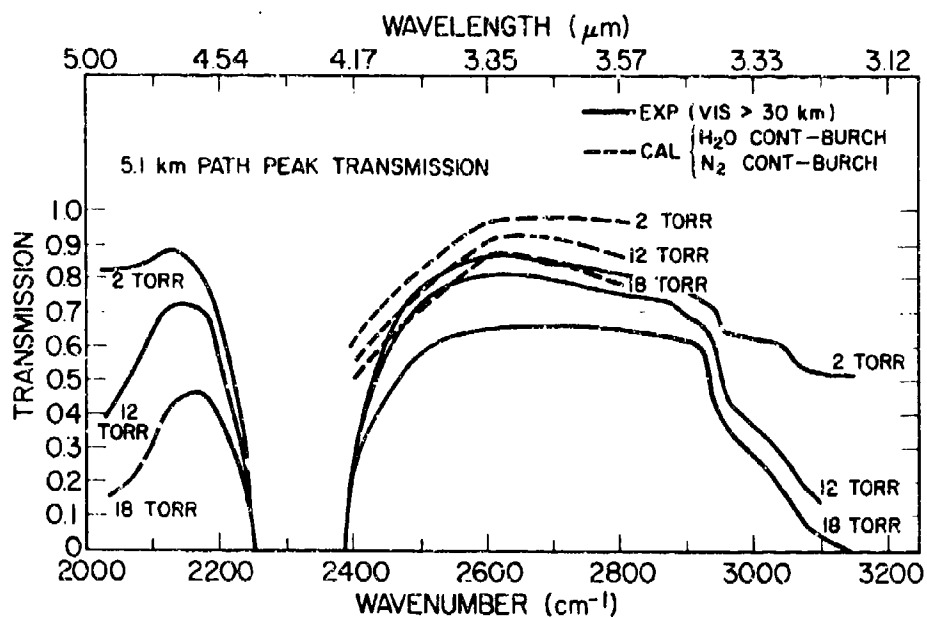


Figure 13. A Comparison of Data Shown in Figure 12 to the N₂ Continuum and H₂O Continuum Models of Burch, et al (see text for reference).

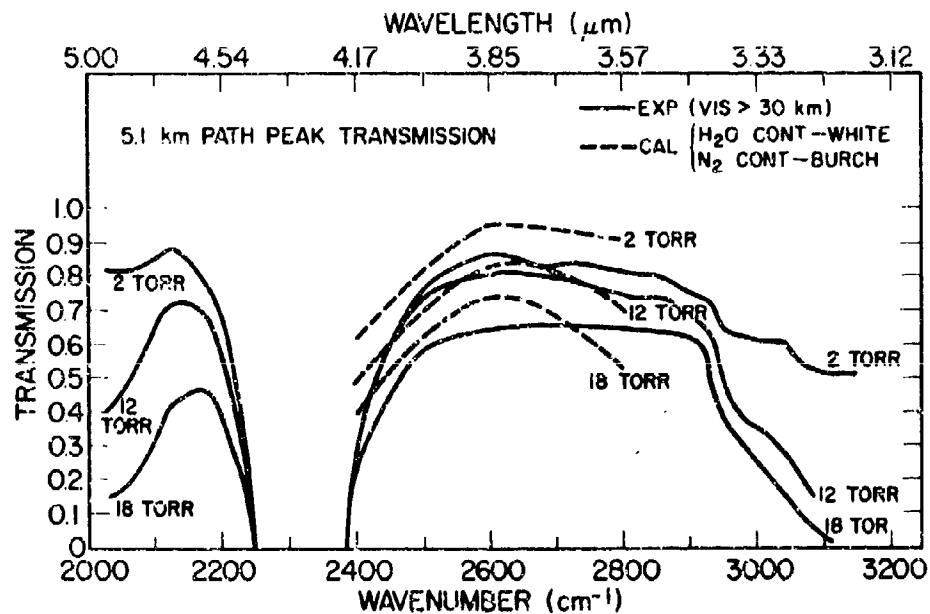


Figure 14. A Comparison of Data Shown in Figure 12 to the N₂ Continuum Model of Burch, et al, and the H₂O Continuum Model of Watkins and White (see text for reference).

RECENT FIELD OPERATIONS
OPTICAL RADIATION BRANCH
LASER/AEROSOL INTERACTION SECTION

FEB-MAR 75 NRL 5560 CCAFS, FLA	JUN 75 NRLC SAN DIEGO, CA	AUG-SEP 75 NRL 5560 CAPISTRANO, CA
MAR 76 U OF FLA GAINESVILLE, FLA	JULY 76 NMC TRINIDAD, CA	SEP-NOV 76 NRL 5560 PATUXENT NAS, MD
MAR-APR 77 NRL 5560 CCAFS, FLA	APR 77 NSMC DAHLGREN, VA	APR 77 AFGL BEDFORD, MA
MAY-JUN 77 USNS HAYTS NORTH ATLANTIC & MEDITERRANEAN	SEP 77 NRL 5560 CAPISTRANO, CA	FEB-MAR 78 NRL/CBD CHESAPEAKE BEACH, MD

Figure 17. List of Recent Field Operations Conducted by the Laser/Aerosol Interaction Section, Optical Radiation Branch (NRL Code 5568).

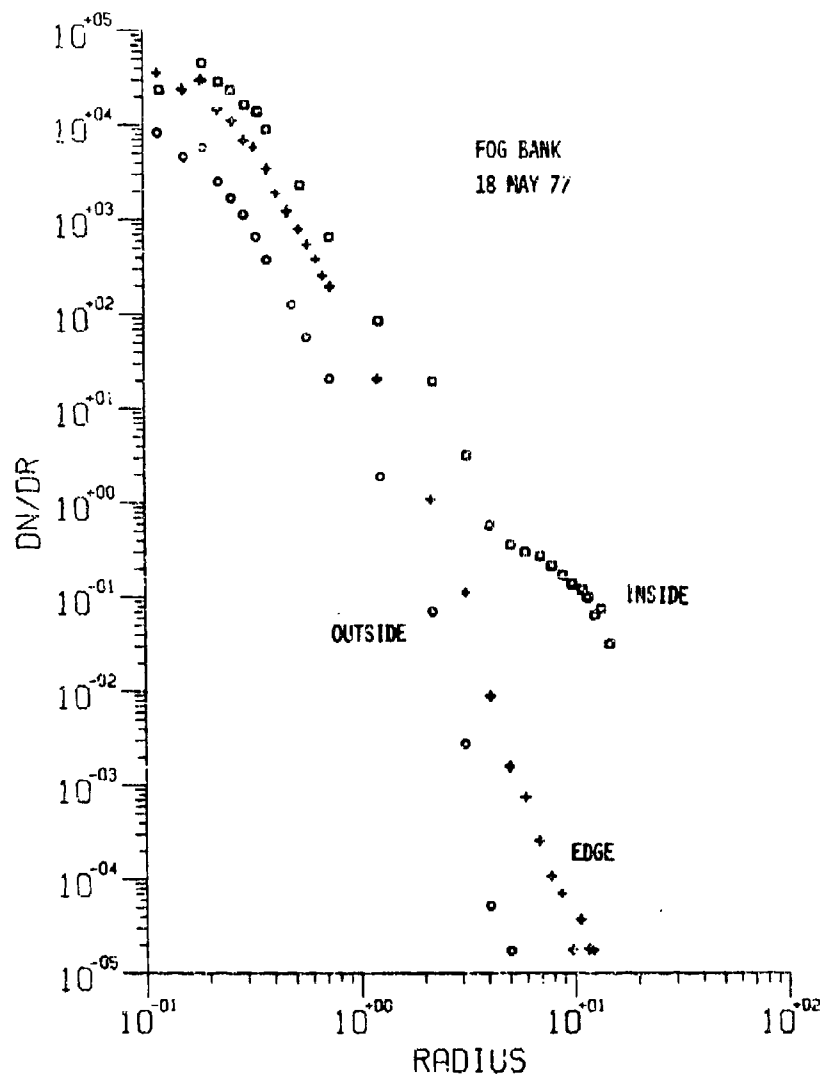


Figure 18. Aerosol Distribution Measurements Obtained on the Open Sea.

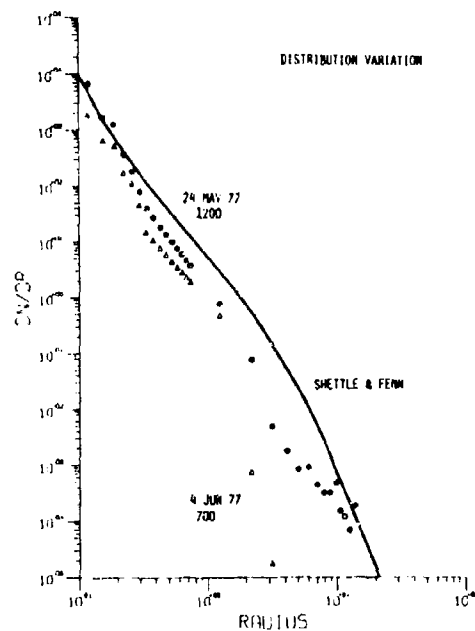


Figure 19. Measured Aerosol Distributions from the North Atlantic (circles) and the Mediterranean (triangles) Compared to the Maritime Aerosol Model Used in LOWTRAN 3b.

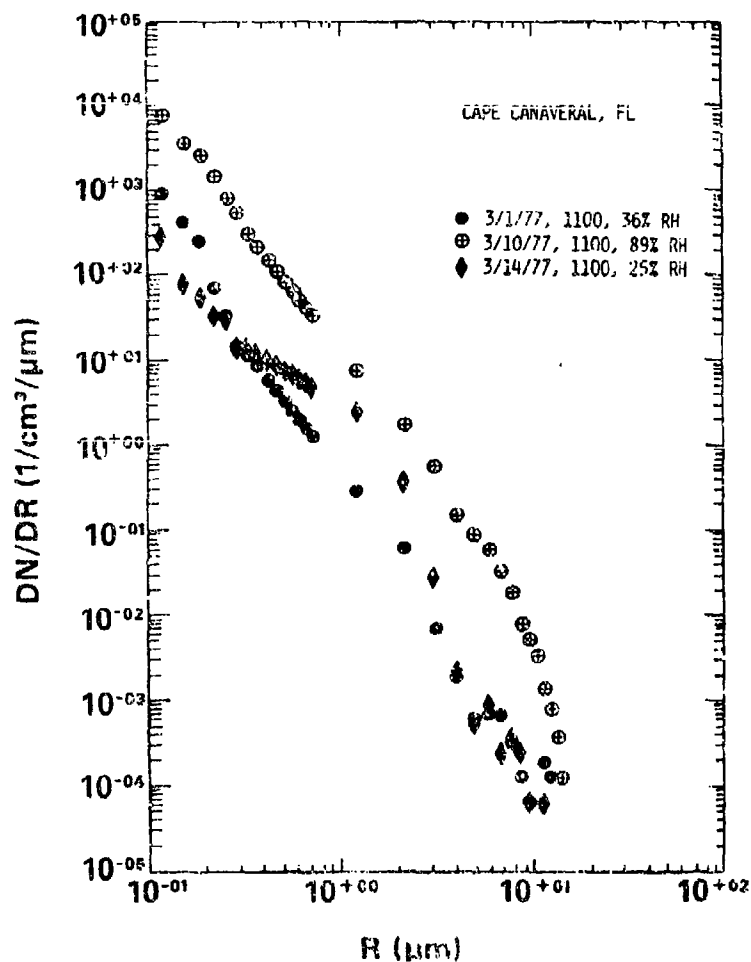


Figure 20. Aerosol Distribution Measurements Obtained on the Coast of Florida for Different Relative Humidity and Wind Conditions.

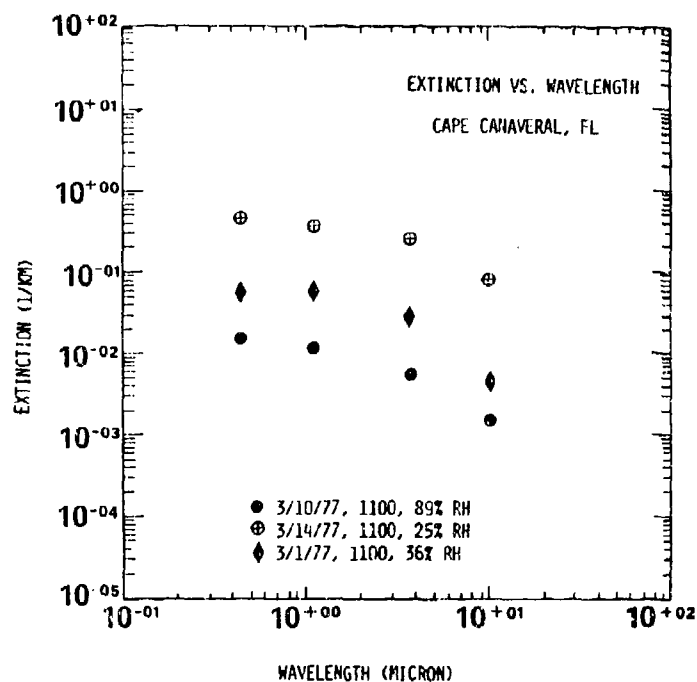


Figure 21. Extinction Coefficients for Various Wavelengths Calculated from the Data Shown in Figure 20.

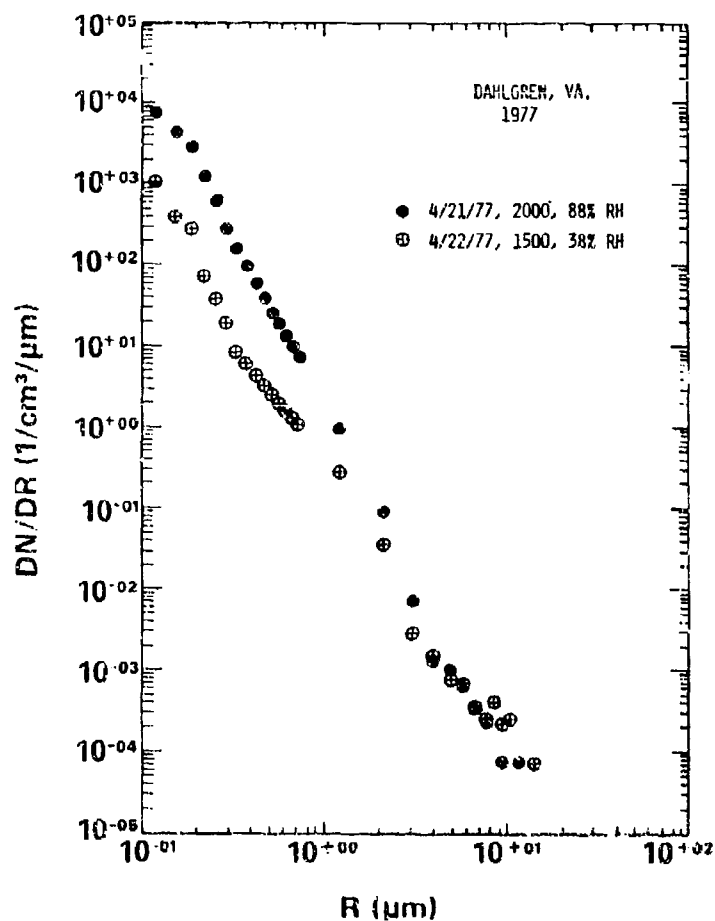


Figure 22. Aerosol Distributions from a Series of Measurements at Dahlgren, Virginia.

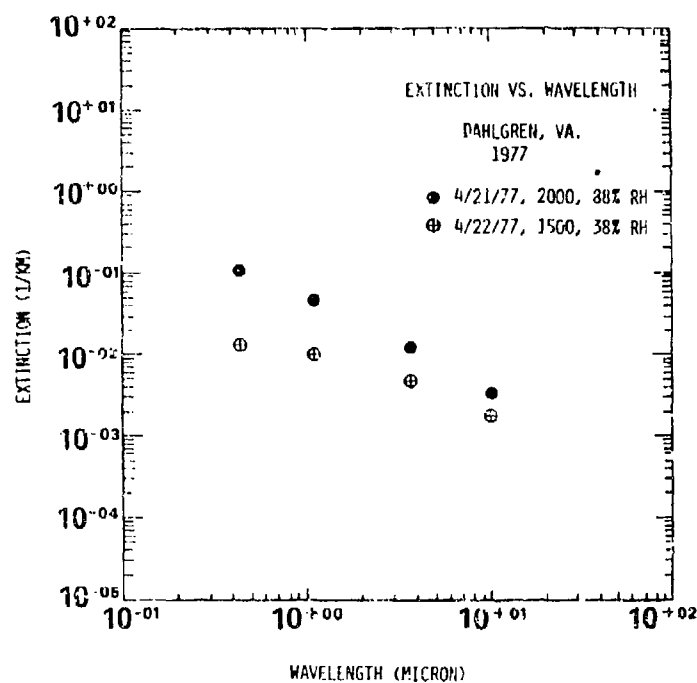


Figure 23. Extinction Calculations for Four Wavelengths Based on the Data Shown in Figure 22.

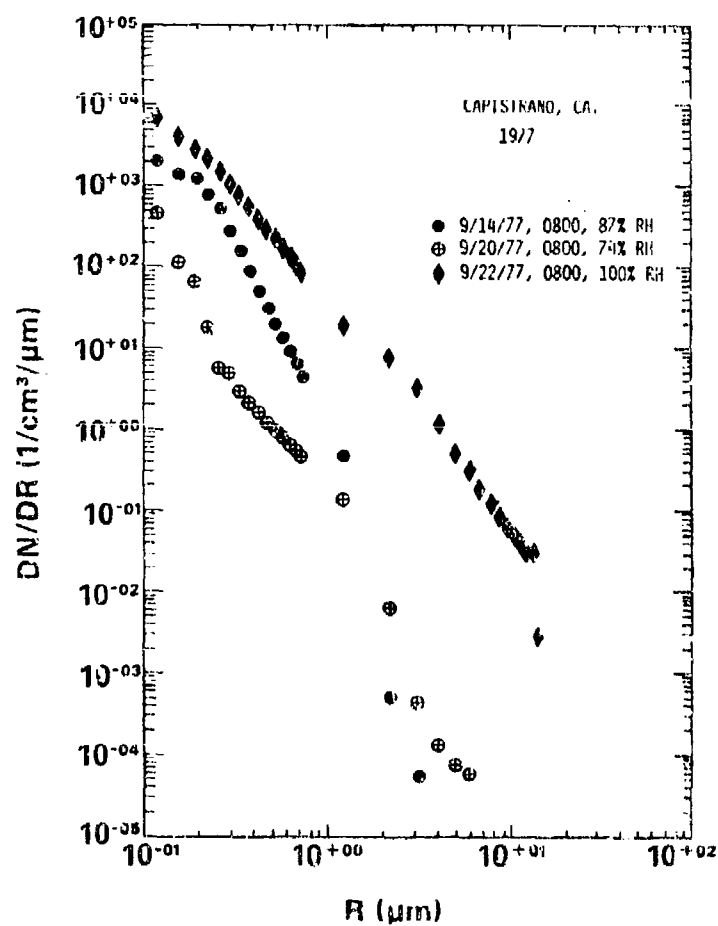


Figure 24. Aerosol Distributions Measured at a Site 6.5 km Inland from San Clemente, California.

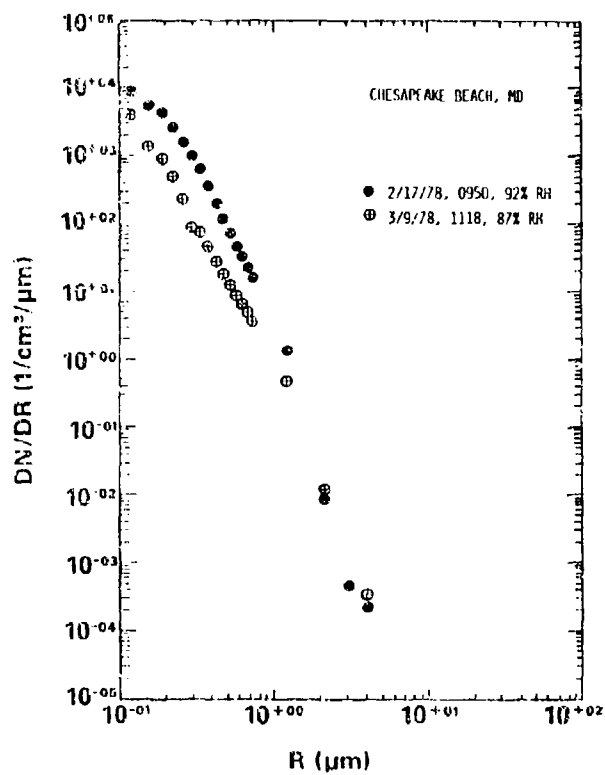


Figure 25. Aerosol Distributions Measured on the Shore of the Chesapeake Bay, 60 km East of Washington, D. C.

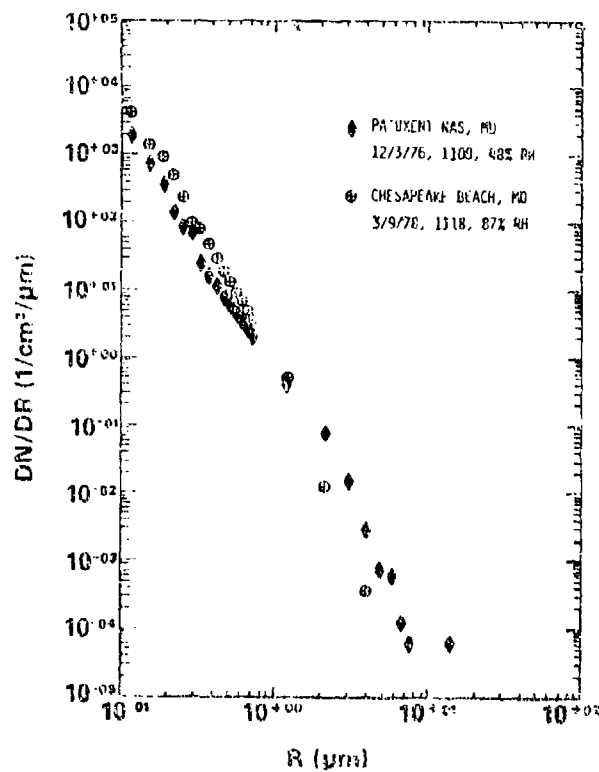


Figure 26. A Comparison of Aerosol Distributions Measured at Two Locations on the Shore of the Chesapeake Bay During Winter Conditions.

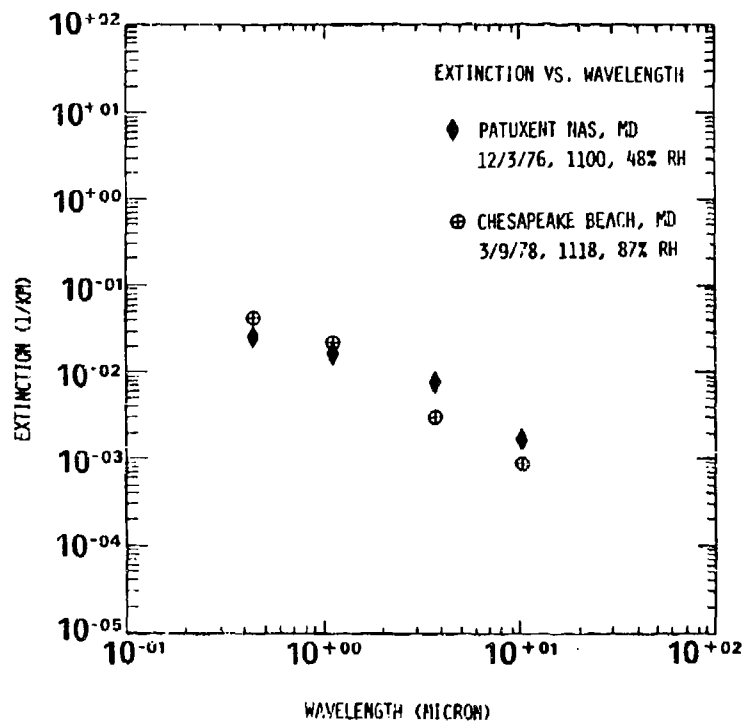


Figure 27. Extinction Calculations for Four Wavelengths Based on the Data Shown in Figure 26.

DISCUSSION

R.A. McClatchey, US

Size distribution measurements are quite difficult to perform, especially for the larger particle sizes. How were the NRL measurements calibrated and how much confidence do the authors have in the measurements?

Author's Reply

We have used the calibration provided by the manufacturer in all cases. In the past we have compared calculated extinctions with simultaneous measured transmissions. The comparisons, when wind direction and relative humidity are taken into account, give us fairly high confidence in the measurements.

J. Abele, FRG

You have shown the large fluctuations of the aerosol with regard to concentration and size distribution. Do you intend to include turbulence measurements in your aerosol measuring programme to get an idea of the magnitude of the fluctuations by correlating turbulence and aerosol measurements?

Author's Reply

We have considered measuring the turbulence along with the aerosols but have not yet done so.

A MODELING PROGRAM FOR THE PREDICTION OF ATMOSPHERIC EFFECTS ON E-O SENSOR PERFORMANCE

Richard B. Gomez
US Army Atmospheric Sciences Laboratory
Electronics Research and Development Command
White Sands Missile Range, New Mexico 88002, USA

ABSTRACT

United States and NATO Military forces are increasingly relying on new sophisticated weapons systems which have greater range, accuracy, and lethality than those of previous wars. Characteristic of most of these systems is their dependence on electro-optical (E-O) sensors which are strongly influenced by the operating atmospheric environment. Therefore, it is extremely important that the effects of the atmosphere (or smoke obscuration) on the effectiveness of E-O sensors be clearly characterized in an analytical form that permits reliable assessment through simulation of the actual E-O sensor field performance.

Both natural and battlefield induced adverse atmospheric conditions impose severe limitations on the performance and battlefield effectiveness of E-O surveillance and weapons systems. There are limited programs in the US and NATO which are addressing the effects of countermeasures (CM) smoke, natural atmospheric dust, fog, haze, rain and snow on E-O systems. These efforts which are beginning to provide the information needed for quantitative answers to questions concerning natural and CM smoke atmospheric limitations should be strengthened and better coordinated. There is also a need for special emphasis in the area of battlefield induced contaminants (BIC), since this area is not now being adequately addressed. BIC refers to the incidental manmade battlefield aerosols that arise as a result of military activities other than deliberate employment of countermeasure smoke. Studies have shown that anthropogenic dust, explosion debris, smoke from burning wreckage and vegetation, and related materials can seriously impede the use of E-O systems. In some cases BIC and/or natural adverse weather can exceed CM smoke in ability to disrupt the performance of E-O weapons systems.

The Atmospheric Sciences Laboratory (ASL) has an ongoing atmospheric modeling program, supported by laboratory and field measurements, aimed at characterizing and predicting the effects of battlefield aerosols and gases on the effectiveness of E-O sensors. Details of this program and an overview of a supporting measurement work effort are described in this paper.

1. INTRODUCTION

The incorporation of electro-optical (E-O) sensors into modern military equipment and weaponry has revealed deficiencies in the capability to predict the effectiveness of such devices. These deficiencies are greatest for low visibility conditions resulting from either adverse weather, the deployment of smoke as a screening agent, or battlefield induced contaminants (BIC). By BIC we mean the incidental anthropogenic battlefield gases and particles that are the natural by-products of weapon firings and explosions and other military activities other than deliberate employment of countermeasure smoke. It has been shown that vehicular dust, explosion debris, smoke from burning wreckage and vegetation, and related materials can seriously impede the use of E-O systems. In some cases the adverse weather or BIC can exceed countermeasures smoke in ability to disrupt the performance of E-O weapons systems. As such, in order to optimize intelligent decisions concerning design, development, procurement, and tactical deployment of these systems it is essential that all battlefield environmental limitations be adequately understood on a theoretical or a sufficiently substantiated empirical basis.

The scientific community has much information about the natural atmospheric environment but not all that it needs. In particular, the vertical characteristics of clouds and fog, etc., including liquid water content, are not sufficiently known. Furthermore, the climatology data which exists does not have sufficient vertical definition. Even so, enough is known to answer many basic questions. For battlefield environmental conditions, however, there are some important unknown areas that arise. The first real difficulty lies in simply determining what a battlefield aerosol really is. It is not known with certainty what materials (gases or particulates) will be present, which materials or optical phenomena have the most impact of E-O systems, or which contribute only minor effects in terms of general military operations. It is known that the size distributions of vehicle dust and high energy shell impact dust will be much different from those of known natural atmospheric dust. But no information is available on what new distributions to expect, or the impact of such distributions on the performance of imaging systems. BIC will have a wide range of new materials present, particularly in the form of smoke from burning equipment and vegetation. There is a potential for some surprising effects in the area, particularly as far as laser propagation is concerned. Anthropogenic dust will have important optical properties that are dependent on geographic locality (soil type, for example), season (soil moisture) and meteorological conditions. One of the most pressing problems in atmospheric optics today is to relate the aerosol effects on the battlefield to measurable meteorological parameters. BIC may pose special problems in establishing these relationships. It is not feasible to measure all of the potentially important combinations of battlefield aerosols and measurable meteorological parameters. One must progress in a way that systematically samples some situations and then extrapolates and interpolates the rest through a viable modeling program.

There are limited programs today in the US and NATO which are addressing the effects of countermeasure smoke and natural adverse weather on E-O systems. These efforts are beginning to provide the information needed to give quantitative answers to questions concerning natural atmospheric and smoke screening limitations. These efforts should be strengthened and better coordinated. In addition there is a need for special emphasis in the area of battlefield environmental conditions since this area is not now being adequately addressed. The problem of assessing the impact on E-O systems of battlefield gases and aerosols whether naturally, unintentionally, or deliberately produced needs additional emphasis. This paper presents the modeling program of the US Army Atmospheric Sciences Laboratory (ASL) and associated laboratory and field measurement work designed to help provide this additional emphasis.

2. BACKGROUND

E-O systems capabilities are closely related to the mesoscale meteorological parameters. However, these mesoscale parameters (observables) for the most part are not directly applicable to E-O systems performance determination (hence referred to as secondary EOMET parameters). These data need to be reduced to a meaningful form through the development of relationships between bulk meteorological data affecting E-O systems performance and microscale atmospheric meteorological and optical parameters used directly in the modeling of atmospheric effects on E-O systems performance determination. The micro-scale optical and meteorological factors used directly in assessing the E-O systems performance are referred to collectively as primary EOMET. In many cases the mesoscale weather parameters can be predicted (either in a probabilistic or deterministic sense) from local or regional weather observations. However, rigorous connectives between secondary EOMET and primary EOMET have yet to be demonstrated. Certain connections such as the relationship between molecular concentrations and molecular line absorption are well known and have been rigorously validated. However, even here, differences of opinion exist as to how to incorporate most efficiently and accurately these results in simple modeling codes. For other situations, such as aerosol haze and fog conditions frequently encountered in Western Europe, many approaches have been suggested but none have been adequately validated.

In response to the requirements for a better understanding of the atmospheric optical environment expressed at the Office of the Director of Defense Research and Engineering (ODDR&E) Atmospheric Workshop in December 1976 [ODDR&E, 1976] and by the Joint Deputies for Laboratories Committee's Night Vision Technology Panel, the Tri-Service Atmospheric Optics Working Group developed a strategy plan [US ARMY ERADCOM, 1977] for the development and validation of a library of algorithms and computer codes that describe the atmospheric effects on E-O sensors. The computer modeling portion of this approach for the US Army is already underway in the ASL in the effort entitled "Electro-Optical Sensor Atmospheric Effects Library (E-O SAEEL)". The objective of the ASL E-O SAEEL program is the development and validation of an operational propagation code or library of codes for the accurate representation of the effects of atmospheric aerosols/gases/BIC on the effectiveness of E-O sensors. These codes will accept secondary EOMET (measurables) parameters and produce information needed for the assessment of the effectiveness of E-O sensor performance under projected battlefield environmental conditions. This work is providing to the US and NATO the atmospheric effects description of the gas and aerosol limitations on E-O weapons systems and identifying the knowledge and data deficiencies that prevent adequate modeling of E-O systems performance. The E-O SAEEL models naturally lead to field and laboratory experimental work required to fill data base deficiencies.

The problem itself is extremely complex. It requires the sorting out of a large number of related problems (composition and size distributions of aerosols, combustion products, gaseous components, explosive debris, synergistic effects, geographic variation, meteorological conditions, etc.). A strictly empirical approach of performing field tests for all potential environmental and battlefield conditions is, of course, impractical. Consequently, a balance between empirical and theoretical approaches is considered in order. Field tests and laboratory studies will be particularly useful in developing computerized atmospheric propagation models for E-O systems applications.

Long-term field activity cannot be planned with high degree of detail because measurements needed in one time frame are going to depend on what was learned just a few months earlier. However, ASL is planning FY78-79 activities aimed at measuring particle size distribution and transmission effects of two of the obvious battlefield dust constituents: explosion debris and vehicular dust. Analysis of these data will establish the need and extent of further measurements. As FY78 data becomes available preliminary models will be constructed (using data available from other sources as well). These models will then be tested in more general situations.

A variety of individual atmospheric effects models (algorithms, computer codes or data sets) is in existence and in use to some extent within the E-O community. Major deficiencies have been identified as currently existing in these models that seriously limit their applicability for E-O sensor performance analysis. The most apparent shortcomings for the most widely used models are the following:

(1) The models have not been subjected to broad experimental reviews to validate their applicabilities for desired analysis tasks. In addition none addresses the question of the effect of BIC on the performance of E-O systems.

(2) For the most part, detailed sensitivity analyses to determine the sensitivity of input parameters to output predictions have not been undertaken.

(3) The most widely used model, i.e., LOWTRAN [SELBY, 1978] is currently used for both gaseous absorption and natural aerosol scattering propagation predictions. There currently exists serious concern in the model user community as to the validity of the aerosol portion of the model for application to low visibility atmospheric paths. On the other hand, the gaseous absorption portion of LOWTRAN for the visible and infrared spectral regions appears suitable for current technology E-O sensors calculations. There is, however, the question as to the validity of LOWTRAN gaseous absorption calculations for the advanced FLIRs where transmission well below 10% must be accurately predicted. In addition the spectral region is generally ignored above 30 micrometers, at least from a practical analysis standpoint, and the LOWTRAN procedure is not valid for spectral resolutions finer than 20 cm^{-1} .

The version of E-O SAEEL which will address these deficiencies will consist of a library of validated atmospheric optics models which can be used with confidence in predicting the atmospheric effects on the performance of E-O systems for Army missions throughout the world. The initial phase of this investigation (interim version of E-O SAEEL) will focus on meteorological conditions and empirical relationships which produce lower bounds on E-O system performance for missions in the European theater. Since the system limitations here are strongly related to aerosol/smoke attenuation/obscuration, these phenomena will receive primary emphasis. The final objective of this preliminary investigation to be concluded by 4QFY79 is to provide the user with a single source library (interim E-O SAEEL) which can provide an appropriate validated atmospheric optics model for his particular application. Later phases of the investigation will consider a wider range of theaters and optical effects.

3. DESCRIPTION OF BATTLEFIELD ATMOSPHERIC ENVIRONMENTAL EFFECTS ON E-O SYSTEMS

We shall now describe those measurements which are necessary for the determination of the initial input parameters for modeling the battlefield atmospheric environmental effects on E-O systems. In all cases where feasible the following climatology should be recorded: unconditional probabilities (frequency of occurrence percentages), conditional probabilities (recurrence) and persistency. Time scales should include time periods of an hour or less. The discussion will follow the flow chart given by Figure 1.

The sources of atmospheric obscuration can be placed into two categories: those arising from natural sources (natural weather) and those arising from man's interaction with the environment (anthropogenic sources). Molecular absorption phenomena for the natural weather category will not be discussed because, for the most part, existent models provide adequate answers and hence require minimal model development.

3.1 Natural Sources of Obscuration

We shall distinguish between cases of relatively high visibility for E-O systems ($V > 5$ km) and cases of relatively low visibility ($V < 5$ km) in order to deal separately with the problems of light haze and generally bright skies on the one hand and very hazy or foggy conditions on the other hand.

3.1.1 High Visibility

If we consider generally sunny or bright days or clear nights with light haze and discrete clouds, then it is necessary to develop so-called haze models, cloud models, and turbulence models.

(1) Haze Models

Models used for characterizing atmospheric haze need measurements of the spectral optical thickness spectral optical depth versus altitude and the volume scattering and volume extinction coefficients. In addition, one should also have estimates of the complex refractive index or composition of the aerosols and the particle number density distribution.

(2) Turbulence Models

Because turbulence eddies exist in the atmosphere, radiation does not propagate along straight lines but wanders along the path. This large-scale effect, along with the small-scale effects of scintillation and image distortion, necessitates the measurement of the coefficient of temperature fluctuation (C_T) in the atmosphere. These measurements should be performed as a function of time of day and altitude for various haze and cloud conditions.

(3) Cloud Models

Clouds which are finite in size can alter the radiation field in the atmosphere. In addition, there is some correlation between cloud type and haze condition. Measurements are needed to determine the spectral optical thickness, water content, size, altitude, temperature, and types of clouds. A measurement of these parameters will enable modelers to calculate the scattering and emission properties of clouds.

3.1.2 Low Visibility

For atmospheres of low visibility ($V < 5$ km) more detailed measurements are necessary because of the greater number of variables and inhomogeneities affecting the optical observations. We can generally categorize these atmospheres into two states: (1) stable weather, i.e., those conditions which are characterized by steady-state conditions, and (2) unstable weather, i.e., those conditions represented by rapidly changing weather such as variable wind and storms.

(1) Stable Weather

Stable weather can be divided into two classes: one which is characteristic of moist or humid conditions and one which is representative of dry conditions.

(a) Moist

Moist weather can also be subdivided into two classes: precipitating and suspended. Precipitating conditions are represented by rain, snow, sleet and hail and require transmission measurements as well as measurements of total rate, e.g., in gm/cm²-sec along with size and temperature of the particles. Suspended conditions are represented by fog, mist, and haze. For this case measurements are needed of the spectral optical thickness, spectral optical depth versus altitude, and volume scattering and volume extinction coefficients, the single scattering phase function, the particle number density distribution and the complex refractive index of the particles. In addition, it would be desirable to measure the liquid water column density or mass column density. All of these measurements should be made at various altitudes in order to obtain a vertical profile of each parameter.

(b) Dry

Dry weather can be characterized by the lack of water vapor and liquid water in the atmosphere. Representative examples include dry haze, dust, and smoke. In order to model such conditions it is necessary that measurements be made of the spectral optical thickness and all of the other parameters which are measured for the case of moist suspended conditions with the exception of liquid water content. In addition, the temperature of the smokes should be measured.

(2) Unstable Weather

Unstable weather can be characterized by rapidly changing conditions. Generally, moist and dry conditions also exist here as in the stable weather conditions.

(a) Moist

Moist weather is represented by violent activity such as hurricanes, cyclones and blizzards. General measurements include the size or extent of the storm, pressure variations and wind speed.

(b) Dry

Dry weather is represented by dust storms and dust devils. As in the moist condition, measurements should be made of the size or extent of the storm, pressure variations, and wind speed.

3.2 Anthropogenic Sources of Obscuration

We shall now consider sources of atmospheric obscuration resulting from human intervention with the environment. There are two classes of these sources: those arising from inadvertent modification of the atmosphere and those arising from deliberate interaction with the environment.

3.2.1 Unintentional

In the category of unintentional sources of environmental modification we consider gases, particulates, and thermal gradients resulting from non-combat related anthropogenic sources (industries, cities, etc.) and BIC.

(1) Gases

Extraneous gases are often introduced into the atmosphere as a result of, for example, exhaust emission from vehicles, debris from explosions, and combustion processes. The concentrations and types of the gaseous products should be measured.

(2) Particulates

Extraneous particulates are often introduced into the atmosphere as a result of, for example, bombs or bombardment of the terrain, exhaust emission, smoke from fires, vehicular dust, and explosion debris. Measurements should be made of the spectral optical thickness of the medium, the volume scattering and volume extinction coefficients, the complex refractive index of the particulates, and the size distribution (to include number densities or mass concentrations).

(3) Thermal Gradients

Thermal gradients arise from populated areas as a result of space heating, industrial activity, and vehicles. Major sources of local thermal gradients on the battlefield include burning vehicles, high energy explosions, etc. This inadvertent heating of the environment can alter the optical properties of the atmosphere. As a result, it is necessary that one measure the temperature and wind velocity as a function of time in areas immediate to the sites of interest.

3.2.2 Deliberate (Screens)

Gases and particulates may also be introduced into the atmosphere in a deliberate manner such as in countermeasure tactics.

(1) Gases

Gases may be deliberately injected into the atmospheric medium. Their type, concentration, and dispersive character should be known or measured.

(2) Particulates

Particulates (to include dust, foam, bubbles, etc) may also be deliberately injected into the atmosphere as a countermeasure tactic. This could be accomplished by smoke munitions or intentional bombardment of the terrain. The refractive index, size distribution and concentration of particulates should be measured as well as the volume scattering and volume extinction coefficients of the medium as a function of time and location.

4. RELATIONSHIPS OF MEASUREMENTS TO MODEL UNCERTAINTIES

The matrices shown in Figures 2 and 3 illustrate the close relationships between the E-O SACL critical modeling uncertainties and associated measurements. The letter in each matrix position indicates the priority a particular measurement is assigned for solving a particular modeling problem. E, as a matrix element indicates that the measurement is absolutely essential for the modeling effort. E₁ indicates a measurement which is highly desirable. U indicates useful types of data, such as long-path spectral transmission and path radiance, for example, which provide useful auxiliary information for aerosol growth model verification. Blank spaces indicate the measurement is of no use or value or irrelevant for addressing that particular model uncertainty.

Figure 2 shows the relevant modeling uncertainties and associated measurements required for E-O modeling of naturally occurring atmospheric attenuation. Although the entries in the matrix indicate the value of various measurement techniques there are many subtle considerations which cannot be represented in this simple format. For example, in order to model the altitude dependence of aerosols the LIDAR can be

a valuable tool. However, LIDAR data is presently difficult to interpret and answers only part of the problem. On the other hand, balloon-borne point sampling measurements can provide valuable information on aerosol altitude dependence. However, this type of measurement is difficult logistically and relatively slow in collecting data. The measurement techniques selected must also be consistent with the current modeling status. For example, although models can be used to attack fundamental problems of aerosol growth, the direct size distribution sampling is preferred. Once local aerosol growth models have been developed it may be more advantageous to use a LIDAR measurement to collect large statistical samples of aerosol spatial distributions.

The relationships between the modeling and measurements required for modeling BIC characterization are illustrated in Figure 3. The problems here are somewhat different from those with the naturally occurring aerosols since BIC consists of a much more diverse range of materials generated by multiple point sources. Most aerosols arising from natural sources are relatively homogeneous in contrast to aerosols arising from anthropogenic sources which are localized and result in smoke or dust plumes which have large spatial and temporal variations. Because of this atmospheric mixing, it is even difficult to obtain source mass release rates for such aerosols as battlefield smokes and vehicle dust clouds. BIC modeling is in a very primitive state. Thus, the emphasis in the near term should probably be to get quick results to bound the seriousness of various anthropogenic sources and guide detailed measurements and modeling. The BIC modeling in some cases also requires unique measurement capabilities as compared to other conditions. In these cases, it may be desirable to utilize advanced remote measurement techniques similar to those being developed for pollution monitoring problems. These methods might include the development of new measurement techniques, such as molecular-sensitive LIDAR, or improved analysis for current instrumentation, such as development of automatic analysis programs for Fourier Transform Spectrometer (FTS) data.

5. CURRENT EFFORT

The ASL has an ongoing atmospheric effects modeling and measurement program, established several years ago, with general objectives to further develop the capability to predict the effects of battlefield environments on E-O systems. Models have been developed which address the atmospheric effects of absorption and scattering in a comprehensive manner requiring as input detailed knowledge of the physical and optical properties of the particular aerosol/gas data. These codes represent the state-of-the-art in radiative transfer and atmospheric transmission modeling and range in scope from Monte Carlo multiple scattering codes to specialized band models for the treatment of molecular absorption and aerosol obscuration models. The ASL can perform line-by-line spectral calculations of molecular absorption utilizing Lorentzian, Doppler, collisionally-narrowed, Voigt or generalized Voigt line shapes. Results have been published in these and other areas, such as pressure-broadening effects for the CO₂ molecular system calculated from basic semi-quantal theory and computerized methods for the Lorentz and Voigt line shape computation [GOMEZ, et al., 1975; 1977; 1978; ROBBAS, et al., 1976; 1977; 1978; 1979; 1980; PIERLUISSI, et al., 1975, 1976, 1977, 1978]. The fact that the ASL has a strong complementary program in the measurement and characterization of aerosol and molecular absorption properties has aided the modeling work considerably.

6. MODELING PROGRAM STRATEGY

Although the gathering and archiving of EOMET data is extremely important, it is not an end in itself. For one thing, observable meteorological parameters, for the most part, are secondary EOMET parameters which are not directly applicable to E-O system performance determination. These data need to be reduced to a meaningful form through the development of relationships between bulk observations and primary EOMET parameters directly affecting E-O system performance. The development of models to provide this link between systems performance and atmospheric observables is widely recognized by numerous groups as the necessary key to successful exploitation of E-O systems technology. This requirement has surfaced in recommendations by Tri-Service Working Groups such as the E-O Sensor Atmospheric Optics and Atmospheric Propagation Working Group [US ARMY ERADCOM, 1977] as well as in the recent OODR&E and Remote Sensing of the Boundary Layer Workshops [OODR&E, 1976; RUHNKE, 1977]. Models also provide requirements on accuracy and resolution of field measurements and insure that measurements are not willy-nilly but actually contribute to our phenomenological understanding of the atmospheric effects on the performance and effectiveness of the E-O weapon or communication systems.

The detailed input requirements of the comprehensive research atmospheric radiative transfer models are rarely available in a battlefield environment. Only secondary EOMET parameters may be available. Hence, current modeling and measurements efforts at the ASL aim to develop methods to link these secondary EOMET parameters to E-O system performance. The success of these efforts will allow optimization of sensor deployment and tactics for various weather and battlefield environments in different scenarios.

The approach is dependent on well-documented climatological data which is currently crude or non-existent. Time scales in the order of three hour periods are unacceptable if battles are won or lost in an hour or less. With the available or near-term modern technology, this will probably be the case. Hence, better climatology is needed. Most of the currently available historical measurements do not relate to specific E-O requirements. This needs to change. The current effort addresses these problems.

The current program strategy also involves the development of an interim E-O atmospheric effects code or codes based largely on measurements. Measurements are planned to allow "brute force" methods to be used to provide adequate results within a reasonable time frame. Advanced versions of E-O SALT will be dependent on the more fruitful but higher risk technology of effectively parameterizing primary EOMET data to achieve the desired engineering solution. This approach will run in parallel with the "brute force" approach. Hence, more field and laboratory measurements will be needed.

E-O SALT codes will be modular, simple and understandable, adaptive, easy to control, complete in important matters, and easy to communicate with. They will bridge the gap between the specialist in atmospheric optics and the operational user of these techniques. This is necessary if there is to be

a constructive exchange of information between user and modeler, which is needed to meet the Army's requirements in this area.

Since the modeling of the aerosol extinction is one of the highest priorities in the findings of the recent ODD&E Workshop [ODD&E, 1976], we need measurements of the spatial and temporal variations of aerosol properties to include the explicit dependence of the aerosol on relative humidity and wind. Current aerosol models generally vary only the total number density, keeping the shape of the particle size distribution and its composition invariant with altitude [SHUTTLE, 1976]. This has to change because in the real world all three quantities may vary. Hence, under present plans, good surface level aerosol measurements, as well as vertical profiles will be made.

Currently models are being applied to determine the magnitude of error which can be tolerated for each of the EOMET parameters. This sensitivity analysis will provide preliminary guidelines for further field work. Aside from the natural aerosols such as fog and haze, the current modeling effort addresses white phosphorus smoke. Other smokes will be addressed later. In particular, models are being used to determine the characteristics of the atmosphere which will be useful in predicting the effects of variable atmospheres on the performance of E-O sensors under conditions of low visibility. The first step in this process is establishing criteria for assessing and evaluating algorithms as to their utility and accuracy for E-O SAEEL. Having established the criteria which existing algorithms and codes must have in order to be incorporated into the proposed E-O SAEEL, it will then be necessary to acquire all models which are available and exercise the computer codes to such an extent that their ranges of validity are delineated. The current spectral region of interest is from the visible to 4mm to include the particular lasers Nd, YAG, CO₂, DF, HF, and GaAs. The spatial scale over which the models should be valid is of the order of 3 to 5 kilometers in the horizontal direction and below 5 km altitude and the state of the atmosphere should be characterized generally by a visibility less than 5 kilometers.

Decreased visibility is caused by a variety of conditions: fog, dust, smoke, and hazes of different kinds; and not all models can be expected to account for all of these conditions for the entire spectral region considered. It will therefore be necessary to identify the "gaps" which exist and are not covered by existing models. Suggestions will then be made either to modify the current models or to develop new models in order to provide the capability which is needed for inclusion into the E-O SAEEL.

A conceptual illustration of how E-O SAEEL might be configured is shown in Figure 4. The executive routine may consist of the code that communicates inputs/outputs (I/O) with the user as well as control the call-up and I/O flow of the subroutines.

7. CLOSING REMARKS

The ASL plan includes near-term and long-term activities aimed at understanding, quantifying, and predicting the battlefield environmental effects on E-O systems. The near-term work will include two of the obvious battlefield constituents: explosion debris and vehicular dust. This work will provide the beginning of some of the answers to the modeling problems mentioned earlier, and sensitivity analysis calculations made on the data will establish the need and extent of further measurements. As data become available, preliminary models will be constructed by using data available from various sources. It will then be necessary to test these models in situations more representative of the complex situation expected under European battlefield conditions. Further work will be required to address the geographic dependent problems.

Field measurements and model validation work will move from specific field situations (such as fog) toward more complex cases. The near-term goals are to: (1) develop and validate interim E-O SAEEL, (2) characterize the battlefield environment and identify the data gaps, (3) establish atmospheric characterization and transmission technological data bases with mobile measurement capabilities, and (4) establish a climatological data and model base. The long-term goals include: (1) development of advanced E-O SAEELs, (2) validation of models, (3) development of advanced atmospheric sensors and remote sensing techniques, (4) publication of manuals and handbooks in atmospheric optics, and (5) development of a prototype system for tactical use of E-O SAEEL. To do this, the ASL E-O atmospheric transmission program divides into four major efforts, each with its own objective and approach as outlined below.

7.1 MAJOR EFFORT: CLIMATOLOGY

7.1.1 Objectives:

(1) To acquire, analyze, store, retrieve, and disseminate information on primary and secondary EOMET parameters which constitute adverse atmospheric conditions for E-O systems.

(2) To develop probabilistic statistical climatology models for adverse weather and EOMET parameters for use in design and evaluation of tactical E-O systems.

(3) To identify data gaps and model deficiencies, and initiate means to bridge these gaps and correct these deficiencies.

(4) To provide a consultant service to internal and external users.

7.1.2 Approach:

(1) Survey repositories (personal, national and international) climatological data to determine the extent and availability of the data.

(2) Categorize the data according to the adverse effects on the operation of the dominant tactical E-O systems.

(3) Develop a data and model base for the frequency of occurrence and the recurrence probability for atmospheric conditions related to models of the atmospheric aerosol.

(4) Computerize the data bank.

(5) Identify data gaps and model deficiencies and implement action to correct these problems through in-house, contract, or grant research.

(6) Provide information summaries to both internal and external users.

7.2 MAJOR EFFORT: MODELING

7.2.1 Objectives:

(1) To develop the capability of predicting atmospheric transmission under battlefield conditions within the spectral region from the visible to the millimeter as a function of user or research input elements (e.g., wavelength, temperature, pressure, visibility, atmospheric path, etc.).

(2) To model the atmospheric aerosol and gases to include BIC to provide input to transmission and radiative transfer models.

(3) Address other modeling requirements such as turbulence, smoke obscuration, and transport and diffusion models.

7.2.2 Approach:

(1) Establish an initial predictive capability to provide transmission, transport and diffusion, radiation transfer, smoke obscuration, and turbulence predictions based on a state-of-the-art assemblage of information and existent models.

(2) Based on prototype transmission and radiative transfer models, initiate model improvements to address adverse weather, countermeasure smokes, and BIC.

(3) To relate user input elements (measurables) to those required by the analytical transmission, turbulence, smoke obscuration, transport and diffusion, and radiative transfer models.

(4) Develop and tailor the aerosol and gaseous models to provide the input information required by transmission, smoke obscuration, and radiative transfer models for realistic battlefield environments.

(5) Determine the minimum measurement requirements for a realistic user model (minimum set of measurables).

(6) Acquire and exercise turbulence and transport and diffusion models for addressing the smoke obscuration problem.

(7) Evaluate and validate the models by utilizing laboratory and field studies.

7.3 MAJOR EFFORT: LABORATORY MEASUREMENTS

7.3.1 Objectives:

(1) To measure, under controlled laboratory conditions, those characteristics of the battlefield gases and particles which affect the propagation of EM energy (in the spectral region from visible to millimeter wavelengths).

(2) To measure, under controlled laboratory conditions, the interaction of EM energy (in the spectral region from 0.3 to 4000 micrometers) with various types of the atmospheric aerosols and gases found in battlefield environments.

7.3.2 Approach:

(1) Specify those gaseous and particulate components of the atmosphere and BIC which significantly affect the propagation of EM energy.

(2) Measure the significant spectral, physical and/or chemical properties of samples of these gases and particulates specified under (1) for wavelengths from visible to millimeter.

(3) Measure the interaction of EM energy with various natural and anthropogenic gases at low, medium and ultrahigh spectral resolution.

(4) Extend gas and particle sampling to a global scale.

(5) Develop or modify equipment as dictated by program needs.

7.4 MAJOR EFFORT: FIELD MEASUREMENTS

7.4.1 Objectives:

(1) To measure the spatial and temporal distribution of the atmospheric aerosols and gases over a variety of meteorological and geographical conditions.

(2) To establish mobile capability for measuring the effect of the atmospheric medium (including BIC) on the propagation of energy in the spectral range from 0.3 to 4000 micrometers.

(3) To measure the atmospheric transmission and scattering effects associated with selected EM devices under a variety of meteorological conditions for natural and projected battlefield situations.

7.4.2 Approach:

(1) Establish mobile computer-centered systems for measuring the temporal and spatial variabilities of projected battlefield environments.

(2) Establish a measurement capability to: (1) test model and laboratory predictions of EM interaction with the atmospheric medium (including battlefield conditions), (2) evaluate the performance of a given EM device, and (3) make in situ propagation measurements for specific applications.

(3) Make measurements at a variety of locations (continental, coastal, oceanic, and high and low latitude).

(4) Initiate a program for the development and utilization of LIDAR and other remote sensors for the measurements of the atmospheric, natural and battlefield aerosols.

REFERENCES

- GOMEZ, R. B., C. Petracca, C. Querfeld, and G. B. Holdale, 1975, "Atmospheric Effects for Ground Target Signature Modeling III. Discussion and Application of the ASL Scattering Model". ASL, ECOM-5558.
- GOMEZ, R. B., E. W. Stuebing, and J. J. Pinto, 1975, "PGUASS-LT: A Program for Computing Optical Properties of Single Scattering Aerosol Clouds of Homogeneous Particles", ASL and Frankford Arsenal, ECOM-5562.
- GOMEZ, R. B. and J. H. Pierluissi, 1975, "Incomplete Gamma Function Approximation for King's Strong Line Transmittance Model", ASL, ECOM-5567.
- GOMEZ, R. B., M. T. Potter and J. H. Pierluissi, 1977, "Application of an Efficient Method for Calculating Transmittance Profiles", Proceedings of the Society of Photo-Optical Instrumentation Engineers, Volume 125, p. 24.
- GOMEZ, R. B., 1977, "Application of Semiquantal Theory to Atmospheric Infrared CO₂ Band Spectral Absorption", 24th Canadian Spectroscopy Symposium, Ottawa, Canada, 23-26 October.
- GOMEZ, R. B., J. H. Pierluissi and R. E. Bruce, 1977, "Computationally Fast and Accurate Method for the Voigt Profile", Transactions, American Geophysical Union, 58, p. 1149.
- GOMEZ, R. B. and L. D. Duncan, 1977, "Atmospheric Modeling for Electro-Optical Systems and Combat Developers", presented at the Military Operations Research Society Symposium, Naval Postgraduate School, 13-15 December.
- GOMEZ, R. B. and L. D. Duncan, 1978, "Description and Application of the ERADCOM Smoke Obscuration Model", Technical Cooperation Program Symposium on Smoke and Adverse Weather Effects on Electro-Optical Systems, Royal Signals Research Establishment, Malvern, England, 22-24 May.
- HOIDALE, G. B., R. B. Gomez and Bobby Hinds, 1976, "Occurrence of Dust Over Selected Geographical Areas", Topical Meeting on Atmospheric Aerosols, Their Optical Properties and Effects, sponsored by NASA-Langley and the Optical Society of America, Williamsburg, Virginia, 13-15 December.
- HOIDALE, G. B., B. D. Hinds and R. B. Gomez, 1977, "Worldwide Data on Reduced Visibility Due to Airborne Dust", J. Opt. Soc. Am., 67, pp. 1668-1690.
- LOW, R. D. H. and R. B. Gomez, 1976, "Analysis of Radiative Properties of Warm Clouds at Infrared Wavelengths", Topical Meeting on Atmospheric Aerosols, Their Optical Properties and Effects, sponsored by NASA-Langley and Optical Society of America, 6-8 December.
- ODDR&E Symposium and Workshop, 1976, Proceedings of the Optical-Submillimeter Atmospheric Propagation Conference", US Air Force Academy, Colorado Springs, CO, 6-9 December.
- PIERLUISSI, J. H. and R. B. Gomez, 1975, "A Study of Transmittance Models for the 15-Micron CO₂ Band", ASL, ECOM-5559.
- PIERLUISSI, J. H., R. B. Gomez and R. E. Bruce, 1976, "Application of Transmittance Models to Inhomogeneous Paths", Seventh Conference on Aerospace & Aeronautical Meteorology and Symposium on Remote Sensing from Satellite, American Meteorological Society, Melbourne, FL, 16-19 November.
- PIERLUISSI, J. H., R. B. Gomez and R. E. Bruce, 1976, "Model for Transmittance Calculations Along Inhomogeneous Paths for Gases with Variable Mixing Ratios", American Geophysical Union Meeting, San Francisco, CA, 6-10 December.
- PIERLUISSI, J. H., G. A. Gibson and R. B. Gomez, 1976, "Approximation to the Incomplete Gamma Function for Strong-Line Absorptance Model", Applied Optics, 15, 19.
- PIERLUISSI, J. H., R. B. Gomez and R. E. Bruce, 1977, "Transmittance Model for Absorbing Gases with Variable Mixing Ratios in Inhomogeneous Atmospheres", Applied Optics, 16, 18.
- PIERLUISSI, J. H., G. A. Gibson and R. I. Gomez, 1977, "Computationally Fast Approximation to the Lorentzian Profile for Spectral Transmittance Calculations", Transactions, American Geophysical Union, 58, 401.

- PIERLUISSI, J. H., P. C. Vanderwood and R. B. Gomez, 1977, "Fast Calculation Method for the Voigt Profile", J. Quant. Spectrosc. Radiation Transfer, 18, pp. 555-558.
- PIERLUISSI, J. H., R. B. Gomez and L. D. Duncan, 1977, "Use of Prony's Method in Band Modeling of Atmospheric Transmittance", Transactions, American Geophysical Union, 58, p. 1149.
- PIERLUISSI, J. H., G. A. Gibson and R. B. Gomez, 1978, "Approximation to the Lorentzian Coefficient for the Efficient Calculation of Transmittance Profiles", accepted by Applied Optics for publication.
- PIERLUISSI, J. H., R. B. Gomez and L. D. Duncan, 1978, "Application of Prony's Method to the Modeling of Spectral-Band Transmittance", accepted by Applied Spectroscopy for publication.
- RUNKE, L. H., Editor, 1977, "Proceedings on a Workshop on Remote Sensing of the Marine Boundary Layer", Naval Research Laboratory Memorandum Report 3430, Workshop was held in Vail, CO, in August 1976.
- SELBY, J. E. A., 1978, "LOWTRAN IV STATUS", Presented at the 5th Meeting of E-O Sensor Atmospheric Optics Working Group, ASI, White Sands Missile Range, New Mexico. John Selby is currently working with the Grumman Aerospace Corporation, Bethpage, NY 11714, USA. A technical report on LOWTRAN IV is scheduled to be released by the Air Force Geophysics Laboratory as AFGL-TR-78-0053.
- SHETTL, E. P. and R. W. Fenn, 1976, "Models of the Atmospheric Aerosols and Their Optical Properties", AGARD Conference Proceedings, No. 183, Optical Propagation in the Atmosphere, pp. 2.1-2.16.
- UNITED STATES ARMY ELECTRONICS RESEARCH & DEVELOPMENT COMMAND, NIGHT VISION & ELECTRO-OPTICS LABORATORY, 1977, "Interim Summary Report of E-O Sensor Atmospheric Optics Working Group Joint PARCOM/NMC/AFLC/AFSC Panel on the Field of Night Vision Technology", prepared for Joint Deputies for Laboratories Committee, Department of Defense.

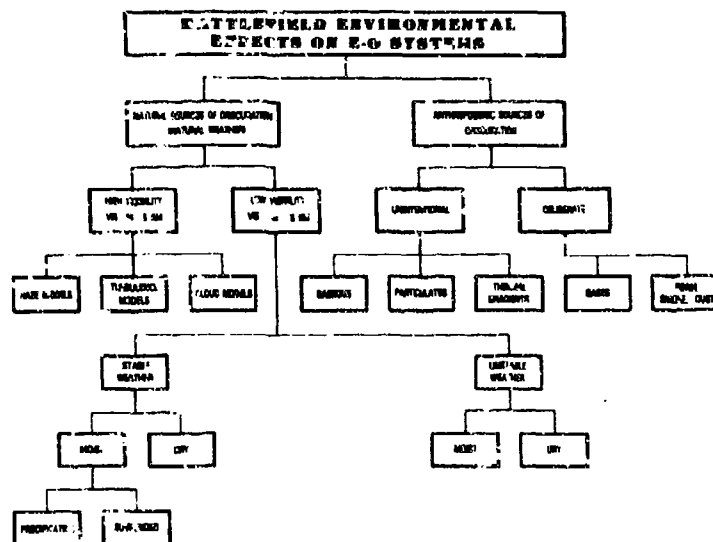


FIGURE 1: Categories of battlefield environmental effects on electro-optical systems.

CRITICAL MODELING UNCERTAINTIES FOR PREDICTION OF NATURAL AEROSOL ATTENUATION														
	OPTICAL PROPERTIES	TEMPERATURE PROFILES	WIND SPEED DIRECTION	WIND SPEED DIRECTION	WIND SPEED DIRECTION	WIND SPEED DIRECTION	WIND SPEED DIRECTION	WIND SPEED DIRECTION	WIND SPEED DIRECTION	WIND SPEED DIRECTION	WIND SPEED DIRECTION	WIND SPEED DIRECTION	WIND SPEED DIRECTION	WIND SPEED DIRECTION
TEMPERATURE PROFILES	E ₁	E ₁	E ₁	E ₁	E ₁	E ₁	E ₁	E ₁	E ₁	E ₁	E ₁	E ₁	E ₁	E ₁
WIND SPEED DIRECTION	E ₁	E ₁	E ₁	E ₁	E ₁	E ₁	E ₁	E ₁	E ₁	E ₁	E ₁	E ₁	E ₁	E ₁
LOCAL WEATHER DISTRIBUTION	E ₁	E ₁	E ₁	E ₁	E ₁	E ₁	E ₁	E ₁	E ₁	E ₁	E ₁	E ₁	E ₁	E ₁
TIME, LOCATION							E ₁	E ₁	E ₁	E ₁	E ₁	E ₁	E ₁	E ₁
LIQUID WATER CONTENT	E ₁	U		U	U	U	U	U	E ₁	E ₁	E ₁	E ₁	U	E ₁
SOLAR AUGMENT	E ₁	U		E ₁	U	U	E ₁	U	U	U	E ₁	E ₁	U	E ₁
TO-AIR TRANSMITTANCE	E ₁					U	E ₁	E ₁		E ₁	E ₁	E ₁	U	U
WIND SPEED DIRECTION	U	U	U	U			E ₁	E ₁	U		E ₁	E ₁	U	U
WIND SPEED DIRECTION							U	U	E ₁	U	E ₁	E ₁	E ₁	E ₁
WIND SPEED DIRECTION	E ₁	U				U	E ₁	E ₁	U	U	E ₁	E ₁	U	U
WIND SPEED DIRECTION	U	U	U	U			E ₁	E ₁	U		E ₁	E ₁	U	U
WIND SPEED DIRECTION	U						E ₁	E ₁		U	U	U	U	E ₁
WIND SPEED DIRECTION											U	U	E ₁	E ₁
WIND SPEED DIRECTION							U	E ₁					E ₁	U
WIND SPEED DIRECTION									U				U	E ₁
WIND SPEED DIRECTION	U			E ₁										U
WIND SPEED DIRECTION													U	U
WIND SPEED DIRECTION														U

E₁ ABSOLUTE UNCERTAINTY
 E₂ MODERATE UNCERTAINTY
 U UNKNOWN
 VALUE UNLESS NOTED OR OTHERWISE

FIGURE 2: Relationships between critical modeling uncertainties and associated measurements for the case of natural weather.

CRITICAL MODELING UNCERTAINTIES FOR PREDICTION OF BIC ATTENUATION										
	ALBEDO COEFFICIENT	ATMOSPHERIC EXTINCTION	SPATIAL STRUCTURE	TEMPORAL STRUCTURE	SMALL SCATTERING ALBEDO	SMALL SCATTERING PHASE FUNCTION	REFRACTIVE INDEX OF ATMOSPHERE	ATMOSPHERIC WATER VAPOR CONTENT	SMALL SCALE FACTORS	SPATIAL SCALE STRUCTURES
SKY RADIANCE	U	U	E ₂	E ₁	U	E ₂	E ₂	E ₂	E ₂	
ALBEDO DATA SAMPLING FOR CHARACTERIZATION AND MODEL ANALYSIS	E ₁	E ₂	E ₂	E ₂	E ₂	U	U	U	U	
WIND AND DIFFUSION MEASUREMENTS			E ₂	E ₂			E ₁	E ₂	E ₂	E ₁
POINT TRANSMITTANCE MEASUREMENTS AT 0.5 MICRONS EXT COEFF	E ₂	U	E ₂	E ₂	E ₁		U	U		
LONG PATH SPECTRAL TRANSMITTANCE	U	U	E ₂	E ₁		U	U	E ₂		
SKY RADIANCE	U	U	U	E ₂	E ₂	E ₂	U	U		
AEROSOL SIZE DISTRIBUTION	U	E ₁	U	U	E ₂	U			U	
POLAR REFLECTANCE	U	U	U	U	E ₂	E ₁	U			
MOLECULAR POINT SAMPLING			E ₂	E ₂						E ₁
PATH RADIANCE	U	U			E ₂	E ₂			U	
LEAK			E ₁	E ₁						
LAPSE RATE			E ₂	E ₂						U
ITS HIGH RESOLUTION TRANSMITTANCE	U	U					U			E ₂
STANDARD METEOROLOGICAL DATA			U	U			U	U	U	
CLIMATOLOGY	U	U	U	U			U			

E₁ - ABSOLUTELY ESSENTIAL
 E₂ - HIGHLY DESIRABLE
 U - USEFUL
 BLANK SPACES - MINOR OR IMPRELEVANT

FIGURE 3: Relationships between critical modeling uncertainties and associated measurements for the case of battlefield induced contaminants (BIC).

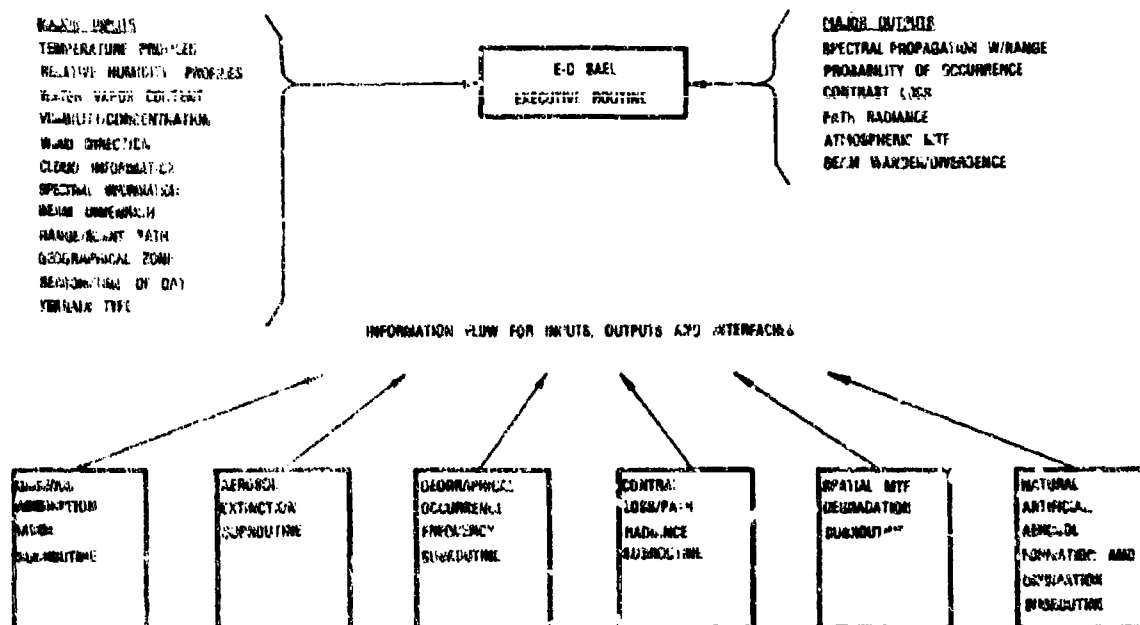


FIGURE 4: A conceptual illustration of how E-O SHEL might be configured [US ARMY ERADCOM, 1977].

DISCUSSION

N.G.Gerson, US

Under battlefield conditions a great number of particles or aerosols are injected into the atmosphere. These can cause both attenuation of the signal and a rise in the background (scattered) noise level. To what extent will this condition degrade optical systems by decreasing ratio of signal/noise.

Author's Reply

The extent of the signal/noise degradation under battlefield conditions depends upon many factors such as the types and concentrations of the aerosols (or smokes), sky illumination, viewing angle, sensitivity, field of view (FOV), and spectral response of the sensor. It depends on whether you are using an active system (laser) or a passive system (FLIR) and possibly even the type of weather and terrain around you. We are currently investigating at the Atmospheric Science Laboratory the answers to these questions using an obscuration model named ASLSOM.

INTERPRETATION OF AIRBORNE MEASUREMENTS OF ATMOSPHERIC EXTINCTION AND
IRRADIATING FLUXES IN GERMANY AND THE NETHERLANDS

H. von Redwitz
G.H. Ruppertsberg
R. Schellhase
J. Weidner

DEUTSCHE FORSCHUNGS- UND VERSUCHSANSTALT FÜR LUFT- UND RAUMFAHRT E.V.

DFVLR - Institut für Physik der Atmosphäre
8031 Oberpfaffenhofen / Germany

ABSTRACT

Atmospheric contrast transmittance is dependent on the atmospheric extinction and the irradiating fluxes, and is severely influenced by weather conditions.

In addition to the corresponding research in the OPAQUE project, the DFVLR carries out airborne measurements in the region between northern Germany, the Netherlands and southern Germany. The optical equipment is simpler than the instrumentation used in the C-130 of the AFGL. But measuring flights are performed during a 2-years period at different times of the day for one week each month. The main attention therefore is set to interpretations, in one hand standing in relation as close as possible to visibility problems in practice, and in the other hand allowing to be classified by meteorological routine-parameters. Beside beam transmittance and path reflectance, the slant meteorological visibility range and in relation the slant detection range for visibility air-to-ground and ground-to-air seem to meet with this request under the prescribed conditions, as is shown in examples.

1. INTRODUCTION

During the NATO-project "OPAQUE" (Optical Atmospheric Quantities in Europe) (BAKKER), the DFVLR Institute for Atmospheric Physics connects the OPAQUE ground stations in southern Germany, the Netherlands and northern Germany every month by means of a series of measurement flights. As our measuring aircraft is much smaller than that of the AFGL, we can, of course, only measure a limited number of parameters. The large number of measuring flights as well as the extension of the area we have to overfly, allows and at the same time requires a classification according to meteorological points of view which have to be developed together with the Amt für Wehrgeophysik (Department for Military Geophysics). The evaluation refers to the comprehensive research work of the AFGL (DUNTLEY, JOHNSON and GORDON). In order to find out appropriate marks of classification, as far as they are not yet known, cases of practical interest are simulated by means of a calculating programme. A further extension of the programme will also deal with the influence of different cloud forms.

2. MEASURING PROGRAM

The propeller aircraft BE 65 serves for the measuring purposes, having a ceiling of 10.000 ft. The OPAQUE measuring flights are usually flown without oxygen in altitudes of 10.000 ft. The average speed is 150 kts, the rate of climb respectively of vertical descent during the measuring flights is approximately 800 - 1000 ft per minute.

Every month, for a week's time, day after day the northern and southern route are flown starting from the base airport Cologne. The northern route (cruising altitude 10.000 ft) begins in the early hours of the morning, if possible before the formation of thermal convection, with take-off at Cologne, leading over Wildenrath (low go), Ypenburg (low go near the OPAQUE measuring station) to Bremen, this being the appropriate airport situated nearest to the OPAQUE measuring station in Meppen. In the afternoon flying back to Cologne is done in opposite direction. Like the northern route, the southern one (cruising altitude 9.000 ft) begins in the early hours of the day before the formation of thermal convection with take-off at Cologne, then leads - at IFR - over Stuttgart (low go) to Oberpfaffenhofen, and in the afternoon, vice versa, back to Cologne. In case of VFR the low go will be effected right next to the OPAQUE ground station Birkhof instead of Stuttgart.

The wish, however, to effect the morning flights before the formation of thermal convection is contradictory to the demand that irradiance should not change too much. As a compromise between these requirements and the technical reasons of the airport the following flight times will be observed:

Dec.	Jan./Nov.	Febr./Oct.	March/Sept.	Apr./Aug.
9.00 - 12.00	8.30 - 11.30	8.00 - 11.00	7.30 - 10.30	7.00 - 10.00
12.30 - 15.30	13.00 - 16.00	13.30 - 16.30	14.00 - 17.00	14.00 - 17.00
May/July	June			
6.30 - 9.30	6.00 - 9.00			
14.00 - 17.00	14.00 - 17.00			

In addition to this program measuring flights were effected together with the C-130 of AFGL (DUNTLEY et al. 1977) and during the measuring campaigns of our Visibility Group (HOFFMANN) at Meppen and Eckernförde.

The optical measuring equipment is installed in a temperature-stabilized nose container of the BE 65 (fig. 1). It consists of a photometer system, two pyranometers and a backscatter sonde. The photometer system comprises 6 single photometers, 4 of which are periodically deflected all 2 s for one second by an angle of 15° to mark inhomogeneities of the radiance in the sky (the sun e.g.). Measuring is done at wavelengths of $400\mu\text{m}$, resp. $550\mu\text{m}$ resp. $900\mu\text{m}$ with a halfwidth of approximately $50\mu\text{m}$. The logarithms of the measured quantities are taken and are once a second transferred on tape.

Seen in flight direction, the photometers are mounted as follows (fig. 2):

photometer 1, view to the left; visual angle 50° normal to flight direction; $\pm 6.5^\circ$ in flight direction

photometer 2, upwards; $\pm 27.5^\circ$ normal to flight direction; $\pm 6.5^\circ$ to flight direction

photometer 3, forward; 3° above horizon (in normal straight flight at constant altitude); visual angle $\pm 27.5^\circ$ horizontal; $\pm 6.5^\circ$ vertical; periodically deflected upward by 15° .

photometer 4, view to the right; visual angle 55° normal to the flight direction; $\pm 6.5^\circ$ in flight direction; periodically deflected by 15° in flight direction.

photometer 5, upwards; cos-characteristic with an aperture of 160° .

photometer 6, downwards; cos-characteristic with an aperture of 160° .

Thus in the sky photometers 1, 2, 4 together have an angle of view of 165° . Their angle as well as that of photometers 5 and 6 was chosen smaller than 180° so that flying motions do not disturb the measurements signals with regard to sky and ground.

pyranometer 1, upward view; cos-characteristic with an aperture of 160°

pyranometer 2, downward view; cos-characteristic with an aperture of 160°

The backscatter sonde views vertically upwards. It measures once per second - at a wavelength of $550\mu\text{m}$ - the radiation of a Xenon-flash lamp backscattered by the air molecules and the aerosol particles. Approximately 97% of the radiation received are originating - in a homogeneous atmosphere - from a scattering volume extending between about 0.2 m and 10 m in front of the instrument. Due to an electronic gate, signals from strong reflectors (clouds) being farther away than 300 m can no longer be received.

For the extrapolation of the spectral course into the IR-range, the measurements taken by the OPAQUE ground stations have to be used.

In addition to this time, static pressure, speed, static temperature, relative humidity, attitude and heading of the aircraft are recorded. Photos are taken of the respective cover of clouds. The tape recording contains $384\text{ bit/s} = 1.4 \cdot 10^6\text{ bit/h}$.

4. ACQUISITION OF MEASUREMENTS

The measurements recorded on tape are converted into physical values with the Amdahl 470 V/6 computer of DFVLR using a special program. Data of each flight are clearly plotted. Fig. 3 e.g. shows the plot of 9/2/77. The various measurements are plotted together with the agreed dimension depending on the flight time. In the following some data referring to the flight are given: Take-off Cologne at 9.00 GMT; 8.20 Koblenz; sunny, partially slightly covered, fog in the valleys; 8.30 Bingen loop, increasing stratus under and over aircraft; 8.40 Worms; 9.00 Suebian Alp; scattered rests of snow, stratus becoming dark grey, increasing sunny; looks through to the ground; 9.05 alteration of heading with approach to Stuttgart, fog in the valleys, visibility 100 m. The backscatter shows very well the diving into the layer of haze as well as the thermal variation, i.e. first increase of temperature, then fall of temperature at low altitude. At 9.23 "low go" Stuttgart; 9.52 Augsburg, now partly in clouds (see backscatter), strato-cumulus, heavily covered; 10.06 landing at Oberpfaffenhofen. The temperature at take-off was 2°C , visibility 4.5 km, sky half-covered. The sun being south-east, near the horizon (Azimuth 127° ,

elevation 9.5°) photometer 3 measures direct irradiance of the sun after the aircraft had headed for 127° . According to extraterrestrial irradiance at wavelengths of $0.4\mu\text{m}$; $0.5\mu\text{m}$ and $0.9\mu\text{m}$ and measuring at an altitude of 2500 m and a sun elevation of 9.5° , follows, e.g. a transmittance of $\tau_1 = 0.62$; $\tau_2 = 0.77$ and $\tau_3 = 0.99$ related to the relative air mass 1. The regular transmittance alone comes up to $\tau_1 = 0.59$; $\tau_2 = 0.74$; $\tau_3 = 0.97$ (green-prple blue horizon).

From 8.05 o'clock the curve of photometer 3 appears strongly spread, the folding mirror makes the photometer, by turns, view to the sun, respectively to the sky 15° above it. The irradiances vary up to factor 5. Hence regular transmittance can be computed. Together with the measurements of photometers 1 to 4 which additionally record the different spots of the sky at variable flying attitudes, it is possible to draw conclusion on the scattering function. It can, however, be disturbed by multiple scattering and probably also by clouds. The Albedo depending on the altitude is resulting from those values measured by photometers and pyranometers in the upper and lower halfspace. Disturbances may arise from shadowing clouds or reflecting ground.

5. INTERPRETATION

The processed data thus furnish, besides the horizontal variability of the single measurements, the extinction coefficient $\sigma_e(z)$ as the function of altitude above sea level as well as the irradiances produced by the sun and the different spots of the sky at the measuring point. Horizontal homogeneity is assumed for $\sigma_e(z)$ when evaluating it. Areas having horizontally different $\sigma_e(z)$ are treated as separate ones. Visibility from such an area into a neighbouring one is of practical interest only in special cases which are dealt with separately. It is, however, taken into consideration on evaluating the data that irradiances can strongly vary horizontally under the influence of clouds laying over the sight path. All measurements are valid for a special wavelength, even if not explicitly mentioned in the text or in the formulae.

It is reasonable to use KOSCHMIEDER's horizontal meteorological visibility* instead of the extinction coefficient, as it is directly comparable to visibility found out by way of routine by all meteorological service stations.

$$(1) \quad \sigma_e(z) = \frac{3.9}{V_N(z)} = \frac{3.0}{V_S(z)}$$

V_N is relative to 2%, V_S to 5% threshold of contrast. They are equivalent to the distances between target and observer having 2% respectively 5% regular transmittance. The meteorological visibility (V_N or V_S) normally refers to a $0.55\mu\text{m}$ wavelength (RUPPERSBERG) and the layer near the ground. According to equation (1) it is, however, possible and in praxi common usage to convey this term to other wavelengths (HOEHN) and other altitudes.

Analogous to the horizontal one there can also be defined a slant meteorological visibility V_{NS} respectively V_{SS} . According to a suggestion of J. WEISS (also FOITZIK 1960) it is the projection of the slant sight path having 2% respectively 5% regular transmittance (or as defined by DUNTLEY et al.: beam transmittance) upon the (horizontal) ground (fig. 4). If observing conditions at this beam transmittance still admit a detection of objects on the ground, also an observer from the altitude z_{ob} (fig. 4) can overlook an area (on the ground) with a radius V_{NS} resp. V_{SS} . The slant meteorological visibility apparently has the advantage of great distinctness and is, as we will see, particularly appropriate for a classification.

$V_N(0)$ be the (horizontal) meteorological visibility on the ground, $V_N(z)$ be that in the altitude z above ground and z_{ob} be the observer's altitude. Hence follows for the slant meteorological visibility:

$$(2) \quad \frac{V_{NS}(z_{ob})}{V_N(0)} = \frac{z_{ob}}{V_N(0)} \sqrt{\frac{1}{\left\{ \frac{z_{ob}/V_N(0)}{V_N(z)} d\left(\frac{z}{V_N(0)}\right) \right\}^2 - 1}}$$

*Footnote: In Germany the term "Normsichtweite" proposed by FOITZIK in 1947 (DIN 5037) has generally become used as denomination of this value. In English literature nowadays obviously "meteorological visibility" is preferred besides the term "meteorological range" which was defined by DUNTLEY in 1948 and taken over by MIDDLETON. The terms "standard visibility", "standard visual range", "visual range" or simply "visibility" are used as well. The term "meteorological optical range" proposed by the WMO for the 5% beam transmittance is closely related to it, but is defined slightly different.

The same equation is valid for V_{55} , however, with the index "5" instead of "N".

Fig. 5 shows the course of the slant meteorological visibility as a function of the observing altitude for the following status: On the ground there is a fog layer with 300 m meteorological visibility reaching up to an altitude of 90 m (curve 1), resp. 180 m (curve 2) or 270 m (curve 3). Above this, up to the upper border of the boundary layer in an altitude of 1440 m, there is a meteorological visibility of 10 km. After a jump to 50 km the meteorological visibility steadily increases together with the altitude in the free atmosphere above 1440 m. Whereas an observer on the ground can, at best, detect objects within a horizontal radius of 300 m, an observer e.g. sitting in a helicopter flying at an altitude of 300 m, can overlook an area of V_N resp. $V_{55} = 873$ m radius, supposed the observing conditions admit a detection up to 2% resp. 5% beam transmittance (see curve 1). The radius would be 1598 m from a flying altitude of 600 m, and 5880 m from a flying altitude of 3000 m. At a fog altitude of 180 m (curve 2) the area to be overlooked from 300 m (600 m; 3000 m) shrinks to 301 m (720 m; 2660 m) radius. At a fog altitude of 270 m (curve 3) the area to be overlooked from all the flying altitudes is smaller than that to be seen from the ground. From flight altitudes of more than 1270 m the ground is no longer visible.

Because of the already known spectral neutrality of fog these values are not only valid in the visible spectral range. Beyond the absorption bands they are most probably valid - by approximation from UV to the far IR - only at 10.5 to 11.5 μm with significant deviations (RUPPERSBERG, SCHELLHASE, SCHUSTER).

In equation 2 the different meteorological visibilities and altitudes appear in relation to the meteorological visibility on the ground, i.e. $V_N(0)$ resp. $V_5(0)$. The same, therefore, is valid for the result: at half the meteorological visibility on the ground, i.e. 150 m, all other numerical values of the above example are halved. Hence the observer in the helicopter at 150 m altitude has 437 m of slant meteorological visibility if there is a fog layer of a density of 45 below him, etc. For the classification of the slant meteorological visibility it is only required to know - apart from the horizontal meteorological visibility on the ground - the relative course of the extinction, which is very favourable as a property.

Analogous to the horizontal meteorological visibility the slant meteorological visibility is likely to be the upper limit for the detection range of (cool) black objects. The contrast transmittance c_T of the turbid atmosphere in all observations not having the horizontal sky as background is, indeed, not equal to the regular transmittance (beam transmittance) τ_r . On the contrary, in these observations the ratio b_{L_0} / b_{L_r} enters out of inherent and apparent background radiance:

$$c_T(z_{ob}, \theta_1, \phi_1) = \frac{C_r(z_{ob}, \theta_1, \phi_1)}{C_0(z_1, \theta_1, \phi_1)}$$

(3)

$$c_T(z_{ob}, \theta_1, \phi_1) = \tau_r(z_{ob}, \theta_1) \frac{b_{L_0}^L(z_1, \theta_1, \phi_1)}{b_{L_r}^L(z_{ob}, \theta_1, \phi_1)}$$

C_r is the apparent contrast, C_0 the inherent contrast. Fig. 6 shows the observation coordinates which have been taken over from DUNTLEY et al. (1957), as well as the respective terms. In the meantime, only some of the signs were adapted to CIE-standards which are customarily used.

A target having the inherent contrast C_0 against its surroundings is thus detectable up to the distances r in which the apparent contrast $C_r = c_T C_0$ has sunk down to the contrast threshold value.

From equation (3) follows, with the path radiance $L_r^x = b_{L_r} - \tau_r b_{L_0}$

(4)

$$c_T(z_{ob}, \theta_1, \phi_1) = \frac{1}{1 + \frac{L_r^+(z_{ob}, \theta_1, \phi_1)}{\tau_r(z_{ob}, \theta_1) b_{L_0}^L(z_1, \theta_1, \phi_1)}}$$

The path radiance L_r^{\pm} is the result of the luminance of the sight path:

$$(5) \quad L_r^+(z_{ob}, \theta_t, \phi_t) = \int_{z=z_t}^{z_{ob}} \sigma_s(z) \tau(z, \theta_t) \left\{ \beta'(z, \varphi_{su}) E(z, \theta_{su}, \phi_{su}) + \int_0^{2\pi} \int_0^{\pi} \beta'(z, \varphi_{sk}) L(z, \theta_{sk}, \phi_{sk}) \sin \theta_{sk} d\theta_{sk} d\phi_{sk} \right\} \frac{dz}{\cos \theta_t}$$

Apart from equation (4) and some other software it is the contents of the main procedure (fig. 7). By means of an σ - and an E-program the scattering coefficients $\sigma_s(z)$, transmittances $\tau(z, \theta_t)$, radiance of the sky $L(z, \theta_{sk}, \phi_{sk})$ and irradiance from the sun $E(z, \theta_{su}, \phi_{su})$ extracted from the measuring data are given in. The type of the scattering function $\beta'(z, \varphi_{su})$ has to be given in - as far as it doesn't result from the measurements (see par. 2) - on the basis of assumptions. Also, β_{L_0} values characteristic for the observation problem to be detected are given in. The main procedure then furnishes - apart from those data also given out by DUNTLEY et al. (1977) - the slant detection ranges $V_s(z_{ob}, \theta_t, \phi_t)$ characteristic for this very observation problem. Analogous to the slant meteorological visibility (fig. 4), the slant detection range is the projection of the sight path under which a detection is still possible upon the (horizontal) ground.

Fig. 8 (curve 2) shows slant detection range from 720 m altitude dependent on the Azimuth difference against the sun, i.e. the area on the ground which can be overlooked by an observer from this altitude. To simplify the matter, in this example it is assumed that objects up to 5% contrast transmittance are still detectable. The turbidity layer corresponds to the above mentioned example (fig. 5). The sun elevation is 30° ($=60^\circ$), the angular dependency of the luminous density of the sky which is dependant δM_z has not yet been considered, the ground reflectance is 0.2 (meadow)

The slant visibility from 720 m altitude (curve 2) is smaller than the slant meteorological visibility (curve 1) but still larger than the horizontal meteorological visibility $V_c(0) = 300$ m on the ground. Towards the sun the slant visibility is smallest and having the sun slantly in the back one looks farthest.

Curve 3 shows the range an observer can overlook from the ground, all the other conditions being the same, as per the level of a helicopter. Apart from the absolute values, this difference is likely to be an interesting parameter for the reconnaissance models. We hope to be able to indicate it if there is an appropriate meteorological optical classification with a sufficiently small scattering range. However, in the example mentioned the inherent contrast has not yet been considered at all. It can change the range considerably. Therefore it is a special object of research of our Visibility Group (Hoffmann). We are going to include their results in our further evaluation.

6. CONCLUSIONS

The slant meteorological visibility is an appropriate parameter for the indispensable classification of the amount of data which have been measured. For this procedure it is necessary to fit in firstly the ground visibility which is routinely recorded by meteorological services, secondly the relative vertical profile of the extinction coefficient which is in close correlation with the temperature profile of the existing air mass. In addition, the slant meteorological visibility can be taken as the upper limit for the slant detection range of usually interesting visual targets; the detection range of very bright targets may be increased by only a small portion.

Moreover, starting points for the classification of the impact of the irradiance still must be developed. For this purpose several parameters of practical interest, e.g. the relation visibility air-to-ground / visibility ground-to-air, are simulated by a computer under variable conditions. Those atmospheric optical parameters which are highly effecting the result then are classified together with the slant meteorological visibility.

7. REFERENCES

BAKKER, T., 1975, "The Measurement Program OPAQUE of AC/243 (Panel IV/RSG.8) on "sky and terrain radiation"", AGARD-CP-183, p. 14.1-10.

CIE, 1970, "International Lighting Vocabulary", 3rd edition, International Commission on Illumination, Bureau Central de la CIE, 4 Av. du Recteur Poincaré, 75 Paris 16e, France.

DIN 5037, 1963, "Lichttechnische Bewertung von Scheinwerfern, sheet 2, Deutsche Industrie-Normen.

DUNTLEY, S.Q., 1948, "The Visibility of Distant Objects", J. Opt. Soc. Am. 38: 237-249.

DUNTLEY, S.Q., BOILEAU, A.R., PREISENDORFER, R.W., 1957, "Image Transmission by the Troposphere I", J. Opt. Soc. Am. 47: 499-506.

DUNTLEY, S.Q., JOHNSON, R.W., GORDON, J.L., 1977, "Airborne Measurements of Atmospheric Volume Scattering Coefficients in Northern Europe", AFGL-PR-77-0078.

FOITZIK, L., 1947, "Theorie der Schrägsicht", Zeitschr. f. Meteorologie, 1:161-175.

FOITZIK, L., 1960, "Bestimmung der Schrägsicht nach einer Komponentenmethode", Beitrag Phys. Atmosph., 33:28-35.

HOEHN, D., 1975, "Atmospheric Vision $0.35/\mu\text{m} \leq \lambda \leq 14/\mu\text{m}$ ", Applied Optics 14: 404-412.

HOFFMANN, H.E., 1978, "Der Eigenkontrast militärischer Objekte auf dem Lande und auf dem Wasser (The inherent Contrast of Military Objects on Land and Sea)", to be published.

MIDDLETON, W.E.K., 1952, "Vision through the Atmosphere", University of Toronto Press.

RUPPERSBERG, G.H., 1978, "The Correct Spectral Weighting of the Meteorological Visibility. To be published in contribution to Atmospheric Physics.

RUPPERSBERG, G.H., SCHIELHASE, P., SCHUSTER, H., 1975, "Calculations about the Transmittance Window of Clouds and Fog at about $10.5/\mu\text{m}$ Wavelength", Atmospheric Environment, 9, 723-730.

WEISS, J., 1976, "Die Möglichkeit der Vorhersage der Schrägsicht beim Landeanflug mit Hilfe routinemäßig anfallender Wetterbeobachtungen nach einer niederländischen Studie", Flugsicherheit 3, 4-6.

It is regretted that Figures 7 and 8 are not available.



Fig. 1a : The AFGL C-130 "Hercules" and the DEVLB BE 65 "Queen Air" after a side by side measurement at Wunstorf

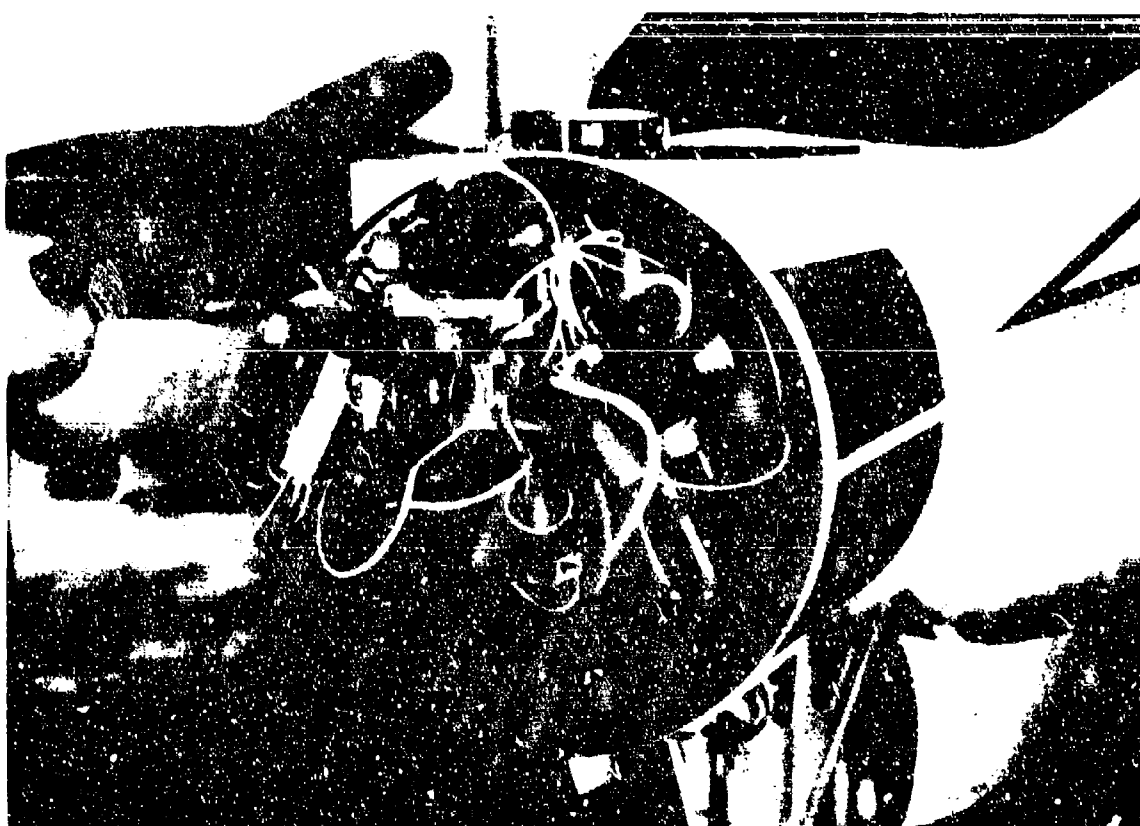


Fig. 1b : Optical measuring equipment installed in the nose container of the BE 65

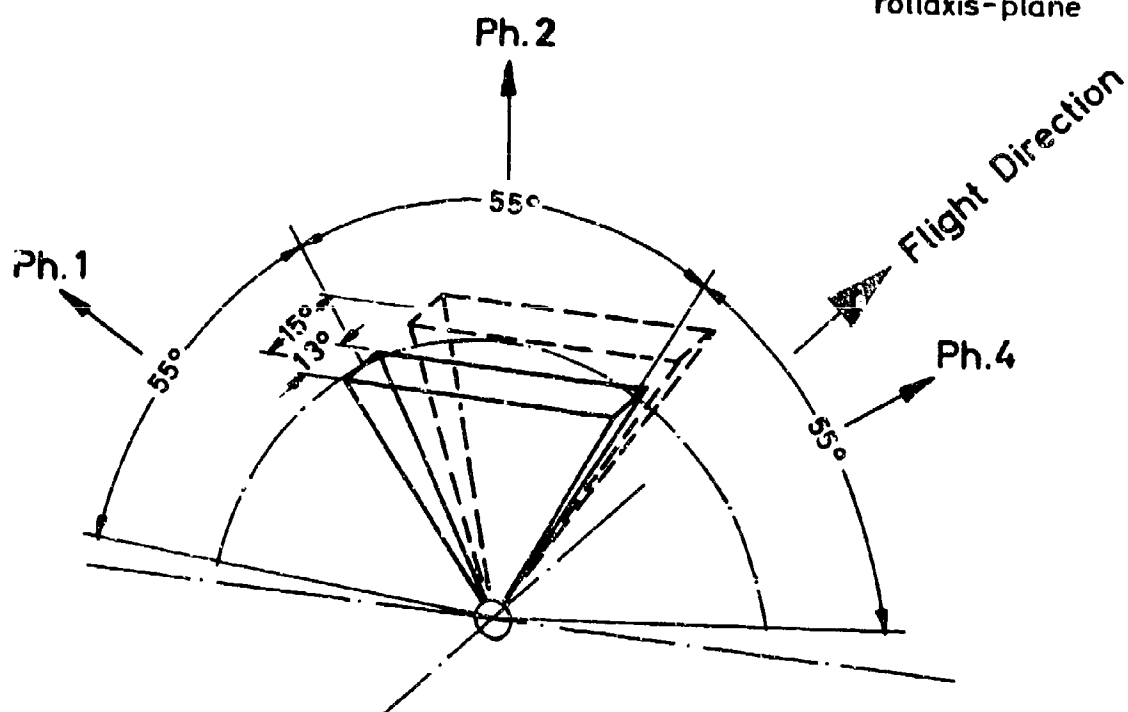
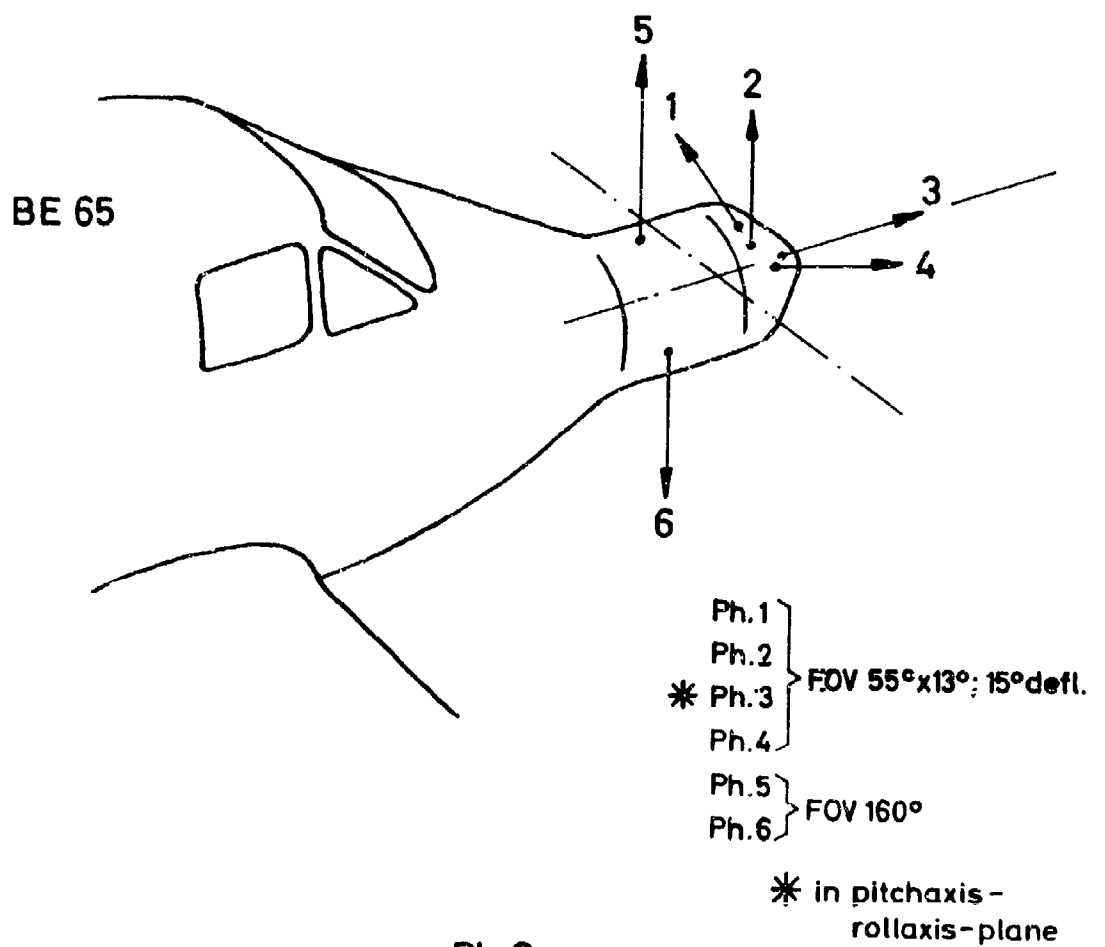


Fig. 2 : Photometers: Field of view

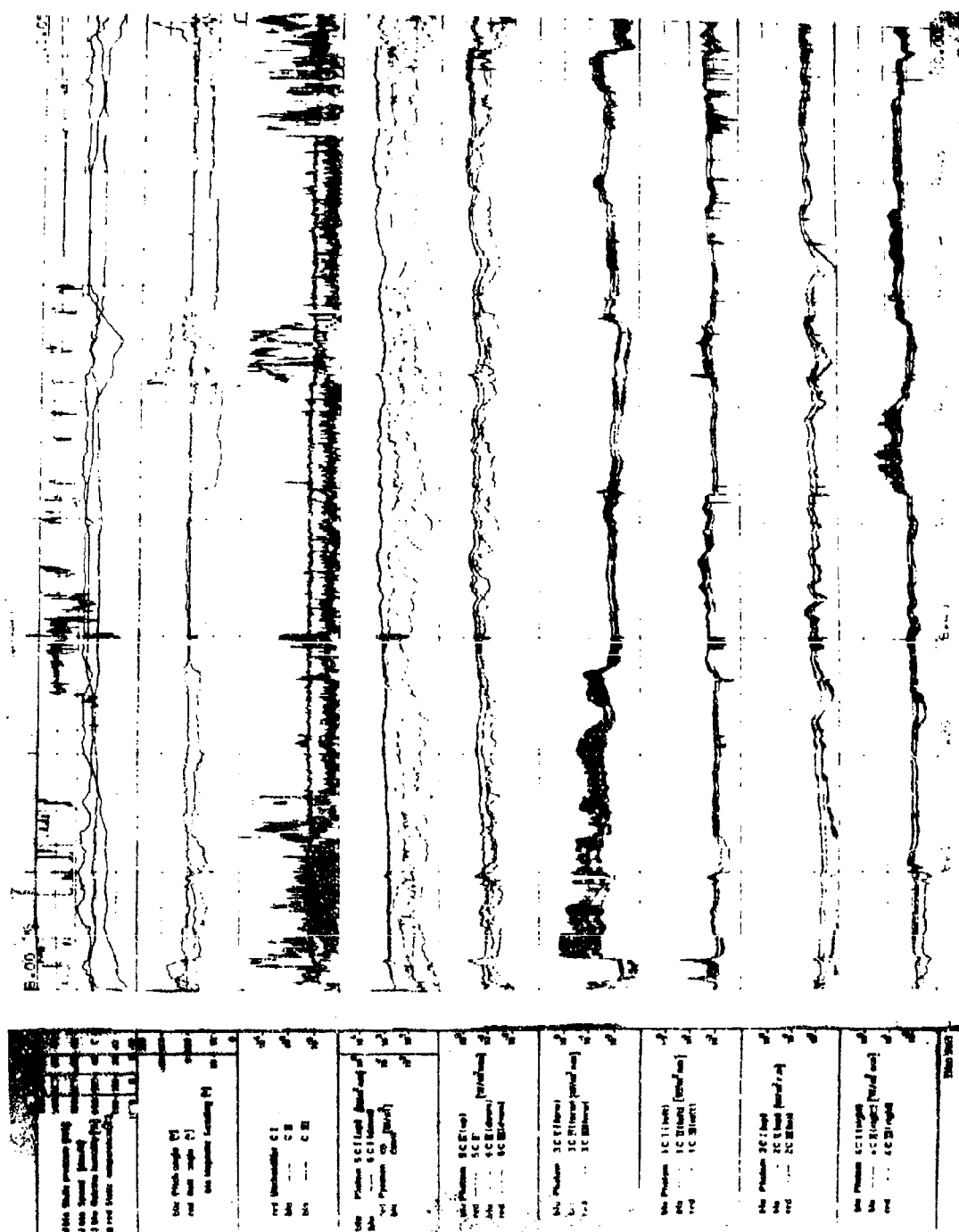


Fig. 3 : Plot of the based physical data

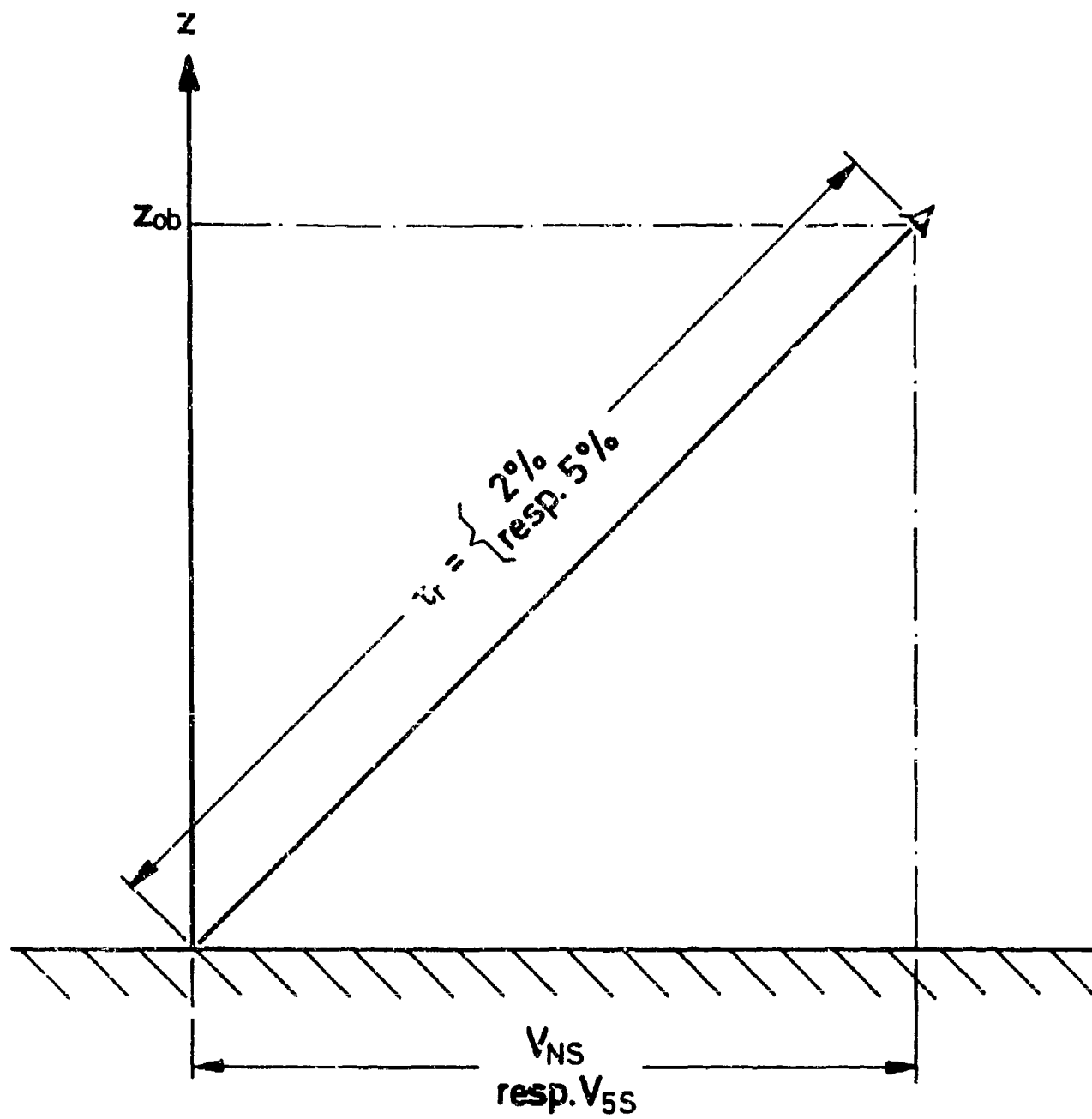


Fig. 4 : Definition of the slant meteorological visibility

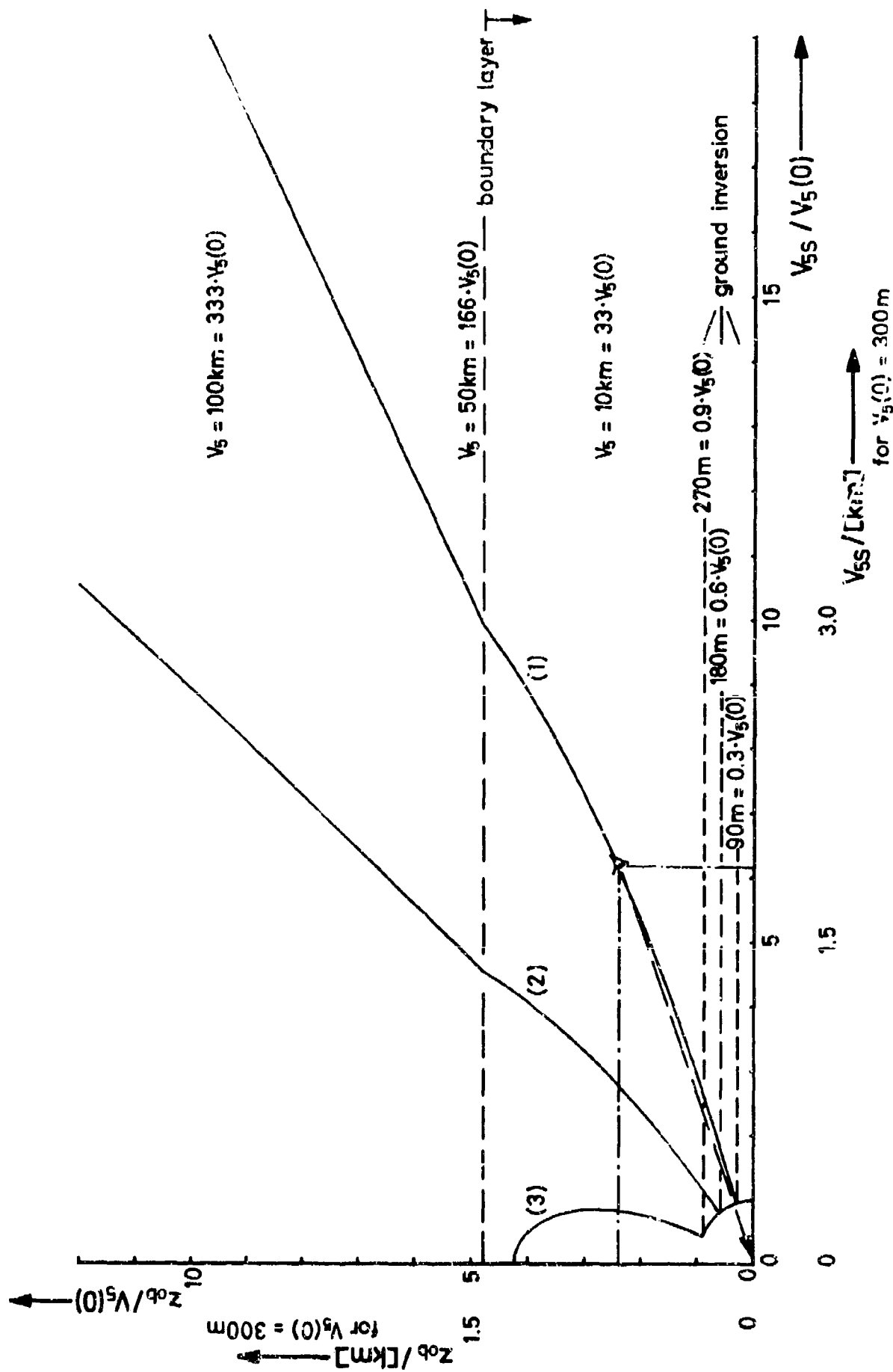


Fig. 5 : Slant meteorological visibility at ground fog situations.
 The meteorological visibility is 300 m beyond the ground inversion which is 90 m, 180 m or 270 m above the ground.

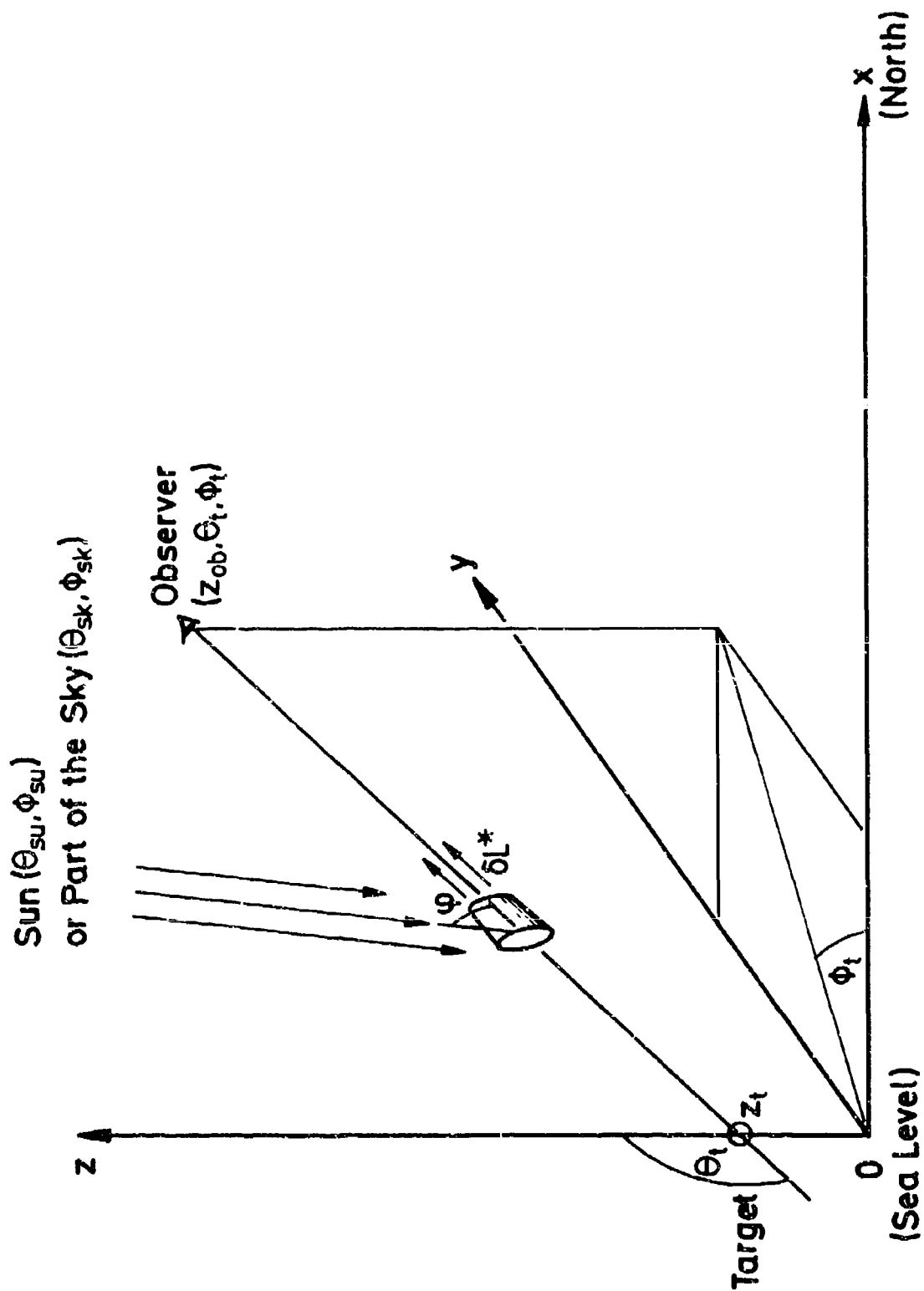


Fig. 6 : Coordinates for estimation of slant detection range

DISCUSSION

L.F.Drummster, US

Is it more common to use 2% or 5% as the contrast threshold for detection?

Author's Reply

The answer to this question depends on the measurement of contrast thresholds of human eyes (Blackwell, Middleton, et al.). In former times a contrast threshold of 2% was in use.

For military use, the 5% contrast threshold for detection is more common.

401

THE INFLUENCE OF METEOROLOGICAL PARAMETERS ON ATMOSPHERIC
TRANSMISSION AT $10.6\ \mu\text{m}$ (CO_2 -LASER RADIATION) AND $0.63\ \mu\text{m}$
(HeNe-LASER RADIATION) FROM MEASUREMENTS AND CALCULATIONS

J. Abele, H. Raidt, W. Jessen, R. Kirschmer
Forschungsinstitut für Optik der FGAN
Schloss Kressbach, D-7400 Tübingen, F.R. Germany
Report 1978 / 6

SUMMARY

This paper presents an experimental and theoretical study on atmospheric transmission of HeNe and CO_2 -laser radiation and in the photopic range. A continuously operating transmissometer designed and developed in the institute measured the attenuation of the two wavelengths simultaneously and over a common path length.

Besides the laser transmissometer measurements in the photopic range were performed by commercial visibility meters. Results are compared with semiempirical formula, with deductions from Mie theory and with a model describing transmission through rain.

1. INTRODUCTION

Atmospheric transmission of laser beams is important for several military and civilian applications, e.g. optical telecommunication engineering, modulation systems, anemometry, lidar systems, range finders, pointers and laser weapon systems. The operational usefulness of all these systems will be determined by the characteristics of the atmosphere through which the laser radiation must pass. Therefore further theoretical and experimental research on atmospheric absorption and scattering by molecules, aerosols, cloud and rain droplets and snowflakes is necessary to improve the mathematical description of atmospheric laser radiation transmission.

The prime objective of this study is to report on the comparative measurement of atmospheric attenuation of CO_2 - and HeNe-laser radiation and in the photopic range under a variety of meteorological conditions. Simple correlations with meteorological parameters will perhaps enable the performance that laser attenuation can be predicted if meteorological records are available. In this study a practical and a theoretical approach to the problem has been made.

2. EXPERIMENTAL SET-UP

2.1 LASERTRANSMISSOMETER AND VISIBILITY METERS

A scheme of the optical layout of the laser transmissometer is shown in Fig. 1. Besides a CO_2 -laser a HeNe-laser is installed. The radiation of the two lasers is collimated by means of a small CdTe plate. This plate is a window for the CO_2 -laser beam, whereas for the HeNe-laser beam it serves as a partial reflector. By means of a ZnSe beam splitter the two laser beams are separated into a reference and a measuring beam. A Cassegrainian-System sends the beams through the atmosphere. The primary mirror is an off-axis parabolic one, the second is a spherical one. At the end of the measuring range (distance 160 m) the laser beams are reflected by a retroreflector. Before reaching the detectors the beams are separated by an additional CdTe plate. The reference beam serves as a control for the laser power. For controlling the line stability of the CO_2 -laser a spectrum analyzer is used; therefore a further CdTe plate which serves as a partial reflector is mounted. The CO_2 -laser radiation is detected by a pyroelectric detector, the HeNe-laser radiation by a silicon detector. The measuring and the reference beam are chopped with 16 and 70 cycles resp. The electronic signal processing is performed by means of

phase sensitive rectifiers (lock-in technique).

The transmission in the photopic range was measured with a transmissometer (ELTRO) and a "Videograph" (Impulsphysik). The ELTRO transmissometer belongs to the double-ended devices. The instrument operates on two base lengths ($L_1 = 2 \times 15$ m; $L_2 = 2 \times 150$ m) and measures transmittance τ due to total atmospheric extinction along the optical path. The source of the device consists of a tungsten filament lamp, the receiver has a photopic response. To obtain optimal accuracy an automatic switching between the two base lengths is installed.

The "Videograph" belongs to the category of backscatter instruments and does therefore not require an extended baselength. It consists of a projector and a receiver in the same housing. The receiver measures the light scattered back from a certain volume of the atmosphere illuminated by the outgoing beam. Therefore scattering from angles between 177° and 179° is recorded. As a light source serves a high powered xenon spark lamp. The spectrum of the lamp contains practically no IR and lies in the blue-white region.

2.2 METEOROLOGICAL SET-UP

Air temperature was measured by means of a standard bimetallic thermometer. As humidity measuring device served a classical hair hygrometer. Since the accuracy of hair hygrometers is about 5% future measurements will be performed by electrically ventilated aspiration psychrometers to achieve higher accuracy. To measure the precipitation rate a commercial rain gauge was installed at the range. A cup anemometer combined with a wind vane was installed about two meters above the ground. Finally, the ambient carbon dioxide concentration was measured by a URAS 2T gas analyzer (Hartmann & Braun).

2.3 AEROSOL SET-UP

Aerosol spectra were measured by a Royco particle counter, Model 225, and a device of Particle Measuring Systems, Model ASAS-300 B. Table 1 shows some details of the aerosol measuring equipment.

Table 1: Some details of the aerosol measuring set-up

characteristics	Royco Model 225	PMS Model ASAS-300 B
measuring principle	light scattering	light scattering
light source	Incandescent lamp	HeNe-laser TEM ₀₀ mode
sampling area	0.5 mm ²	0.018 mm ²
sampling flow rate	47.2 or 4.72 cm ³ /sec	0.12 cm ³ /sec
measuring range	channel 1: 0.4 - 0.6 μ m " 2: 0.6 - 1.4 " " 3: 1.4 - 3.0 " " 4: 3.0 - 5.0 " " 5: 5.0 - (~ 20) "	range 1: 0.15 - 0.30 μ m, 0.01 channel width " 2: 0.23 - 0.605 ", 0.025 " " 3: 0.40 - 1.00 ", 0.04 " " 4: 0.60 - 3.00 ", 0.16 " "
sizing accuracy (as stated by the manufacturer)	stated size, $\pm 5\%$ based on pulse height measurements	RMS size errors: $\pm 10\%$

3. THEORY

3.1 DESCRIPTION OF MONOCHROMATIC TRANSMITTANCE AT 0.63 AND 10.6 MICRONS

In general the monochromatic transmittance τ_λ of radiation along an atmospheric path is defined as follows:

$$\tau_\lambda = \exp. (-\gamma_\lambda L), \quad (1)$$

where γ_λ is the extinction coefficient and L is the path length traversed by the radiation. The exponent in equation (1) $\gamma_\lambda \cdot L$ is denoted as the optical thickness t . After [1] equation (1) is valid if the relation: $t \leq 14$ holds. The extinction coefficient γ_λ is given by

$$\gamma_\lambda = \gamma_{\lambda,m} + \gamma_{\lambda,a}, \quad (2)$$

where $\gamma_{\lambda,m}$ is the extinction coefficient by molecules, whereas $\gamma_{\lambda,a}$ means extinction by aerosols. Both extinction coefficients are composed of both scattering and absorption. With regard to CO_2 -laser radiation absorption by water vapour and carbon dioxide molecules has to be considered. Because of their smaller concentration absorption of other molecules can be neglected (e.g. CO , N_2O , CH_4). Finally extinction of aerosols is very essential. Therefore, atmospheric extinction of CO_2 -laser radiation $\gamma_{10.6}$ can approximately be written as follows:

$$\gamma_{10.6} = km(\text{H}_2\text{O}) + km(\text{CO}_2) + \gamma_a, \quad (3)$$

where $km(\text{H}_2\text{O})$ and $km(\text{CO}_2)$ denote absorption by water vapour and carbon dioxide. γ_a means extinction caused by aerosols.

In case of fog (visibility ≤ 1 km) and precipitation extinction by fog droplets (γ_f) and rain drops (γ_p) becomes dominant, so extinction by molecules can in generally be neglected [2, 3]. Thus equation (3) can be rewritten in

$$\gamma_{10.6} \approx \gamma_f \text{ or } \gamma_{10.6} \approx \gamma_p. \quad (4)$$

The propagation of HeNe-laser radiation is determined by extinction owing to aerosols. Therefore, for extinction at 0.63 micron ($\gamma_{0.63}$) holds:

$$\gamma_{0.63} \approx \gamma_a. \quad (5)$$

Analog to Equ.(5), it holds for atmospheric extinction in the visual range γ_{vis} :

$$\gamma_{vis} \approx \gamma_a. \quad (6)$$

The extinction due to air molecules can be ignored for visibilities less than about 50 kilometers. The visibility V_N can then be computed by means of the wellknown Koschmieder formula, using also only γ_a :

$$V_N = \frac{3.912}{\gamma_a}. \quad (7)$$

Besides of semiempirical formula determining atmospheric broad band and laser transmission there are several computer programs on the basis of atmospheric and aerosol models, e.g. LOWTRAN [4], HITRAN [5] and ATRAN [6,7]. At the FFO an approximative formula for extinction at 10.6 micron was used based on the available literature until 1973 [1, 2, 3, 8, 9, 10]. Here $\gamma_{10.6}$ is defined after equation (3) with

$$k_m(\text{CO}_2) = 144 (295/T)^{3/2} \exp(-2230/T), \quad (8)$$

where T denotes the air temperature in Kelvin. Further absorption by water vapour is given as follows:

$$k_m(\text{H}_2\text{O}) = 4.32 \cdot 10^{-6} p_{\text{H}_2\text{O}} (p + 193 p_{\text{H}_2\text{O}}), \quad (9)$$

where $p_{\text{H}_2\text{O}}$ denotes the water vapour partial pressure in Torr whereas p means atmospheric pressure in Torr.

Finally extinction by aerosols is expressed by the following approximation formula:

$$\gamma_a = 0.245 V_N^{-1} \left\{ \exp[(Hr - 50 + \delta) ((V_N/km)^{0.3}/50)] \right\}. \quad (10)$$

Here V_N is the visual range in km, Hr is the relative humidity in percent.

Equation(10) is valid as an first order approximation with the limitations

$$V_N \leq 100 \text{ km} \\ \delta = \begin{cases} 0 & ; 45\% \leq Hr \leq 77\% \\ 0.38 (Hr - 77) & ; 77\% \leq Hr \leq 90\%. \end{cases}$$

More accurate approximation formula have to take into account the relevant aerosol size distribution; therefore the visibility V_N cannot replace the aerosol size distribution for Infrared wavelengths.

3.2 MIE CALCULATIONS - AEROSOL SIZE DISTRIBUTIONS

The extinction coefficient for atmospheric particulate matter γ_a is related to the size distribution and optical properties of the particles by Mie's theory. Although atmospheric aerosols are not uniform homogeneous spheres, Mie's theory approximately describes extinction by aerosols. The particle extinction cross section is commonly written in terms of the cross-sectional area πr^2 of particles times an efficiency factor for extinction Q_{EXT} . Thus γ_a becomes:

$$\gamma_a = \pi r^2 Q_{EXT} \quad (11)$$

for a single particle. The extinction efficiency factor, expressed in terms of the Mie amplitude functions [11] a_n and b_n is

$$Q_{EXT}(m, x) = \frac{2}{x^2} \sum_{n=1}^{\infty} (2n+1) \text{Re}(a_n + b_n), \quad (12)$$

where $m = (n_{Re} - i n_{Im})$ is the complex index of refraction of an aerosol particle and $x = 2\pi r/\lambda$ is a size parameter relating the radius r of the sphere to the wavelength λ of the incident electromagnetic wave (Mie parameter).

In the same way the efficiency factor for scattering is

$$Q_{SCA}(m, x) = \frac{2}{x^2} \sum_{n=1}^{\infty} (2n+1) \{ |a_n|^2 + |b_n|^2 \}. \quad (13)$$

For a monodisperse aerosol having N_a particles per unit volume γ_a is given by

$$\gamma_a = \pi r^2 Q_{EXT} N_a. \quad (14)$$

Similarly, the total extinction due to a polydisperse distribution of particles is given by the integral over the size distribution:

$$\gamma_a = \int_{r_1}^{r_2} \pi r^2 Q_{EXT} n(r) dr, \quad (15)$$

where $n(r)$ is a continuous function defined within the radius interval from r_1 to r_2 representing the concentration of particles per unit volume and per unit increment of dr . An overview of frequently used size distribution functions is given in [12].

The techniques employed to count and measure particles usually provide data on the number of particles per specific interval of radius. If the radius intervals are small enough, equation (15) can approximately be rewritten in

$$\gamma_a = \sum_{i=1}^z \pi r_i^2 Q_{EXT}(m, x_i) n_i(r_i), \quad (16)$$

where r_i is the mean radius of each radius interval, n_i is the population of the corresponding radius interval and z is the total number of radius intervals. Equation (15) represents extinction by aerosols much better than equation (10) where extinction is calculated via visibility and relative humidity, but it requires the measurement of the aerosol size distribution.

3.3 TRANSMISSION THROUGH RAIN

Most atmospheric extinction models do not consider the effect of precipitation but include only extinction by gaseous constituents and aerosols. However, especially in the 3 - 15 μm region extinction by rain is of considerable importance.

In order to model IR-extinction by precipitation the rain-drop size distribution is required. The distribution mostly used by modellers has been proposed by Marshall and Palmer [13]:

$$N(D) = N_0 \exp(-\Lambda D) \quad [\text{cm}^{-4}] \quad (17)$$

with

$$\Lambda = \Lambda(R) = 41 R^{-0.21}, \quad (18)$$

where the following notation holds:

$N(D) dD$	=	Number of drops per unit volume with diameter between D and $D+dD$ [cm^{-4}].
D	=	Drop diameter [cm].
N_0	=	Intercept parameter, found to be constant ($= 0.08 \text{ cm}^{-4} = 8000 \text{ m}^{-3} \text{ nm}^{-1}$) by Marshall and Palmer.
Λ	=	Slope parameter of the Marshall-Palmer distribution [cm^{-1}].
R	=	Rain rate [mm h^{-1}].

Thus via (18) the rain rate is related to the spectrum which generally is unknown, unless measured by special equipment. The rain rate itself can at least be estimated from routine observations. As far as the parameter N_0 is concerned there are indications today that it can no longer be treated as a constant as summarized by Markowitz [14]. Other suggestions, e.g. to express N_0 as a function of R are given in [15], [16], [17].

Equ. (17) should be valid for many cases of steady rain at continental mid-latitudes. However, stochastic deviations from the "straight line" (on a log-plot) are expected in heavy rain, e.g. during showers or thunderstorms.

To relate rain rate to the total amount of precipitation, the terminal velocity of the rain drops is needed. Here we use the relationship given by Goldstein [16]:

$$V(D) = 9.6 (1 - \exp(-5.5 D)) \quad [\text{m sec}^{-1}], \quad (19)$$

with

$$V = \text{Velocity} \quad [\text{m sec}^{-1}].$$

Following van de Vrie [19] the procedure to calculate the transmission τ through rain is as follows:

$$1) R = N_0 \frac{\pi}{6} \int_0^\infty \exp(-\Lambda D) V(D) D^3 dD,$$

$$2) \quad N_0 = \frac{R}{\frac{\pi}{6} \int_0^{\infty} \exp(-\Lambda D) V(D) D^5 dD}$$

$$3) \quad A = N_0 \frac{\pi}{4} \int_0^{\infty} \exp(-\Lambda D) D^2 dD = \frac{N_0 \pi \Gamma(3)}{4 \Lambda^3} = \frac{3 \pi N_0}{2 \Lambda^3},$$

$$4) \quad \gamma_p = -10^5 \ln(1 - A \cdot Q_{EXT}) \quad [\text{km}^{-1}],$$

$$5) \quad \tau = \exp(-\gamma_p \cdot L) \quad ; L \text{ in } [\text{km}].$$

The factor A means the total geometric cross-section of all rain drops. The weighting factor Q_{EXT} is the Mie-extinction-efficiency factor, which is a function of the Mie size parameter $x = \frac{\pi D}{\lambda}$. For large values of x , i.e. $D \gg \lambda$, Q_{EXT} approaches the value of 2. This approximation is made in this simple model. γ_p is the extinction coefficient, τ the transmission through rain and L the atmospheric path in km.

τ as a function of R and L after Equ. (17), (18), (19) is presented in Fig. 2. The integration has been performed between 0.1 and 5 mm drop diameter. (The contribution to the integrals from smaller and larger drops is negligible.)

4. EXPERIMENTAL AND COMPUTATIONAL RESULTS

4.1 ANALYSIS OF DIFFERENT EXTINCTION CONTRIBUTIONS

In the following section examples of the diurnal variation of extinction coefficients from our measurements at 0.63, 10.6 μm and in the visual range, together with different extinction contributing atmospheric constituents are presented.

Fig. 3a shows the extinction coefficient γ_{vis} in the visual spectral region with the aerosol population n_1 , which means the aerosol population in the radius range 0.2 - 1.5 microns, measured by means of the Royco aerosol counter. Fig. 3 b indicates the measured extinction coefficients at 10.6 microns $\gamma_{10.6}(\text{exp.})$ and the computed extinction after Equ. (7), $\gamma_{10.6}(\text{theor.})$ together with the computed absorption coefficient for water vapour $\text{km}(\text{H}_2\text{O})$ (after Equ. (8)) and carbon dioxide $\text{km}(\text{CO}_2)$ (after Equ. (9)). In this figure the carbon dioxide concentration is fixed on 300 ppm; therefore the curve mirrors the diurnal variation of the air temperature. In Fig. 3c the aerosol population n_2 is plotted, where n_2 is the aerosol population in the radius range 1.5 - 10.0 μm measured by the Royco aerosol counter. Finally in Fig. 3 d the diurnal variations of the absolute (Ha) and relative (Hr) humidity are shown. The time resolution of the extinction coefficients as well as the count rate of the Royco counter was 10 minutes, whereas the time resolution of the computed values and the meteorological data was 30 minutes.

Fig. 3 shows that in the case of fog (visibility ≤ 1 km) the courses of γ_{vis} , $\gamma_{10.6}(\text{exp.})$ and n_2 are in good agreement. The course of n_1 is - as expected - different. During light and moderate fog the relation $\gamma_{10.6} < \gamma_{vis}$ holds. For dense fog (visibility ≤ 0.2 km) one obtains: $\gamma_{10.6} \approx \gamma_{vis}$. If the visibility becomes greater than 1 kilometer the influence of n_1 to γ_{vis} becomes evident as it can be seen after noon. Here, $\gamma_{10.6}$ continues following n_2 . The insufficient consideration of the aerosol by Equ. (7) is demonstrated by the course of $\gamma_{10.6}(\text{theor.})$. $\lambda_{10.6}(\text{theor.})$ is similar to the course of γ_{vis} .

An additional diurnal variation is presented in Fig. 4. Part a) shows n_1 and instead of γ_{vis} as in Fig. 3 the extinction coefficient $\gamma_{0.63}$ of HeNe-laser radiation is shown. Part b demonstrates $\gamma_{10.6}(\text{exp.})$, $\text{km}(\text{CO}_2)$ and $\text{km}(\text{H}_2\text{O})$. In part c the aerosol population n_2 is plotted, whereas part d shows the diurnal course of Hr and Ha.

The courses of n_1 and $\gamma_{0.63}$ coincide fairly well until noon. No analogy can be seen between the course of $\gamma_{0.63}$ and n_2 . As in Fig. 3 $\gamma_{10.6}(\text{exp.})$ follows to some extent n_2 . Partially the relation $\gamma_{0.63} < \gamma_{10.6}(\text{exp.})$ holds. Comparing Fig. 3 and 4 this relation may be explained by a reduced aerosol population n_1 in Fig. 4 (approx. factor 5), whereas the

aerosol population n_2 is about the same. A further diurnal variation is plotted in Fig. 5. Part a) shows the extinction coefficients $\gamma_{0.63}$ and γ_{vis} , part b) the extinction coefficient $\gamma_{10.6}$ together with $\gamma_{10.6}$ (theor.) and $km(H_2O)$ and $km(CO_2)$. (A mean carbon dioxide concentration of 300 ppm assumed). Part c) demonstrates the relative and absolute humidity. Fig. 5a shows an analog course of $\gamma_{0.63}$, $\gamma_{10.6}$ (exp.) and to some extent of γ_{vis} . From 4 to 6 a.m. the fluctuations of the extinction coefficients are caused by precipitation. The course of $\gamma_{10.6}$ (theor.) bears analogy to the course of γ_{vis} , but there is no coincidence with $\gamma_{10.6}$ (exp.).

The whole data set of about 60 days was statistically processed. Mean correlation coefficients between several parameter combinations are presented in table 2.

Table 2: Mean correlation coefficients

correlation values	correlation coefficients	number of days
$H_a / \gamma_{10.6}$ (exp.)	- 0.9449	49
$\gamma_{vis} / \gamma_{10.6}$ (exp.)	0.21	38
$\gamma_{0.63} / \gamma_{10.6}$ (exp.)	0.39	24
H_r / γ_{vis}	0.25	38

The next table shows the trial to classify the relationship between γ_{vis} and $\gamma_{10.6}$ (exp.) for different visual ranges.

Table 3: Mean correlation coefficients $\gamma_{vis} / \gamma_{10.6}$ for different visual ranges V_N

atmospheric condition	visual range	correlation coefficient $\gamma_{vis} / \gamma_{10.6}$ (exp.)	number of days
moderate, dense, thick fog	$V_N < 0.5$ km	0.72	5
light fog	$0.5 \text{ km} < V_N \leq 1$ km	0.51	5
thin fog	$1.0 \text{ km} < V_N \leq 2$ km	0.41	6
haze	$2.0 \text{ km} < V_N \leq 4$ km	- 0.07	16
light haze	$4.0 \text{ km} < V_N \leq 10$ km	0.11	32
clear	$V_N > 10$ km	- 0.07	24

The low correlation coefficients in table 2 clearly show that investigations of the relationship between atmospheric transmission at $\lambda = 0.63 \mu m$, $\lambda = 10.6 \mu m$ and in the visual range can only be done by selecting special meteorological conditions where several extinction contributing atmospheric parameters can be fixed or neglected, so that extinction by one parameter is dominant. Table 3 demonstrates that for fog (thick, dense, moderate, light) and to some extent for thin fog the relationship is fairly close because of the dominance of giant particles. Therefore it is obvious that extinction at $10.6 \mu m$ is by a factor of about 4 smaller with the trend to equality at dense fog, when compared with the visual range.

Selected meteorological situations will be discussed where extinction by aerosols is approximately constant.

In both following figures a diurnal mean of the carbon dioxide concentration is used.

Fig. 6 demonstrates a diurnal variation with an approximately constant course of n_2 while n_1 partially fluctuates. Fig. 6a indicates the course of $\gamma_{0.63}$ and n_1 . To some extent the similarity is obvious. In Fig. 6 b $\gamma_{10.6}$ (exp.), km (H_2O) and km (CO_2) are plotted. Finally part c) shows the aerosol population n_2 whereas in part d) relative (Hr) and absolute (Ha) humidity are presented. The relationship between $\gamma_{10.6}$ (exp.) and Ha from 3 a.m. to 2 p.m. is evident.

A further example which points out the relationship between $\gamma_{10.6}$ and Ha is illustrated in Fig. 7. Fig. 7 a shows $\gamma_{10.6}$ (exp.), $\gamma_{10.6}$ (theor.), km (H_2O) and km (CO_2). Fig. 7 b presents the diurnal variation of the absolute humidity. In table 4 correlation coefficients $\gamma_{10.6}/Ha$ are listed. Part a) shows correlation coefficients for an approximately constant aerosol population n_2 ; part b) presents correlation coefficients for visibilities exceeding 15 kilometers.

Table 4: Correlation coefficients $\gamma_{10.6}/Ha$

Part a): aerosol population n_2 approximately constant

date	10 23 76	10 24 76	10 26 76	06 24 77	mean
$\gamma_{10.6}/Ha$	0.49	0.64	0.76	0.56	0.61

Part b): visibility ≥ 15 km

date	10 04 76	10 07 76	10 12 76	10 15 76	07 27 77	mean
$\gamma_{10.6}/Ha$	0.94	0.63	0.61	0.75	0.52	0.69

Table 4 shows firstly the supposed relationship between CO_2 -laser transmission and atmospheric water vapour, secondly that in general it is difficult to study separately the influence of one extinguishing atmospheric constituent on transmission without disturbances by other constituents.

A further lack is the short measuring range (length 0.32 km). In general reduction of CO_2 -laser transmission from water vapour was about 4 percent at the range. Therefore the influence of water vapour can easily be hidden by other quantities. The extinction contribution from carbon dioxide to CO_2 -laser radiation is smaller if compared with extinction by water vapour (about 2 - 3 percent at our range). Because of the drift of the carbon dioxide measuring device only mean diurnal values could be used to give an order of magnitude of carbon dioxide extinction.

EXTINCTION BY AEROSOLS

To study the influence of atmospheric aerosols meteorological situations were selected where km (H_2O) was approximately constant or negligible in comparison to γ_u . km (CO_2) is always smaller compared to km (H_2O). Figure 8 a demonstrates the diurnal variations of γ_{vis} and $\gamma_{10.6}$ (exp.). In part b) the aerosol population K1 - K5 (channel 1 - 5) are plotted (see table 1). Finally part c) shows the diurnal course of the absolute and relative humidity.

Looking at Figure 8 a one confirms that the courses of γ_{vis} and $\gamma_{10.6}$ (exp.) coincides fairly well. Until 6 a.m. during dense fog the courses of γ_{vis} and $\gamma_{10.6}$ (exp.) are practically identical. In this time extinction by particles in the radius range 1.5 - 10.0 μm is dominant.

From 6 a.m. on $\gamma_{10.6}$ (exp.) follows the course of K4 and K5, whereas the course of γ_{vis} is essentially determined by the particle populations K1 - K3.

A further example which emphasizes the influence of aerosols on extinction is given in Fig. 9. Instead of K1 - K5 in Fig. 8

here n_1 and n_2 are plotted in part b). As in Fig. 8 the analog course of $\gamma_{10.6}$ (exp.) and n_2 is evident. During fog the relation $\gamma_{10.6} < \gamma_{vis}$ holds again. Without regard to fog the influence of n_1 on γ_{vis} becomes obvious.

To show the extinction due to the different aerosol size ranges simple statistical calculations were performed. Table 5 shows correlation and regression coefficients.

Table 5: Mean correlation and linear regression coefficients (A = slope, B = intercept)

correlation values	correlation coefficient	regression coefficient		number of days
		A	B	
$K3 / \gamma_{10.6}$	0.43	0.11	0.11	11
$K4 / \gamma_{10.6}$	0.67	1.23	1.04	11
$K5 / \gamma_{10.6}$	0.75	6.50	1.03	11
$n_2 / \gamma_{10.6}$	0.71	1.34	1.01	11
n_2 / γ_{vis}	0.54	2.64	1.78	10
$n_2 / \gamma_{0.63}$	0.27	3.55	0.44	2
n_1 / γ_{vis}	0.33	0.01	1.97	11
$n_1 / \gamma_{0.63}$	0.59	0.01	0.52	2

The results show the predominant influence of giant aerosol particles on CO_2 -laser extinction. Furthermore it is obvious that the extinction by smaller particles cannot be neglected. The low correlation coefficient n_1 / γ_{vis} is caused by the fact that only selected measuring days were evaluated with respect to CO_2 -laser extinction.

4.4 COMPUTED EXTINCTION BY AEROSOL VIA MIE THEORY

It has been shown that the computation of extinction due to aerosols via simple meteorological records like visibility and relative humidity generally is not possible. Section 4 clearly demonstrated empirically—in agreement with Mie's theory—that particles in the radius range $0.6 - 10 \mu m$ are the main contributors to CO_2 -laser extinction. Therefore equation (16) was used instead of equation (10) to compute the extinction by aerosols. The aerosol size distribution was measured by a Royco and a PMS aerosol counter (see table 1).

The Fig. 10 and 11 give a good comparison between measured and computed CO_2 -laser extinction via Equ. (8), (9), (16). In both figures the diurnal variation of $\gamma_{10.6}$ (exp.) and $\gamma_{10.6}$ (theor.) is presented. Additionally the complex index of refraction used for Mie calculations as well as the aerosol measuring device is specified.

Both figures show that in case of fog there is a surprisingly good agreement within a factor 2 between measurement and calculation. Without fog the deviations become larger. The main reason is the rough size resolution of the Royco counter. Other uncertainties with regard to Mie calculations shall not be discussed at this point.

Fig. 12 presents the diurnal variation of extinction in the visual range (γ_{vis}) and at $0.63 \mu m$ ($\gamma_{0.63}$). The third curve is the calculated HeNe-laser extinction coefficient via the measured aerosol size distribution by a PMS device. Additionally the complex index of refraction is given. To some extent there is a rather good agreement between measured and calculated HeNe-laser extinction. The deviations may be caused by the upper limit of the measuring range of the PMS device (ASAS-300 B). A further lack is that all aerosol measurements at the range were point measurements. It is known that the measuring results may be changed due to atmospheric turbulence and the sensibility of the aspiration systems against wind velocity and direction.

The quality of the rain-extinction model presented in section 4.3 has been checked for 17 cases of rainfall with a total amount of approximately 640 measuring points taken during 32 hours of precipitation.

As a typical example one of the 17 rain cases is plotted in Fig. 13. Part a) shows the course of the transmission on July 19 according to calculation (full line) and from measurements in the photopic range (dashed line), for $0.63 \mu\text{m}$ (dash-dotted) and at $10.6 \mu\text{m}$ (dotted line). Relations between τ_{vis} , $\tau_{10.6}$ and $\tau_{0.63}$ have been discussed elsewhere (section 4). Here we concentrate only on $\tau_{10.6}$ and τ_{cal} and obtain the following gross features:

The trends in both, calculated and measured transmission agree fairly well in all cases. However, a systematic positive difference ($\tau_{\text{cal}} - \tau_{10.6}$) is observed in practically all cases. This difference can be explained by a neglected aerosol and molecule extinction. The total calculated transmission would be obtained by multiplication of the rain case with the transmission due to all other atmospheric constituents (e.g. from LOWTRAN).

Sharp peaks in the measured (and calculated) transmission coincide very well with those of the rain rate (part b). The largest differences between calculation and measurement occur for high rain rates, as to be seen from part c, where $\tau_{\text{cal}}/\tau_{10.6}$ is plotted. The reason is twofold:

The evaluation of the rain rate introduces the largest errors for high rain rates, because it is obtained by differentiating the rainfall-recorder curve. Furthermore the raindrop spectrum itself may be erroneous for heavy rainfall, as already indicated earlier.

Finally it can be said that the simple model gives surprisingly good results. Statistical calculations showed a mean value for $\tau_{\text{cal}}/\tau_{10.6}$ of 1.34. The mean correlation coefficient for all 17 rain cases turned out to be 0.83.

5.

CONCLUSIONS

Measurements with our laser transmissometer show that in general a prediction of atmospheric extinction at 0.63 and $10.6 \mu\text{m}$ from meteorological parameters, e.g. relative humidity, absolute humidity, air temperature, air pressure and visibility is not possible.

Measuring visibility only aerosol particles in the radius region $0.2 - 1.0 \mu\text{m}$ are taken into account, whereas CO_2 -laser extinction is essentially determined by the particle radius range $0.5 - 15.0 \mu\text{m}$. Therefore the only way to improve the mathematical description of HeNe- and CO_2 -laser radiation extinction in the atmosphere seems to be possible by the accurate measurement of the aerosol size distribution with sufficient size resolution as input for Mie calculations together with the above mentioned meteorological parameters. Further research has to prove to what extent information of the aerosol size distribution can be derived from meteorological data including air mass analysis and the history of the general weather pattern [20]. Analog to the visibility V_N an additional quantity, e.g. the transmission at 10.6 microns itself may have to be added to the daily usual set of meteorological data to be able to predict additionally infrared transmission. The use of aerosol counters seems to be restricted to research work, and cannot be recommended for routine meteorological work. Extinction by rain seems to be describable by an improved rain model including the actual measurement of the rain drop size distribution or at least accurate data on rain-rates.

ACKNOWLEDGMENTS

Our thanks are due to D.H. Höhn for his encouraging support during the experimental phase of this study and his valuable suggestions. Furthermore we are grateful to A. Jetter for his assistance in the field experiments.

REFERENCES

- [1] Höljer, S., Atmospheric attenuation of a light beam due to scattering and absorption, Förstvarets forskningsanstalt Stockholm, FOA 2C 2659-E1, E2, E3, E4, (1974).
- [2] Höhn, D.H., Raidt, H., Gruner, W., Atmospheric Transmission of Focused Laser Beams (at 6328 Å and 10.6 μm) Bericht FFO (1973).
- [3] Gruner, W., Höhn, D.H., Raidt, H., Atmosphärische Transmission bei 10.6 μm (CO_2 -Laserstrahlung) Bericht FFO 1974/33.
- [4] Selby, J.E.A., et al., Atmospheric Transmittance from 0.25 to 28.5 μm : Supplement LOWTRAN 3 B (1976) AFGL-TR-76-0258 (1976).
- [5] LaRocca, A., Methods of Calculating Atmospheric Transmittance and Radiance in the Infrared, Proceedings of the IEEE, Vol. 63, No. 1 (1975).
- [6] Miller, A., et al., Research in the Area of Atmospheric Modeling: High-Resolution Atmospheric IR Transmittance Prediction, NMSU-Phys 537-75-1 (1975).
- [7] Miller, A. et al., Research in the Area of Atmospheric Modeling: High-Resolution Atmospheric IR Transmittance Prediction (Part II) New Mexico State University, ECOM 75-3 (1975).
- [8] McClatchey, R.A. et al., Atmospheric Transmittance, 7 - 30 μm : Attenuation of CO_2 -Laser Radiation, AFCRL-72-0611.
- [9] McCoy, J.M., Rensch, D.B., Long, R.K., Water Vapour Continuum Absorption of Carbon Dioxide Laser Radiation near 10 μm , App. Optics 8, 1471 (1969).
- [10] Sokolov, A.V., Attenuation of Visible and Infrared in Rain and Snow, Radio Engineering and Electronic Physics 15, 2175 (1970).
- [11] Giese, R.H.: Tabelle von Mie-Streufunktionen. 1. Gemische dielektrischer Teilchen, Bereich Extraterrestrische Physik, Ruhr Universität Bochum (1971).
- [12] Abele, J., Hipp, H., Höhn, D.H. Modelling of atmospheric aerosol size distributions, KB FFO 1977/43 - OPAQUE N/GE - 7706 (1977).
- [13] Marshall, J.S. and Palmer, W.M.K., The distribution of raindrops with size, J. Met. 5, 165-166 (1948).
- [14] Markowitz, A.H., Raindrop size distribution expressions, J. App. M., Vol. 15, 1029 - 1031 (1976).
- [15] Czerwinski, N., and Pfisterer, W., Typen von Regentropfenspektren von polaren bis tropischen Zonen und ihre Abhängigkeit von Elementen des Regens. Met. Rdsch., 25. Jahrg., Heft 3, 88-94 (1972).
- [16] Strantz, R., Typen der Regentropfenspektren, Met. Rdsch., 24. Jahrg., Heft 1, 19-29 (1971).
- [17] Diem, M., and Strantz, R., Typen der Regentropfenspektren II, Met. Rdsch., 24. Jahrg., Heft 1, 23-26 (1971).
- [18] Rensch, D.B., and Long, R.K., Comparative studies of extinction and backscattering by aerosols, fog and rain at 10.6 μm and 0.63 μm , Appl. Opt. 9, No. 7, 1563-1573 (1970).
- [19] van de Vrie, Theory and measurements of the effect of rainfall on Infrared transmission, Phys. Lab. TNO, The Hague, Netherlands, Rept. No. PHL 1976-07 (1976).
- [20] Abele, J., Aerosol size distributions as dependent on general weather situations, Report FFO 1976/40.

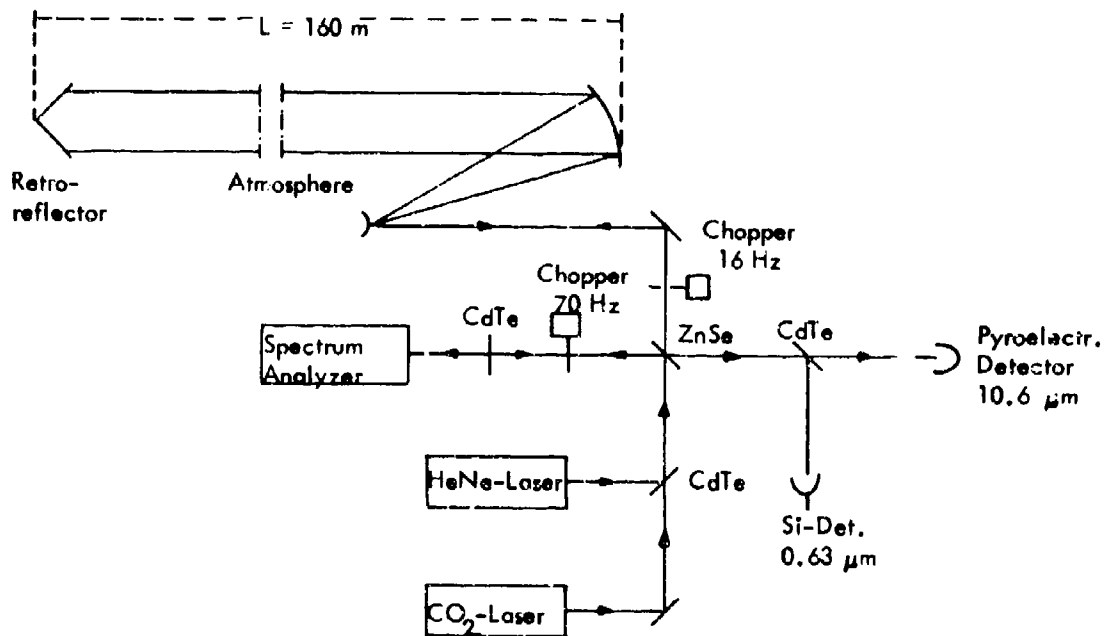


Fig. 1: Optical layout of the laser transmissometer

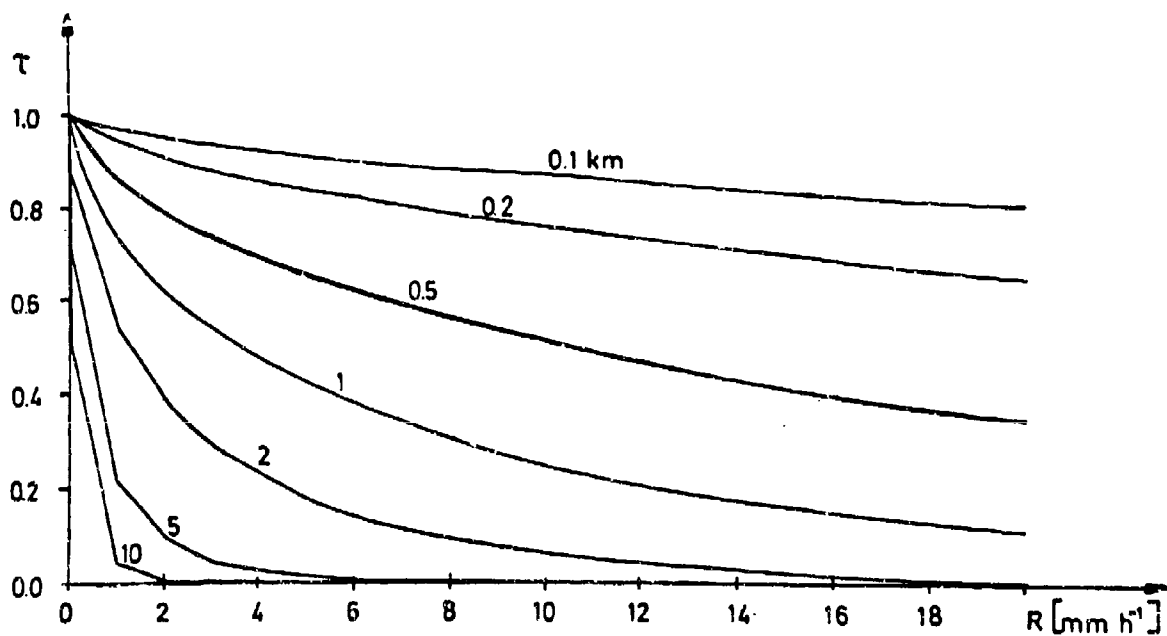


Fig. 2: Transmission through rain as a function of rain-rate R (after Equ. (17), (18), and (19)). Parameter is the atmospheric path L . The actual transmission is obtained by multiplication with the transmission of the rainless case, e.g. from LOWTRAN (Valid for $3 \mu\text{m} < \lambda < 15 \mu\text{m}$).

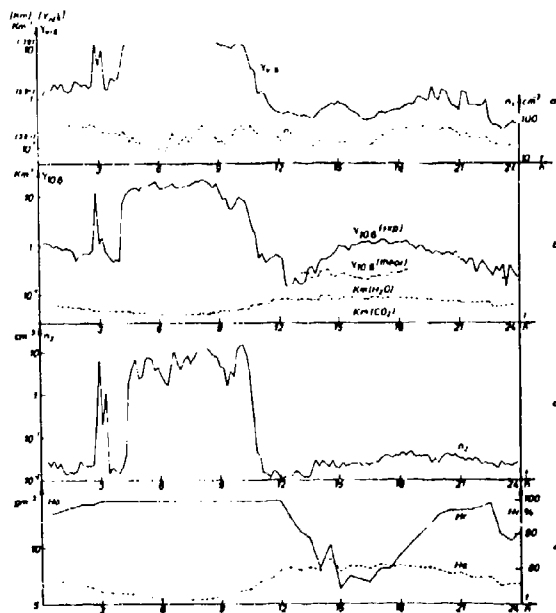


Fig. 3:

Diurnal variation on Oct. 23, 1976.

- a) Extinction coefficient γ_{vis} with aerosol population n_1 (radius range: 0.2 - 1.5 μm).
- b) Extinction coefficient $\gamma_{10.6}$ (exp.) with $\gamma_{10.6}$ (theor.) and absorption by molecules, $km(H_2O)$, $km(CO_2)$.
- c) Aerosol population n_2 (radius range: 1.5 - 10.0 μm).
- d) Relative (Hr) and absolute (Ha) humidity.

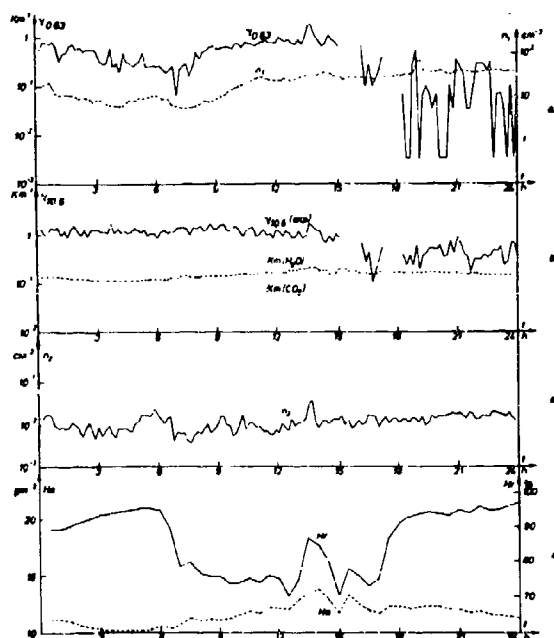


Fig. 4:

Diurnal variation on June 25, 1977.

- a) Extinction coefficient $\gamma_{0.63}$ with aerosol population n_1 (radius range: 0.2 - 1.5 μm).
- b) Extinction coefficient $\gamma_{10.6}$ (exp.) with absorption by molecules $km(H_2O)$ and $km(CO_2)$.
- c) Aerosol population n_2 (radius range: 1.5 - 10.0 μm).
- d) Relative (Hr) and absolute (Ha) humidity.

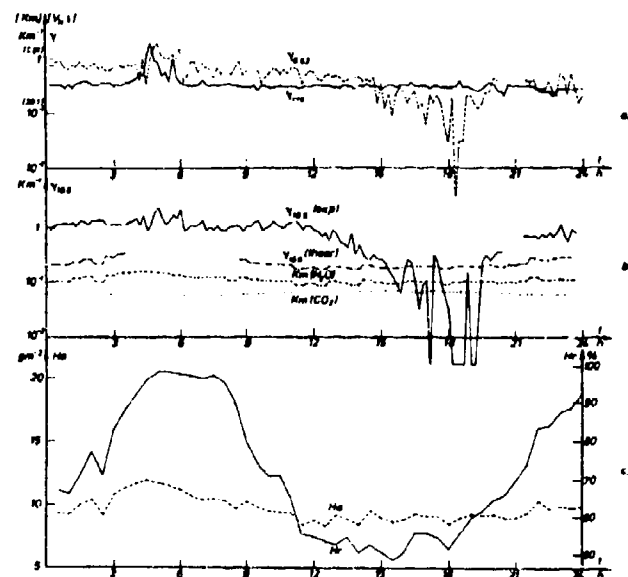


Fig. 6:

Diurnal variations on June 24, 1977.

- a) Extinction coefficient $\gamma_{0.63}$ with aerosol population n_1 (radius range: $0.2 - 1.5 \mu\text{m}$).
- b) Extinction coefficient $\gamma_{10.6}$ (exp.) and absorption by molecules $k_m(H_2O)$ and $k_m(CO_2)$.
- c) Aerosol population n_2 (radius range: $1.5 - 10.0 \mu\text{m}$).
- d) Relative (Hr) and absolute (Ha) humidity.

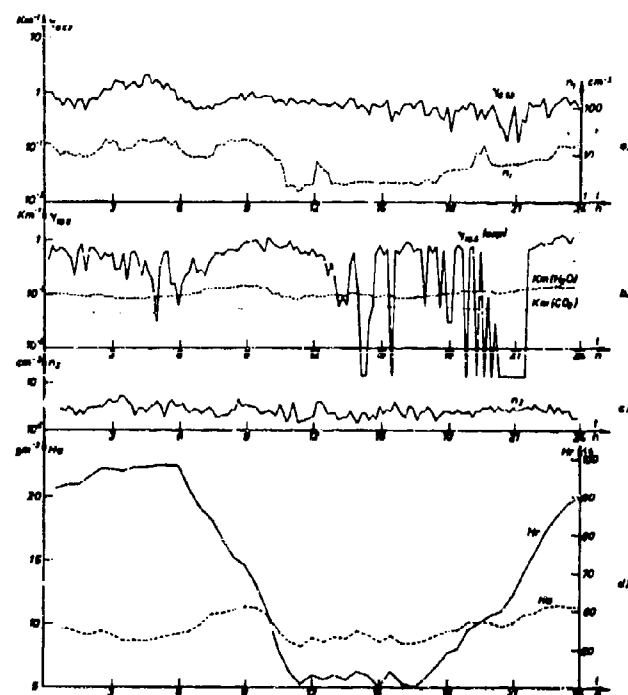


Fig. 5:

Diurnal variation on July 19, 1977.

- a) Extinction coefficients $\gamma_{0.63}$ and γ_{vis} .
- b) Extinction coefficients $\gamma_{10.6}$ (exp.) and γ_{10} (theor.) with absorption by molecules $k_m(H_2O)$ and $k_m(CO_2)$.
- c) Relative (Hr) and absolute (Ha) humidity.

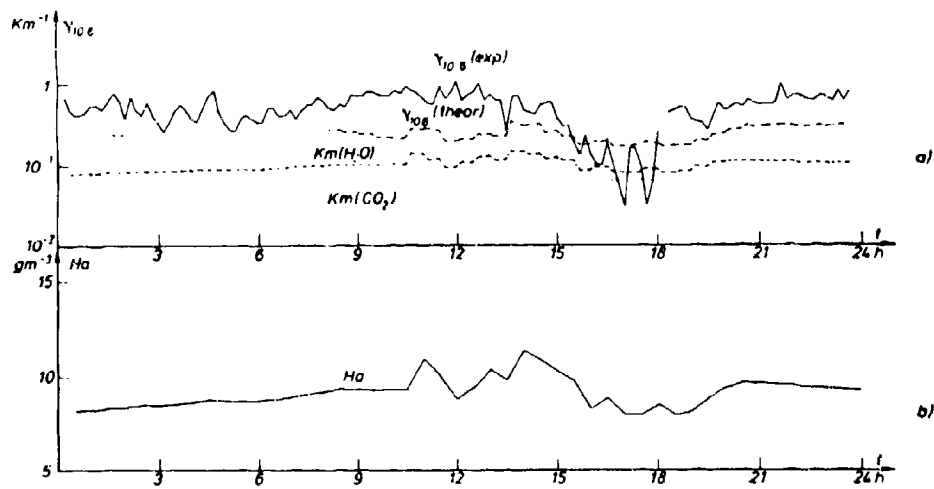


Fig. 7: Diurnal variation on July 27, 1977.
 a) Extinction coefficient $\gamma_{10.6} (exp.)$ with $\gamma_{10.6} (theor.)$.
 b) Absolute humidity Ha .

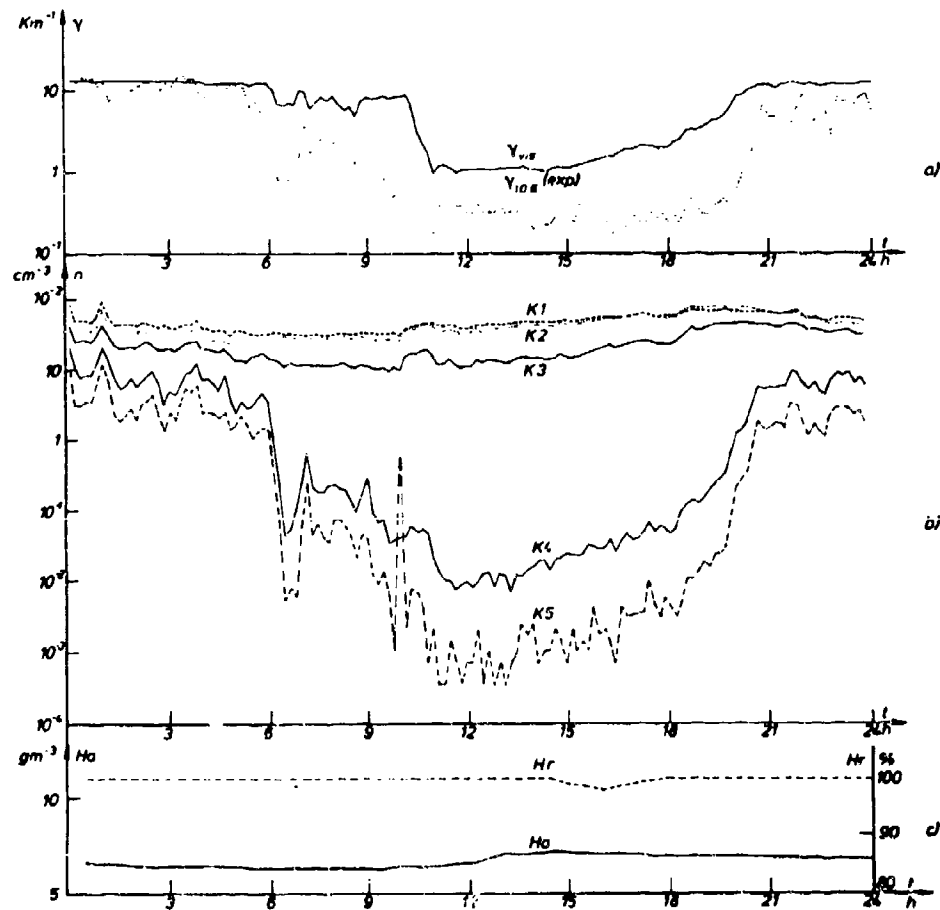


Fig. 8: Diurnal variation on Oct. 27, 1976.
 a) Extinction coefficients γ_{vis} and $\gamma_{10.6} (exp.)$.
 b) Aerosol population in the channels 1 to 5, measured by the Royco counter (see table 1).
 c) Relative (Hr) and absolute (Ha) humidity.

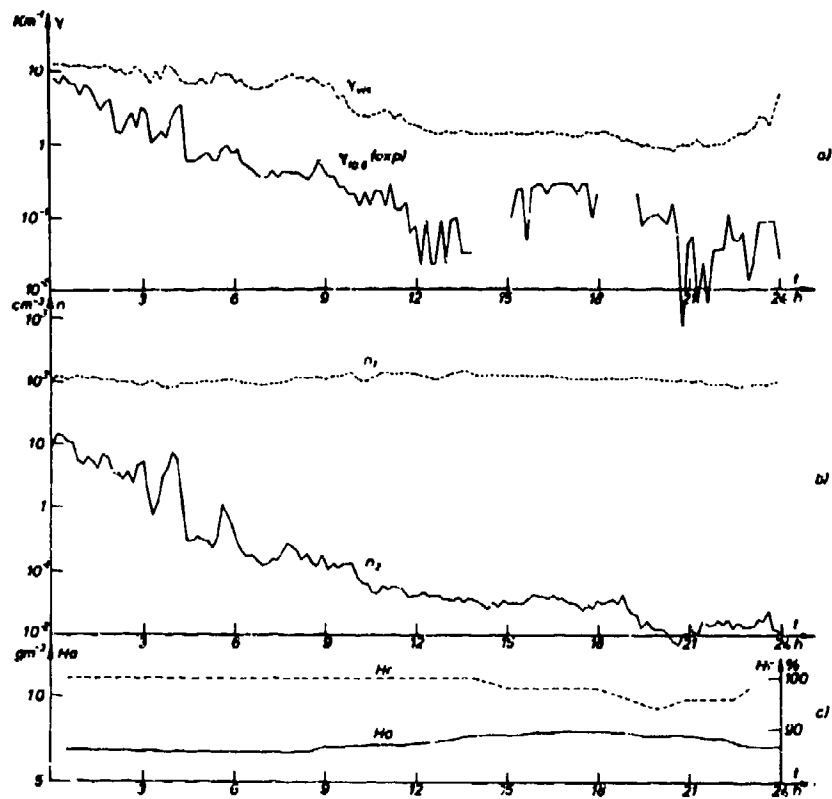


Fig. 9

Diurnal variation on Oct. 28, 1976.

a) Extinction coefficient γ_{vis} and $\gamma_{10.6}$ (exp.).

b) Aerosol population n_1 (radius range: 0.2 - 1.5 μm) and n_2 (radius range: 1.5 - 10.0 μm).

c) Relative (Hr) and absolute (Ha) humidity.

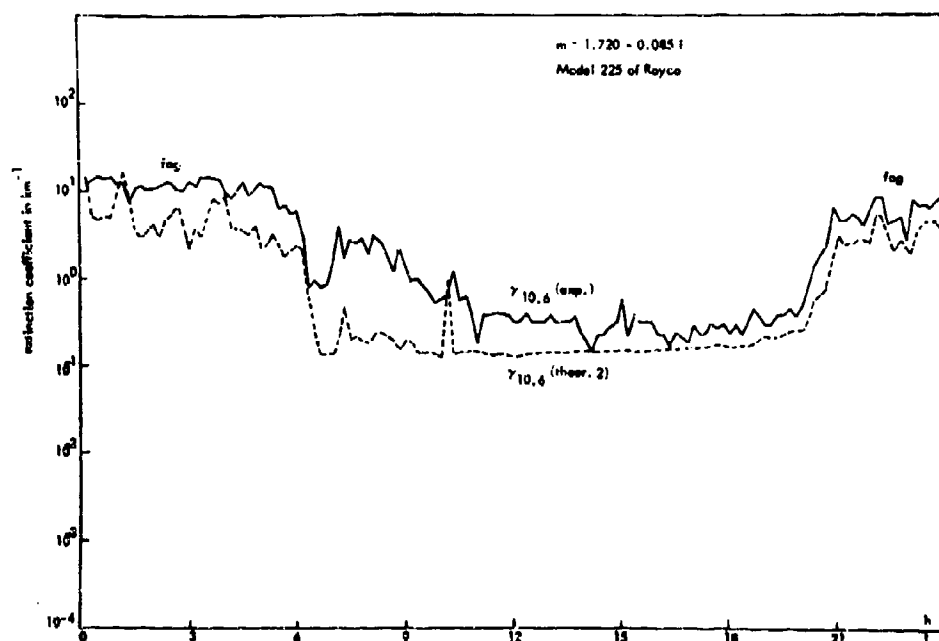


Fig. 10:

Diurnal variation of measured ($\gamma_{10.6}$ (exp.)) and computed ($\gamma_{10.6}$ (theor.)) CO_2 -laser radiation extinction coefficient on Oct. 27, 1976.

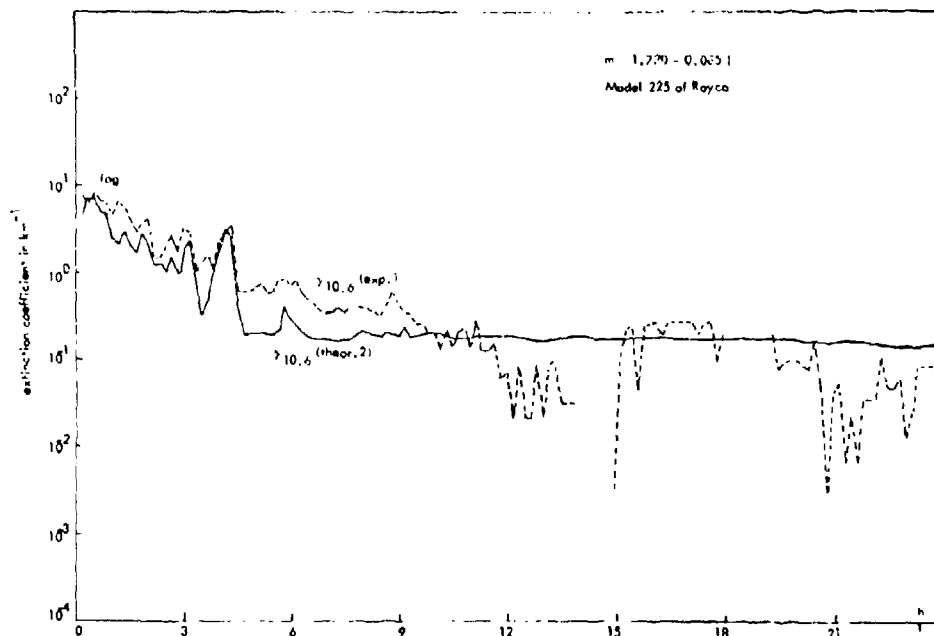


Fig. 11: Diurnal variation of measured ($\gamma_{10.6}(\text{exp.})$) and computed ($\gamma_{10.6}(\text{theor. 2})$) CO_2 -laser radiation extinction coefficient on October 28, 1976.

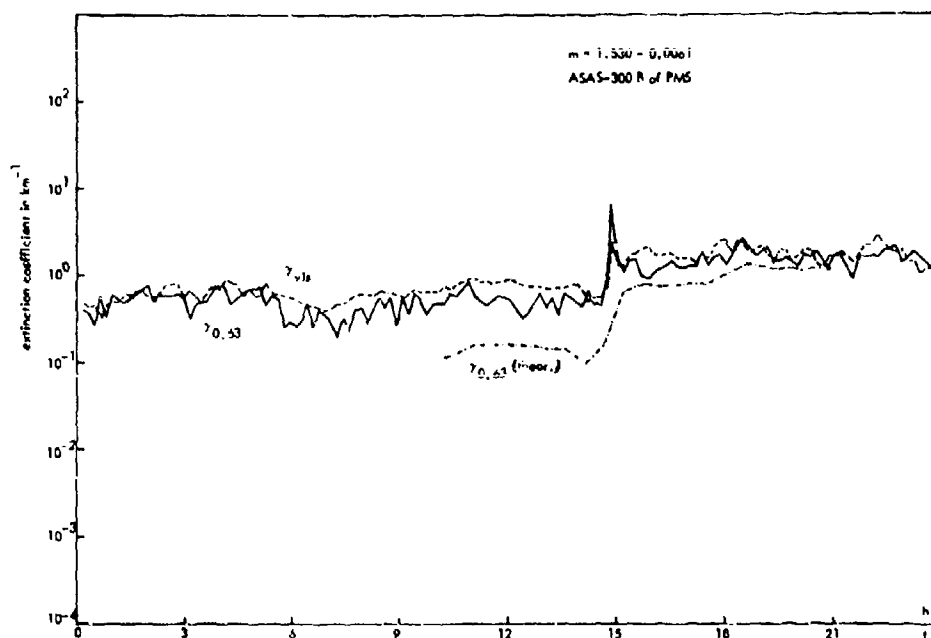


Fig. 12: Diurnal variation of $\gamma_{0.63}$ (measured), γ_{vis} (measured) and $\gamma_{0.53}$ (computed).

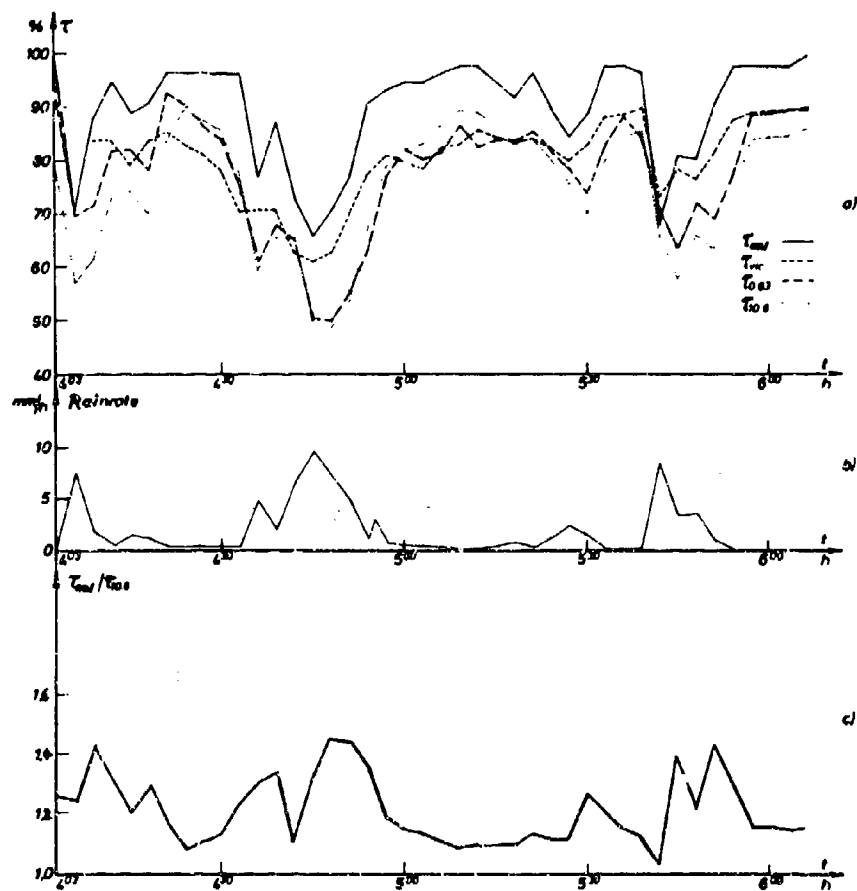


Fig. 13: Transmission during rainfall (July 19, 1977, 4.03 - 6.09 h).

- a) τ_{cal} = calculated transmission,
- τ_{vis} = photopic transmission,
- $\tau_{0.63}$ = transmission at 0.63 μm ,
- $\tau_{10.6}$ = transmission at 10.6 μm .
- b) Rain rate [mm h^{-1}].
- c) $\tau_{cal}/\tau_{10.6}$.

DISCUSSION

J.Röttger, FRG

It seems to me that the calculated and measured transmission curves show a phase shift of a few minutes. Is this shift significant?

Author's Reply

The transmission was calculated assuming a Marshall Palmer raindrop size distribution and using the rain rate measured at the range. Rain rate recordings and laser transmission recordings are different recordings. Therefore, the shift is caused by the limited time resolution (within a few minutes) of the recordings.

L.F.Drummeter, US

Could you discuss the calibration procedure for the transmissiometer described?

Author's Reply

The intensity is measured when, by means of a spherical mirror, the laser beam is focussed on a detector. The measurements are carried out twice daily at each end of a 320 meter measurement range. From the two measured intensities the actual transmission may be calculated.

ELECTRO-OPTICS SYSTEMS PERFORMANCE ANALYSIS
IN SELECTED MARINE ENVIRONMENTS

Barry S. Katz
Naval Surface Weapons Center
White Oak Laboratory
Silver Spring, Maryland 20910

Kenneth C. Hepfer
Naval Surface Weapons Center
Dahlgren Laboratory
Dahlgren, Virginia 22448

SUMMARY

In order to support electro-optics system planners, designers and users with probability of occurrence information on surface marine propagation conditions, techniques have been developed to convert large quantities of previously stored weather products to statistics of specific propagation parameters. The meteorology to propagation parameter models include Lowtran 3B, which converts temperature and absolute humidity to absorption coefficients, Naval Postgraduate School semi-empirical models, that convert air-sea temperature difference and surface winds to the refractive index turbulence structure function C_N^2 , and an aerosol model that uses wind and relative humidity to produce both aerosol size and number distributions, and a complex index of refraction. Using a modified Monte Carlo approach that preserves correlations between meteorological parameters, these statistics are coupled to E/O system models in order to calculate the probability of performing various system tasks versus target range in a variety of marine locations. Optical systems in both visible and IR wavelength bands have been studied.

Introduction

A number of electro-optical systems are in various stages of development and will hopefully be released for Fleet use beginning in a few years. These include applications in connection with surveillance, intelligence gathering, ASMD search and track and weapons control. Due to the degrading influence that the marine atmospheric conditions have on visible and IR wavelengths associated with these systems, it is important that early in the design stages these systems are optimized for use in such environments. This optimization procedure includes a proper mix of optical bands to keep effectiveness constantly high and prevention of expensive over-design that cannot be used a large percentage of the time. The systems analyst plays an important role in this procedure and should have available statistical information on atmospheric conditions and their influence on system components for all locations in which these systems must operate.

A first step in determining quantitatively the atmospheric limitations on system use is to specify the optical parameters that describe the magnitude of the interaction of optical waves with specific environmental conditions. This listing would include the atmospheric turbulence structure function C_n^2 , aerosol extinction values for various wavelengths or bands and molecular absorption when applicable. Since average values of meteorological parameters are readily available from marine atlases, the development, improvement or collection from the E/O community-at-large of propagation codes relating optical parameters to atmospheric conditions allows one to determine nominal operating conditions for areas of interest. Unfortunately this procedure, while providing a set of inputs for system codes, does not allow for determination of statistical effectiveness for different system configurations. When considering the cost for new systems, it is not an unjust question for the operational community to ask, "Just how often can I expect to effectively use this system?" In order to help answer these questions a program was initiated to do a statistical evaluation of propagation conditions in marine environments. Emphasis has been placed on TV, 1.06 μ m designator and FLIR optical bands. The basic premise as shown in block diagram form in Figure 1 was to acquire large quantities of stored meteorological raw products from ship reports and convert each observation individually into a set of propagation parameters using propagation codes obtained from the E/O community. These multiple sets of propagation parameters were converted into a probability of occurrence statistics and randomly selected to yield a small subset for driving system codes. The codes used and the procedure for using this large matrix of data will be described in subsequent sections of this report.

Propagation Codes and Sources of Data

The majority of the meteorological ship data was obtained from the National Climatic Center in Asheville, North Carolina. They process and store weather reports from ships of U.S. and foreign registry in addition to U.S. government ships. Most of these ships report synoptic weather observations by radio while underway. This historic surface marine data file is known as Tape Data Family - 11 (TDF-11) and presently consists of approximately 50 million observations. There are, however, collection problems inherent in this world-wide marine data file. The uncertainties of TDF-11 are attributed to different levels of observer experience in recording the state of marine environment from an unstable platform and paucity of observations over certain large areas of the ocean. Another ambiguity has been induced by improved radio communication and optimum track ship routing. These advances have increased the likelihood of "fair weather bias" (i.e., a decrease in frequency of heavy weather observations).

This latter uncertainty can be reduced by considering observations from a unique subset within TDF-11. The Ocean Weather Station (OWS) section of TDF-11 contains data that are nearly serially complete for relatively fixed locations at sea. Experienced meteorological personnel aboard OWS vessels record the state of the marine environment at least eight regularly scheduled times a day. The standard synoptic observation times are midnight, Greenwich Mean Time, and at three hour intervals thereafter.

The most important set of parameters from each observation included air, sea and dew point temperatures, wind speed, barometric pressure, visibility and present weather condition (rain type). The surface observations also include cloud height and coverage which will be used in future guided projectile effectiveness studies and ship signature studies respectively where cloud-free line-of-sight statistics are needed.

The computer code that was developed to convert the weather data to optical parameters can be broken down into the following: (1) molecular absorption coefficients as a function of air temperature and absolute humidity derived from Lowtran 3B calculations; (2) semi-empirical turbulence model relating the refractive index structure constant C_n^2 to air-sea temperature difference, surface winds gradient, and absolute humidity; (3) aerosol model that uses relative humidity and wind speed to produce an aerosol size/number distribution, a complex index of refraction and finally aerosol extinction values.

The Lowtran 3B code developed at AFGL¹ provided transmission calculations for evenly spaced wavelengths in the 8-12 μ m and 3.4-5 μ m band at various values of temperature, water vapor (gm/m³) and range. For a given absolute humidity, temperature and range each transmission value was weighted by the thermal derivative of Planck's radiation equation (300°K source). These values were then averaged over wavelength to provide an effective transmission for the two IR bands. This effective transmission value for a specified atmospheric condition was converted into an effective molecular absorption coefficient (R_m^{-1}) by assuming an exponential decrease with range. These effective extinction coefficients were used to derive a scaling law for temperature and water vapor content. This scaling law was necessary since tens of thousands of calculations are needed.

473

The scaling laws for the 3.4-5 μ m and 8-12 μ m bands (over a 10 kilometer path) are shown as function of temperature (10, 20 and 30°C) and absolute humidity (gm/m³) in Figure 3. The most obvious feature of these band comparisons is the large difference in the molecular absorptions at high absolute humidities. In humid marine locations (within 30° of the equator) where visibilities tend to be 20 kilometers or better, the calculated performance statistics for IR imaging systems are directly related to this difference in molecular absorption. This difference in molecular absorption increases as the performance range extends beyond 10 kilometers. The effective molecular absorption coefficient in the 3.4-5 μ m band decreases by approximately 40% over a 30 kilometer path due primarily to the importance of individual absorbing lines that deplete large amounts of radiation in the first few kilometers. In the 8-12 μ m band the dominant absorption mechanism is the gaseous H₂O continuum which is a slowly varying effect over the entire wavelength interval. This slow variation with wavelength causes only a minor range dependence for band averaged effective molecular absorption coefficient associated with this band.

The basic aerosol distribution model used in this report was provided by Dr. Mike Munn², Lockheed, Palo Alto, California. This model was developed by fitting data that was taken over water and published in the open literature. It uses relative humidity and wind speed to calculate an aerosol size and number distribution. Constants associated with the wind velocity were changed to improve comparisons with aerosol distributions and scattering data taken by the Optical Science and the Atmospheric Sciences Branches at the Naval Research Laboratory. Mie scattering calculations were done with a four region closed form approximation scheme developed by Van De Hulst³. Comparisons with full Mie codes indicate a maximum 5% error. The complex index is varied from that of a high concentration salt water mixture to pure water as aerosols grow with increasing relative humidity.

A direct comparison of this aerosol extinction model (K/R) and the Lowtran 3B Maritime model is found in Figure 3 where the relationships between visible (.55 μ m) and 8-12 μ m extinction are plotted. The K/R curves represent pairs of extinction values for RF from 70-98% (five curves) and equally spaced wind speed from 1-17 m/sec (nine per curve). The most obvious difference is the lack of uniqueness in relating $\tau(.55)$ to values in other bands (K/R calculations). Each pair of wind speed and RH creates its own distinctive wavelength relationship that in the case of the 8-12 μ m band varies from 20:1 at good visibilities to 2:1 at a 2 km visual range. The Lowtran Maritime model has a constant 4.76:1 ratio which falls in the center of the K/R variation. The K/R calculations are more optimistic in the IR regions for good visibilities while being more pessimistic in the more turbid windy conditions.

Before using the K/R model aerosol extinctions in systems performance calculations a series of trials were made comparing a calculated visibility to the observer estimated visual range (EVR). Since the purpose of these calculations was to provide the Navy community with statistical performance of their E/O systems, it was felt necessary that any aerosol extinction model used in these calculations should relate well to the stored visibility data in both a direct and statistical manner. The three hundred per season random sets of observations from OWS and passing ships were used with the K/R model for this comparison. Each observation provided an estimated visual range and the meteorological parameters necessary to calculate a visual range (VR). The calculated VR assumed a two percent threshold of brightness contrast and a Bouguer-Lambert Law (Beers' law) for atmospheric attenuation with range⁴:

$$VR \text{ calc.} = 3.91/\tau(.55) \text{ calculated}$$

The observations and calculations for each season were compared in a cumulative probability form. The results are plotted in Figure 4 for winter and summer seasons at the Mediterranean (WD2) and Ship J locations (WDJ). The straight line segmented curves (VISC X) in these figures represent the cumulative probabilities of the EVR's while the noisy curves (VISC*) represent the calculated visual ranges.

Using the assumption that the subjective visibilities were equally distributed over their respective ranges (re: EVR at 20 km were equally weighted between 20 and 50 kms), the medium estimated visual range increased from 15 km in Winter J to over 35 km in Winter Med. This large variation in medium EVR was tracked very well by the model calculations. At all visibilities below one kilometer the model calculation of visual range was forced to be equal to the EVR.

The previously described molecular absorption and aerosol extinction models were combined with sets of weather observations to produce individual sets of optical parameters related to TV, 1.06 μ m and two FLIR systems. These sets of propagation parameters were then used individually in systems performance calculations and collectively for probability of occurrence statistics. Examples of these curves for the 8-12 μ m band are shown in the next two figures (5 and 6).

In Figure 5 sets of curves represent the seasonal variation in the cumulative probability of occurrence of the total molecular absorption and the aerosol extinction for Weather Ship J and a combined Eastern and Western Mediterranean data set. The ordinate is the probability that the specific parameters will be equal to or greater than the abscissa value. The seasons are three months long with SP denoting the spring months of March, April and May. The summer (SU), fall (FA) and winter (WI) seasons correspond to sequential sets of three month periods.

The North Atlantic Ship J calculations reveal higher aerosol extinction values but lower molecular absorption coefficients than does the Mediterranean data. This is a consequence of higher winds and relative humidity and lower absolute humidity in the Ship J location.

In Figure 6 the same parameters are plotted together with the statistics of the total extinction coefficient for the summer and winter months. In the North Atlantic, aerosols dominate the 8-12 μ m total extinction 20-35% of the time depending on the season and location. In this region the total extinction values and statistics are more suspect than those in the Mediterranean due to the greater uncertainties in the aerosol models. This variation in aerosol influence with changing location and season is even more acute in the 3.4-5 μ m region.

System Performance Considerations

The performance range for a particular optical system depends critically upon the target and the scenario as well as on the environmental factors. The deterministic approach to sensor performance for a given system, scenario and target combination, provides the prediction of a unique performance range (in this case detection) for each set of atmospheric optical parameters.

An aperiodic detection scheme based on signal-to-noise and spatial size consideration is combined with a medium-size ship target that has a uniform temperature difference with the background to provide detection range versus total extinction curves for a variety of TV, 1.06 μ m and FLIR systems. The following range performance equation was used to fit the parametric outputs of the complicated aperiodic FLIR model⁵:

$$R_{\text{detection}} = (A + B \cdot B_{\text{atm}}^2)^{-1/2}$$

where R_{det} is the predicted range (kilometers) for a 50% probability of detecting the target, A and B are constants associated with the choice of FLIR system and altitude, and B_{atm} is the total extinction coefficient in units of inverse kilometer. Some examples of current and projected future 8-12 μ m FLIR systems performance (detection range) versus total extinction are shown in Figure 7. The FLIRs were placed at various altitudes to emphasize horizon limitations. The greater the horizon limitation the smaller the detection range improvement associated with more advanced systems of the same wavelength.

The systems performance models, target and receiving systems were combined with individual sets of atmospheric optical parameters to produce detection range statistics for different seasons, locations and receiver altitudes. The resulting performance range statistics were plotted together to show the dramatic variation in predicted detection range with altitude for different competing systems.

In the next three figures the 20, 50 and 80% cumulative performance points for FLIRs operating on-board a ship in a ship detection mode are plotted as a function of latitude for summer months. Figure 8 contains only detection statistics for a current generation 8-12 μ m FLIR. The poor performance near the equator is due entirely to the high humidity conditions. In more northern climates the humidity decreases allowing for much larger detection ranges during good visibility days. The 80% curve remains fairly flat with latitude indicating that as humidity effects decrease with increasing latitude the aerosol effects are becoming more severe statistically even though there are many very clear days (20% points). In Figure 9 the performance statistics of a near term focal plane array 8-12 μ m FLIR is superimposed on the current generation system. The increased sensitivity provides improved detection ranges. In Figure 10 a near term 3.4-5 μ m system is superimposed on the current generation 8-12 μ m system statistics. This dramatic difference in performance between the two bands is based entirely on the aerosol models since, as shown earlier, the molecular absorption in the 3.4-5 μ m band is insensitive to change in absolute humidity or temperature and therefore latitude. As the visibilities improve (lower latitudes) the detection range associated with the 3.4-5 μ m FLIR increases while the 8-12 μ m is encumbered by the increasing water vapor content.

- ¹ Selby, J. E. A., and McClatchy, R. A., "Atmospheric Transmittance from 0.25 to 28.5 m: Supplement to LOWTRAN 3B," AFGL-TR-76-0258, 1976.
- ² Wells, W. C., Gal, G., and Munn, M. W., Applied Optics 16, No. 3, March 1977, pg. 654
- ³ Van De Hulst, H. C., Light Scattering by Small Particles, John Wiley & Sons, Inc., 1957, Chapter 14.
- ⁴ Middleton, W. E. K., Vision Through the Atmosphere, University Toronto Press, Toronto, Canada, 1952
- ⁵ Sendell, R. L., and Rosell, F. A., "E-O Sensor Performance Analysis and Synthesis (TV/IR Comparison Study)," AFAL-TR-72374, April 1973.

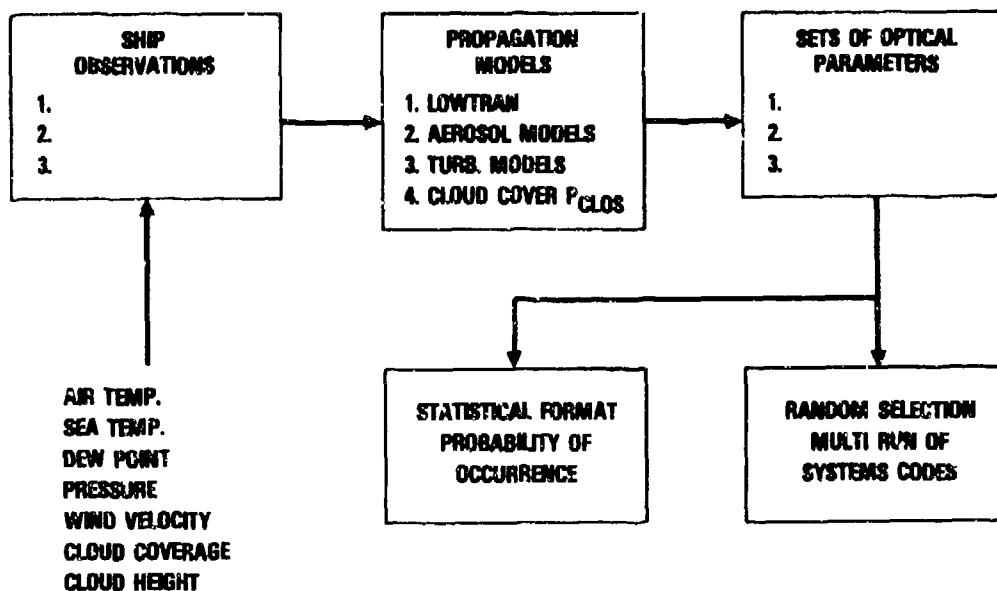


Figure 1 - Block Diagram for Conversion of Meteorological Observations to Optical Parameters

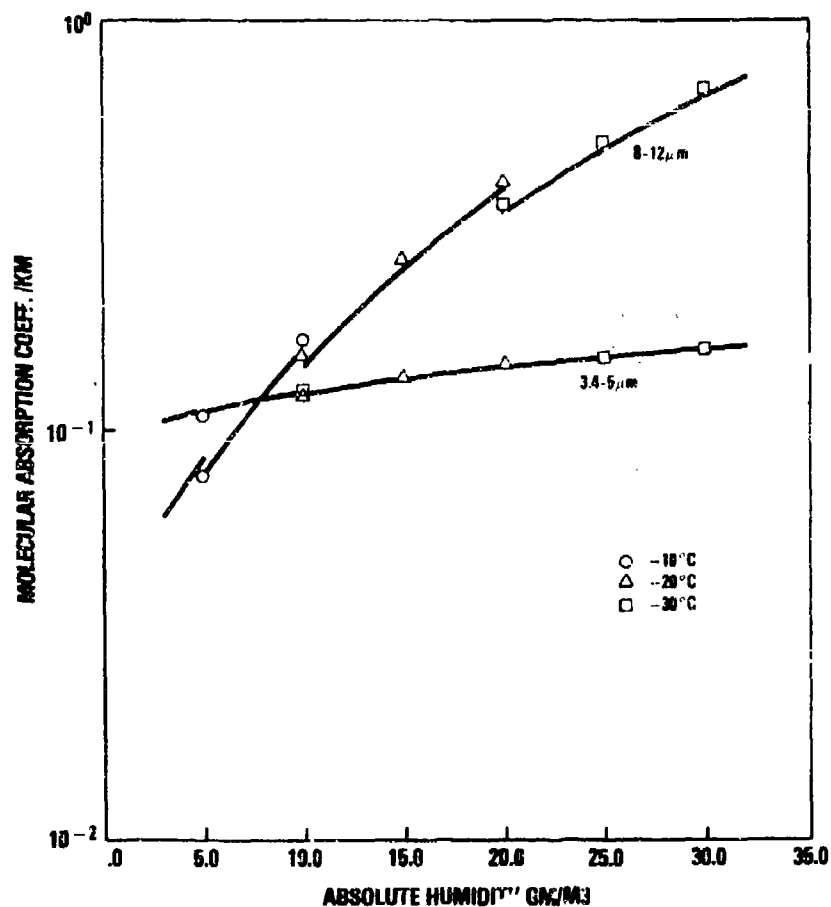


Figure 2 - Total Molecular Absorption Coefficient as a Function of Absolute Humidity for both 3.4-5 μ m and 8-12 μ m Bands at a Range of 10 Km and Three Temperatures

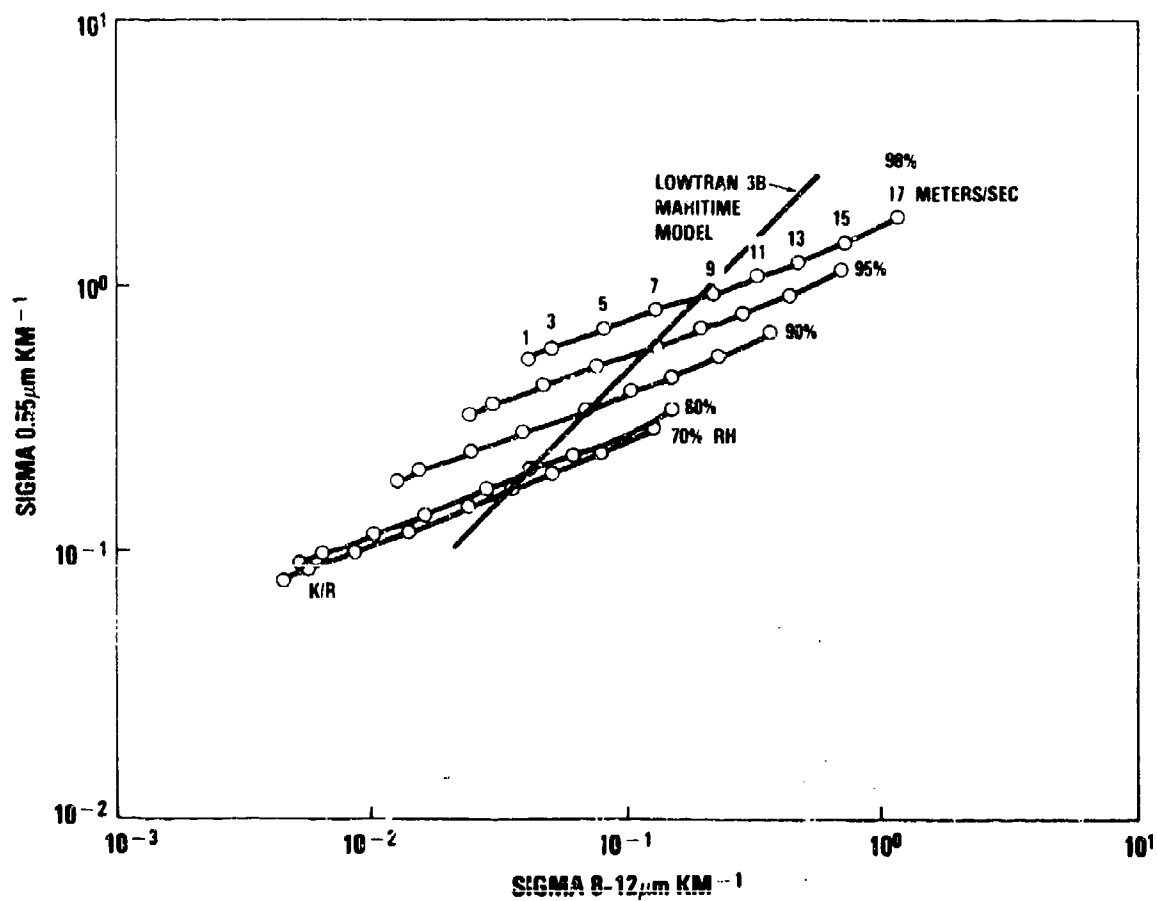


Figure 3 - K/R Model Comparison of Visible ($0.55\mu\text{m}$) and $8-12\mu\text{m}$ Aerosol Extinction Coefficients at Five RH Values and Nine Wind Speeds for each RH (LOWTRAN 3B Maritime Model Curve also shown)

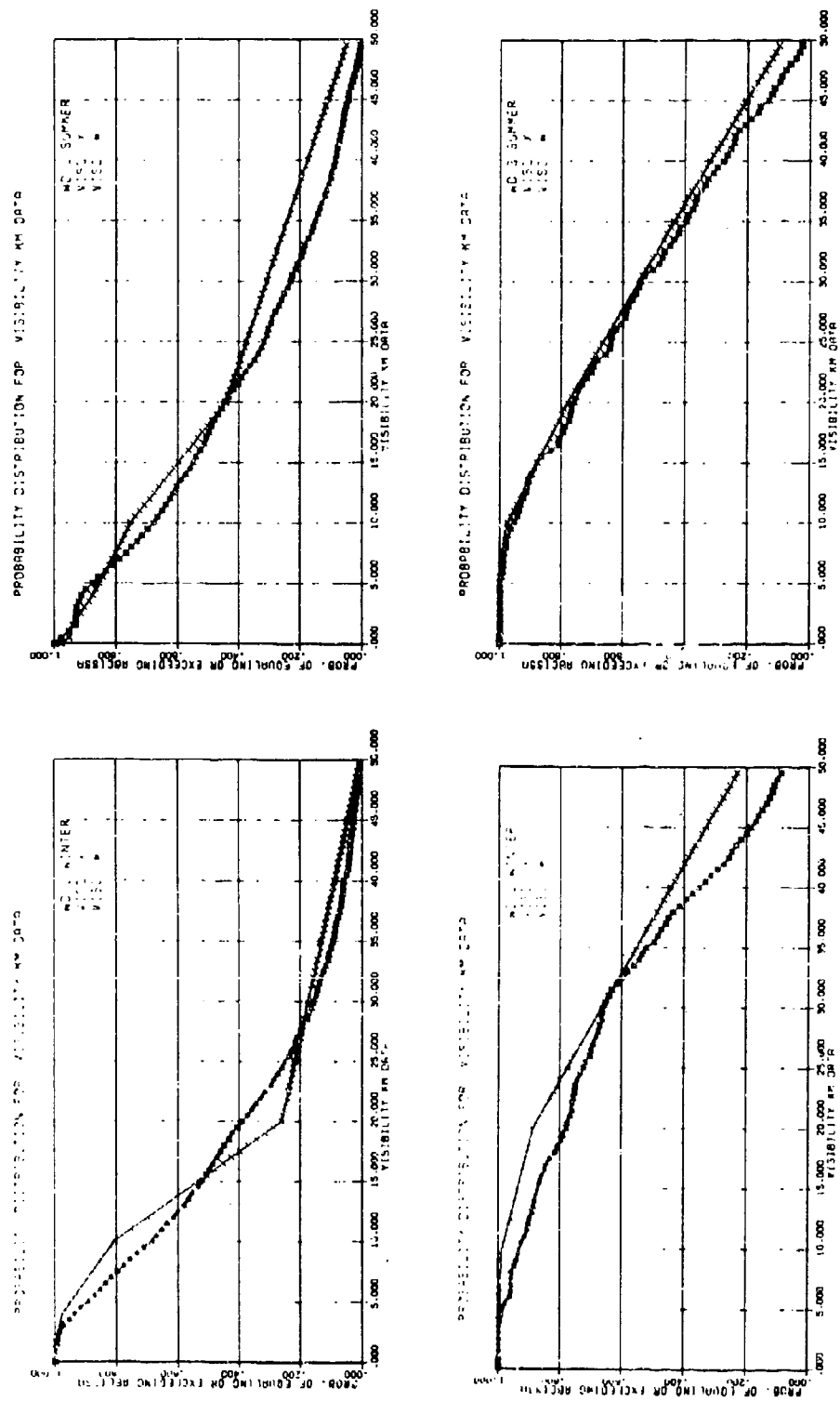


Figure 4 - Cumulative Probability Distribution Comparisons of Calculated Visibility (VISC) and Estimated Visibility (VSD) in the North Atlantic (WDJ) and Mediterranean (WDJ) during Summer and Winter

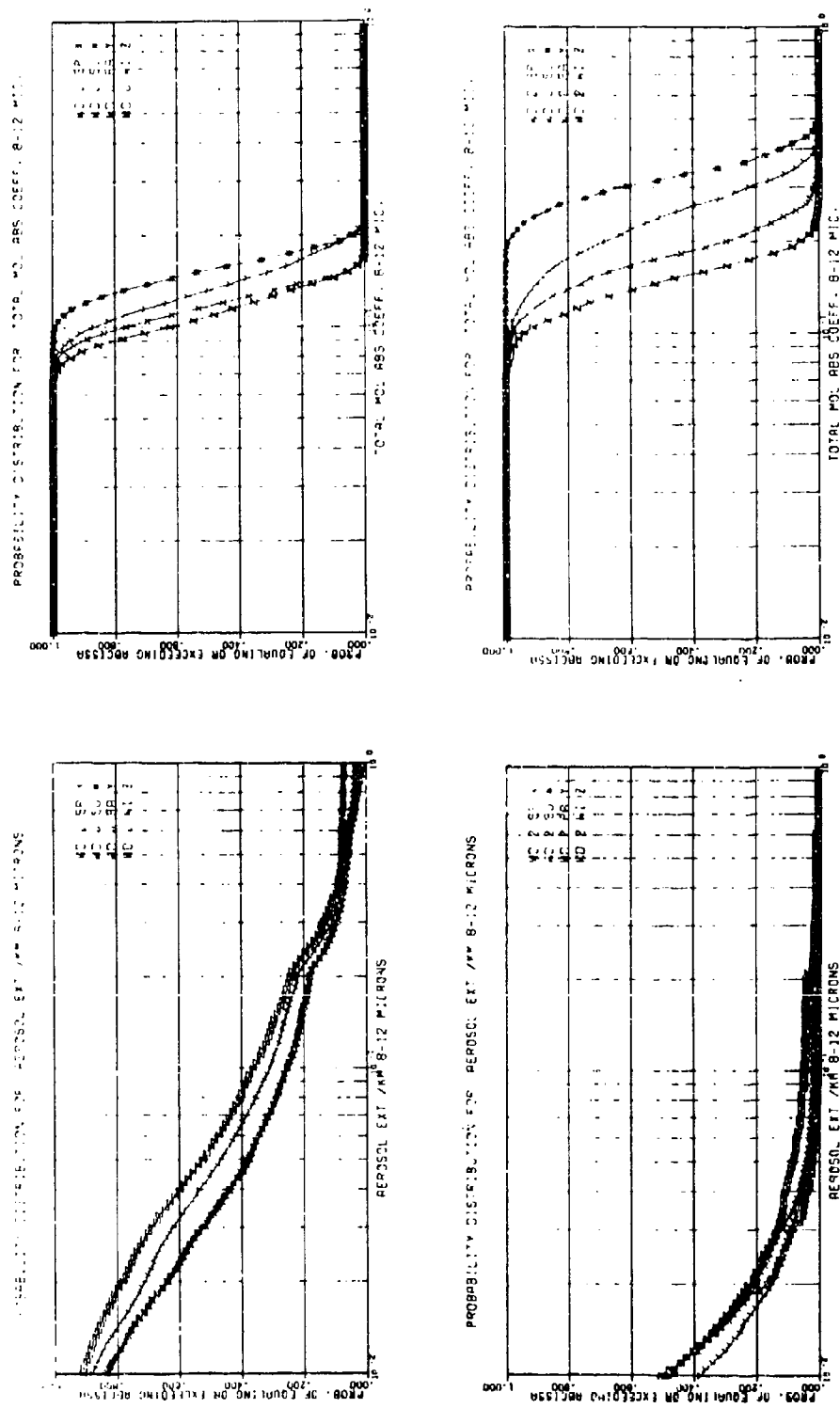


Figure 5 - Cumulative Probability Distributions for North Atlantic (WDJ) and Mediterranean (WDJ) locations. Aerosol and Molecular Absorption statistics in the 8-12 μ m band are presented for individual seasons

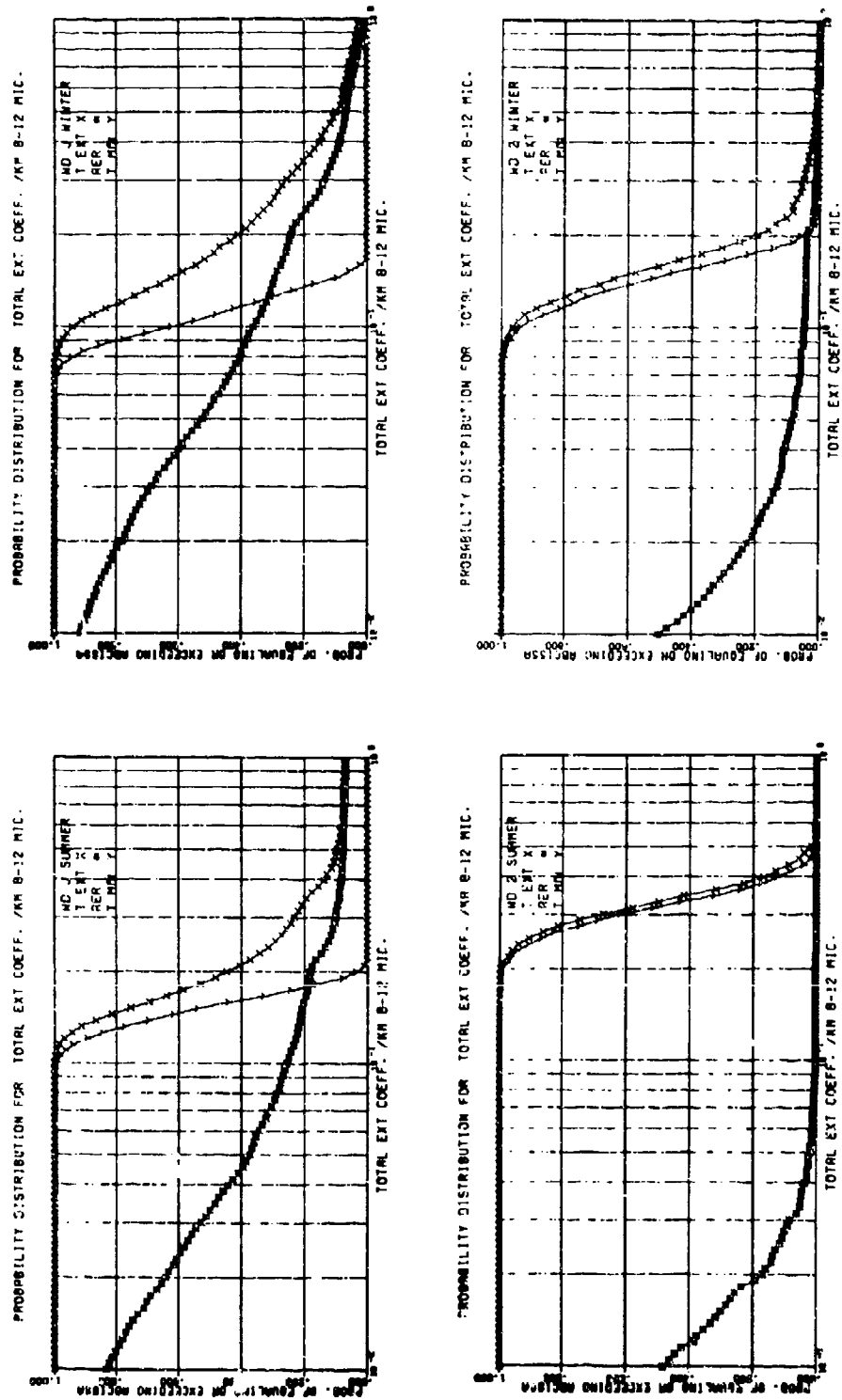
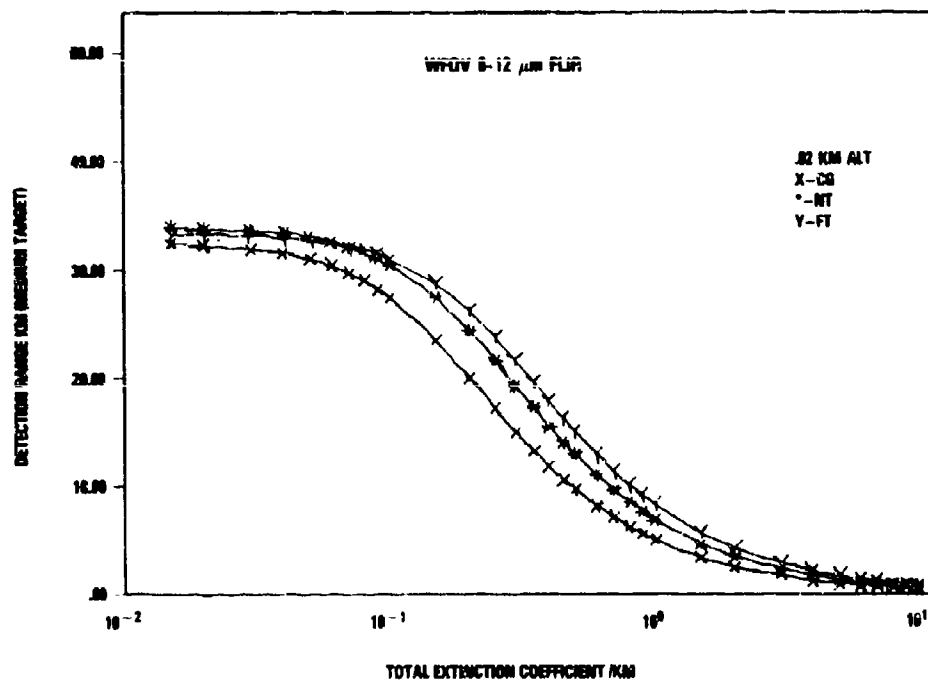
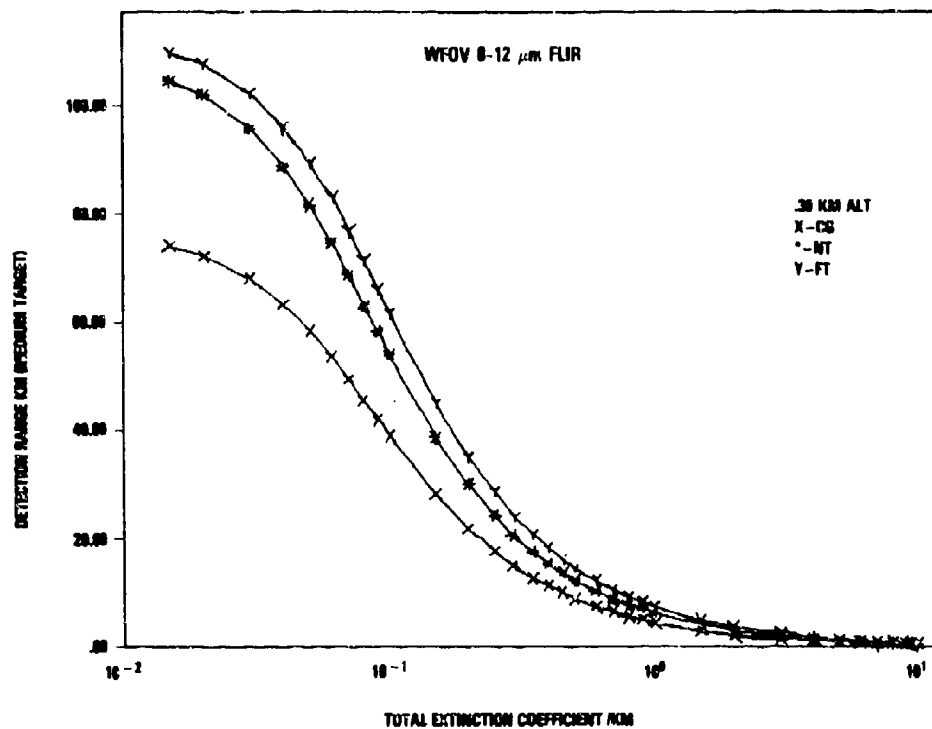


Figure 6 - Cumulative Probability Comparisons of 8-12 μ m Aerosol Extinction, Molecular Absorption and the Total Extinction Coefficients



Figures 7 Detection Range Performance Curves for Current Generation,
A&B Near-Term and Far-Term FLIRs (WFOV 8-12 μ m) with Medium Target,
and Receiver Altitudes of (A) 300 meters, and (B) 18 meters

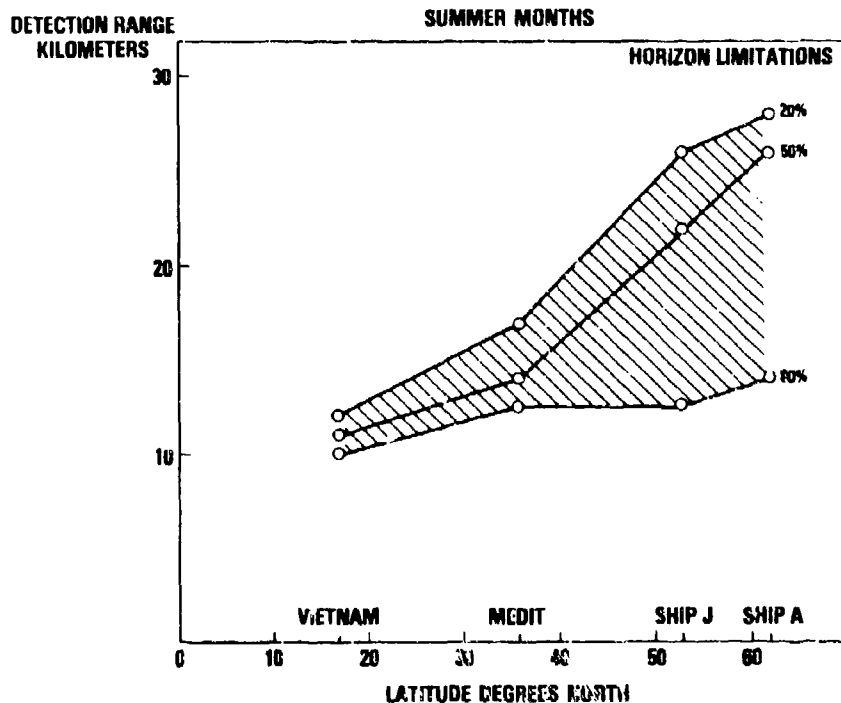


Figure 8 - Detection Range vs. Latitude for Current Generation 8-12 μ m WFOV FLIR, 18 meters Altitude during Summer with Medium Target (20%, 50%, and 80% Cumulative Probability Curves shown)

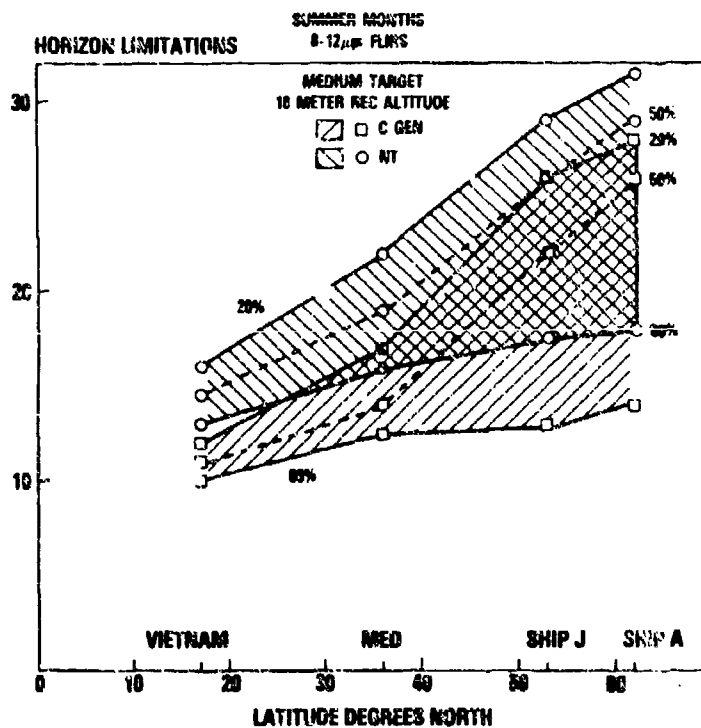


Figure 9 - Detection Range vs. Latitude for Current Generation and Near-Term WFOV 8-12 μ m FLIRs, 18 meters Altitude during Summer with Medium Target (20%, 50%, and 80% Cumulative Probability Curves shown)

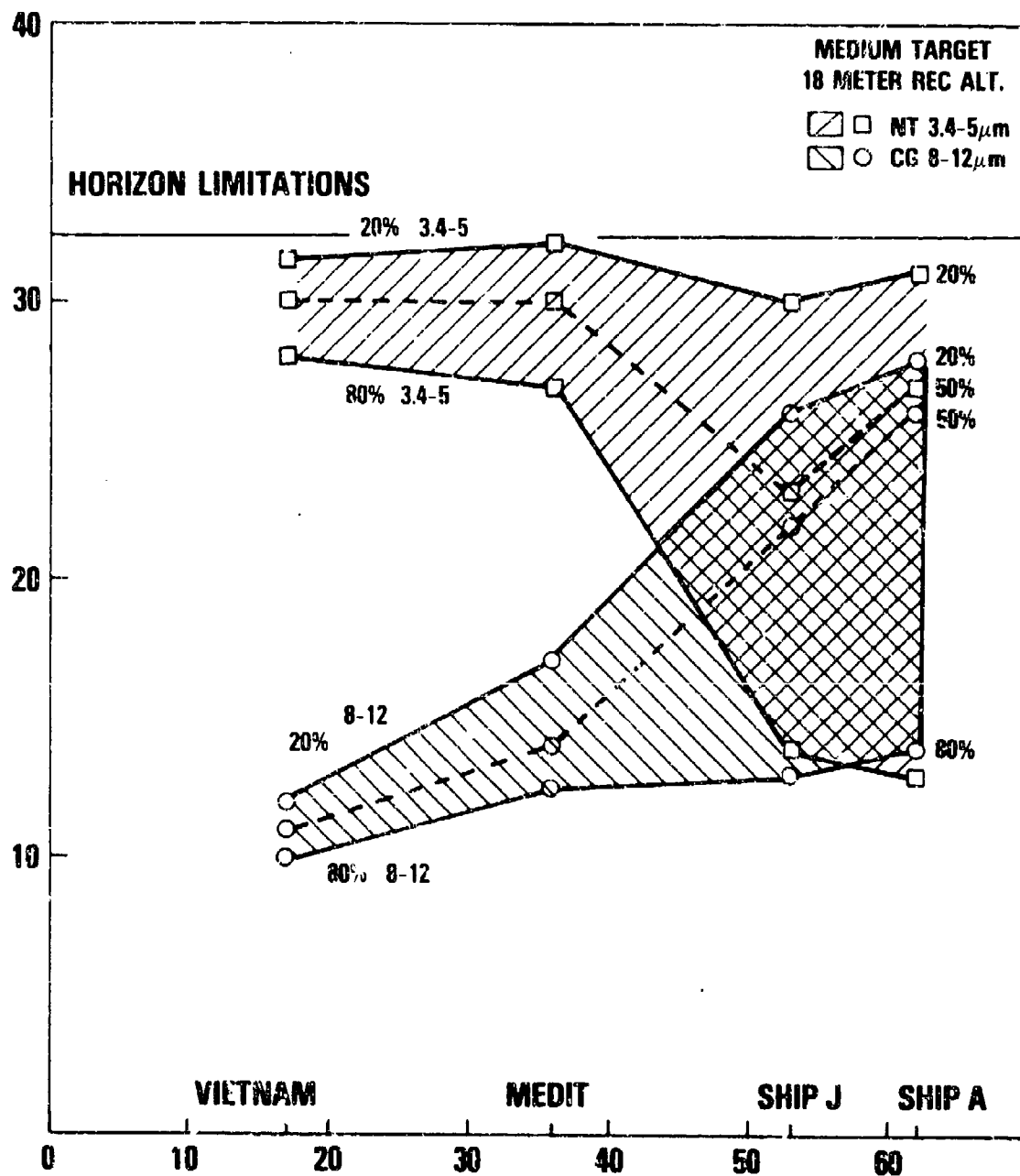


Figure 10 - Detection Range vs. Latitude for Current Generation 8-12 μ m and Near-Term, 3.4-5 μ m WFOV FLIRs, 18 meters Altitude during Summer with Medium Target (20%, 50%, and 80% Cumulative Probability Curves shown)

SUMMARY OF SESSION IX
TROPOSPHERIC TURBULENCE

by

Dr H. Soicher
Editor

The effects of atmospheric turbulence due to temperature fluctuations and wind on the performance of optical systems are well known. In particular, system degradations include loss of image resolution, difficulty in detection of dim objects, and loss of tracking accuracies. Papers during this session concentrated on the comparison of atmospheric turbulence measurements with models of corresponding parameters, and on the simulation of turbulence conditions for propagation analysis.

Yura seeks to determine whether any correlation exists between measured values of both stellar scintillation and phase coherence and the corresponding values predicted from a recent model of atmospheric turbulence profile. He finds good agreement with the scintillations data, while the phase data is only of fair-to-good agreement.

Hanson describes measurements of the temperature turbulence profiles and the coherence diameter conducted at the ARPA Maui Optical Station (AMOS). These measurements are compared with existing models. He concludes that while the coherence diameter measurements are in reasonable agreement with existing models, temperature turbulence profiles are not.

Lyon describes the simulation of turbulent atmospheric propagation as part of a procedure for the development of an optical tracking system.

OPTICAL PHASE AND SCINTILLATION AT AMOS: COMPARISON BETWEEN OBSERVATION AND PREDICTION

H. T. Yura

The Ivan A. Getting Laboratories
The Aerospace Corporation
P.O. Box 92957
Los Angeles, California 90009

Abstract

Atmospheric turbulence has a significant impact on the performance of large aperture optical systems. Degradations observed include loss of resolution when imaging, increased difficulty in detecting dim objects, loss of tracking accuracy, as well as a number of other effects. The evaluation of the performance of any system and the specification of operating parameters for systems designed to eliminate or minimize these degradations require sufficient knowledge in order to provide a characterization of the turbulent environment in which they must operate.

A primary objective of an operational model of the aerospace propagation environment is to provide sufficient understanding for the system analyst to compute performance estimates under various operational conditions. To this end we present in this paper a comparison between measured values of both stellar scintillation and optical phase coherence and the corresponding values predicted from a recent model of the atmospheric turbulence strength profile. The optical measurements under consideration were performed by members of the AVCO Everett Research Laboratory (AVCO) at the ARPA Maui Optical Station (AMOS) atop Mt. Haleakala on the island of Maui, Hawaii in the fall of 1975. We employ here Hufnagel's recent statistical model of atmospheric turbulence for heights greater than three kilometers above mean sea level together with a model for low altitude turbulence developed from the empirical data of Koprov and Tsvang, and Bufton. The appeal of this turbulence model is that it is relatively simple to implement in system studies and that only one free parameter is needed for its quantitative use. This parameter is the root mean square wind speed for the altitude range of five to twenty kilometers above sea level.

We first discuss the statistical turbulence model in its full generality (i.e., both its temporal and spatial variations). We next present an average or non-random model which can be used by those not interested in the fine structure, as is the case here since available data does not warrant the use of the full random model of atmospheric turbulence.

It is necessary to have knowledge of the statistical characterization of both the optical phase coherence diameter r_0 and the scintillation index σ_I^2 of a stellar source. Expressions for these quantities are presented and discussed. Using measured values of the wind speed parameter for the appropriate dates of the experiment, we then calculate the appropriate values of r_0 and σ_I^2 and compare with the corresponding values, as measured by AVCO. We find good agreement with the scintillation data, the agreement with the phase data being only fair to good. Although the results presented here are encouraging, more data comparison is needed before the validity for general use of the turbulence model used here can be established. Finally, possible improvements with the turbulence model are discussed.

I. INTRODUCTION

The purpose of this paper is to seek to determine if any correlation exists between measured values of both stellar scintillation and phase coherence and the corresponding values predicted from a recent model of the atmospheric turbulence profile. Specifically, we employ here Hufnagel's (Ref. 2) recent model of the index structure constant profile $C_n^2(h, V)$, where h is the altitude above mean sea level and V is a root mean square wind speed (defined below) to calculate both the variance and covariance of the log-amplitude σ_I^2 and phase coherence diameter r_0 of an optical wave due to a stellar source. We then compare these quantities to the corresponding quantities as measured by AVCO and AMOS during November 1975.

We first discuss Hufnagel's recent model of C_n^2 and present expressions for the appropriate wave statistical quantities. Using measured values of the wind speed parameter V for the appropriate dates of the experiment, we then proceed in Section IV to calculate the normalized log-amplitude variance and compare with the corresponding values, as measured by AVCO. For the three experimental dates considered, fairly good agreement is obtained.

In the design and deployment of the AMOS compensated imaging system, it is necessary to have knowledge of the statistical characterization of the phase coherence diameter of the atmosphere r_0 of an optical stellar source. In Section III we present the results of our calculation of r_0 and compare with AVCO's experimental results. The present calculation of r_0 is based on Hufnagel's recent model of C_n^2 together with a low altitude C_n^2 model (i.e., 0-3 km above the AMOS site) abstracted from the experimental results of Bufton (Ref. 1) and Koprov and Tsvang (Ref. 3). Our calculated values of r_0 are a little larger than AVCO's measured average values, although not as large as AVCO's value of r_0 as calculated on the basis of measured turbulence profiles.

Although the present results are encouraging, more comparison with experimental data is needed before the validity of the turbulence model used here can be established. However, at this point we are cautiously optimistic.

II. ATMOSPHERIC TURBULENCE PROFILE

Recently R. E. Hufnagel (Ref. 2) presented an empirical model for the altitude profile of the index structure function C_n^2 . In its full generality, the random turbulence version of the Hufnagel turbulence model has the form (in units of $m^{-2/3}$)

$$C_n^2(h) = 5.98 \times 10^{-23} (V/27)^2 h^{10} e^{-h} + 10^{-16} \times e^{-h/1.5} \exp[r(h,t)], \quad h > 3 \text{ km} \quad (1)$$

where h is in kilometers above mean sea level, V is the root mean square wind speed in meters/sec in the 5 to 20 km altitude range, i.e.,

$$V = \left[\frac{1}{15 \text{ km}} \int_{5 \text{ km}}^{20 \text{ km}} v^2(h) dh \right]^{1/2}, \quad (2)$$

where $v(h)$ is the wind speed profile in m/sec. The quantity $r(h, t)$ is a gaussian random variable which depends on altitude and time. As defined by Huftnagel, r has zero mean and a correlation function given by

$$\langle r(h + h', t + \tau) r(h, t) \rangle = A(h'/100) \exp(-\tau/5) + A(h'/2000) \exp(-\tau/80) \quad (3)$$

where t is time measured in seconds and the function A is given by

$$A(x) = 1 - |x|, \quad |x| \leq 1 \\ = 0, \quad |x| > 1 \quad (4)$$

In some cases it may be more convenient computationally to use an exponential decay function, i. e., $A(x) = \exp(-|x|)$.

As is discussed below, the available data does not warrant the use of the full random model of C_n^2 . Accordingly, we employ the non-random model, obtained by taking the ensemble average of Eq. (1). We obtain $\langle e^r \rangle \equiv e = 2.72$

$$C_n^2(h, V) = 5.98 \times 10^{-23} (V/27)^2 h^{10} e^{-h} + 2.72 \times 10^{-16} e^{-h/1.5} \quad (5)$$

where V is given by Eq. (2). As discussed by Huftnagel (Ref. 2), V appears to be normally distributed about some average value. For example, for the state of Maryland, V appears to be normally distributed with an average value of 27 m/sec and a standard deviation of 9 m/sec. Below we use the value of V obtained from the wind speed profiles for the dates of the measurements, as supplied by the Air Weather Service.

Strictly speaking, Eq. (1) or (5) is valid for $h \geq 3$ km. Since the measurements were performed at AMOS, i. e., at an altitude of 3 km, Eq. (5) will suffice for the present analysis. However, for completeness we present a model developed from the empirical data of Koprov and Tsvang (Ref. 3), and J. Bufton (Ref. 1) for the value of C_n^2 at altitudes below 3 km:

$$C_n^2 = \begin{cases} 7.0 \times 10^{-14} h^{-4/3}, & 10 \text{ m} < h < 100 \text{ m} \\ 1.5 \times 10^{-16} & 100 \text{ m} < h < 500 \text{ m} \\ 1.5 \times 10^{-16} - 1.125 \times 10^{-16} \left(\frac{h-500}{500} \right), & 500 \text{ m} < h < 1000 \text{ m} \\ 3.75 \times 10^{-17} + 7.95 \times 10^{-17} \left(\frac{h-1000}{1000} \right), & 1000 \text{ m} < h < 2000 \text{ m} \\ 1.17 \times 10^{-16} - 5.85 \times 10^{-17} \left(\frac{h-2000}{2000} \right), & 2000 \text{ m} < h < 3000 \text{ m} \end{cases} \quad (6)$$

The model presented above is simple in many respects. It does not explicitly account for possible high turbulence peaks generated at frontal interfaces or sharp inversion layers. And, conceivably the numerical coefficients in model should be different over mountainous terrain. Nevertheless, it does seem to yield reasonable agreement with most of the observed stellar scintillation measurements taken in the past. The appeal of the model lies in the fact that there is only one parameter, the root mean square wind speed V , which characterizes the altitude dependence of C_n^2 . This parameter is readily available for many experimental sites and in particular it is available for AMOS. Finally, we note that it is expected that the largest variability of C_n^2 is obtained near the ground, the high altitude turbulence being insensitive to effects of local terrain. As is discussed below, the effects of low altitude turbulence have little effect in producing scintillation. However, both low and high altitude turbulence are important in producing optical phase distortions.

III. IRRADIANCE STATISTICS

In all cases considered here we are in the regime of weak optical scintillation; that is, we are in unsaturated regime of scintillation where the results of the Rytov approximation apply. The regime of weak scintillation is such that the normalized variance of log-amplitude, σ_I^2 , is much less than unity. In this regime it is known (Ref. 6) that the probability distribution of irradiance is log-normal (i. e., the natural logarithm of irradiance is normally distributed); that is, the probability density of irradiance is given by

$$P(I) = \frac{1}{\sqrt{2\pi} \ln(\sigma_I^2 + 1)} \left(\frac{1}{I} \right) \exp \left\{ - \frac{[\ln I + 1/2 \ln(\sigma_I^2 + 1)]^2}{2 \ln(\sigma_I^2 + 1)} \right\} \quad (7)$$

where

$$I = \frac{I}{\langle I \rangle}, \quad (8)$$

$$\sigma_I^2 = \frac{\langle I^2 \rangle - \langle I \rangle^2}{\langle I \rangle^2}, \quad (9)$$

I is the instantaneous value of irradiance, and angular brackets denote the ensemble average. Thus, I is the instantaneous value of irradiance normalized by its mean, and σ_I^2 is the normalized variance of irradiance. Examination of Eq. (7) reveals that the probability distribution of normalized irradiance is

characterized by the single parameter σ_I^2 , the normalized variance of irradiance.

For log-normal statistics, the normalized variance of irradiance for a point receiver is related to the variance of log-amplitude, σ_I^2 , by the relation

$$\begin{aligned}\sigma_I^2 &= \exp(4 \sigma_I^2) - 1 \\ &\approx 4 \sigma_I^2, \quad \sigma_I^2 \ll 1\end{aligned}\quad (10)$$

The introduction of the quantity σ_I^2 as the basic parameter is operationally useful as this is the quantity that is usually measured. Thus for a given value of σ_I^2 , the probability distribution of irradiance is determined completely.

We next present expressions that relate the log-amplitude statistics to the index structure profile, optical wavelength and propagation path. For weak scintillation conditions the log-amplitude correlation function for a point (i.e., stellar) source at infinity is given by (Ref. 6)

$$B_A(\rho) = 4 \pi^2 k^2 \sec \theta^{11/6} \int_{h_1}^{\infty} C_n^2(h) dh \int_0^{\infty} J_0(K\rho) \Phi_n(K) \sin^2 \left[\frac{K^2(h-h_1)}{2k} \right] K dK \quad (11)$$

where ρ is the separation in a plane transverse to the mean direction of propagation, θ is the zenith angle, h_1 is the altitude of the receiver, k is the optical wave number ($= 2\pi/\lambda$, where λ is the optical wavelength), J_0 is the Bessel function of zero-order of the first kind, $C_n^2(h)$ is the index structure profile, and $\Phi_n(k) \approx 0.033 K^{-11/3}$.

The variance of log-amplitude is then given by

$$\begin{aligned}\sigma_I^2 &= B_A(0) = 4 \pi^2 k^2 \sec \theta^{11/6} \int_{h_1}^{\infty} C_n^2(h) dh \int_0^{\infty} \Phi_n(K) \sin^2 \left[\frac{K^2(h-h_1)}{2k} \right] K dK \\ &\approx 0.563 k^{7/6} \sec \theta^{11/6} \int_{h_1}^{\infty} C_n^2(h) (h-h_1)^{5/6} dh\end{aligned}\quad (12)$$

Examination of Eq. (12) reveals that owing to the $h^{5/6}$ weighting function in the integrand, the value of σ_I^2 is determined primarily from high altitude turbulence. Examination of Eqs. (5) and (12) reveals that for $V \geq 10$ m/sec the main contribution to σ_I^2 is determined by the turbulence near the tropopause, i.e., at $h \sim 10$ km. The integrand of Eq. (12) has a relative maximum for $h = 10.83$ km, falling to one-half its maximum value at $h \approx 7.5$ and 15.5 km.

Equation (12) for σ_I^2 pertains to the statistics of irradiance at a point. As the experiments at AMOS were performed with a finite size receiving aperture, it is necessary in our analysis to account for aperture smoothing. As is discussed below, the effects of aperture smoothing are determined not only by the log-amplitude variance σ_I^2 but also by the shape of the correlation function $B_A(\rho)$. As such, it will also be necessary to compute the full correlation function $B_A(\rho)$ for $\rho \leq D$, where D is the diameter of the receiving aperture ($= 35.6$ cm for the AMOS experiments). This calculation is discussed in more detail later on in this section.

Upon substituting Eq. (5) into Eq. (12), we find that the log-amplitude variance at a point is given by

$$\begin{aligned}\sigma_I^2 &\approx \left[4.14 \times 10^{-2} \left(\frac{V}{27} \right)^2 + 2.48 \times 10^{-3} \right] \left[\frac{0.5}{\lambda(\text{microns})} \right]^{7/6} \sec \theta^{11/6} \\ &= 4.14 \times 10^{-2} \left(\frac{V}{27} \right)^2 + 2.48 \times 10^{-3}, \quad \text{for } \lambda = 0.5 \mu\text{m}, \theta = 0\end{aligned}\quad (13)$$

and is plotted in Fig. 1 as a function of V for the case $\lambda = 0.5 \mu\text{m}$ and $\theta = 0$. In order to compare with experiment, one must correct these values for the smoothing effect of the finite size collecting aperture.

As alluded to above, scintillation measurements performed with a finite sized collector include an aperture smoothing effect referred to in the literature as the aperture averaging effect. Thus, the log-amplitude variance obtained from a collector of diameter D , $\sigma_I^2(D)$, is related to the corresponding point log-amplitude variance by

$$\sigma_I^2(D) = A \sigma_I^2 \quad (14)$$

where the aperture averaging factor $A(\leq 1)$ is given by (Ref. 4) (we assume here that the collecting aperture is circular)

$$A = 8 \int_0^1 \frac{C_1(Dx)}{C_1(0)} M_L(x) x dx \quad (15)$$

where

$$\begin{aligned}M_L &= \frac{2}{\pi} \left[\cos^{-1} x - x \sqrt{1-x^2} \right], \quad 0 \leq x \leq 1 \\ &= 0, \quad x > 1\end{aligned}\quad (16)$$

$$C_1(\rho) = \exp \left[4 B_A(\rho) \right] - 1 \quad (17)$$

and $B_A(\rho)$ is given by Eq. (11). Examination of Eqs. (11) and (17) reveal that the value of A depends on the characteristic correlation length of the log-amplitude correlation function p_L . For $D \ll p_L$, $A \approx 1$ and there is no aperture averaging effect, the receiver is essentially a point receiver. On the other hand, for

$D \geq p$, several "independent" fluctuations with differing signs are collected, and they partially compensate one another leading to a value of $A < 1$. For uniform turbulence condition the amplitude correlation length is of the order $\sqrt{\lambda L}$, where L is the path length and λ is the optical wavelength.

Examination of Eqs. (15) and (17) reveal that for $B_A(0) = \sigma_f^2 < 1$ the value of A depends on the form of the normalized log-amplitude covariance function $b_A(\rho) = B_A(\rho)/\sigma_f^2$ only. For values of V greater than about 10 m/sec the dominant contribution to $b_A(\rho)$ results from the turbulence in the tropopause, i.e., the first term on the right-hand side of Eq. (1). In the experiments discussed below the value of V is in the 20 to 30 m/sec range. As a result, it can be shown for this case that $b_A(\rho)$ is nearly a universal curve; that is, $b_A(\rho)$ is independent of V for $V \geq 10$ m/sec. This implies that A is nearly independent of V . These results have been confirmed numerically for all values of V that were obtained in the AMOS experiments. We find that $A \approx 0.019$ for the 14-inch diameter collector used at AMOS.

AVCO has performed scintillation measurements using a star sensor built by NOAA Environmental Research Laboratory. This instrument consists of a 35.6 cm Schmidt-Cassegrain telescope. When a stellar source is received through this system, measurements of the spatial frequency content of the atmospherically produced scintillation pattern are obtained. Details of the experimental apparatus and results obtained are reported elsewhere (Ref. 5). We have chosen three separate days to compare with. These days were chosen because the environmental profile $C_n^2(h)$ was also measured independent of the optical measurements. Further details of the C_n^2 measurements are also given in Ref. 5.

The nights chosen to compare our results to experiment are Nov. 17, 18 and 21, 1975. The experiments were generally run between 1900 to 2400 hours local time.

The wind speed data, obtained through Maj. John Madura of SAMSO, was taken at Hilo, Hawaii, at 2400 hours. Although Hilo, Hawaii, is about 100 miles from Maui, it is not expected that the values of V over Maui were significantly different than those over Hawaii, owing to the fact that the main contribution to V is at high altitude (5-15 km) and the terrain between the two islands is primarily open ocean. The value of V obtained are 21.3, 20.5, and 30.8 m/sec for Nov. 17, 18, and 21, respectively.

In Table 1 we have tabulated the values of σ_f^2 obtained by AVCO at 0.5 μ m and the results of our calculations.

TABLE 1
Log-Amplitude Data Comparison
($D = 35.6$ cm, $A \approx 0.019$)

Date	σ_f^2 , AVCO		σ_f^2 , Aerospace Corp., $\theta = 0$	
	Range $\times 10^{-4}$	Average, $\times 10^{-4}$	Average, $\times 10^{-4}$	V (m/sec)
Nov 17	2.79 - 18.20	7.92	5.37	21.3
Nov. 18	2.28 - 5.03	3.76	4.95	20.5
Nov 21	5.17 - 8.21	6.00	10.70	30.8

The AVCO data presented in the second column is a summary of twenty-minute log-amplitude variance measurements. The theoretical zenith angle dependence of $(\sec \theta)^{11/6}$ was not removed by AVCO because "all data was collected on starts at low zenith angle (typically 10-20°, 30° maximum) and this effect should not be large." Our results are based on zenith propagation, i.e., $\theta = 0$.

No attempt was made by AVCO to compare their optical scintillation results to the corresponding results obtained from the C_n^2 profile that was measured on the dates of the experiments. Furthermore, an analysis of the variance of the σ_f^2 was not performed, although enough data was recorded so that this information can be readily obtained.

Examination of Table 1 reveals that our calculated values of σ_f^2 are in good agreement with AVCO's measured values; in two cases the calculated values is in the experimental range, while in the third case it is about 25% high. In view of the fact that some zenith angle biasing may be present [$(\sec 30)^{11/6} = 1.3$] and the experiments were performed over several hours on each night, we feel that the results obtained here are encouraging enough to warrant further comparisons as more data is made available. We are in the process of doing this.

IV. PHASE COHERENCE STATISTICS

Here we relate the coherence diameter r_0 to the rms wind speed V and compare these results to the experimental values obtained by AVCO during Nov. 17, 18 and 21, 1975.

The mutual coherence function can be written as

$$M(r) = \exp \left[-3.44 \left(\frac{r}{r_0} \right)^{5/3} \right] \quad (18)$$

where the coherence diameter r_0 is given by

$$r_0 \approx \left[\frac{3.44}{1.45 k_v^2 \sec \theta \int_{h_1}^{\infty} C_n^2(h) dh} \right]^{3/5} \quad (19)$$

Examination of Eq. (19) reveals that in contrast to the case of scintillation, the coherence diameter depends both on low and high altitude turbulence (the weighting factor in the integrand of Eq. (19) being unity in the present case).

AVCO's measured turbulence profiles averaged over the complete data runs taken on 17, 18, and 21 Nov. 1975 are shown in Fig. 2. The lowest height (15 m) data points were obtained from the ground-based

microthermal sensors. Data from 37 m to 2.5 km were provided by NOAA from a reduction of their (nighttime) airborne microthermal data. The line segments from 1 km to 24 km were derived from Star Sensor data and represent the approximate width of the weighting functions used in the data reduction. The horizontal scale is in height above the observatory which is at an altitude of approximately 10,000 ft. The tropopause height was determined from rawinsonde temperature profiles obtained from the two Hawaiian Weather Bureau stations.

For comparison, the turbulence profile used for our calculation, i. e., Eqs. (5) and (6) are given by the dashed curve in Fig. 2, along with the value of V for the date in question.

We have computed r_0 based on the assumption that the plane of the receiver is 10 m above local ground and the use of Eq. (5) for high altitude turbulence and Eq. (6) for turbulence near the ground. The numerical results for $\theta = 0$ are plotted in Fig. 3 as a function of V (upper curve). Also, we have computed the values of r_0 based on Eq. (5) above and these results are also shown in Fig. 3 (lower curve). Examination of Fig. 3 reveals that for $5 \leq V \leq 15$ m/sec the values of r_0 obtained by including turbulence near the ground are within a factor of two to that obtained otherwise. For larger values of V , the corresponding values of r_0 approach one another asymptotically. This is expected since for large values of V the main contribution to r_0 results from turbulence values at high altitudes.

The use of Eq. (6) for low altitude turbulence values may not be representative of the conditions above the AMOS site as it was developed from measurements over different times of the year. Thus, it should represent, in our opinion somewhat of a worst case estimate of turbulence above local ground and is used here as such. The values of r_0 obtained by employing Eq. (6) represents a worst case estimate at low values of V (≤ 15 m/sec), while the values obtained for large values of V should be looked upon with less uncertainty.

In summary, for small values of V (i. e., low integrated turbulence strength) the predicted values of r_0 are to be regarded as a lower limit with the real value being as much as a factor of two larger. On the other hand, for large values of V (i. e., high integrated turbulence strength) the corresponding uncertainty in the predicted value of r_0 is much smaller than a factor of two; that is, the confidence by which we predict r_0 is larger for strong turbulence conditions than it is for weak turbulence conditions.

AVCO's average measured values of r_0 at $0.633 \mu\text{m}$ and $\theta = 0^\circ$ and the corresponding values obtained from the measured turbulence profiles are presented in Table 2 along with the results of our calculations.

TABLE 2
 r_0 Data Comparison, $\lambda = 0.633 \mu\text{m}$

Date	AVCO Seeing Monitor, r_0 (cm)		AVCO, From Measured Turbulence Profile, r_0 (cm)	Aerospace	
	Range	Average		r_0 (cm)	V (m/sec)
Nov 17	9.3 - 13.5	10.4	25.7	17.1	21.3
Nov 18	13.3 - 18.2	15.4	24.9	17.4	20.5
Nov 21	9.4 - 14.4	11.8	16.6	14.4	30.8

The corresponding value of r_0 at $\lambda = 0.5 \mu\text{m}$ are obtained from those given in the table by multiplication by $(0.5/0.633)^{6/5} \approx 0.75$. Examination of Table 2 reveals that our values of r_0 are in fair agreement with the experimental value. On the other hand, AVCO's calculated values based on the measured turbulence profile are larger than the measured value by a factor of 1.5-2.

Note that for the three days considered the measured average values of r_0 are somewhat less than the corresponding calculated values. At this point it is not clear why this should be the case, although it may just be an artifact. Although the airborne microthermal probe measurement of C_n^2 between 37 m and 2 km above the AMOS site were performed at night, the airplane was not directly above the mountain top, but instead was slightly off to one side. This suggests that the lower altitude measured values of C_n^2 the AVCO calculated value of r_0 is about a factor of two too large. We wait with anticipation for reliable low altitude C_n^2 profile measurements above the AMOS site (i. e., from the NOAA acoustic sounder). On the other hand, we arbitrarily used a model of low altitude turbulence that, strictly speaking, applies (if at all) to conditions over level ground near sea level. For the value of V that applied, the contribution to r_0 from turbulence in the first three kilometers above the site is about equal to the corresponding contribution from turbulence in the tropopause (See Fig. 2). On this basis we would expect that an r_0 calculated with such a turbulence profile would result in too small a value. Since our calculated values of r_0 are a little on the high side, we are left in a quandary. Rather than speculate we defer further discussions on this point until more data is analyzed.

Based on our results obtained for the three dates in question, we are encouraged to make further comparisons with more data.

In conclusion we are cautiously optimistic about the use of the model of C_n^2 used here to obtain phase and log-amplitude statistics. More data comparison is clearly needed until the general use of the model can be ascertained. In particular, it is very desirable to obtain wind speed data that pertain to the time and location of the experiment. We have been in contact with P. Zieske, AVCO/Maul, and he is in the process of seeing what can be done for the experiments that will be performed at AMOS this spring and summer.

References

1. BUFTON, J. L., 1973, "Comparison of Vertical Turbulence Structure with Stellar Observations," Appl. Opt. 12, 1785.
2. HUFNAGEL, R. E., July 9-11, 1974, "Variations of Atmospheric Turbulence," Paper WAI appearing in the Digest of Technical Papers, Topical Meeting on Optical Propagation Through Turbulence, Univ. Colorado, Boulder, CO.
3. KOPROV, V. R. and TSVANG, L. R., 1966, "Characteristics of Very Small Scale Turbulence in a Stratified Boundary Layer," Atmos. and Oceanic Phys. 22, 1142.
4. LUTOMIRSKI, R. F., HUSCHKE, R. E., MEECHAM, W. C., and YURA, H. T., June 1973, "Degradation of Laser Systems by Atmospheric Turbulence," Rand Report No. R-1171-ARPA/RC.

- 42-0
5. MILLER, M., ZIESKE, P., AND HANSON, D., March 1976, "Characterization of Atmospheric Turbulence," SPIE Symposium on Imaging Through the Atmosphere, Paper 7505, Reston, VA.
 6. TATARSKII, V. I., 1961, "Wave Propagation in a Turbulent Medium," McGraw Hill Book Co., New York.

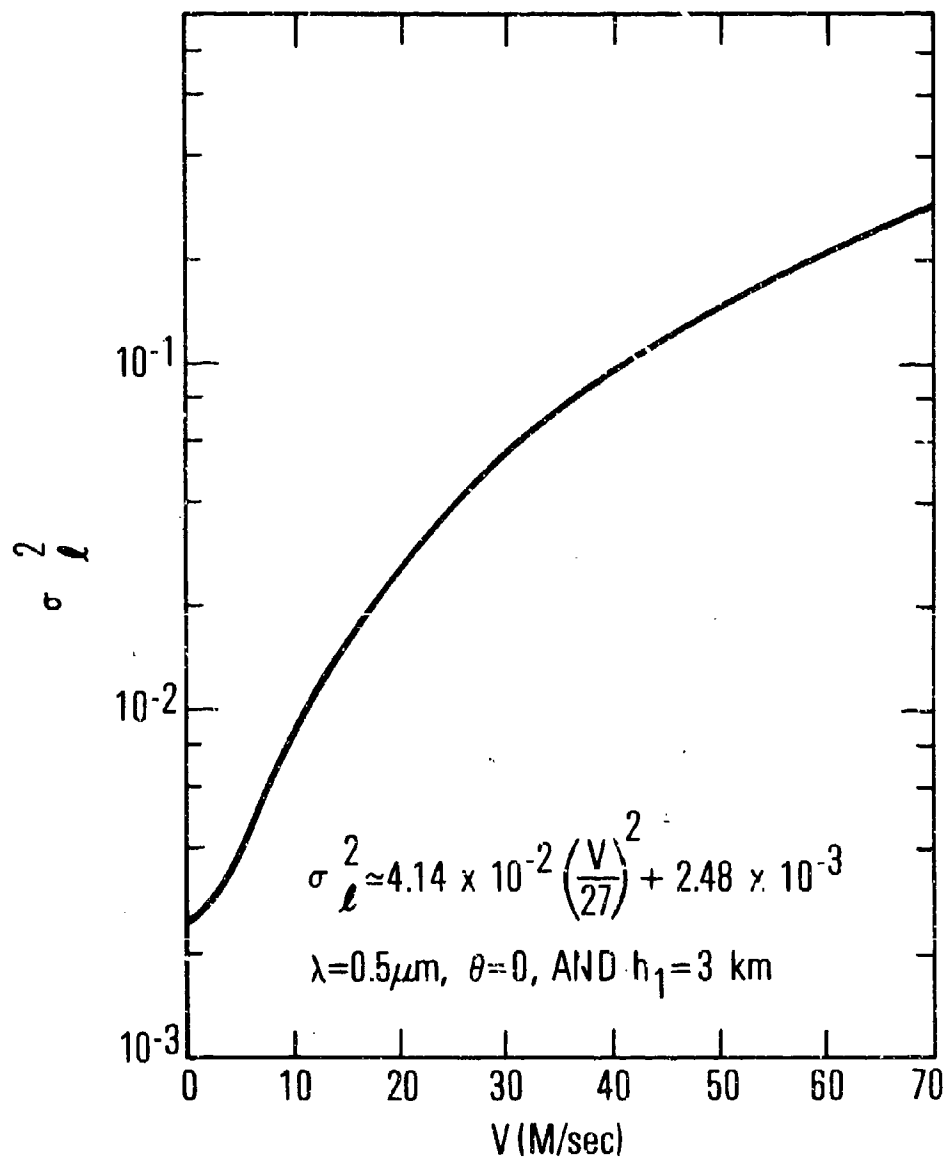


Fig. 1 Calculated value of the log-amplitude variance at a point as a function of the rms wind speed.

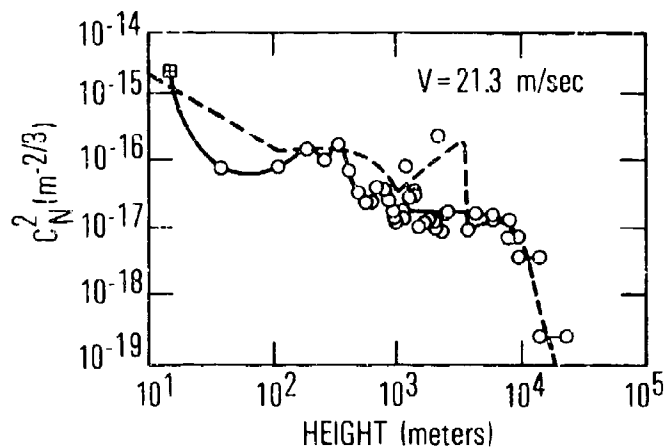


Fig. 2a Turbulence Profile vs. Height Above the Observatory - 17 November 1975. Ground Based Microthermal Data = \bullet ; Airborne Microthermal Data = $+$; Star Sensor Data = \circ . Estimated tropopause height of 11-55.5 km. The dotted curve is the sum of Eqs. (5) and (6) for the value of V indicated.

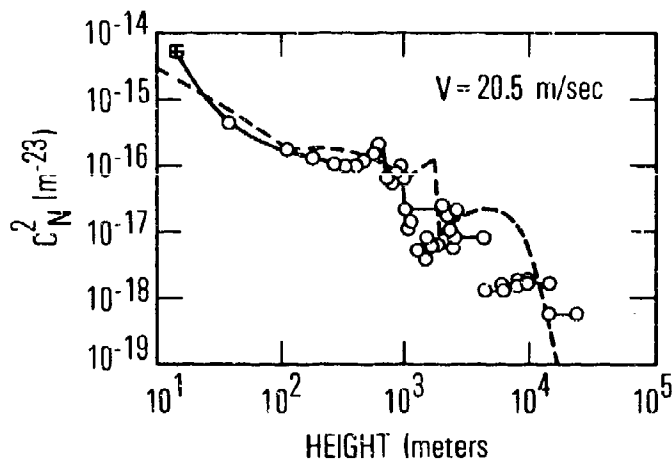


Fig. 2b Same as Figure 2b for 18 November 1975. Estimated tropopause height of 9-15.5 km.

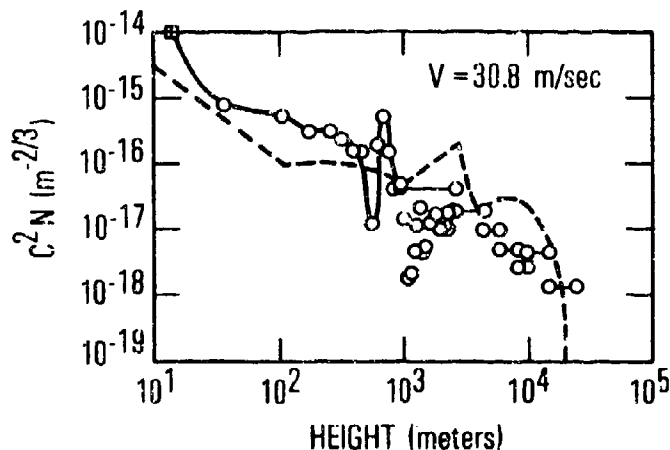


Fig. 2c Same as Figure 2b for 21 November 1975. Estimated tropopause height of 9-15.5 km.

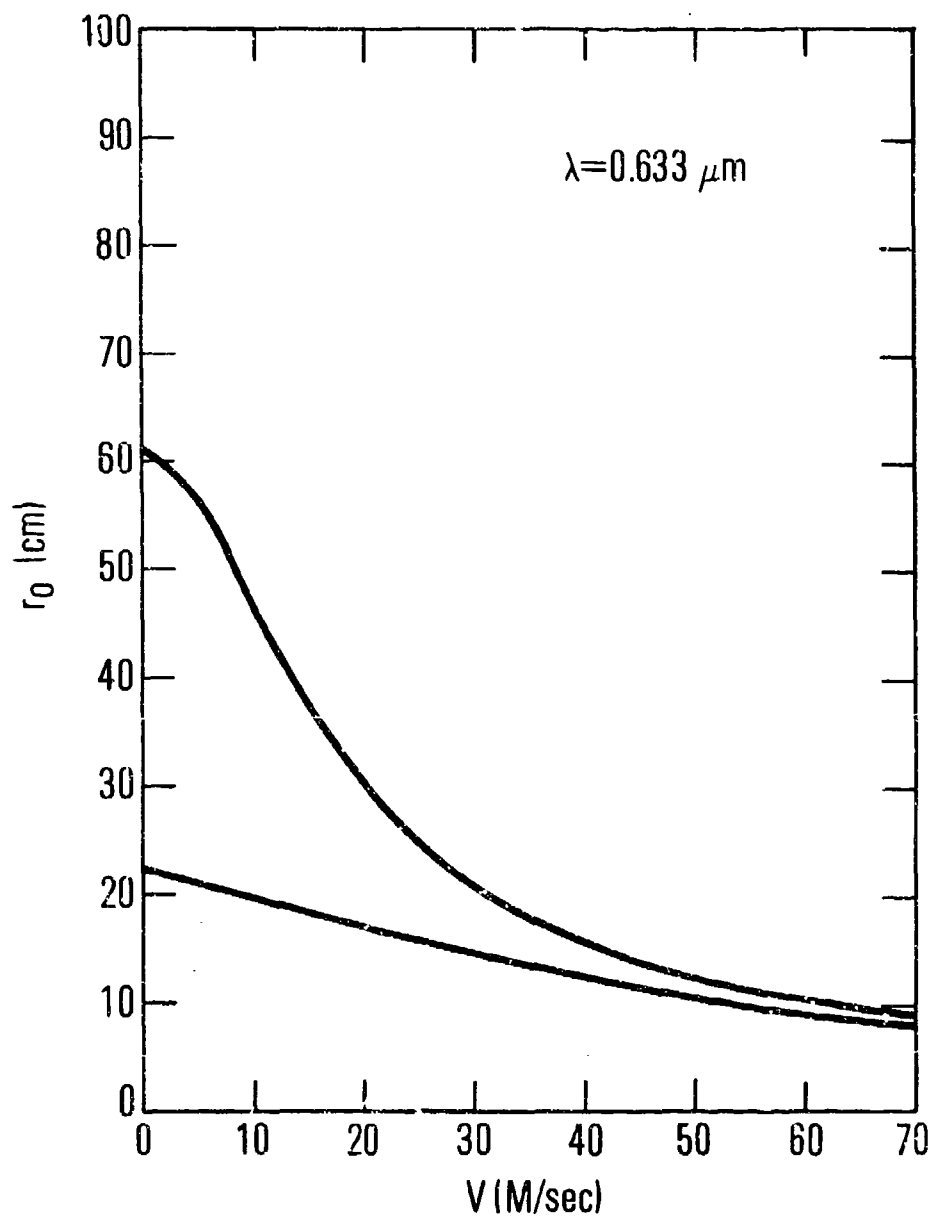


Fig. 3 The phase coherence diameter $\lambda = 0.633 \mu\text{m}$ as function of rms wind speed. The upper curve is based on Hufnagel's model for high altitude turbulence while the lower curve includes the contribution from low altitude turbulence as given by Eq. (16).

DISCUSSION

R.A. McClatchey, US

Why is it that C_n^2 -Profile does *not* depend on deviation of wind speed from some uniform mean speed, and on the vertical stability of the atmosphere (e.g., temperature gradients)?

Author's Reply

As discussed by Hufnagel in 1974 (Ref. 1), the model is purely empirical and it was found that about 70% of the optical data he looked at correlated well with the rms wind speed. Recent work of T. VanZandt and K. Gage (of NOAA) on the vertical profile of C_n^2 in the microwave region is based on a model of vertical stability and shows a somewhat different profile which seems to compare well with radar backscatter measurements of C_n^2 .

REAL TIME SIMULATION OF TURBULENT ATMOSPHERIC PROPAGATION

I.D. Lyon,
British Aerospace Dynamics Group,
Bristol - Stevenage Division,
Stevenage, Herts. SG1 2DA
England.

SUMMARY

Simulation of turbulent atmospheric propagation during the development of a tracker can reduce the amount of field trials necessary. A particular beacon/tracker system is described followed by the simulator requirement and its realisation. Finally the utilisation of the simulator is described.

INTRODUCTION

In many defence applications there is a need to track the position of one's own vehicles. These vehicles can be remotely piloted vehicles, guided weapons or similar. This paper describes an optical tracking system using a vehicle carried xenon-arc pulsed beacon operating in the near infra-red. To avoid extensive field trials during hardware development, a simulator was built to give statistically repeatable effects of the atmospheric propagation, turbulence, and beacon motion.

SYSTEM

The optical tracking system comprises a vehicle carried xenon-arc beacon, pulse modulated at a precise frequency and a static, near infra-red, four quadrant (8 element) tracker. Analog voltage signals are provided by the tracker which are, within limits, proportional to the off-axis cartesian coordinates of the beacon. These voltages would normally be used to servo drive the tracker to maintain the beacon image on the optical axis. In order to maintain the signal to noise ratio as the beacon range increases, the tracker optics are varied to increase the beacon to background ratio at the detector. Automatic gain control stabilises the gain about a reference level which can be externally adjusted to follow the field of view size.

Beacon

Figure 1 shows the xenon-arc beacon which is fairly conventional. Pulse energy is held constant to within 10% for periods long compared with the turbulence. Longer term drift is inevitable as the flashtube lifetime is used up. In order to achieve a compact beacon, a new flashtube was developed which fits axially into a complex solid of revolution reflector. The reflector is required to give a substantially constant output over a large cone angle.

Tracker

Figure 2 shows the optical tracker. To reduce the noise in the processing system as the beacon range increases, the detector field of view is reduced. The first reduction is made by the zoom lens. Further reduction is made by an adjustable field stop in the focal plane of the telescope. Also at the focal plane is a fibre optic diffuser. Vignetting is minimised to keep the tracker transfer function as linear as possible over the angles of interest.

The static split silicon detector quadrant differences are normalised as usual in the signal processing to provide the error output signals. Channel width effects, giving dead areas between quadrants are minimised by irradiating a relatively large detector area via the fibre optic diffuser, which provides a uniform circular spot. To maintain the transfer function slope, the spot size is varied by moving the detector relative to the diffuser as a function of field stop aperture. The diffuser also gives the important advantage of minimising atmospheric scintillation, so that variations in intensity distribution across the lens aperture do not affect the tracker's output.

Both inner and outer quadrant signals are amplified until the beacon spot, decreasing with range, covers only the inner quadrants. Then the outer quadrants are disconnected and only the inner quadrant signals are amplified. The dark current noise of the non-irradiated outer quadrants is then eliminated. The detector cell geometry is also shown in Figure 2. Insulating channels divide the cell into quadrant elements. The silicon photodetector can be thermo-electrically cooled to keep it below +40 degC in hot environments.

Tracker Electronics

Figure 2 illustrates the general signal flow through the tracker. The servos which adjust the telescope zoom, focal plane stop, and detector are not shown. Four head amplifiers are provided, one for each quadrant pair of inner plus outer. Selection of either inner or inner plus outer is made externally, again as a function of range. Impedances of the amplifiers are simultaneously changed to match the detector areas and fields of view.

Following the pre-amplifiers are the sum and difference amplifiers giving the raw X and Y errors. The sum signal is peak detected in each pulse cycle. An adjustable fraction of the difference between successive peaks is fed back to alter the system gain at a proportional rate. Excessive automatic gain changes due to atmospheric turbulence modulation are avoided. Part of the simulation function is to optimise the automatic gain function in the laboratory without prolonged field trials.

'Integration and hold' maintains the beacon signals between pulses. Finally the difference signals are divided by the sum signal to normalise them.

Figure 3 is a photograph of a tracker development model with laboratory packaged electronics beside it. Figure 4 shows the inside of the tracker. Fixed focal length lenses were used at this stage.

SIMULATOR REQUIREMENT

The simulator is designed to be compact, portable and self-contained. Its major capabilities are:-

- * beacon range variations:
From 100 m to 4 km.

There is no requirement to vary beacon image size with range. Only the slope of the tracker transfer function is affected, which does not matter since the tracker output signals are monitored and not fed back at this level of testing.

- * beacon movement:

A beacon can move in a circle about the tracker optical axis, providing sine wave of variable amplitude and frequency in the tracker X and Y channels. This function does not vary with range.

- * variation in meteorological visibility:

Visibilities of infinity, 10 km, 8 km, 4 km, 2 km and 1.2 km using 5% definition.

- * effect of atmospheric turbulence:

Time varying amplitudes of the simulated beacon pulses seen by the tracker to have a log-normal distribution such that 95% of the pulse amplitudes lie within $\pm 1:1$ (= no turbulence), or $\pm 1.414:1$, or ± 2.236 or $\pm 5:1$ of the mean value, as required (i.e. from $1/5$ mean to $5x$ mean).

- * background irradiance:

A background irradiance on the tracker focal plane of 0 to 24 Wm^{-2} in the band $0.75 \mu\text{m}$ to $1.1 \mu\text{m}$.

ATMOSPHERIC MODEL

The atmospheric model was chosen for its simplicity to instrument, yet including enough relevant factors to realistically test the tracker. Vehicle altitudes are predominately below 30 m in the current application and therefore the sightline is essentially horizontal through the atmosphere.

The mean power received by the tracker from the beacon is given by:

$$P = I \cdot \frac{\pi D^2}{4} \cdot \frac{e^{-\sigma_v R}}{R^2} \cdot \Delta \lambda \cdot Z$$

where I is the mean radiant intensity over the spectral band

D is the tracker objective lens diameter

R is the beacon range

σ_v is the mean atmospheric extinction coefficient
($\approx 3 + \text{meteorological visibility}$)

$\Delta \lambda$ is the spectral band

Z is the normalised fading parameter due to atmospheric turbulence which is a lognormal random variable with probability density function:

$$p(Z) = \frac{1}{\sqrt{2\pi} \sigma Z} \cdot \exp \left\{ - \frac{\left[\ln(Z) + \frac{\sigma^2}{2} \right]^2}{2 \sigma^2} \right\}$$

where σ^2 is the normalised log-intensity variance.

Pulse to pulse correlation is provided by low pass filtering of the white noise generator from which the lognormal function Z is derived. Single order filters with 3 dB points 1.95 kHz, 376 Hz and 62.4 Hz are selectable. The filters simulate a range of closed loop lags in the overall tracking system.

DESCRIPTION OF SIMULATOR

Optics

The basic optical scheme is shown in Figure 5.

Light emitting diodes (LED) are used to simulate the beacon and a tungsten halogen lamp the sky background.

Due to the large variation in beacon brightness required, two LED's are provided. The short range LED changes over to the long range LED at approximately 1.5 km. The difference in optical transmission between the paths is about 130. Although the exact changeover distance is not critical, the brightness and optical superposition are important. The diodes are 0.5 mm square with a substantially uniform intensity in the forward hemisphere.

The LED rays reach the tracker via beam splitter 2 and mirror 2. Mirror 2, which is flat, is mounted on a pair of circular wedges. Relative preadjustment of the wedges tilts the mirror with respect to its mounting shaft. This shaft is driven by a variable speed motor, causing the beacon image to circle the tracker sightline. One degree movement between the wedges changes the mirror inclination by 1 mrad.

The tungsten halogen lamp is driven from a variable constant current source to provide the sky background. This illumination reaches the tracker via a diffuser and lens 3.

Meteorological visibility effects are generated electronically as described below. Figure 6 is a photograph of the complete simulator with a 30 cm ruler alongside.

Electronics

A simplified electronics block diagram is illustrated in Figure 7. For simplicity the sky background electronics are omitted.

For a stable simulator, needing infrequent calibration, great care was taken to ensure low thermal and ageing drifts. In consequence, the circuits are complex although their function is simple. On the top line the pulse clock and generator, which is crystal controlled, is followed by a shaper which simulates the xenon-arc beacon response. The shaped pulse is then amplitude modulated in proportion to the control signal Z ($\exp(-\sigma R)/R^2$). After the LED driver, a changeover relay operating at 1.5 km directs the pulse current to either the long or short range light emitting diode.

The range signal for the purposes of simulation is generated open loop, by a ramp voltage. Range changeover at 1.5 km is also provided. As well as switching the LED's, the changeover also selects pre-set adjustments in gains so that the intensity perceived by the tracker does not alter at changeover.

Following the upper line from the Range Generator, the first block is a switched attenuator simulating the various meteorological visibilities required. The resulting R is exponentiated by the $e^{-\sigma R}$ block which is based on a diode voltage-current characteristic. Gain adjustment for range changeover matching follows.

A divider produces the inverse square law from a squarer (V_{in}^2) followed by another range changeover gain adjustment. The divider output: $e^{-\sigma R}/R^2$ is then multiplied by the turbulence fading factor Z which is generated as follows. A white noise generator has an output flat from below 25 Hz to 37 kHz dropping at 6 dB/octave thereafter. The band pass filters are arranged to all have the same r.m.s. output. Selection of a particular filter gives choice of pulse to pulse correlation as described in the atmospheric model above. The filtered noise is amplified to different levels such that the final turbulence fading factor Z has 95% of pulse amplitudes between extremes which are harmonically symmetrical about the mean. The extremes selectable are $\pm 1:1$ (= no turbulence), $\pm 1.414:1$, $\pm 2.236:1$, and $\pm 5:1$. Thus $\pm 5:1$ gives max/min amplitudes of 25.

Another $e^{-V_{in}}$ generator shapes the filtered noise distribution to lognormal. Finally the mean level change caused by the $e^{-V_{in}}$ generator is removed by the turbulence selector, giving the normalised turbulence fading factor Z .

Z and $e^{-\sigma R}/R^2$ derived above, are multiplied together and via another range changeover gain adjustment, and applied to the pulse amplitude modulator, which has greater than 1000:1 dynamic range.

UTILISATION OF THE SIMULATOR

Worsening range, visibility and turbulence combine to degrade the performance of the tracker. A convenient parameter for assessing the performance is the output noise power spectral density of the tracker error outputs.

The error outputs are measured by a true r.m.s. voltmeter with a 1.6 s time constant, via a 20 Hz low pass filter. A 5th order Butterworth filter was chosen to give a well defined cut-off. Each reading in volts r.m.s. is the average of 10 samples. The readings are then converted from millivolts to milliradians by the calibrated transfer function

slope of the tracker. To compare these results with theoretical figures, the r.m.s. errors are converted to power spectral density by squaring and dividing by the bandwidth in rad.s^{-1} .

The units are then $\text{radians}^2/\text{radian/sec.}$ as previously described, the constant simulated beacon image size keeps the transfer function slope constant.

Comparison of practical and theoretical results for a particular tracker showed agreement within ± 4.4 dB over a theoretical range of 20,000:1 in power.

Due to the difficulty of theoretically predicting the expected performance of the tracker in turbulence conditions, correlation of practical and theoretical results is not yet established. However, one of the purposes of the simulator is to overcome this difficulty. Field trials results were analysed to establish the extreme range of correlation times and turbulence variations to be included in the simulator.

Simulation of beacon circular motion at different amplitudes and frequencies enables the tracker's transfer function to be quickly established. This facility is particularly useful for mapping the edge of the vignetting, where the transfer function slope becomes non-linear.

ACKNOWLEDGEMENTS

The work was carried out by members of the Electro-Optical Department of British Aerospace Dynamics Group at Stevenage, England, to whom thanks are due for the information presented in this paper.

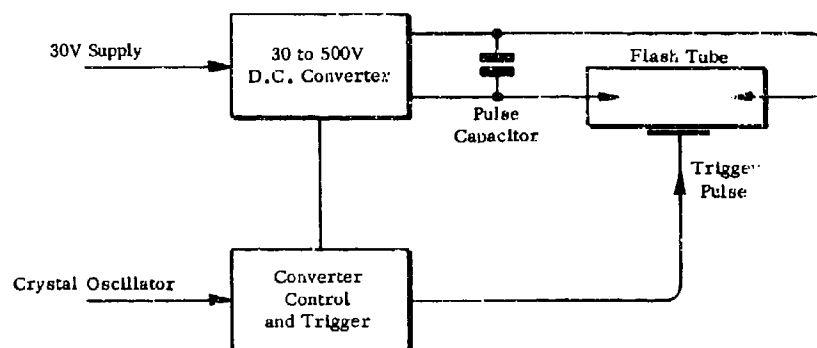


Fig.1 Xenon arc beacon

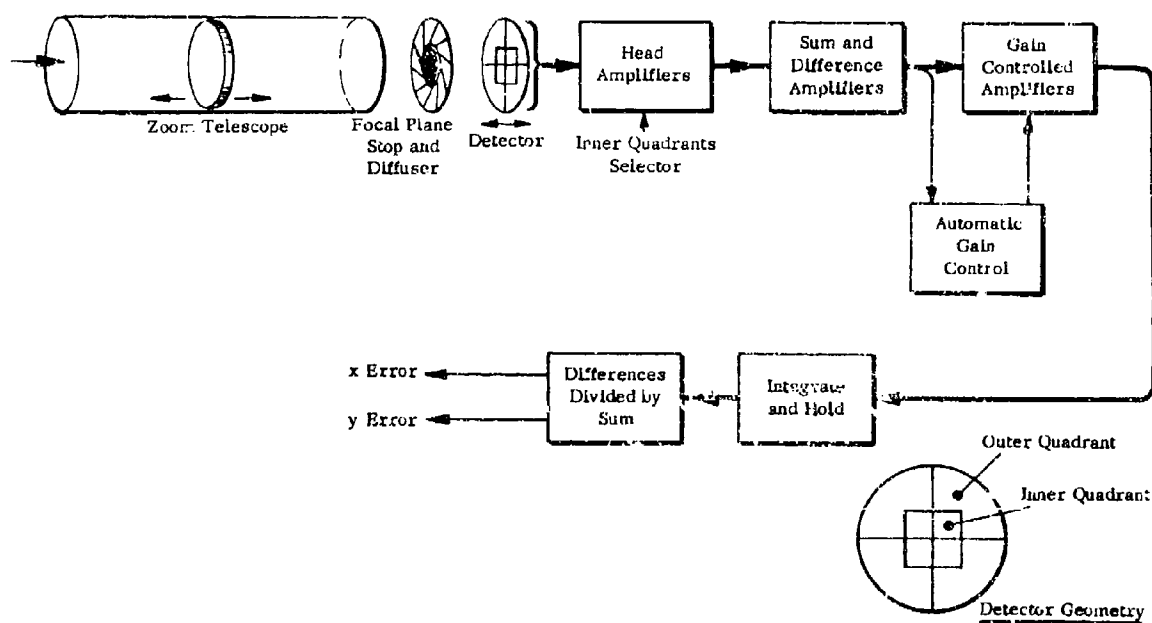


Fig.2 Optical tracker schematic

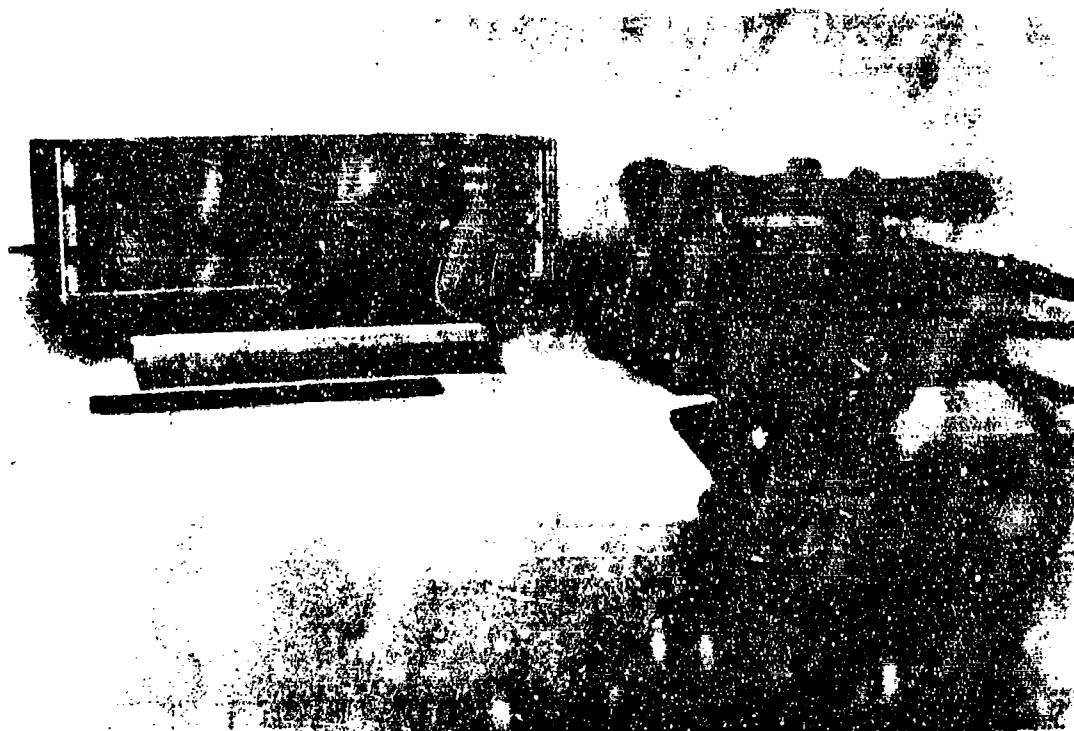


Fig.3 Tracker and electronics

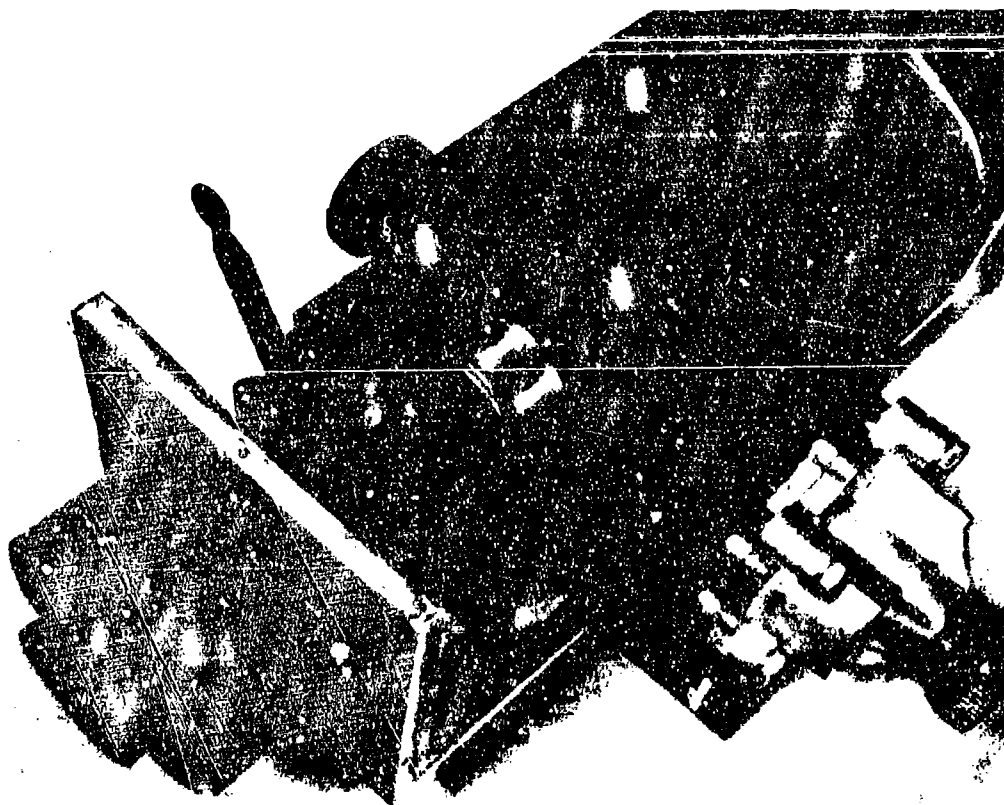


Fig.4 Tracker close-up

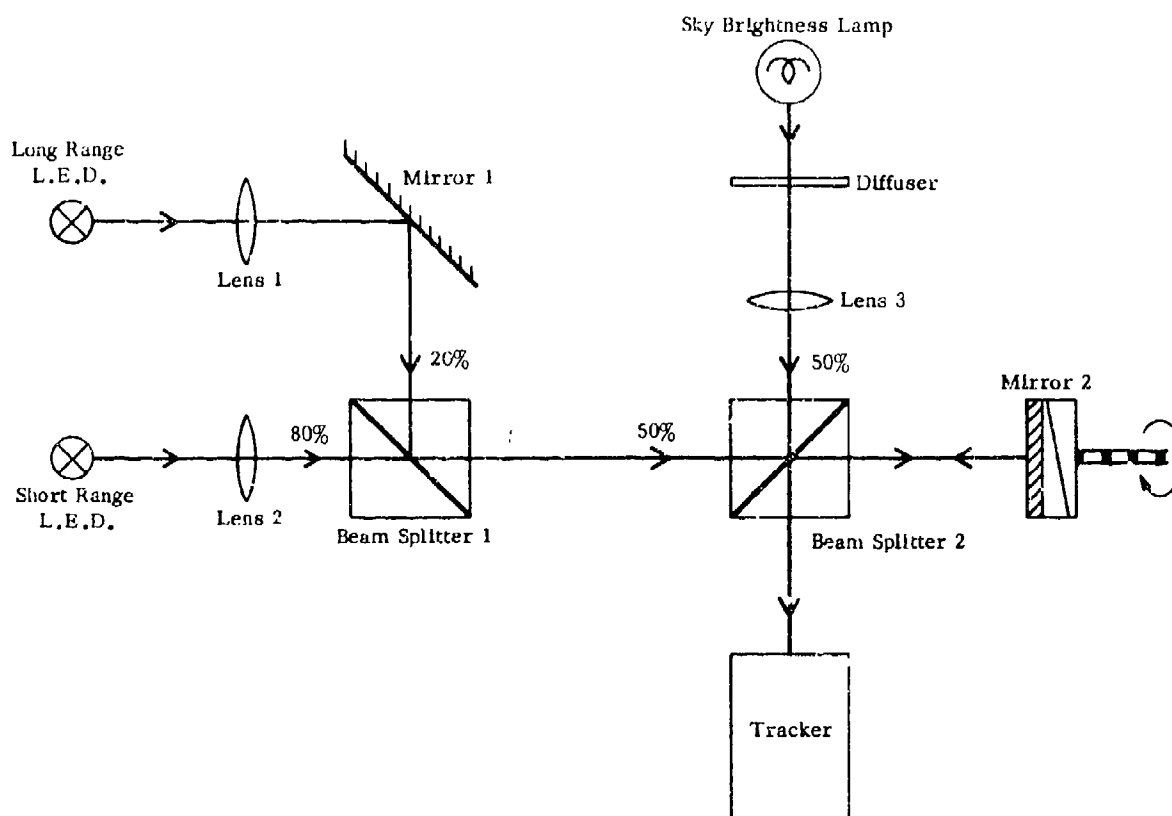


Fig.5 Simulator optics



Fig.6 Simulator

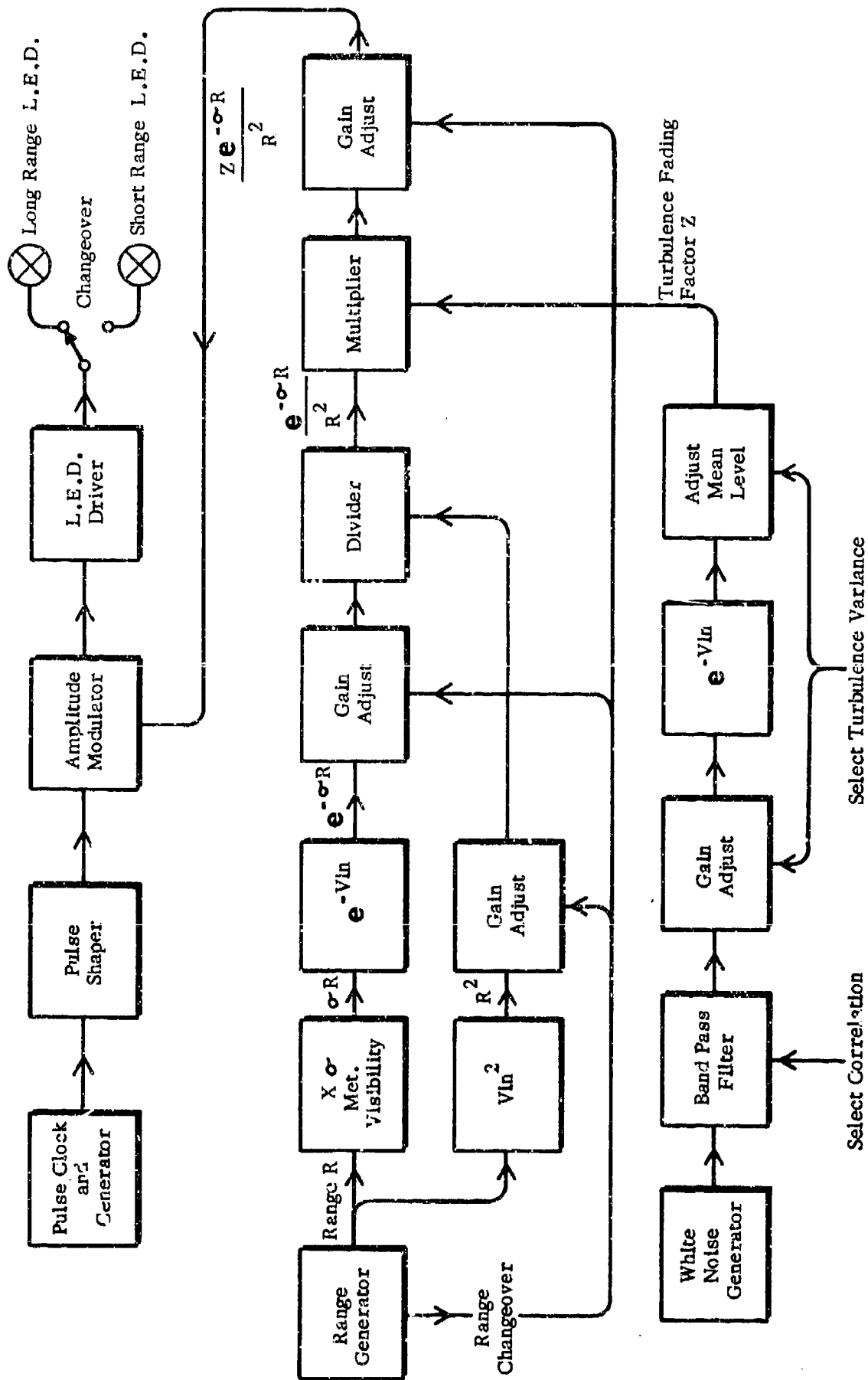


Fig. 7 Simulator electronics

DISCUSSION

M. Tavis, US

Are clouds taken into account in the background simulation?

Author's Reply

The tracker has a diffuser in front of the detector which averages the sky background across the aperture. For simulation it is sufficient to provide a diffused, substantially even, background.

TEMPERATURE TURBULENCE MEASUREMENTS AT AMOS

Donald W. Hanson
Rome Air Development Center
Griffiss AFB, New York 13441

SUMMARY

Atmospheric temperature turbulence is created by random, small scale, high frequency fluctuations in air. This turbulence degrades the performance of optical systems which image through the atmosphere. Extensive theory has been developed which relates the propagation of light through the atmosphere to the temperature turbulence. Measurements of the temperature turbulence above Mount Haleakala on the island of Maui, Hawaii have been made. The emphasis of these measurements has been to measure vertical profiles of temperature turbulence, however the integrated value of the profiles has also been measured. The measurement data has been compared with existing models.

1. INTRODUCTION

Atmospheric temperature turbulence is created by random, small scale, high frequency temperature fluctuations in air. This temperature turbulence degrades the performance of optical systems which image through the atmosphere. Extensive theory has been developed which relates the propagation of light through the atmosphere to the temperature turbulence.

1.1 Temperature Turbulence

Temperature turbulence can be described by its spatial structure function, $D_T(r)$, as shown below:

$$D_T(r) = \langle (T(\vec{r}_1) - T(\vec{r}_2))^2 \rangle$$

where $T(\vec{r}_1)$ is the temperature at \vec{r}_1 , $T(\vec{r}_2)$ is the temperature at \vec{r}_2 , $r = |\vec{r}_1 - \vec{r}_2|$, and the brackets $\langle \rangle$ indicate an ensemble average. It is known that, for certain conditions

$$D_T(r) = C_T^2 r^{2/3}$$

where C_T^2 is called the temperature structure parameter. C_T thus provides a measure of the level of the temperature turbulence.

1.2 Optical Propagation

The temperature turbulence described above creates changes in the refractive index of air. The spatial structure function for changes in the index of refraction of air, D_n , is directly proportional to the temperature turbulence structure function, thus

$$D_n(r) = C_n^2 r^{2/3}$$

where C_n^2 is called the refractive index structure parameter and has units of $m^{-2/3}$. The relationship between C_n^2 and C_T^2 at a wavelength of light of $0.5\mu m$ is given below:

$$C_n^2 = \left[79.2 \times 10^{-6} \frac{p}{T^2} \right]^2 C_T^2$$

where p is pressure in mbar and T is temperature in $^{\circ}K$. C_n^2 thus provides a measure of the degrading effect that temperature turbulence will have on light propagating through the atmosphere. As C_n^2 increases the degrading effects on light beams propagating through the atmosphere increases. A basic parameter, r_0 , can be used to determine the performance of optical imaging systems when viewing through the atmosphere (Fried, D.L., 1966). The parameter r_0 , in units of meters, is related to C_n^2 as shown below.

$$r_0 = \left[.423 \left(\frac{2\pi}{\lambda} \right)^2 \int_0^L C_n^2(z) dz \right]^{-3/5}$$

where λ is the wavelength of light, L is the length of the optical path through the atmosphere, and $C_n^2(z)$ is the value of C_n^2 at each point along that path. The significance of r_0 is that it can be thought of as the diffraction limited aperture of the atmosphere. For telescopes with diameters smaller than r_0 , imaging performance which is directly related to telescope quality can be expected. For telescopes with diameters greater than r_0 imaging performance limited by an effective aperture of the size of r_0 can be expected.

2. Measurement Program

Measurement of the atmospheric turbulence above Mount Haleakala on the island of Maui, Hawaii have been conducted over the past several years. Emphasis has been placed on measuring vertical temperature turbulence and r_0 . Both measurements are made using ground based sensors (Miller, M.G. et al, 1976).

2.1 Measurement of Profiles

The turbulence profiles were measured with an instrument called a Stellar Scintillometer. The instrument was made by the Wave Propagation Laboratory of the National Oceanic and Atmospheric Administration of the U.S. Basically the instrument measures stellar scintillation as a function of spatial frequency to estimate the strength and location of the turbulence causing the scintillation. The instrument provides data from 2.5km up through the atmosphere. A detailed description of the instrument can be found in Ochs, G.R. et al, 1977.

2.2 Measurement of r_0

The parameter r_0 was measured using an instrument called the Seeing Monitor. This instrument was built by the Hughes Research Laboratories. This instrument measures the atmospheric Modulation Transfer Function. From this data an estimate of r_0 can be made. For a complete description of this instrument see Giuliano, C.R. et al, 1976.

3. Turbulence Models

3.1 Profile Models

Based on empirical data Hufnagel has developed a model for temperature turbulence as shown below (Hufnagel, R.E., 1974).

$$C_n^2 = \left[(2.2 \times 10^{-53}) h^{10} (W/27)^2 \exp(-h/1000) + 10^{-16} \exp(-h/1500) \right] \exp r(h,t) m^{-2/3}$$

Where:

h = altitude above sea level in meters

$$W = \frac{1}{15 \times 10^3} \left[\int_{5 \times 10^3}^{20 \times 10^3} V^2(h) dh \right]^{1/2}$$

$V(h)$ = wind speed at altitude h m/sec

The parameter $r(h,t)$ is a zero mean Gaussian random variable with variance 2. Complete details on the covariance function of $r(h,t)$ are given in the Hufnagel reference. The mean value of C_n^2 predicted by the model is given below:

$$C_n^2 = (6.0 \times 10^{-53}) h^{10} (W/27)^2 \exp(-h/1000) + 2.7 \times 10^{-16} \exp(-h/1500)$$

Since the probability density function associated with $\exp[r(h,t)]$ is skewed the mean value is not necessarily a good description of the density function. The median for C_n^2 is given below:

$$C_n^2 = 2.2 \times 10^{-53} h^{10} (W/27)^2 \exp(-h/1000) + 10^{-16} \exp(-h/1500)$$

3.2 r_0 Model

Based on empirical data Fried and Mevers have proposed the following model for the median of r_0 (Fried, D.L. and Mevers, G.E., 1974).

$$r_0 = .114 (\lambda/5.5 \times 10^{-7})^{3/5} (\sec \theta)^{-3/5}$$

where r_0 is log-normally distributed, θ is zenith angle, and one standard deviation factor is x1.36.

4. Results & Analysis

4.1 Profile Data

Measured temperature turbulence profiles are shown in Figures 1-4. These profiles are an average profile for the entire evening. Also shown in the figures are the mean and median values predicted by a slightly modified version of Hufnagel's model. Rawinsonde data, from launches made at Hilo, Hawaii, were used to calculate W in the Hufnagel model. The profile data was typically taken within four hours of the rawinsonde data. The rawinsonde data was provided by USAF Environmental Technical Applications Center (ETAC). The model was found to provide a better fit to the measured data when the altitude, h , was taken to be the height above Mount Haleakala (3,000m). From previous data better agreement between the Hufnagel model and the measured profile data was expected. However an error has been discovered in the earlier data which negates that agreement.

4.2 r_0 Data

The parameter r_0 has been measured at various times throughout the year. Data for the period 11 November 1975 to 13 July 1976 is shown in figure 5 (Miller, M.G. and Zieske, P.L. 1977). The solid line is a least square fit to a Gaussian cumulative density curve. This data has been replotted as shown in figure 6 to see how well the data might also conform to a log-normal distribution. The correlation coefficients for the fit of the regression to the data is .984 for the normal distribution and .985 for the log-normal distribution. The cumulative probability density thus conforms to a log-normal distribution as well as it does to a normal distribution. More r_0 data has been collected since 13 July 1976. In total 670 measurements of r_0 have been made. The range of measured r_0 values has been from 3.6 to 17.8cm with a mean value for the 670 data points of 9.8cm, at $\lambda=5.0 \times 10^{-7}$ m. The Fried and Mevers model predicts a median value of $r_0=10.8$ cm. The cumulative probability density function of the data taken since 13 July 1976 has not yet been analyzed.

5. Conclusions

More work needs to be done before a model for the temperature turbulence profile above Mt. Haleakala can be developed. The r_0 data is in reasonable agreement with the Fried and Mevers model.

REFERENCES

- Fried, D.L., 1966, "Optical Resolution Through a Randomly Inhomogeneous Medium for Very Long and Very Short Exposures", J. Opt. Soc. Am. 56,1372.
- Fried, D.L. and Mevers, G.E., 1974, "Evaluation of r_0 for Propagation Down Through the Atmosphere", Applied Optics Vol. 13, No. 11, 2620.
- Giuliano, C.R., et al., 1976, "Space Object Imaging", RADC-TR-76-54.
- Hufnagel, R.E., 1974, "Variations of Atmospheric Turbulence", USA Topical Meeting on Optical Propagation Through the Atmosphere, paper WA1.
- Miller, M.G., Zieske, P.L., and Dryden, G., 1976, "Turbulence Characterization and Control", RADC-TR-76-189.
- Miller, M.G., Zieske, P.L., 1977, "Turbulence Environment Characterization", RADC-TR-77-70.
- Ochs, G.R., Wang, T., and Merrem, 1977, "Stellar Scintillometer Model II for Measurement of Refractive-Turbulent Profiles" NOAA Technical Memorandum ERL WPL-25.

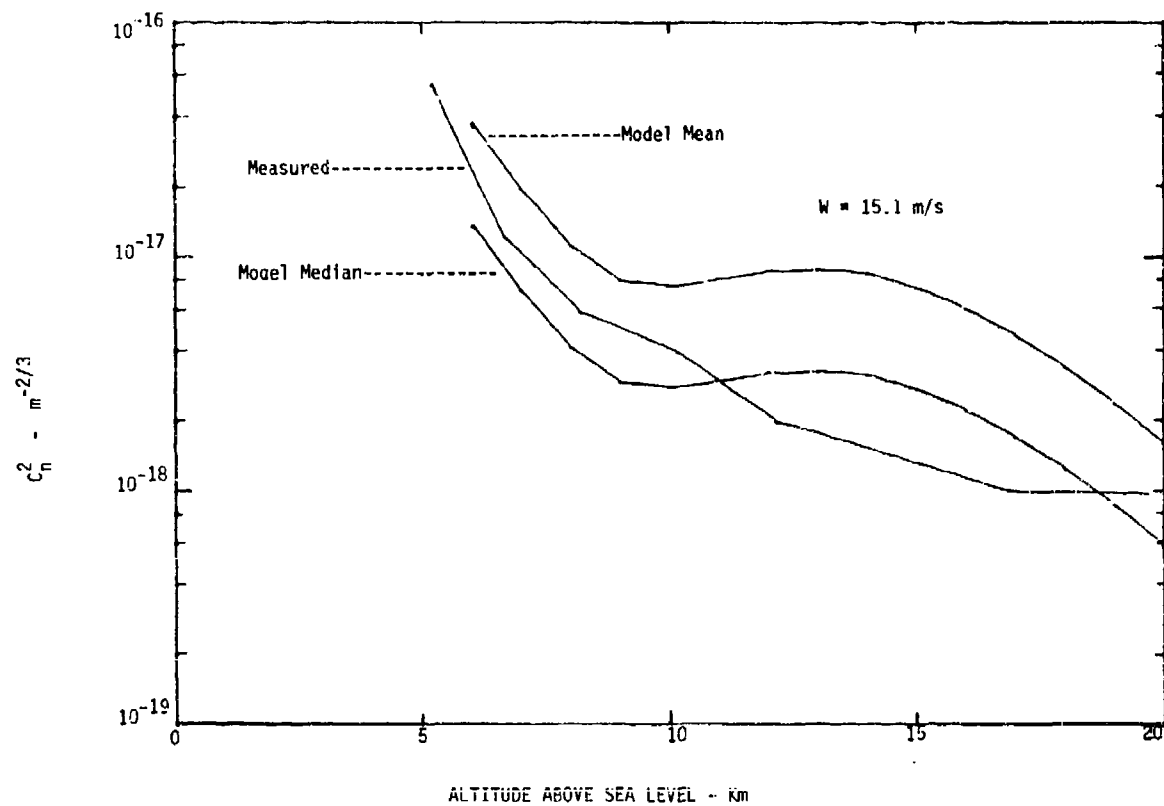
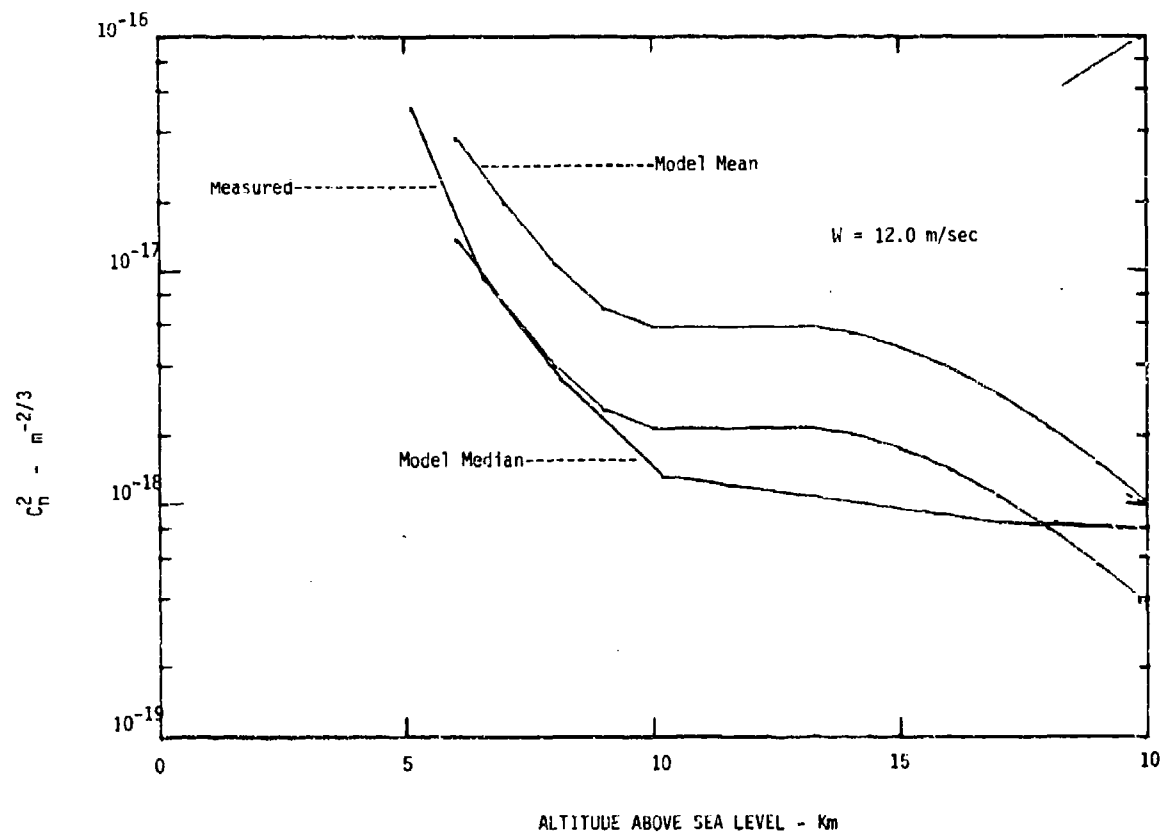


FIGURE 1 - Turbulence Profiles for 1 September 1978



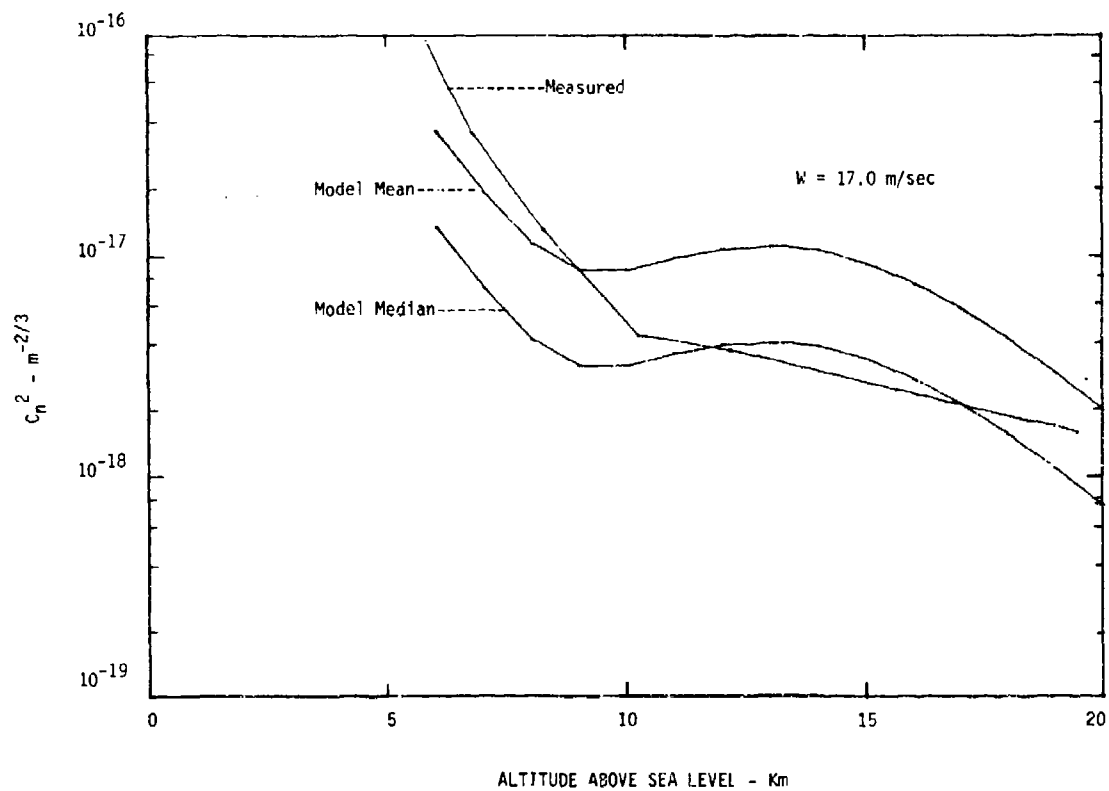
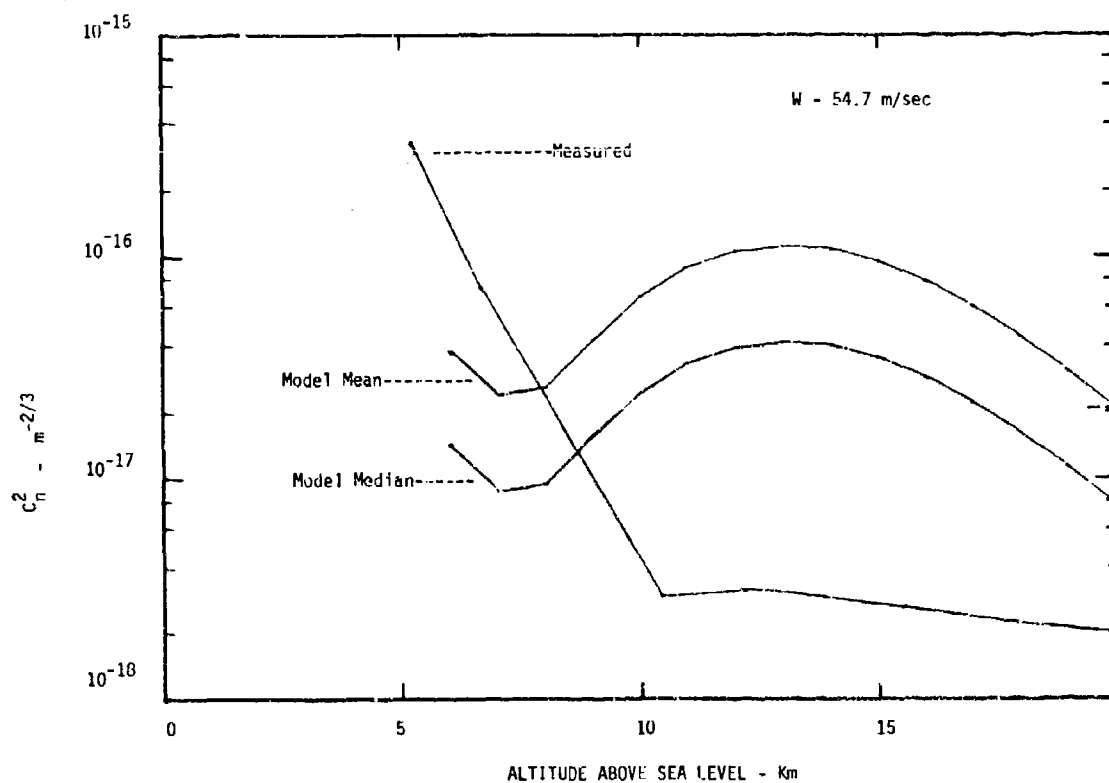
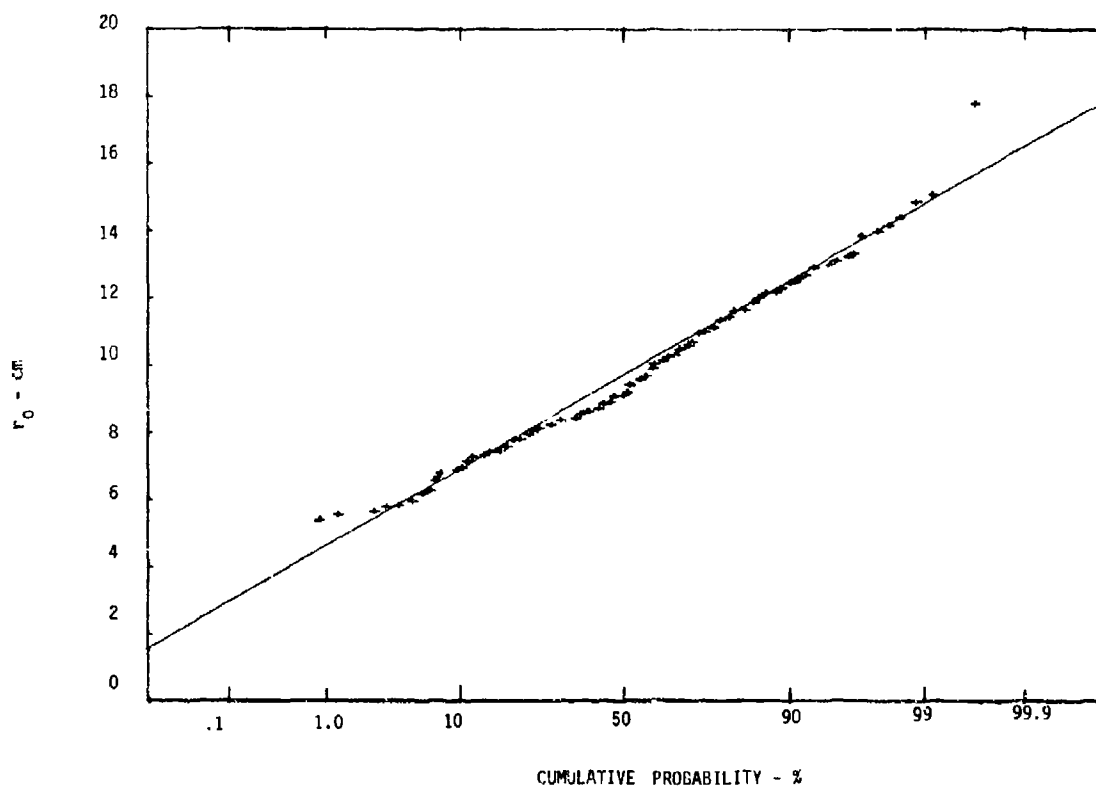
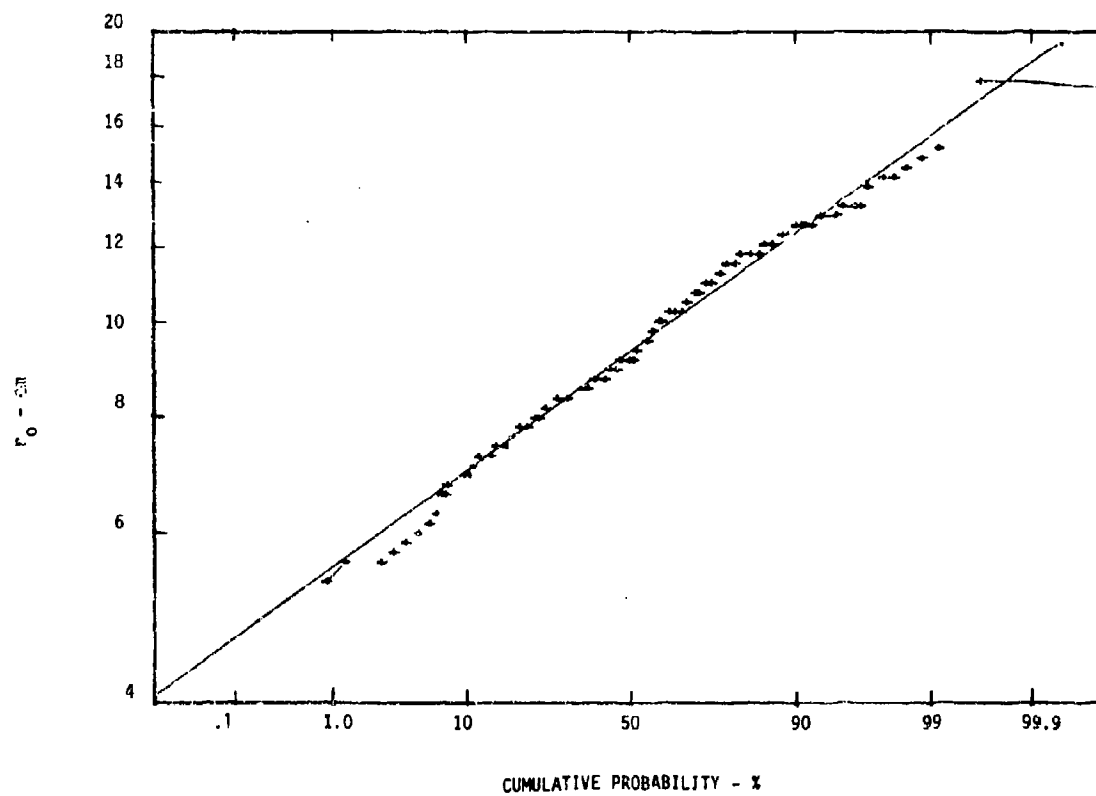


FIGURE 3 - Turbulence Profiles for 22 September 1978



FIGURE 5 - Measured r_0 Data and Least Square Linear Fit

DISCUSSION

M.Tavis, US

I note that your comparison is good for low rms wind speeds and very bad for high values.

Is the acoustic sounder operating now?

Author's Reply

The acoustic sounder data has not yet been analyzed. We intend to publish further work in this area when this data has been analyzed.

J.Röttger, FRG

- (1) Do you include wind shears to predict the C_n^2 -profile?
- (2) It should be checked if the discrepancy of predicted and measured C_n^2 -profiles at greater heights might be explained by the possibility that at these heights the turbulence for these very short wavelengths is no longer in the inertial subrange.

Author's Reply

- (1) The rms wind speed is calculated using a wind speed profile. Changes in wind direction are not included.
- (2) I believe that proper theory has been used in the developing of the instrumentation used to measure C_n^2 .

R.A.McClatchey, US

It seems to me that models of turbulence should depend on vertical wind shear and vertical temperature gradients and not only on wind speed. Perhaps differences between measurement and Hufnagel model could be used to generate a somewhat more sophisticated model, still dependent on ordinarily measured meteorological parameters.

Author's Reply

Other more complicated models for turbulence profiles do exist which include the parameters mentioned above.

L.W.Barclay, UK

I note that there is a change in the ordinate scale in Figure 4. In the four days of results, there is a much bigger change in the model than in the measurements for heights above 10 km. Would you confirm this?

Author's Reply

The ordinate scale in Figure 4 is correct.

SUMMARY OF SESSION X

EHF PROPAGATION

by

Dr B. Van Dijl
Session Chairman

The need for reliable means for the design of radio systems, is extending more and more to the higher frequencies. This statement was true 40 years ago, it is still true now. At that earlier time the higher frequencies were in the VHF-band (30 - 300 MHz); now they are in the EHF-band (30-300 GHz). To spend one session on this latter band, is timely; to accept for this session also papers dealing in part or mainly with the VHF-SHF-band, was a wise decision, since it appears that still a lot can be learned about the properties of the propagation medium for those lower frequencies.

In the paper by **Liebe** and **Hopponen**, dealing with the frequency range $20 < f < 300$ GHz, it is shown that for an assumed clear, inhomogeneous, nonturbulent atmosphere, it is possible to predict with sufficient accuracy the behaviour of the medium for a radio wave under various slant path angles.

The data presented in the paper by **Fluess**, for the frequency range $1 < f < 300$ GHz, are under same assumed conditions as above, in agreement. In this paper however also the type and probability of precipitation and clouds are taken into consideration for their effects on the transfer characteristic of the atmosphere.

The paper by **Maseng** and **Bakkén**, considering a Stochastic Dynamic Model of Rain Attenuation, is based on the work of S.H.Lin, who has shown that rain attenuation in dB is lognormally distributed. By the introduction of one extra parameter, not only the stationary properties of rain are taken into account, but also the dynamic behaviour. The latter is done in order to be able to offset the effects of rain attenuation by power control of the satellite communication system.

The paper by **Johnson** and **Gierhart** deals with a propagation model and a computer programme for the frequency range $0.1 < f < 20$ GHz. The model includes allowances for: average ray bending, horizon effects, long term power fading, vertical plane patterns of antennas, surface reflection and tropospheric multipath, atmospheric absorption, ionospheric scintillations, rain attenuation, reflection from an elevated counterpoise, smooth earth diffraction and forward scatter.

A computer-based propagation prediction programme is discussed in the paper by **Palmer**. It provides an accurate means of predicting coverage areas for VHF and UHF systems. A topographic data-base enables detailed path-loss or field-strength calculation to be carried out in the Ottawa region. This data-base can be extended to other areas of Canada.

The paper by **Marguinaud** aims to determine the preferred transmission procedure for a digital tropospheric scatter circuit at a frequency of 6 GHz over a distance of 135 km and a bit rate of 10 Mb/sec.

ATMOSPHERIC MEDIUM CHARACTERIZATION AND MODELLING

OF

EHF PROPAGATION IN AIR

H. J. Liebe

Institute For Telecommunication Sciences
National Telecommunications and Information Administration
U. S. Department of Commerce
Boulder, Colorado 80303 USA

and J. D. Hopponen

Lockheed Missiles and Space Company
Sunnyvale, California 94088 USA

SUMMARY

It is possible to predict the behavior of an EHF (frequencies up to 300 GHz) radio wave traversing a clear, inhomogeneous, nonturbulent atmosphere at various slant path angles θ . Molecular absorption spectra of major (O_2 , H_2O) and minor (e.g., O_3 , CO, N_2O) air constituents cause frequency dependent signal attenuation, phase delay, ray bending, and medium noise. The interaction between radiation and air is expressed through a complex refractivity N , which is a function of frequency ν , total pressure p , partial water vapor pressure p_w , temperature T , earth magnetic field strength H (O_2 -Zeeman effect), and trace gas densities. The N -calculation takes into account 36 O_2 lines, 6 H_2O lines plus a nonresonant spectrum, and, if needed, includes trace gas spectra ($>100 O_3$, 2 CO, 64 N_2O lines), which are generally very weak. The calculation scheme has been verified to a large extent by recent laboratory measurements of the 22 GHz H_2O line, and the 60 GHz O_2 band plus 119 GHz line spectra (LIEBE and GIMMESTAD, 1978). Assuming a distribution of the gas variables for neutral air ($h=0$ to 100 km) as a function of height and the radio path geometry (ground-to-ground, -aircraft, -satellite, -outer space) provides the basis for calculating the various propagation effects. The height distributions $p(h)$, $p_w(h)$, and $t(h)=300/T$ may be obtained from in situ data (e.g., radiosonde) or from models simulating atmospheres as a function of altitude, latitude, and season (NOAA, 1976).

A tractable propagation model employs a spherically stratified atmosphere ("onion-shell" model of thin quasi-homogeneous layers) to be amenable to computer calculations of five integrals: cumulative attenuation (i.e., transmittance), radio range, curved path length, and noise temperature due to upwelling and downwelling radiation. These integrals are evaluated by numerical integration applying the Romberg method to optimize computer time. Low ($\theta < 1^\circ$) elevation angle cases employ an analytical approximation to circumvent numerical instabilities. Since the integration method uses finer steps than the input data provide, interpolation is applied for intermediate values of $N(\nu, p, t, H, p_w)$. Various aspects typical of EHF propagation will be exemplified by giving results for specific cases.

1. INTRODUCTION

The relatively stable neutral air mass represents a unique filter over the EHF (20-300 GHz) range with transfer, shielding, and emission properties caused by microwave spectra of oxygen, water vapor, and trace gases, not found at any lower frequency. The spectra cause selective attenuation, transit time variations, and increases in the background noise affecting amplitude, phase, and direction of propagating radio waves as well as limiting their detectability. Confidence in EHF system design and recommendations on the optimum use of specific EHF bands hinges on the ability to predict atmospheric propagation effects. Those inherent to the gaseous atmosphere are of foremost importance since they are always present.

Any simulation of radio wave propagation requires an accurate correlation between the physical state and the electromagnetic properties of the medium. Thus, EHF applications are dependent on a description of the somewhat complicated interaction between millimeter waves and the molecules that comprise the atmosphere. Scattering is neglected since the air mass is assumed to be calm and clear. The primary motivation for the work described here is to translate molecular spectroscopy into an engineering data base which, in turn, is applied to generate attenuation, phase dispersion, and emission rates for modelled radio paths within, into, and through the neutral atmosphere ($h=0$ to 100 km). The complex refractivity N in parts per million (ppm) is a suitable measure of the interaction. Over the EHF range, several air molecules (O_2 , H_2O , O_3 , CO, N_2O , and other trace gases - KOLBE et al., 1977) exhibit more than 500 spectral lines leading to a complicated expression for N .

For the spectroscopic basis of modelling N we resorted to a variety of sources (LIEBE and GIMMESTAD, 1978 and references therein), including the October 1977 version of the Air Force Cambridge Research Laboratory absorption line parameter compilation (abbreviated ALPC) tape (ROTHMAN and McCLATCHY, 1976). The first problem is to express N as a function of the following variables:

dry air pressure	$p(h)$	10^5 to 10^{-2} Pa (Pascal = N/m^2 = 0.01 mbar),
water vapor pressure	$p_w(h) \leq p^s(t)$	≤ 6 kPa,
temperature parameter	$t(h) = 300/T$	0.9 to 2,
earth magnetic field strength	H	2 to 8×10^{-5} T (Tesla = 10^{-4} Gauss),
frequency	ν	30 to 300 GHz,
slant angle of radio path	θ	0 to 90° = zenith.

(1)

The various trace gas spectra (e.g., O_3 , CO, N_2O), which require additional variables, will not be treated in this paper.

The EHF refractivity N is formulated in Section 2. Accurate knowledge of $N(\nu, p, p_w, t, H, \text{trace gas density})$ due to detectable atmospheric absorption lines is important in various radio science fields (e.g., wave propagation, remote sensing, radio astronomy). A little-understood anomalous water vapor absorption, particularly noticeable in the four window ranges (30-50, 70-110, 130-160, 220-280 GHz), introduces some uncertainty into the otherwise well confirmed calculation scheme. In Section 3, the second problem is addressed by numerical experimentation, namely radio path behavior modelling for various assumed geometries.

2. SPECTROSCOPIC BASIS

2.1 Formulation

The complex EHF refractivity can be expressed as

$$N = N_0 + \sum_1 (S_1 I_1') + N'_w + j \left\{ \sum_1 (S_1 F_1'') + N''_w \right\} \quad (\text{ppm}) , \quad (2)$$

where N_0 is the frequency-independent refractivity of moist air,

$$N_0 = [2.589p + (2.39 + 41.6t)p_w]t \quad (\text{ppm}) . \quad (3)$$

The frequency-dependent molecular spectra are of two types:

- the line spectra of absorption (amplitude attenuation) SF'' and dispersive refraction (nonlinear phase shift) SF' with a strength S in units of kHz and shape factors F' and F'' in units of GHz^{-1} ; the sums range over all spectral lines given in Tables 1-4; and
- nonresonant water vapor spectrum N'_w and N''_w due to wing terms of very strong infrared lines plus additional contributions not fully understood.

Power attenuation and phase delay rates, the standard propagation factors, are simply

$$\alpha = 0.1820\nu \text{ Im } N \quad (\text{dB/km}) , \quad (4)$$

$$\phi = 0.0209\nu \text{ Re } N \quad (\text{radians/km}) , \quad (5)$$

where Im stands for "imaginary part of" and Re for "real part of".

2.2 Shape Functions

Common to each spectroscopic feature is an intensity-versus-frequency distribution function, the shapes $F'(\nu)$ and $F''(\nu)$. For $h < 20 \text{ km}$, resonant and nonresonant spectra exist. Their shape functions are (ROSENKRANZ, 1975):

(resonant)	(nonresonant, Debye shape)
$F'_R = \left(\frac{\nu}{\nu_0} \right) \left[\frac{(\nu_0 - \nu) + \gamma I}{(\nu_0 - \nu)^2 + \gamma^2} - \frac{(\nu_0 + \nu) + \gamma I}{(\nu_0 + \nu)^2 + \gamma^2} \right]$ $F''_R = \left(\frac{\nu}{\nu_0} \right) \left[\frac{\gamma - (\nu_0 - \nu) I}{(\nu_0 - \nu)^2 + \gamma^2} + \frac{\gamma - (\nu_0 + \nu) I}{(\nu_0 + \nu)^2 + \gamma^2} \right]$	$F'_D = I^2 / (\nu^2 + I^2) \quad (6), (7)$ $F''_D = 2\nu I / (\nu^2 + I^2) \quad (8), (9)$

which introduce the spectroscopic parameters center frequency ν_0 , widths γ , I , and overlap interference 1.

For $h > 20 \text{ km}$, only isolated resonant lines are present, spread over a megahertz frequency scale. Equations (6) and (8) reduce to Lorentzian shapes

$$F'_L = (\nu_0 - \nu) / [(\nu_0 - \nu)^2 + \gamma^2] \quad \text{and} \quad F''_L = \gamma / [(\nu_0 - \nu)^2 + \gamma^2] . \quad (10)$$

Peak dispersion at $\nu = \nu_0 \mp \gamma$ and maximum absorption at $\nu = \nu_0$ are given by

$$\pm \Delta N_0 = S/2\gamma \quad \text{and} \quad N_0'' = S/\gamma \quad (\text{ppm}) . \quad (11)$$

For $h > 40 \text{ km}$, further decrease in pressure converts the pressure-broadened Lorentzian into a Doppler-broadened Gaussian with a different width

$$\gamma_D = 6.20 \cdot 10^{-6} \nu_0 / \sqrt{M t} \quad (\text{GHz}) , \quad (12)$$

where M is the molecular weight (e.g., $O_2: M=32$, $t=1$, $\nu_0=60 \text{ GHz}$, $\gamma_D=65.8 \text{ kHz}$). The convolution of Lorentz and Gaussian shape functions is called the Voigt profile, which is governed by the parameter, $x_V = \gamma/\gamma_D$.

The Voigt profile is prominent when x_V falls in the range between ≈ 10 and 0.1 and the numerical evaluation of the height-dependent complex Voigt function requires considerable computational effort. We adopted for F_V' the fast algorithm (FORTRAN IV program) reported by PIERLUSSI et al. (1977).

For total atmospheric transfer calculations associated with ground-to-satellite paths it is quite adequate to keep the Lorentzian shape (10) but replace the width γ with

$$\gamma_h = \sqrt{\gamma^2 + \gamma_D^2} \quad (13)$$

The treatment of high-altitude oxygen lines introduces further complications due to Zeeman splitting (see 2.4 below).

2.3 EHF Spectrum of Oxygen (O_2 -MS)

All pertinent information on the O_2 -MS is contained in Table 1. The line parameters have been reduced to five coefficients a_1 - a_5 and are listed in Table 1 together with the center frequencies ν_0 . Water vapor influences the O_2 -MS through (15). The dependences on atmospheric variables are:

$$S = a_1 p t^3 \exp[a_2(1-t)] \quad (\text{kHz}), \quad (14)$$

$$\gamma = a_3 (p + 1.3p_w) t^{0.9} \quad (\text{GHz}), \quad (15)$$

$$I = a_4 p t^{a_5} \quad (16)$$

The nonresonant oxygen spectrum ($\nu_0=0$) exhibits a Debye shape (7), (9) with a width of

$$\Gamma = a_3^0 p t^{0.9} \quad (\text{GHz}). \quad (17)$$

The associated strength is

$$S_0 = a_1^0 p t^2 \quad (\text{ppm}). \quad (18)$$

The nonresonant EHF contributions $S_0 F_0^H$ and $S_0 F_0^D$ amount to a small constant attenuation (e.g., for $p=101$ and $t=1$, $\alpha=0.0064$ dB/km) and a negligible dispersion, but they are an integral part of the oxygen spectrum, necessary in the ROSENKRANZ formulation to keep predicted low altitude ($h < 10$ km) attenuation rates for $\nu > 180$ GHz from becoming slightly negative and to describe the O_2 -MS for $\nu < 30$ GHz. Without eqns. (7) and (9), $N''(O_2\text{-MS}) > 0$ at all frequencies when the a_4 -coefficients of lines 1-21(5'), 26(3) are reduced by 6 percent. Such arbitrary adjustment does not alter the significant results (i.e., > 0.01 dB/km) of the O_2 -MS in the EHF range.

Typical examples of the atmospheric O_2 -MS are depicted in Fig. 1, representing conditions for $h \approx 0-30$ km.

2.4 The O_2 -MS Zeeman Effect

For altitudes $h > 40$ km, Zeeman splitting of O_2 -MS lines under the influence of the earth's magnetic field introduces considerable complications (LENOIR, 1968). A consequence of the Zeeman effect is a polarization-dependent, anisotropic refractivity N . The presence of a steady magnetic field H splits each line into $3 \times (2K^2 + 1)$ sub-lines with their center frequencies located at

$$\nu_0^Z = \nu_0 + n(M, K) \cdot 28.03 \text{ H} \quad (\text{GHz}). \quad (19)$$

The calculation scheme for the relative frequency shift n of each Zeeman component is given in Table 2. Whereas unsplit lines are identified by one quantum number K^2 (Table 1), the Zeeman components require the additional magnetic quantum number M varying in integers between the K -limits given in Table 2. The maximum frequency spread of the components is $\nu_0^Z \pm 2.2$ MHz ($n=1$, $H=8 \times 10^{-3}$ T).

The Zeeman line strengths are calculated by substituting in eqn. (14) for a_1 the value

$$a_1^Z = a_1 f(M, K), \quad (20)$$

where the calculation procedure for the relative intensity factors f follows from Table 2. The Voigt profile is applied to each component; these are summed-up in three groups labeled σ^+ , σ^- , and π . Depending on the polarization and orientation of the intervening wave or observing antenna, one or a mixture of the three groups will contribute to the resonance interaction. We will later discuss several examples of atmospheric Zeeman patterns at $h=55$ and 100 km and then elaborate on this point. Table 3 lists all shifts n and relative intensities f for the lines $K^2=1$ to 7 .

2.5 EHF Spectrum of Water Vapor

From ALPC, we read 1838 H_2O lines up to 31 THz when a maximum intensity ($\nu=\nu_0$) cutoff of 2×10^{-3} dB/km (300°C) is applied. For the EHF range, we must consider six (see Table 4) and the remaining ones are lumped into a nonresonant wing contribution. Table 4 continues to list the spectroscopic parameters for lines up to 1000 GHz. An individual line is described by

$$S = b_1 p_w t^{3.5} \exp[b_2(1 - t)] \quad (\text{kHz}), \quad (21)$$

$$\gamma = b_3(p + 4.80 p_w) t^{0.6} \quad (\text{GHz}), \quad (22)$$

$$\text{and} \quad I = 0. \quad (23)$$

At altitudes above 60 km ($p < 20$ Pa), Doppler-broadening has to be considered. The Voigt profile ($x \gamma < 10$, see Sec. 2.2) or the approximation (13) are used for line calculations. Water vapor lines exhibit a hyperfine structure on a kilohertz scale. For example, for the 22 GHz line five sub-lines have been measured spread over an interval of roughly $v_0 + 3 \gamma_p$. This effect shows in the line shape function when $h > 70$ km; however, the water vapor concentration in the upper atmosphere is quite uncertain (see Fig. 15) and may not produce a measurable contribution.

The nonresonant H_2O spectrum was cast into the form (LIEBE and GIMESTAD, 1978)

$$N''_w = b_4 p p_w t^y (v/30)^z + b_5 (v/30)^{1.6} t^{12} p_w^2 \quad (\text{ppm}), \quad (24)$$

where

$$b_4 = 1.97 \times 10^{-5}, \quad b_5 = 5 \times 10^{-4} \quad (\text{ppm/kPa}^2), \quad y = 3.5, \quad z = 1.3. \quad (25)$$

This compares with an empirical fit of reported background H_2O absorption, where

$$b_4 = 5.6 \times 10^{-5}, \quad b_5 = 0, \quad y = 3.1, \quad z = 1. \quad (26)$$

The example in Fig. 2 underlines the considerable uncertainties in formulating the nonresonant H_2O spectrum. Model 1 [(4), (24), (26)] is based upon an empirical fit to scarce experimental data obtained between 100 and 1000 GHz. Model 2 [(4), (24), (25) and $b = 0$] is a kind of "best theoretical estimate" obtained by fitting the wing contributions of all APLC-listed H_2O lines up to 13 THz. Model 3 [(4), (24), (25)] accounts for 30/60 GHz laboratory measurements yielding an "anomalous" p_w^2 -term. Further work is needed to clarify the nonresonant H_2O EHF attenuation, which is important in the four window (see Fig. 4) regions.

The most glaring unknown in the spectroscopic basis [(2)-(26)] for modelling EHF radio path behavior (excluding trace gases) in the clear atmosphere is the correct treatment of nonresonant H_2O absorption.

3. RADIO PATH MODELLING

The complex refractivity N determines homogeneous atmospheric EHF channel characteristics and is adequate to assess short-hop horizontal transmission. For slant paths (e.g., satellite-to-ground links, radar tracking, atmospheric noise), radio path calculations are complicated by the inhomogeneous refractivity of the total air mass. The cumulative refractivity along a curved ray path starting at some ground level height h_0 with a slant angle θ (90° at zenith) and ending at some high altitude h_1 ($h_1 = \infty$ is outer space) leads to the following four integrals of interest to systems engineers:

$$1. \quad \text{Curved path length,} \quad L = \int_{h_0}^{h_1} s(\theta) dh \quad (\text{m}). \quad (27)$$

$$2. \quad \text{Radio range, approximated as} \quad R \approx \int_{h_0}^{h_1} [1 + \text{Re } N \cdot 10^{-6}] s(\theta) dh \quad (\text{m}). \quad (28)$$

since ray tracing in lossy media might require the full, complex N (JONES, 1970).

$$3. \quad \text{Cumulative attenuation (with eqn. 4),}$$

$$A = 0.1820 \nu \int_{h_0}^{h_1} (\text{Im } N) s(\theta) dh = \int_{h_0}^{h_1} \alpha(h) s(\theta) dh \quad (\text{dB}) \quad (29)$$

defining power transmittance τ (0, 1 for opaque, transparent, respectively) to be

$$\tau = \exp(-A/4.343). \quad (30)$$

$$4. \quad \text{Medium noise temperature caused by molecular emission upwelling (\uparrow) and downwelling (\downarrow) along the ray to } h_1 \text{ (employing the Rayleigh-Jeans approximation),}$$

$$T_B^{\uparrow, \downarrow} = \int_{0, h_1}^{h_1, \infty} T(h) \alpha(h) \tau^{\uparrow, \downarrow}(h) s(\theta) dh \quad (\text{K}). \quad (31)$$

Common to all four integrals is a differential of height, dh multiplied by an extension factor, $s(\theta)^{-1}$, of the geometric path increments, which accounts for the secant law and refractive ray bending. By applying the spherical form of Snell's law and neglecting $\text{Im}N$, the factor $s(\theta)$ becomes

$$s(\theta) = \left\{ 1 - \left[\frac{10^6 + \text{Re } N(h_0)}{10^6 + \text{Re } N(h)} \left(\frac{r_0 + h_0}{r_0 + h} \right) \cos \theta \right]^2 \right\}^{-1/2} \quad (32)$$

($r_0 = 6370$ km, earth's radius).

At this point, we resort to modelling (computer simulating) the various "forces" that "drive" equations (27) to (32). Infrared line-by-line transmittance calculations using the AIPA data base (more than 100,000 lines) show how to set up a portion of the mathematical framework needed to arrive at practical answers. Two newer IR works are those by TRAUB and STIER (1976) and SUSSKIND and SEARL (1976). The spectroscopic basis for the CHF range is much smaller (Sec. 2) and has the added advantage of being validated by us through extensive laboratory measurements.

The EHF prediction model for clear air properties is meant to utilize the fundamental data of the first part (where insignificant details have already been left out) as universally as practical for atmospheric transfer properties that are different from those at lower frequencies. Such a model extends the field of microwave propagation and lessens time and tedium for designers, planners, spectrum policy makers, etc.

3.1 Model Atmosphere

For spectroscopic calculations, it is useful to adopt the principles that led to the 66-level stratification model by SUSSKIND and SEARL (1978). Mean conditions are modelled by the U.S. Standard Atmosphere and its various seasonal and geographical modifications (NOAA, 1976). In situ data are available from radio descents made by the U.S. Air Force Global Weather Center or NASA, among others. Whatever the atmosphere may be, model or data, it is converted in the computer into a spherically-stratified medium with n -layers each having an assigned set of values for $p(h)$, $p_w(h)$, $t(h)$. Of these three, only the dry air pressure $p(h)$ follows to first order a simple physical law, namely the hydrostatic equation, $p(h) = p(h_0) \exp(-h/7)$ [see eqn. (34)]. The inverse temperature structure $t(h)$, $10/T$ follows no simple law below $h = 80$ km and has to be taken in any case from models or data. Water vapor pressure $p_w(h)$ is the most capricious atmospheric variable. First of all, it is highly variable within the first kilometer from the surface; then, water vapor is restricted by temperature up to the saturation pressure (e.g., $t=1$, $p_w \leq 3.52$ kPa). Models of tropospheric H_2O distributions are in NOAA (1976); a rough approximation is given by: $p_w(h) = p_w(h_0) \exp(-h/2.5)$. Various proposed water vapor distributions above the tropopause are shown in Fig. 15.

3.2 EHF Ray Tracing Program

The radio path is assumed to be a "ray" (plane wave case). A computer simulation combines the spectroscopic and atmospheric data bases to perform the calculations for (27)-(31). The difficulties in evaluating these equations center on (32) and $t(h)$. In view of the involved expression for $N(h)$, the integrals are calculated by numerical integration. Adaptive Romberg integration is used, which begins with a trapezoidal approximation and shifts to higher order modes to accelerate convergence. This method affords a balance between accuracy and computing time.

The general procedure is to calculate the local $N(h)$ for the programmed altitude grid reporting p , p_w , t and to store N_p , $\text{Re}N(v)$ and $\text{Im}N(v)$ separately on (disc-) file. The ray starts at a surface height h_0 with an elevation angle θ and is then guided by the program through the inhomogeneous medium until it reaches the intended final height h_1 .

The following approximations and refinements are built into the program:

- 1) Refraction is most pronounced between the two lowest data points causing substantial ray bending when θ is small. Therefore, at the beginning a large number of sub-intervals are generated, the first ten layers spaced 0.5 meters apart, the next ten 5m, then 50 meters and so on until the next reporting level is reached, after which the normal Romberg integration is performed for all subsequent intervals.

For $\theta < 1^\circ$, the computer evaluation of $s(\theta)$ requires an analytical approximation since (32) becomes numerically unstable. An expression was developed following BLAKE (1968).

- ii) For any height h between data points $h_a - h_b$, the HOPFIELD (1969) expression is used to interpolate

$$\text{Re}N(h) = \text{Re}N(h_a) \left\{ 1 - \left(\frac{h - h_a}{h_b - h_a} \right) \left[1 - \left(\frac{N_0(h_b)}{N_0(h_a)} \right)^{1/\mu} \right]^\mu \right\}, \quad (33)$$

where $\mu = g(h_b - h_a) / R [T(h_b) - T(h_a)]$ (R is the gas constant and g is the gravitational acceleration being a function of altitude and latitude). Equation (33) is based upon the hydrostatic equation

$$dp/dh = -g\rho/R T \quad (34)$$

The refractivity $N(h) \approx N_0(h)$ is used in (33) since the spectral contributions $\text{Re } N(\nu)$ are generally less than 1 percent of N_0 .

The values $t(h)$ and $\text{Im } N(\nu) \equiv \alpha(h)$ are found by linear interpolation from the values calculated at h_a, h_b .

- iii) Housekeeping chores are performed by the sub-program ATMO, which converts data to S.I. units, removes redundant values, and interpolates for missing levels.
- iv) The frequency grid for calculations of the total EHF range had a 5 GHz spacing (Figs. 4, 10, 11); for line details the spacings need to be as small as 0.1 γ and the line centers ν_0 are treated separately or forced to fall on the grid points.

A number of test calculations were performed; e.g., a ray tracing $h = 0 - 100$ km at one frequency requires about 3 seconds computer time (UNIVAC 1110).

3.3 EHF Radio Path Characteristics

Close to surface levels, the 60 GHz O_2 -MS lines are merged into a more or less unstructured band shape (Fig. 1a) whose maximum intensity is pressure-proportional until the lines separate ($h > 10$ km). Figure 4 gives an example of sea level EHF attenuation. The window ranges are very sensitive to the amount of water vapor.

Spectra are evaluated up to the altitude where they have vanished ($< 2 \times 10^{-3}$ dB/km) due to a lack of resonant molecules or line strength. The interaction $N(\nu)$ is always a function of the amount of the absorbing gas. The peak intensities (eqn. 11) are generally independent of pressure as long as the width is pressure proportional (e.g., Fig. 1b). A fixed width (eqn. 12) causes the line to diminish with decreasing pressure. The transition between γ and γ_0 occurs in the EHF range around $h \approx 70$ km, in contrast to an infrared line which begins to disappear when $h \approx 20$ km (Fig. 3). Stronger O_2 -MS Zeeman components exceed the intensity cutoff even at $h = 100$ km; however, dissociation to atomic oxygen ($h = 90, 120$ km leads to $O_2/O = 99, 25$ percent, respectively) accelerates their disappearance. We assume 100 km to be the boundary to outer space for EHF radio path spectra.

Tracking the maximum attenuation of one of the stronger O_2 -MS lines (γ^-) with height, as depicted in Fig. 5, we see that the approach to zero depends upon various assumptions all related to the Zeeman effect. Figures 6 and 7 show the complete Zeeman patterns for several lines at $h = 100$ and 55 km. Their calculation followed the procedure outlined in section 2.4. Each Zeeman component was treated as an individual line and a fast algorithm for the Voigt profile F_V (PIERLUISSI et al., 1977) was employed. The results show that around 55 km all components are merged into one line (Fig. 7) while around 100 km the individual Zeeman components, weak though they may be, appear for O_2 -MS lines with low (≤ 13) K^- numbers (Fig. 6). The component at $\nu = \nu_0$ is not necessarily the largest (i.e., 0.0033 compared to 0.0068 dB/km at $\nu_0 + 1.65$ MHz for ν^-). Linearly polarized radiation "sees" (a) the π -pattern when H is parallel to EHF magnetic field component \mathcal{H} in a plane perpendicular to the direction of propagation or (b) the $\sigma = \sigma^+ + \sigma^-$ pattern when H is perpendicular to \mathcal{H} . Circular-polarized radiation responds either to the σ^+ or σ^- pattern depending on \odot or \ominus . For cumulative calculations, an approximation similar to (13) can be made by replacing (15) with

$$\gamma_h = \sqrt{\gamma^2 + (25 H)^2} \quad (35)$$

Equation (35) tracks closely the attenuation $\alpha(\sigma, \nu_0)$ as seen in Fig. 5.

Figure 8 shows attenuation α as a function of height for three frequencies in the 60 GHz band. The pressure proportional behavior of $\alpha(h)$ is valid up to about 15 km, above which isolated line behavior takes over if there happens to be a line close to the frequency of interest [e.g., $\nu_0(15^+) = 62.998$ GHz]. Figure 9 gives an example of cumulative attenuation $A(h)$ at the 60 GHz O_2 -MS band center. Comparing the results for A (Fig. 9) with those for α (Fig. 8), we can define a "thickness" of the inhomogeneous medium in terms of the equivalent homogeneous attenuation path length,

$$R_g = A/\alpha \quad (\text{km}) \quad (36)$$

For example, $R_g = 155/13.5 = 11.5$ km at 60 GHz against zenith for a path starting at $h_0 = 0$.

Figure 10 displays the cumulative earth-to-space attenuation A along a nadir path through a warm, moist summer atmosphere and a cool, dry winter atmosphere. The winter attenuation is less than in the summer except in the regions of the two O_2 -MS resonances (60 and 119 GHz). Lower winter temperatures increase the line strengths and reduce the linewidths (eqn. 15) due to lower water vapor pressure. The insert shows the fine structure between 50 and 70 GHz for a dry U.S. Standard Atmosphere 1965. The frequency range 55 to 64 GHz is opaque for any sea level system looking into space. As a prospective application gains altitude, this shielding effect breaks down and several radio channels open up with interesting transfer properties. The transmittance (30) is measurable when the atmosphere is somewhat transparent, and then it can be determined either by the absorption of a signal coming from the outside (sun emission, satellite beacon) or by the thermal emission originating predominantly from 8 kilometer thick layers.

Figure 11 gives a result of atmospheric noise temperature calculations. The evaluation of (31) was done compatible with the surface-to-space methodology adopted (see Sec. 3.2). The integral factors of both sums, downwelling and upwelling, are stored as a "ray" is traced and then assembled by use of the recursion relations

$$(T_B^{\downarrow})_n = \int_{h_n}^{h_{n+1}} T \alpha \cdot \tau(f)_n^h \cdot s(\theta) dh + (T_B^{\downarrow})_{n+1} \tau(f)_n^{h_{n+1}} \quad (37)$$

and

$$(T_B^{\uparrow})_{n+1} = \int_{h_n}^{h_{n+1}} T \alpha \cdot \tau(f)_n^{h_{n+1}} \cdot s(\theta) dh + (T_B^{\uparrow})_n \tau(f)_n^{h_{n+1}} \quad (38)$$

to yield, additionally, noise temperature at all grid points. In regions of strong attenuation, the downwelling noise temperature nearly equals the ambient air temperature T_a , while the upwelling noise results from layers in the upper atmosphere. The summer atmosphere yields similar curves with slightly higher peaks.

In Figure 12, we look at examples of EHF phase dispersion $\psi(v) = \text{Re } N(v)$ (eqn. 5) at three frequencies as a function of height. The frequencies 57 and 63 GHz approximately yield the maximum and minimum phase dispersion for the 60 GHz band close to surface level. Range difference (Fig. 13) serves as a measure of the effect of dispersion in the refractive index. Rays at 57, 60, and 63 GHz were traced with and without the $\text{Re } N(v)$ -contributions. The difference at 60 GHz was negligible; however, at 57 and 63 GHz appreciable range differences occur with respect to the 5 millimeter wavelength. The refractive electrical path length, $R(N_0) = 3.38, 103.17$ meters for $\theta = 45^\circ, 0^\circ$, respectively, plus the dispersive path length ΔR lead to a propagation delay time

$$\zeta + \Delta \zeta(v) = [R + \Delta R(v)]/c \quad (s), \quad (39)$$

where c is the speed of light.

3.4 Atmospheric Remote Sensing at EHF

At selected EHF frequencies, the air mass can be utilized as frequency variable attenuator, phase shifter, and temperature, pressure, and/or density indicator. For example, the 60 GHz O_2 -MS band reveals average temperature and pressure over a line-of-sight path from a measurement of signal amplitudes at different frequencies or from a differential phase measurement at two frequencies bracketing the 60 GHz band. The change in strength of a radio signal at 118.8 GHz (1 line center) is a good indicator of path-averaged temperature fluctuations (LIEBE and HOPPONEN, 1977). Temperature-independent attenuation in the lower atmosphere, where O_2 -MS band and line contribution balance, could serve as pressure measure. Figure 14 gives the result of such a search in the U.S. Standard Atmosphere.

Several atmospheric molecules besides O_2 and H_2O exhibit a rich EHF spectrum. None of these lines is detectable in the troposphere unless somehow enriched in its abundance, which is naturally below 1 ppm. Above $h = 30$ km, however, the lines are relatively narrow, the natural abundance can increase, and several stronger lines may affect the transfer and emission characteristics at frequencies where the atmosphere is not opaque. It is possible from a measured absorption or emission line shape to infer the height distribution of that particular species if the spectroscopic parameters are well known. That technique has been successfully employed for ground-based measurements of O_3 (SHIMABUKURO et al., 1975), CO (WATERS et al., 1976) and for aircraft-based measurements of H_2O , O_3 , CO_2 , ClO , N_2O in the 165 to 280 GHz range (WATERS and WOFSEY, 1978). Typical results are given in Fig. 15. The quantitative measurements are accomplished with a multi-channel receiver detecting "emission" against the cold (≈ 3 K) cosmic background or "absorption" in the sun's emission continuum (≈ 5800 K) to within 0.1 K.

A potential application to upper ($n \approx 15$ to 150 km) atmospheric research lies in observing (e.g., from the orbiting Spacelab) intensity and spectral character of EHF limb emission. Weak signals are enhanced manifold by the largest possible path lengths ($> 10^3$ km) at a given level and by seeing them against the cosmic background. Parameters to be sensed include atmospheric composition, thermal structure, motion (winds) along the line of sight relative to that of the observation point (Doppler shift of ν_0), and, from O_2 -MS lines, reference pressures (the intensities of the lines, $K^2 = 17$ are almost independent of T) and magnetic field strength (WATERS and WOFSEY, 1978).

Cosmic background radiation fills the universe (≈ 3 K noise temperature). Planck's radiation intensity for 3K peaks around 180 GHz. Results from high altitude (aircraft, balloon) radiometric EHF measurements confirm the existence of nearly uniform outer space emission when the results are corrected for atmospheric path behavior. The anisotropy of the 3K radiation is investigated to support theories on asymmetric expansion of the universe or irregularities in the distribution of matter or energy (GORENSTEIN et al., 1978).

4. CONCLUSIONS

Molecular absorption increases over the EHF range thus posing persistent limitations to EHF systems operating through the earth's atmosphere. Transfer and emission properties depend upon frequency, and vary with pressure, temperature, magnetic field strength and with the nature and length of the radio path. Methods have been presented to model these properties based upon meteorological height profiles. A reliable answer on, say, just one attenuation value requires a large number of molecular parameters and elaborate calculations. Major uncertainties remaining are due to the nonresonant water vapor absorption, which is particularly important in the window regions.

Acknowledgment

We would like to thank Dr. G. G. Gimmetstad who performed the Zeeman calculations (Fig. 5-7, Table 3) and contributed many valuable comments.

REFERENCES

- BLAKE, L. V., 1968, "Ray height computations for a continuous non-linear refractive index profile", *Radio Science* 3(1), 85-95.
- GOENSTEIN, M. V., R. A. MULLER, G. F. SMOOT, and J. A. TYSON, 1978, "Radiometer system to map the cosmic background radiation", *Rev. Sci. Instr.* 49(4), 440-448.
- HOPFIELD, H. A., 1969, "Low quartic tropospheric refractivity profile for correcting satellite data", *J. Geophys. Res.* 74, 4487-4499.
- JONES, R. M., 1970, "Ray theory for lossy media", *Radio Science* 5(5), 793-801.
- KOLBE, W. F., H. BUSCHER, and B. LESKOVAR, 1977, "Microwave absorption coefficients of atmospheric pollutants and constituents", *J. Quant. Spectr. Rad. Transfer* 18, 47-64.
- LENOIR, W. B., 1968, "Microwave spectrum of molecular oxygen in the mesosphere", *J. Geophys. Res.* 73, 361-376.
- LIEBE, H. J., and G. G. GIMMESTAD, 1978, "Calculation of clear air EHF refractivity", *Radio Science* 13(2), 245-251.
- LIEBE, H. J., and J. D. HOPPONEN, 1977, "Variability of EHF air refractivity with respect to temperature, pressure, and frequency", *IEEE Trans. Antennas Propagat.* AP-25(1), 336-345.
- NOAA, 1976, "U. S. Standard Atmosphere 1976", NOAA-S/T 76-1562, U. S. Government Printing Office, Washington, DC.
- PIERLUISSI, J. H. P. C. VANDERWOOD, and R. B. GOMEZ, 1977, "Fast calculation algorithm for the Voigt profile", *J. Quant. Spectr. Rad. Transf.* 18, 555-558.
- ROSENKRANZ, P. W., 1975, "Shape of the 5mm oxygen band in the atmosphere", *IEEE Trans. Antennas Propagat.* AP-23(4), 498-506.
- ROTHMAN, L. S., and R. A. McCLATCHEY, 1976, "Updating of the AFGL atmospheric absorption line parameters compilation", *Appl. Optics* 15(11), 2616-2617 (abbr. ALPG).
- SHIMABUKURO, F. I., P. L. SMITH and W. J. WILSON, 1975, "Estimation of ozone distribution from mm wavelength absorption measurements", *J. Geophys. Res.* 80(7), 2957-2959.
- SUSSKIND, J., and J. E. SEARL, 1978, "Synthetic atmospheric transmittance spectra near 15 and 4.1 m", *J. Quant. Spectr. Rad. Transfer* 19, 195-215.
- TRAUB, W. A., and M. T. STIER, 1976, "Theoretical atmospheric transmission in the mid- and far-infrared at four altitudes", *Appl. Optics* 15(2), 364-377.
- WATERS, J. W., W. J. WILSON and F. I. SHIMABUKURO, 1975, "Microwave measurements of mesospheric carbon monoxide", *Science* 191(3), 1174-1175.
- WATERS, J. W. and S. C. WOFSY, 1978, "Applications of high resolution passive microwave satellite systems to the stratosphere, mesosphere, and lower thermosphere", NASA Committee on High Resolution Passive Microwave Satellite Systems; available from JPL-Pasadena, CA 91103.

TABLE 1. DATA BASE FOR O_3^+ SPECTRAL LINES IN AIR UP TO 1000 GHz
(after LIEBE and GIMESTAD, 1978 and references therein).

i	Center Frequency ν_0	Strength μ_1	Temp., Exp. μ_2	Width μ_3	Interference μ_4	Temp., Exo. μ_5	ID
1	GHz	km/kPa		GHz/kPa	1/kPa		
1	0	3.07 E-4 (Units: dyn/kPa)	-	5.6 E-3	-	-	Nonresonant
5	50.4736	0.94 E-6	9.69	8.6 "	5.2 E-6	1.79	31"
	50.9873	2.44 E-6	8.69	8.7 "	5.5 "	1.66	35"
	51.50202	6.04 E-6	7.74	8.9 "	5.6 "	1.77	33"
	52.02117	1.41 E-5	6.84	9.2 "	5.5 "	1.81	31"
	52.54223	3.08 E-5	6.00	9.4 "	5.69 "	1.79	29"
10	53.06680	6.37 E-5	5.22	9.7 "	5.28 "	1.89	27"
	53.59572	1.24 E-4	4.48	10.0 "	5.44 "	1.82	25"
	54.12937	2.265 E-4	3.81	10.2 "	4.80 "	1.99	23"
	54.67116	3.893 E-4	3.19	10.5 "	4.84 "	1.90	21"
	55.22136	6.274 E-4	2.62	10.79 "	4.17 "	2.07	19"
15	55.78380	9.471 E-4	2.115	11.10 "	3.75 "	2.07	17"
	56.26478	5.453 E-4	0.0138	16.46 "	7.74 "	0.89	1*
	56.36339	1.335 E-3	1.655	11.44 "	2.29 "	2.29	15"
	56.96218	1.752 "	1.255	11.81 "	2.12 "	2.53	13"
	57.61249	2.125 "	0.910	12.21 "	0.94 "	3.76	11"
20	58.32386	2.369 "	0.621	12.66 "	-0.55 "	-11.2	9"
	58.44660	1.447 "	0.0827	14.49 "	5.97 "	0.79	82 3*
	58.16422	2.387 "	0.386	13.19 "	-2.44 "	0.07	7"
	58.59998	2.097 "	0.207	13.60 "	3.44 "	0.49	5*
	60.30604	2.109 "	0.386	13.82 "	-4.35 "	0.68	7*
25	60.43178	2.444 "	0.910	12.97 "	1.32 "	-1.20	5"
	61.15057	2.486 "	0.621	12.48 "	-0.36 "	5.84	9*
	61.80017	2.281 "	0.910	12.07 "	-1.59 "	2.84	11*
	62.44236	1.507 "	1.255	11.71 "	-2.66 "	2.26	13*
	62.59800	1.492 "	0.0827	14.68 "	-5.03 "	0.85	3"
30	63.56854	1.079 "	1.655	11.39 "	-3.34 "	2.18	15*
	64.12778	7.281 E-4	2.115	11.06 "	-4.17 "	1.96	17*
	64.67892	4.601 E-4	3.19	10.78 "	-4.48 "	2.00	19*
	65.22408	2.727 E-4	3.81	10.5 "	-5.15 "	1.84	21*
	65.76474	1.52 E-4	4.48	10.0 "	-5.07 "	1.92	23*
35	66.30206	7.94 E-5	5.22	9.7 "	-5.67 "	1.78	25*
	66.84677	3.51 E-5	6.00	9.4 "	-5.49 "	1.74	27*
	67.38951	1.81 E-5	7.74	9.2 "	-5.88 "	1.71	29*
	67.90073	7.95 E-6	8.69	8.9 "	-5.8 "	1.73	31*
	68.4308	3.28 E-6	9.49	8.7 "	-5.7 "	1.63	33*
39	118.75934	9.341 E-4	0.0138	15.92 "	-0.441 "	0.39	37*
40	258.4590	6.79 E-5	0.202	15.6 "	0	-	1*
	428.7839	6.43 E-4	0.0112	15.6 "	0	-	1,3
	467.170	2.39 E-4	0.0112	15.6 "	0	-	1,3
	715.3944	9.73 E-5	0.0991	14.4 "	0	-	3,5
	773.341	5.71 E-4	0.0798	14.4 "	0	-	3,5
45	824.147	1.63 E-4	0.0798	14.4 "	0	-	3,5

X) revised

D - Doublet

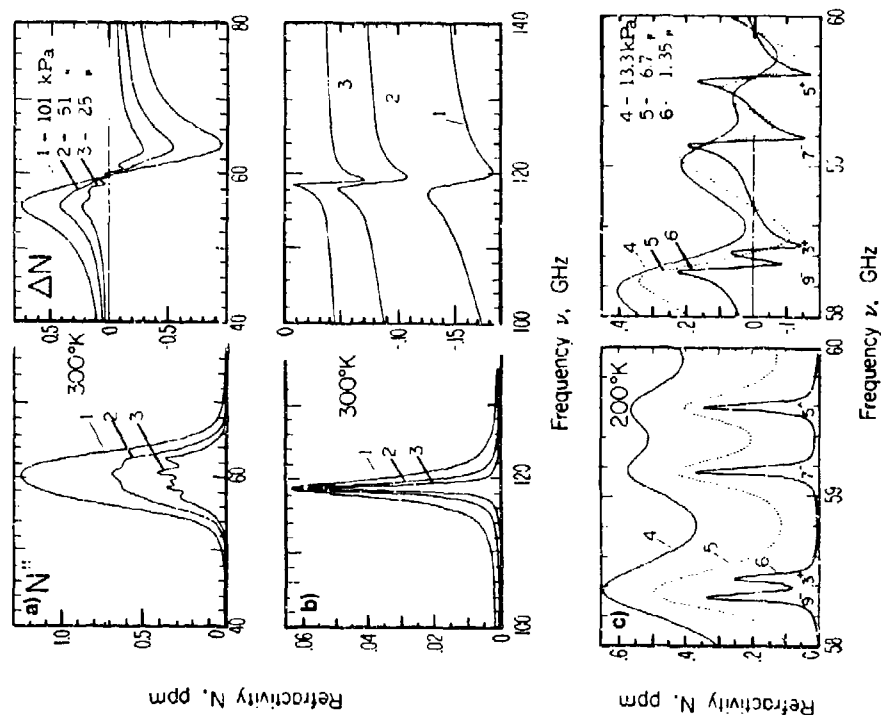


Fig. 1. Examples of the complex O_3^+ NS refractivity $\Delta N+1N''$ in dry air (LIEBE and HOPFEN, 1977):

- a) 60 GHz band structure at 3 pressure levels ($h \approx 0 - 10$ km),
- b) 119 GHz line shape at 3 pressure levels ($h \approx 0 - 10$ km),
- c) Four resolved lines between 58 and 60 GHz ($h \approx 15 - 30$ km).

TABLE 2. CALCULATION SCHEME FOR THE FREQUENCY SHIFT $\eta(M, K)$ AND THE RELATIVE INTENSITY FACTOR $f(M, K)$ OF Q_{-} -HS ZEMAN COMPONENTS (See for Examples of $K^{\pm} = 1$ to 7 Lines in Table 3).

Final State: $K, J, |M| \leq J \leftarrow$ Initial State: $K, J', |M'| \leq J'$

$$\Delta M = H' - M$$



Zeeman Transitions	Polarization		$K^+ - \text{Line}$		$K^- - \text{Line}$	
	linear	circular	$n(M, K) < \pm 1$	$f(M, K) < 1$	$n(M, K) < \pm 1$	$f(M, K) \leq 1$
σ_+ ($\Delta M = 1$)	$\vec{E} \perp \vec{H}$	 left	$\frac{M(1-K)-K}{K(K+1)}$	$\frac{3(K+M+1)(K+M+2)}{4(K+1)(2K+1)(2K+3)}$	$\frac{(M+1)(K+2)-1}{K(K+1)}$	$\frac{3(K+1)(K+M)(K+M-1)}{4K(2K+1)(2K^2+K-1)}$
			$\pm M \leq K$		$K-2 \geq M \geq -K$	
σ_- ($\Delta M = -1$)	$\vec{E} \perp \vec{H}$	 right	$\frac{M(1-K)+K}{K(K+1)}$	$\frac{3(K-M+1)(K-M+2)}{4(K+1)(2K+1)(2K+3)}$	$\frac{(M-1)(K+2)+1}{K(K+1)}$	$\frac{3(K+1)(K+M)(K+M-1)}{4K(2K+1)(2K^2+K-1)}$
			$\pm M \leq K$		$K \geq M \geq -(K-2)$	
π ($\Delta M = 0$)	$\vec{E} \parallel \vec{H}$		$\frac{M(1-K)}{K(K+1)}$	$\frac{3[(K+1)^2 - M^2]}{(K+1)(2K+1)(2K+3)}$	$\frac{M(K+2)}{K(K+1)}$	$\frac{3(K+1)(K^2 - M^2)}{K(2K+1)(2K^2+K-1)}$
			$\pm M \leq K$		$K-1 \geq M \geq -(K-1)$	

TABLE 3. THE FREQUENCY SHIFTS $\eta(M, K)$ AND RELATIVE INTENSITIES FACTORS $f(M, K)$ FOR ALL ZEEMAN COMPONENTS OF THE $K^{\pm} = 7$ TO 1 O_n -MS LINES.

	i	22	19	20	21	18	26	13	39
	K	7	6	5	4	3	2	1	
	M	i	f	i	f	i	f	i	f
b	7	-.0720	.0082	0	0	0	0	0	0
	6	-.7679	-.0772	0	0	0	0	0	0
	5	-.4607	.0069	.9466	-.0111	-.6355	.0154	0	0
	4	-.0536	.0074	-.7679	.0033	-.7000	.0562	0	0
	3	-.3464	.0085	.6250	.0066	-.5667	.0787	.9200	.0030
	2	-.3393	.0074	-.0643	.0116	-.4335	.0679	-.5667	.0071
	1	-.3221	.0331	.3336	.0265	-.3000	.0090	-.3333	.0162
	0	-.6250	.0667	.1822	.0233	-.1667	.0367	.2500	.0303
	-1	-.0174	.0206	-.0179	.0308	-.0333	.0272	-.0333	.0055
	-2	.0093	.0154	-.1168	.0196	-.1100	.0175	-.0833	.0357
	-3	-.1934	.0110	-.3393	.0093	-.2333	.0105	-.5000	.0088
	-4	.0036	.0074	-.5000	.0044	-.3667	.0057	-.7333	.0091
	-5	-.0167	.0044	-.6607	.0725	.5000	.0017	-.9467	.1364
-6	-.5179	.0722	-.8214	.0857	0	0	0	0	
-7	.6250	.0007	-.9821	.1000	0	0	0	0	
b	7	-.6250	.0007	.9821	.1000	0	0	0	0
	6	-.5179	.0722	.8214	.0857	0	0	0	0
	5	-.0167	.0044	.6607	.0725	-.5000	.0017	.9467	.1364
	4	-.0036	.0074	.5000	.0044	-.3667	.0057	.7333	.0091
	3	-.1934	.0110	-.3393	.0093	-.2333	.0105	-.5000	.0088
	2	-.0093	.0154	.1168	.0196	-.1100	.0175	.0833	.0357
	1	-.0174	.0206	-.0179	.0308	-.0333	.0272	.0333	.0055
	0	-.4252	.0367	.1822	.0233	-.1667	.0367	.2500	.0303
	-1	-.3333	.0162	.3000	.0090	.3333	.0105	.5000	.0088
	-2	-.3393	.0093	.4643	.0110	.4333	.0049	.5667	.0071
	-3	.4464	.0085	.6250	.0066	.5667	.0787	.9200	.0030
	-4	.5536	.0570	-.7679	.0033	-.7000	.0562	0	0
	-5	.6607	.0725	-.9821	.0857	-.9467	.1364	0	0
-6	.7679	.0772	0	0	0	0	0	0	
-7	.8750	.0982	0	0	0	0	0	0	
b	7	-.7500	-.0221	0	0	0	0	0	0
	6	-.6429	.0412	.9433	.0266	0	0	0	0
	5	-.3357	.0074	.8036	.0527	-.4667	.0505	0	0
	4	-.4766	.0076	.6429	.0725	-.5333	.0679	.9200	.0030
	3	-.3214	.0091	-.0821	.0074	-.4000	.0578	-.6888	.0033
	2	-.2193	.0082	.3214	.0989	-.2667	.1139	.4667	.1273
	1	-.1071	.0096	.6887	.1855	-.2533	.1224	.7333	.1355
	0	-.6250	.0741	.6000	.1877	.6250	.1112	.6000	.1764
	-1	-.3071	.0426	-.1607	.1055	-.1333	.1224	-.2333	.1455
	-2	-.2143	.0802	-.3214	.1969	-.4667	.1873	.3333	.1429
	-3	.3214	.0096	-.6821	.0074	-.4000	.0578	.6888	.0033
	-4	.4766	.0076	-.6429	.0725	-.5333	.0679	.9200	.0030
	-5	.3357	.0074	-.8036	.0527	.4667	.0505	0	0
-6	.4479	.1112	-.7643	.0266	0	0	0	0	
-7	.7500	.0721	0	0	0	0	0	0	

Table 4

DATA BASE FOR H_2O^{16} SPECTRAL LINES IN AIR UP TO 1000 GHz

1	Center Frequency γ_0	Strength b_1	Temperature Exponent b_2	Width b_3	ID (lower Quant. No.)	Remark
	GHz	kHz/ μ Pa		GHz/kPa		
1	22.23518	0.112	2.143	28.1 E-3	5 2 3	
	68.052	0.018	8.75	28 "	3 2(1) 1	
	183.310091	2.41	0.653	28.2 "	2 2 0	
	321.225444	0.044	6.16	22 "	9 3 6	
	325.152919	1.59	1.52	29 "	4 2 2	
6	380.197372	12.40	1.02	28.5 "	3 2 1	
7	390.18	0.004	7.33	16 "	11 2 10	
	437.34667	0.062	5.02	15 "	6 6 0	
	439.150812	0.921	3.56	17.5 "	5 5 0	
10	443.018295	0.187	5.02	14.8 "	6 6 1	
	448.001075	10.7	1.37	24.6 "	3 3 0	
	470.888947	0.328	3.57	18.1 "	5 5 1	
	474.689127	1.24	2.34	21 "	4 4 0	
	488.491133	0.256	2.81	22.2 "	7 1 7	
15	503.56	0.035	6.69	12.7 "	7 7 0	
	504.46	0.012	6.69	13 "	7 7 1	
	556.936002	542	0.114	31.7 "	1 0 1	
	620.700807	4.69	2.34	21.6 "	4 4 1	
	658.34	0.460	7.76	32.8 "	1 0(1) 1	
20	752.033227	259	0.336	30.2 "	2 0 2	
	841.01	0.012	8.11	17 "	11 2 9	
	859.81	0.015	7.99	27 "	2 0 2	
	899.38	0.091	7.94	30 "	1 1 1	
	903.28	0.064	8.35	28 "	2 2 1	
25	906.21	0.179	5.04	20.4 "	8 3 5	
	916.62	8.90	1.37	24.9 "	3 3 1	
	970.31	9.40	1.84	24.6 "	4 3 1	
28	987.94	145	0.18	29.9 "	1 1 1	
Plus 1810 additional lines up to 31 THz, of which 362 lines have strengths, $b_1 > 1000$. The strongest lines are at:						
	2640.5	2530	0.656	28.5 "	3 0 3	Max. strength
	6076.5	2500	1.37	20.4 "	3 3 0	Max. attenuation

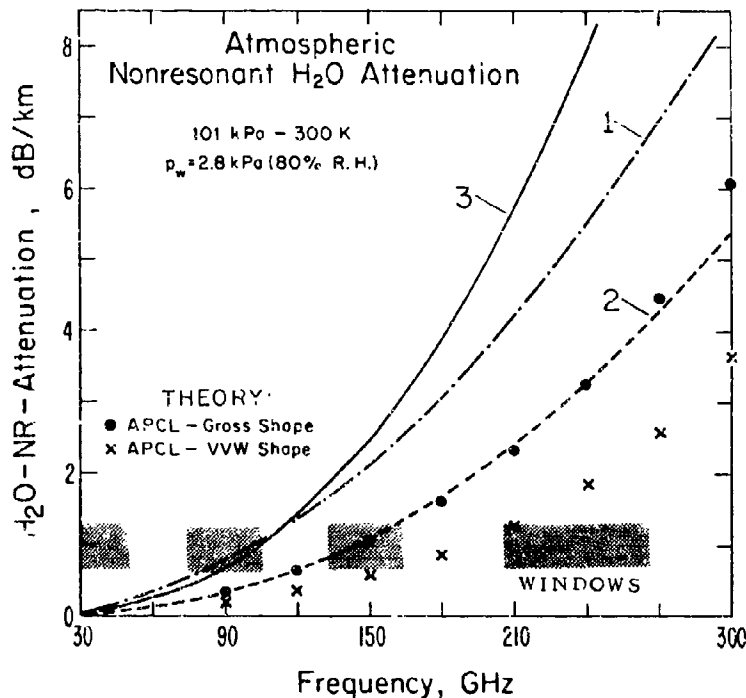


Figure 2.

Example of EHF nonresonant water vapor attenuation for sea level conditions with 80% relative humidity (RH). The prediction models 1-3 are discussed in the text (eqs. 23-26).

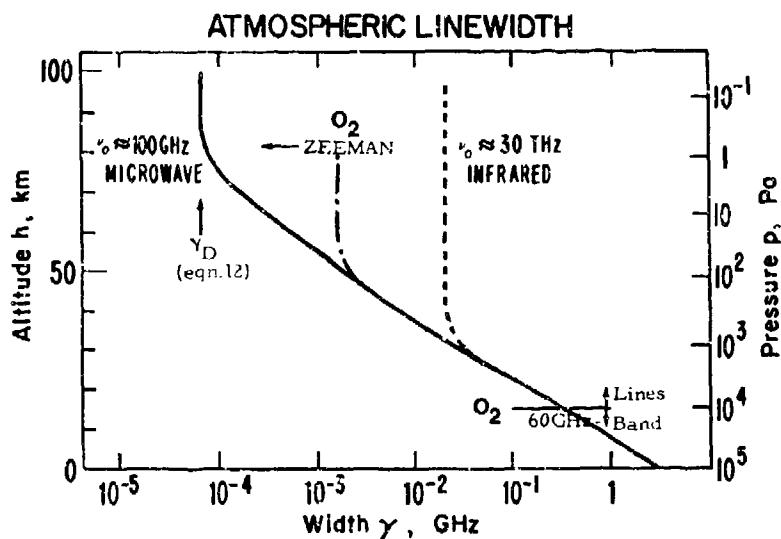


Fig. 3. Schematic atmospheric linewidth γ_h versus altitude h and pressure p . The EHF range of the pressure-proportional regime extends up to $h \approx 70$ km, the infrared range is limited to $h \approx 20$ km. The Zeeman effect of the O_2 spectrum causes line shape complications when $h > 40$ km (see Figs. 5-7).

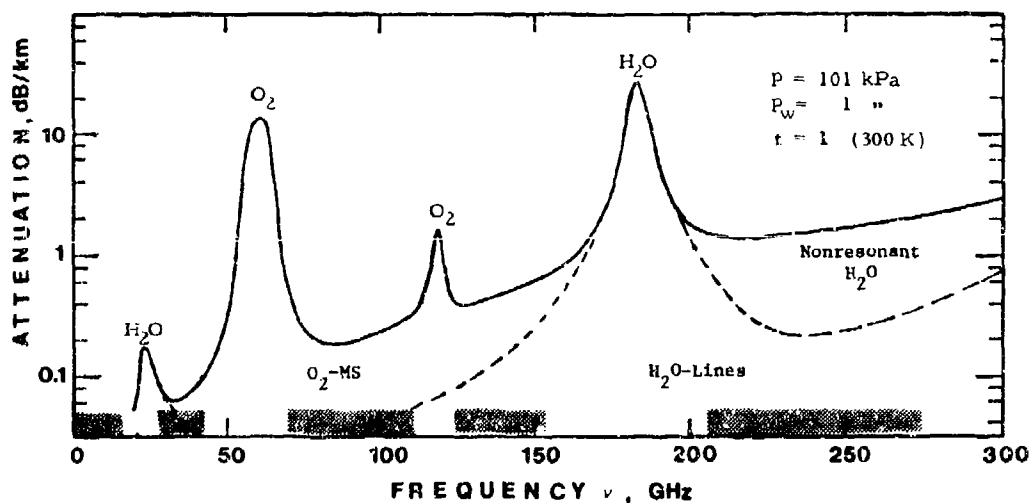


Fig. 4. Example of EHF attenuation in clear air at a typical surface level condition with $\approx 30\%$ relative humidity. The computation used $i=1$ to 39 from Table 1, $i=1$ to 6 from Table 4, and Model 1 (eqs. 24, 26, 4) for nonresonant water vapor attenuation.

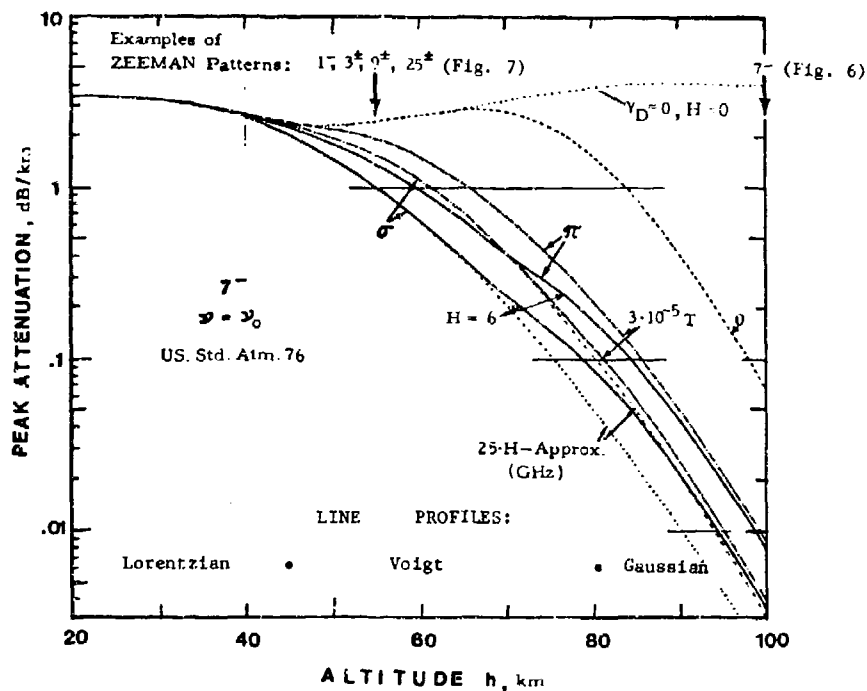


Fig. 5. Attenuation rate α_0 at line center (max.) of the 7^- line as a function of altitude h for both Zeeman patterns (π, σ) and two magnetic field strengths (6 and $3 \times 10^{-5} \text{ T}$). Also shown are the influence upon $\alpha_0(h)$ for Doppler broadening alone ($H=0$), for the $25 \cdot H$ approximation, and for the neglect of Doppler broadening ($\gamma_D=0, H=0$).

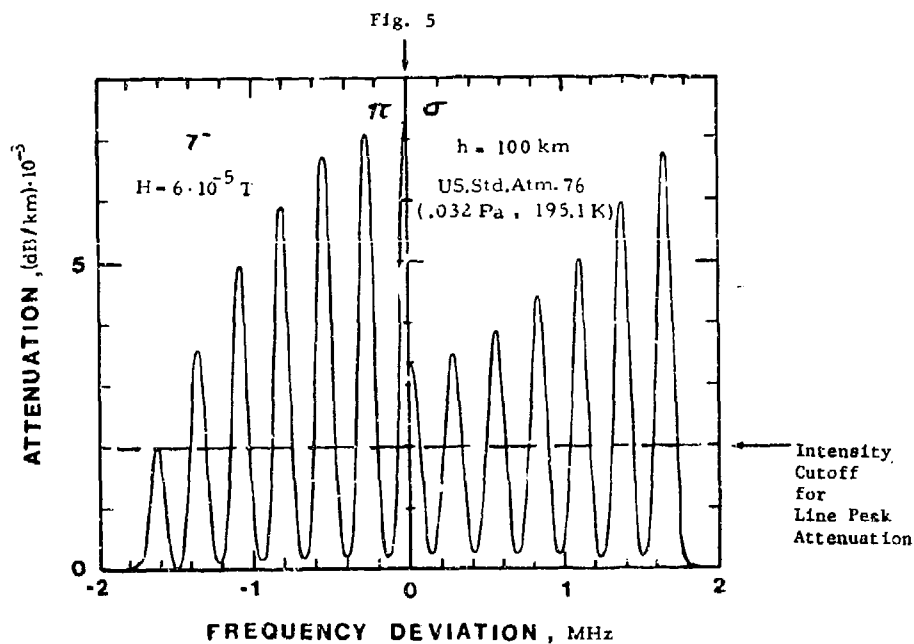


Fig. 6. Zeeman patterns π and $\sigma = \sigma^+ + \sigma^-$ for the 7^- line at an altitude, $h = 100 \text{ km}$.

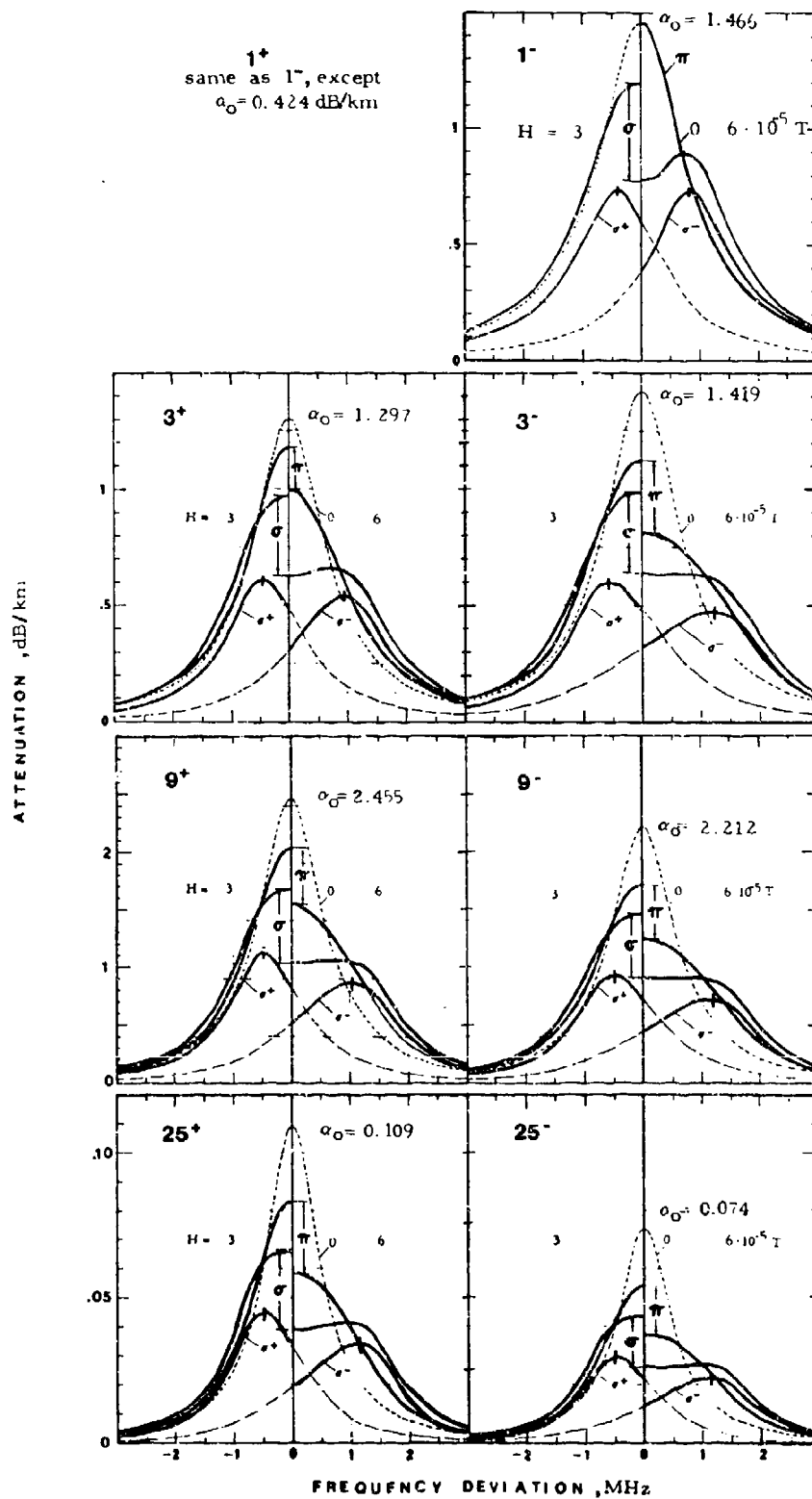


Fig. 7. Typical examples of O_2 -MS Zeeman patterns for $K^+ = 1, 3, 9$, and 25-lines at $h = 53 \text{ km}$ ($p = 42.5 \text{ Pa}$ and $T = 260.8 \text{ K}$ -U.S. Std. Atm. 76) for two magnetic field strengths, $H = 3$ (left half), $H = 6$ (right half) $\times 10^{-5} \text{ T}$, and the unsplit line, $H = 0$.

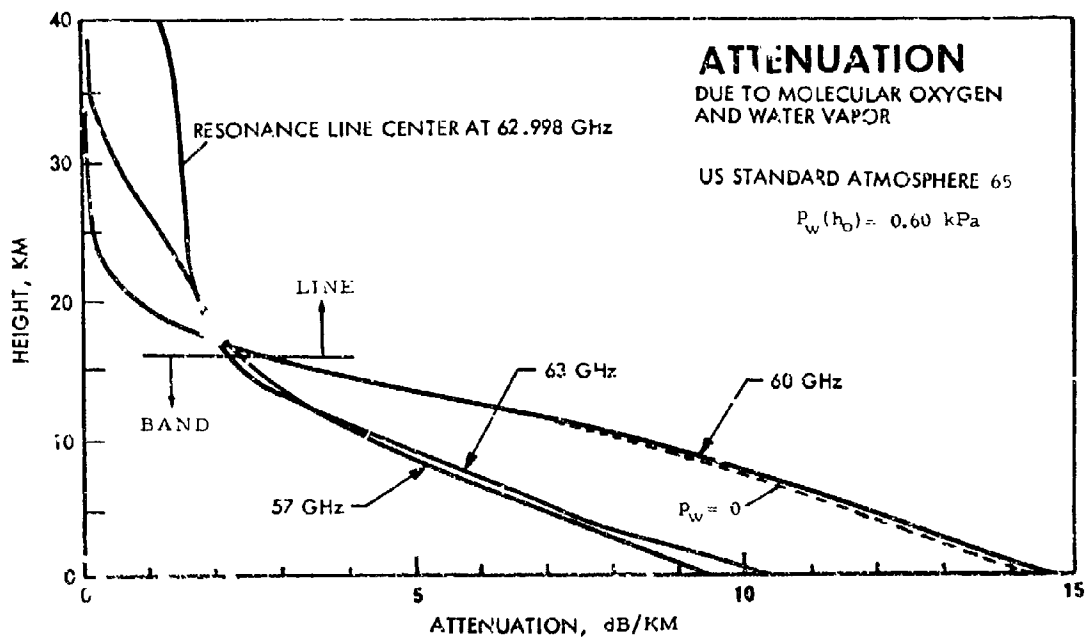


Fig. 8. Attenuation rates α versus altitude h at three frequencies within the O_2 -MS band.

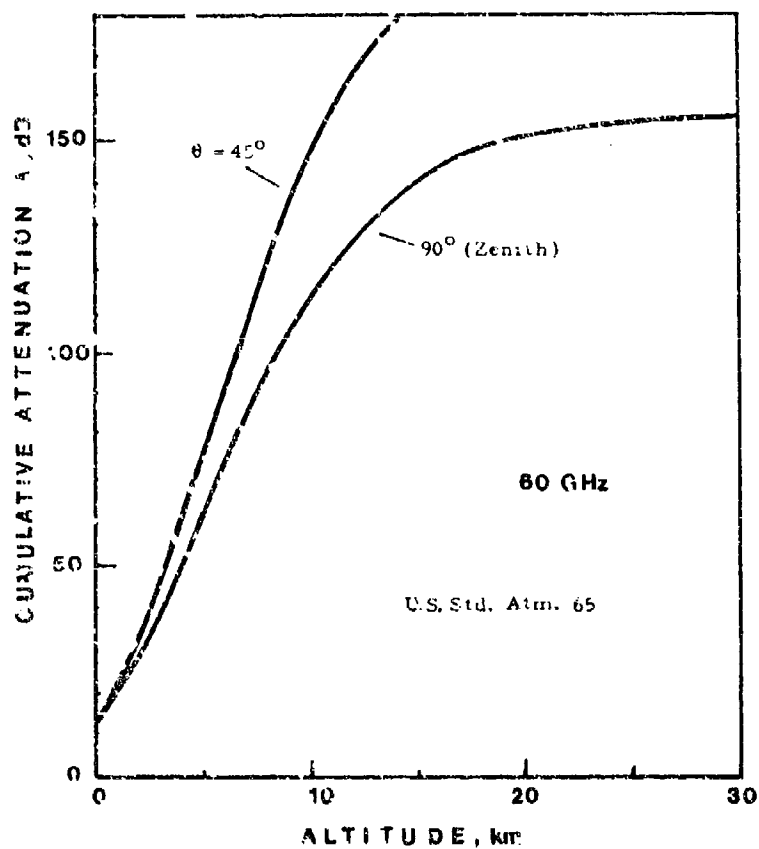


Fig. 9. Increase in cumulative attenuation A with altitude h at 60 GHz for two slant path angles θ .

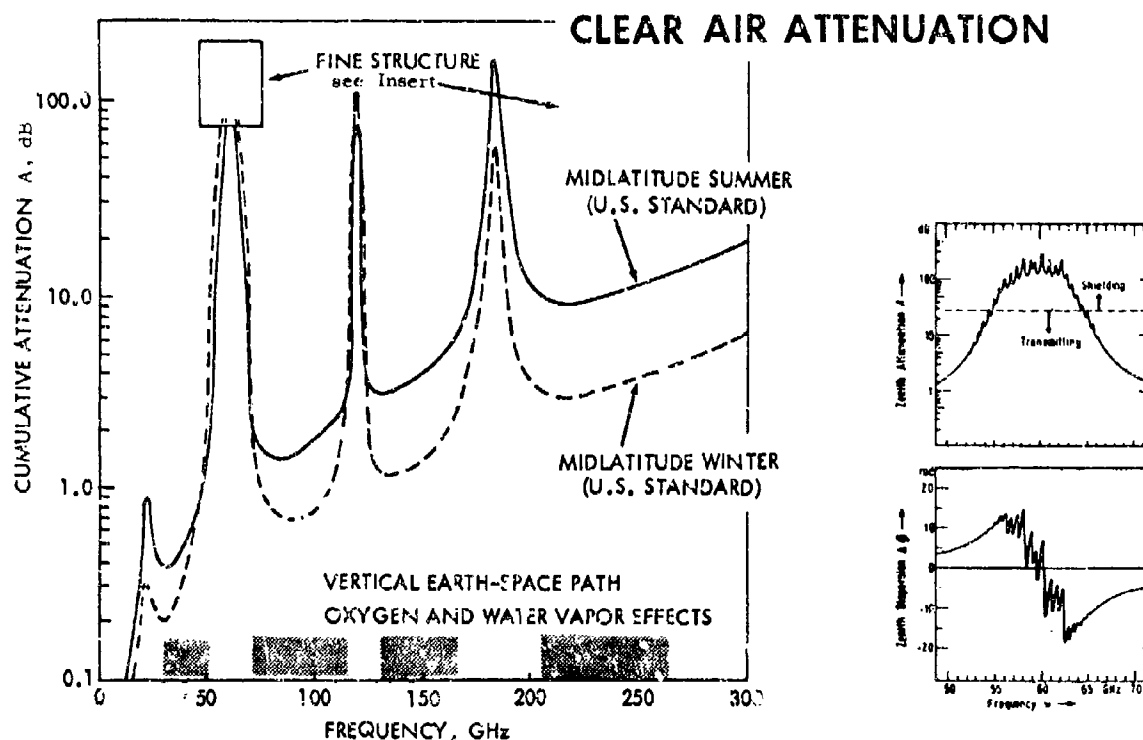


Fig. 10. Cumulative EHF zenith attenuation from surface ($h_0 = 0$) to outer space ($h_1 = 100$ km) for a summer (at $h_0 = 0$: $p = 101$, $p_w = 1.90$ kPa, $t = 1.020$ or 21°C) and winter ($p = 101$, $p_w = 0.44$ kPa, $t = 1.102$ or -1°C) atmosphere.

Cumulative phase dispersion, $\Delta\phi = \int_0^{80\text{ km}} \varphi(\nu) d\nu$.

ATMOSPHERIC NOISE TEMPERATURE

RAYLEIGH-JEANS APPROXIMATION
VERTICAL RAY PATH

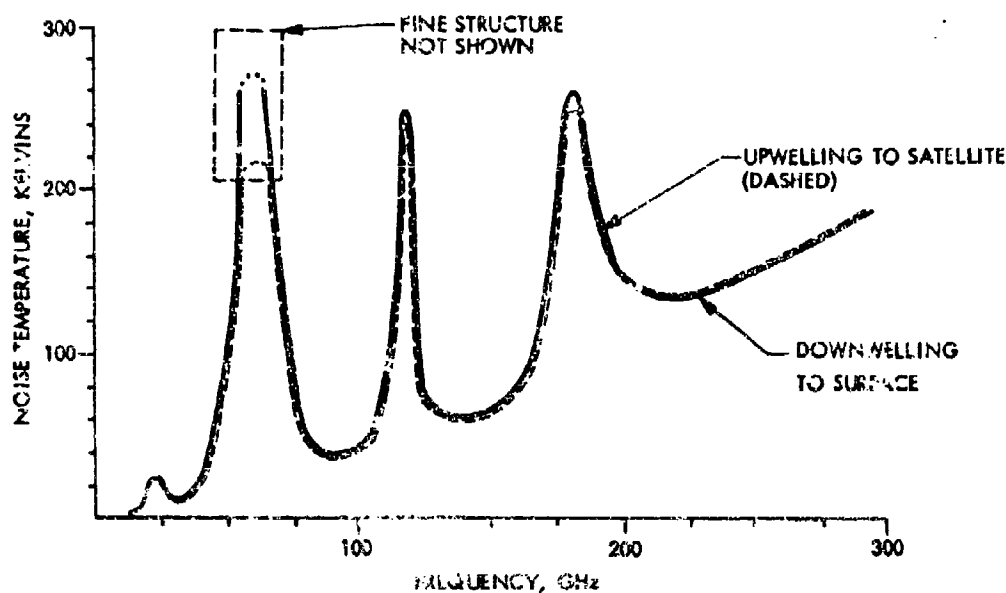


Fig. 11. Atmospheric noise temperature downwelling to the surface and upwelling to a satellite in zenith direction from the U.S. Standard midlatitude winter atmosphere.

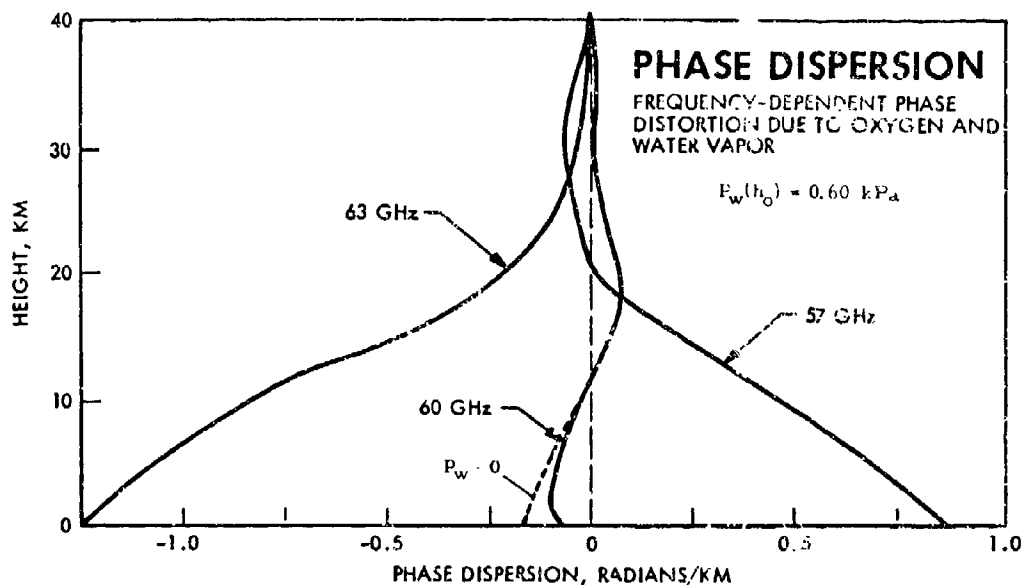


Fig. 12. The dispersive phase rate $\varphi(v)$ as a function of altitude for three frequencies in the O_2 -MS band.

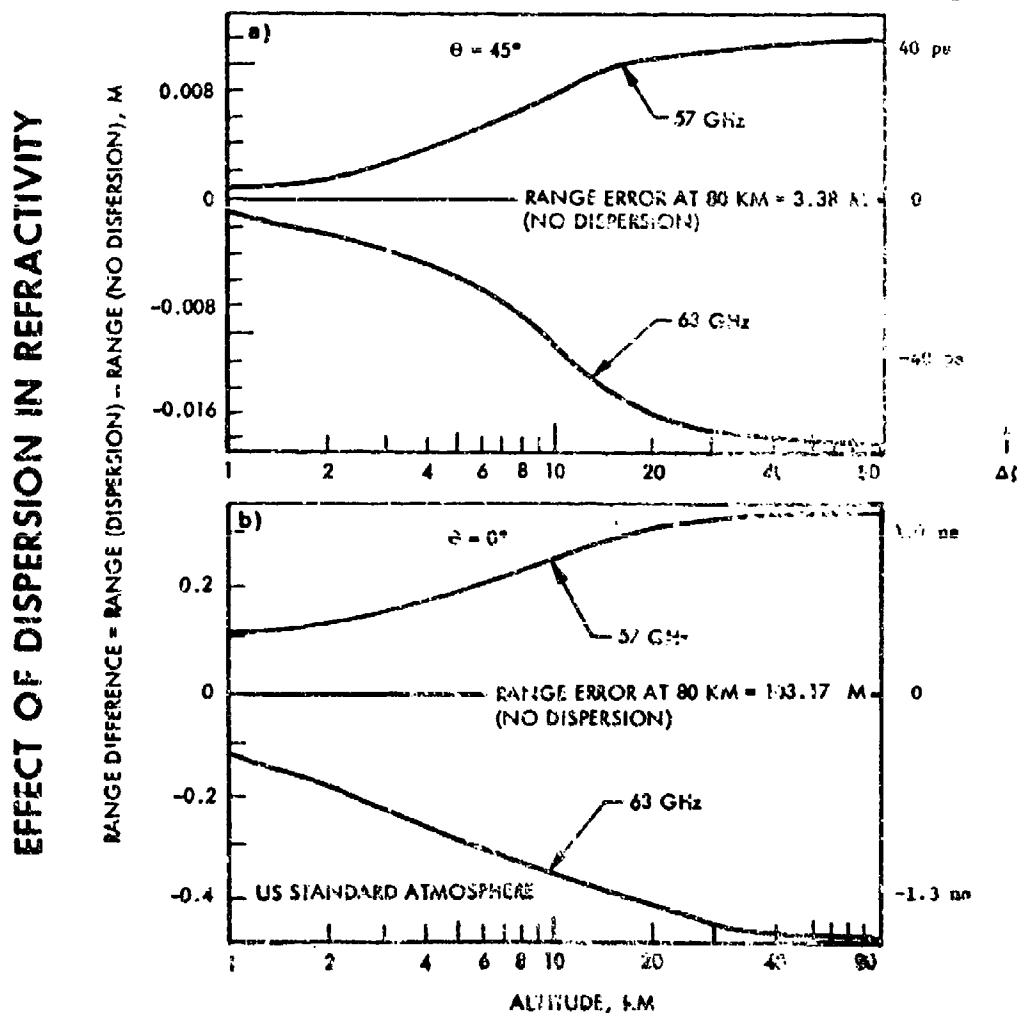


Fig. 13. Range error due to molecular phase dispersion (see Fig. 12) as a function of altitude for two frequencies within the O_2 -MS band: a) $\theta=45^\circ$ and b) $\theta=0^\circ$ (tangential path). The refractive radio range $R(N_0)$ for $h=0$ to 80 km is also given.

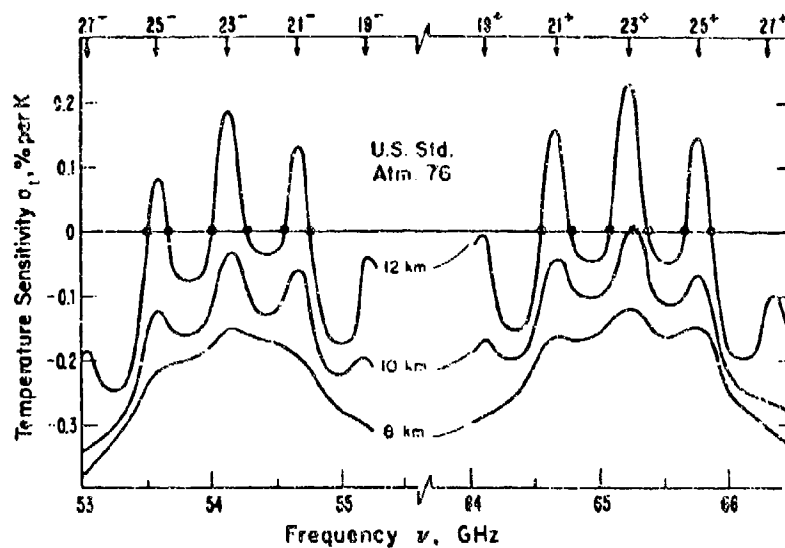


Fig. 14. Search for temperature-independent O_2 -MS attenuation [$a_t = (\partial a/\partial T)/a$] in the U.S. Standard Atmosphere 1976 (NOAA, 1976).

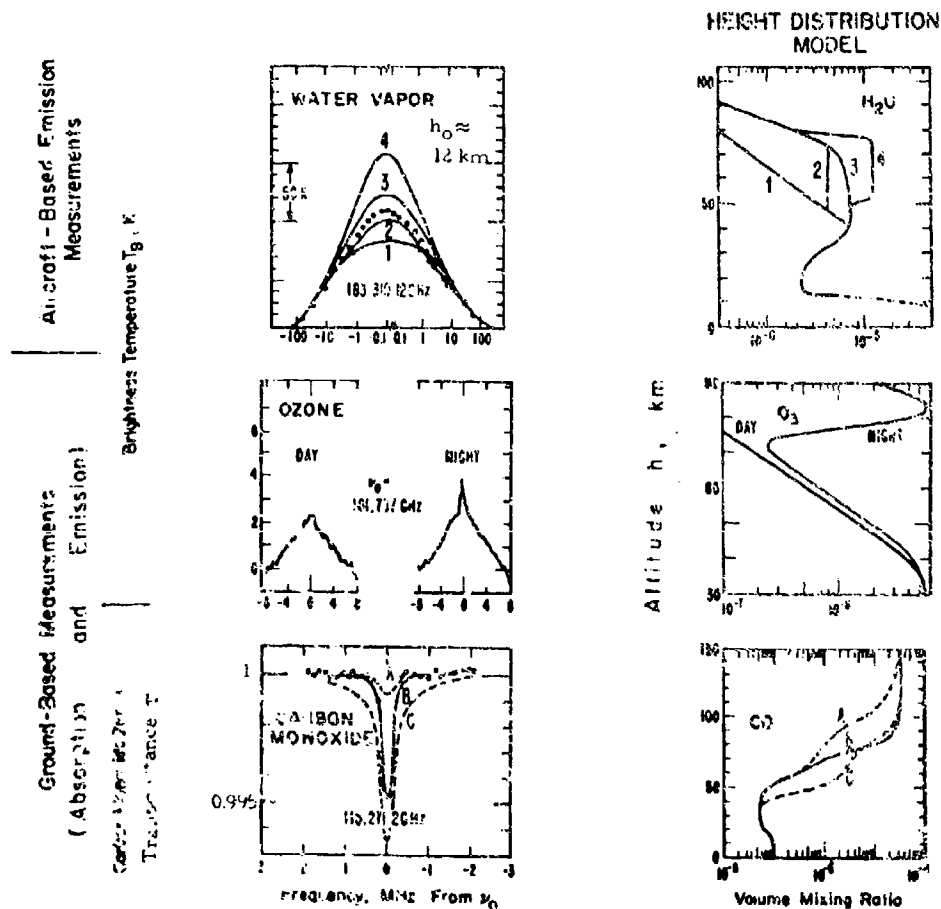


Fig. 15. Aircraft- and ground-based emission and absorption high altitude line shape measurement of H_2O (WATERS and WOPSY, 1974), O_3 (SHIMABUKURO et al., 1975), and CO (WATERS et al., 1976) and various height distribution models of the species for attempts to fit the data.

DISCUSSION

Z. Houminer, Israel

How would the irregular structure of the atmosphere affect mm-wave propagation and do you have models describing it?

Author's Reply

The amplitude spectrum for mm-waves propagating in a turbulent, clear atmosphere, characterized by a complex refractive index, is modified by the imaginary (loss) part (see Ott, R.H., and M.C. Thompson, 1978, "Atmospheric Amplitude Spectra in Absorption Region", IRE Trans Antennas and Propagation, *AP-26* (2), 329-332 and references therein)

A COMPUTER MODEL DESCRIBING ATMOSPHERIC PROPAGATION OF MICROWAVES
FROM 1 TO 300 GHz INCLUDING DETAILED ATMOSPHERIC CONDITIONS AND
COMPARISON WITH EXPERIMENTAL DATA

H.J. Fluess

Messerschmitt Bolkow Blohm, GmbH, Unternehmensbereich Flugzeuge
 D-8000 München 80, Postfach 801160

SUMMARY

For the frequency region from 1 to 300 GHz, a computer model was written describing the most important atmospheric effects on microwave propagation. The calculation of attenuation, scattering and refraction is based upon existing theoretical and experimental investigations and fundamental physical relations. Since this model should primarily produce representative results for Germany, meteorological data evaluated from German significant weather map types were inserted into the model. These meteorological data include the probability of occurrence, temperature, pressure and humidity profile, type and probability of precipitation and clouds. Based upon these data some basic results were obtained and compared with available data of the statistical US-model atmospheres. For practical application of this computer model the reduction of the detection range of radars is shown as a function of different atmospheric conditions. In addition, first results of experimental and theoretical propagation investigations are presented.

1. INTRODUCTION

There are several different methods of determining the influence of the atmosphere on microwave propagation. It is a very reliable way to study the performance of each microwave system such as communication links and reconnaissance systems under varying atmospheric conditions by experimental test series. This has the disadvantage of being time-consuming and expensive. Another way is to use physical relations in computer models to simulate and predict atmospheric effects on microwave propagation. This saves time and costs. But the physical description in such models is often not adequate when the modelling has been simplified with respect to computer time and to special purposes. Therefore it is desirable to estimate the confidence level of a computer model by experiments at least in some points, in order to modify the model if necessary. For the wavelength region from 0.25 to 28 cm such a computer model is LOWTRAN 3B (SELBY, J.E.A. et al., 1976) which has been modified for general German weather situations (ECKL, W. et al., 1977). To cover the microwave region from 1 to 300 GHz, for operation research purposes (Integriertes Bewertungsmodell für Aufklärung, BORINET, E., 1977) a computer model was written which calculates

- signal attenuation
- scattering
- propagation path parameters for
 - any sensor target configuration and
 - realistic atmospheric conditions.

This paper describes the complete computer model, presents results for typical applications and first experimental data of propagation investigations together with theoretical ones.

2. TRANSFER CHARACTERISTICS OF THE ATMOSPHERE

The atmosphere influences electromagnetic waves in several ways: signal attenuation and scattering, changes in phase and polarisation, bending of propagation path and increase of background noise. These effects have been subjects of numerous theoretical and experimental investigations which each cover only single parts of the microwave region and/or some atmospheric conditions. However, the task consisted of finding out appropriate references and of adapting these to each other to treat the most important propagation effects in the microwave region from 1 to 300 GHz for the most occurring atmospheric conditions, adequately. The physical relations upon which the computer model is based are outlined as follows.

2.1 Attenuation and Scattering

The attenuation and scattering of signals is due to atmospheric gases, precipitation and clouds. As the physical law of superposition is valid for these effects too, their contributions can be treated separately and added.

2.1.1 Absorption by Atmospheric Gases

Absorption throughout the 1 to 300 GHz frequency region is due to molecular spectra of major (O_2 , H_2O) and minor (e.g. O_3 , CO , N_2O) constituents. Radiative transfer, spectral line absorption, total absorption through and emission by atmospheric gases have been reviewed by WATERS, J.W., 1976. Water vapor and oxygen have to be considered in the microwave region whereas the minor constituents can be ignored up to an altitude of 30 km. The mathematical description of the molecular spectra of water vapor and oxygen is based on the investigations of ROSENKRANZ, P.W., 1975 and LIEBE, H.J., 1977. For water vapor the spectroscopic parameters of 15 lines are taken into account, for oxygen the data of 41 lines (LIEBE, H.J., 1977).

2.1.2 Attenuation and Scattering by Precipitation and Clouds

Attenuation by water and ice particles is due to two physical effects: absorption and scattering. Both effects are considered for the different particles. To calculate attenuation and scattering by rain the single scattering theory of MIE, G., 1908 is used. Data of RAY, P.S., 1972 are used for the description of the dependency of the complex index of refraction of water and ice on temperature and frequency. Scattering in the near field is neglected because of a lack of appropriate descriptions. First-order multiple scattering may be expressed using the radar equation or in terms of the specific intensity (ISHIMARU, A., 1977). In principle, polarisation effects can be calculated (OGUCHI, T., HOSOYA, Y., 1974). In the computer model they are only roughly estimated, because no adequate meteorological description for deformed rain drops is available.

Attenuation and backscattering by snow is calculated according to CUNN, K.L.S., EAST, T.W.R., 1954. The results are reliable only for frequencies lower than 30 GHz, where the Rayleigh approximation is still valid. For higher frequencies, the complexity of snowflakes allows only rough approximations.

Rayleigh approximation is used to determine attenuation and scattering by clouds and fog up to frequencies of about 100 GHz because of the small size of water droplets and ice particles.

For frequencies greater than 100 GHz the complete Mie-formalism is used.

2.2 Refraction Effects

The index of refraction influences on one hand the propagation velocity of electromagnetic waves and on the other hand the propagation path outlined as follows. Since the tropospheric index of refraction is greater than unity the propagation velocity is slightly less than free space velocity. This produces a time delay which affects time-measuring systems. The deflection of the propagation path is caused by the variation of the real part of the air refractivity. In this computer model a ray tracing method based upon the integral method (EDENHOFER, P. et al., 1972) is used to determine the path parameters such as range and angle of refraction and angle of arrival. The index of refraction profile can be inserted directly into the program or is calculated from the meteorological parameters: temperature, pressure, and humidity. For frequencies less than 20 GHz the index of refraction is determined by the formulae of SMITH jr. E.K. and WEINTRAUB, S., 1952. In order to take into account dispersion, the refractivity of air is calculated for frequencies equal to and greater than 20 GHz according to LIEBE, H.J., 1977. For a wide application of the computer model an iteration technique was developed to calculate the position of an unknown target from radar data by forward recursion. By backward recursion this technique enables the determination of elevation angle and radar range for given radar and target position.

3. METEOROLOGICAL DATA

The computer model has been designed for two purposes, namely operational analysis and data correction. For operation research, system design and prediction purposes model atmospheres are used in this program whereas actual meteorological data are required for propagation measurements. To cover possible variations of atmospheric conditions the German Military Geophysical Office - GMGO - has determined two different types of model atmospheres

- statistical model atmospheres and
- model atmospheres representing the significant weather map types for West Germany.

3.1 Statistical Model Atmospheres

For pre-design purposes and very rough estimations 12 statistical model atmospheres, which were extracted from meteorological observations of the year 1973 in Germany, can be used (GMGO, 1975). They contain pressure, temperature and water vapor profiles and cover altitudes from 0 to 12 km in layers of 1 km. These model atmospheres are based upon the separate evaluation for

- the southern part of Germany (Munich area) and the northern part (Hannover area) and represent for each area
- the mean and extreme values for
 - summer (April - September) and
 - winter (October - March).

3.2 Significant Weather Map Types

For operational analysis and prediction characteristic and more detailed atmospheric conditions have to be considered. The GMGO has provided 64 vertical profiles of 8 significant weather map types for this purpose (GMGO, 1975). These are the - North, West, East and High one for summer and winter - . Their occurrence in 1973 is shown in figure 1. The weather map type West has a high percentage of occurrence of 60% per year due to the geographic location of Germany. Furthermore, each significant weather map type is divided into 4 profiles representing a day in six-hour intervals. These weather situations have been evaluated for North and South Germany. To take into account typical irregularities (inversion etc.) of the lower troposphere the vertical profiles are spaced in 100m intervals up to an altitude of 2km. Above this height the spacing is 1km up to 12km. The profiles of the significant weather map types contain not only pressure, temperature and humidity, but also precipitation rates and probability of occurrence for rain

and snow, and type of clouds with their typical size spectrum of droplets and their vertical extent. Following cloud types are considered:

- (1) Cumulus congestus, (2) Cumulus humilis, (3) Stratus fractus, Cumulus fractus
- (4) Stratocumulus, (5) Altostratus, (6) Altostratus, (7) Stratus, (8) Cirrus and combinations of these.

As rain drop size distribution we use the Marshall-Palmer spectrum which seems to be most appropriate for radar applications (ATLAS, D., 1964).

In table 1, for example, the meteorological data of the weather map type: West, Winter, South Germany, 12.00 - 18.00 are listed. The precipitation rate of 0,7 mm/hr indicates a steady rainfall in the order of one hour which is typical for this weather situation.

The general weather situations can be improved by weather reports from special stations in 1973 in order to make very realistic simulations of a given area for operation research (GMGO, 1976). Investigations of the GMGO have shown that the behaviour of the atmosphere in 1973 was normal with respect to other years (GMGO, 1977).

3.3 Actual Meteorological Data

For measurements of microwave propagation and correction of data obtained by microwave systems actual meteorological parameters have to be used. The structure of the computer model enables an easy exchange of data.

In addition to the set of the model atmospheres described above, model atmospheres for other areas, e.g. US-profiles, can easily be inserted into the program.

4. RESULTS

To show the variation of attenuation in the frequency region from 1 to 300 GHz for different atmospheric conditions some basic results obtained by the computer model are presented. Furthermore applications of this model for system design of communication and radar systems are shown. In addition, calculated and measured values of a propagation experiment are compared with respect to critical meteorological parameters and radar data.

4.1 Basic Statistical Results

To determine the design parameters of a communication link or of a radar the attenuation based upon statistical meteorological data is of interest. For this purpose an example is shown in figure 2, representing the upper and lower extreme values of attenuation per unit path length dependent on frequency for the Munich area, Summer '73 and sea level. One recognizes the absorption lines of water vapor at 22,235 GHz and 183,310 GHz and the absorption band of oxygen at 60 GHz and the isolated π line of oxygen at 118,750 GHz. Between these lines and bands there are the known atmospheric windows of relative high transmission. The attenuation values in the 30 GHz window ranges from 0,07 to 0,18 dB/km, in the 90 GHz region from 0,2 to 0,6 dB/km. The attenuation of the 130 GHz region is in the order of 1 dB/km. Corresponding calculations based upon the US-Standard Atmosphere of 1962 and the Supplemental Atmospheres as compiled in the Handbook of Geophysics and Space Environment (VALLEY, 1965) have shown that the upper values of attenuation are similar to those obtained with the Midlatitude Summer Atmosphere and the lower ones correspond with those obtained with the US-Standard Atmosphere of 1962.

As the meteorological data permit the use of winter and summer atmospheric conditions the average values of attenuation for winter and summer of the Munich Area are plotted versus frequency for comparison purposes in figure 3.

The winter values do not differ very much from the summer values due to the fact that the climate in Mid-Europe is maritime in comparison to the continental climate in USA. The variation of attenuation in one season is greater than the difference of the average values for summer and winter (compare fig. 2 and 3).

The absorption bands are very sensitive to changes in the content of water vapor and oxygen. The dependence of absorption from height can be seen in figure 4, in which absorption rates versus frequency are illustrated for sea level and an altitude of 10 km. The absorption peak and width of the water vapor lines are decreasing with increasing height. For oxygen the decrease is not so obvious. This sensitivity in peak and width of the molecular absorption offers possibilities to sense remotely the physical state of the atmosphere.

4.2 System Considerations

To determine the cumulative transfer characteristics along a slant path a numerical integration assuming a straight-line path through a spherically stratified, layered atmosphere must be carried out.

4.2.1 Influence of the Atmosphere on Communication Links

For ground to space links the total attenuation through the atmosphere has to be considered. The length of the propagation path varies with the zenith angle for links to aircraft and non-stationary satellites. Figure 5 gives an impression of the variation of attenuation for the following parameters: general weather situation West, Winter, South Germany without hydrometeors (table 1) and zenith angle and frequency. The calculations have been carried out for zenith angles of 0,30 and 80 degrees for the troposphere up to 12 km height. In this example the frequency region was limited to 100 GHz. Up to 20 GHz attenuation does not exceed 2 dB, in the 30 GHz-band it ranges

from 0,3 to 2 dB and in the 90 GHz region from 1 to 6 dB. In figure 6 the attenuation of the 60 degree zenith angle versus frequency is plotted for the weather conditions West, Winter, South Germany with and without a rainrate of 0,7 mm/hr and clouds as listed in table 1. Up to 20 GHz this light rain is not serious (less than 1 dB) whereas the rain becomes a detrimental factor (10 dB), for frequencies greater than 80 GHz. Therefore transmission in this frequency region can hardly be achieved under these weather conditions without space diversity.

4.2.2 Influence of the Atmosphere on Detection Radars

The performance of an active remote sensing system was investigated for different atmospheric conditions. The probability of detecting a target (SWERLING, P., 1954) by means of a Ku-band radar (17 GHz) was calculated for the propagation conditions: free space, clear air (a statistical model atmosphere) and rainrates of 6 or 12 mm/hr superimposed. Rain backscatter suppression was assumed to be better than 30 dB. The probability of detection versus range is illustrated in figure 7. For the 50% probability the relative difference of range is about 20% between free space (curve 1) and a rainrate of 12 mm/hr (curve 4).

For the weather situation West, Winter, South Germany with and without rainfall the probability of detection by two radars operating at 31 GHz and 90 GHz non-coherently with the same antenna (Diameter 1m) and peak power (20 KW) were calculated. The radar cross section of the target was assumed to be 10 m² for both frequencies. The rain backscatter was not suppressed. Figure 8 shows the results of the calculations. For the 50 per cent probability the reduction of range is about 50% for both radars (curve 1 - 2 for 31 GHz and curve 3 - 4 for 90 GHz). This can easily be explained when considering the volume backscatter of rain. For rain rates of 1, 6 and 12 mm/hr the volume backscattering cross section versus frequency is illustrated in figure 9. The cross sections have been calculated for linear polarized waves. The gradient of the backscattering cross section decreases with increasing frequency up to 100 GHz. Above this frequency the cross section decreases according to the rain rate. The volume backscatter coefficient of the rain rate of 1 mm/hr for 90 GHz is about five times greater than for 31 GHz. Having the same antenna the beamwidth in elevation and azimuth for 90 GHz is one third of that for 31 GHz. Although the attenuation for 90 GHz is about 6 times greater than for 31 GHz, the backscattering of rain causes the same relative reduction of radar range for both frequencies without rain clutter suppression.

4.3 Actual Propagation Measurements and Comparison with Theory

As outlined already it appears highly desirable to find out the conformity between the theoretical model and experimental results. Therefore propagation measurements are carried out to investigate the influence of the atmosphere on a high precision tracking system. One point of concentration is to study the diurnal variations of range and angle. A further aim is to find out by which meteorological data - statistical refractivity profile or actual profile - the atmospheric influence can be described adequately.

4.3.1 Measuring Range and Equipment

The experimental test series was started in summer 1977. The measuring equipment (LUTZ, G., 1977) consists of
- the tracking radar AN/MPS 36 operated by the DfVLR/German Space Operation Center operating in the C-band with a resolution of 0,9m and
- a transponder.

The tracking radar stands in Workorzell near Ingolstadt on a hill 536m high. The transponder is placed on the top of the Zugspitze, the highest mountain in Germany at 2963m (figure 10). Both locations are geodetical points so that the slant range between the antennas can be determined exactly with 167,144 km with an error less than 0,3m. The elevation angle for line of sight is 0,07 degrees. The profile of the terrain is plotted in figure 11. There is one critical region for the radar beam up to a distance of 10 km from the radar location where the beam of 1,2 degrees width might touch the ground. The measurements might therefore be influenced by ground reflections.

4.3.2 Comparison of Measured and Calculated Data

The measured ranges were not corrected for any atmospheric effects in the radar processor. Measured radar ranges on 20th July 1977, and the theoretical range values obtained with the computer model are illustrated in figure 12. The dots represent the mean values of 300 range measurements during 5 minutes. Before and after these measurements the radar was calibrated in range and angle. The measurements carried out every half hour show an increase of 4m in the range of 167,187 km for 9.00 a.m. up to 11.00 a.m. due to the diurnal variation of the refractivity. An increasing cloud cover of 3/5 to 8/8 from 11.30 a.m. to 5.00 p.m. had a stabilizing influence on radar range. The variation of the radar range of 167,191 km is about 1,5m for this time interval. The range calculated for moon with the actual profile, represented by a cross in figure 12, lies within the error bars of the measured one. Using the CCIR-profile (figure 13) we obtained a radar range (cross with circle) which corresponds to the value of 10 a.m. It differs from the measured range by 2m and by 1,5m from the other one. It must be pointed out that the measured range is greater than the calculated one due to the fact that the actual profile is smoothed by interpolation, and

the natural fluctuations of the index of refraction over the propagation path are not grasped (fig. 13).

The experimental and theoretical results of five other days obtained as described above are shown in figure 14. The measured radar ranges agree well with those calculated. It seems to be sufficient to use actual meteorological data obtained half way between two points to determine the range in the order of 150 km with an accuracy of less than 2m. Therefore position determination could be done by a few range measurements of a high precision radar.

How far the exact position can be found out by measurements of range and angle the following diagram (fig. 15) demonstrates. A great discrepancy exists between measured and calculated elevation angle by this method due to ground reflections for angles less than 1,5 degrees (beam width 1,2 degrees). Furthermore, elevation angles less than 5 degrees suffer from strong scintillations indicated by the great error bars in figure 15.

The consideration of fluctuations of the index of refraction in the lower atmospheric layers near the measuring system might lead to better results for the critical parameter elevation angle. This test series is going on and there will be a report later and in more detail.

5. CONCLUSION

The results have demonstrated that the important atmospheric effects on wave propagation in the frequency region from 1 to 300 GHz can be sufficiently described by a computer model. This comprehensive model can be used for system design and evaluation problems in the Mid-European weather szenario because statistical and characteristic model atmospheres were made available by the GMDG. The program structure enables the easy insertion of other statistical and actual meteorological data for example for other areas and for special investigations of microwave propagation. The test series carried out to study atmospheric effects on precise position determination has shown that range measurements provide results with sufficient accuracy using one refractivity profile measured in the middle of the range. Measuring and calculating elevation angles by this method has proved to be critical.

6. ACKNOWLEDGEMENTS

This work was partially sponsored by the Ministry of Defense, under contract number T/R720/R7600/52002. I am very indebted to the scientists of the German Military Geophysical Office for providing the meteorological data and to the radar operators of the DfVLR/Oberpfaffenhoefen. It is a pleasure to thank Dr. W. Eckl and Dr. H.J. Albrecht for helpful comments regarding this work.

REFERENCES

- | | | |
|---|------|--|
| Atlas, D. | 1964 | "Advances in Radar Meteorology" Advances in Geophysics <u>10</u> 317-478, Academic Press, N.Y. |
| Bodinet, E. | 1977 | INBA 77, Zwischenbericht zum "Integrierten Bewertungsmodell für Aufklärung" Stand: Ende 1977 IABG B-SO-2064/06 |
| Edenhofer, P.
Glesner, D.
Harnischmacher, E.
Stein, V. | 1972 | "A Correction Method for Tracking Errors due to Atmospheric Refraction", Space Research XII, 1205-1214, Akademie Verlag, Berlin. |
| Eckl, W.
Flüß, H.
Hallwachs, H. | 1977 | "Calculations of Extinction and Scattering in the Wavelength Range of 0.25 - 15 μ m by Hydrometeors in General German Weather Situations", Proceedings of AGARD - Symposium on "Operational Modeling of the Aerospace Propagation Environment", this issue |
| German Military
Geophysical Office | 1975 | "Problemanalyse Wetterabhängigkeit von Aufklärungssensoren" Studie Nr. 75146 |
| | 1976 | "Vertikalprofile, Tropfenspektren und daraus abgeleitete Größen für die Atmosphäre in Mitteleuropa", Studie Nr. 76148 |
| | 1977 | Das Referenzjahr 1973 Studie Nr. 77135
Das Bodenwetter - Szenarium Studie Nr. 77169 |
| Gunn, K.L.S.
East, T.W.R. | 1954 | "The microwave properties of precipitation particles", Quart. J. Roy. Meteorol. Soc., <u>80</u> , 522-542 |
| Ishimaru, A. | 1977 | "Theory and Application of Wave Propagation and Scattering in Random Media", Proceed. of the IEEE, vol. 65,7. |
| Liebe, H.J. | 1977 | "EHF Properties of Air", NTZ <u>30</u> , 1, 76-84 |
| Liebe, H.J.
Gimnestad, G.G.
Hopponen, J.D. | 1977 | "Atmospheric Oxygen Microwave Spectrum - Experiment versus Theory", IEEE AP-25,3, 327-345 |

- Lutz, G. 1977 "Kurzbeschreibung des Bahnvermessungsradar" AN/MPS 36 DfVLR, Oberpfaffenhofen.
- Mie, G. 1908 "Beiträge zur Optik trüber Medien, speziell Kolloidaler Metallösungen", Ann. Phys., 25,377-445
- Oguchi, T. 1974 "Differential Attenuation and Differential Phase Shift of Radio Waves due to Rain", J. de Recherches Atmospheriques, 8, 1-2, 121-128
- Ray, P.S. 1972 "Broadband Complex Refractive Indices of Ice and Water", Appl. Optics 11,8,1836-1843.
- Rosenkranz, P.W. 1975 "Shape of the 5mm Oxygen Band in the Atmosphere", IEEE AP-23,4, 498-506.
- Selby, J.E.A. 1976 "Atmospheric Transmittance from 0.25 to 28.5 μ m: Supplement LOWTRAN 3B", Air Force Geophysics Lab. Rep. No. AFGL-TR-76-0258.
- Shuttle, E.P.
McClatchey, R.A. 1952 "The Constants in the Equation for Atmospheric Refractive Index at Radio Frequencies", CRPL, NBS, Boulder Co. Rep. No. 1938.
- Smith Jr., E.K.
Weintraub, S. 1954 "Probability of Detection for Fluctuating Targets." RM-1217.
- Swerling, P. 1965 "Handbook of Geophysics and Space Environments", AFCL
- Valley, S.L,Ed. 1976 "Absorption and emission of microwave radiation by atmospheric gases" in "Methods in Experimental Physics", vol. 12B, M.L. Meeks, Ed. N.Y. Academic Press.
- Waters, J.W.

Table 1: Vertical profile for general German Weather condition:
West, Winter, South Germany, 12.00 - 18.00 Z,
Probability of Occurrence 28%

HEIGHT [KM]	PRESSURE [MHAR]	TEMPERAT. [KELVIN]	ABSOLUTE HUMIDITY [G/M3]	DWINE DENSITY [G/M3@-5]	H2O-CONT. OF CLOUD [G/M3]	CLOUD SPECTRUM	PROB. OF CLOUDS [%]	PRECIPITATION [MM/HR]	PRECIPIT. RATE [MM/HR]	UNDERCOOL. OF PRECIP. [K]	PROBAB. OF PREC. [%]
0.000	958.	279.3	6.50	3.8	0.00		0.00	RAIN	.70	0.0	20.0
.100	946.	282.7	6.40	3.8	0.00		0.00	RAIN	.70	0.0	20.0
.200	934.	287.7	6.40	3.8	0.00		0.00	RAIN	.70	0.0	20.0
.300	922.	292.6	6.10	3.8	0.00		0.00	RAIN	.70	0.0	20.0
.400	911.	291.9	6.00	3.8	0.00		0.00	RAIN	.70	0.0	20.0
.500	900.	291.1	5.80	3.8	0.00		0.00	RAIN	.70	0.0	20.0
.600	890.	289.7	5.70	3.8	0.00		0.00	RAIN	.70	0.0	20.0
.700	879.	279.2	5.20	3.8	0.00		0.00	RAIN	.70	0.0	20.0
.800	868.	279.3	5.50	3.8	0.00		0.00	RAIN	.70	0.0	20.0
.900	858.	279.7	6.40	3.8	.16	4	75.00	RAIN	.70	0.0	20.0
1.000	848.	280.5	7.70	3.8	.16	4	75.00	RAIN	.70	0.0	20.0
1.100	838.	280.6	7.70	4.0	.16	4	75.00	RAIN	.70	0.0	20.0
1.200	827.	286.3	6.90	4.1	.16	4	75.00	RAIN	.70	0.0	20.0
1.300	817.	280.2	6.50	4.3	0.00		0.00	RAIN	.70	0.0	20.0
1.400	807.	280.1	6.10	4.4	0.00		0.00	RAIN	.70	0.0	20.0
1.500	796.	280.1	5.70	4.6	0.00		0.00	RAIN	.70	0.0	20.0
1.600	786.	279.5	5.30	4.8	0.00		0.00	RAIN	.70	0.0	20.0
1.700	776.	279.0	4.90	4.9	0.00		0.00	RAIN	.70	0.0	20.0
1.800	767.	278.6	4.50	5.1	0.00		0.00	RAIN	.70	0.0	20.0
1.900	759.	278.0	4.10	5.2	0.00		0.00	RAIN	.70	0.0	20.0
2.000	749.	277.4	3.80	5.4	0.00		0.00	RAIN	.70	0.0	20.0
2.100	740.	276.9	3.70	5.0	.12	6	75.00	SNOW	.70	0.0	20.0
2.200	734.	263.7	2.00	5.7	0.00		0.00		0.00	0.0	0.0
2.300	727.	258.2	.70	5.2	0.00		0.00		0.00	0.0	0.0
2.400	720.	252.9	.45	4.9	0.00		0.00		0.00	0.0	0.0
2.500	714.	246.1	.75	4.7	.02	8	25.00		0.00	0.0	0.0
2.600	707.	235.2	.15	4.4	.02	8	25.00		0.00	0.0	0.0
2.700	697.	231.1	.10	5.0	0.00		0.00		0.00	0.0	0.0
2.800	687.	229.2	.05	7.2	0.00		0.00		0.00	0.0	0.0
2.900	677.	229.0	0.00	11.0	0.00		0.00		0.00	0.0	0.0
3.000	670.	228.8	0.00	14.0	0.00		0.00		0.00	0.0	0.0

4 Stratocumulus
6 Altostratus
8 Cirrus

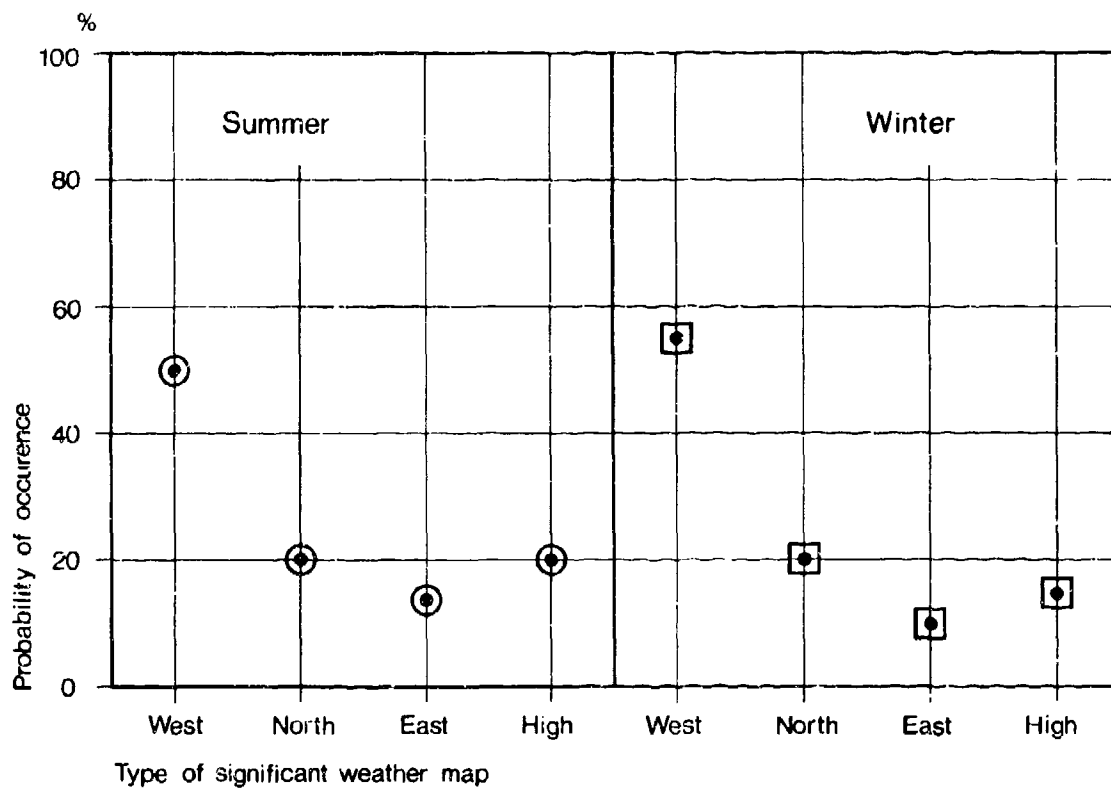


Figure 1. Probability of occurrence of significant German weather map types

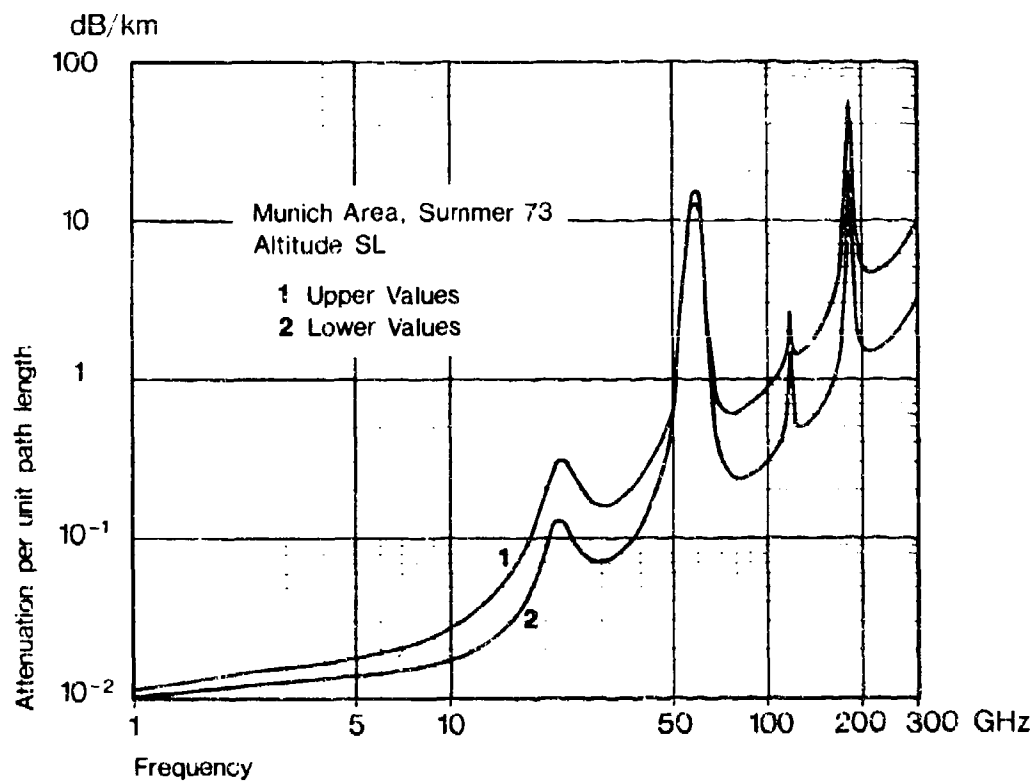


Figure 2. Upper and lower attenuation coefficients versus frequency for Summer 73, Munich Area and sea level

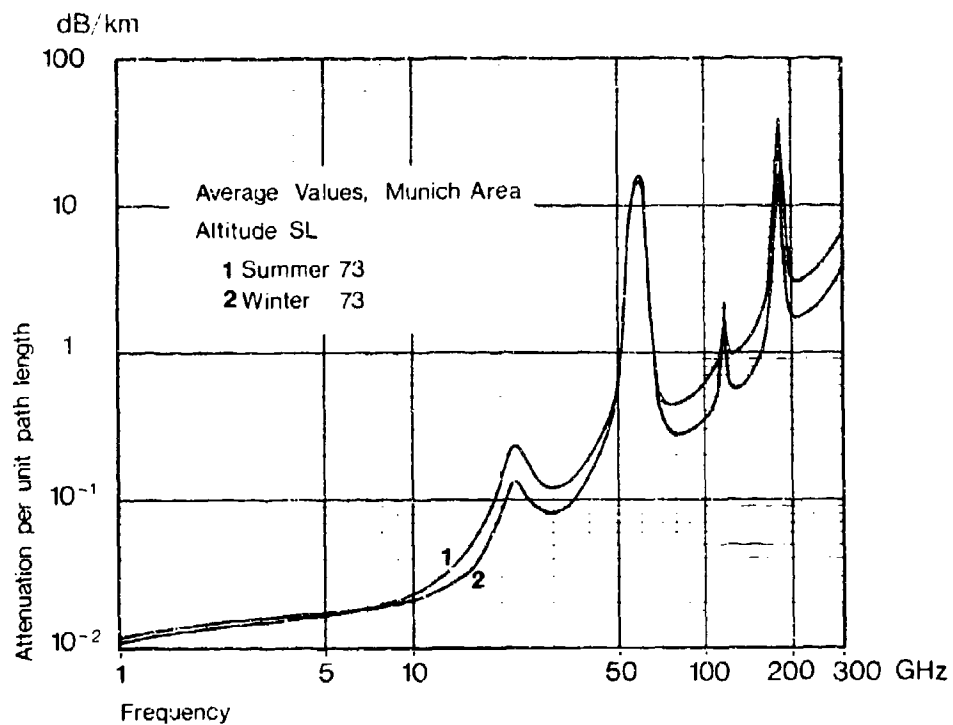


Figure 3. Comparison of summer and winter attenuation coefficients

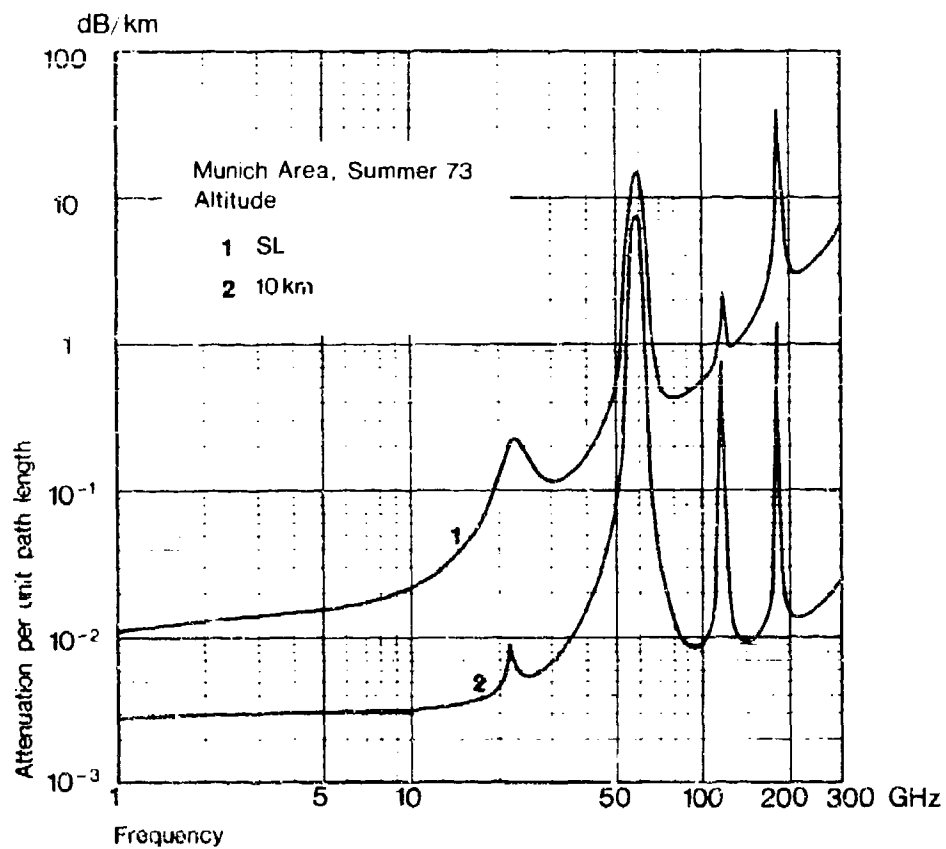


Figure 4. Attenuation coefficients versus frequency for sea level and 10 km height

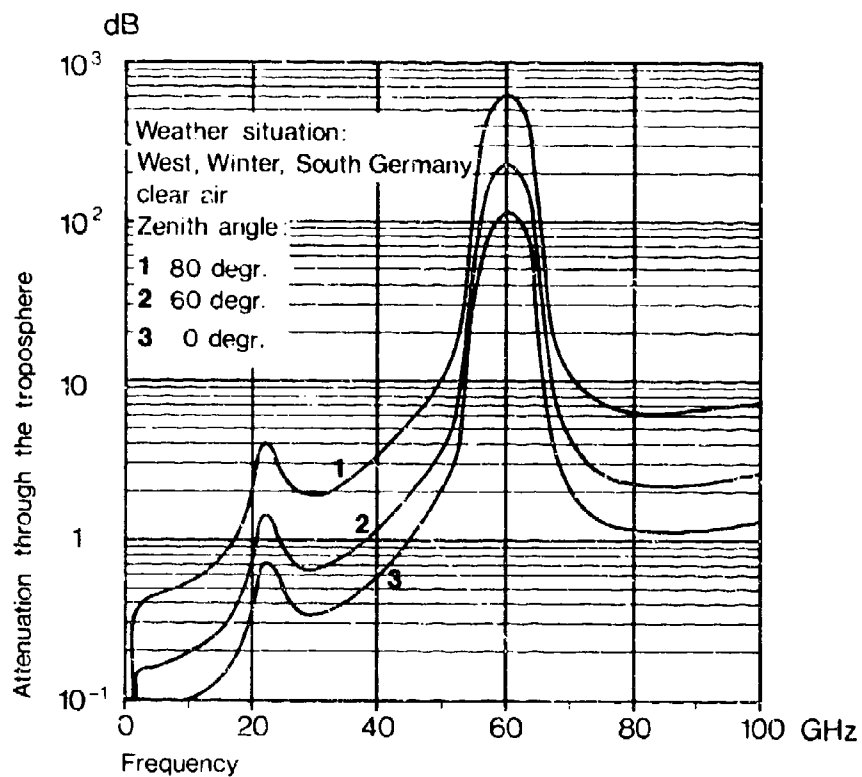


Figure 5. Total attenuation through the troposphere versus frequency for a general German weather situation without precipitation

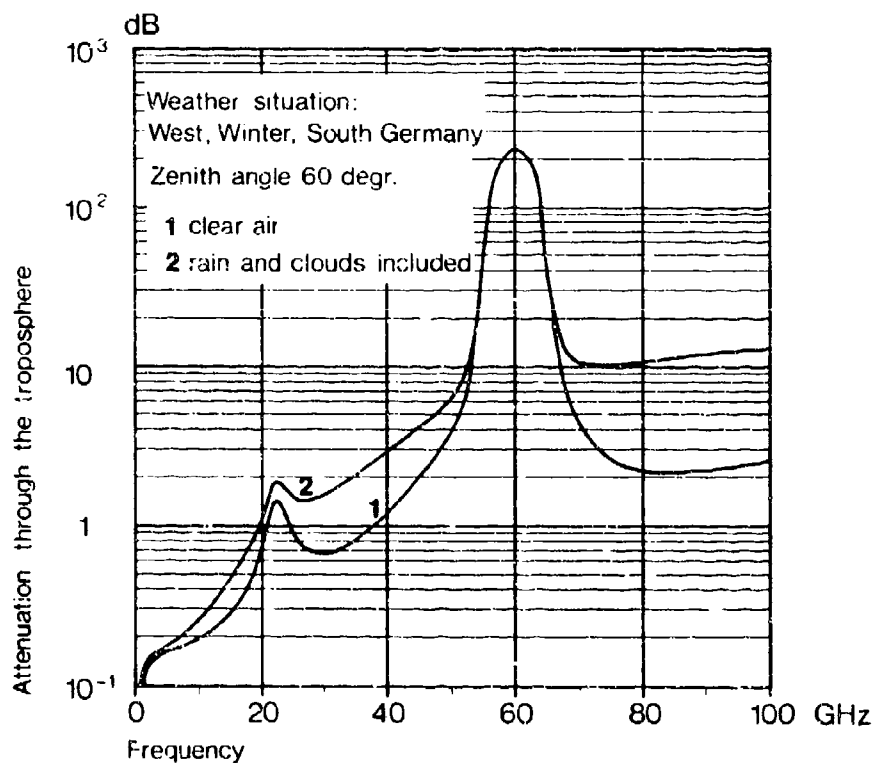


Figure 6. Total attenuation through the troposphere versus frequency for a general German weather situation with precipitation

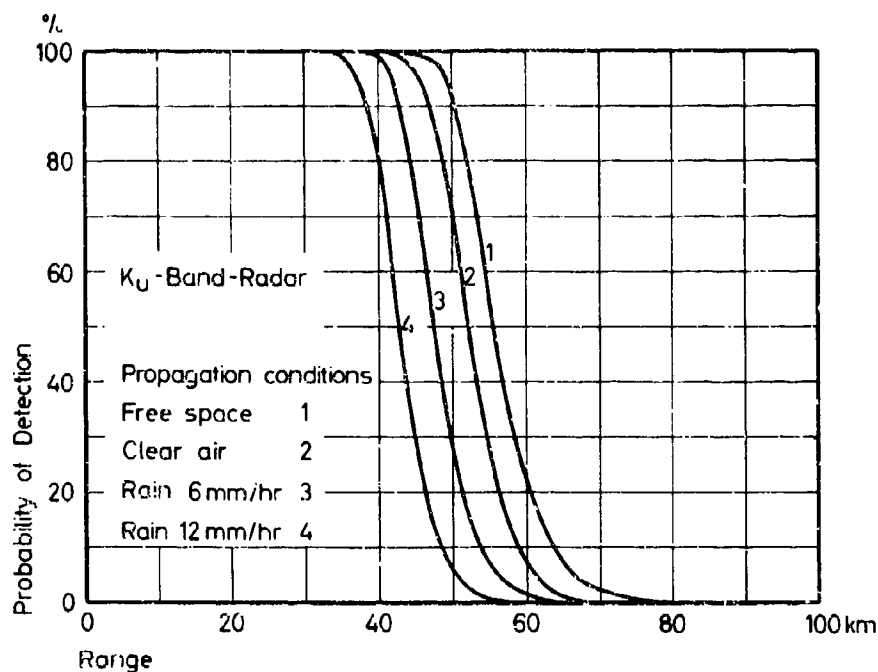


Figure 7. Influence of different propagation conditions on the probability of detection of a K_U-band radar

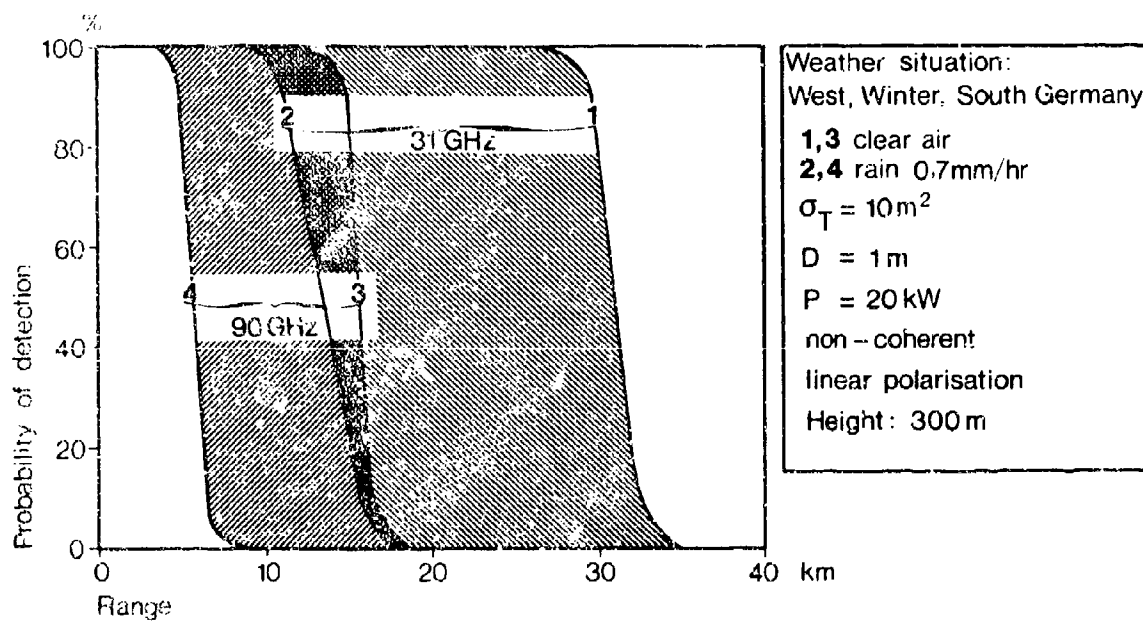


Figure 8. Reduction on the detection range of a 31 GHz and 90 GHz radar for different atmospheric conditions

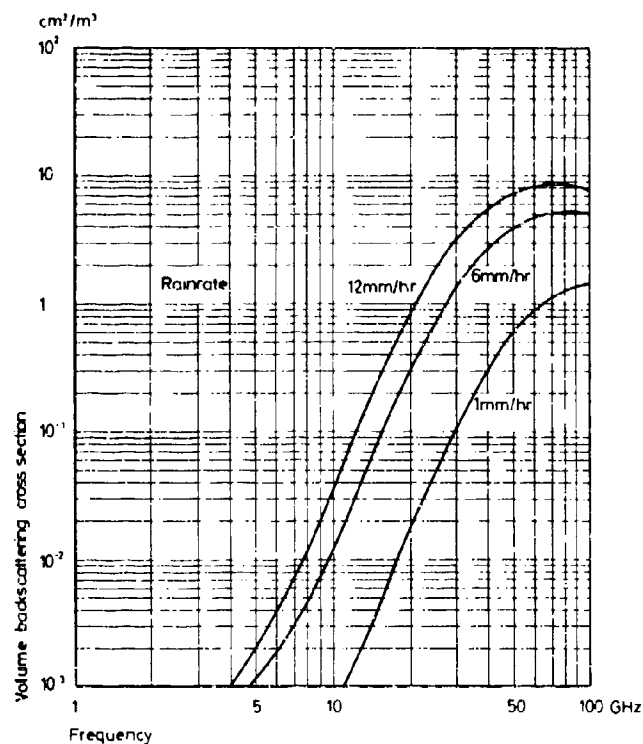


Figure 9. Volume backscattering cross section (linear polarisation) for different rain rates

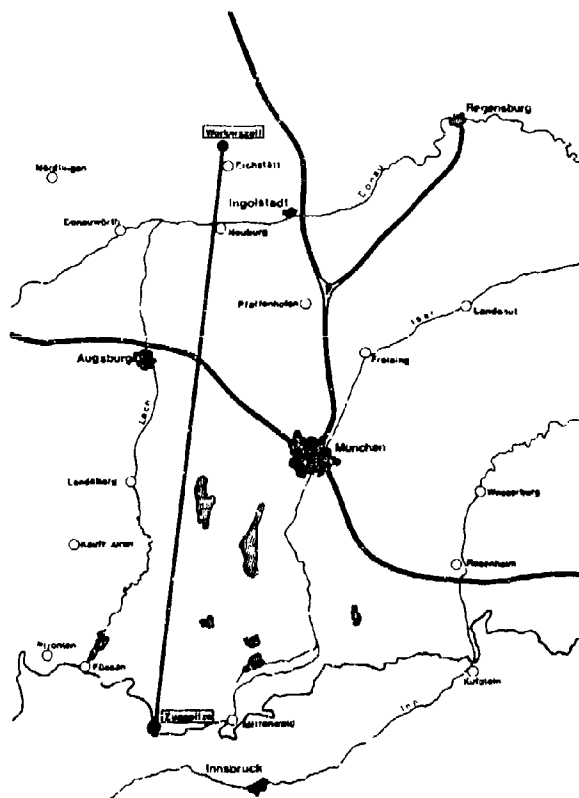


Figure 10. Map of the measuring range

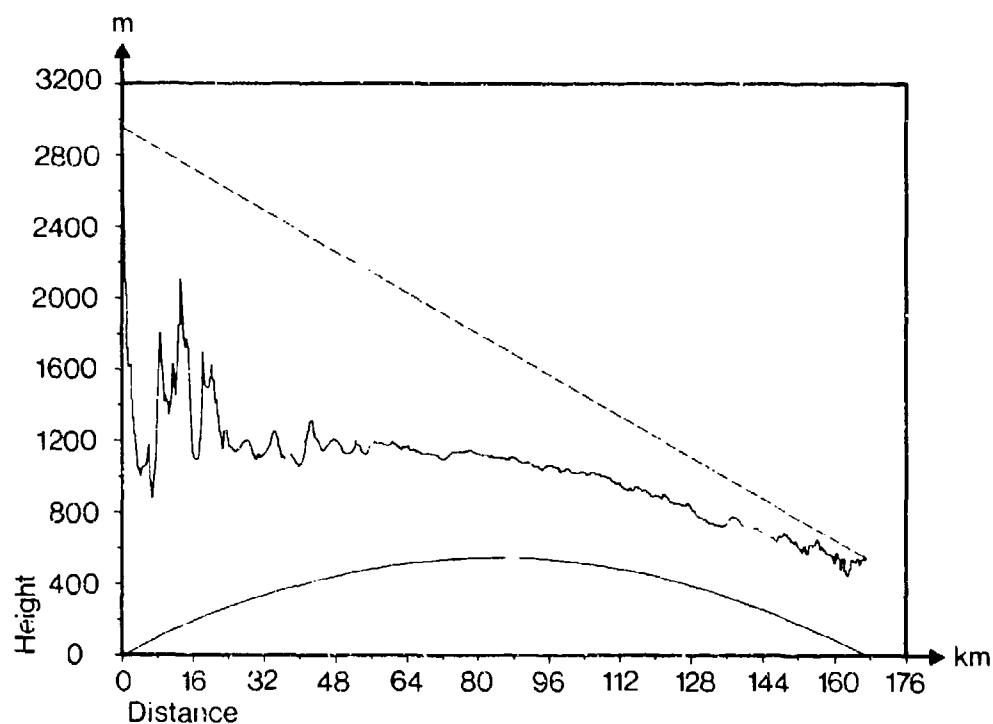


Figure 11. Terrain profile for the measuring range

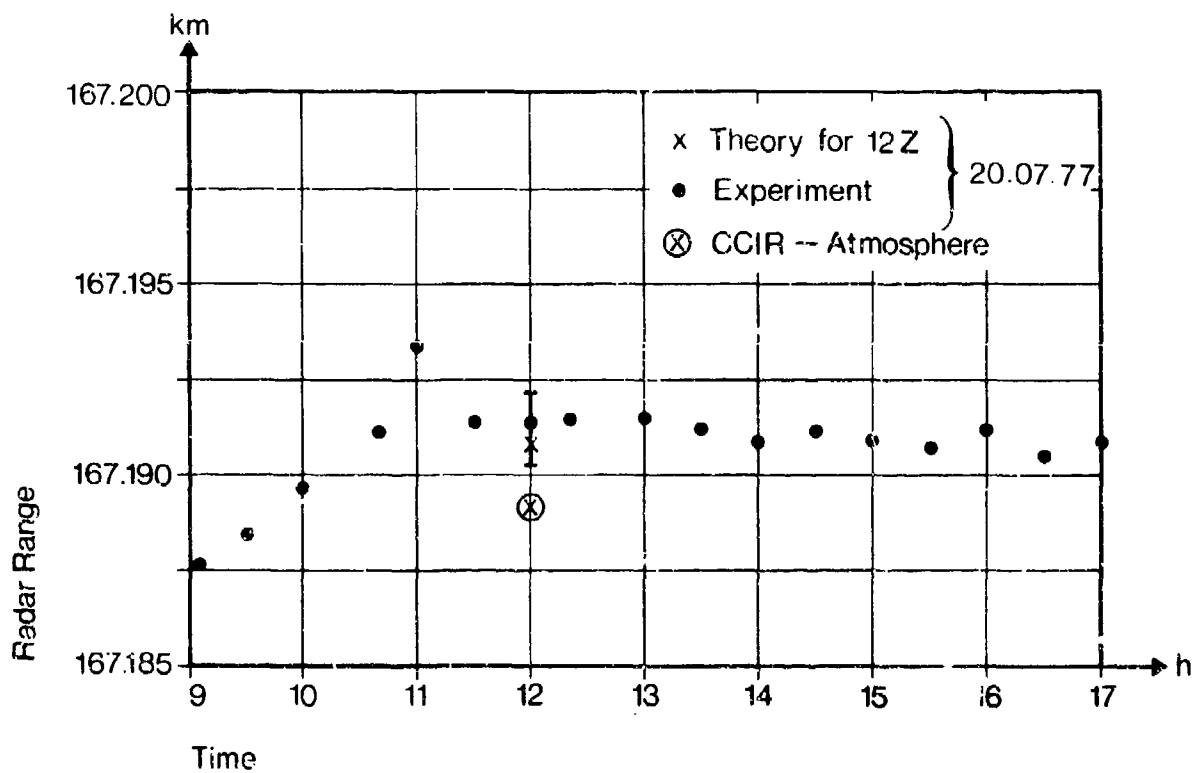


Figure 12. Measured range and calculated range on 20th July 1977

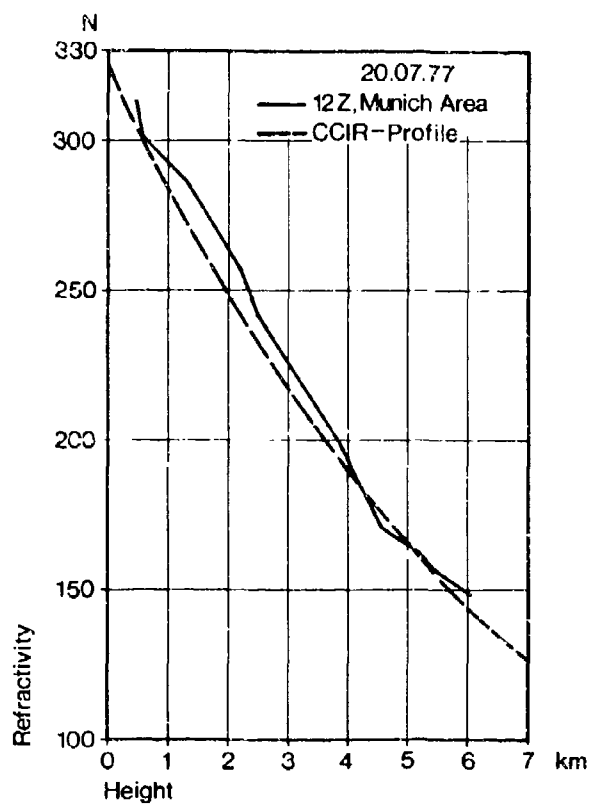


Figure 13. Refractivity profiles

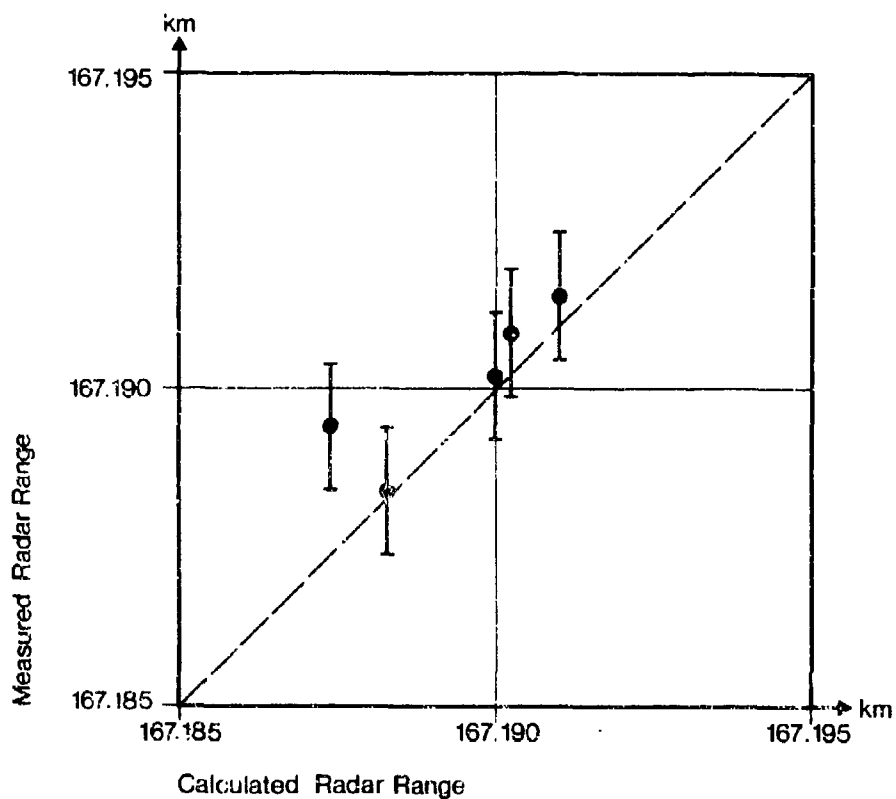


Figure 14. Comparison of measured and calculated radar ranges

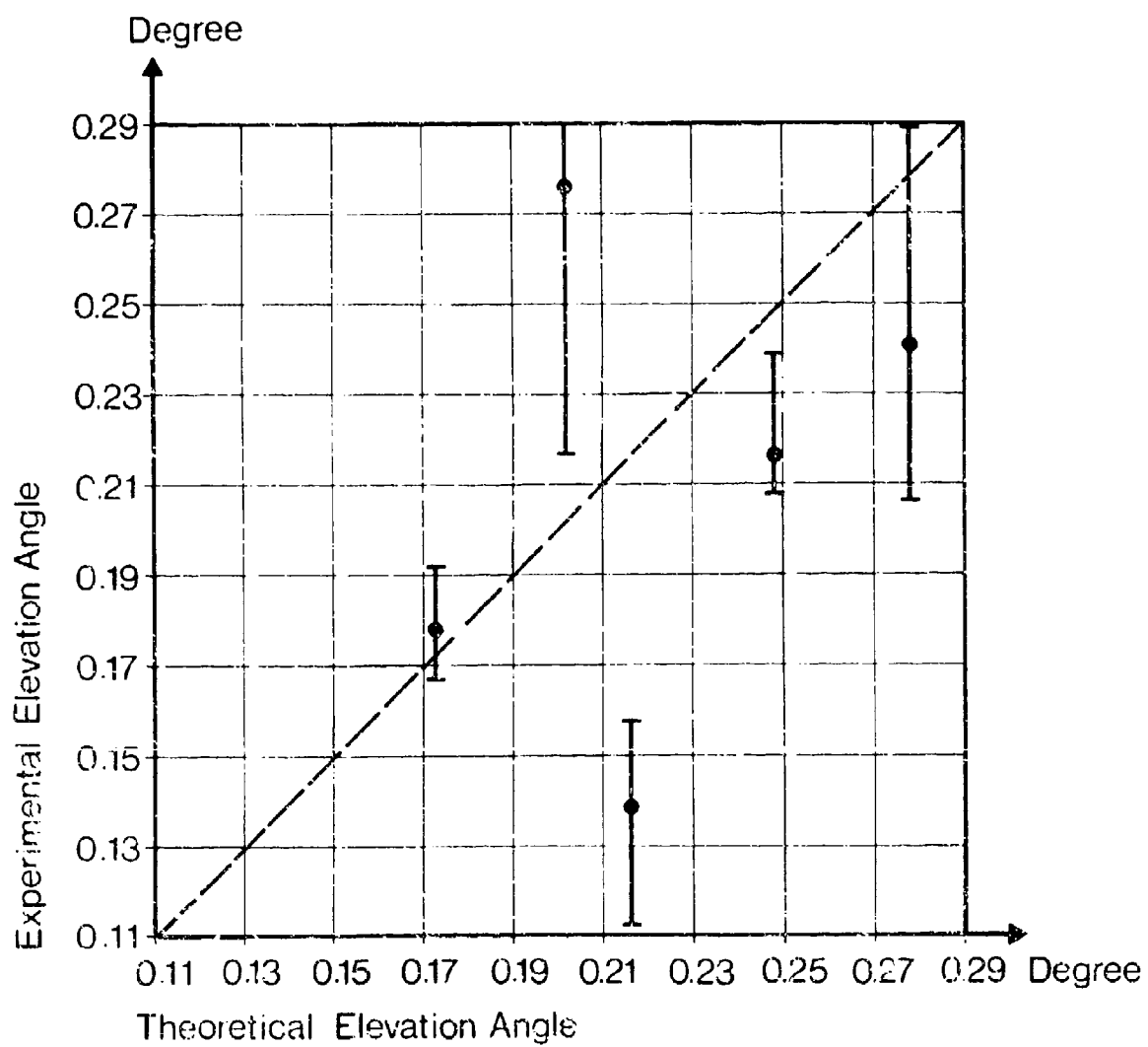


Figure 15. Comparison of experimental and theoretical elevation angles

DISCUSSION

J. Röttger, FRG

What defines the shape of the shown curve of the detection probability as function of distance for free space propagation?

Author's Reply

The shape of the detection curve is dependent on atmospheric attenuation and free space loss and on the detection mechanism which is used for the fluctuation of the target. Here we used the pulse-to-pulse fluctuation according to Swerling's case II.

Discussion note by J. Röttger

The accuracy of your method might be improved if you take into account the small-scale structure of refractivity variations in the troposphere. In Figure 1 I show an example for typical structures observed with a vertical-looking VHF radar operated by the Max-Planck-Institut für Aeronomie. This structure plot indicates time-varying layers of enhanced radar reflectivity which are caused by humidity and temperature variations (ref.: Röttger J., Klostermeyer J., Czechowsky P., Rüster R., Schmidt G., Remote Sensing of the Atmosphere by VHF Radar Experiments, to be published in Die Naturwissenschaften, 1978).

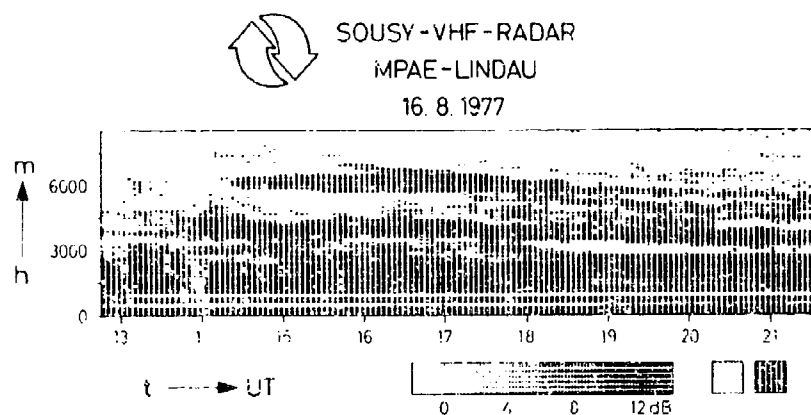


Figure 1

CARACTERISATION DE LA DISTORSION DU CANAL TROPOSPHERIQUE

par
A. Marguinaud
Thomson-CSF/DITM
55, rue Greffulhe
92301 Levallois-Perret

RESUME

L'exposé traite de trois sujets:

- description du dispositif expérimental permettant d'évaluer le canal,
- présentation et synthèse des résultats de mesure,
- remarques sur la conception du système de réception.

1. Le dispositif expérimental permet de mesurer en fonction du temps (100 fois par seconde), la fonction de transfert du milieu sur les 2 canaux d'une diversité d'espace.

Un autre dispositif permet d'obtenir avec une fréquence d'échantillonnage rapide (8000 fois par seconde) la valeur de l'amplitude et du retard de transmission.

Les valeurs mesurées sont enregistrées sur bandes magnétiques qui sont ensuite traitées par ordinateur.

2. Les mesures ont été effectuées pendant une durée de un an environ sur une liaison d'une distance de 140 km à 6 GHz, sur une bande de 10 MHz.

Les traitements réalisés sur ordinateur permettent d'évaluer la bande de cohérence, la stationnarité de la fonction de transfert, l'importance de la distorsion du point de vue énergétique et retard de propagation, la corrélation entre les paramètres caractéristiques de la distorsion, etc. .

3. Dans le cas de transmission numérique empruntant un canal distordu, on peut, soit chercher à corriger la fonction de transfert puis utiliser un démodulateur adapté à un canal parfait, soit comparer le signal reçu aux différentes versions de signaux élémentaires estimées d'après les signaux déjà démodulés. On montre que cette deuxième solution est toujours supérieure à la première si l'on tient compte des signaux précurseurs et postcurseurs.

1.- INTRODUCTION

Depuis quelques années, la technique de transmission par diffusion troposphérique permet d'envisager des débits élevés à condition de prendre en compte l'évolution de la distorsion du canal. Par exemple RAYTHEON et SYLVANIA présentent des équipements prévus pour 6 et 12 Mb/s. Plusieurs conceptions sont proposées pour la modulation, la démodulation, la mise en oeuvre de la diversité : modulation en quadrature à 4 phases (4 PSK), modulation de fréquence à déviation minimale (MSK), portillonnage temporel (time gating), filtre transverse, combinaison après démodulation, etc... La collecte de données précises et variées (temps et espace) est donc d'un grand intérêt, ce qui explique les campagnes de mesure actuellement menées par les organismes militaires. Cet exposé décrit le principe du banc de mesure réalisé pour enregistrer sur le terrain l'évolution de la fonction de transfert instantanée du canal. Ces enregistrements numériques sont prévus pour tester par simulation divers principes de réalisation de modem et de diversité dans les mêmes conditions. Par ailleurs, on propose une fonction caractéristique de la distorsion que l'on utilise ensuite pour évaluer le degré de corrélation entre les principaux paramètres de la liaison.

2.- DISPOSITIF EXPERIMENTAL

2.1 Description de la liaison

La liaison est réalisée en FRANCE, la partie émission est située à SERANS (région parisienne), la partie réception se trouve à LE BAHOT sur la Manche.

Les caractéristiques de la liaison sont les suivantes :

. distance géographique	135 km
. angle de site émission	- 1,62 mrd
angle de site réception	- 0,55 mrd
. distance de l'émission à son horizon	22 km
distance de la réception à son horizon	38,3 km
. altitude de l'émission	223 m
altitude de la réception	60 m
. diamètre de l'antenne émission	3,6 m
diamètre de l'antenne réception	3 m
. fréquence	6,375 GHz
. puissance émission	1 kW

On caractérise habituellement la difficulté rencontrée pour utiliser ce canal par leur bande de cohérence, c'est-à-dire l'écart de fréquence à partir duquel le coefficient de corrélation entre les amplitudes de deux fréquences porteuses est inférieur à $\frac{1}{e}$.

On considère que le débit en Mb/s que l'on peut transmettre sans précaution particulière est numériquement de l'ordre de grandeur de la bande de cohérence (en MHz).

Les calculs effectués à partir des modèles classiques donnent les valeurs médianes ci-dessous :

Modèle	SUNDE	RICE	BELLO-DANIELL
Bande de cohérence en MHz	3,4	9,3	30

Le dépouillement des mesures donne des valeurs instantanées variant entre 5 et 15 MHz. Ces résultats numériques confirment la nécessité d'une mise en oeuvre de procédés adaptés au canal.

2.2 Mesure de la fonction de transfert (fig. 1 et 2)

Le dispositif expérimental est construit autour d'un MLA (Microwave Link Analyser).

La fréquence porteuse du signal émis est de la forme $F + \Delta F \cdot \sin 2\pi f t$, expression dans laquelle les valeurs typiques pour les mesures sont :

$$F = 6,375 \text{ GHz}$$

$$\Delta F = 5 \text{ MHz}$$

$$f = 100 \text{ Hz}$$

La modulation est constituée par un signal dont le spectre présente deux composantes principales distantes de 1 MHz. A la réception, la comparaison de la phase de ces composantes permet l'estimation du temps de propagation de groupe. En pratique, le MLA récepteur est précédé d'un contrôle automatique de gain rapide (200 ns) qui fournit au MLA un signal de niveau variant dans une plage de 15 dB. Il en résulte que l'estimation de l'amplitude du signal doit être réalisée par un circuit développé spécialement pour l'application.

Les signaux analogiques enregistrés sont filtrés par un passe-bas de fréquence de coupure 3 kHz, puis échantillonnés et multiplexés à la fréquence de 8 kHz, et enfin numérisés (8 bits par échantillon) et enregistrés sur bande magnétique. Les principaux signaux enregistrés sont : la fréquence porteuse, l'amplitude et l'estimation du temps de propagation de groupe.

2.3 Mesure du temps de propagation de groupe (fig. 3)

L'émetteur émet avec une porteuse de valeur fixe, de sorte qu'en utilisant le même dispositif de réception et de numérisation que ci-dessus, on dispose de 8 000 valeurs du paramètre au lieu de 100 dans la mesure de la fonction de transfert. Par ailleurs, le principe utilisé fournit une estimation du retard de propagation. Notons qu'on enregistre en même temps l'amplitude du signal, ce qui permet, par exemple, d'étudier la corrélation du retard de propagation avec l'amplitude.

2.4 Etude de la diversité spatiale

L'objet de cette troisième approche était de déterminer si la décorrélation des niveaux des deux signaux reçus entraînait la décorrélation des distorsions aussi bien sur l'amplitude que sur le temps de propagation de groupe.

Le dispositif expérimental est identique à celui de l'émission de la liaison unique.

A l'autre extrémité de la liaison, on trouve deux chaînes de réception fournissant chacune le temps de propagation de groupe et l'amplitude en fonction de la position de la porteuse. Ces signaux sont ensuite échantillonnés, multiplexés et numérisés par le dispositif déjà décrit.

3.- TRAITEMENTS REALISES SUR ORDINATEUR

3.1 Préparation des mesures

On rappelle que les valeurs numériques citées ne sont que des exemples et qu'il faudrait des campagnes de mesures intensives pour en vérifier la stabilité statistique.

Tout d'abord, il s'agit de vérifier que les 3 paramètres caractéristiques du signal émis ont bien la valeur convenable ; il s'agit de la largeur de bande explorée (ΔF), de la fréquence de balayage (f) et de l'écart des composantes principales du signal de mesure. Après quelques tâtonnements, on a abouti aux valeurs citées au § 2.2 ; ce compromis a été déterminé à partir des caractéristiques du MLA et de l'enregistreur magnétique, des objectifs de l'expérimentation (10 Mb/s) et de la stationnarité du milieu. Les figures 4 et 5 représentent les histogrammes des écarts de mesures à une même fréquence en fonction de l'intervalle de temps qui les sépare. Ces résultats donnés à titre indicatif montrent que la qualité des mesures est suffisante pour les traitements décrits par la suite.

Un calcul simple montre qu'il ne serait pas raisonnable d'enregistrer les mesures sur de longues périodes, c'est pourquoi on enregistre seulement pendant des intervalles d'une minute déclenchés par un séquenceur. On a constaté expérimentalement que cet échantillonnage de l'information ne perturbait pas de façon sensible l'étude de la distorsion instantanée du signal.

Avant de procéder aux traitements intéressants sur l'étude du canal, on commence par valider les enregistrements, par exemple en vérifiant que la restitution de porteuse fournit

une courbe proche de la sinusoïde théorique (en phase et en fréquence). Une fois acquise la validation de l'enregistrement, il est nécessaire de remplacer par un calcul d'interpolation le balayage sinusoïdal en fréquence par un balayage linéaire pour ne pas biaiser les résultats des traitements ultérieurs.

3.2 Calculs de corrélation

La corrélation est pratiquement le seul outil utilisé, c'est la raison pour laquelle il convient de dégager avec soin les principes de ce calcul.

La formule 1 ci-dessous est l'expression classique permettant, en principe, de calculer le coefficient de corrélation ρ entre les variables x et y dont on connaît la suite des échantillons x_i, y_i .

$$(1) \quad \rho = \frac{\sum (x_i - \bar{x})(y_i - \bar{y})}{\sqrt{[\sum (x_i - \bar{x})^2][\sum (y_i - \bar{y})^2]}}$$

Pour calculer cette formule d'une façon générale, on se heurte à trois difficultés :

- . échelle de représentation des échantillons x_i, y_i .
- . estimation de \bar{x} et \bar{y} .
- . nombre d'échantillons à prendre en compte.

La solution adoptée dans les traitements a été de remplacer chaque valeur x_i par son rang. C'est-à-dire que x_i est remplacé par le nombre d'échantillons de x qui sont plus petits que x_i . Ces problèmes de statistiques de rang sont bien connus (KENDALL) et conduisent naturellement à s'affranchir de l'estimation des valeurs moyennes. Du point de vue théorique, ces méthodes sont plus robustes que les procédés de la statistique paramétrique (cf. (1)) et, du point de vue pratique, l'organisation des calculs est plus simple que dans le cas paramétrique.

On a vérifié de façon expérimentale que les valeurs de ρ calculées étaient pratiquement indépendantes de l'échelle de représentation : amplitude, dB ou rang, ce qui justifie le choix de la méthode de calcul.

Quant à la dernière difficulté, on a constaté expérimentalement que l'on obtenait des résultats identiques que l'on prenne 5, 10, 20 ou 30 secondes de signal. Comme on s'intéresse à l'aspect instantané de la distorsion, on effectue le calcul sur un intervalle de 5 à 10 secondes.

3.3 Caractérisation de la distorsion

La méthode habituelle consiste à appliquer la formule (1) aux amplitudes seulement, il est tentant d'appliquer la même méthode au temps de propagation de groupe. Les histogrammes de ces deux estimations sont représentés sur les figures 6 et 7.

Une autre façon de caractériser la distorsion consiste à calculer l'histogramme des retards de propagation (cf. fig. 8). De cet histogramme on peut estimer l'écart type σ de ce retard, et ainsi calculer la bande de cohérence B_c en amplitude par la formule (2) :

$$(2) \quad B_c = \frac{1}{4\sigma} \quad \text{avec} \quad \begin{array}{ll} B_c & \text{en MHz} \\ \sigma & \text{en ms} \\ \frac{1}{4} & = \frac{1}{\pi} \approx 0,32 \end{array}$$

Les résultats obtenus par la formule (2) sont comparables à ceux de la figure 6, on ne peut toutefois se prononcer car le dispositif expérimental ne permet pas une réalisation simultanée des deux expériences.

Les estimations précédentes fournissent une indication moyenne du comportement du canal, il a donc été nécessaire de définir une mesure de la distorsion instantanée.

Dans cette conférence, on en propose 2. La première est décrite dans la suite de ce paragraphe et a l'intérêt de fournir une estimation simple de la corrélation entre niveau moyen du signal et distorsion. La seconde sera exposée dans le paragraphe 4 car elle résulte de considérations théoriques sur les MODEM.

La figure 9 montre le procédé utilisé pour résumer la distorsion instantanée du canal. Le procédé est applicable aussi bien au temps de propagation de groupe qu'à l'amplitude. Si le canal n'était pas distordu, ces deux quantités seraient constantes dans le bande. Etant donné un écart d'amplitude ΔA (exprimé en dB) on cherche la valeur de l'amplitude A (centre de la fenêtre) qui correspond au plus grand nombre d'échantillons d'amplitude à l'intérieur de l'intervalle $(A - \frac{\Delta A}{2}, A + \frac{\Delta A}{2})$. Plus ce maximum est élevé, moins le canal est distordu. Bien entendu, le procédé est applicable au temps de propagation de groupe, avec un écart de temps $\Delta \tau$ et un centre de fenêtre temporel τ .

3.4 Corrélation amplitude-temps de propagation de groupe (TPG)

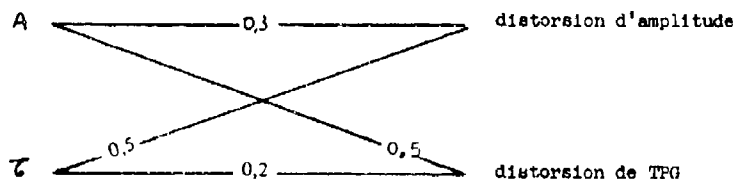
Lorsqu'on observe, avec un ralentissement de l'ordre de 20, les courbes d'amplitude et de temps de propagation de groupe sur 10 ou 20 MHz, on constate que les 2 courbes "s'agitent" ensemble. On vérifie à partir des enregistrements que le coefficient de corrélation entre la distorsion d'amplitude et la distorsion de temps de propagation de groupe est de l'ordre de 0,70.

C'est la seule corrélation que l'on a trouvée entre l'amplitude et le temps de propagation de groupe. En effet, on vérifie que la valeur de la bande de cohérence calculée à partir de l'amplitude est décorrélée de celle calculée à partir du temps de propagation de groupe.

Enfin, le coefficient de corrélation de l'amplitude et du temps de propagation à une même fréquence reste inférieur à 0,2. Ces résultats montrent qu'il faut estimer les 2 types de distorsion pour démoduler.

3.5 Corrélation niveau-distorsion

Pour ΔA et $\Delta \tau$ fixés, on dispose des deux valeurs des centres de fenêtre A et τ que l'on peut corréler avec les 2 distorsions. On a obtenu les valeurs du coefficient de corrélation données par le schéma ci-dessous :



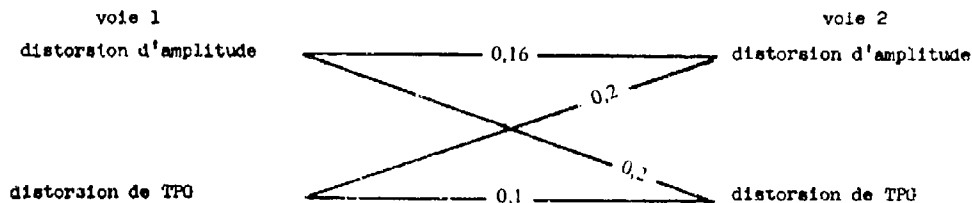
Ces valeurs numériques concernent le comportement instantané du signal et on peut obtenir des résultats apparemment différents si on s'intéresse par exemple à la corrélation du niveau médian avec la fréquence dans le cas de fortes distorsions.

L'ordre de grandeur des valeurs numériques du schéma ci-dessus montre qu'il y a peu à espérer de la prise en considération du niveau du signal ou de son retard pour estimer le risque d'erreur entraîné par la distorsion du canal. Ce résultat est important pour l'utilisation de la diversité puisqu'il démontre que chaque récepteur doit posséder son estimateur de degré de confiance instantané.

3.6 Corrélation d'espace

Les emplacements des deux aéronefs de réception ont été choisis de façon à s'assurer que, pour toute fréquence, les paramètres d'amplitude (ou de temps de propagation de groupe) sont décorrélés sur les deux voies de réception.

Les premières exploitations montrent que les distorsions sont décorrélées sur les deux voies comme le montre le schéma ci-dessous :



Ces résultats sont favorables car ils montrent que la diversité permet de réduire le taux d'erreur dû aux distorsions.

4.- REMARQUES SUR LA CONCEPTION DU SYSTEME DE RECEPTION

4.1 Choix du code de modulation

Les valeurs numériques obtenues montrent qu'il est nécessaire de mettre en oeuvre des méthodes adaptatives. Cette adaptation permanente est équivalente à une estimation en temps réel de la fonction de transfert. On conçoit que cette estimation sera facile à mettre en oeuvre si les spectres des signaux élémentaires sont égaux ou proportionnels entre eux. En effet, la connaissance de la distorsion subie par un seul signal élémentaire permet de construire la distorsion subie par les autres signaux élémentaires. Cette remarque limite donc le choix aux modulations par saut de phase ou d'amplitude. Dans l'état actuel des besoins on peut s'en tenir à la modulation en quadrature de phase.

4.2 Utilisation de la diversité

Avec une bonne approximation, on peut considérer que les erreurs dues à la dégradation du rapport signal sur bruit étaient indépendantes de celles dues à la distorsion.

Il faut donc prévoir une mesure du degré de confiance attaché à chaque décision élémentaire sur chaque voie.

L'évolution des coûts et des possibilités de traitement incite fortement à utiliser un démodulateur adapté avec l'indicateur de qualité sur chaque voie réceptrice.

4.3 Démodulation adaptée

L'adaptation à la réception comprend donc quatre types de traitements :

- . estimation de la distorsion,
- . prise en compte de la distorsion,
- . reconnaissance de la suite de signaux élémentaires,
- . combinaison des informations recueillies sur chaque voie de diversité.

Ces opérations ne sont pas forcément réalisées dans l'ordre ci-dessus. Par ailleurs, nous allons montrer que la reconnaissance des signaux élémentaires doit être organisée d'une façon différente de celle utilisée dans les transmissions de données pour lesquelles la distorsion d'amplitude est faible.

En effet, on peut soit corriger le signal reçu pour qu'il ressemble à un signal parfait, soit comparer chaque signal reçu aux versions distordues estimées.

On peut représenter le signal émis par une série trigonométrique de la forme (3) :

$$(3) \quad s(t) = \sum_i a_i \cos(\omega_i t + \varphi_i)$$

La transmission introduit du bruit additif désigné par la suite des valeurs n_i et une distorsion des composantes représentées par les couples de paramètres (h_i, ψ_i) .

On peut donc représenter le signal reçu par la série trigonométrique (4) de FOURIER :

$$(4) \quad r(t) = \sum_{i=1}^M [a_i h_i \cos(\omega_i t + \varphi_i + \psi_i) + n_i \cos(\omega_i t + \theta_i)]$$

Comme la stationnarité du canal est convenable sur plusieurs centaines de signaux élémentaires, on peut aboutir à une excellente estimation des couples de paramètres (h_i, ψ_i) sauf peut-être pour les composantes très affaiblies.

Dans ces conditions, le signal corrigé (procédé classique) est donné par (5) :

$$(5) \quad \hat{s}(t) = \sum_i \left[a_i \cos(\omega_i t + \varphi_i) + \frac{n_i}{h_i} \cos(\omega_i t + \theta_i') \right]$$

Le démodulateur réalise l'opération suivante :

$$(6) \quad E \left(\int \hat{s}(t) s(t) dt \right) = \sum_i \left[a_i^2 + \left(\frac{n_i}{h_i} \right)^2 \right]$$

Le rapport signal sur bruit vaut alors ρ_c :

$$(7) \quad \rho_c = \frac{\sum_i a_i^2}{\sum_i \left(\frac{n_i}{h_i} \right)^2}$$

Dans la démodulation adaptée le signal de référence est le signal distordu dont l'expression est donnée par (8) :

$$(8) \quad \hat{r}(t) = \sum_i a_i \cos(\omega_i t + \varphi_i)$$

Le démodulateur adapté réalise l'opération (9) :

$$(9) \quad E \left(\int \hat{r}(t) r(t) dt \right) = \sum_i \left[(a_i h_i)^2 + n_i^2 \right]$$

Le rapport signal sur bruit vaut alors :

$$(10) \quad \rho_a = \frac{\sum_i (a_i h_i)^2}{\sum_i n_i^2}$$

Pour effectuer la comparaison des expressions (7) et (10) il est commode de prendre tous les n_i égaux à n et tous les a_i égaux à a ce qui donne les expressions (11) :

$$(11) \quad \rho_c = \frac{a^2}{n^2} \cdot \frac{1}{\frac{1}{M} \sum_i \frac{1}{h_i^2}}$$

$$\rho_a = \frac{a^2}{n^2} \cdot \frac{\sum_i h_i^2}{M}$$

Une inégalité classique du combinatoire (cf. STEGUN et ALBRAMOWITZ) montre que l'on a toujours :

$$(12) \quad \rho_a \geq \rho_c$$

Cette inégalité (12) s'explique physiquement par le fait que le bruit du récepteur situé dans les parties affaiblies du spectre est remonté par le filtre correcteur de distorsion.

Le rapport $\frac{P_a}{P_c}$ peut donc servir de paramètre caractéristique de la distorsion instantanée du canal.

$$(13) \quad d = \frac{P_a}{P_c} = \frac{1}{M^2} \cdot \left(\sum_i R_i^2 \right) \left(\sum_i \frac{1}{R_i^2} \right) \gg 1$$

La figure 10 qui représente un histogramme des valeurs relevées pour ce paramètre d montre que la perte due à une correction mal adaptée de la distorsion est supérieure à 2 dB pendant 1 % du temps.

Dans l'expression (13), la distorsion de phase n'apparaît pas, ce qui ne signifie pas qu'on n'a pas à s'en préoccuper. Par exemple si l'on utilise une modulation à 2 voies en quadrature (4 PSK, MSK), on ne peut extraire ces 2 voies à la réception par un hétérodynage en quadrature car les composantes spectrales du signal n'ont pas tourné de la même quantité. Il en résulte qu'il faut introduire une correction de la distorsion de phase avant de séparer les 2 voies en quadrature.

Cette dernière remarque ainsi que les résultats de mesures de la corrélation suggèrent une organisation de la réception représentée sur la figure (11).

5.- CONCLUSION

Cet exposé a mis en relief l'aspect logiciel de la transmission numérique par diffusion troposphérique en raison de la nouveauté des procédés à mettre en oeuvre. Cette nouveauté résulte de l'introduction de traitements élaborés du signal que l'on ne rencontre pas de façon habituelle dans les faisceaux hertziens analogiques. En dépit de l'intérêt considérable de ces études, il ne faut pas perdre de vue que le coût des équipements de traitement continuera de décroître en valeur relative, de sorte que la partie onéreuse et difficile à réaliser sur le plan technique restera l'étage de puissance à l'émission. En résumé, l'augmentation des débits est envisageable grâce aux progrès conceptuels et technologiques dans le domaine du traitement mais les performances restent limitées par les données de la thermodynamique et de la propagation.

REMERCIEMENTS

L'auteur tient à remercier la DRET (Direction des Recherches Etudes et Techniques de l'Armement) qui a soutenu l'étude et les services techniques de THOMSON-CSF/TFH qui ont installé et maintiennent la liaison expérimentale.

REFERENCES BIBLIOGRAPHIQUES

ADRAMOWITZ (M), STEGUN (I.A), 1965 . "Handbook of mathematical functions"
Ed. Dover, New York

BELLO (P.A), Apr. 1969 . "A troposcatter channel model".
IEEE Trans. Commun. Technol., vol. COM-17, pp. 130-137.

BRANHAM (R.A), June 1970 . "Correlation bandwidth measurements over troposcatter paths".
Tech. Rep. ECOM-0251-F.

DANIEL (L.D), REINMAN (R.), June 1976 . "Performance prediction for short range troposcatter links".
IEEE Trans. on Communication.

KENDALL (M.G), 1975. "Rank Correlation Methods"
Ed. Charles Griffin Co. London 4th edition.

KENNEDY (T.J), Apr. 1972 . "A comparison of measured and calculated frequency correlation functions over 4,6 - 7,6 GHz troposcatter paths"
IEEE Trans. on Communication, pp. 173-175.

MONSEN (P), KERN (P.R), GRZENDA (C.J), 1975. "Megabit digital troposcatter system".
IEEE Nat. Telecom. Conf.

MONSEN (P), RICHMAN (S.H), 1973. "A comparison of digital techniques for troposcatter applications".
IEEE Nat. Telecom. Conf.

RIKE (S.O), Feb. 1953 . "Statistical fluctuations in radio field strength far beyond the horizon".
Proc. IRE, vol. 41, pp. 274-281.

SHERWOOD (A.R), PANIERA (I.A), 1975 . "Multipath measurements over troposcatter paths with application to digital transmission".
IEEE Nat. Telecom. Conf. pp. 28-1 à 28-4.

SUNDE (E.D), Jan. 1964. "Digital troposcatter transmission and modulation theory".
Bell Syst. Tech. J., vol. 43, pp. 244,214.

UNKAUF (M), BAGNELL (R), TAGLIA FERRI (O.A), 1975. "Tactical tropo performance of a distortion adaptive receiver".
IEEE Nat. Telecom. Conf.

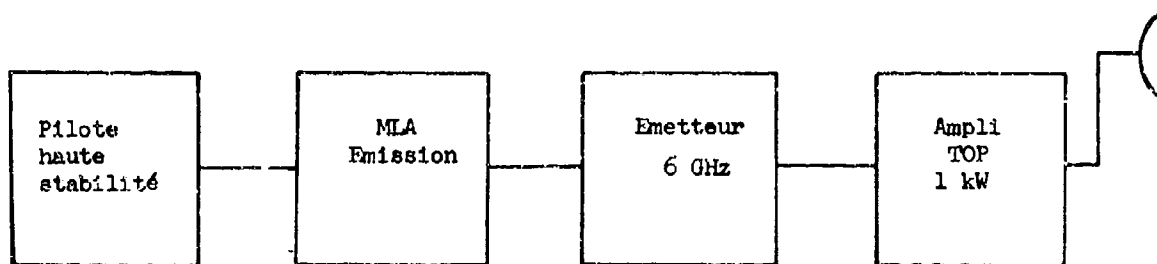


Fig.1 Terminal emission

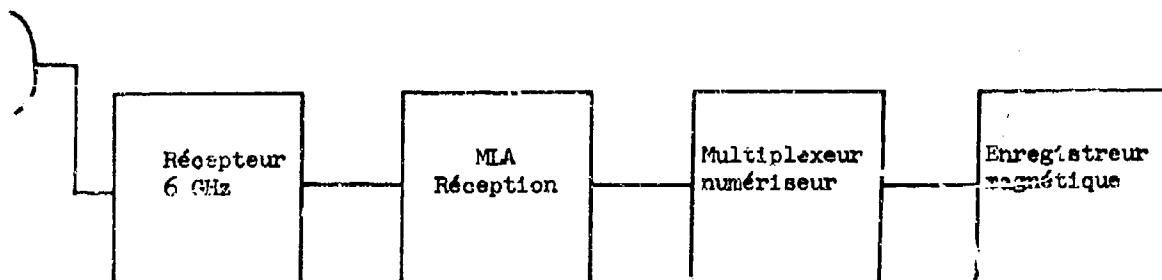


Fig.2 Terminal réception

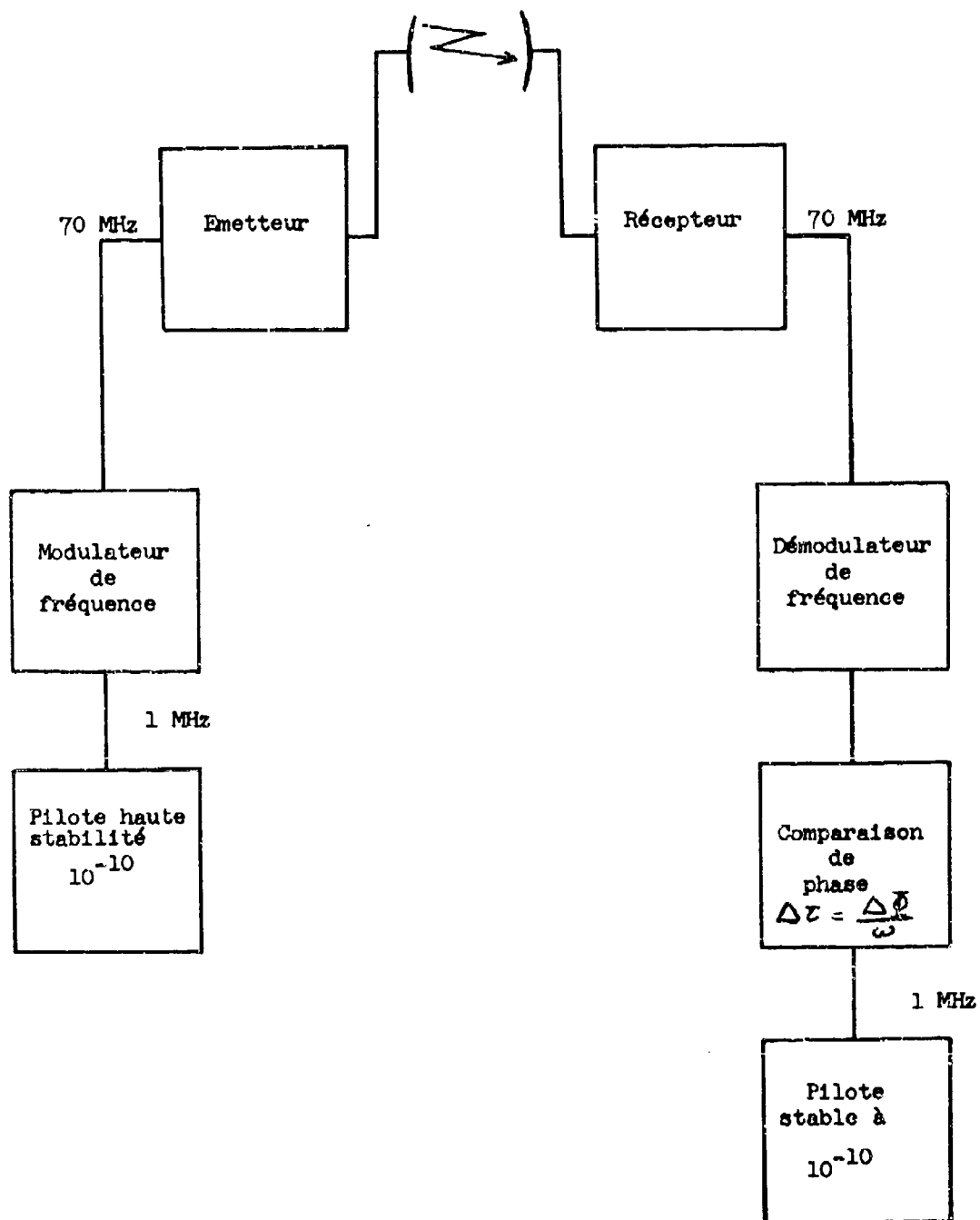


Fig.3 Mesure du temps de propagation de groupe

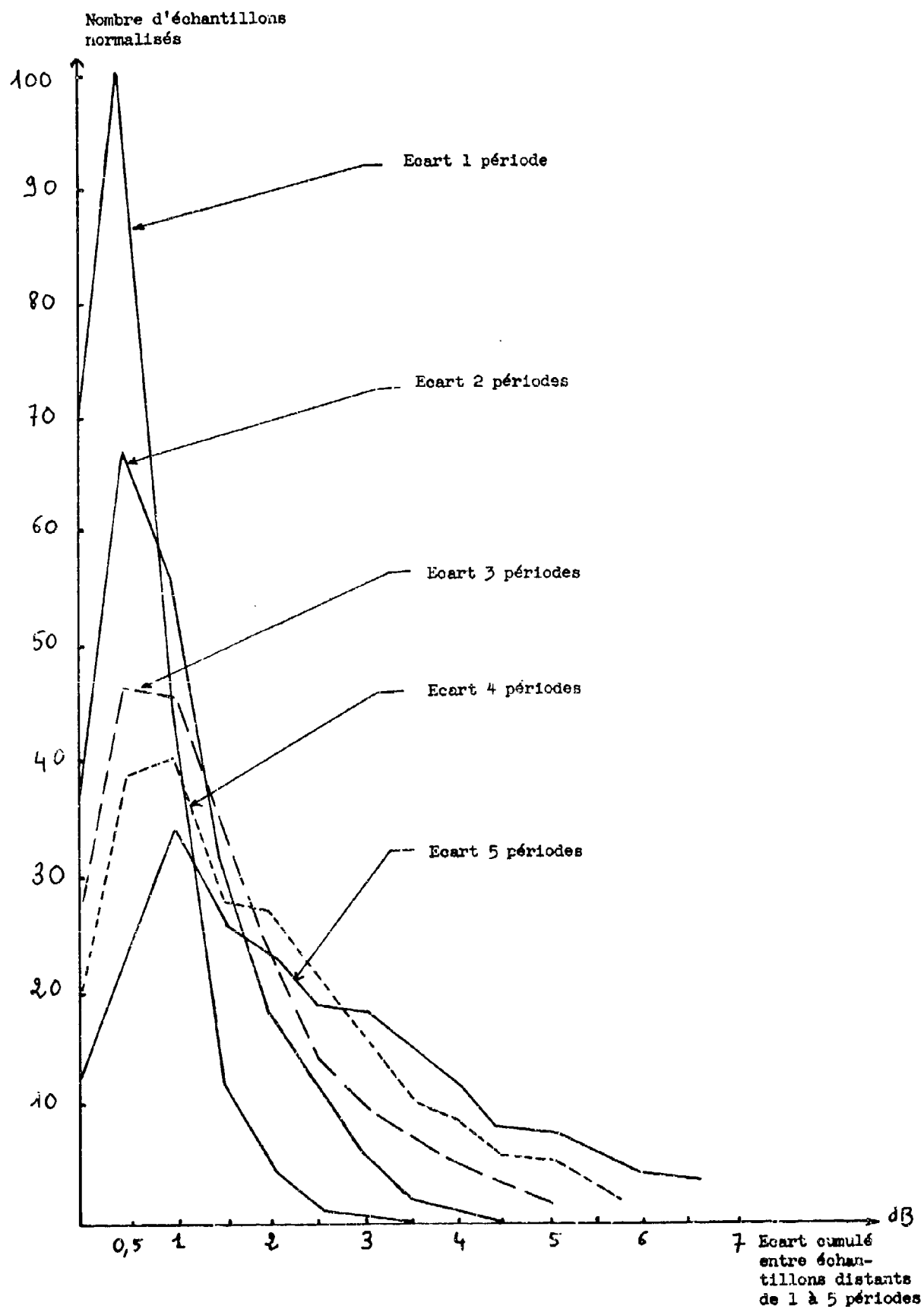


Fig.4 Stationnarité de l'amplitude

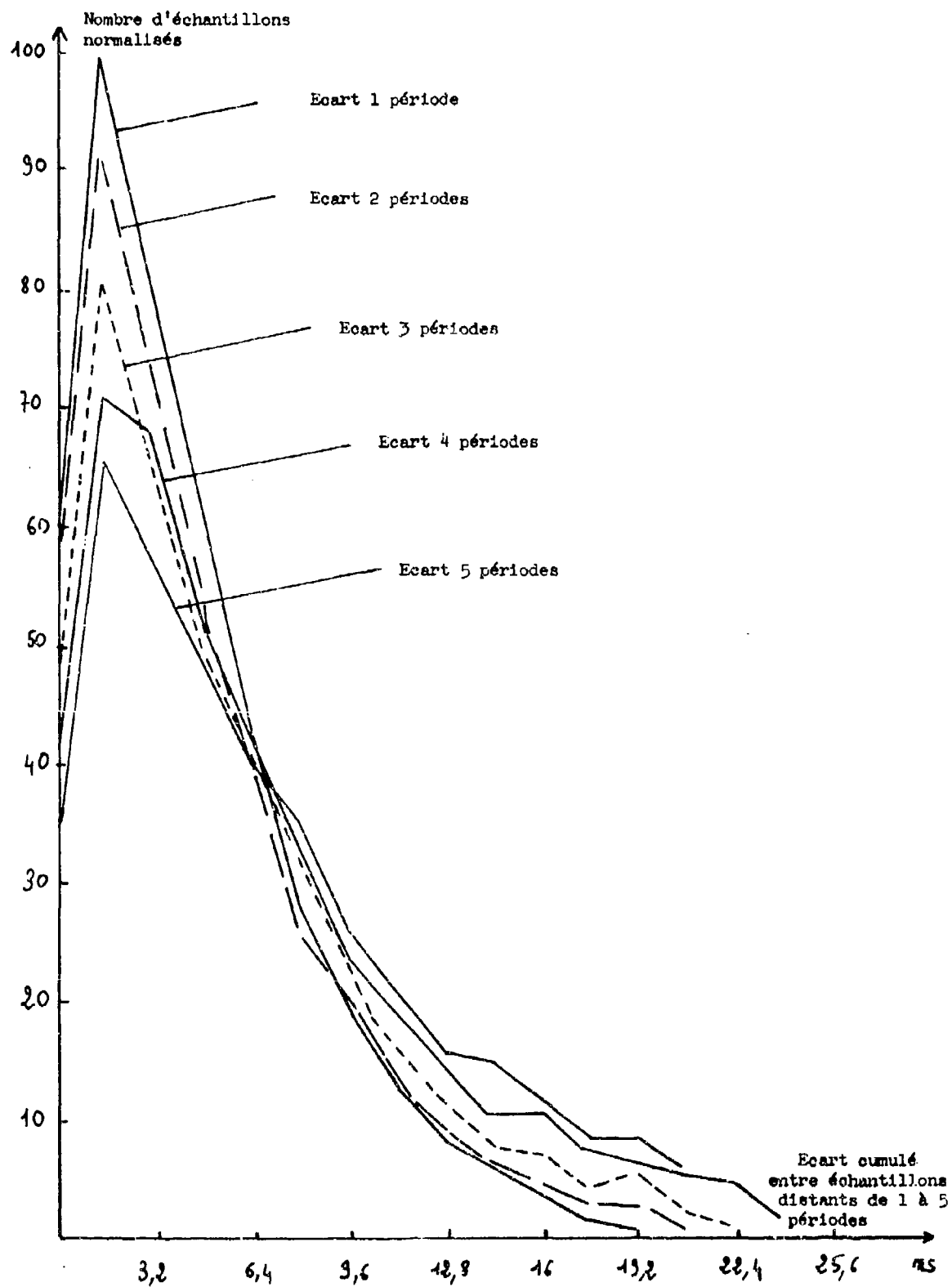


Fig.5 Stationnarité du temps de propagation de groupe

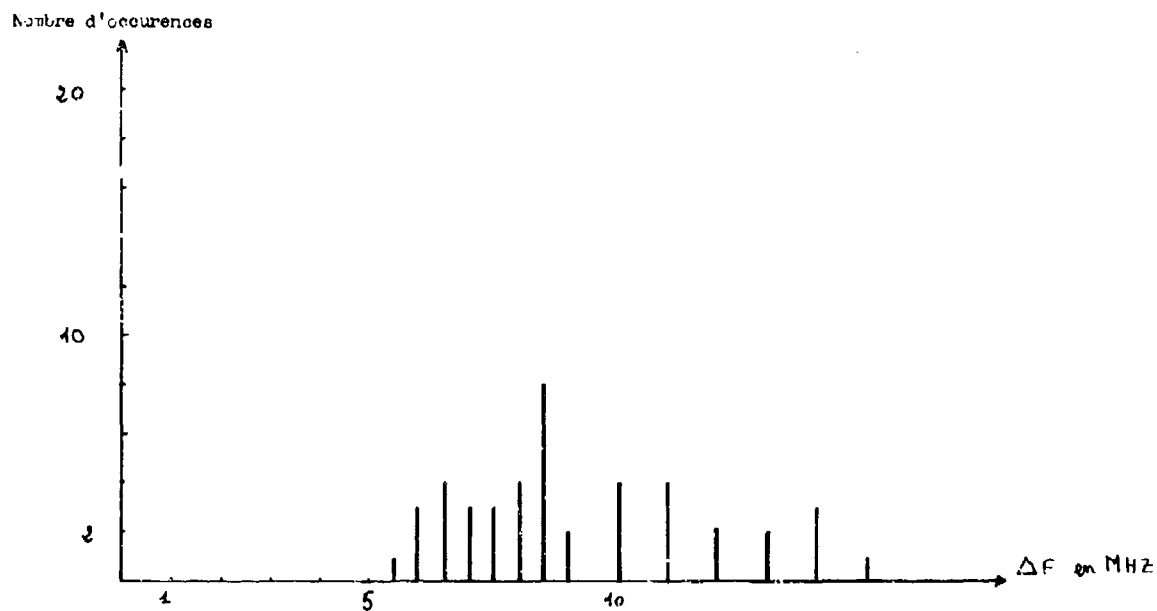


Fig. 6 Histogramme de la valeur de la bande de cohérence pour l'affaiblissement

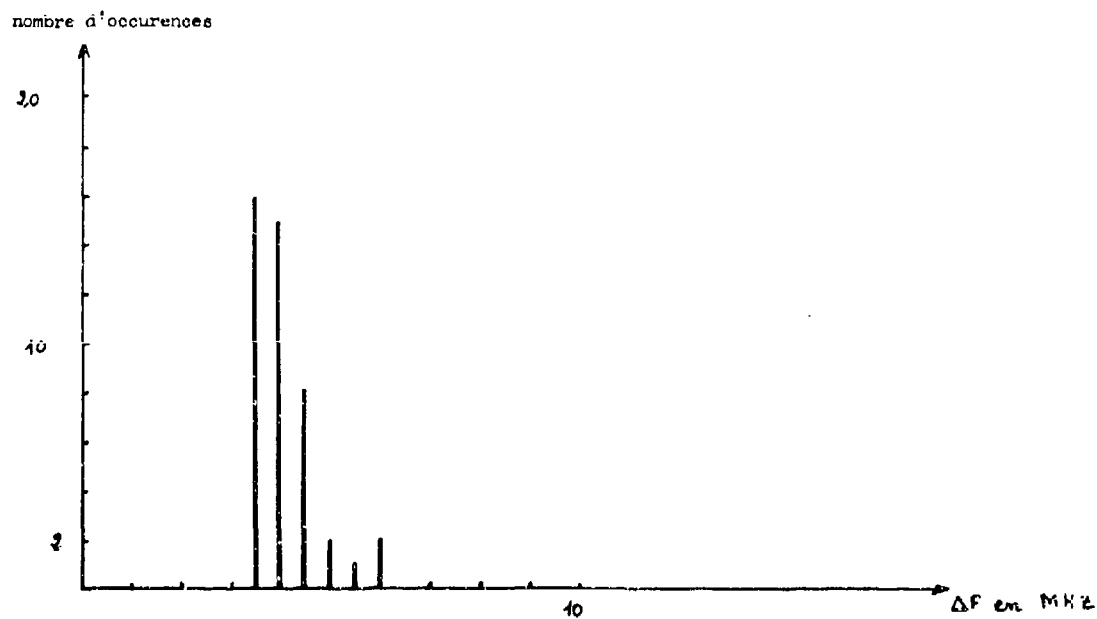


Fig. 7 Histogramme de la valeur de la bande de cohérence pour le temps de propagation de groupe

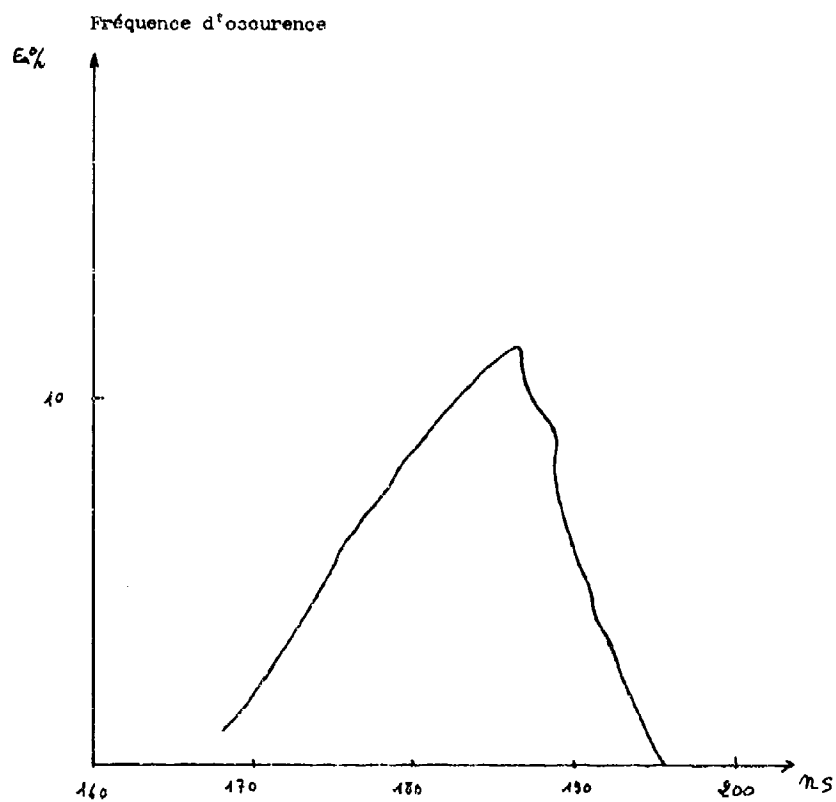


Fig.8 Histogramme des valeurs du retard de transmission

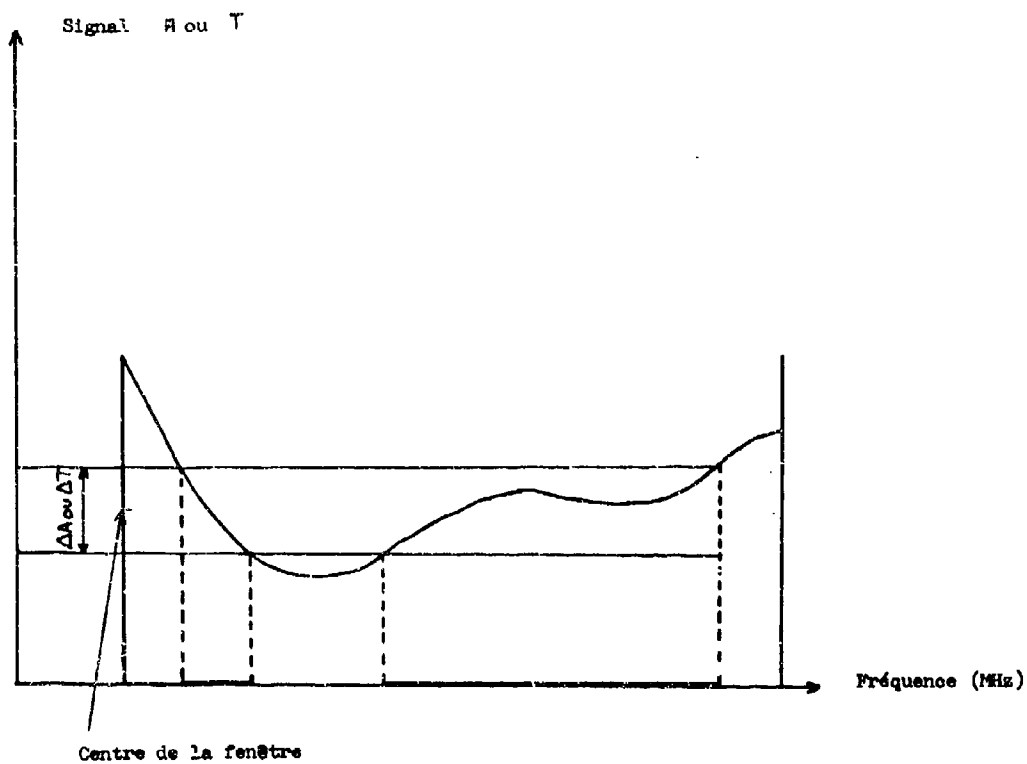


Fig.9 Principe d'évaluation de la distorsion

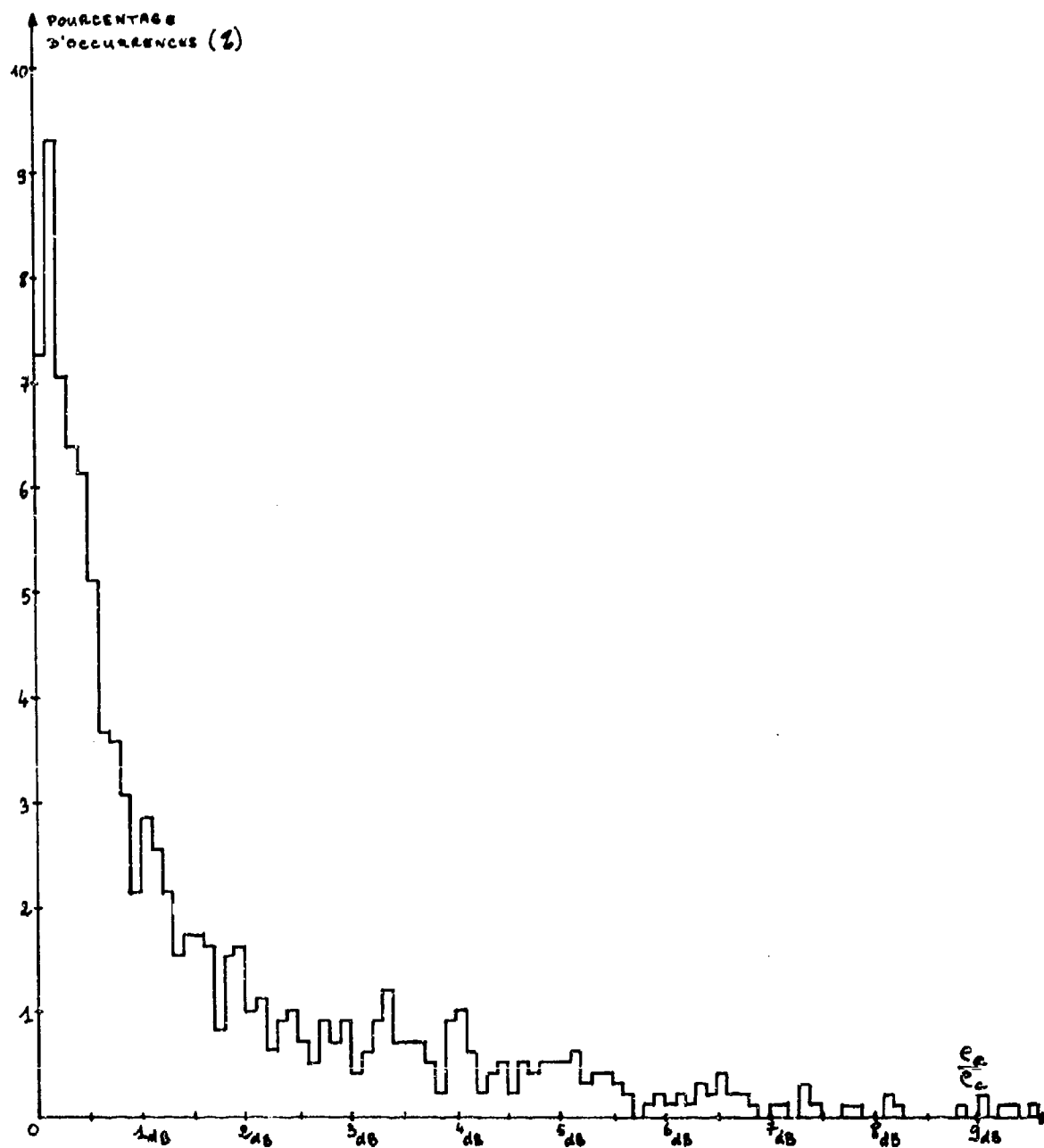


Fig.10 Histogramme de la distorsion instantanée

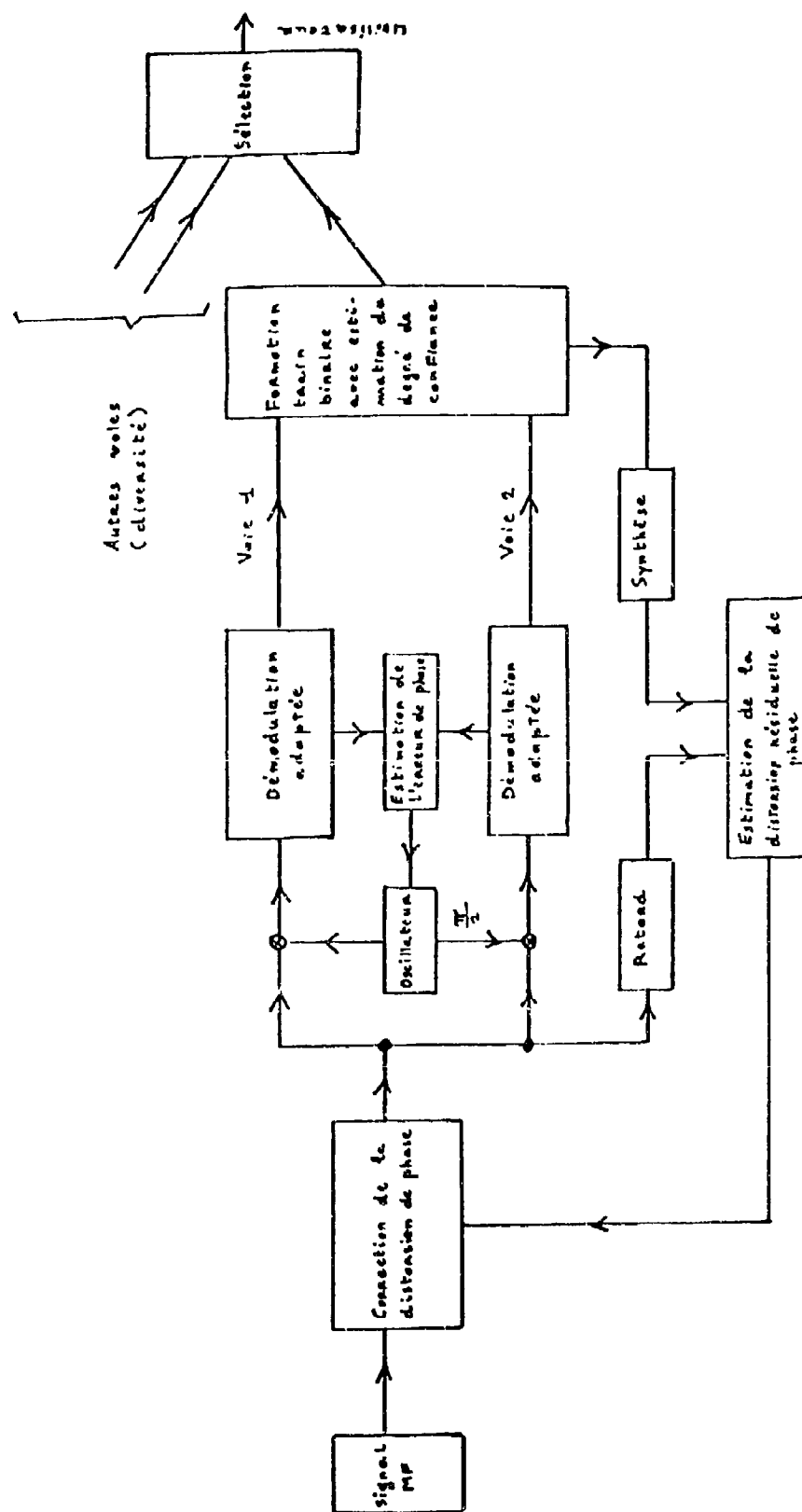


Fig.11 Organisation du récepteur

AEROSPACE PROPAGATION PREDICTION CAPABILITIES ASSOCIATED WITH THE IF-77 MODEL

M. E. Johnson and G. D. Gierhart
Office of Telecommunications
Institute for Telecommunication Sciences
Boulder, Colorado 80303, U.S.A.

SUMMARY

The United States Department of Commerce (DOC) has been active in radio wave propagation research and prediction for several decades, and has provided the Federal Aviation Administration (FAA) with many propagation predictions relevant to the coverage of air navigation and communications systems. During 1960-1973, an air/ground propagation model applicable to irregular terrain was developed by the Office of Telecommunications/Institute for Telecommunication Sciences (OT/ITS) for the FAA and was documented in detail. This IF-73 (ITS-FAA-1973) propagation model has evolved into the IF-77 model, which is applicable to air/ground, air/air, ground/satellite, and air/satellite paths. It can also be used for ground/ground paths that are line-of-sight, smooth earth, or have a common horizon. Model applications are restricted to telecommunication links operating at radio frequencies from about 0.1 to 20 GHz with antenna heights greater than 0.5 m. In addition, the elevation of the radio horizon must be less than the elevation of the higher antenna. The radio horizon for the higher antenna is taken either as a common horizon with the lower antenna or as a smooth earth horizon with the same elevation as the lower antenna's effective reflecting plane.

This propagation model has been incorporated into ten computer programs. These programs may be used to obtain a wide variety of computer-generated microfilm plots such as transmission loss versus path length and desired-to-undesired signal ratio at a receiving location versus the distance separating the desired and undesired transmitting facilities. Such capabilities are useful in estimating the service coverage of aerospace radio systems, and are currently being used to establish station separation requirements for VHF/UHF/SHF air navigation aids. This paper provides (1) a brief discussion of the IF-77 propagation model, (2) a summary of the prediction capabilities available, and (3) remarks concerning model validation work.

1. INTRODUCTION

Assignments for aeronautical radio in the radio frequency spectrum must be made so as to provide reliable services for an increasing air traffic density. Potential interference between facilities operating on the same or on adjacent channels must be considered in expanding present services to meet future demands. Service quality depends on many factors including the desired-to-undesired signal ratio at the receiver. This ratio varies with receiver location and time even when other parameters, such as antenna gain and radiated powers, are fixed.

The prediction capabilities mentioned in this paper were developed at OT/ITS with the sponsorship of the FAA. Although these were intended for use in predicting the service coverage associated with ground- or satellite-based VHF/UHF/SHF air navigation aids, they can be used for other services.

2. PROPAGATION MODEL

At 0.1 to 20 GHz, propagation of radio energy is affected by the lower nonionized atmosphere (troposphere), specifically by variations in the refractive index of the atmosphere. Atmospheric absorption and attenuation or scattering due to rain become important at SHF. The terrain, along and in the vicinity of the great circle path between transmitter and receiver also plays an important part. In this frequency range, time and space, variations of received signals, and interference ratios lend themselves readily to statistical description.

Conceptually, the model is very similar to the Longley-Rice propagation model for propagation over irregular terrain, particularly in that attenuation versus distance curves calculated for the (a) line-of-sight, (b) diffraction, and (c) scatter regions are blended together to obtain values in transition regions (Longley and Rice, 1968). In addition, the Longley-Rice relationships involving the terrain parameter Δh are used to estimate radio horizon parameters when such information is not available from facility siting data. The model includes allowance for

- (a) average ray bending (Bean and Dutton, 1968; sec. 3),
- (b) horizon effects (Gierhart and Johnson, 1973, sec. A.4.1),
- (c) long-term power fading (Rice et al., 1967, sec. 10),
- (d) vertical plane patterns for both antennas (Hartman, 1974, sec. CI-D.3),
- (e) surface reflection multipath (Hartman, 1974, sec. CI-D.7),
- (f) tropospheric multipath (Gierhart and Johnson, 1973, sec. A.7),
- (g) atmospheric absorption (Rice et al., 1967, sec. 3),
- (h) ionospheric scintillations (Whitney et al., 1971),

- (i) rain attenuation (Samson, 1975, sec. 3),
- (j) reflection from an elevated counterpoise (Gierhart and Johnson, 1973, sec. A.4.2),
- (k) smooth earth diffraction (Longley and Rice, 1968, sec. 3.2),
- (l) knife-edge diffraction (Longley and Reasoner, 1970, sec. 3.5), and
- (m) forward scatter (Rice et al., 1967, sec. 9).

Input parameters for IF-77 are summarized in figure 1. Note that the minimum parameter requirement is frequency and antenna elevations (H1 and H2).

The above discussion provides a very brief description of the IF-77 model and contains sufficient specific references to allow readers to pursue topics of interest to them. However, additional discussion is provided here for some parts of the model that may be of particular interest in connection with the predictions made for aerospace systems with line-of-sight service limitations; i.e., power available (sec. 2.1), median basic transmission loss (sec. 2.2), and variability (sec. 2.3).

2.1. Power Available

Power available as calculated in IF-77 is taken as the power available from the receiving antenna terminals under matched conditions when internal heat losses of the receiving antenna and path antenna gain loss are neglected. Compensation for internal heat loss or gain-loss factors needed to refer the available power to some point in the receiving system other than the receiving antenna terminals can be made by an appropriate adjustment to the radiated power or antenna gains used for computer program input.

Power available $P_a(q)$ levels exceeded for a fraction of time q are determined using

$$P_a(q) = \text{EIRPG} + G_{NT} + G_{NR} - L_b(0.5) + Y_e(q) \text{ dBW}, \quad (1)$$

$$\text{EIRPG} = \text{EIRP} + G_R \text{ dBW}, \quad \text{and} \quad (2)$$

$$\text{EIRP} = P_{TR} + G_T \text{ dBW}. \quad (3)$$

Here EIRP is equivalent isotropically radiated power, P_{TR} in decibels greater than 1 W (dBW) is the total power radiated by the transmitting antenna, and G_T in decibels greater than isotropic (dBi) is the maximum gain of the transmitting antenna or receiving antenna respectively. Losses (e.g., lines) associated with the transmitting system should be considered in calculating radiated power from transmitter output power. Normalized antenna gain (G_{NT} or G_{NR}) in decibels greater than maximum gain (G_T or G_R) is included in (1) to allow for antenna directivity when maximum gain is not appropriate (i.e., the antennas are not pointed at each other). A tracking option is available that keeps antenna main beams pointed at each other. Methods used to calculate the median basic transmission loss, $L_b(0.5)$, and the total variability with time, $Y_e(q)$, are discussed in section 2.2 and 2.3. Note that $Y_e(q)$ is the only term on the right-hand side of (1) that contains variability with time when path parameters (e.g., distance, heights, etc.) are fixed, and EIRP is considered to be constant with time.

2.2. Median Basic Transmission Loss

Median basic transmission loss $L_b(0.5)$ is calculated from

$$L_b(0.5) = L_{bf} + A_a + A_{cr} - V_e(0.5) \text{ dB}, \quad (4)$$

where L_{bf} is basic transmission loss for free space, A_a is average atmospheric absorption, A_{cr} is a reference attenuation calculated for the propagation mode(s) applicable for a particular path (e.g., line-of-sight variability, line-of-sight lobing, diffraction, scatter, or transition regions), and $V_e(0.5)$ is a median adjustment associated with long-term variability.

With the variability option, lobing associated with a specular reflection from the earth's surface is suppressed inside the far portion of the horizon lobe. When lobing is suppressed in this way, an appropriate increase in the variability associated with short-term variability (sec. 2.3) is made. A conditional adjustment factor, A_{cr} , that is a function of the long-term variability is used to prevent available power levels from exceeding levels expected for free-space propagation by an unrealistic amount when the long-term variability about $L_b(0.5)$ is large; i.e., A_{cr} is increased so that the long-term power does not exceed its free-space value by 3 dB for more than 10 percent of the time. Lobing associated with a counterpoise reflection is included in A_{cr} even when the variability option is used.

With the lobing option, lobing associated with interference between the direct ray and specular reflections from both the counterpoise and the earth's surface are allowed to determine A_{cr} for the first 10 lobes inside the smooth earth radio horizon. Contributions to short-term variability associated with the specular earth's surface reflection are neglected when A_{cr} is based on lobing. The program calculates several points for each of the 10 lobes inside the horizon. One of these will be the lobe null if no counterpoise reflected ray is present and the phase change associated with reflection

is 180°. Otherwise, calculations may not actually be made for the null case. Conditions most likely to result in missed nulls involve the propagation of vertical polarization over sea water or transition regions where both the earth surface and counterpoise reflected rays are significant.

Calculation of A_{rr} in the diffraction region involves a weighted average of rounded earth and knife-edge diffraction attenuations. Transition between the line-of-sight and diffraction regions is made using a straight line connecting a diffraction value at the radio horizon with a point in the line-of-sight region where the ray optics formulation is valid.

2.3. Variability

The variability term of (1) is calculated from

$$Y_r(q) = \pm \sqrt{Y_e^2(q) + Y_m^2(q) + Y_r^2(q) + Y_i^2(q)} \quad \text{dB}, \quad (5)$$

+ for $q \leq 0.5$
- otherwise

where $Y_e(q)$ is long-term (hourly-median) variability, $Y_m(q)$ is variability associated with surface reflection and tropospheric multipath, $Y_r(q)$ is rain attenuation variability, and $Y_i(q)$ is variability associated with ionospheric scintillation. The short-term (within the hour) variabilities $Y_e(q)$, $Y_m(q)$, and Y_i are neglected if the option for long-term variability only is selected; i.e., $Y_r(q) = Y_r(q)$ when the option to predict the distribution of hourly median levels is selected. The median level of $P_a(q)$ is not dependent on $Y_r(q)$ since $Y_r(0.5) = Y_e(0.5) = Y_m(0.5) = Y_i(0.5) = 0$.

The IF-77 model contains long-term variability options which allow variabilities for different climates or time blocks within a continental temperate climate to be selected. These variabilities are similar to, but not identical with, those provided by Technical Note 101 (Rice et al., 1967), or the CCIR, (1970). Techniques used in IF-73 to prevent excessive long-term variability are still used.

Nakagami-Rice distributions are used for $Y_r(q)$ (Rice et al., 1967, p. V-8). These distributions provide statistics for the case where a constant vector is added to a Rayleigh-distributed vector. The particular distribution applicable is selected by a parameter K where K is the ratio in decibels between the steady component of received power and the Rayleigh fading component. If K is large (> 40 dB), $Y_r(q) = 0$, and if K is small (< -20 dB), $Y_r(q)$ is a Rayleigh distribution. Power for the Rayleigh distributed vector is taken as the sum of relative powers associated with surface reflection multipath and tropospheric multipath.

Surface reflection multipath is calculated from effective reflection coefficients for specular and diffuse reflection from the earth's surface. When the specular component is used to produce lobing (i.e., lobing option selected), it is neglected in the calculation of surface reflection multipath power. These effective reflection coefficients include allowances for surface constants, frequency, surface roughness, relative direct-reflected ray antenna gain, relative direct-reflected ray lengths, counterpoise shadowing, and divergence. Counterpoise reflection is always allowed to cause lobing and is never allowed to contribute to $Y_r(q)$. For beyond-the-horizon paths, surface reflection multipath contributions are neglected.

The tropospheric multipath power formulation for the line-of-sight region was derived from an outage time formulation developed for microwave relay links (Lenkurt, 1970, pp. 60, 13-2, 119). Just beyond the horizon, the formulation involves a linear interpolation between the K parameter value applicable at the radio horizon and a $K = -20$ dB value used in the scatter region. Data (Jones, 1955) were used to determine the distance beyond which short-term fading for beyond-the-horizon paths can be characterized as Rayleigh ($K < -20$ dB).

Rain attenuation variability is based on an extension of work done by Samson, (1975, sec. 3). The formulation involves

$$Y_r(q) = \begin{cases} 0 & \text{for } q \leq 0.98 \\ A_{rr}(q)r_s & \text{otherwise} \end{cases} \quad \text{dB} \quad (6)$$

where $A_{rr}(q)$ is the rain attenuation rate determined using rain rate statistics, and r_s is an in-storm ray length. Note that $Y_r(q) = 0$ for time availabilities less than 98%. Ionospheric scintillation variability is described with the distribution given by Whitney et al., (1971). The model does not predict the ionospheric scintillation index; i.e., an appropriate value is selected for an ionospheric scintillation group number which is a model input parameter.

3. PROGRAMMED CAPABILITIES

The IF-77 model has been incorporated into ten computer programs which provide 28 plotting capabilities. These programs cause the computer to produce parameter summary sheets and microfilm plots. A guide to the plotting capabilities currently available is provided in figure 2, and a sample parameter sheet is shown in figure 3. An applications guide covering these programs is being prepared (Johnson and Gierhart, 1978).

Capabilities 1 through 10 are outputs from a single program called LOBING (Hartman, 1974, sec. CII). This program uses an abbreviated version of IF-77 that is applicable only to the line-of-sight region for a spherical earth in which variability with time and horizon effects are neglected. Various parameters such as transmission loss, reflection coefficient, time lag, and elevation angle are plotted against path distance. Figure 4 is a transmission loss curve in which the lobing caused by interference between direct and reflected ray is shown along with limiting and free space values. Flight through such a lobing structure will cause periodic variation in received level, and the lobe or doppler-beat modulation frequency (Read and Russell, 1964, sec. 10) associated with it can be estimated using the lobing frequency plots of capabilities 5 and 6. These plots are normalized with respect to carrier frequency, and aircraft velocity such that the radial component of velocity is used with capability 5 and the vertical component is used with capability 6 (Hartman, 1974, secs. CII-C.6, CII-C.7).

Capabilities 11 through 23 provide information relevant to received signal level as power available, power density, transmission loss, or the equivalent isotropically radiated power needed to obtain a specified power density. The selected quantity may be used as the ordinate for capabilities 11 through 16, or shown as contours for specific levels in the altitude versus distance plane for capabilities 17 through 23.

Figure 5 was produced by using capability 13 for parameters of figure 3 which are identical to those used for figure 4 except that the option to include lobing as part of the time variability was used along with the nautical mile plotting option. Figure 5 shows the transmission loss predicted under free space conditions along with loss levels expected to be unexceeded during 5, 50, and 95 percent of the time. In addition, the lobing pattern from figure 4 has been superimposed to illustrate the difference between the two ways of treating lobing. Note that the 95 percent loss is not as great as the loss encountered in a null, but that it is usually greater than the loss predicted by the lobing model. The monotonic nature of the curves developed with the variability option make them more convenient to use in service range predictions. However, if the frequency and antenna heights are such that only a few lobes are present, the lobing option is probably preferable since it provides information on the location of strong and weak signal regions. These regions are both large and stable in that changes of refractive conditions or uncertainty associated with the precise aircraft location would not drastically alter the received signal level.

Capabilities 24 through 28 provide information on the desired to undesired signal ratio, D/U, available at the aircraft when transmissions from two facilities are received simultaneously. The interference configuration is illustrated in figure 6. Note that station separation, S , is defined as the sum of d_D and d_U so that S is equal to the great-circle facility separation, S_F , only when the facilities and the aircraft are along the same great circle.

Capabilities 24 and 25 provide curves of D/U versus S or d_D , respectively. Figure 7 was developed using capability 24. It can be used to estimate the station separation needed to obtain a required D/U value for the specified aircraft location (altitude and d_D).

Figure 8 was developed using capability 26. Curves showing the relative azimuthal orientation of the undesired facility, ϕ_U , with respect to the great-circle path connecting the desired and undesired facility are plotted versus the facility separation required to achieve a required D/U ratio or better at each of six specified protection points. Each curve represents a different relative azimuthal orientation of the desired facility, ϕ_D , with respect to the path connecting facilities.

Orientation geometry for the protection points is illustrated in figure 9. Protection point C is used to illustrate the difference between facility separation, S_F , used in figure 8, and station separation, S , used elsewhere (fig. 7). In particular, $S_F \leq S$ since S need not be measured along the great-circle path connecting the facilities. Note that (a) the d_U to point C changes as ϕ_D changes even if S_F remains fixed, and (b) the angle from the undesired facility to point C changes with both ϕ_D and ϕ_U , so that the applicable gain for the undesired facility varies in accordance with its horizontal pattern even if S_F remains fixed.

The geometrical consequences of these complications are handled as part of the calculations performed by program TWIRL. These calculations would be very tedious to perform by hand even if appropriate signal ratio graphs (fig. 9) were available. A graph similar to figure 8 is constructed for each protection point, and the maximum S_F for each combination of ϕ_D and ϕ_U is selected for the final graph (fig. 8). The intermediate graphs have a format identical to figure 8 and are available as computer output even though no samples are provided here.

Capabilities 27 and 28 provide contours for fixed D/U values in the altitude versus distance plane for a fixed facility separation. With capability 27, a single D/U value is used with 3 different time availabilities, whereas capability 28 involves a fixed time availability and several D/U values. Figure 10 was produced using capability 28.

4. MODEL VALIDATION

Model validation work is being done by comparing predictions made using IF-77 with measured data and other predictions. While this work will eventually involve comparisons with data from many sources, the remarks made here involve only those data obtained from a single data source (Longley et al., 1971). This source was selected for our initial effort because it (a) "...summarizes measurements of tropospheric transmission loss and its long-term variability for nearly 800 paths in various parts of the world"; (b) contains sufficient information on path parameters, including path profiles, for IF-77 input; and (c) provides predictions based on two other widely used models.

Figure 11 is a sample of the comparison being made. It is a copy of a figure from the data source to which a prediction made with IF-77 (labeled FAA) has been added. The

other predictions were made with the Technical Note 101 method (Rice et al., 1967), and the ESSA 70 Model (Longley and Reasoner, 1970).

About 200 paths in the data source can be predicted using IF-77, and figures similar to figure 11 are being developed for them. Then statistics for the difference between predicted and measured median transmission loss values will be determined as a function of path type for each of the three models mentioned here.

5. REFERENCES

- Bean, B. K., and E. J. Dutton, 1968, Radio Meteorology (Dover Publications, Inc., New York, N. Y.).
- CCIR, 1970, Estimation of tropospheric-wave transmission loss, Report 244-2 XII Plenary Assembly, New Delhi, Vol. II, Part I (Intl. Telecomm. Union, Geneva).
- Gierhart, G. D., and M. E. Johnson, 1973, Computer programs for air/ground propagation and interference analysis, 0.1 to 20 GHz, DOT Rept. FAA-RD-73-103 (NTIS, AD 770 335).
- Hartman, W. J., editor, 1974, Multipath in air traffic control frequency bands, DOT Rept. FAA-RD-74-75, I and II, (NTIS, AD/A 006 267, and AD/A 006 268).
- Jones, H. B., 1955, An analysis of within-the-hour fading in the 100-to-1000 Mc transmission, J. Res. NBS 54, No. 4, 231-250.
- Johnson, M. E., and G. D. Gierhart, 1978, Applications guide for propagation and interference analysis computer programs (0.1 to 20 GHz), DOT Rept. FAA-RD-77-60 (to be printed).
- Lenkurt, 1970, Engineering considerations for Microwave Communication Systems (GTE Lenkurt Dept., CI34, San Carlos, Calif., \$10.00).
- Longley, A. G., and R. K. Reasoner, 1970, Comparison of propagation measurements with predicted values in the 20 to 10,000 MHz range, ESSA Tech. Rept. 148-ITS 97 (NTIS, AD 703 579).
- Longley, A. G., R. K. Reasoner, and V. L. Fuller, 1971, Measured and predicted long-term distributions of tropospheric transmission loss, OT Rept. OT/THER 16 (NTIS, COM 75-11205).
- Longley, A. G., and P. L. Rice, 1968, Prediction of tropospheric radio transmission loss over irregular terrain, a computer method--1968, ESSA Tech. Rept., ERL 79-ITS 67 (NTIS, AD 676 874).
- Reed, H. R., and C. M. Russell, 1964, Ultra High Frequency Propagation (Boston Tech. Publishers, Lexington, Mass.).
- Rice, P. L., A. G. Longley, K. A. Norton, and A. P. Barsis, 1967, Transmission loss predictions for tropospheric communication circuits, NBS Tech. Note 101, I and II revised (NTIS, AD 687 820, and AD 687 821).
- Samson, C. A., 1975, Atmospheric considerations in radio systems engineering at 10 to 30 GHz, OT Rept. 75-66 (NTIS, COM-75-11093/AS).
- Whitney, H. E., J. Aarons, and D. R. Seemann, 1971, Estimation of the cumulative amplitude probability distribution function of ionospheric scintillations, AF Cambridge Res. Labs. Rept. AFCRL-71-0525, Cambridge, Mass.

PARAMETER

RANGE

Aircraft (or higher) antenna height above mean sea level (msl), H1

> Facility horizon height

Facility (or lower) antenna height above facility site surface (fss), H2

> 1.5 ft (0.5 m) above fss

Frequency

0.1 to 20 GHz

Specification of the following parameters is optional

Aircraft antenna type options

Isotropic,* or as specified*

Polarization options

None, identical with facility

Tracking options

Directional* or tracking

Effective reflection surface elevation above msl

At fss* or specified value above msl

Equivalent isotropically radiated power

0.0 dBW* or specified

Facility antenna type options

Isotropic* or as specified

Counterpoise diameter

0* to 500 ft (152 m)

Height above fss

0* to 500 ft (152 m)
Below facility antenna by at least 3 ft (1 m) but no more than 2000 ft (610 m)

Polarization options

Horizontal,* vertical, or circular

Tracking

Directional* or tracking

Gain, receiving antenna (main beam)

0* to 60 dBi

Transmitting antenna (main beam)

0* to 60 dBi

Transmitting antenna location

Aircraft or facility*

Horizon obstacle distance from facility

From 0.1 to 3 times smooth earth horizon distance (calculated)*

Elevation angle above horizontal at facility

<12 deg (calculated)*

Height above msl

0* to 15,000 ft-msl (4572 m-msl) and \leq aircraft altitude

Ionospheric scintillation options

No scintillation* or specified

Index group

0* to 5, 6 for variable

Rain attenuation options

None* or computed with dB/km or zone

Attenuation/km

0 dB/km and up

Storm size

5, 10,* 20 km

Zone

1 to 6

Refractivity

Effective earth's radius

4010 to 6070 n mi (7427 to 11,242 km)

or minimum monthly mean, N_0

200 to 400 N-units (101 M-units)*

Surface reflection lobing options

Contributes to variability* or determines median level

Surface type options

Poor, average* or good ground, fresh or sea water, concrete, metal

Sea state

0-glassy,* 1-rippled, 2-smooth, 3-slight, 4-moderate, 5-rough, 6-very rough, 7-high, 8-very high, 9-phenomenal

or rms wave height, σ_h

0 to 50 m (164 ft)

Temperature

0, 10,* or 20°C

Terrain elevation above msl at facility

0* to 15,000 ft-msl (4572 m-msl)

Parameter, Ah

0* or greater

Time availability options

For instantaneous levels exceeded* or for hourly median levels exceeded

Climates

0*-Continental all year, 1-Equatorial, 2-Continental subtropical, 3-Maritime subtropical, 4-Desert, 5-Continental Temperate, 7a-Maritime Temperate Overland, 7b-Maritime Temperate Overseas

or time blocks

1, through 8, summer, winter

*Values or options that will be assumed when specific designations are not made are flagged by asterisks.

Figure 1. Input parameters for IP-77.

CAPABILITY	REMARKS*
1. LOBING**	Transmission loss versus path distance.
2. REFLECTION COEFFICIENT**	Effective specular reflection coefficient versus path distance.
3. PATH LENGTH DIFFERENCE**	Difference in direct and reflected ray lengths versus path distance.
4. TIME LAG**	Same as above but with path length difference expressed as time delay.
5. LOBING FREQUENCY-D**	Normalized <u>distance</u> lobing frequency versus path distance.
6. LOBING FREQUENCY-H**	Normalized <u>height</u> lobing frequency versus path distance.
7. REFLECTION POINT**	Distance to reflection point versus path distance.
8. ELEVATION ANGLE**	Direct ray elevation angle versus path distance.
9. ELEVATION ANGLE DIFFERENCE**	Angle by which the direct ray exceeds the reflected ray versus path distance.
10. SPECTRAL PLOT**	Amplitude versus frequency response curves at various path distances.
11. POWER AVAILABLE	Power available at receiving antenna versus path distance or central angle for time availabilities of 5, 50 and 95%, and fixed antenna heights.
12. POWER DENSITY	Similar to above, but with power density ordinate.
13. TRANSMISSION LOSS	Similar to above, but with transmission loss ordinate.
14. POWER AVAILABLE CURVES	Power available curves versus distance are provided for several aircraft altitudes for a selected time availability, and a fixed lower antenna height.
15. POWER DENSITY CURVES	Similar to above, but with power density as ordinate.
16. TRANSMISSION LOSS CURVES	Similar to above, but with transmission loss as ordinate.
17. POWER AVAILABLE VOLUME	Fixed power available contours in the altitude versus distance plane for time availabilities of 5, 50, and 95%.
18. POWER DENSITY VOLUME	Similar to above, but with fixed power density contours.
19. TRANSMISSION LOSS VOLUME	Similar to above, but with fixed transmission loss contours.
20. EIRP CONTOURS	Contours for several EIRP levels needed to meet a particular power density requirement are shown in the altitude versus distance plane for a single time availability.
21. POWER AVAILABLE CONTOURS	Similar to above, but with power available contours for a single EIRP.
22. POWER DENSITY CONTOURS	Similar to above, but with power density contours.
23. TRANSMISSION LOSS CONTOURS	Similar to above, but with transmission loss contours.
24. SIGNAL RATIO-S	Desired-to-undesired, D/U, signal ratio versus station separation for a fixed desired facility-to-aircraft distance, and time availabilities of 5, 50, and 95%.
25. SIGNAL RATIO-D0	Similar to above, but the abscissa is desired facility-to-aircraft distance and the station separation is fixed.
26. ORIENTATION	Undesired facility antenna orientation with respect to the desired-to-undesired station line versus required facility separation curves are plotted for several desired facility antenna orientations.
27. SERVICE VOLUME	Fixed D/U contours are shown in the altitude versus distance plane for a fixed station separation and time availabilities of 5, 50, and 95%.
28. SIGNAL RATIO CONTOURS	Contours for several D/U values are shown in the altitude versus distance plane for a fixed station separation, and time availability.

*Additional discussion, by capability, will be provided in an "Applications Guide", which should be published in 1978 (Johnson and Gerhart, 1978).

**Applicable only to the line-of-sight region for spherical earth geometry. Variability with time and horizon effects are neglected.

Figure 2. Plotting capability guide for IF-77 programs.

PARAMETERS FOR ITS PROPAGATION MODEL IF-77
77/07/13. 22.15.49 RUN

TRANSMISSION LOSS
SPECIFICATION REQUIRED

AIRCRAFT (OR HIGHER) ANTENNA ALTITUDE: 45000. FT (13716.M) ABOVE MSI.
FACILITY (OR LOWER) ANTENNA HEIGHT: 50.0 FT (15.2M) ABOVE FSS
FREQUENCY: 125. MHZ

SPECIFICATION OPTIONAL

AIRCRAFT ANTENNA TYPE: ISOTROPIC
POLARIZATION: HORIZONTAL
EFFECTIVE REFLECTION SURFACE ELEVATION ABOVE MSL: 0. FT (0.M)
EQUIVALENT ISOTROPICALLY RADIATED POWER: 14.0 DBW
FACILITY ANTENNA TYPE: ISOTROPIC
POLARIZATION: HORIZONTAL
HORIZON OBSTACLE DISTANCE: 8.69 N MI (16.09KM) FROM FACILITY*
ELEVATION ANGLE: -0/ 6/30 DEG/MIN/SEC ABOVE HORIZONTAL*
HEIGHT: 0. FT (0.M) ABOVE MSL
REFRACTIVITY:
EFFECTIVE EARTH RADIUS: 4586. N MI (8493.KM)*
MINIMUM MONTHLY MEAN: 301. N-UNITS AT SEA LEVEL
SURFACE REFLECTION LOBING: CONTRIBUTES TO VARIABILITY
SURFACE TYPE: AVERAGE GROUND
TERRAIN ELEVATION AT SITE: 0. FT (0.M) ABOVE MSL
TERRAIN PARAMETER: 0. FT (0.M)
TIME AVAILABILITY: FOR INSTANTANEOUS LEVELS EXCEEDED

* COMPUTED VALUE

- Notes: 1) Parameter values (or options) not indicated are taken as the assumed values (or options) provided on the general parameter specification sheet (fig. 1).
- 2) To simulate computer output, only upper case letters are used. Dual units are not provided on actual computer output.

Figure 3. Parameter sheet for capability 13.

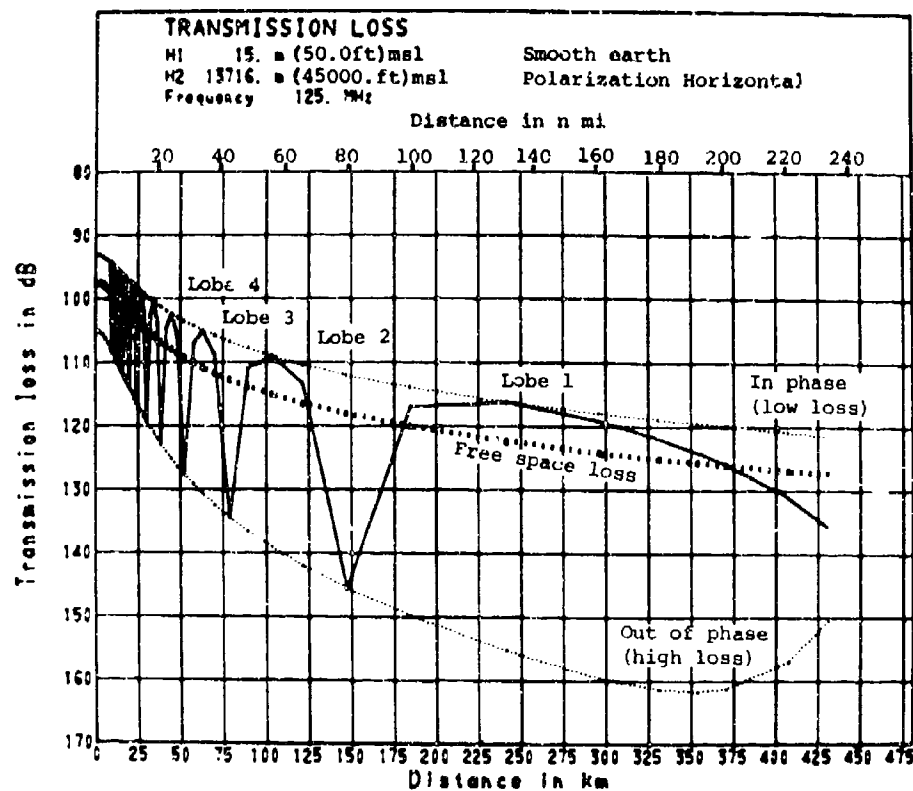


Figure 4. Plot for capability 1, LOBING.

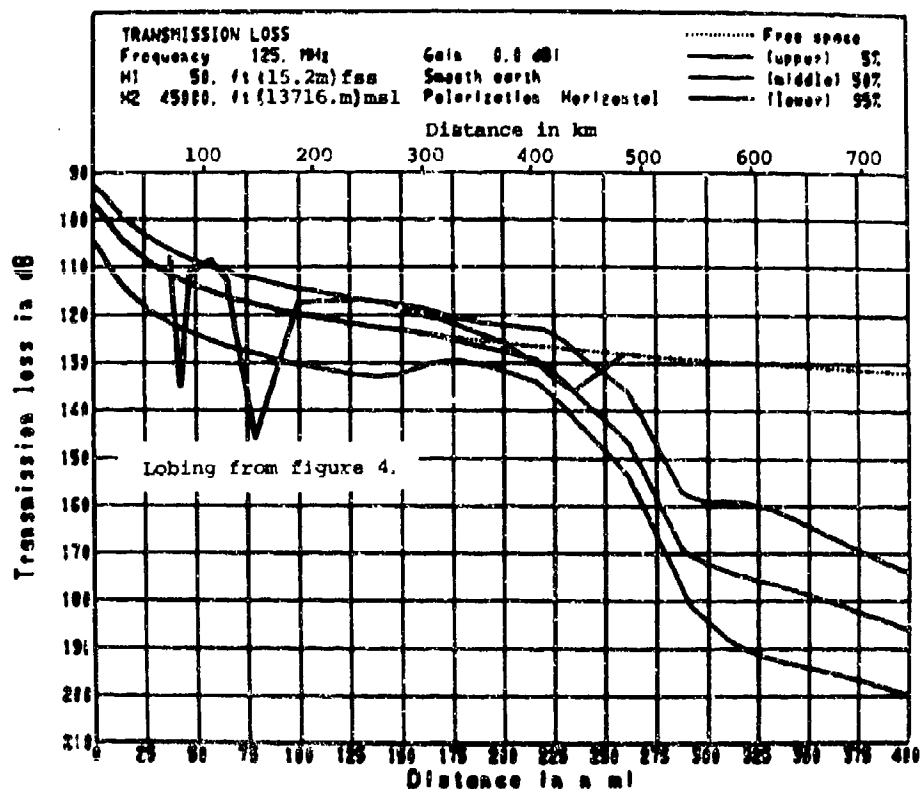


Figure 5. Plot for capability 13, TRANSMISSION LOSS.

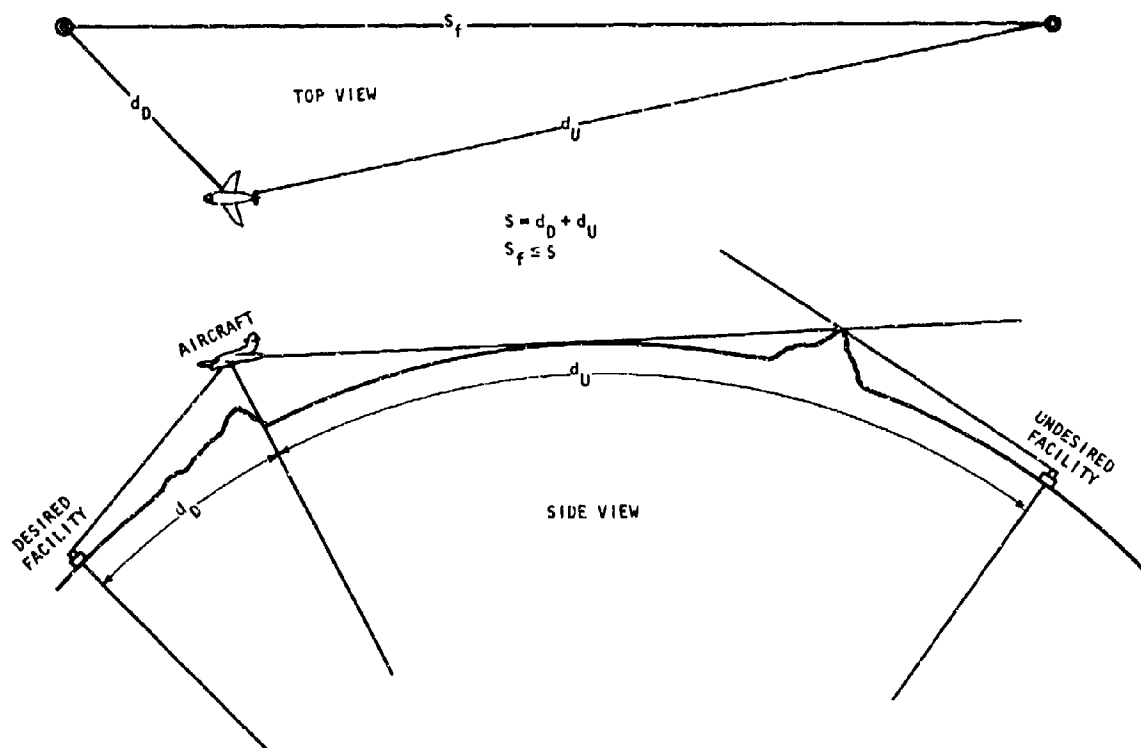


Figure 6. Sketch illustrating interference configuration.

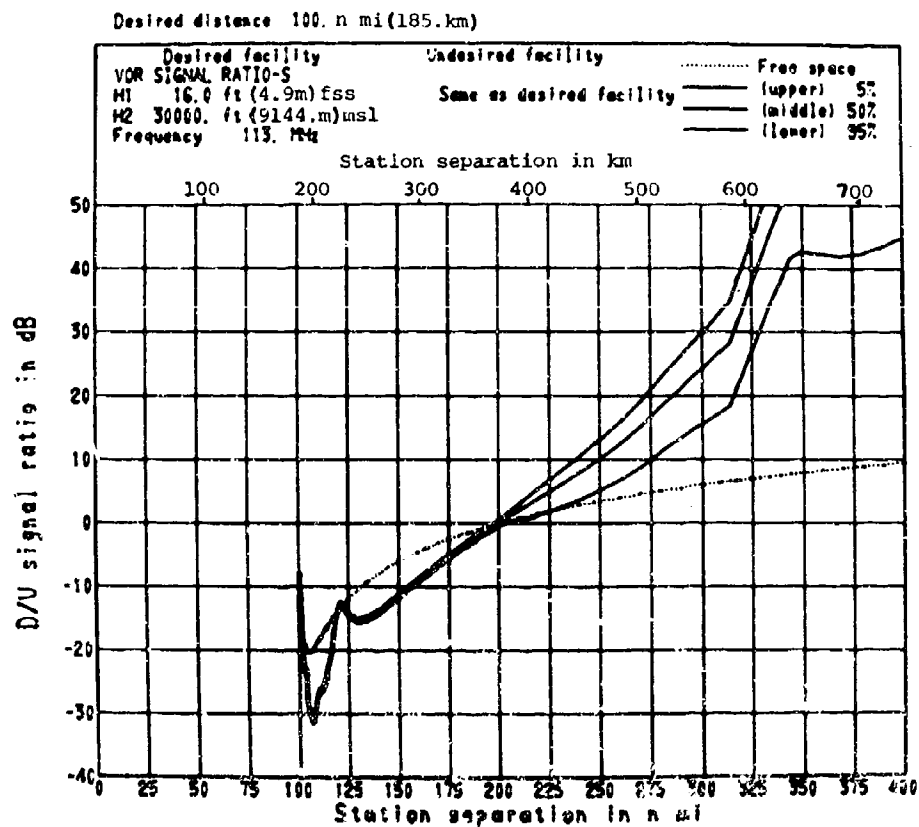


Figure 7. Plot for capability 24, SIGNAL RATIO-S.

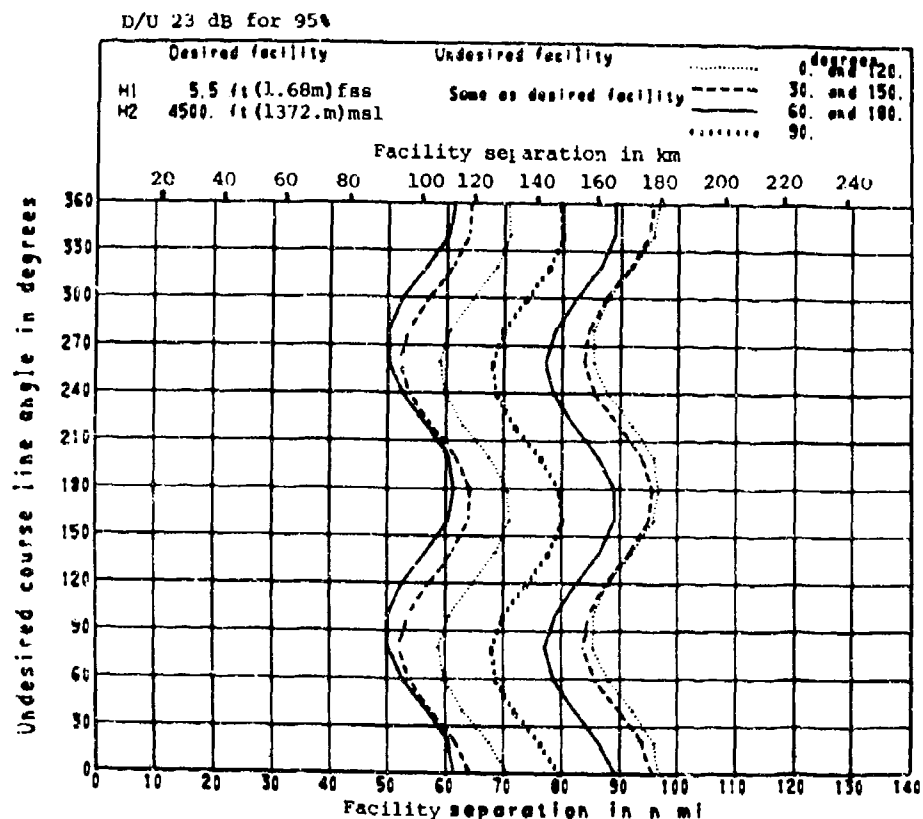
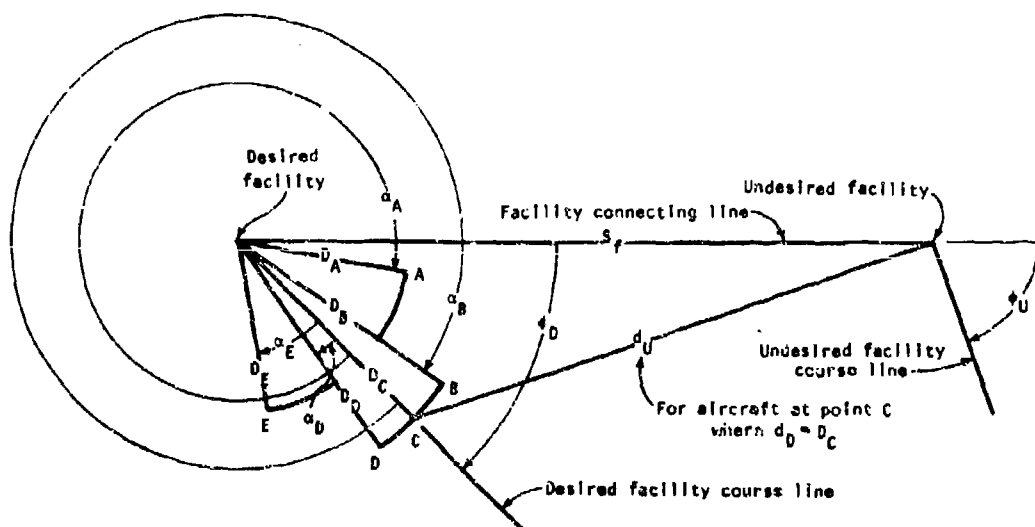


Figure 8. Plot for capability 26, ORIENTATION.



All angles are positive clockwise.

Angles to course lines, $\phi_{D,U}$, are measured from facility connecting line.

Angles to protection points, $\alpha_{A,B,C,D,E}$, are measured from the desired station course line.

Point C is along the course line so that $\alpha_C = 0$, but this is not a required condition.

Facility separation, S_f , is in general less than station separation, S , when S is calculated from $S = d_D + d_U$ where $d_{D,U}$ are facility to aircraft distances. This is illustrated for protection point C.

Figure 9. Sketch illustrating protection point geometry.

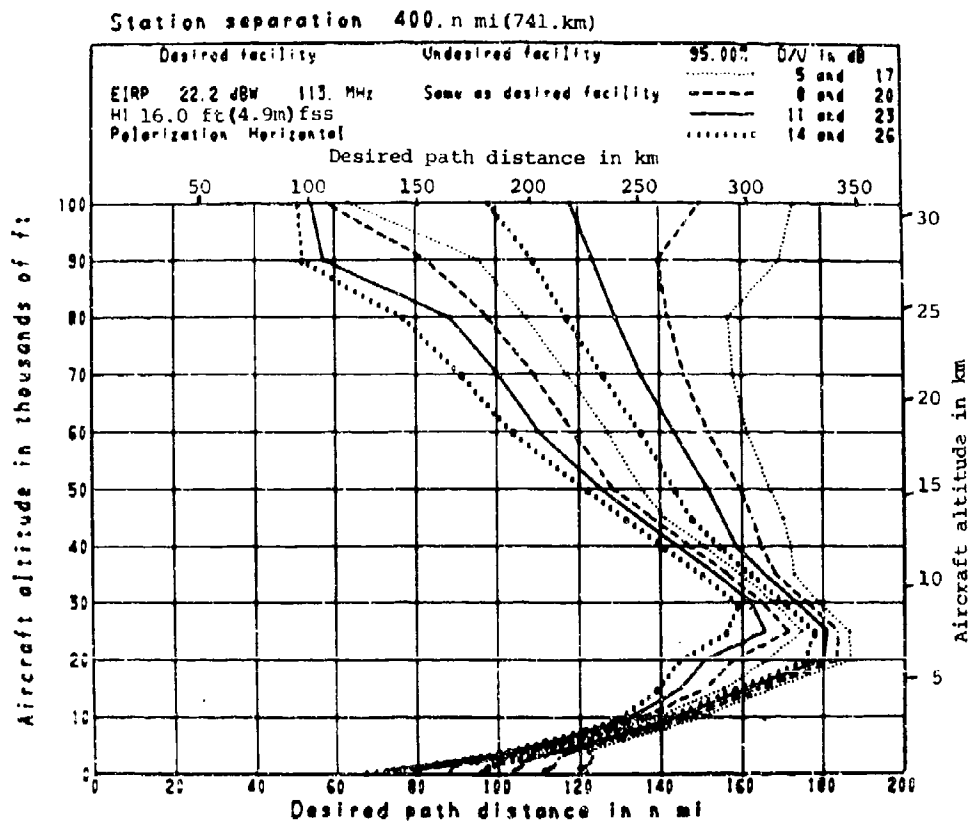


Figure 10. Plot for capability 28, SIGNAL RATIO CONTOURS.

PATH 92 ATLANTA GA - FORSYTH GA

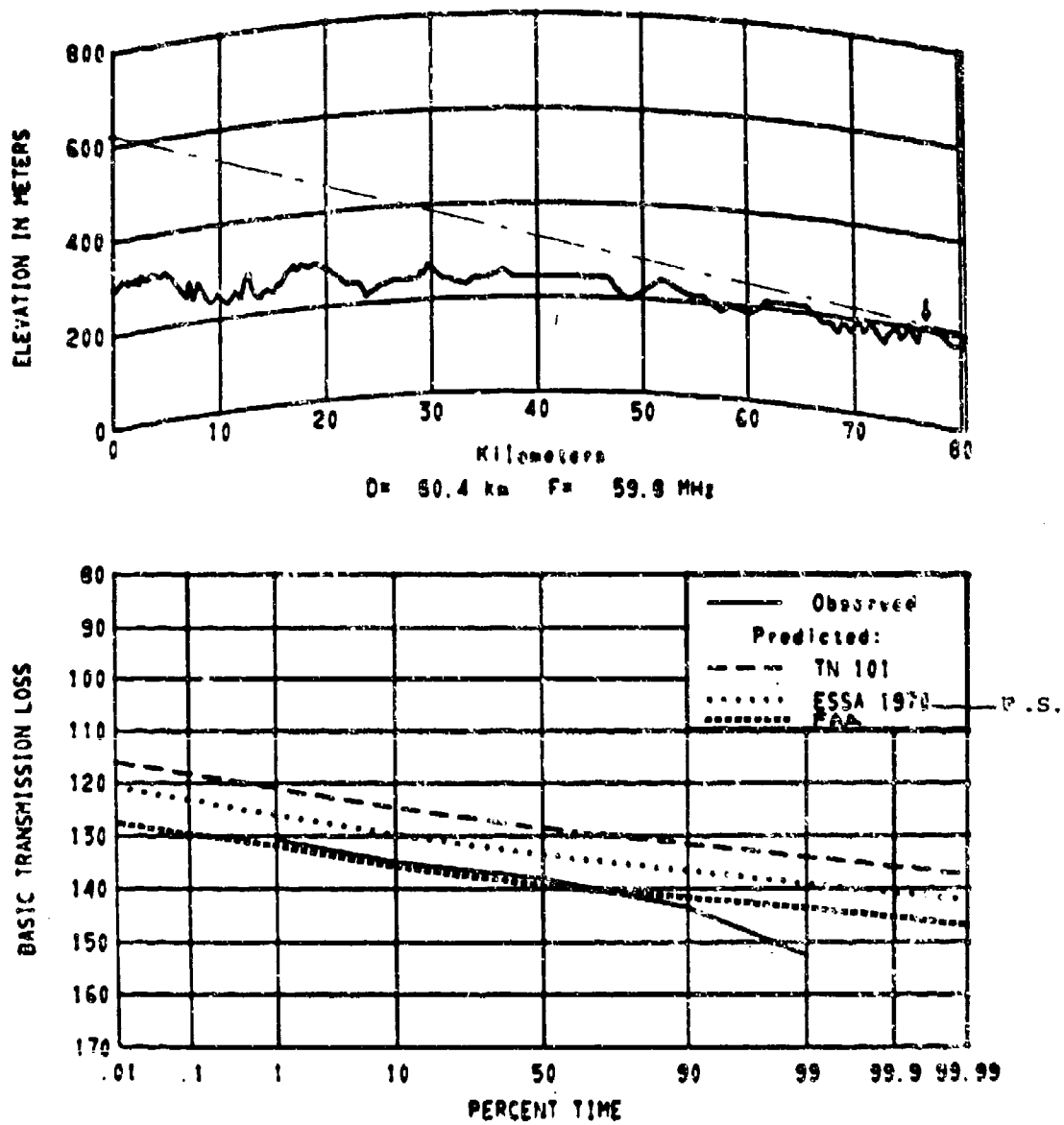


Figure 11. Profile, data and predictions for path 92.

DISCUSSION

H. Vissinga, Netherlands

Is distortion by multipath propagation included in the IF-77 model, and if not, are there plans to include it?

Author's Reply

Distortion, as such, is not predicted, and such model extensions are not currently planned. However, the time lag (Figure 2, # 4) and spectral plot (Figure 2, # 10) capabilities may be useful in distortion estimation for multipath due to a specular reflection from the earth.

J. Röttger, FRG

What is the reason why you have not included specifically the role of quasi-specular reflection at thin stratified layers in your model?

Author's Reply

While the model does not treat these reflections in a deterministic manner, their effects are accounted for in the long-term variability portion of our model (Sec. 2.3).

THE CRC VHF/UHF PROPAGATION PREDICTION PROGRAM:
DESCRIPTION AND COMPARISON WITH FIELD-MEASUREMENTS

F.H. Palmer
Communications Research Centre
Department of Communications
Ottawa, Canada

SUMMARY

A computer-based propagation prediction program has been developed which provides an accurate, easy-to-use means of predicting coverage areas for VHF and UHF systems, for the planning of radio links, both terrestrial and air/ground, and for use in electromagnetic compatibility analysis problems. A topographic data-base enables detailed path-loss or field-strength calculations to be carried out in the Ottawa area by users who need only specify the transmitter and receiver parameters and define the area in which results are required. This data-base can be extended to other areas of Canada.

Comparisons of predictions with measured values of path-loss show that the detailed method of prediction is significantly better than statistical techniques and is the only method capable of identifying low signal areas in the shadows of terrain obstructions.

1. INTRODUCTION

While the Communications Research Centre (CRC) has had extensive experience in the behaviour of radio waves throughout most of the radio spectrum, very few propagation studies have been carried out at VHF and UHF in recent years. In view of this, a VHF/UHF Propagation Group was established in 1974. The purpose of this group was to study the following areas of interest, to identify the outstanding problems, and to provide solutions where possible.

1.1 Computer Techniques

In areas for which VHF/UHF propagation prediction techniques are relatively well developed, the efficient use of the techniques is often compromised by the time required to perform adequate calculations. The implementation of complex and numerous path-loss or field strength calculations by means of computer-based techniques offers the possibility of significantly improving prediction accuracies over those currently available for routine operations.

1.2 Urban Environments

The planning and management of the VHF/UHF parts of the radio spectrum require the ability to accurately predict the field strength expected at any location due to both existing and proposed transmitters. The increasing demand for frequency assignment in these bands is creating acute problems in urban and near-urban areas where current prediction techniques are least reliable.

1.3 'Remote' Environments

It is anticipated that there will be an increasing utilization of VHF/UHF communication systems in remote areas of Canada. Such systems will operate in climates and terrains the effects of which have been relatively little studied to date. Although propagation studies have been performed by other countries for their own use, the environmental conditions in Canada are unique and it is not clear whether existing techniques can be applied without modification.

Field trials have been used by CRC to determine the accuracies with which currently available techniques model the propagation characteristics of typical Canadian environments. Paths up to 100 km in length have been studied and improvements carried out where possible. The results of these studies have been incorporated into a computer-based propagation prediction program which includes a topographic data-base relevant to the Ottawa area.

This paper is in three main parts. The first presents a brief summary of the organization of the propagation prediction program. The second discusses the conversational subroutine and the propagation and topographic models that are included in the prediction program and the third part presents comparisons between predicted and measured path-losses.

2. A SUMMARY OF THE PREDICTION PROGRAM

Based on an extensive review of existing propagation modelling techniques, a computer prediction program was constructed which incorporates a number of existing techniques. In addition, a number of new features were introduced which include the following:

- (a) A 'conversational' subroutine 'PREDICT', which acts as an interface between the user and the main computational subroutines. This routine is intended to make the prediction program relatively easy to use by persons lacking a wide knowledge of computer and prediction techniques.

- (b) A topographic data-base encompassing 13,440 square kilometers of Eastern Ontario, centred on Ottawa.
- (c) A fully automatic 'detailed' mode of calculating path-loss or signal-strength which uses path-profiles provided either by the user or extracted automatically for paths in the Ottawa area from the topographic data-base stored in the computer.
- (d) An environmental 'clutter' correction factor that may be calculated, if the user wishes, to account for the effects of the local antenna environments.

The program itself breaks naturally into three main segments (see Figure 1)

- The conversational routine 'PREDICT'
- The main computational routine 'RUN'
- The topographic data-base 'TOPO'

3. THE PREDICTION PROGRAM

3.1 The 'Conversational' Routine 'PREDICT'

The purpose of 'PREDICT' is to construct a data file 'INPUT' based on user responses to questions provided by the computer, and to set a series of flags that identify the specific types of calculation to be carried out. 'RUN' then uses this input file to perform the appropriate calculations.

The type of calculation desired by the user is determined by his responses to questions such as

- (a) Are path-loss or signal-strength calculations required?
- (b) Do you require
 - i) Point-to-point
 - ii) Radial coverage, or
 - iii) Complete area coverage calculations?

The user is subsequently asked only those questions concerning equipment and terrain parameters that are relevant to the particular type of calculation required. For example, if the user elects to compute path-loss rather than signal-strength, questions concerning transmitter output power, line-losses, etc., do not appear. In this way, the user is not faced with the complete set of all possible questions that might be asked, regardless of their relevance.

If the propagation path defined by the user is contained within the topographic data-base 'TOPO' all terrain parameters will be deduced automatically by 'RUN' as required. If the computer determines that the path is not contained within the data-base, the user may then be asked:

- (a) Can you supply your own terrain profile?, or
- (b) Is the propagation path entirely contained in an urban core area?, or
- (c) Choose a terrain type from the following list:
 - i) Don't know
 - ii) Smooth plains
 - iii) Rolling plains
 - iv) .
 - v) .
 - vi) .
 - vii) Extremely rugged mountains

The responses to these questions determine the specific subroutine in 'RUN' that will be used to calculate path-loss or field-strength. If the propagation path is contained within the data-base, or if a terrain profile can be inverted by the user, calculations will be done using a 'detailed' path-loss model. If the path lies entirely within an urban core area, calculations will be carried out using a statistical model relevant to those areas. If the user chooses a terrain type from the list given above, a statistical 'irregular terrain' model will be used for calculations except for the case of the 'don't know' response. In this case, calculations are carried out using a smooth-earth propagation model.

At this point, the user may be requested to provide additional parameters such as antenna heights, transmitter power, antenna line-losses, and antenna polarizations and radiation patterns.

The user may also supply his own values of average ground conductivity and permittivity and surface value of atmospheric refractivity if he so wishes. Finally, he is asked if he knows anything of the transmitter and receiver antenna environments. If he does, he is asked to specify the type, height, distance, and other parameters relating to local obstacles along the transmitter-receiver line-of-sight. 'RUN' later uses these parameters to calculate values of transmission loss through the obstacles or of diffraction loss over or around the obstacles.

At this point the user may review and edit the input data file if he so wishes, and then submit the input file 'INPUT' to 'RUN' either in real-time or as a batch job.

3.2 The Topographic Data-Base 'TOPO'

The topographic data-base comprises the city of Ottawa and surrounding suburban and rural areas. A rectangular area 112 by 120 kilometres (13,440 sq. km.) has been scaled with a resolution of 1.0 km.

Each of the 13,440 grid points in 'TOPO' consists of the coordinates of the grid point, the maximum, minimum, and average elevations occurring in a 1 km square cell centred on the grid point, and a code representing the average type of terrain cover in the 1 km square cell.

It is anticipated that knowledge of the maximum and minimum terrain heights will later enable more refined computer estimates of path-loss location variability to be made. The terrain cover codes are used to provide estimates of ground conductivity and permittivity and of average terrain cover heights. These heights are added to the topographic elevations to define the 'effective' heights along the profile.

An example of a computer-derived path-profile, together with the actual profile as measured directly from topographic maps, is shown in Figure 2.

3.3 The Computational Routine 'RUN'

Based on a review of existing propagation prediction techniques, a number of models were selected for inclusion in 'RUN'. It was anticipated that these techniques would be modified and extended after comparisons of the initial predictions of the program with observed values of path-loss over known paths. To this end, measurement programs have been carried out in the Ottawa area and at Inuvik and Resolute Bay, N.W.T.

It is evident that the particular type of path-loss calculation used in any given situation depends upon a number of factors which include the location of the propagation path (urban core area or open terrain) and the amount of information available to the user concerning the nature of the terrain. (Terrain profile or a statistical description of path parameters).

To make the computer program relevant to all types of propagation paths, and levels of user knowledge concerning these paths, it was decided to incorporate into it a number of different propagation models. The choice of the model or models to be used in any given situation is made automatically by the computer, depending upon user responses to questions set by 'PREDICT'.

The propagation models included in the prediction program are:

- (a) Smooth-earth model
- (b) Urban-area model
- (c) Irregular-terrain model
- (d) A detailed model which uses path-profiles either supplied by the user or generated automatically from 'TOPO'
- (e) Antenna environment 'clutter' model.

3.3.1 The Smooth-Earth Model

This model is used in cases where smooth-earth path-losses are desired as references or where user knowledge of the propagation path characteristics is minimal. The model used in the present program is a modified version of that described by Sachs/Freeman Associates, Inc. (1970). It is a simplified version of the van der Pol and Bremmer (1937) and Norton (1941) smooth-earth techniques which were used for the calculation of the CCIR (1955) Atlas curves. In addition, a tropo-scatter term is added for beyond-the-horizon calculations, following Frazier and Anderson (1963).

3.3.2 The Urban-Area Model

Two slightly different urban area models are incorporated into 'RUN'. The first is used when a propagation path lies wholly within an urban area. The second is used in conjunction with the 'detailed' model when either the transmitter or receiver end of the path is located in an urban area. This second version will be discussed later as part of the 'detailed' model.

The topography of urban areas has a profound effect on observed path-losses, but is too complex to model in any detailed way. Only statistical techniques are currently available. The most commonly used model is due to Egli (1957), although a number of other models exist (Murphy, 1971; McMahon, 1974). These models are usually of the form

$$L = a_1 + a_2 \log f + a_3 \log d + a_4 \log h_t + a_5 \log h_r \quad \text{dB}$$

where f is frequency in MHz, d is distance in km, and h_t and h_r are transmitting and receiving antenna heights in metres. The a_i are chosen to minimize the rms error between predicted values of path-loss and those measured over actual propagation paths. Different investigators use different sets of data, collected in different areas, with the result that a variety of different values are found for the a_i . The coefficients currently used are those due to Egli (1957):

$$a_1 = 85.9; a_2 = 20.0; a_3 = 40.0; a_4 = -20.0; a_5 = -20.0 \quad \text{for } h > 10 \text{ m}$$

$$a_1 = 76.3; a_2 = 20.0; a_3 = 40.0; a_4 = -20.0; a_5 = -10.0 \quad \text{for } h \leq 10 \text{ m}$$

It is anticipated that these coefficients will be modified as experimental data becomes available for Canadian urban areas.

3.3.3 The Irregular-Terrain Model

This model was developed by A.G. Longley and P.L. Rice and is described in detail in ESSA Technical Report ERL 79-ITS 67 (1968). It is applicable to propagation over irregular terrain in suburban and rural areas. Calculations of path-loss are based on analytic techniques. However, the values of parameters such as horizon distance, obstacle height, etc., that are used in these calculations are statistical medians based on a terrain irregularity height, Δh , which is chosen to be typical of the propagation path. Thus, "slightly rolling plains" correspond to $\Delta h = 30$ m and "hills" correspond to $\Delta h = 115$ m, etc.

It is clear that a model such as this is suited to propagation loss calculations for paths over 'statistically uniform' types of terrain where there are no isolated large obstacles. If such isolated obstacles exist along the propagation path, this model may seriously underestimate the path loss in the 'shadows' of such obstacles.

It should also be noted that the predicted values of path-loss are medians and are intended to represent the average path-loss that would be measured over some area in the vicinity of the receiver. If the terrain is hilly or mountainous, large variations may be measured about the predicted medians as the receiving antenna is moved up or down the slopes of the hills or mountains.

This model is not restricted to relatively short paths, as was the urban model, because of the inclusion of a tropo-scatter term.

3.3.4 The 'Detailed' Model

When sufficient knowledge of path characteristics exists, the 'detailed' model, which takes into account the detailed nature of the path topography, is used to calculate path-loss. Basically, this involves computing diffraction losses due to obstacles which may exist along the path, reflection losses from flat surfaces, and tropo-scatter losses. The model thus accounts for shadow losses behind terrain irregularities of essentially any type. For over-the-horizon paths, tropo-scatter levels are calculated and the appropriate values of either diffraction or scatter loss are used to define the total path-loss. This model can also account for the effects of limited types of environmental 'clutter' in the vicinity of the transmitting or receiving antennas. At present, local effects due to trees and buildings may be included. This clutter routine is also used in the smooth-earth and irregular terrain models.

1) Derivation of Path-Profiles

The manner in which path-profiles are deduced from a topographic data-base depends upon the size of the data-base as well as its organization. In the present case, profiles are interpolated from the data-base grid with the use of plane rather than spherical geometry. This results in a saving in time and complexity and, for profiles derived from a data-base of the present size, does not result in significant errors in path position with respect to the data-base resolution. For longer paths, the projection of the propagation path and data-base grid onto the earth's surface must be done using the appropriate geometry.

To the average terrain height h_t at each distance d_t along a profile is added a 'ground-cover correction height' derived from the terrain cover code at that point. This correction is designed to take into account the height of buildings and trees under the propagation path. In the present model these height corrections are:

Woods/Forest	10 metres
Suburban buildings	10 metres
Urban core	30 metres
Other	0

Finally, the corrected terrain elevations (above sea-level) are modified to take into account the effective radius of the earth's surface. This effective radius is computed using the value given by the user for the surface atmospheric refractivity N , or by using a default value of 300 N-units. With the use of this effective radius, radio waves may be considered to travel in straight lines and simple plane trigonometry can be used to determine the actual path of a radio wave with respect to the earth's surface.

1i) Propagation Paths Completely Outside Urban Areas

If the propagation path is interpolated from the topographic data-base, each of the terrain cover codes is checked to see if either end of the propagation path lies in an urban area. Cases in which these codes are found involve certain additional calculations. These will be discussed in section (1ii).

In all cases, a subroutine is called to determine the location and other parameters of whatever obstacles exist along the given profile. Obstacles are determined by the "stretched string" technique in which a string may be imagined to be tightly stretched over the terrain between transmitter and receiver. Then a subroutine determines if large obstacles are to be considered as single or multiple, e.g. is a large hill cut by ravines a single or multiple obstacle? Finally, individual path-loss calculations are carried out once the appropriate obstacles and their parameters have been determined.

The first subroutine uses simple geometrical techniques to determine whether the propagation path is: line-of-sight with adequate Fresnel-zone clearance ($N_F > 0.6$), line-of-sight with restricted Fresnel-zone clearance, or obstructed. In the first case, diffraction losses are assumed to be zero. If the propagation path is obstructed, or has a restricted Fresnel-zone clearance, the parameters d_x , d_y , H , and c are determined for each obstacle. The radius of the obstacle crest is determined by a three point parabolic fit. The definitions of each of these parameters, for a path containing two obstacles, are given on Figure 3. These parameters are then used to define the first Fresnel-zone radius, $R = (\lambda d_x d_y / (d_x + d_y))^2$ and the curvature factors of the obstacle, $a = \lambda^2/8 r^2/R$ where λ is the wavelength.

The main obstacle, at location 1 in the example, is defined to be the obstacle having the largest value of H/R . The effective height of the secondary obstacle is its height above the line-of-sight between the crest of the main obstacle and the transmitting or receiving antennas (receiving antenna in the example). H is defined to be negative for obstacles below the line-of-sight and positive otherwise. The method of obstacle parameter determination can be extended to paths containing any number of obstacles, and is due to Deygout (1966).

The diffraction loss over each obstacle is computed as a function of the parameters H/R and α . Nomograms giving diffraction loss as a function of these parameters have been presented by Dougherty and Maloney (1964) and by d'Assis (1971). These nomograms have been extended and approximated by polynomial expressions suitable for machine calculation. The total diffraction loss is the sum of the diffraction losses due to each obstacle.

Reflection 'losses' between obstacles or between transmitter and receiver over unobstructed paths are determined next. The magnitude and phase of the reflected ray is calculated for any segment of terrain that is smooth, horizontal, and satisfies the geometrical requirements for interference between the direct and reflected rays. Reflection coefficients are determined using the available values of surface conductivity and permittivity. The total reflection 'loss' is the sum of the 'losses' due to each reflecting surface. It is possible, of course, for a net gain to be realized if the direct and reflected waves combine in phase.

The path-loss L_d is defined to be the sum of the individual diffraction losses, reflection losses, and free-space loss. For each obstructed path, a tropo-scatter loss term L_s is calculated using a technique similar to that described by CCIR (1966). The smaller of L_d and L_s is taken to represent the actual path-loss expected over the propagation path.

iii) One End of Propagation Path in an Urban Area

In all cases the computer checks the terrain cover codes for each point at which a path-loss or field-strength calculation is required. If such a point is found to lie in an urban area, two separate path-loss calculations are carried out. The first is the detailed calculation as previously described, and the second is a statistical loss calculation related to that used in the urban area model. The statistical loss model used here is not identical to that used in the urban model since, in this case, only one end of the propagation path lies in the urban area. Currently, expressions equal to $L = L_{CLI} - 1000/f(\text{MHz})$ dB are used. These expressions were empirically determined to best fit the Ottawa area measurements, where one end of the propagation path lay in the urban core area. The final value of path-loss is the maximum of the statistical and detailed calculation values of path-loss.

iv) The Environmental 'Clutter' Routine

This routine accounts for the presence of buildings or trees in proximity to the transmitting or receiving antennas.

Numerous measurements of excess path-loss in or near built-up or treed areas have been carried out. Few models have been developed from the data which enable predictions to be made in the general case. The routine incorporated into the present program is a composite and summarizes existing data and models thus far available. (Rice, 1971; Head, 1960; LaGrone et al., 1953; Saxton and Lane, 1955; Okumura et al., 1968; etc.).

Trees

Path-losses due to trees may be considered in the following three categories:

(a) Entering a wooded area from the transmitter (receiver) side in the case of clutter around the receiver (transmitter) antenna. The path-loss increases at the rate of:

$$L_v = 1637\alpha + \left[\frac{\exp(-90/f) \log(1 + f/100)}{2.99} \right] \quad \text{dB/metre}$$

$$L_h = 1637\alpha + \left[\frac{\exp(-210/f) \log(1 + f/200)}{2.34} \right] \quad \text{dB/metre}$$

where v and h stand for vertical and horizontal polarization respectively, f is in MHz, and α depends upon tree type (Rice, 1971).

(b) Inside a wooded area. After the initial increase in attenuation described above, the path-loss relative to free-space in a wooded area reaches a more or less constant value, independent of distance. 30 dB is a typical value for this limiting attenuation for the UHF band (Head, 1960). In the present program the loss is taken to increase linearly with tree height above the antenna to a maximum of 30 dB when the tree cover extends 30 metres or more above the antenna.

(c) Antenna behind a wooded area. At distances greater than five times the mean tree height above the antenna, the tree-tops are taken as defining a knife-edge, and the resultant path-loss is that expected as a result of diffraction over this edge. For distances behind the trees of less than five times the mean tree height above the antenna, the knife edge loss is smoothly joined to the constant value found within the wooded area.

Buildings

Three separate loss factors are calculated and the minimum value is taken as the predicted additional loss. The loss through the structure of the buildings is given empirically by $L_1 = M \cdot d/15$ (dB) where d is the extent of the building(s) along the line-of-sight, and M is a loss factor dependent upon

the construction type. ($M = 15$ dB for wood, 30 dB for concrete, and 45 dB for steel). Diffraction losses over the building(s) are accounted for by $L_2 =$ knife-edge diffraction loss. An empirical maximum path-loss of $L_3 = 20 \log f$ is assumed.

In the case of both buildings and trees, a factor $(1 - \exp(-\Delta L/d))$ is introduced to account for the finite extent of the obstructions perpendicular (across) the line-of-sight. ΔL is the minimum extent of the obstruction across the line-of-sight and d is the distance between the antenna and the closest part of the obstruction.

4. COMPARISON OF PREDICTED AND MEASURED PATH-LOSS

There are numerous sets of measured path-loss data available with which the results of the propagation prediction program could be compared. Many of these, however, fail to describe the relevant terrain parameters in sufficient detail to be of real use in the present work. Examples of parameters which are seldom reported include the type of ground surface, or terrain cover, radii of curvature of obstacle crests, and the nature of the 'clutter' in the vicinity of the transmitter and receiver antennas.

4.1 Ottawa-Area Measurements

An Ottawa-area measurement program was initiated in January 1975. This program used two existing television transmitters as sources (CKGN at 38 MHz, and CFVO at 572 MHz). Measurements of received signal-strength were made along a number of radials from each transmitter at distances up to about 45 km. At each measurement 'site' five to ten separate measurements of field-strength, at locations separated by 50-100 metres, were made in order to obtain a measure of the spatial variability of signal-strength at each site. The radiation patterns and output powers of the transmitters were known, enabling path-loss to be determined from the corresponding field-strength measurements. More than one thousand individual path-loss measurements were made between April 1975 and April 1976.

4.2 'Remote' Area Measurements

Between August 1976 and May 1977, a series of propagation measurements were made at Inuvik and Resolute Bay, N.W.T. Path-losses were measured in both summer and winter at the two sites. Both horizontally and vertically polarized signals at 150 and 450 MHz were used, together with transmitting antenna heights of 7.2 and 16.5 metres and receiving antenna heights of 1.5 and 3.0 metres. Over two thousand individual measurements of path-loss were made, for all combinations of system parameters, in the 10 month period.

Examples of measured path-losses along radials from the 88 MHz (CKGN) and 572 MHz (CFVO) transmitters, together with the values of path-loss predicted by the 'detailed' and 'irregular terrain' models incorporated into 'RUN' are shown in Figures 4a and 5a. The corresponding path-profiles are shown in Figures 4b and 5b.

Examples of path-loss measured at 150 MHz along radials at both Inuvik and Resolute Bay, again with values of path-loss predicted by both the 'detailed' and irregular terrain models, are shown in Figures 6a and 7a. The corresponding path-profiles are shown in Figures 6b and 7b.

The 'irregular terrain' calculations were carried out using the following values of ΔH :

- i. Ottawa, 88 MHz (Fig. 4a): 55 m
- ii. Ottawa, 572 MHz (Fig. 5a): 15 m
- iii. Inuvik, NWT (Fig. 6a): 45 m
- iv. Resolute Bay, NWT (Fig. 7a): 3 m

The CKGN and CFVO path-profiles shown in Figures 4b and 5b were derived automatically from the topographic data-base. The profiles shown in Figures 6b and 7b were derived manually from topographic maps. The corrections for the earth's curvature, easily visible on paths of this length, were done automatically.

4.3 'Irregular Terrain' Model Predictions

It is clear that the values of path-loss predicted by this model are good approximations to the median values of loss which are measured over lengths of the propagation path which are large compared to the dimensions of typical terrain obstructions. However, in the vicinity of these obstructions, the path-loss may be seriously under or over-estimated depending upon whether the receiving site is at the foot or crest of the obstruction.

4.4 'Detailed' Model Predictions

The CKGN and CFVO radials shown in Figures 4b and 5b cross 'urban' areas at various points along their length. At these points, path-losses are automatically taken to be the larger of those calculated using the terrain loss subroutines and those calculated using a statistical 'urban' subroutine. The resulting increases in predicted path-loss, relative to the losses in neighbouring 'non-urban' areas, can be seen at a distance of about 35 km in Figure 4a and at distances of about 12, 16, and 22 km in Figure 5a. The predicted losses are good approximations to the measured (median) losses in these areas.

All path-loss curves illustrated show the highly variable (spatial) nature of path-loss in irregular terrain. The effects of 'isolated' obstacles are most clearly seen in Figure 7a. The receiving site in the 'shadow' of the obstacle at a distance of 5 km has an associated path-loss approximately 60 dB above that predicted by the irregular terrain model. It is well appreciated by the predictions of the detailed model. The oscillation in path-loss at distances of about 17 and 30 km along this radial are due to reflections from the smooth terrain found along this path.

5. CONCLUSIONS

The propagation prediction program initially constructed during 1975/1976 has been modified as necessary and validated as far as possible for propagation ($d \leq 100$ km) over the types of terrain found in both southern and northern areas of Canada. The following are two major areas in which the present program should be checked against experiment and extended where required.

5.1 Urban Core Areas

A number of statistical models exist which are intended to predict path-losses for propagation paths in urban areas. A comparison of a number of these models indicates that their validity depends upon how closely the urban area in question resembles the city or cities in which the propagation data used to construct the model was collected. Observed path-losses are dependent upon building heights and density; factors which are ignored in most of the present models. It is hoped that, starting in 1978, the existing models can be improved by taking such factors explicitly into account. In addition, multipath effects in these areas can have a profound effect upon digital transmission systems and it is hoped that a start can be made toward modeling these phenomena.

5.2 'Long' Paths

Although tropo-scatter terms are included in the present prediction models, their accuracy has not yet been verified by the experimental programs carried out to date. Large errors are not anticipated for paths in many areas of southern Canada since the original loss expressions are based on large amounts of data collected in areas of the U.S. and Europe. It is not clear, however, that the existing models can be used without modification in the Arctic or Great Lakes areas where climatic factors can differ greatly from those found elsewhere.

To realistically model tropospheric effects, the results of long-term measurement programs are required. One such program was initiated in the summer 1977 as part of a joint project between the Canadian Department of Communications and the Federal Communications Commission of the United States. Signals from 16 Canadian and U.S. VHF/UHF television stations are being monitored from a receiving site at the University of Western Ontario at London, Ontario. Path-lengths range from 130 to 225 km. Eight stations, having a similar range of path-lengths, are being monitored at CRC. Path-loss statistics are currently being derived from the data. At the completion of the project these statistics will be used to modify or extend the troposcatter loss model that is presently incorporated into 'RUN'.

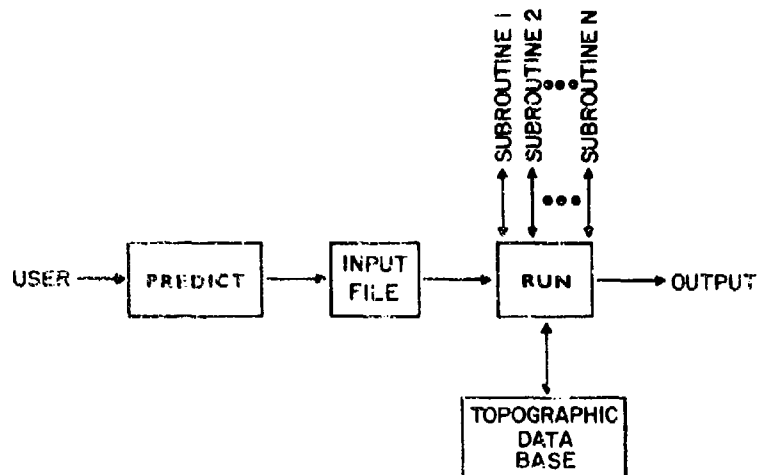
6. REFERENCES

- CCIR, 1955, "Atlas of Ground-Wave Propagation Curves for Frequencies Between 30 Mc/s and 300 Mc/s", 170, Geneva.
- CCIR, 1966, "Documents of the XI Plenary Assembly; Vol. II, Propagation", p. 143, Oslo.
- d'ASSIS, M.S., 1971, "A Simplified Solution to the Problem of Multiple Diffraction Over Rounded Obstacles", IEEE Trans. Ant. and Prop., AP-19, 292-295.
- DEYGOUT, J., 1966, "Multiple Knife-Edge Diffraction of Microwaves", IEEE Trans. Ant. and Prop., AP-4, 480-489.
- DOUGHERTY, R.T. and L.J. MALONEY, 1964, "Application of Diffractions by Convex Surfaces to Irregular Terrain Situations", Radio Science, 68D, 239-250.
- EGLI, J.J., 1957, "Radio Propagation Above 40 Mc/s Over Irregular Terrain", Proc. IRE, 45, 1383-1391.
- FRAZIER, W.E. and D.S. ANDERSON, 1963, "A Propagation Model for Electromagnetic Compatibility Analysis", Proc. Ninth Tri-Service Conference on EMC.
- HEAD, B.T., 1960, "The Influence of Trees on Television Field Strengths at Ultra High Frequencies", Proc. IRE, 48, 1016-1020.
- LAGRONE, A.B., P.E. MARTIN, and C.W. CHAPMAN, 1953, "Height Gain Measurements at VHF and UHF Behind a Grove of Trees", IRE Trans. on Broadcasting, BC-9, 37-54.
- LORNGLEY, A.G. and P.L. RICE, 1968, "Prediction of Tropospheric Radio Transmission Loss Over Irregular Terrain, A Computer Method - 1968", U.S. Dept. of Commerce, Environmental Science Services Administration, ESSA Technical Report ERL 79-ITS 67.
- McMAHON, J.H., 1974, "Interference and Propagation Formulas and Tables Used in the Federal Communications Commission Spectrum Management Task Force Land Mobile Frequency Assignment Model", IEEE Trans. on Vehic. Technology, VT-23, 129-134.
- MURPHY, J.P., 1971, "Statistical Propagation Model for Irregular Terrain Paths Between Transportable and Mobile Antennas", AGARD Conf. Proceedings, CP-70-71, 49.1-49.20.
- NORTON, K.A., 1941, "The Calculation of Ground-Wave Field Intensity Over a Finitely Conducting Spherical Earth", Proc. IRE, 29, 623-639.
- OKUMURA, Y., et al., 1968, "Field Strength and its Variability in VHF and UHF Land-Mobile Radio Service", Review of the Electrical Communication Laboratory, 16, No. 9-10, 825-873.
- RICE, P.L., et al., 1966, "Transmission Loss Predictions for Tropospheric Communications Circuits: Vols. I and II", National Bureau of Standards Technical Note 101.

SACHS-FREEMAN ASSOC MIES, INC., 1970, "Time-Sharing Computer Techniques for Spectrum Management and EMC", SFA, Inc., 7515 Annapolis Road, Suite 408, Hyattsville, Md. 20784.

SAXTON, J.A. and J.A. LANE, 1955, "VHF and UHF Reception - Effects of Trees and Other Obstacles", Wireless World, 61, 229-232.

VAN DER POL, D. and H. BREMMER, 1937, "The Diffraction of Electromagnetic Waves from an Electrical Point Source round a Finitely Conducting Sphere, with Applications to Radiotelegraphy and the Theory of the Rainbow", Part I: Phil. Mts., 141-176. Part II: Phil. Mag., 24, 825-864.



CRC VHF/UHF PROPAGATION PREDICTION PROGRAMME

Fig. 1 Organization of the prediction program.

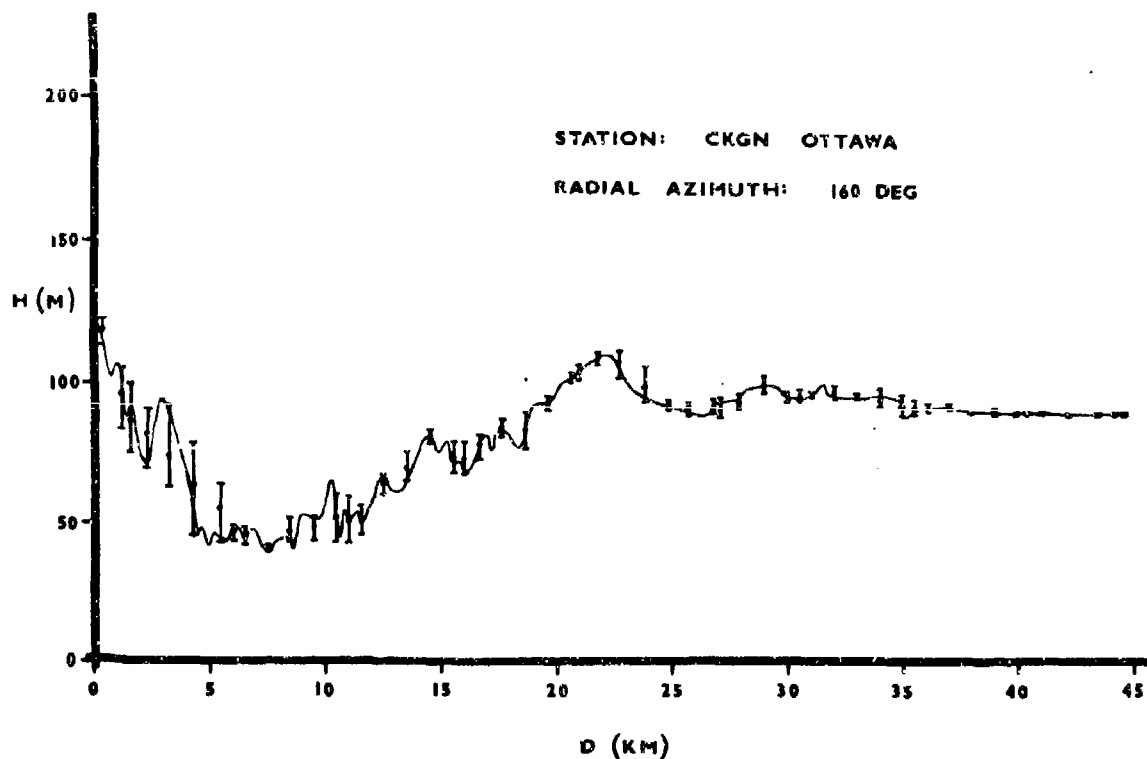


Fig. 2 Example of an actual profile and its reconstruction from the topographic data-base. The vertical bars with dots show the maximum, minimum, and average terrain heights calculated from the corresponding data in the 1 km square cells of the data-base.

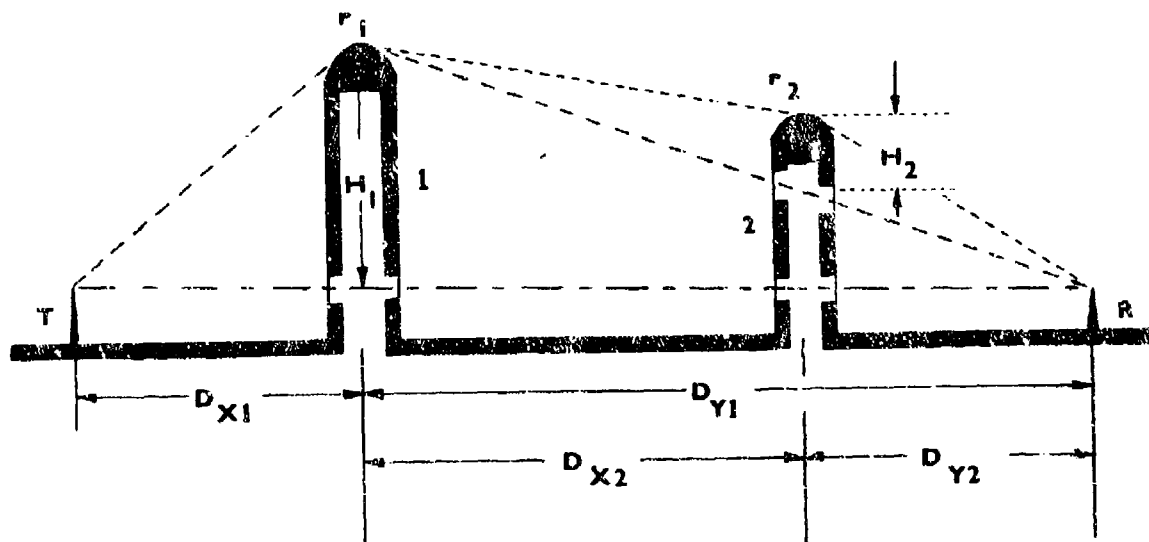
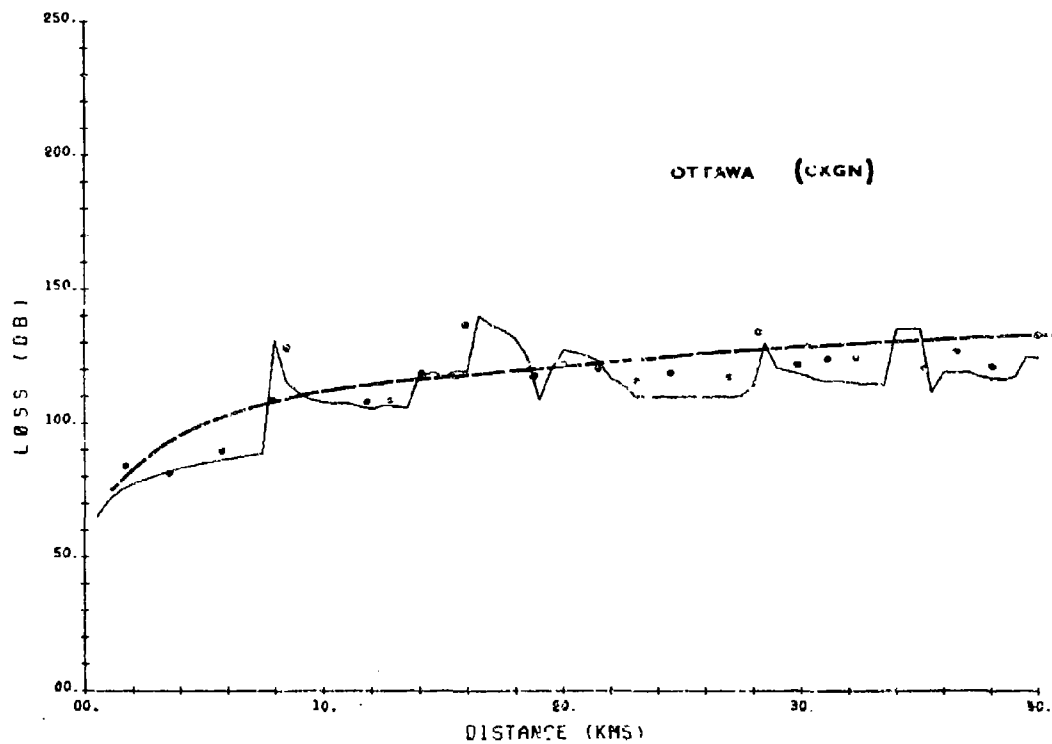
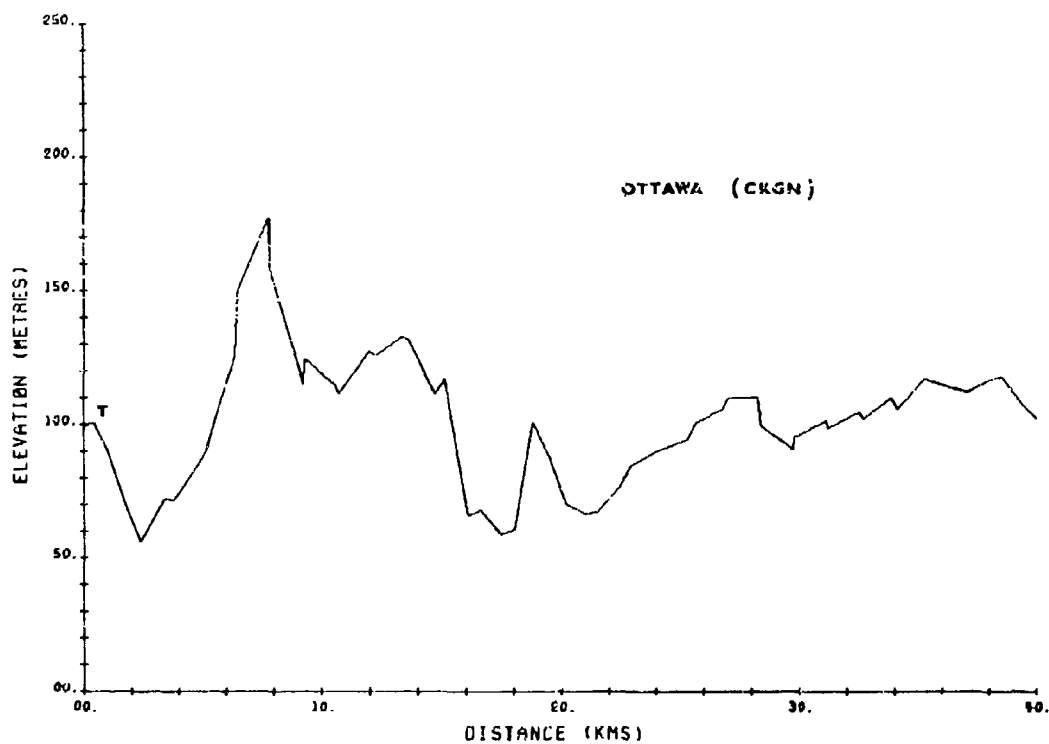


Fig. 3 Example showing the determination of obstacle parameters for a two obstacle path.



(a)



(b)

Fig. 4 (a) Plots of path-loss as a function of distance from the CKGN transmitter; Ottawa.
 f : 88 MHz; h_t : 46 m; h_r : 7 m. Solid line: detailed model; dotted line: irregular-terrain model.

(b) Profile of radial from television station CKGN, Ottawa.

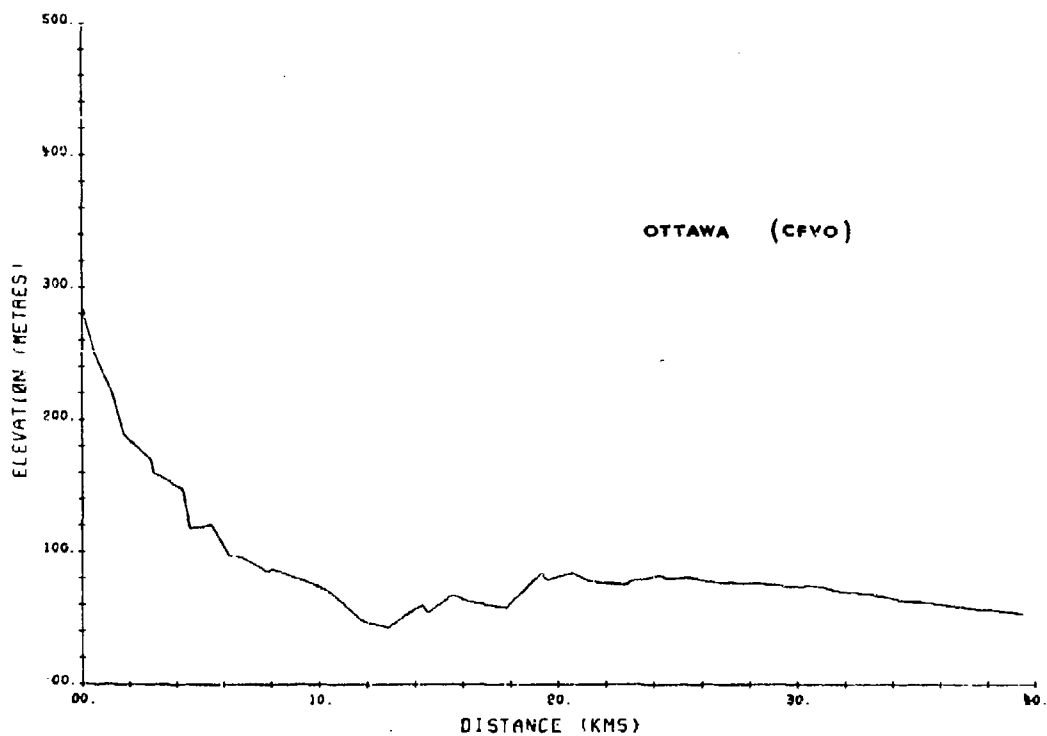
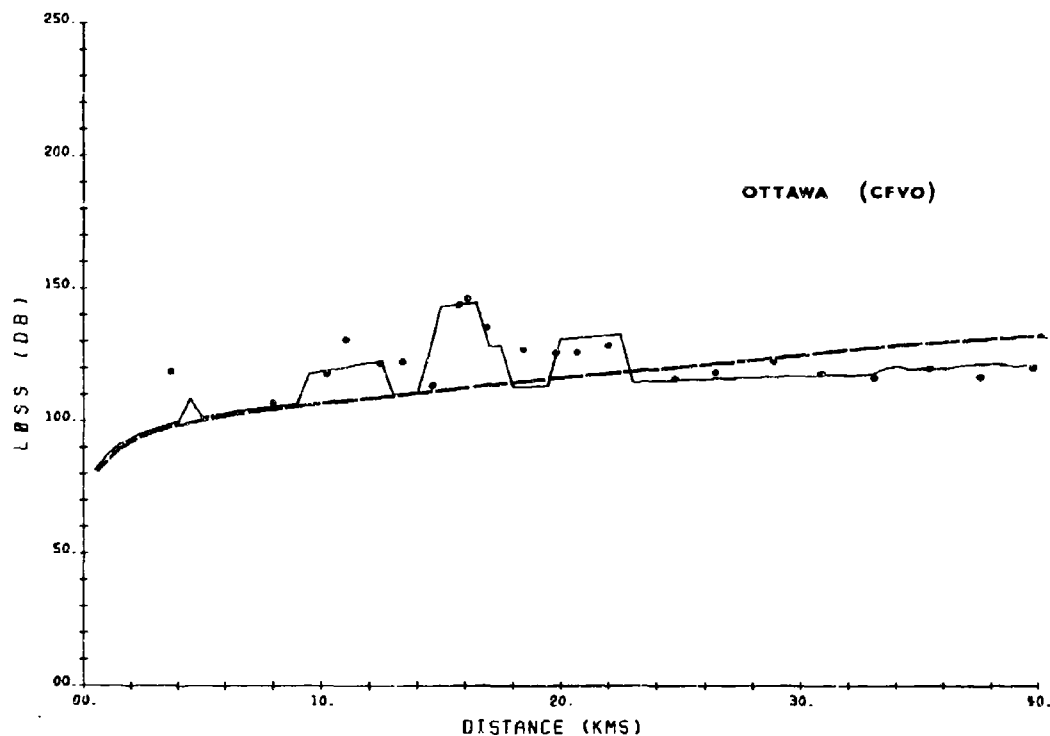
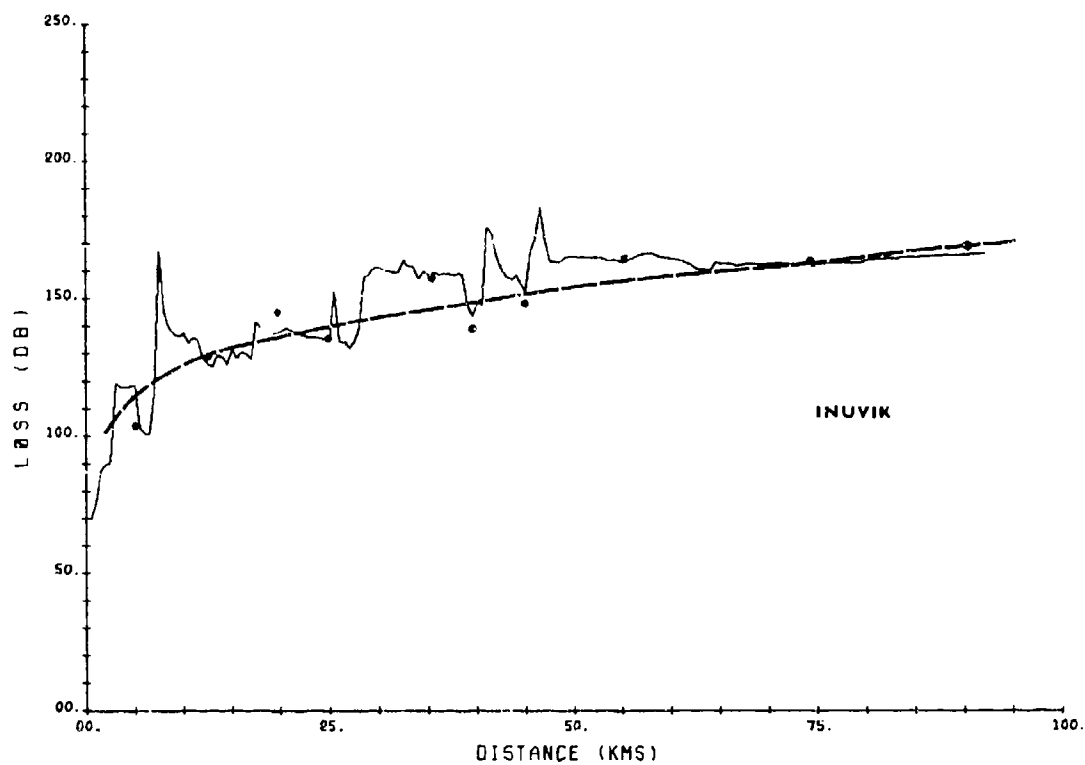
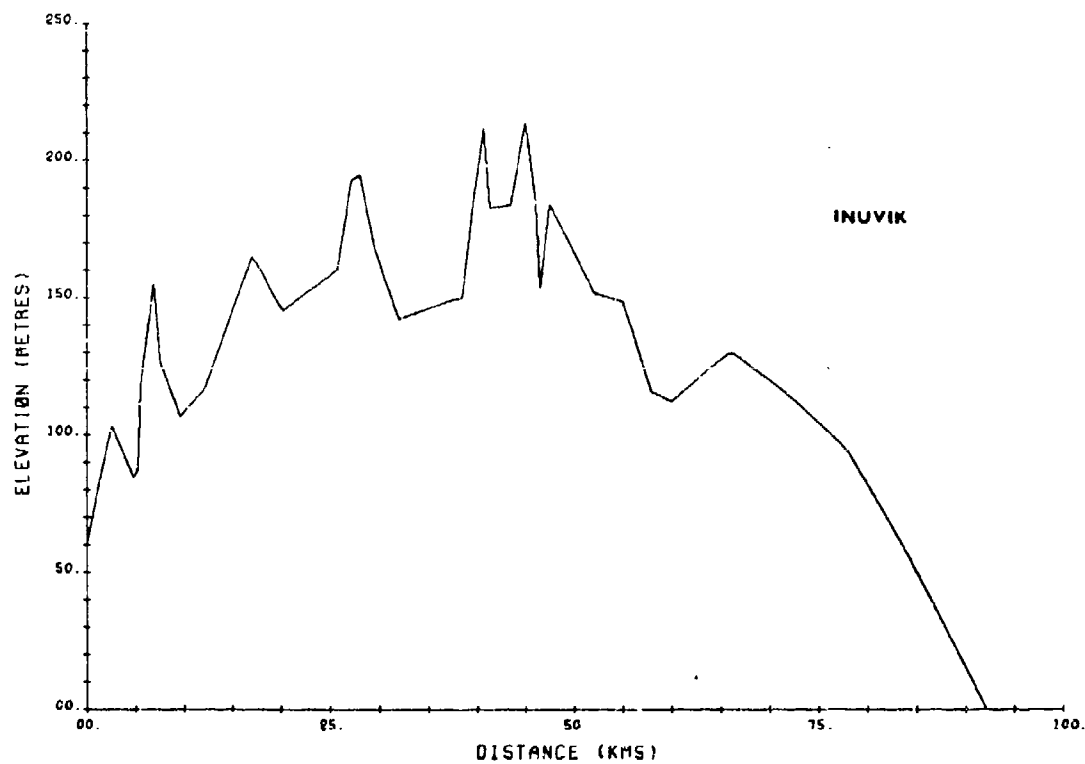


Fig. 5 (a) Plots of path-loss as a function of distance from the CFVO transmitter; Ottawa
 f : 572 MHz; h_t : 142 m; h_r : 7 m. Solid line: detailed model; dotted line: irregular-terrain
 model.

(b) Profile of radial from television station CFVO, Ottawa



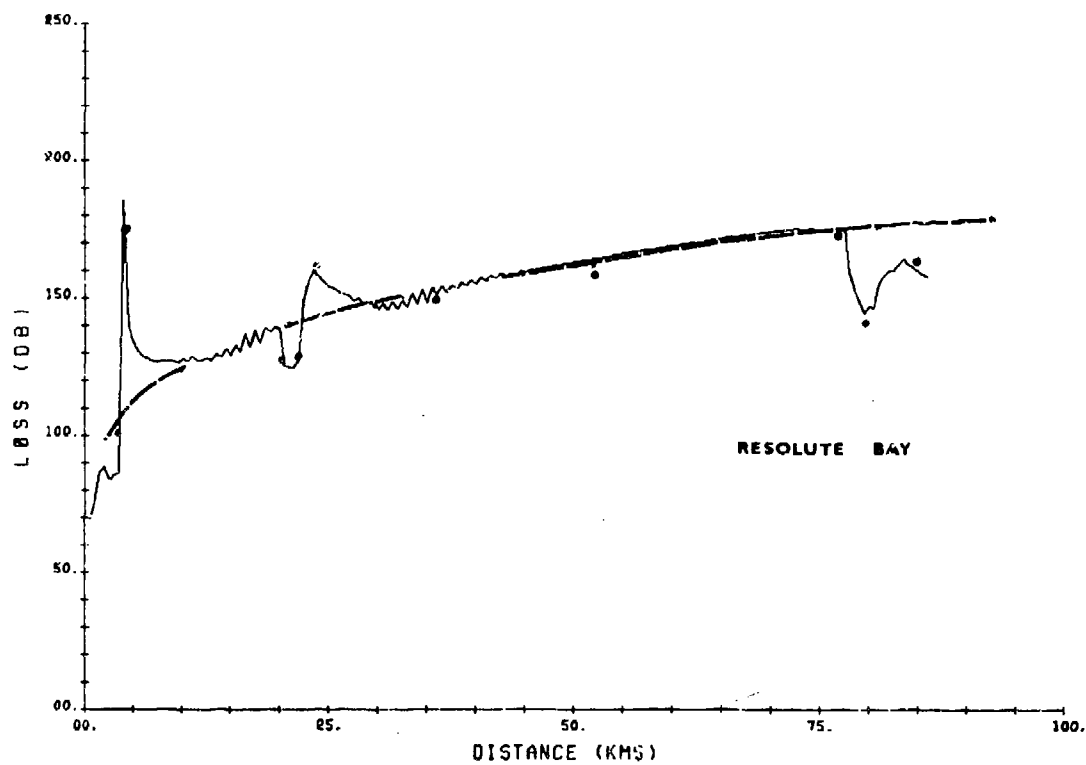
(a)



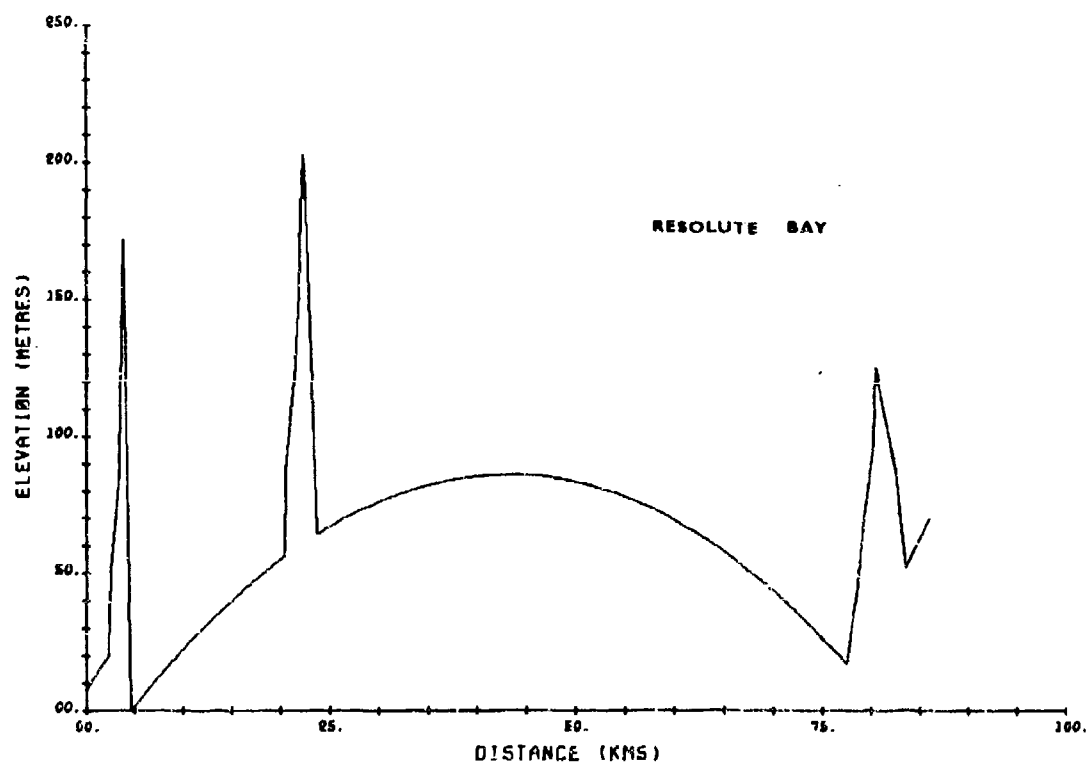
(b)

Fig. 6 (a) Plots of path-loss as a function of distance from the CRC transmitter at Inuvik, N.W.T.
 f : 150 MHz; h_t : 16 m; h_r : 3 m. Solid line: detailed model; dotted line: irregular-terrain model.

(b) Profile of radial from CRC transmitter at Inuvik, N.W.T.



(a)



(b)

Fig. 7 (a) Plots of path-loss as a function of distance from the CRC transmitter at Resolute Bay, N.W.T.
 f : 150 MHz; h_t : 16 m; h_r : 3 m. Solid line: detailed model; dotted line: irregular-terrain model.

(b) Profile of radial from CRC transmitter at Resolute Bay, N.W.T.

DISCUSSION

H. Vissinga, Netherlands

The dots in the graphs you showed represent median values of several measurements. Can you tell me how these measurements were taken and what the spread in these measurements is?

Author's Reply

We have made measurements of the location-variability of VLF/UHF signals and find that in urban areas the standard deviation of a series of measurements, made over a distance of 10-100 meters, ranges up to about 10 dB. In Arctic areas, where there is little or no ground cover, the standard deviation of a similar set of measurements can be very small, perhaps a dB or so.

We are accumulating location variability data but we have not yet incorporated a model into our program.

E. Lampert, FRG

In systems with low antenna height especially, calculated path losses using ordinary two-dimensional path profiles often deviate considerably from measured values. Have you, therefore, tried to include the third dimension in your calculation, or are you aware of such attempts?

Author's Reply

We realize that in certain areas, off-path reflections can significantly affect received signal-levels. We do not presently include such effects, but this does not seem to have significantly affected prediction accuracy for the paths we have modelled thus far.

There is a paper dealing with the modelling of off-path reflection in a recent issue of one of the IEEE Transactions

A STOCHASTIC DYNAMIC MODEL OF RAIN ATTENUATION

T. Maseng and P.M. Bakken
STAF Technical Centre
The Hague, Netherlands

SUMMARY

A dynamic mathematical model of rain attenuation has been developed at STC and is presented in this paper. This model permits the expression of analytic relationships between parameters commonly used to describe the properties of interest for communication. The model utilizes a memoryless nonlinear device to transform attenuation and rain intensity into a one dimensional Gaussian stationary Markov process. Hence, only one parameter is required to introduce the dynamic properties of rain attenuation into the model.

Experimental results and the known properties of rain have been used to derive and to verify the model. Comparative results are presented and demonstrate a good correspondence. Further the analysis described in this paper shows how the dynamic properties of rain attenuation should be measured to provide a complete characterization in the model.

The application of the model to the statistical analysis of the performance of communications systems is illustrated in the paper. The use of a dynamic rain attenuation model is necessary in order to analyze radio communication systems with transmit power control to offset the effects of rain attenuation and where the finite response time of the control system affects the performance.

An advantage of the model is the simplicity with which it allows simulation of communication link performance under the influence of rain attenuation. Such simulations are of great interest for complex models of adaptive networks where several deteriorating effects, including finite response times, are present.

1. INTRODUCTION

In satellite communication systems operating at X-band frequencies and higher, large signal margins are generally assigned to cater for the signal fading caused by precipitation. As spectrum congestion drives the system planner to higher and higher frequencies, larger and larger margins must be taken. The methods available to reduce these margins and thereby make the most efficient use of satellite communication systems fall broadly into two categories: one employing diversity techniques and the other employing adaptive compensation techniques. The work described in this paper was undertaken to determine the response time requirements of an adaptive system to compensate for fades caused by precipitation.

1.1 Background and Purpose

Previous work by SAC (Ref. 1 and 2) has shown that the use of satellite ground terminal (SGT) transmitter power control is a valuable method of reducing the outage time caused by rain attenuation. It is therefore planned that the next generation NATO SATCOM system shall utilize power control with automatic implementation of commands. The control system will employ a mini-computer with appropriate software at the control centres. Input data will be made available by an automatic data reporting system (ADRS), reporting from each of the fixed SGTs.

The system input noise temperature and the level of the satellite beacon will be among the measurements made by the fixed SGTs. The beacon measurements will be performed very accurately by comparison with an injected reference carrier. Since the output level of the satellite beacon is very stable, a beacon level measurement will give an accurate measure of the link loss at that location, at any given instant. The mini-computer, with a knowledge of the up- and down-link losses for each carrier, can order transmit-power changes to compensate for any increased losses which may be caused by rain or other environmental effects.

Delay is a very important factor considered in the evaluation of the control concept. From the sudden onset of rain attenuation, no control actions can be taken for a time determined by the delay in the ADRS and the delay while commands are computed and transmitted. The effect of these delays is that a somewhat higher margin on each link will be required.

To evaluate the effect of the delays, a statistical model of rain attenuation was developed. The model takes into account not only the stationary properties of rain, but also, with the introduction of one additional parameter, the dynamic behaviour of rain.

1.2 Related Work

S. H. Pan has shown that rain attenuation in dB is lognormally distributed (Ref. 3), a result which is supported by experimental results reported by Turner et al. (Ref. 4 to 6) and F.M. Galante (Ref. 7). Pan also suggested that the fade duration T is lognormally distributed with parameters dependent on the fade threshold used. However, the threshold value dependence is not given.

To determine the parameters required to predict the statistical properties of rain attenuation, long-term propagation measurements are necessary. For terrestrial links, well-established techniques are available (Ref. 10) for evaluating the expected path loss per kilometre from meteorological observations. For satellite paths through the atmosphere, this is more difficult to achieve based only on point measurements of rain statistics, because the rain intensity changes with altitude and the wind direction influences the attenuation. However, Bussey (Ref. 11) and Holtzer (Ref. 12) have both produced computational procedures for evaluating statistical properties of path losses at slant angles through the atmosphere.

A more accurate procedure for predicting attenuation statistics on a slant satellite path from rain gauge measurements was developed by Ippolito (Ref. 13 and 14), who used a set of ten tipping bucket rain gauges deployed along the azimuth track of the satellite path. The results were compared with those predicted from on-beam radar measurements.

For the NATO SATCOM SGT sites, the SHAPE Technical Centre has used both Bussey's method and Hotzler's to evaluate from meteorological information the long-term cumulative distribution of X-band rain attenuation. These results (Ref. 15) are utilized in this paper to obtain the power margin requirements of ten NATO SATCOM links when an automatic power control system with a finite response time is employed.

1.3 Approach to the Problem

It has been accepted that the attenuation of a microwave radio signal caused by rain has a lognormal stationary distribution (Ref. 3). In the planning of communication systems the dynamic properties of rain attenuation are also of interest, especially the fade duration distribution, of which extensive measurements have been made for a wide range of fade thresholds. These measurements are summarized in Ref. 3. For the planning and performance evaluation of the NATO SATCOM adaptive power control system, a dynamic stochastic model is required to enable the effects of finite system response time to be calculated.

The model selected for this purpose transforms, by a memoryless nonlinear device, the attenuation α (in dB) into a Gaussian stationary Markov process of the Ornstein-Uhlenbeck type. The model allows the static statistical distribution description of rain attenuation to be described by two parameters, average attenuation μ_a and standard deviation σ_a of $\lg_{10} \alpha$. The time dependence is described by a single parameter β . When these three parameters have been determined, properties of interest, such as the auto-correlation function for the rain attenuation and the complete transition probability density, may be found by calculation. Fade duration statistics may be derived from the passage time properties of the Ornstein-Uhlenbeck process.

It must be emphasized that this dynamic model is applicable only during the rain periods, because no dynamic transition mechanism between rainy weather and clear-sky conditions has been incorporated.

2. CONCEPTION OF THE MODEL

For the intended application of the rain attenuation model, it is considered highly desirable to use the relatively simple first-order Markov process. This implies that, given the rain attenuation at a time t , the model allows statistics to be generated for future rain attenuation, and that these statistics cannot be improved upon by consideration of the rain attenuation prior to t . The fluctuation equation may then be written as (Ref. 16),*

$$\frac{d\alpha}{dt} = K_{1a}(\alpha) + \sqrt{K_{2a}(\alpha)} n(t) \quad (1)$$

where $n(t)$ is white Gaussian noise of unity variance and zero mean, and K_{1a} and K_{2a} are deterministic functions of α corresponding to

$$K_{na}(\alpha) = \lim_{\Delta t \rightarrow 0} \frac{1}{\Delta t} E \{ (\alpha(t+\Delta t) - \alpha(t))^n | \alpha(t) \} \quad n = 1 \text{ and } 2 \quad (2)$$

Lin (Ref. 3) has shown that the stationary probability distribution of α is lognormal (Ref. 17) $A(\mu_a, \sigma_a^2, \alpha)$. Kontorovich and Lyndras (Ref. 16) have shown that for reflecting boundaries, when the stationary density is given, only one of the two functions $K_{1a}(\alpha)$ or $K_{2a}(\alpha)$ remains to be selected to characterize the process fully. Assuming $K_{2a}(\alpha)$ to be chosen,

$$K_{1a}(\alpha) = \frac{1}{2} \left[\frac{dK_{2a}(\alpha)}{d\alpha} + \frac{d^2 A(\alpha)}{d\alpha^2} \left(\frac{dA(\alpha)}{d\alpha} \right)^{-1} K_{2a}(\alpha) \right] \quad (3)$$

and the probability density of $\alpha(t)$, $p(\alpha, t)$ can be found from the Fokker-Planck equation

$$\frac{dp(\alpha, t)}{dt} = \frac{1}{2} \frac{\partial^2}{\partial \alpha^2} (K_{2a}(\alpha) p(\alpha, t)) - \frac{\partial}{\partial \alpha} (K_{1a}(\alpha) p(\alpha, t)) \quad (4)$$

Since the number of classes of Fokker-Planck equations that have been solved is limited (Ref. 18), $K_{2a}(\alpha)$ will be chosen so that Eq. (4) can be converted to one of them.

Furthermore, observations have shown (Ref. 19) that the random rate of change of $\alpha(t)$ increases with α . It is shown later that these two requirements can be met by the following choice:

$$K_{2a}(\alpha) = 2\beta^2 M^2 \sigma_a^2 \alpha^2 \quad (5)$$

where β is the parameter selected to describe the rate of change of the process modelled. This choice enables the fluctuation equation of $\alpha(t)$ (Eq. 1) to be transformed by

$$x(t) = \frac{\lg_{10}(\alpha(t)) - \mu_a}{\sigma_a} \sim \frac{\ln \alpha - \ln \alpha_m}{M \sigma_a} \quad (6)$$

* A list of symbols is given in Appendix A

into that of Ornstein and Uhlenbeck (Ref. 20 and 21) by the use of Itô differentiation rules (Ref. 22)

$$\frac{dx}{dt} = -\beta x + \sqrt{2} n(t) \beta \quad (7)$$

The complete dynamic solution of the corresponding Fokker-Planck equation for x (using $K_{11}(x) = -\beta x$ and $K_{22}(x) = 2\beta^2$ in Eq. (4)) has been obtained (Ref. 18 and 20) and results in the normal first-order stationary Markov process.

The substitution of Eq. (5) into the conditional probability density of the Ornstein and Uhlenbeck process gives the conditional probability density of $\alpha(t)$. This lognormal distribution can be written

$$P_r(\alpha(t+\Delta t) < \alpha | \alpha(t) = \alpha_0) = \int_0^\infty (p_1(\alpha_0), p_2; \alpha_0) \cdot \\ = \Lambda(\mu_a M(1 - \exp(-\beta|\Delta t|)) + \lg_{10}(\alpha_0) M \exp(-\beta|\Delta t|), \sigma_a^2 M^2(1 - \exp(-2\beta|\Delta t|)); \alpha) \quad (8)$$

The relationship between the generating white Gaussian noise source $n(t)$, the Ornstein and Uhlenbeck distributed intrinsic model stochastic variable $x(t)$, and the instantaneous rain attenuation $\alpha(t)$ in dB is illustrated in Fig. 1.

Figure 2 shows how the conditional probability density of $\alpha(t+\Delta t)$ changes with Δt , given the instantaneous value of $\alpha(t) = \alpha_0$ for $\sigma_a = 0.5$, $\alpha_m = 0.5$ dB and $\alpha_0 = 6$ dB.

The moments of the conditional density of α are $\lambda_{aj} = E(\alpha^j | \alpha_0) = \int_0^\infty \alpha^j d\Lambda(\alpha)$

$$= \exp\{jM[\mu_a(1 - \exp(-\beta|\Delta t|)) + \lg_{10} \alpha_0 \exp(-\beta|\Delta t|)] + \frac{1}{2} M^2 \sigma_a^2 j^2 [1 - \exp(-2\beta|\Delta t|)]\} \quad (9)$$

from which Eq. (5) can be obtained when

$$K_{\alpha\alpha}(\alpha) = \frac{\partial \lambda_{aj}(t=0)}{\partial t} = 2 \frac{\partial \lambda_{aj}(t=0)}{\partial t} \quad (10)$$

3. POINT RAIN INTENSITY

For short radio paths (Ref. 23), where the rain intensity q can be assumed constant throughout the path, the attenuation is related to rainfall intensity by

$$\alpha = \gamma q^n L \quad (11)$$

where γ and n are frequency-dependent parameters, which are nearly independent of polarization, and L is the length of the path.

Since α is lognormally distributed $\Lambda(\mu_a, \sigma_a^2; \alpha)$, it follows from Eq. (11) that the rainfall intensity q is also lognormally distributed

$$\Lambda(M(\mu_a - \lg_{10} L) - \lg_{10}(\gamma), \sigma_a^2 M^2/n^2; q) = \Lambda(M(\mu_q, M^2 \sigma_q^2; q) \quad (12)$$

which is in accordance with Ref. 23.

This model is developed primarily to represent space-to-earth links at microwave frequencies. The distance through the atmosphere for these links will not be "short" in the sense used in Ref. 23. The fluctuation rate will therefore be slower for the radio path attenuation than for the rain intensity at a single point in the path, thereby giving a higher value of β for the single point rain intensity model.

Equation (11) shows that rainfall intensity can be represented by a lognormal model similar to that for rain attenuation. This makes it possible to support the model not only with rain attenuation statistics, but also with statistics on rainfall intensity.

4. PROPERTIES OF THE MODEL SUITABLE FOR COMPARISON WITH EXPERIMENTAL OBSERVATIONS

The stationary distribution of the rain attenuation of the model is lognormal and is therefore described by two parameters which can be determined from long-term attenuation statistics in the form of a histogram for the attenuation of a given radio path.

As will have been noted from the previous sections, the dynamic properties of the model are described by one additional parameter β , which is the rate of change of attenuation. When β is known, the model can be used to calculate dynamic properties of rain attenuation such as fade duration statistics, typical profiles of rain attenuation as a function of time, and the autocorrelation function.

4.1 The Autocorrelation Function

In Ref. 24 it is shown that the autocorrelation of $x(t)$, $\rho(\tau)$, is exponential with unity correlation for zero time lag. The autocorrelation of α (and q) will, however, be different and is given by

$$R_\alpha(\tau) = \frac{\int_{-\infty}^{\infty} \int_{-\infty}^{\infty} \frac{\sigma_a^2 (x_1 + x_2)}{2\pi \sqrt{1 - \rho(\tau)}} \exp\left(-\frac{x_1^2 + x_2^2 - 2\rho(\tau)x_1 x_2}{2(1 - \rho(\tau))}\right) dx_1 dx_2 \quad (13)$$

since x is $N(0,1;x)$ distributed and the transfer function between x and α is non-singular and memoryless for all values of x .

By integration, Eq. (13) yields: $R_{\alpha}(\tau) = \sigma_m^2 \exp\{M^2 \sigma_a^2 (1-\rho(\tau))\}$ (14)

Normalization and the removal of bias yield: $r_{\alpha}(\tau) = \frac{\exp\{M^2 \sigma_a^2 \rho(\tau)\} - 1}{\exp\{M^2 \sigma_a^2\} - 1}$ (15)

where $\rho(\tau) = \exp(-R|\tau|)$ (16)

is the correlation function for the Gaussian variable $x(t)$.

Equations (15) and (16) are shown graphically in Fig. 3, with σ_a as a parameter. It can be seen that the correlation decreases with increasing σ_a . This is a consequence of the model property expressed in Eq. (5).

4.2 Time Profiles

If at a time $t = 0$ an attenuation $\alpha = \alpha_0$ is given, the mean profile for $t > 0$ will be determined from the first conditional moment (Eq. (9)).

$$E\{\alpha(t) | \alpha_0\} = \lambda_{1\alpha}(t) \quad (17)$$

The variance from the mean profile is

$$\sigma_p^2 = E\{\alpha(t) - E\{\alpha(t)\}^2 | \alpha_0\} = \lambda_{2\alpha}(t) - \lambda_{1\alpha}^2(t) \quad (18)$$

Figure 4 shows normalized mean and $\pm \sigma$ profiles for $\omega/\alpha_0 = 47.6$ and 166.7 , $\alpha_0 = 0.42$ dB, and $C' = 0.61$. To facilitate comparison with the experimental results given in Section 5.2, the parameter values are chosen to comply with those found in Ref. 19.

4.3 Fade Duration Statistics

A fade is experienced when the attenuation exceeds a fade threshold α_0 . Because the fade threshold can be referred to the statistical variable $x(t)$ by the nonlinear transform (Fig. 1), the statistics of the fade duration T_x of the model are found from the level crossing properties of the Ornstein-Uhlenbeck process.

The fade duration properties of this process have received special attention in the literature. S.O. Rice (Ref. 8), A.J.F. Siegert (Ref. 25), and McFadden (Ref. 26) have studied the process and shown that the probability density of the fade duration for this model does not exist as normally defined.

The power spectrum of the Ornstein-Uhlenbeck process can be written:

$$W(f) = \frac{1}{1 + \left(\frac{2\pi f}{B}\right)^2} \quad (19)$$

The power carried by the high frequencies in the spectrum of this process is so large that the average fade duration is zero. In a practical system used for measuring

fade duration characteristics, however, effects such as finite sampling frequency, hysteresis in the level crossing detectors and bandwidth limitations in the level measurement equipment will cause the observed average fade duration to be finite.

In this paper it will be assumed that a measurement filter is used to enable fade duration statistics to be defined. The filter characteristics can be chosen quite freely as long as the bandwidth ω_m is much larger than β .

Figure 5 shows a proposed equipment measurement configuration to enable the model parameters to be determined from reported fade duration measurements.

The use of the approach given in Ref. 8 illustrates the fact that the average fade duration is dependent on the measurement bandwidth superimposed on the process. Independent of the measurement bandwidth, however, the distribution function of fade duration is given by (Ref. 9)

$$P\{\tau < t\} = 1 - \exp(-t/\bar{T}_x) \quad (20)$$

where the average fade duration \bar{T}_x for threshold α_0

is given by $\bar{T}_x = \bar{T}_0 \exp(x_0^2/2) \text{erfc}(x_0/\sqrt{2})$ (21)

The complementary error function is defined in Appendix A.

In Ref. 8 it is shown how the fade duration statistics can be obtained when the measurement filter used is of the type:

$$W_m(f) = \frac{1}{(1 + (\frac{2\pi f}{\omega_m})^2)^2} \quad \omega_m \gg \beta \quad (22)$$

Then \bar{T}_O is given by (Ref. 8)

$$\bar{T}_O = \pi \sqrt{\frac{3}{2\frac{\omega_m}{\beta} - 3\omega_m^2 + \beta^2/\omega_m(\omega_m - \beta)}} \quad (23)$$

Note that \bar{T}_O goes to zero as ω_m approaches infinity.

5. COMPARISON OF MODEL PROPERTIES WITH OBSERVATIONS OF RAIN

In the previous section, properties of the model suitable for comparison with measured properties of rain were obtained. In this section, these properties are compared with the known properties of rain.

5.1 The Autocorrelation Function

No measurements of rain attenuation or rain intensity have been found in the literature which have or can be processed to yield the autocorrelation function.

5.2 Time Profiles

In Section 4.2 time profiles for rain attenuation were obtained from the conditional moments. However, unprocessed measured time profiles are not available from reported trials. Norbury and White (Ref. 19) have conducted experiments over four years at Slough, England, recording all rainfall intensity events with amplitudes larger than 20 mm/h. For the experiments a special rapid-response rain gauge was employed (Ref. 28). The sampling rate was 0.1 sample per second. The results were normalized with respect to the peak intensity within the interval considered and the time scale referred to the time of the peak. These results (Fig. 6) show the normalized mean and the standard deviation profiles for rain intensities in the range 20 mm/h to 70 mm/h.

For the model no analytic expressions have been found for the moments of the expected decay of the rain intensity from a given maximum. Since the unprocessed data of Ref. 19 was not available a computer simulation was carried out at STC using the algorithms given in Appendix B. The results of an STC simulation, consisting of 100 event sequences, are included in Fig. 6 for $\beta = 0.11 \text{ min}^{-1}$, $q_m = 0.42 \text{ mm/h}$, $\sigma_q = 0.61$, in accordance with Ref. 19 and 23.

5.3 Fade Duration Statistics

It was pointed out in Section 4.3 that the probability distribution of the duration of a fade exceeding a given threshold x was given by eq. (19 and 20) for any type of measurement filter. To determine β from fade duration statistics only was not a convenient method since the measurement equipment would tend to influence the results.

In figure 9 the results on the statistics of fade duration from experiments using the ATS-6 satellite (Ref. 14) are compared with those obtained from eq. (19). The results are plotted on lognormal grid using fade duration normalized with respect to average fade duration as abscissa and fade threshold as a parameter.

Table 1 shows some of the results from reported trials on fade duration statistics. If the table had contained more measurements of the effect of different thresholds, Eq. (20) could have been compared.

6. MARGIN REQUIREMENTS OF NAFO SATCOM LINKS

In FDM* satellite communications it is possible to combat rain losses by increasing the transmit powers for the carriers affected by rain (Ref. 29 and 30). The transmit power must be regulated to the value necessary to maintain communication plus a margin to cater for imperfections in the system. In this section a margin Z that does not depend on the attenuation x_0 is considered, while in Section 6.2, the margin is attenuation dependent. The probability of an increase Z in attenuation for a time Δt can be found as a function of x_0 by means of Eq. (8), which is subsequently averaged over the distribution of $\alpha_0 = \alpha(t=0)$

$$P\{\alpha(t+\Delta t) > \alpha_0 + Z | \text{RAIN}\} = \int_{\text{RAIN}(x,0)}^{\infty} (1 - A(F_1(\alpha_0), P_1; \alpha_0 + Z)) dA(M, \alpha_0^2 M; \alpha_0) \quad (24)$$

where the parameters $p_1(\alpha_0)$ and p_2 are the same as those used in eq. (8). The substitution $s = \ln(\alpha/\alpha_0)/\sqrt{2}\sigma_a M$ gives for the integral

$$\int_{\alpha_0}^{\infty} \frac{1}{\sqrt{2\pi}} \exp(-s^2) \text{erfc}\left(\frac{\ln(\alpha_0 + Z \exp(s\sigma_a M\sqrt{2})) - s\sqrt{2}\exp(-\beta|\Delta t|)\sigma_a M - \ln\alpha_0}{M\sigma_a\sqrt{2(1-\exp(-2\beta|\Delta t|))}}\right) ds \quad (25)$$

where the lower integration limit is

$$u_z = \begin{cases} -\alpha & z \geq 0 \\ \ln(\frac{-Z}{\alpha_0})/\sqrt{2}\sigma_a M & z < 0 \end{cases}$$

* Frequency Division Multiple Access.

Equation (24) yields $\frac{1}{2}$ for $z = 0$. Hence, the probability of increase and decrease in attenuation is the same. Another property of Eq. (24) is that, when Δt approaches zero, it yields 1 for $z = 0$ and 0 for $z \neq 0$.

Since no analytic solution has been found to the integral of Eq. (24), numerical integration was used to obtain a solution. Because of the Gaussian factor in the integrand, and because of the double infinite integration range ($z \pm \infty$), a Hermitian numerical integration was used (20 points).

The atmospheric attenuation statistics for ten NATO SATCOM SGT sites were estimated in Ref. 15. For two of these sites, the parameters σ , α , and β were obtained by fitting a lognormal distribution through the curves given in Ref. 15. (The curves obtained from Bussey's method were used and are therefore expected to represent "worst case figures".) The parameter β was set to $0.11 \text{ (min}^{-1}\text{)}$ for both links. Figures 8 and 9 illustrate the results of the application of Eq. (24). Note that the margin savings using a power control system increase with increasing availability requirements.

6.2 Partial Countering of Time Delay by Attenuation-Dependent Margins

In the previous section, the effects of the delay in the control system were calculated in terms of margin requirements. With the advanced power control system planned for NATO SATCOM however, it is not necessary to use the same margin for all links, nor need the margin for a link be time-independent. An obvious method of reducing the degradation of the power control system caused by time delay is to let the links with a high probability of a sudden increase in rain attenuation operate with higher margins than the remaining links.

The model offers a possibility of calculating how the available satellite effective isotropic radiated power (EIRP) should be allocated to the various links, taking into account not only the clear-weather loss of the link, but also the differences in rain attenuation statistics throughout the network. As an example of the use of the model, a single link with an observed rain attenuation α_0 is considered. The objective is to assign to this link a margin K , which depends on α_0 in such a way that the probability of an outage in the next Δt seconds, where Δt is the delay time of the power control system, remains constant.

The probability of exceeding the level $\alpha_0 + K$ at time $t + \Delta t$ is

$$\Pr(\alpha(t+\Delta t) > \alpha_0 + K | \alpha_0) = 1 - A(P_1(\alpha_0); P_2; \alpha_0 + K) = P_K \quad (26)$$

where the righthand side of Eq. (26) can be found from Eq. (8) using the definition of the A -integral given in the list of symbols. The optimum control strategy in this simplified example is to keep the argument of the complementary error function constant with changing attenuation α_0 by the introduction of corresponding changes in the margin K . (This statement contains an approximation because the probability of exceeding $\alpha_0 + K$ in the time Δt and then returning to a lower level is neglected. The approximation is good for $\Delta t \ll 1/\beta$.)

For $\beta \Delta t \ll 1$ Eq. (26) yields

$$K = \alpha_0 (\exp(\xi) - 1) \quad (27)$$

where

$$\xi = \text{erfc}^{-1}(2P_K) \alpha_0 M \sqrt{2\beta \Delta t} \quad (28)$$

The results of Eq. (27) and (28) are plotted in Fig. 10 for $P_K = 10^{-2}$ and 10^{-3} . From the figure it can be seen that this strategy implies an increase in margin (in addition to the actual increase in path loss attenuation) of approximately 1.5 dB for each dB increase in rain attenuation, when the delay before execution of a command is 20 seconds and the outage probability when it is raining is set to 10^{-3} at this site.

7. CONCLUDING REMARKS

The results obtained from the mathematical stochastic model of rain attenuation show good correspondence with the available experimental results. The model enables analytical expressions to be formulated showing the inter-relationship between commonly-used statistical parameters. It also indicates how a communication link should be measured in order to yield a statistical characterization.

Fade duration statistics are of particular interest for communication purposes. These properties of rain attenuation have been measured extensively for fixed threshold values. Since level crossing evaluation of stochastic processes is an extremely difficult topic, and few analytic expressions are known, such measurements are not entirely suited for characterization of the process. As shown in Sections 4.1 and 4.2, mean attenuation profiles, and long-term measurements of the autocorrelation function, are more directly applicable for this purpose and further measurements of these properties, to support the model, are desirable.

By the use of the model, it has been possible to estimate the availability of the NATO SATCOM links (considering rain attenuation only), when the power of a link is controlled by a control system with a finite response time, but otherwise perfect. With a link availability requirement of 99.9% and a total response time of 40 seconds, the margin requirements for an up- or down-link can be reduced by 1-2 dB (depending on the site) compared to the margin required if no control system were used.

An advantage of the model is the simplicity with which it allows simulation of communication link performance under the influence of rain attenuation. Such simulations are of great interest for complex models of adaptive networks where it is necessary to include the deteriorating effects of finite response times due to the practical limitations of telemetry systems.

This paper records work undertaken as part of the continuing effort to design and evaluate an automatic power control technique for NATO SATCOM. The main purpose of the control system is to combat the increased attenuation experienced during adverse weather conditions. For a realistic evaluation, the degrading effects of measurement errors and limited ground terminal EIRP are being considered in current studies.

8. APPENDIX A

List of Symbols

$N(\mu, \sigma^2; x)$	-	Cumulative normal distribution of x with average value of $x = \mu$ and standard deviation of $x = \sigma$:
		$= \frac{1}{\sigma\sqrt{2\pi}} \int_{-\infty}^x \exp\left(-\left(\frac{u-\mu}{\sigma}\right)^2\right) du = 1 - \frac{1}{2} \operatorname{erfc}\left(\frac{x-\mu}{\sigma\sqrt{2}}\right)$
$\Lambda(\mu, \sigma^2; \alpha)$	-	Cumulative lognormal distribution (Ref. 24) of α with average value of $\ln(\alpha) = \mu$ and standard deviation of $\ln(\alpha) = \sigma$
		$= \frac{1}{\sigma\sqrt{2\pi}} \int_0^{\alpha} \frac{1}{u} \exp\left(-\left(\frac{\ln u - \mu}{\sigma}\right)^2\right) du = 1 - \frac{1}{2} \operatorname{erfc}\left(\frac{\ln \alpha - \mu}{\sigma\sqrt{2}}\right)$
$\operatorname{erfc}(x)$	-	Complementary error function (Ref. 27)
		$= \frac{2}{\sqrt{\pi}} \int_x^{\infty} \exp(-t^2) dt$
λ_j	-	Moment of order j of lognormal distribution
$\alpha, A, k, z, \alpha_0$	-	Attenuation in dB
q, Q	-	Rain intensity in mm/h
μ_a	-	Mean value of $\lg_{10}(\alpha)$; $\mu_a = \lg_{10}(\alpha_v)$
β	-	Inverse time constant
x	-	Intrinsic model stochastic variable
$\rho(\tau)$	-	Autocorrelation function of x
$r(\tau)$	-	Normalized, unbiased autocorrelation function of the external stochastic variable of the model
$R(\tau)$	-	Non-normalized, biased autocorrelation function of the external stochastic variable of the model
$W(f)$	-	Power spectrum
M	-	Mathematical constant ($\ln 10 = 2.302585$)
χ	-	Radio frequency dependent constant
ψ	-	Radio frequency dependent constant
L	-	Equivalent link length, in km
P_0	-	Probability of rain
t, τ, T	-	Time
$K_n(x)$	-	n^{th} order moment of stochastic variable x
p	-	Probability density

α_m	-	Median value of attenuation = $\exp(M\mu_a) = 10^{4a}$
ω_m	-	Measurement bandwidth
σ	-	Standard deviation of x

9. APPENDIX B

Aspects of Simulation

The model is so designed as to enable simple hardware or software simulation experiments to be conducted.

Hardware Simulation

The equipment shown in Fig. 1 consists of a noise source, a first-order RC filter, and an exponential amplifier. An analogue value is produced which can be used to control an attenuator with a linear relationship between attenuation in dB and control voltage.

Software Simulation

An algorithm suitable for computer simulation can be obtained using the properties of a sequence of sample values ($x_1, \dots, x_k, x_{k+1}, \dots$) of the stationary Markovian process of first order (Ref. 35):

$$x_k = \rho x_{k-1} + \sqrt{1-\rho^2} n_k \quad (A1)$$

where $x_k = x(t_k)$

$$t_k = t_{k-1} + \Delta t$$

n_k is white and normally distributed with mean value zero and unity variance

and $\rho = \exp(-\beta \Delta t)$

The relation between α and x given by Eq. (6) yields:

$$\alpha_{k+1} = \left(\frac{\alpha_k}{\alpha_m}\right)^\rho \alpha_m 10^{\sqrt{1-\rho^2} n_k} \quad (A2)$$

Equation (A2) is directly applicable for computer simulation and requires a subroutine for generation of independent random Gaussian numbers $N(0,1)$ for n_k . This technique was used to produce the model results in Section 5.2 for comparison with the experimental results.

10. REFERENCES

1. G. Coupé et al., "A preliminary report on the method of control for Phase II Stage 1 of the NATO SATCOM System", STC Technical Memorandum TM-259, May 1970. (NATO Unclassified)
2. D.W. Brown, J.A. Midgley, "A study of the effectiveness of various power control methods for the NATO Phase II SATCOM System", STC Technical Memorandum TM-373, August 1973. (NATO Unclassified)
3. S.H. Lin, "Statistical behaviour of rain attenuation", BSTJ April 1973, pp 557-581.
4. D.J.W. Turner and D. Turner, "Attenuation due to rainfall on a 24-km microwave link working at 11, 18 and 36 GHz", Electr. Ltrs. 6, No. 10, 14 May 1970, pp 297-298.
5. B.J. Easterbrook and D. Turner, "Prediction of attenuation by rainfall in the 10.7 to 11.7 GHz communication band", Proc. IEE, 114, No. 5, May 1967, pp 557-565.
6. D. Turner, B.J. Easterbrook and J.E. Golding, "Experimental investigation into radio propagation of 11.0 to 11.5 Gc/s", Proc. IEE, 113, No. 9, September 1966, pp 1477-1489.
7. F.M. Galante, "Statistical evaluation of rain fades and fade duration at 11 GHz in European Region", IEE Cont. Publ. No. 126, April 1975.
8. S.O. Rice, "Distribution of the duration of fades in radio transmission", BSTJ Vol. 28, No. 3, May 1958, pp 581-635.
9. A.N. Denisenko, "Estimate of the distribution of surge durations of random processes." Radiotekh. Elektron., Vol. 20, pp 1529-1532, July 1975 (English transl. Radio Eng. Electron).
10. J. Dutton et al., "Prediction of European rainfall and link performance coefficients at 8 to 30 GHz", ACC-ACO-16-74.

11. H.E. Bussey, "Microwave attenuation statistics estimated from rainfall and water vapour statistics", Proc. IRE, 38, pp 781-785, July 1950.
12. W. Holtzer, "Atmospheric attenuation in satellite communications", Microwave Journal, 8, No. 3, March 1965, pp 119-125.
13. L.J. Ippolito, "The ATS-F millimeter wave propagation experiment", NASA/GSFC Doc. X-751-71-460, October 1971.
14. L.J. Ippolito, "ATS-6 millimeter wave propagation and communications experiments at 20 and 30 GHz", IEEE Trans. on Aerospace and Electr. Syst. Vol. AES-11: No. 6, November 1975.
15. D.W. Brown, "Estimation of the long-term statistics of atmospheric attenuation at the NATO SATCOM Phase II terminals", STC Technical Memorandum TM-291, Volume 1, November 1971 (NATO Unclassified)
16. V. Ya. Kontorovich and V.Z. Lyandres, "Fluctuation equation generating a one-dimensional Markovian process", Radio Engineering and Electronic Physics, Vol. 17, July 1972, pp 1093-1096.
17. Aitchison and Brown, "The lognormal distribution", Cambridge University Press, 1957.
18. E. Wong, "The construction of a class of stationary Markov processes", Proc. Amer. Math. Soc. Symp. Appl. Math. 16, 1963, pp 264-276.
19. J.R. Norbury and W.J.K. White, "Intensity-time profiles of high-intensity rainfall", Meteorological Magazine Vol. 104, 1975, pp 221-227
20. L.S. Ornstein and G.E. Uhlenbeck, "On the theory of Brownian motion", Phys. Rev. 36, 1930, pp 823-41.
21. M.C. Wange and G.E. Uhlenbeck, "On the theory of Brownian motion II", Rev. Mod. Phys. Vol. 17, 1945, pp 323-342.
22. Jazwinski, "Stochastic processes and filtering theory", Academic Press, 1970.
23. S.H. Lin, "A method for calculating rain attenuation distribution on microwave paths", BSTJ July/Aug. 1975, pp 1052-1086.
24. M. Rosenblatt, "Random processes", New York, Oxford University Press, 1962.
25. A.J.F. Siegert, "On the first passage time probability function", Phys. Rev. Vol. 81, 15 February 1951, pp 617-623.
26. J.A. McFadden, "The axis crossings of a stationary Gaussian Markov process", IRE Transactions on Information Theory, Vol. IT-7, No. 3, July 1970, pp 130-153.
27. M. Abramowitz and A. Stegun, "Handbook of mathematical functions", Dover Publications Inc., New York, 1968.
28. J.R. Norbury and W.J.K. White, "A rapid response rain gauge", J. Phys. E. Scient. Instrum. London 4, 1971, pp 601-602.
29. A.N. Ince, D.W. Brown and J.A. Midgley, "Power control algorithms for satellite communications systems", IEEE Trans. on Communications, Vol. COM-24, No.2, February 1976.
30. R.G. Lyons, "A statistical analysis of transmit power control to compensate up- and down-link fading in an FDMA satellite communication system", IEEE Trans. on Communications, Vol. COM-24, No. 6, June 1976.
31. R.W. Wilson, "Sun tracker measurements of attenuation by rain at 16 and 30 GHz", BSTJ, 48, No. 5, May-June 1969, pp 1383-1404.
32. P.G. Davies, "Radiometer studies of attenuation of solar emission at 19 GHz, Proc. IEEE (London), 118, No. 6, June 1971, pp 737-741.
33. G.B. Stracca, "Propagation tests of 11 GHz and 18 GHz on two paths of different lengths", Alta Frequenz (Italy), 38, 1969, pp 345-360.
34. R.A. Semple and R.H. Turin, "Some measurements of attenuation by rainfall at 18.5 GHz", BSTJ 48, No. 6, July/Aug. 1969, pp 1767-1797.
35. W. Feller, "An introduction to probability and its applications", Vol. II, John Wiley & Sons Inc., 1971.

Table 1
Experimental results on fade characteristics

No.	Author	Ref.	Location	Freq. (GHz)	Path length (km)	Fade threshold (dB)	σ_r	τ_a	τ (min)	σ_m (dB)	P_0	Threshold X_0	Time
1	Wilton and Pucic	31	Crawford Hill N.J.	16	Earth-space	9	0.76	0.71	8	0.33	5.23	2.02	8 December 1957 - 26 February 1963
2	"	31	"	30	"	9	0.76	0.57	7.7	1.6	5.23	1.96	"
3	"	31	"	30	"	21	0.67	0.57	11.4	1.6	5.23	1.32	"
4	Davies	32	England	19	"	5	0.53	0.46	4.4	0.4	8.5	2.38	6 June 1963 - 31 May 1970
5	Staccia	33	Italy	11	20	10	0.75	0.71	4.8	0.45	6	1.90	May - October 1967
6	Szeplak & Turin	34	Crawford Hill N.J.	18.5	6.4	5	0.65	0.85	7.2	0.11	5.08	1.93	23 June 1957 - 31 October 1957
7	"	34	"	18.5	6.4	10	0.57	0.85	5.8	0.11	5.08	2.27	"
8	"	34	"	18.5	6.4	20	0.63	0.85	5.1	0.11	5.08	2.63	"
9	Barnat et al.	34	Palmetto, Georgia	18	5	36	0.44	0.41	2.4	0.55	5.7	3.02	November 1970 - June 1971
10	Yppolito	14	Austin, Texas	30	Earth-space	5	0.46	0.31	9.13	1.62		0.6	11 July 1974 - 20 May 1975
11	"	14	"	30	"	10	0.46	0.31	7.74	1.62		0.98	"
12	"	14	"	30	"	15	0.46	0.31	9.01	1.62		1.19	"
13	"	14	"	30	"	20	0.46	0.31	7.89	1.62		1.35	"
14	"	14	"	30	"	25	0.46	0.31	8.33	1.62		1.47	"

* Obtained over the time period 1957-1963
 ** Reported in Ref. 3

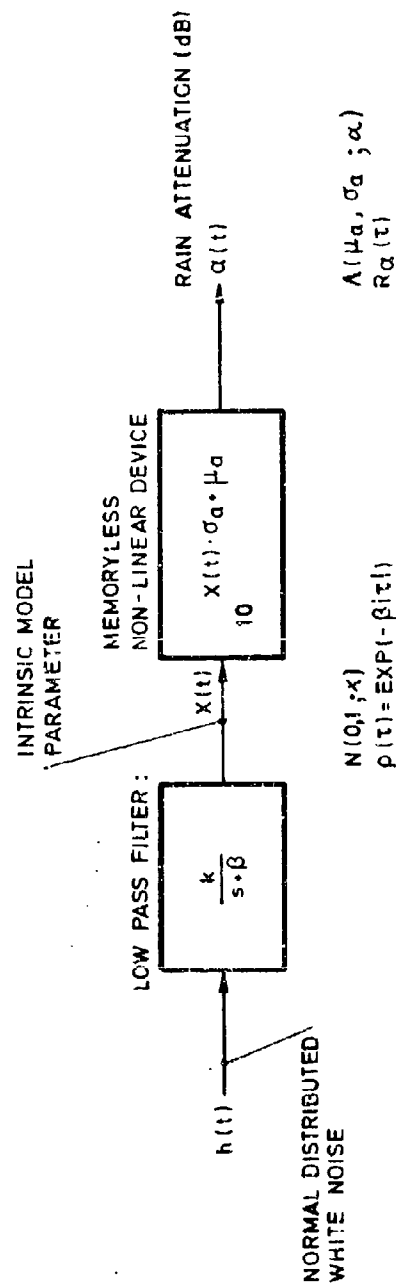


Fig. 1 The stochastic dynamic model of rain attenuation.

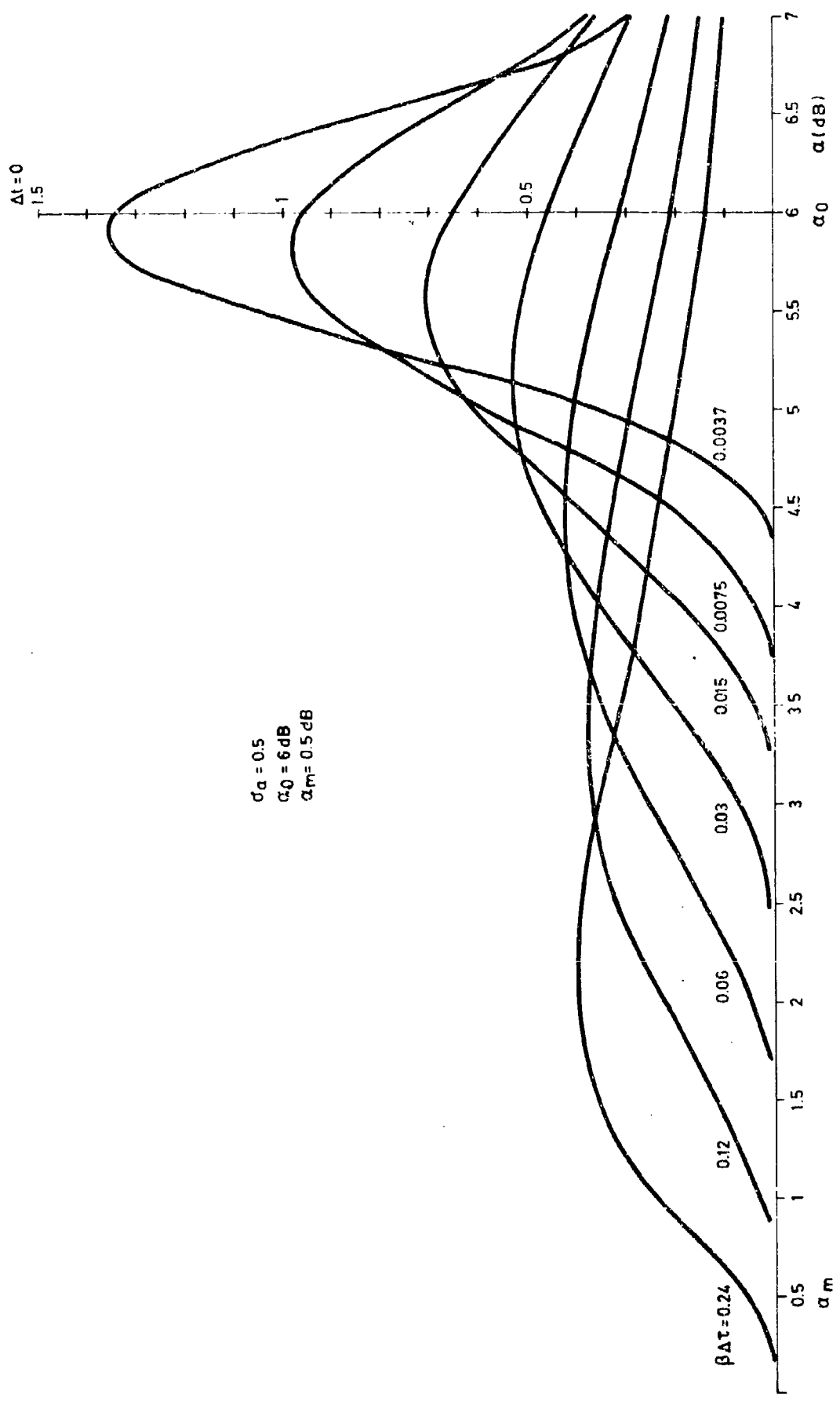


Fig. 2 Conditional probability density of $\alpha(t + \Delta t)$ for various Δt for an initial excursion $\alpha(t) = \alpha_0 = 6 \text{ dB}$.

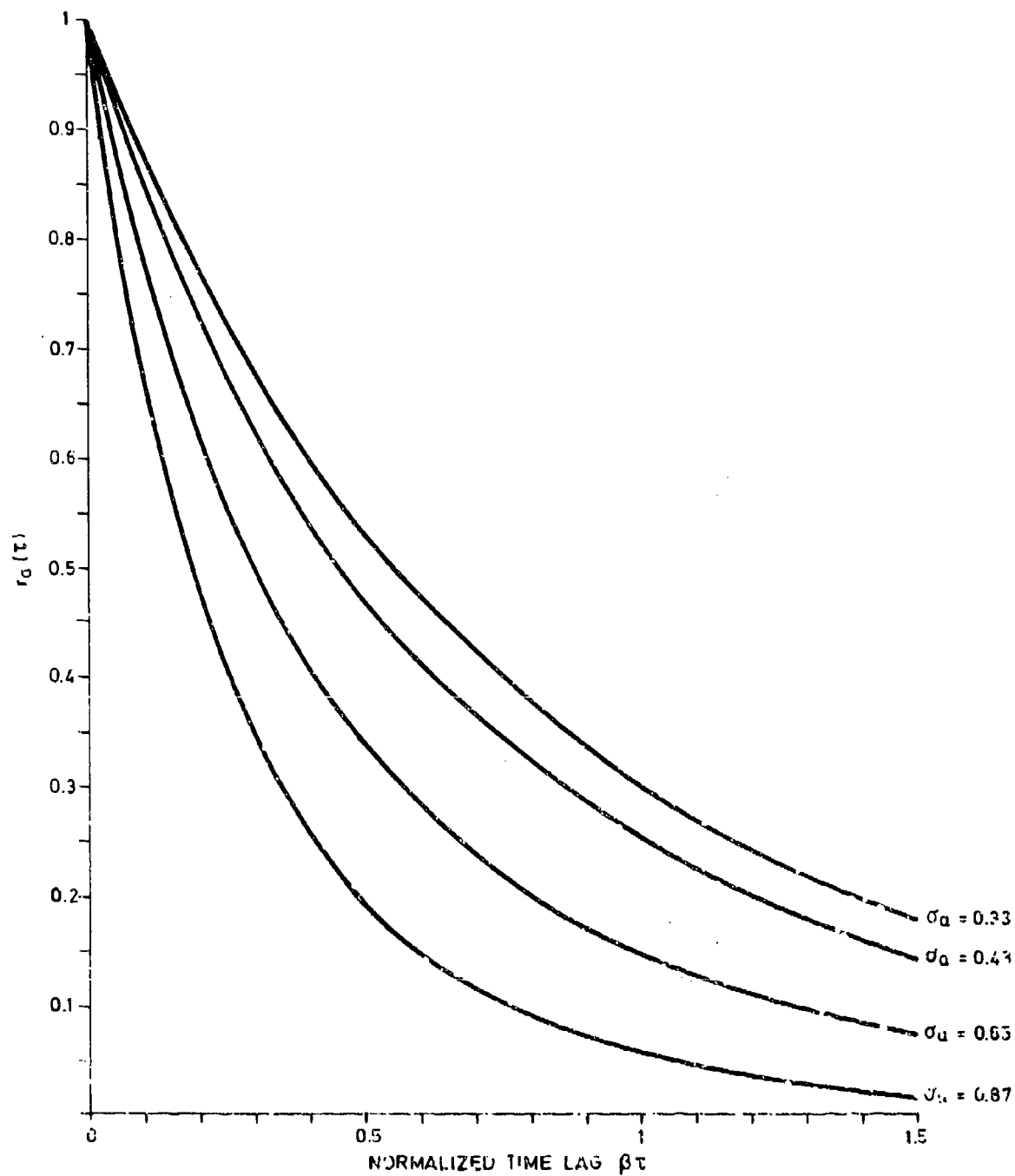


Fig. 3 Normalized autocorrelation function of excess path loss in dB according to the Ornstein-Uhlenbeck hypothesis (one dimension).

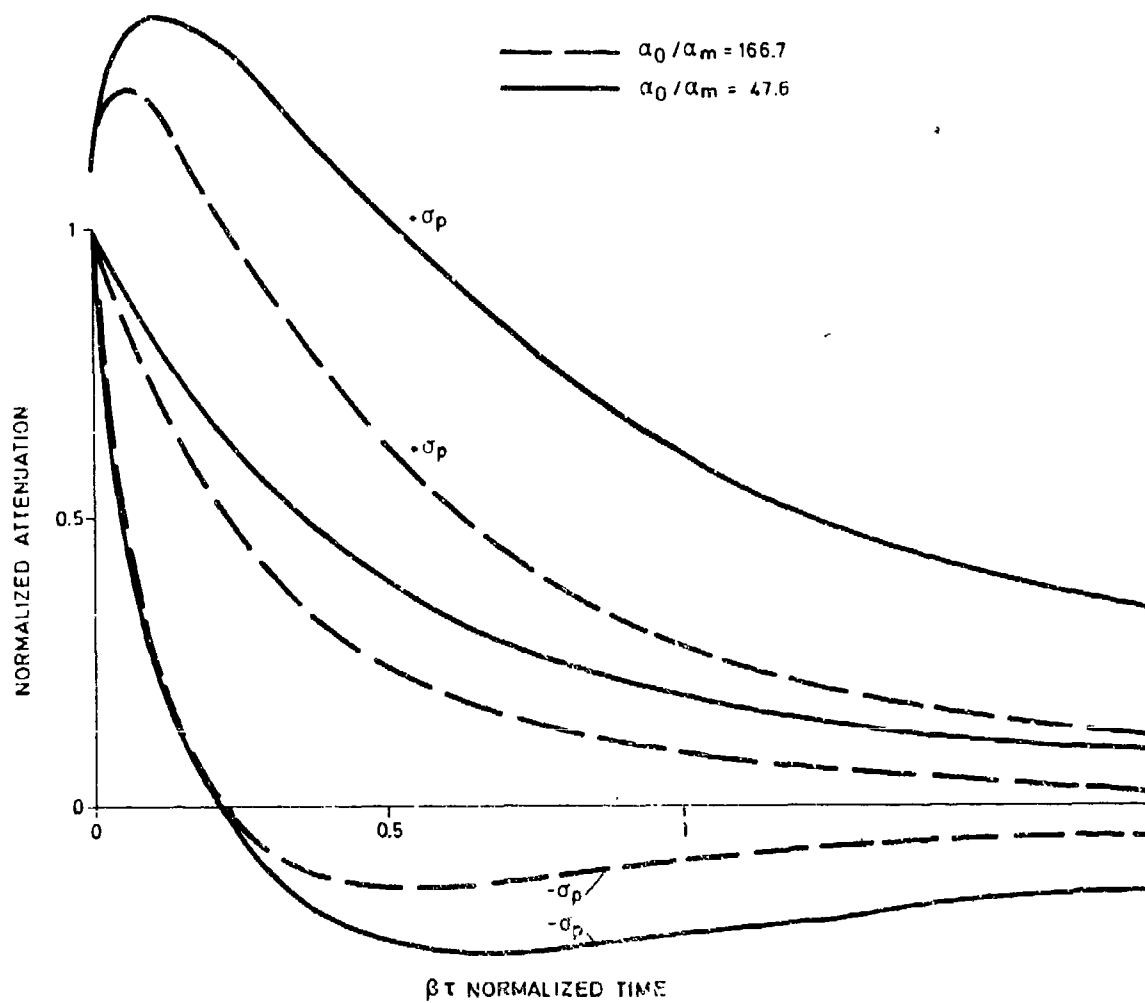


Fig. 4 Normalized mean and standard deviation time profiles of model for $\mu_s = 0.42$ and $\sigma_s = 0.61$. α_m is chosen to facilitate comparison with Fig. 6.

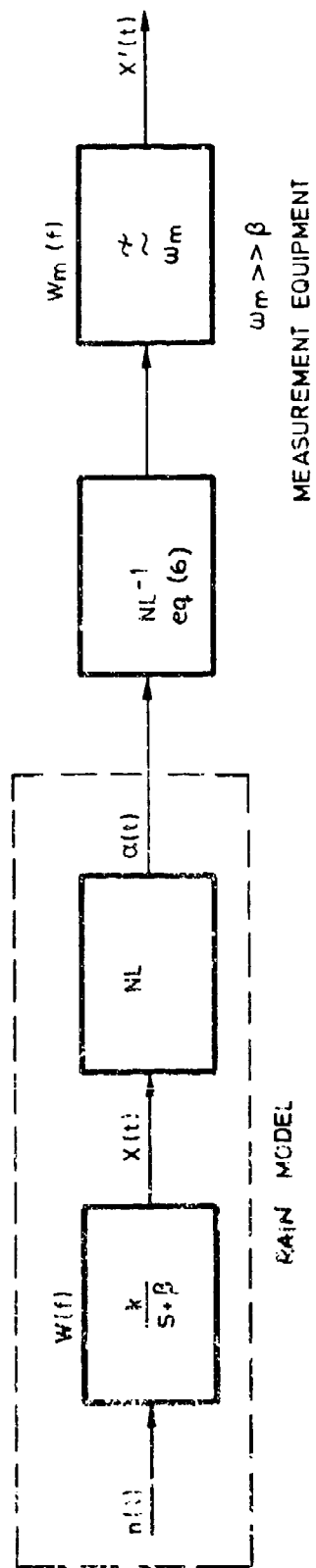
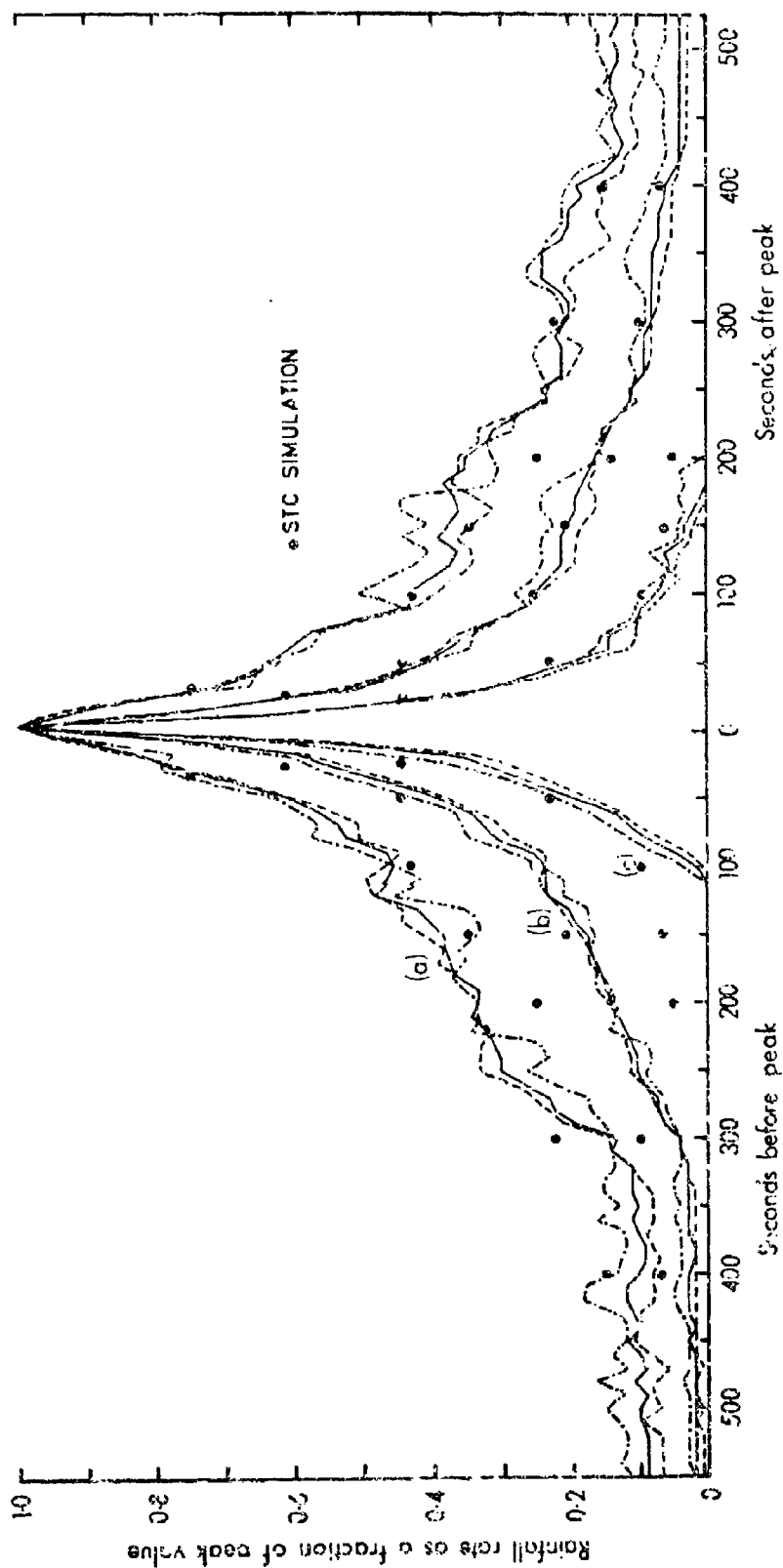


Fig. 5 Proposed equipment configuration to enable the dynamic properties of the model to be determined from fade duration statistics.



MEAN AND STANDARD-DEVIATION PROFILES FOR EVENTS WITH PEAK RATES IN EXCESS OF OR BETWEEN SPECIFIED LEVELS

- (a) mean profile $+ 1 \sigma$
 (b) mean profile
 (c) mean profile $- 1 \sigma$
 --- All events --- Events with peak values in the range 20 mm/h to 50 mm/h
 - - - - - Events with peak values in excess of 50 mm/h.

$q_m = 0.42$ $SR = 1.4$ $q_q = 0.61$

(FROM REF 19)

Fig. 6 Mean and standard deviation profiles for events with peak rates in excess of, or between, specified levels.

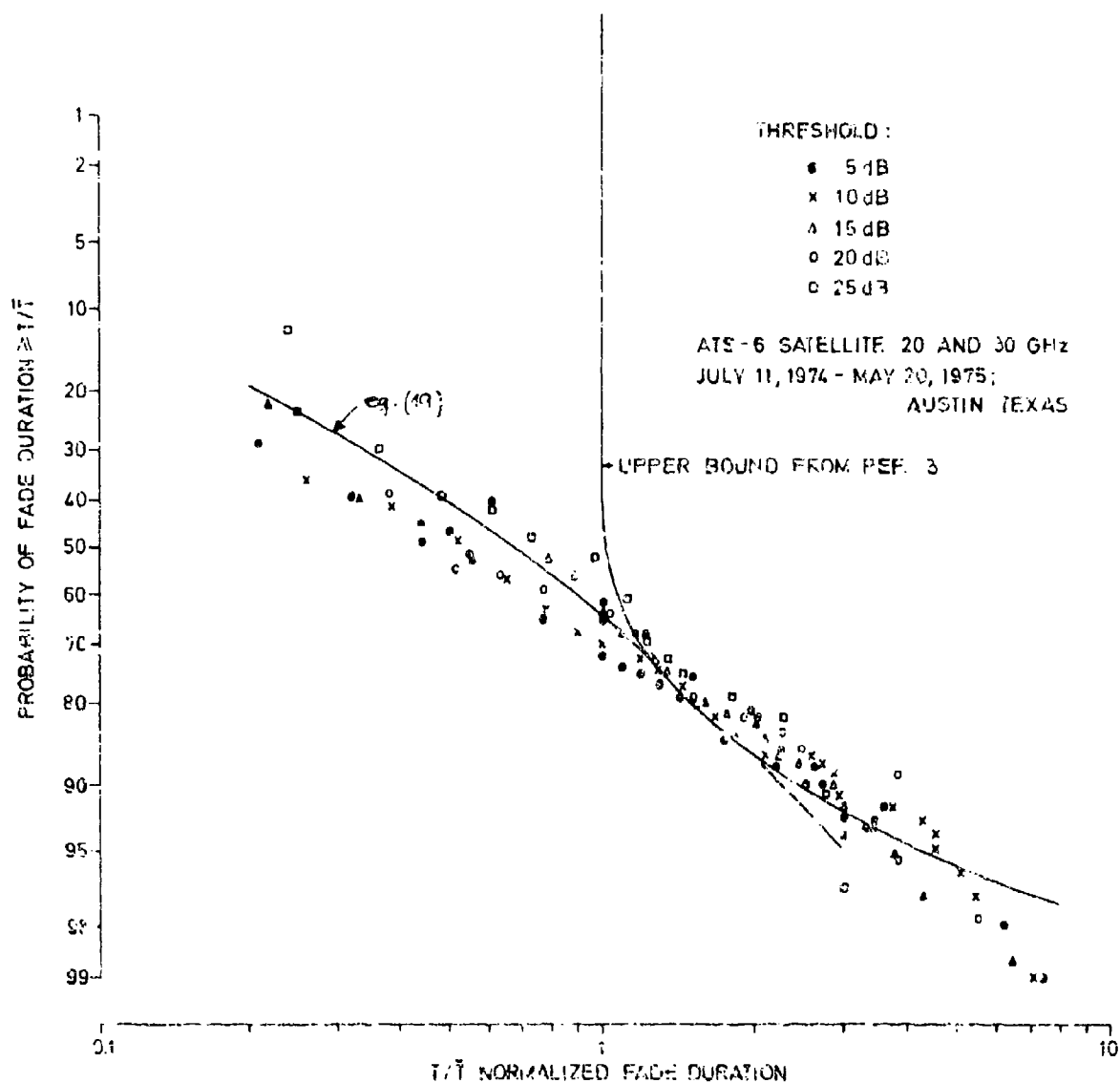
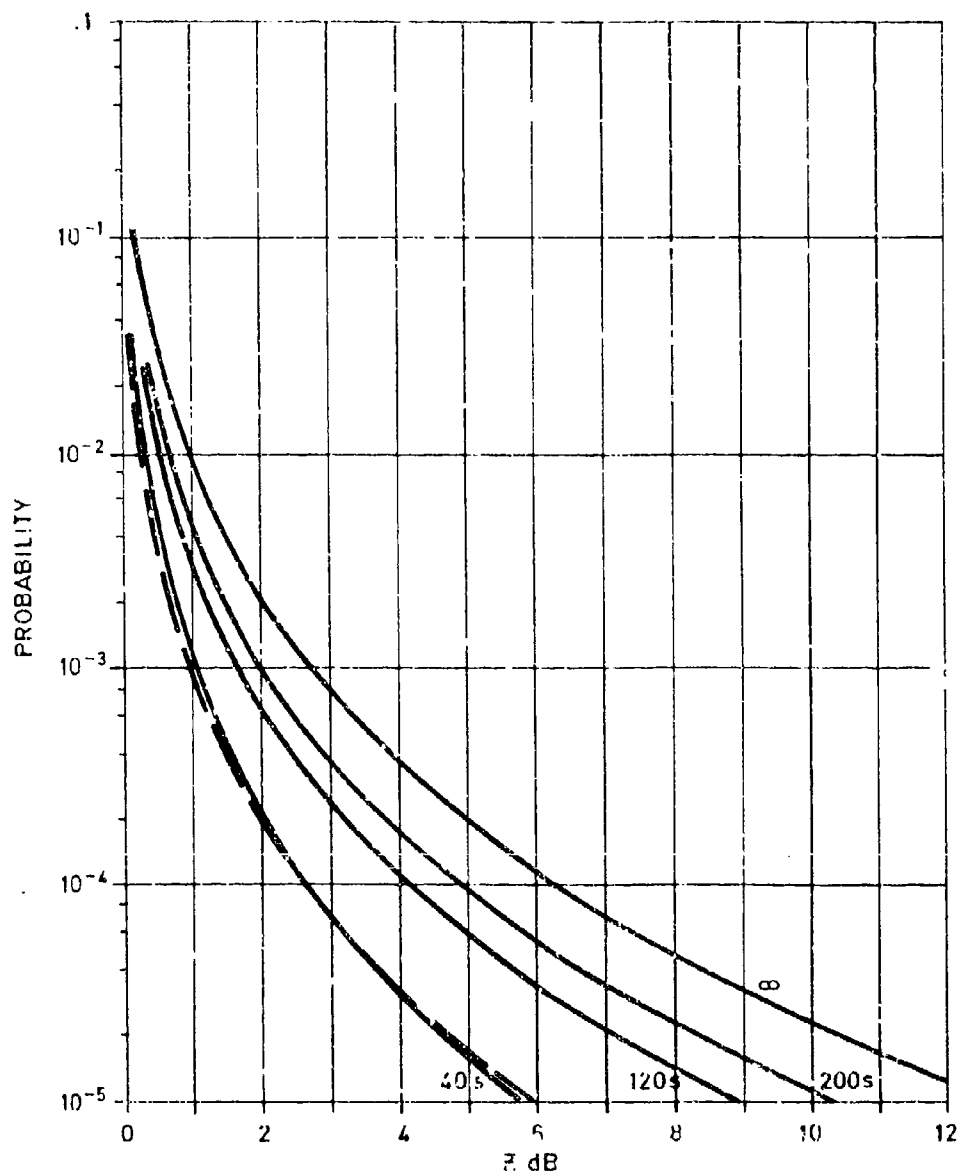


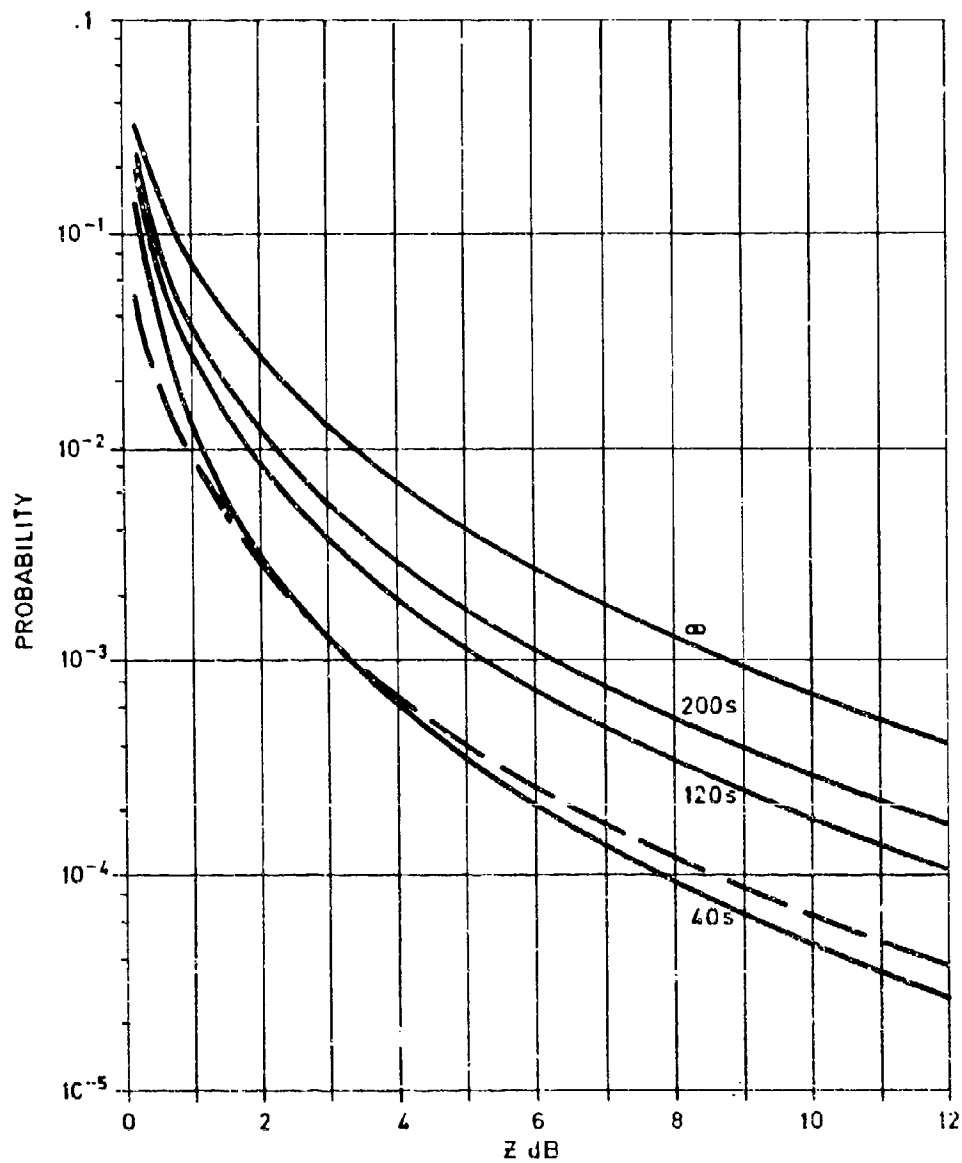
Fig. 7 Experimental results on the statistics of fade duration.



PROBABILITY OF A CHANGE OF MORE THAN z dB
ATTENUATION IN $\Delta t = 40, 120, 200$ AND ∞ SECONDS, GIVEN THAT IT RAINS.

PROBABILITY OF AN ATTENUATION MORE THAN z dB

Fig. 6 Estimated attenuation characteristics for SGT Kester, Belgium
 $P_0 = 0.08$; $\sigma_m = 0.04$ dB; $\sigma_a = 0.55$; $\rho = 0.11 \text{ mm}^{-1}$.



———— PROBABILITY OF A CHANGE OF MORE THAN Z dB
 ATTENUATION IN $\Delta t = 40, 120, 200$ AND ∞ SECONDS, GIVEN THAT IT RAINS.
 - - - - - PROBABILITY OF AN ATTENUATION MORE THAN Z dB

Fig. 9 Estimated attenuation characteristics for SGT Norfolk, USA
 $P_0 = 0.08$; $\alpha_m = 0.24$ dB; $\sigma_m = 0.51$; $\beta = 0.11 \text{ min}^{-1}$.

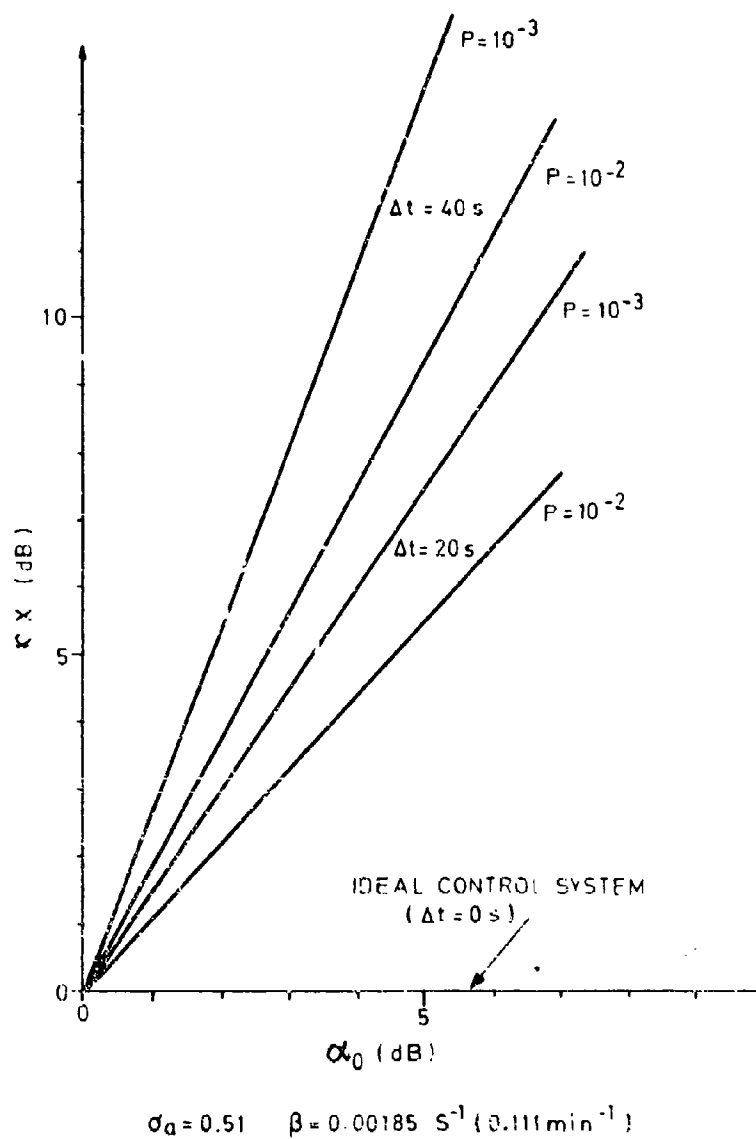


Fig. 10 Margin required as a function of rain attenuation to counter the effect of time delay in the power control system.

APPENDIX A

GENERAL DISCUSSION PROCEEDINGS

SESSION II

C.M.Rush – US: Dr Nisbet, you mentioned in your talk the need or the desire to have coordinated ionospheric modeling efforts. A few years ago, there was within the Government, the makings of a coordinated ionospheric modeling effort; it involved many different Government agencies, and also people in universities. Whatever became of that?

J.S.Nisbet – US: There was a very large ionospheric modeling effort started by ARPA, but it was dropped.

E.J.Fremouw – US: ARPA did call together a panel of people working in radio propagation to review the work. One of the criticisms that came up time-and-time again was where is the output? Where is the application? It was a very large program, but it was viewed, at least by some people, in terms of more immediate output. That's obviously a problem one's always going to have to face in that large scale a program – that the sponsoring agencies are always looking for year-by-year, or even a shorter time-interval application.

J.M.Goodman – US: There is theoretical modeling work being done at the Naval Research Laboratory. Workers are principally concerned with the first principles approach in which they try to develop all of the processes which are responsible for things such as scintillations, plume development, and so on. There is a strong program in equatorial scintillation simulation. There is little bit of work at high latitudes, and virtually nothing at mid-latitudes.

N.G.Gerson – US: Question for Professor Nisbet. You mentioned that you thought you might be able to obtain some dynamical models, and it's on this very case that I feel very pessimistic; and hopefully, you can drive away my pessimism. I view the earth's atmosphere as a conducting fluid in a magnetic field, with unknown energy sources coming not only from the sun, but from energetic particles as well as from layer couplings. Do you reasonably feel that we can construct a dynamic model? Is it a one year, a ten year, a century job? How hopeful do you feel about it?

J.S.Nisbet – US: I think we can produce dynamic models that will reproduce irregularities of the scale of the height distribution of the general time variation; in other words, irregularity structures that will develop in the same way as they are seen by an EM signal from a satellite communications system or a radar. I agree entirely that it's very much more difficult to model the dynamic variations in the ionosphere short of starting from first principles.

F.R.Schmerling – US: I think, personally, that the advances in modelling state-of-the-art are going to come from more emphasis in the overall physics of what is happening in the ionosphere as part of a system in solar-terrestrial relationships; and we have nearly gone as far as we can in the empirical modeling.

C.M.Rush – US: Your points are very well taken, Doctor Schmerling. I think, however, that most of us who are in this game do appreciate that the man who's holding the purse strings does want to see results. It's perhaps a sad testimony to our time, that we have to produce those in a rather short time period and to tailor our work to a specific application rather than to generalize it.

I.J.Rothmuller – US: I think one shouldn't sneer too much at empirical or semi-empirical methods of getting answers, because quite often that's the first step. You form a correlation between two things that you feel are somehow connected, but you are not quite sure. The physics tell you it ought to, but it's so complicated as not to be obvious. I feel there ought to be a balance between modeling totally empirically without looking at the physics at all, and at the other end, modeling only by total understanding of all interrelated processes.

L.W.Barclay – UK: In the comparison of theoretical and empirical models of the ionosphere, I am reminded of a rather simple example; that of modeling the night-time skywave field strength at MF. Early models of this were empirical, but some years ago a major improvement seemed likely when wave-hop methods were developed. These theoretical methods failed to find acceptance due (I think, although the rejection was not expressed in this way) to the lack of an adequate theoretical model of the structure at the lower ionosphere at night. Since then, the prediction of MF field strength has been based on empirical results and the technique has had to become much more complicated, and less related to any physics, to account for the apparently differing results in various parts of the world. An empirical model like this might be challenged and altered at anytime as new results become available, and I regard it as rather unsatisfactory. It should be possible to produce a much more satisfying and scientifically acceptable model when we are able to supply a reliable basic physical model of the lower ionosphere.

I was interested to hear the discussion on sources of funds for long-term studies of ionospheric models in the USA. In my opinion, the position in the UK is even less encouraging. Some sources of funds for universities and research centers may come, with difficulty, from the scientific budgets. So far as other budgets are concerned, however, it has really not been possible to convince the HF users that there is a problem for which long-term modeling studies would provide a solution.

T.B.Jones – UK: As far as our military people are concerned, it's virtually impossible to convince them that any kind of modeling whatsoever is of any value to them. What they do think though, and I think this is worth saying, is that a real-time hardware channel estimation system seems a much more attractive object to someone who's going to put money into a system.

E.R.Schmerling - US: I must take issue with that, to the extent that it's only a partial answer. For short term needs, an adaptive channel estimation system is enormously attractive. But in the long-term need for planning, such systems are inadequate. The modeling community has to convince the authorities of the necessity of better modeling. Perhaps Dr Rush would like to say a few words about CCIR. Wouldn't CCIR like to have some good long term models on the basis on which it could make some good recommendations?

C.M.Rush - US: There's no question about that. Attempts have been made over the course of the years to develop not only MF skywave field strength methods, but HF and now even down to the LF bands. I think it's rather difficult, though, for CCIR to make great strides in these areas without the benefit of the scientific community. The people who participate in CCIR, although we mean well, do not have the benefit of, let's say, flexibility that is normally afforded in the scientific communities. We will see within the next two years the crying need for much improved information on the status of the ionosphere and its impact on all of the radio communications systems as we go into the preparations and actually hold the General World Administrative Conference in 1979. At that point all of the radio regulations as well as the frequency allocations will be up for review, and decisions will be made as to the allocation of the spectrum and the utilization of certain frequencies on the basis of information that's at best incomplete and in some instances, lacking. On the other side of the coin, such decisions will also be made on the basis of political pressures so if one had that information, it's not at all clear that it would be used in the most appropriate way. But you are right, there's no question that CCIR in the ultimate does desire more accurate models, more accurate methods, for long term system planning and utilization of the entire frequency spectrum.

I.J.Rothmalier - US: The point one should make when one looks at the effects of the environment on systems, is that one can deal broadly with all systems rather than tailoring oneself to one particular system.

E.R.Schmerling - US: While it is true that the funds are available in the applications, the applications would have been impossible without the science that went before it.

I think NASA's representative put it very well when he was challenged in Congress about the use of pure science. He said, "Gentlemen, we have taken out from the treasure house of knowledge what has been put in by previous generations and it served us well; and you can get all the examples you know from TV onwards. Now I think it's our problem to put science back into the store-house of knowledge for future applications that aren't even dreamt of". And one Congressman jumped up and very excitedly said, "Do you mean, that you want to restock the barn with seed grain?" The Congressman understood it very well.

I think we're talking about two entirely different things. We are talking on the one hand for results now and applications. This is legitimate, and there's a lot of money in it if the arguments are legitimate. On the other hand there is science - the search for a deeper understanding of the how and why. I think there we want to be very careful not to pretend that we're going to come up with instant answers. What we're really seeking is the intellectual satisfaction of understanding, and maybe one month, one year, one generation ahead, some application will be found from this knowledge.

H.Soicher - US: In view of what has been said in this discussion period, has the scientific community failed in its effort to convince the users and those in positions of funding authority on the relative importance of science and its applications?

J.Aarons - US: Someone ought to defend the current funding system. For example, in the US Department of Defense, we have what we call, 6.1 funds for basic research. This effort emphasizes theoretical and experimental conceptual work, rather than strictly applied work. The National Science Foundation is heavily funded, and it is not tasked with operational tasks.

We are involved here in an operational modeling meeting and therefore, we're putting together all these various operational models which are practical to some users. The tasks of putting together all the parameters involved in producing the various ionospheric effects should be performed. It's a massive effort requiring many groups coming together, and a lot of funds devoted to just this problem over very long periods of time. Perhaps one of the things that we ought to think about, at least within the US concept, is how to put this together in a practical way and sell it to the Government.

N.G.Gerson - US: The funds spent in North America on improving ionospheric predictions over the past two decades were enormous, while the results have been rather small. In some cases, the practical communicator did not change his operating pattern to incorporate new refinements and improvements in prediction techniques.

J.M.Goodman - US: As far as the C³ system designer is concerned, the traditional use of basic research in the radiowave propagation modeling area is based upon a requirement to know the range of channel or link variability. This is so that naval waveform/network adaptation and coding/interleaving schemes can be developed given best estimates of the ranges over which such schemes must adapt or operate against. Nevertheless the designer will generally opt for development of adaptation or mitigation schemes based upon median disturbance models. Large disturbances may still produce outages especially for the small disadvantageous users. It seems to be that the requirement for real-time prediction schemes therefore still exists even if the overall link availability is as good as 99.5% (corresponding to 44 hours/year) since disturbances are generally clustered and not averaged over a year. Typically a few disturbances will contribute to the total channel unavailability is a significant problem; it matters not that the long term availability is 99.5% say.

SESSION III

L.W.Barclay -- UK: In a number of papers this morning, we've heard mention on the use of the Bradley/Dudeney profile for connecting the E-region and F-region. I am going back again to statistics really. For E-region critical frequencies, the models, I think, allow $\pm 5\%$ variation in critical frequency between the 90% and 10% days of the month; and there are much wider variations in the critical frequency in the F-region. There are also variations, and I am not sure how well the statistics are modeled, for the thickness of the F-region. Yet we use a single type of connection, a single type of profile between the E and F-regions. Can I ask Mr Bradley, or some of the other people who use this profile, is there a need for adding a statistical variation onto that interlayer profile?

P.A.Bradley -- UK: Further developments of the Bradley/Dudeney model have been proposed by Dudeney. The proposed model consists of a parabolic F₂-region and a parabolic E-region and some intermediate sections which are trigonometric in form. These sections give a smooth transition through the height profile.

K.Davies -- US: It is very nice to have the sophisticated models that were described in this meeting. The question is, are they of any use to the user? Are we making these models more and more sophisticated for our own sakes rather than for the sake of the user or the designer?

L.W.Barclay -- UK: My job has been to try to interpret the valuable work the scientists do for the man who's got to use it, so my first consideration has always been to try to talk to the user first and find out what he wants, and then to tell him the answer in language that he's used to talking in. And that's not easy, but I think that's the way we have got to go. We have got to somehow turn our predictions with all the sciences built into them into some sort of number, some sort of measure, that the man who's got the job of using HF communications can really hold onto and understand. We are trying, but I think any ideas on how to do it better will be very welcome.

T.B.Jones -- UK: We had in Norway some years ago a gathering of a group of scientists, a group of communications engineers, and a group of military people, who are the actual users. At the beginning of the week the participants didn't even speak the same language let alone understand each other. I think that was a very revealing meeting. Dr Davies summed it up very well at that meeting, saying that one of the major problems in communication research was communications between ourselves and the user community. I think that's a problem that's still outstanding and we, as scientists are a little to blame for not making more effort in this direction. People like Dr Barclay whose job it is to translate ionospheric science into useable terms that he can give to users, have very demanding and difficult jobs.

T.A. Van Geem -- Netherlands: I am an officer with the Air/Staff Training Section of the Netherlands. It seems to me that we have three levels of communication. The first is the scientist, the second is industrial and military liaisons, and the third is the actual user. For fruitful results, there must be a translation between the first level through the second level to the third level, with understandable instructions.

J.Röttger -- FRG: The smooth behavior of the ionosphere shown in the talks this morning presents a very general picture. There are variations in the critical frequencies of these ionospheric layers that can be included into forecasts and predictions, as has been pointed out very properly. We also have some disturbances which can be forecasted by some means. We must, however, realize that at several locations of the globe the ionosphere does not behave smoothly. For example, at polar regions disturbances are quite common; as at the equatorial regions during the post-sunset period. You cannot fit a parabolic profile to the F-layer under such conditions, neither can you define the critical frequency properly due to the strong density gradients. For HF propagation mode in the equatorial zone one must take scatter into account as well as off-great-circle propagation at total reflection. While the equatorial behavior is quite common and possibly predictable, the normal model parabolic fit can not be used.

T.B.Jones -- (US): The point is that there are very large temporal changes in the ionosphere, especially in the auroral zone, and it is very difficult to include these in a model. I don't think this has been done.

C.M.Rush -- US: Some years ago a group of AFRL (now AFGL) attempted to put together a polar ionospheric model. Averaged over all time in any of the simulations, the conclusion was reached that it was no better than that which was already available, namely, in the form of the ITS78 program. This particular model was put together specifically to look at the impact of the high latitude ionosphere on the performance of the backscatter radar system. Even though, on the average, it turned out that the results on the new model were not better than that previously available, it contained certain quasi-permanent features of the high latitude ionosphere such as the high latitude trough and the auroral irregularity zone. That enables one to at least make an assessment of what the potential impact would be on the performance of a radar system if the high latitude trough were to move down under his area and to move back up. I think the primary limitation to forecast and predictions, not only in the high latitudes but also the equatorial region, is the fact that things are changing so rapidly. It makes very little sense to attempt to develop a prediction scheme that requires an observation or assessment of a geophysical phenomenon on such a time scale that by the time you get that information to make it useful, things have changed so much, so rapidly, that it's of no use whatsoever. There's an area beyond which I don't think we can progress, because we really get into the geophysical noise area and all we would be doing raising and lowering the noise floor.

J.S.Nisbet – US: The users and scientists are being talked about as two different people. For some of these models the scientists themselves are users – particularly for high latitude studies. The models which take account of special high latitude features (e.g. cap or trough regions) are very valuable to those who study, for example, damping of ionospheric wind systems.

E.V.Thorne – Norway: I have two comments. One pertains to the predictions at high latitude. Some years ago an attempt was made at our laboratory to compare the behavior of a communication circuit with an ionospheric reflection point in the auroral zone, with predictions. When the operators compared the frequencies actually used with those predicted – there seemed to be no connection. Further, the predictions were compared with ionosonde data just south of the auroral zone with very good agreement. The conclusion was drawn that the predictions hold well up to 65° north geomagnetic latitude, and the break down abruptly as one moves northward. The other comment refers to the paper by Widdel and Lange Hesse. It seems that for the first time there's an indication that one can predict Winter Anomaly absorption. Do the authors have any suggestions as to the physical mechanism that connect the air glow to the actual absorption?

G.Lange-Hesse – FRG: At the present time I have no physical model which could explain the statistical behavior, shown. The only thing that may be said is that the intensity of the red emission in the air glow is proportional to the square of the atomic oxygen concentration in the lower atmosphere, say at about 95 kms. The two factors K1 and K2 depend on the temperature in such a way that increasing temperature would also increase emission. I think there's a future field of activity for theoretical work in this respect.

H.Soicher – US: On many occasions we have tried to update prediction schemes with real time data by ionosondes. Since the ionosondes are located in specific limited areas, what can one say about a correlation distance? For TEC correlation distances of 1000–2000 kms do exist. What are the correlation distances in terms of F-max or critical E for examples?

N.M.Tomljanovich – US: It was pointed out that a highly variable ionosphere there is a limit on how much the prediction accuracy may be improved by a near-real-time update. However, the near-real-time update will give an indication when the ionosphere is highly variable, and as such it is of value.

T.B.Jones – UK: For a signal between 5 and 8 MHz, a path of 1000 km – the correlation of absorption variations dropped to .5 when the separation of the path midpoints was about 300–400 kms.

I.J.Rothmuller – US: We have a complicated matrix of users, modelers and models and what happens is that the same word gets used and different things are implied about it. When a user claims he needs a more accurate model, or a more precise model or a more realistic model, he has to make it clearer what is meant by "greater accuracy". Does he mean he needs to know reaction rates better? Does he need to know the profile better? Does he need to know morphology better? What exactly does he need and what is he going to use it for?

SESSION VII

H.J. Albrecht - FRG: This general discussion period should focus on the future direction of environmental modeling for the optical and IR portions of the spectrum. One should keep in mind the specific requirements of the military community in the design of such modeling efforts. To quote Lord Kelvin - "When one can measure a quantity and express it in numbers, one knows something about it; when one cannot express it in numbers, one's knowledge is meager and unsatisfactory". Environmental models are, of course, somewhat different. In some cases, they pose an iterative approach to the solution of a problem, and must be improved continuously. Some suggestions I would like to offer for discussion: Applicability of Environmental Models to Artificial Modification of the Environment; Aerosol Models; Environmental Tests of Models at a limited geographic area; Determination of Rainfall Rates and Cloud Formations by Remote Sensing and its applicability; humidity as a model parameter.

R.A. McClatchey - US: I am going to respond to a couple of points that our chairman made as well as to raise another very closely related point here. I think that the models have become quite good, in terms of predicting the optical properties of the atmosphere, to the extent that the input data into the models is adequate. The problem that I think we have for the future is how to decide, (1) which models to use for a given situation and (2) how do we establish that the input data is the correct input data. It's particularly pertinent in the case of the aerosol models (and by aerosol I mean haze, fog, dust, clouds - whatever is a particulate matter in the atmosphere). In case of the molecular influences, we have a reasonably good knowledge of the molecular constituents of the atmosphere, thorough standard meteorological measurements, and a reasonable understanding of the variability of, for example, water vapor, which is one of the key molecular constituents that affect propagation characteristics. We have that simply because we know how to measure it pretty well, and we measure it routinely around the world. On the other hand, in the case of aerosols, we don't have a good measurement. We don't have a good predictive capability either, I think, and so even though we have models of a whole range of different aerosol effects (whether now we are talking about rain, or cloud, or haze, or dust) we've got to make some hard decisions (or the user has to make some hard decisions) as to which model to use for a given situation, and how to specify the input data. With regard to growth of particles due to relative humidity, we do intend to include it in all the various aerosol models that will be introduced into the LOWTRAN Code in the six-to-eight months time frame.

H. Fluess - FRG: Computer models are the only useful tools by which to introduce artificial atmospheric constituents and aerosols in order to prevent communication and detection.

B.S. Katz - US: To address the question of aerosol models and the relative humidity - one of the driving factors over water is the relative humidity. If one talks about slant paths, the calculation of the relative humidity as a function of altitude becomes a difficult problem. We saw earlier a model which depends on temperature and absolute humidity but the relative humidity is very much a function in a physical sense; (Are there clouds there? Does it go off to 100% above you? Or are you in between clouds?). Those are the parameters, I think, that should be looked into in future modeling, not just temperature and absolute humidity. The other point, mentioned earlier, is that we do have a community that requires these models. There is a great concern within that community that people spend too much effort on details and do not really provide them the simple things that the users want to know: whether a system will work, be good, or bad or somewhere in between. This may mean that for future modeling you do not need all the details that do come from detailed spectroscopic work.

H.J. Albrecht - FRG: In a recent interesting experiment by the US Air Force, an attempt was made to correlate cloud data obtained by remote sensing (satellite observations), with attenuation on troposcatter links. In the general sense, with reasonable assumptions, the correlation was quite good, and this represents a confirmation on the validity of hypothetical assumptions previously made.

R.B. Gomez - US: One should also be concerned with the effect of winds on the aerosol size distribution. In addition, no mention has been made of the process of transport, diffusion, or the persistency of adverse weather once it has occurred.

H. Fluess - FRG: I agree that it is crucial to choose the correct input data for incorporation into a model. One should take into account atmospheric irregularities, rain, height range of clouds, and the probability of their occurrence.

H.J. Albrecht - FRG: An attempt to use average meteorological conditions for a certain geographic area, including special weather situations, is quite helpful. This was tried in the central region of NATO, which is quite variable as far as weather is concerned. As far as turbulence is concerned, the spectrum is to some degree well defined. The problem at hand is the association of clouds with some kind of turbulence. While one cannot get precise data on the turbulence behavior of clouds, the clouds are one indicator which is measured continually on a statistical phenomenological basis, and may thus be used as an input in modeling.

W. Eckl - FRG: To clarify the aim of the program which I presented, our program aims to set a standard reference, with respect to which various systems will be compared. The reference need not be correct in every detail.

E.Lampert – FRG: The approach of having a general weather situation is well appreciated. However, for transmission ranges of 10 to 20 km the assumptions implied are crude. The introduction of a meteorological statistical grid over the area in question should improve the model considerably.

K.P.Pirwitz – FRG: Measurement taken at weather stations of the German Military Geophysical Service were used to define areas (over distances of 5 km) where the weather is the same.

J.Röttger – FRG: To follow up the discussion on turbulence, I would like to point out that one has to take into account clear air turbulence in addition to cloud turbulence. The former may be of greater influence on the propagation of electromagnetic waves. If one observes the development of Ionospheric Propagation Models during the past twenty years, one would conclude that Tropospheric Propagation Models (at least as far as turbulence is concerned) in the optical and EHF regions are a first step.

H.J.Albrecht – FRG: I would like to turn the discussion to the subject of the determination of rainfall rates by remote sensing. If one knows the rainfall rates with any sort of precision one would have a far better indication of the attenuation behavior of satellite and ground communication and navigation links above ~ 10–20 GHz. Since rainfall rates at ground level are no more than those in existence in clouds, cloud remote sensing by satellites would be extremely helpful.

H.J.Jung – FRG: I would like to address the limitations of the rainfall intensity measurements. At 37 GHz, only rainfall has to be considered as an absorber and/or scatterer. In the analysis, one has to consider the height distribution of rainfall, and the boundary conditions at the ground. Since no measurement or calculations of the distribution of the rainfall at the various atmospheric levels exist, one has to assume a median value.

R.A.McClatchey – US: There is a plan afoot that is probably going to take place within the next few years to put microwave imaging sensors on the DMSP, Defense Meteorological Satellite, which will have as one of its aims to measure rainfall rate, total liquid water content in clouds as well as water vapor. I can't comment on accuracy of that capability; some of those things are still being thought about and worked out, but I think there's a serious interest in this and I think it will be probably a sensor that will be constructed and flown several years from now.

H.J.Albrecht – FRG: To conclude this discussion period, the general conclusion might be that more work is necessary. Perhaps in a few years, the direction of future work indicated in this meeting would result in new information and would be presented at future AGARD symposiums.

APPENDIX B

LIST OF PARTICIPANTS

LIST OF PARTICIPANTS

AARONS, J. Panel Deputy Chairman	Air Force Geophysical Laboratory/PHF Hanscom AFB, Mass. 01731	USA
ABELE, J.	Forschungsinstitut für Optik, Schloss Kressbach, D-7400 Tübingen	FRG
ALBRECHT, H.J. Panel Chairman	FGAN, Königstrasse 2, Wachtberg-Werthhoven	FRG
ATKINSON, G.	Department of Communications, CRC, P.O. Box 11490, Ottawa, Ontario	CANADA
BARRINGTON, R.F.	Department of Communications, CRC, P.O. Box 11490, Ottawa, Ontario	CANADA
BARCLAY, L.W.	Home Office, Directorate of Radio Technology, Waterloo Bridge House, Waterloo Road, London SE1 8UA	UK
BECKER, K.D.	Universität des Saarlandes, Fachrichtung 12, Elektrotechnik, 6600 Saarbrücken	FRG
BELROSE, J.S. Panel Member	Department of Communications, CRC, P.O. Box 11490, Ottawa, Ontario	CANADA
BENT, R.B.	Atlantic Science Corporation, 1901 N A14, Indian Harbour Beach, Florida, 32937	USA
BERNHARDT, P.	Radioscience Laboratory, Stanford University, Stanford, Cal. 94305	USA
BISSONNETTE, L.	Defence Research Establishment, Valcartier	CANADA
BLASCHKE, G.	Standard Elektrik Lorenz AG, Entwicklung Navigation, Hellmuth Hirth-Str. 42, 7000 Stuttgart-Zuffenhausen	FRG
BOSSY, L.	IRM, Geophysique Externe, 3, Avenue Circulaire, 1180 Brussels	BELGIUM
BRADLEY, P.A.	Appleton Laboratory, Science Research Council, Ditton Park, Slough, Berks, SL3 9JZ	UK
BURTON, R.J.	Office of Chief Communications, Security Department of National Defence, 101 Colonel By Drive, Ottawa	CANADA
BURKE, M.J.	CRC, Box 11490, Station H, Ottawa, Ontario	CANADA
CARATORI, J.	Laboratoire d'Etude des Transmissions Ionosphériques, 9 Avenue de la Division Leclerc, 94230 Cachan	FRANCE
CARLSON, J.R.	Office of Chief Communications, Security Department of National Defence, 101 Colonel By Drive, Ottawa	CANADA
COYNE, V. Panel Member	RADC/OCS, Griffiss AFB, N.Y. 13441	USA
DAMBOLDT, Th.	P.O. Box 5000, 6100 Darmstadt	FRG
DAVIES, K. Panel Member	NOAA/ER, SEL, R.43, Ionospheric Physics Program, Boulder, Co. 80302	USA
DEVEREUX, E.L.	Mercury House, Theobalds Road, London WC1 8RX	UK

DIJL, Van, B. Panel Member	Johan de Wittlaan, 18, Eindhoven	NETHERLANDS
DONNELLY, R.F.	Program Chairman STP/P-W, Space Environment Lab. NOAA/FRL, Boulder, Colorado, 80307	USA
DRUMMETTER, L.F., Jr Panel Member	Associate Superintendent, Optical Sciences Division, US Navy Research Laboratory, Washington D.C. 20350	USA
ECKERT, K.D.	Standard Elektrik Lorenz AG, Entwicklung Navigation, Helmutn Hirth-Str. 42, 7000 Stuttgart-zuffenhausen	FRG
ECKL, W.	Elektronik-System GmbH, Postfach 86 03 05, 8000 Munchen	FRG
FENGLER, C.	McGill University, Electrical Engineering Dept. 3460 University Street, Montreal, Quebec	CANADA
FLUESS, H.	Messerschmitt-Bölkow-Blöhm, 8 München 80, Postfach 80 11 60	FRG
FONTANELLA, J.C.S.	ONERA, 29, Avenue de la Division Leclerc, 92320 Châtillon-sous- Bagneux	FRANCE
FREMOUW, E.J.	Physical Dynamics Inc. P.O. Box 3027, Bellevue, WA 98009	USA
GEEM Van, T.A.	Air Staff/Training Section, Princ. Clauslaan 8, 2509 The Hague	NETHERLANDS
GERSON, N.G.	Laboratory for Physical Sciences, College Park, MD 20740	USA
GLADWIN, J.	Department of Communications, CRC, P.O. Box 11490, Ottawa, Ontario	CANADA
GOMEZ, R.B.	US Army Electronics Research and Development Command, Atmospheric Science Laboratory, White Sand Missile Range, NM 88002	USA
GOODMAN, J.M.	Space Environment Branch, Space Systems Division, NFL, Washington D.C. 20375,	USA
COUJELARD, C.	Laboratoire d'Etude des Transmissions Ionosphériques, 9, Avenue de la Division Leclerc, 94230 Cachan	FRANCE
GRFEN, F.	CRC, Box 11490, Ottawa, Ontario	CANADA
HAGG, E.L.	CRC, Box 11490 Ottawa, Ontario	CANADA
HANSON, D.W.	FADC/OCSE, Griffiss AFB, N.Y. 13441	USA
HARTZ, T.R.	CRC, Box 11490, Ottawa, Ontario	CANADA
HIGGINS, J.	DND HO, Ottawa	CANADA
HOUMINER, Z.	National Committee for Space Research, Radio Observatory, Haifa	ISRAEL
JAMPS, H.	Department of Communications, P.O. Box 11490, Ottawa, Ontario	CANADA
JAVED,	Bell Northern Research, Ottawa, Ontario	CANADA
JEAN, G.	Space Environment Laboratory, NOAA, FRL, 325, So Broadway, Boulder, Col. 80302	USA
JENKINS, R.W.	Department of Communications, CRC, P.O. Box 11490, Ottawa, Ontario	CANADA
JONES, T.B.	Physics Department, The University, Leicester	UK

JUNG, H.J.	Institut für Geophysik und Meteorologie, Universität Köln, Derpenerstr. 13, Köln, 41	FRG
KATZ, B.S.	Naval Surface Weapons Center White Oak Laboratory, Silver Springs, MD 20910	USA
KREPLIN, R.W.	Code 7125, Naval Research Laboratory, Washington D.C. 20375	USA
LAMPERT, F.	Siemens AG, Wv fu MS EF 21, 8000 München, 70, Hofmann- strasse 51	FRG
LANGE-HESE, G. Panel Member	Max-Planck Inst. für Aeronomie, Postfach 20, D 3411 Kadenburg- Lindau, 3	FRG
LIEBE, H.J.	US Department of Commerce, OT/ITS, 325 South Broadway, Boulder, Col. 80302	USA
LONG, R.J.	Mail Stop C 380, MIT Lincoln Laboratory Lexington, Mass 02173	USA
LYON, I.D.	British Aerospace Dynamics Group, P.B. 244, Six Hills Way, Stevenage SG1 2DA, Herts	UK
McCLATCHEY, R.A.	Air Force Geophysics Laboratory/OPI, Hanscom AFB, Mass. 02131	USA
MARGUINAUD, A.	Thomson CSF/DITM, 55, rue Greffulhe, 92391, Levallois-Perret	FRANCE
NASENG, T.	Shape Technical Center, P.O. Box 174, The Hague	NETHERLANDS
MONTBRIAND, E.	Department of Communications, CRC P.O. Box 11490, Ottawa Ontario	CANADA
MORLEY, G.	Defence Research Establishment, Valcartier	CANADA
MULDREW, D.B.	Department of Communications, CRC P.O. Box 11490, Ottawa, Ontario	CANADA
NICOLET, M. Panel Member	External Geophysics, Brussels University, 30 Avenue Den Doorn, 1180 Brussels	BELGIUM
NISBET, J.S.	Ionosphere Research Lab., The Pennsylvania State University, University Park, PA 16802	USA
OLIVER, H.E.	Decca Navigator Co Ltd, 2 Biagdon Road, New Malden, Surrey	UK
PALMER, F.H.	Department of Communications, CRC, P.O. Box 11490, Ottawa, Ontario	CANADA
PAPET LEPINL	CNET, Department MIR, 22301 Lannion	FRANCE
PIRWITZ, K.P.	German Military Geophysical Service, Rheinstrasse 32, 2850 Bremerhaven	FRG
REDWITZ von H	DFVLR Institut für Physik der Atmosphäre, 8031 Oberpfaffenhofen	FRG
RICE, R.W.	Department of Communications, CRC P.O. Box 11490, Ottawa, Ontario	CANADA
ROBERTS, L. Panel Member	Director, Office of Energy and Environment (Code 690) Transportation Systems Center, Department of Transportation, Kendall Square, Cambridge, Mass. 02142	USA
ROELCKE, E.C.	John Hopkins University, Applied Physics Lab., John Hopkins Road, Laurel, Maryland 20810	USA
ROSENBAUER, H.	Max-Planck-Institut für Aeronomie, Postfach 20, 3411 Lindenberg/Harz	FRG

ROSS, D.	Department of Communications, CRC P.O. Box 11490, Ottawa, Ontario	CANADA
ROTHMULLER, I.J.	US Naval Ocean Systems Center, 271 Catalina Bld, San Diego, Cal. 92151	USA
RÖTTGER, J.	Max-Planck-Institut für Aeronomie D-3411 Katlenburg-Lindau 3	FRG
RUSH, C.M.	US Department of Commerce, Office of Telecommunications, Institute for Telecommunication Sciences, Boulder, Col. 80302	USA
SCHMERLING, E.R. Panel Member	NASA Code S1-5, NASA Headquarters, Washington D.C. 20546	USA
SCHOLZ, D.	ARFA, Streitkräfteamt, P.O. Box 20 50 03, D-53 Bonn, 2	FRG
SOICHER, H. Panel Member	CORADCOM, DRDCO-COM-RE, Ft Monmouth, N.J. 07703	USA
TAVEL, M.	The Ivan Getting Lab. Aerospace Corporation, P.O. Box 92957, Los Angeles, Cal. 90009	USA
TAM, W.G.	Defence Research Establishment, Valcartier	CANADA
THOMPSON, R.L.	Headquarters Air Force, Global Weather Central, Offutt AFB, NE 68113	USA
THOMSON, E.A.	Department of National Defence, Defence Research Establishment, Ottawa, Ontario	CANADA
THRANL, E.V.	NDRE P.O. Box 25, N-2007, Kjeller	NORWAY
TOMLIANOVICH, N.M.	The Mitre Corporation, Bedford, Mass. 01730	USA
VENIER, G.C.	Department of Communications, CRC P.O. Box 11490, Ottawa, Ontario	CANADA
VISSINGA, H.	Physics Laboratory N.D.R.O. Postbox 2864, The Hague	NETHERLANDS
WEBBER, R.V.	Department of Communications, CRC P.O. Box 11490, Ottawa, Ontario	CANADA
WHITTEKEP, J.H.	Department of Communications, CRC P.O. Box 11490, Ottawa, Ontario	CANADA
WIDDEL, H.U.	Max-Planck Institut für Aeronomie, Katlenburg-Lindau 3, Pechhuiten 4	FRG
WINACOTT, E.L.	Department of Communications, CRC P.O. Box 11490, Ottawa, Ontario	CANADA
WINTER, A.E.	Department of Communications, CRC P.O. Box 11490, Ottawa, Ontario	CANADA
AGARD		
Ch D.G. CARPOTHERS	EPF Executive	
M. M. TESSIER	EPF Secretary	

JUNG, H.J.	Institut für Geophysik und Meteorologie, Universität Köln, Derpenerstr. 13, Köln, 41	FRG
KATZ, B.S.	Naval Surface Weapons Center, White Oak Laboratory, Silver Springs, MD 20910	USA
KREPLIN, R.W.	Code 7125, Naval Research Laboratory, Washington D.C. 20375	USA
LAMPERT, E.	Siemens AG, Wv fu MS EF 21, 8000 Munchen, 70, Hofmann- strasse 51	FRG
LANGE-HESE, G. Panel Member	Max-Planck Inst. für Aeronomie, Postfach 20, D 3411 Katlenburg- Lindau, 3	FRG
LIEBE, H.J.	US Department of Commerce, OT/ITS, 325 South Broadway, Boulder, Col. 80302	USA
LONG, R.J.	Mail Stop C 380, MIT Lincoln Laboratory, Lexington, Mass 02173	USA
LYON, I.D.	British Aerospace Dynamics Group, P.B. 244, Six Hills Way, Stevenage SG1 2DA, Herts	UK
McCLATCHY, R.A.	Air Force Geophysics Laboratory/GPI, Hanscom AFB, Mass. 01731	USA
MARGUINAUD, A.	Thomson CSF/DITM, 55, rue Greffuhle, 92301, Levallois-Perret	FRANCE
MASENG, T.	Shape Technical Center, P.O. Box 174, The Hague	NETHERLANDS
MONTBRIAND, E.	Department of Communications, CRC P.O. Box 11490, Ottawa Ontario	CANADA
MORLEY, G.	Defence Research Establishment, Valcartier	CANADA
MULDREW, D.B.	Department of Communications, CRC P.O. Box 11490, Ottawa, Ontario	CANADA
NICOLET, M. Panel Member	External Geophysics, Brussels University, 30 Avenue Den Doorn, 1180 Brussels	BELGIUM
NISBET, J.S.	Ionosphere Research Lab., The Pennsylvania State University, University Park, PA 16802	USA
OLIVER, H.E.	Decca Navigator Co Ltd, 2 Blagdon Road, New Malden, Surrey	UK
PALMER, F.H.	Department of Communications, CRC, P.O. Box 11490, Ottawa, Ontario	CANADA
PAPET LEPINE	CNET, Department MIR, 22301 Lannion	FRANCE
PIRWITZ, K.P.	German Military Geophysical Service, Rheinstrasse 32, 2850 Bremerhaven	FRG
REDWITZ von H.	DFVLR Institut für Physik der Atmosphäre, 8031 Oberpfaffenhofen	FRG
RICE, R.W.	Department of Communications, CRC P.O. Box 11490 Ottawa, Ontario	CANADA
ROBERTS, L. Panel Member	Director, Office of Energy and Environment (Code 600) Transportation Systems Center, Department of Transportation, Kendall Square, Cambridge, Mass. 02142	USA
ROELOF, E.C.	John Hopkins University, Applied Physics Lab., John Hopkins Road, Laurel, Maryland 20810	USA
ROSENBAUMER, H.	Max-Planck-Institut für Aeronomie, Postfach 20, 3411 Lindau/Lake	FRG

REPORT DOCUMENTATION PAGE

1. Recipient's Reference	2. Originator's Reference AGARD-CP-238 [✓] (In two Volumes)	3. Further Reference ISBN 92-835-0224-8	4. Security Classification of Document UNCLASSIFIED								
5. Originator	Advisory Group for Aerospace Research and Development North Atlantic Treaty Organization 7 rue Ancelle, 92200 Neuilly sur Seine, France										
6. Title	OPERATIONAL MODELLING OF THE AEROSPACE PROPAGATION ENVIRONMENT										
7. Presented at	a Meeting of the Electromagnetic Wave Propagation Panel held in Ottawa, Canada, 24-28 April 1978.										
8. Author(s)/Editor(s)	Various Edited by H. Soicher		9. Date November 1978								
10. Author's/Editor's Address	DRDCO-COM-RF US Army CORADCOM Fort Monmouth, NJ 07703, USA		11. Pages 732								
12. Distribution Statement	This document is distributed in accordance with AGARD policies and regulations, which are outlined on the Outside Back Covers of all AGARD publications.										
13. Key words/Descriptors	<table border="0"> <tr> <td>Electromagnetic wave transmission</td> <td>Telecommunication</td> </tr> <tr> <td>Ionosphere</td> <td>Surveillance</td> </tr> <tr> <td>Earth atmosphere</td> <td>Mathematical prediction</td> </tr> <tr> <td>Mathematical models</td> <td>Navigation</td> </tr> </table>			Electromagnetic wave transmission	Telecommunication	Ionosphere	Surveillance	Earth atmosphere	Mathematical prediction	Mathematical models	Navigation
Electromagnetic wave transmission	Telecommunication										
Ionosphere	Surveillance										
Earth atmosphere	Mathematical prediction										
Mathematical models	Navigation										
14. Abstract	<p>High-performance military and civilian systems operating in the aerospace environment require propagation media characterization to meet reliability and accuracy goals. The atmosphere, ionosphere, and the space environment constitute the media within which waves propagate. The users of communication, navigation and surveillance systems must have continuous background information regarding the state of these media as well as their variability and their response to natural disturbances.</p> <p>Ideally, such information is available through sophisticated forecasting techniques based on media models and supported by periodic (or real-time) updating of data at specified locations. Modelling, and consequently forecasting, can and must be improved significantly through a better understanding of the governing processes of all the interrelated parts of the space environment.</p> <p>This Conference Proceeding is published in two volumes.</p>										

<p>AGARD Conference Proceedings No.238, Vols 1 & 2 Advisory Group for Aerospace Research and Development, NATO OPERATIONAL MODELLING OF THE AEROSPACE PROPAGATION ENVIRONMENT Edited by H.Solcher Published November 1978 in two volumes 732 pages</p> <p>High-performance military and civilian systems operating in the aerospace environment require propagation media characterization to meet reliability and accuracy goals. The atmosphere, ionosphere, and the space environment constitute the media within which waves propagate. The users of communication, navigation and surveillance systems must have continuous</p> <p>P.T.O.</p>	<p>AGARD-CP-238 Volumes 1 and 2</p> <p>Electromagnetic wave transmission Ionosphere Earth atmosphere Mathematical models Navigation Telecommunication Surveillance Mathematical prediction</p>	<p>AGARD Conference Proceedings No.238, Vols 1 & 2 Advisory Group for Aerospace Research and Development, NATO OPERATIONAL MODELLING OF THE AEROSPACE PROPAGATION ENVIRONMENT Edited by H.Solcher Published November 1978 in two volumes 732 pages</p> <p>High-performance military and civilian systems operating in the aerospace environment require propagation media characterization to meet reliability and accuracy goals. The atmosphere, ionosphere, and the space environment constitute the media within which waves propagate. The users of communication, navigation and surveillance systems must have continuous</p> <p>P.T.O.</p>	<p>AGARD-CP-238 Volumes 1 and 2</p> <p>Electromagnetic wave transmission Ionosphere Earth atmosphere Mathematical models Navigation Telecommunication Surveillance Mathematical prediction</p>
<p>AGARD Conference Proceedings No.238, Vols 1 & 2 Advisory Group for Aerospace Research and Development, NATO OPERATIONAL MODELLING OF THE AEROSPACE PROPAGATION ENVIRONMENT Edited by H.Solcher Published November 1978 in two volumes 732 pages</p> <p>High-performance military and civilian systems operating in the aerospace environment require propagation media characterization to meet reliability and accuracy goals. The atmosphere, ionosphere, and the space environment constitute the media within which waves propagate. The users of communication, navigation and surveillance systems must have continuous</p> <p>P.T.O.</p>	<p>AGARD-CP-238 Volumes 1 and 2</p> <p>Electromagnetic wave transmission Ionosphere Earth atmosphere Mathematical models Navigation Telecommunication Surveillance Mathematical prediction</p>	<p>AGARD Conference Proceedings No.238, Vols 1 & 2 Advisory Group for Aerospace Research and Development, NATO OPERATIONAL MODELLING OF THE AEROSPACE PROPAGATION ENVIRONMENT Edited by H.Solcher Published November 1978 in two volumes 732 pages</p> <p>High-performance military and civilian systems operating in the aerospace environment require propagation media characterization to meet reliability and accuracy goals. The atmosphere, ionosphere, and the space environment constitute the media within which waves propagate. The users of communication, navigation and surveillance systems must have continuous</p> <p>P.T.O.</p>	<p>AGARD-CP-238 Volumes 1 and 2</p> <p>Electromagnetic wave transmission Ionosphere Earth atmosphere Mathematical models Navigation Telecommunication Surveillance Mathematical prediction</p>

<p>background information regarding the state of these media as well as their variability and their response to natural disturbances.</p> <p>Ideally, such information is available through sophisticated forecasting techniques based on media models and supported by periodic (or real-time) updating of data at specified locations. Modelling, and consequently forecasting, can and must be improved significantly through a better understanding of the governing processes of all the interrelated parts of the space environment.</p> <p>Papers presented at a Meeting of the Electromagnetic Wave Propagation Panel held in Ottawa, Canada, 24-28 April 1978.</p> <p>ISBN 92-835-0224-8</p>	<p>background information regarding the state of these media as well as their variability and their response to natural disturbances.</p> <p>Ideally, such information is available through sophisticated forecasting techniques based on media models and supported by periodic (or real-time) updating of data at specified locations. Modelling, and consequently forecasting, can and must be improved significantly through a better understanding of the governing processes of all the interrelated parts of the space environment.</p> <p>Papers presented at a Meeting of the Electromagnetic Wave Propagation Panel held in Ottawa, Canada, 24-28 April 1978.</p> <p>ISBN 92-835-0224-8</p>
---	---

<p>background information regarding the state of these media as well as their variability and their response to natural disturbances.</p> <p>Ideally, such information is available through sophisticated forecasting techniques based on media models and supported by periodic (or real-time) updating of data at specified locations. Modelling, and consequently forecasting, can and must be improved significantly through a better understanding of the governing processes of all the interrelated parts of the space environment.</p> <p>Papers presented at a Meeting of the Electromagnetic Wave Propagation Panel held in Ottawa, Canada, 24-28 April 1978.</p> <p>ISBN 92-835-0224-8</p>	<p>background information regarding the state of these media as well as their variability and their response to natural disturbances.</p> <p>Ideally, such information is available through sophisticated forecasting techniques based on media models and supported by periodic (or real-time) updating of data at specified locations. Modelling, and consequently forecasting, can and must be improved significantly through a better understanding of the governing processes of all the interrelated parts of the space environment.</p> <p>Papers presented at a Meeting of the Electromagnetic Wave Propagation Panel held in Ottawa, Canada, 24-28 April 1978.</p> <p>ISBN 92-835-0224-8</p>
---	---

0114
4
AGARD

NATO  OTAN

7 RUE ANCELLE - 92200 NEUILLY-SUR-SEINE
FRANCE

Telephone 745.08.10 - Telex 610176

**DISTRIBUTION OF UNCLASSIFIED
AGARD PUBLICATIONS**

AGARD does NOT hold stocks of AGARD publications at the above address for general distribution. Initial distribution of AGARD publications is made to AGARD Member Nations through the following National Distribution Centres. Further copies are sometimes available from these Centres, but if not may be purchased in Microfiche or Photocopy form from the Purchase Agencies listed below.

NATIONAL DISTRIBUTION CENTRES

BELGIUM

Coordonnateur AGARD - VSL
Etat-Major de la Force Aérienne
Quartier Reine Elisabeth
Rue d'Evere, 1140 Bruxelles

CANADA

Defence Scientific Information Service
Department of National Defence
Ottawa, Ontario K1A 0Z2

DENMARK

Danish Defence Research Board
Østerbrogades Kaserne
Copenhagen Ø

FRANCE

O.N.E.R.A. (Direction)
29 Avenue de la Division Leclerc
92 Châtillon sous Bagneux

GERMANY

Zentralstelle für Luft- und Raumfahrt-
dokumentation und -information
c/o Fachinformationszentrum Energie,
Physik, Mathematik GmbH
Kernforschungszentrum
7514 Eggenstein-Leopoldshafen 2

GREECE

Hellenic Air Force General Staff
Research and Development Directorate
Holargos, Athens, Greece

ICELAND

Director of Aviation
c/o Flugrad
Reykjavik

ITALY

Aeronautica Militare
Ufficio del Delegato Nazionale all'AGARD
3, Piazzale Adensuer
Roma/EUR

LUXEMBOURG

See Belgium

NETHERLANDS

Netherlands Delegation to AGARD
National Aerospace Laboratory, NLR
P.O. Box 126
Delft

NORWAY

Norwegian Defence Research Establishment
Main Library
P.O. Box 25
N-2007 Kjeller

PORTUGAL

Direcção do Serviço de Material
da Força Aérea
Rua da Escola Politécnica 42
Lisboa
Attn: AGARD National Delegate

TURKEY

Department of Research and Development (ARGE)
Ministry of National Defence, Ankara

UNITED KINGDOM

Defence Research Information Centre
Station Square House
St. Mary Cray
Orpington, Kent BR5 3RE

UNITED STATES

National Aeronautics and Space Administration (NASA)
Langley Field, Virginia 23365
Attn: Report Distribution and Storage Unit

THE UNITED STATES NATIONAL DISTRIBUTION CENTRE (NASA) DOES NOT HOLD STOCKS OF AGARD PUBLICATIONS, AND APPLICATIONS FOR COPIES SHOULD BE MADE DIRECT TO THE NATIONAL TECHNICAL INFORMATION SERVICE (NTIS) AT THE ADDRESS BELOW.

PURCHASE AGENCIES

Microfiche or Photocopy

National Technical
Information Service (NTIS)
5285 Port Royal Road
Springfield
Virginia 22161, USA

Microfiche

Space Documentation Service
European Space Agency
19, rue Mario Nikis
75015 Paris, France

Microfiche

Technology Reports
Centre (DTI)
Station Square House
St. Mary Cray
Orpington, Kent BR5 3RE
England

Requests for microfiche or photocopies of AGARD documents should include the AGARD serial number, title, author or editor, and publication date. Requests to NTIS should include the NASA accession report number. Full bibliographical references and abstracts of AGARD publications are given in the following journals.

Scientific and Technical Aerospace Reports (STAR)
published by NASA Scientific and Technical
Information Facility
Post Office Box 8757
Baltimore-Washington International Airport
Maryland 21240, USA

Government Reports Announcements (GRA)
published by the National Technical
Information Service, Springfield
Virginia 22161, USA



Printed by Technical Editing and Reproduction Ltd
Lifford House, 7-9 Charlotte St, London W1P 1HD

ISBN 92-833-0224-6